Polar Oceanography

Part A
Physical Science

Edited by

Walker O. Smith, Jr.
Botany Department and
Graduate Program in Ecology
University of Tennessee
Knoxville, Tennessee

Academic Press, Inc.
Harcourt Brace Jovanovich, Publishers
San Diego New York Boston
London Sydney Tokyo Toronto

This book is printed on acid-free paper. ♾

Academic Press, Inc.
San Diego, California 92101

United Kingdom Edition published by
Academic Press Limited
24–28 Oval Road, London NW1 7DX

Library of Congress Cataloging-in-Publication Data

Polar oceanography / [edited by] Walker O. Smith, Jr.
p. cm.
Includes bibliographical references.
Contents : pt. A. Physical science.
ISBN 0-12-653031-9 (pt. A : alk. paper)
1. Oceanography--Polar regions. I. Smith, Walker O.
GC401.P633 1990
551.46'8--dc20 89-18391
CIP

Printed in the United States of America
90 91 92 93 9 8 7 6 5 4 3 2 1

Contents of Part B
Chemistry, Biology, and Geology

8. **Chemical Oceanography**
   E. P. Jones, David M. Nelson, and Paul Tréguer

9. **Polar Phytoplankton**
   Walker O. Smith, Jr. and Egil Sakshaug

10. **Polar Zooplankton**
    Sharon L. Smith and Sigrid B. Schnack-Schiel

11. **The Upper Trophic Levels in Polar Marine Ecosystems**
    David G. Ainley and Douglas P. DeMaster

12. **Polar Benthos**
    Paul K. Dayton

13. **Particle Fluxes and Modern Sedimentation in the Polar Oceans**
    Susumo Honjo

Contributors

Numbers in parentheses indicate the pages on which the authors' contributions begin.

Robert A. Brown (1), Department of Atmospheric Sciences, University of Washington, Seattle, Washington 98195

Eddy C. Carmack (171), Institute of Ocean Sciences, Sidney, British Columbia, Canada V8L 4B2

Anthony J. Gow (47), USA Cold Regions Research and Engineering Laboratory, Hanover, New Hampshire 03755

Sirpa Häkkinen (335), NASA Goddard Space Flight Center, Greenbelt, Maryland 26771

Miles G. McPhee (287), McPhee Research Company, Naches, Washington 98937

Robin D. Muench (223), Science Applications International Corporation, Bellevue, Washington 98005

Robert G. Onstott (123), Radar Science Laboratory, Environmental Research Institute of Michigan, Ann Arbor, Michigan 48107

Robert A. Shuchman (123), Radar Science Laboratory, Environmental Research Institute of Michigan, Ann Arbor, Michigan 48107

Walter B. Tucker III (47), USA Cold Regions Research and Engineering Laboratory, Hanover, New Hampshire 03755

Preface

The study of the world's oceans has rapidly expanded in the past decade through the use of new and exciting technologies (including the use of remote sensing, moored samplers, acoustic current meters, sonic arrays, and many others), in conjunction with more traditional data collection methods from ships. The merger of these techniques has led to a greater understanding of oceanographic processes at all scales. Yet, in many respects, the study of polar oceanography has lagged behind the study of temperate and tropical regions. The reason for this is simple: the severe logistic constraints imposed by the harsh environments of the Arctic and Antarctic simply preclude a simple extension of temperate oceanography into polar oceans. Many oceanographers who have never studied within the ice do not fully appreciate this fact, and we who do have often wondered how simple our science would be if only we did not have to drill ice holes through 1.5 m of ice to sample, to worry about water freezing as it is drained from Niskin bottles, or to expect the breakdown of equipment at the surface because of the change of physical properties of plastics at low temperatures.

Despite the numerous logistic and environmental difficulties inherent in the study of polar waters, these regions continue to be the focus of study for many oceanographers. In large part this is due to the realization that polar regions play a critical role in many global phenomena. For example, they are implicated as critical regions in controlling the global carbon dioxide cycle, being large sources of CO_2 in winter and spring and potential sinks in summer. They also play a dominant role in the global hydrologic cycle by accounting for approximately 98% of the world's fresh water. Polar regions are major sites of deposition within a number of biogeochemical cycles; they also are the sites for the formation of the ocean's deep water and hence are critical heat sinks to the atmosphere. In short, polar oceans have a profound effect on many large-scale oceanographic processes, and these effects are evident throughout the world's oceans.

Polar oceans are also being critically examined for exploitation of their mineral and biological resources, and there is extensive evidence that global environmental problems will disproportionately impact polar regions. In order to understand the influences of human activities in the Arctic and Antarctic, an appreciation of the role of polar oceans is required, as is the response of polar systems to human-induced perturbations.

Substantial differences exist between the Arctic and Antarctic, a fact which makes a synthesis of the existing knowledge extremely difficult. One major difference between the two areas is that the Arctic is an oceanic basin with its own coherent and restricted circulation, whereas the Antarctic is a continent with the surrounding seas dominated by a circumpolar current which exchanges large amounts of mass and heat with the Pacific, Atlantic, and Indian oceans (Fig. A shows the bathymetry of the two regions). As a corollary to the physiography, the seasonal climate and irradiance variations are more extreme in the Arctic Ocean than in the waters of Antarctica. However, the seasonal difference in the pack ice area is much greater in the Antarctic than in the Arctic (Fig. B shows the average minimum and maximum ice extent and concentration for the Arctic and Antarctic for the years 1978–1986). Hence the oceanographic impacts of ice-related processes tend to be different in each. The unifying and distinguishing characteristics of the Arctic and Antarctic are a major feature of each of the following chapters.

Prior to the initiation of these volumes *(Polar Oceanography, Part A* and *Part B),* a number of researchers commented that our knowledge of polar oceanography is expanding at such a rapid pace that such a synthesis might be premature. It is clear that polar research is now a major portion of oceanographic research; evidence for this can be seen in the budgets of funding organizations, the numbers of polar-related papers presented at oceanographic meetings and published in peer-reviewed journals, and the attention given to international polar expeditions within the oceanographic community. Recent and present large programs in polar waters include MIZEX (Marginal Ice Zone Experiment), AIWEX (Arctic International Wave Experiment), the Greenland Sea Project, Pro Mare, AMERIEZ (Antarctic Marine Ecosystem Research at the Ice-edge Zone), WEPOLEX (Weddell Sea Polynya Experiment), CEAREX (Co-ordinated Eastern Arctic Experiment), ISHTAR (Inner Shelf Transfer and Recycling), and numerous others. These experiments are largely international in nature; in addition, many are interdisciplinary and merge the disciplines of physical, chemical, geological, and biological oceanography in order to understand the processes inherent in each region and their interaction. In this respect polar oceanography is perhaps even more interactive than temperate and tropical oceanography, although similar interdisciplinary projects are underway in nonpolar regions. Yet because of the cost of research on ice-breakers (and their relative rarity), as well as the number of nations which have national interests in polar waters, international projects are the most expedient manner in which to study polar regions. The inclusion of many non-U.S. contributors emphasizes the active role of many nations in polar research.

The two volumes have been organized into thirteen chapters. The first chapter in Part A deals with polar meteorology and air–sea–ice interactions,

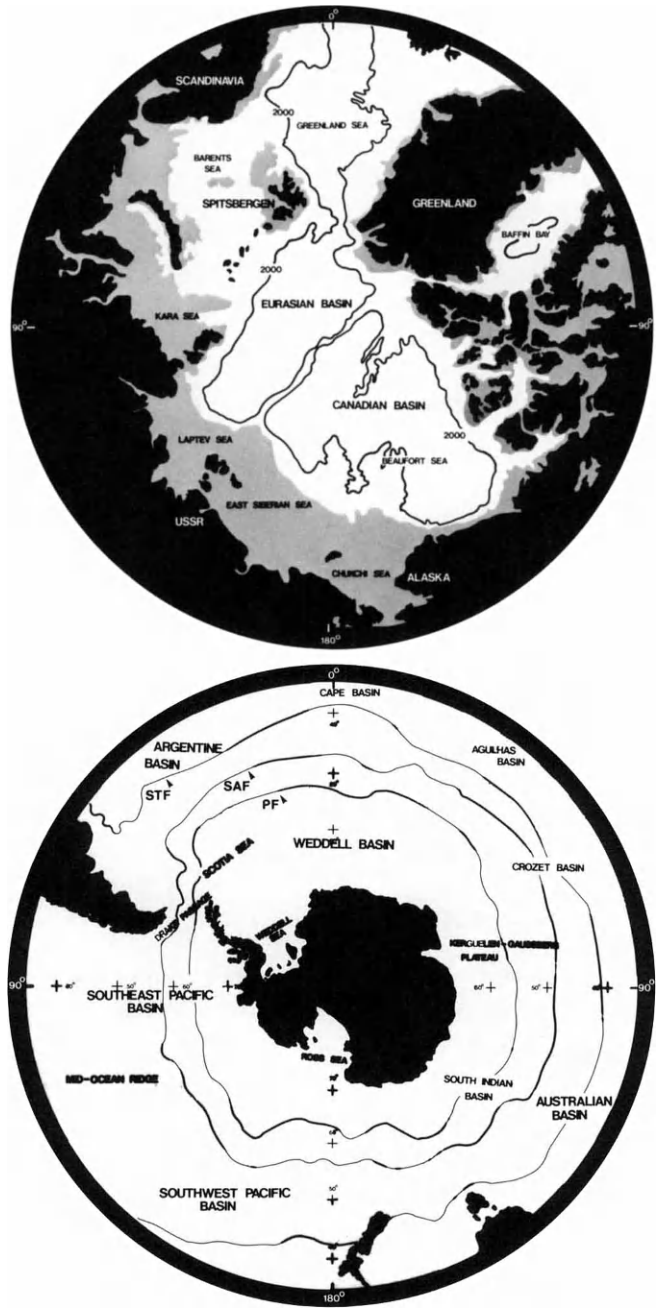

Figure A Physiography of the Arctic Basin and the waters around the Antarctic continent.

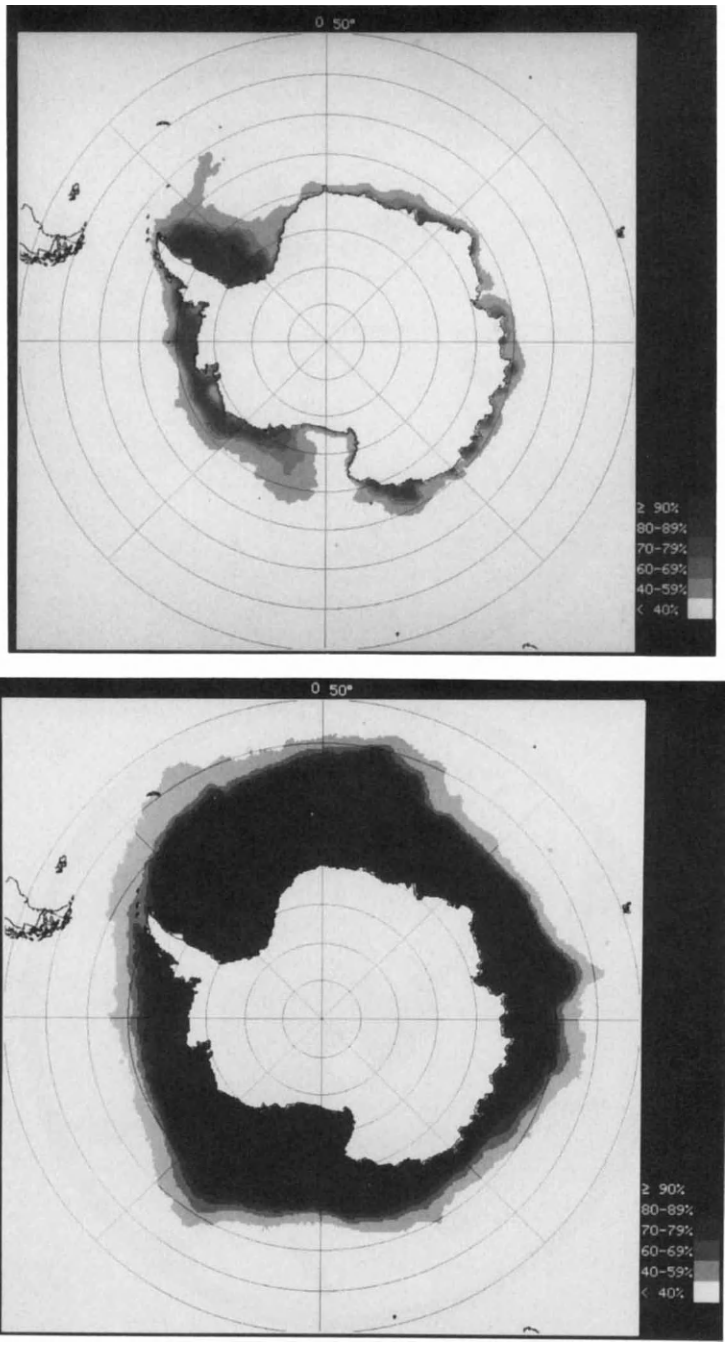
0 50°
≥ 90%
80-89%
70-79%
60-69%
40-59%
< 40%
0 50°
≥ 90%
80-89%
70-79%
60-69%
40-59%
< 40%

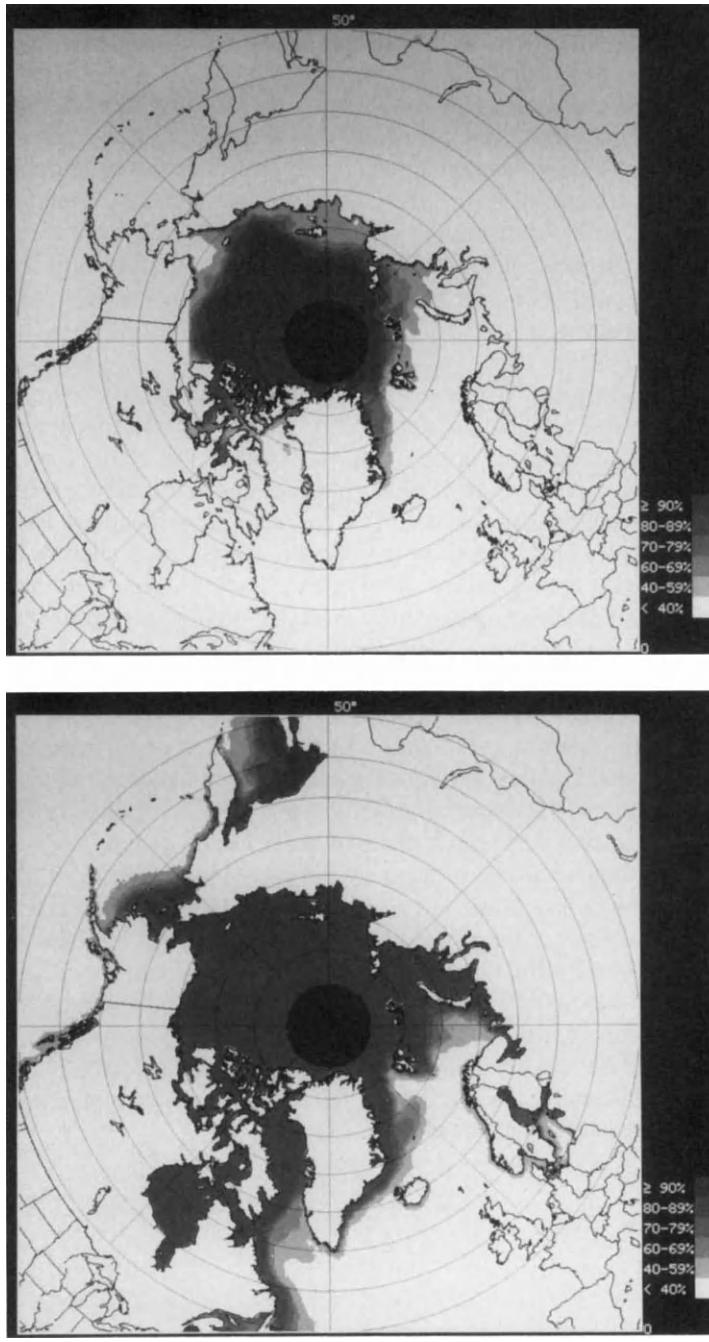

Figure B The average ice distribution and concentration at the minimum and maximum extent for the Antarctic and Arctic. Values represent the means for the years 1978–1986. Figures kindly provided by J. Comiso (NASA Goddard Space Flight Center).

whereas the second covers the properties of sea ice. The third chapter reviews the uses of remote sensing in polar regions, and the following three chapters cover physical oceanographic processes on three different scales: large, meso-, and small. This does not imply that these scales do not interact but provides a convenient manner in which to synthesize the existing information. The last chapter of Part A deals with models in polar systems. Models have played (and will continue to play) an extremely important role in polar oceanography because of the difficulty and expense of conducting long-term studies within and near ice-covered regions; furthermore, they play an extremely important role in hypothesis generation and testing in polar oceanography.

Part B begins with a chapter on chemical oceanography which follows those chapters in Part A on physical oceanography but precedes those in Part B dealing with biological oceanography, because the chapter serves as a transition from a description of physical processes to the effects of biological processes on chemical properties. The following four chapters on biological oceanography are divided by trophic structure (i.e., a chapter on autotrophic processes is first, followed by one on zooplankton, then one which synthesizes the information currently available on higher trophic levels, and finally one on the benthos). These chapters are followed by one on particle fluxes in polar regions, since flux is a function of the physical, chemical, and biological regimes of the water column.

The two volumes are not meant to be all inclusive, and some topics (e.g., bacterial processes, acoustics, optics) have not been exhaustively addressed. However, we hope the material presented provides an updated synthesis of most of the important research areas in polar oceanography.

This work has been encouraged by many oceanographers, both within and outside the polar community, including those within funding agencies of various countries. The editor and authors appreciate and acknowledge their support, both direct and indirect, and hope that this synthesis plays some role in adequately describing past work and providing a basis for discussion of future studies. Dr. Josefino Comiso kindly provided Fig. B. All of the chapters have been reviewed both formally and informally by a great number of colleagues, and without their help the quality of the chapters would have been seriously compromised.

Walker O. Smith, Jr.

1 Meteorology

Robert A. Brown
Department of Atmospheric Sciences
University of Washington
Seattle, Washington

I. Introduction 1
A. Pack Ice 3
B. Marginal Ice Zone 4
C. Wind Stress 5
II. The Winds and Surface Stress 6
A. The Atmospheric Ekman Layer 6
B. The Atmospheric Surface Layer 12
C. Methods of Stress Measurement 15
III. Major Air–Sea Interaction Polar Experiments 17
A. The Arctic Ice Dynamics Joint Experiment (AIDJEX) 17
B. Antarctic Experiments 19
C. The Marginal Ice Zone Experiments (MIZEX) 20
IV. Modeling Methods 23
A. Geostrophic Drag Coefficient 25
B. Similarity Modeling 25
C. Numerical Modeling 28
V. Remote Sensing 30
VI. Large-Scale Interaction 32
VII. Flux Coefficient Summary 33
A. Drag Coefficients 33
B. Heat Flux Summary 37
C. Radiation and Clouds 40
VIII. Conclusions 42
References 43

I. Introduction

The emphasis in this chapter is on polar meteorology as it relates to the interests of polar oceanographers. Aspects of meteorology are crucial to most oceanographic disciplines. Biological activity requires irradiance, which de-

Polar Oceanography, Part A: Physical Science

pends on atmospheric transmissivity, clouds and/or ice cover, and nutrients (wherein regional atmospheric forcing of currents is often a factor). Utilization of polar resources depends not only on air–sea interaction dynamics for production but also on weather analysis and prediction. The sedimentary record under ice-covered seas is important in climate analyses and is complicated by sea ice transport. Finally, the forcing of the ocean by the atmosphere, from short-term and regional wind stress to large-scale and climate-related pressure patterns, is an important element in ocean dynamics.

The common factor in the meteorological input to oceanographic problems is furnishing the air–sea interaction fluxes—primarily the dynamic driving force (the stress) and the heat flux. Only studies in meteorology which directly bear on oceanic dynamics and thermodynamics are included here. Three challenges in meteorology are of primary interest to the oceanographer: (1) Measure the fluxes at the surface. Currently, this mainly means momentum (stress), but it may also include heat, humidity, and CO_2. (2) Relate the fluxes to some easily measured mean flow parameters, such as the sea surface temperature, surface wind, and humidity. (3) Extrapolate the flux parametrizations to the large-scale domain and climatic-scale time intervals. The topics in meteorology which encompass these results involve the following elements of this chapter: discussion of all factors which affect the air stress and heat flux over ice or water; outline of measurement and modeling techniques for the planetary boundary layer (PBL); brief discussion of remote sensing capabilities of use for atmospheric modeling in or near the pack ice; short discussion of prospects for extending stress and flux parametrizations to large scales and long times; and presentation of summary values of drag and heat flux coefficients. The preponderance of material is directed toward the evaluation and modeling of the surface stress, as that is where the most information has been obtained. This restricted scope will be ameliorated as much as possible by frequently including general references for additional reading.

Generally, two types of knowledge about the atmosphere are required in oceanography. First, there is a need to know the winds because these provide the primary forcing of many ocean currents. In this regard, a distribution of surface stress will suffice. Second, the ocean is an important component in the global climate concatenation. Here, the momentum fluxes are less important than heat fluxes, although they are closely linked. On global scales the horizontal transport of heat, moisture, and momentum in each medium becomes important. On the larger time scales, other fluxes, such as CO_2, become of interest. Polar oceans play an important role in the cycle of this crucial greenhouse gas (e.g., see Herman, 1986). For example, abyssal waters contain 50 times the mass of CO_2 present in the atmosphere. Primary productivity in the oceanic mixed layer, transport of high-carbon surface water

to deep water, and deposition are important polar ocean processes in the global carbon cycle.

The significant change in albedo due to sea ice is another important climatic ingredient. There is evidence for an "amplification factor" in the polar temperature responses to climatic changes. Inferred ice-age data indicate that polar Arctic temperatures decreased by about 10–15 °C, compared to 5–7 °C in mid-latitudes. Atmospheric general circulation model (GCM) calculations support these observations and show sensitivity of the temperature to ice extent, due to albedo and heat flux changes (S. Manabe, global model results, personal communication).

In many geophysical problems the feedback between ocean and atmosphere is mutually important. Parametrization of the radiative and turbulent exchanges and mass exchange processes is essential for successful general circulation modeling for weather and climate studies. Radiative processes depend on cloud properties, aerosols, albedo, and atmospheric transmissivity. Turbulent fluxes depend on wind, air and surface temperatures, surface roughness, and moisture. Rain, snow, and brine rejection from sea ice affect the above processes. The basic task for climate applications is to parametrize each of these mechanisms with respect to field variables which appear in the large-scale models.

The atmospheric scientist is interested in the air–sea–ice interaction as it influences the weather and climate (e.g., Radok, 1979). Weather influences take place on scales from hours to days, while climate influences operate on scales from seasons to the life of the planet. Thermal radiation, turbulent fluxes, and precipitation must be measured, generally at fixed times and places, and then parametrized on the appropriate scales.

A. Pack Ice

When the polar regions are considered, pack ice adds dramatic variation to all atmosphere–ocean interactions. The classic problem of air–sea heat and momentum transfer has a new dimension when air–sea–ice interaction is discussed. In cases where the smooth and homogeneous pack ice intervenes in the atmospheric forcing of the ocean, the interaction can be simpler to describe than that over the free ocean. In the latter case, the variations in roughness and stratification are important factors. Although the momentum flux analysis may be easier over the smooth pack ice, stress in the ice now complicates things, heat flux is nearly eliminated, radiation character is greatly changed, and measurements of all quantities become scarce. These new facets of air–sea–ice interaction must significantly influence the character of ocean and atmospheric circulation patterns in polar regions (e.g., Herman and Johnson, 1978; Walsh, 1978; Crane, 1978; Herman, 1986).

Data prior to the past 30 years are suspect for ice–climate statistical correlations (e.g., Walker, 1974). Only within the past decade have adequate pressure sensors been placed on a few buoys in the mid-Arctic, and very few measurements are available for the Antarctic pack ice. Despite the meager data, it is evident that the sea ice extent is correlated with atmospheric forces. The ice extent varies due to ice-edge cyclone activity, planetary-scale stationary waves, and global temperature trends. Walsh (1986) has shown that some predictive information for ice extent is contained within the surface pressure and temperature fields. However, this is significant for prediction for only a month or two. It can still be said that there is no adequate theory for describing the interannual variations of ice cover and its relation to atmospheric circulation.

B. Marginal Ice Zone

When the marginal ice zone (MIZ) is included in consideration of the air–sea–ice interaction, the abrupt changes in boundary conditions can have many local and long-range effects (Rogers, 1978; Egorov *et al.*, 1974). Although the MIZ represents a small percentage of the total ice cover, the dynamical description is crucially important in many processes associated with the pack ice variation. These include: the growth, extent, and breakup of the pack ice; the regional ocean circulations and associated problems of the oceanic mixed-layer dynamics, biology, and thermal structure; the dynamics of bottom-water formation at the MIZ; the enhanced biological activity with high phytoplankton concentrations and large standing stock near the MIZ; and the mechanics of the long-time influence of the pack ice and MIZ on climate and oceanic circulation.

There are characteristic weather phenomena associated with the MIZ, and the climate responds to the variability in sea ice extent. The storm tracks near the MIZ change in response to ice cover extent (and/or vice versa). Interannual variability of the ice extent has been correlated with air and sea temperatures (Greenland Sea ice, Vinje, 1977; Bering Sea, Niebauer, 1980). Bering Sea ice extent is also related to regional storm-track dynamics (Overland and Pease, 1982). The seasonal changes of pack ice are twice as great and more variable in the Antarctic compared with the Arctic. The Antarctic pack ice is mainly first year and the flow is mainly divergent. Antarctic ice extent has been correlated with mean air temperatures (Budd, 1975) and with the position and frequency of cyclones (e.g., Schwerdtfeger and Kachelhoffer, 1973). The growth season is longer and the melt season shorter in the Antarctic. These seasonal changes are probably responses to variations in the atmospheric seasonal variability. At present, there exist only correlations between sea ice anomalies and atmospheric parameters; the physical mechanisms

have yet to be found (Walsh and Johnson, 1979; Lemke *et al.*, 1980; Walsh and Satler, 1981).

In the 1980s, a broad-based effort to measure the environment in the MIZ has produced an excellent set of data. Still, there is a large gap between the scales of the basic physical measurements on buoys and ships, taken only for brief periods, and the climate-scale indicators of connections between ocean, ice, and atmosphere dynamics. There is evidently much room for work on the ocean–ice–atmosphere climate dynamics.

C. Wind Stress

Probably the principal interest of the dynamic oceanographer in meteorology is in the value of the surface wind stress on the ocean. Although the fluid dynamic principles are the same for the ocean and atmosphere boundary layers, there are sufficient differences that investigations in the two regimes generally are separate, with little interchange. This has not always been true, and Ekman's planetary boundary layer solution is a notable example.

The pack ice moves mainly under the influence of the wind, and the uniformity of the surface and PBL stratification lead to good correlation between geostrophic atmospheric flow and ice motion (Thorndike and Colony, 1982). Thus, although meteorological data over the pack ice are sparse, they may be sufficient to provide for simple, large-scale effective models of the ice–ocean forcing.

In the MIZ the air–sea–ice interaction is much more complex. The ice dynamics vary dramatically according to the direction and magnitude of the wind. There is a step change in surface roughness and air–surface temperature differences. Downwelling in this region was found by Røed and O'Brien (1983) to be sensitive to the stress variation due to this change. These processes must all be included in any models of ocean, ice, or atmospheric dynamics which include this domain.

Most air–sea–ice interaction involves the wind, at least as a parametrization factor. We will discuss the basic wind solutions for the PBL. Since stress is the actual driving force on the ocean and ice, the methods of obtaining stress will be discussed next. Empirical parametrization is an essential component of flux modeling, and the major experiments which have contributed to the data base are discussed. Because this data base is far from complete in time and space, and data on some physically important parameters are absent, models are often used to address specific questions.

Some specific applications of satellite remote sensing are mentioned which promise revolutionary changes in data bases for polar meteorology. The problems and prospects of extrapolating flux data to large scales can only be summarized here. Finally, for practical applications, there is a sum-

mary of drag coefficients as a function of the most sensitive parameters—surface roughness, stratification, and wind magnitude.

II. The Winds and Surface Stress

A. The Atmospheric Ekman Layer

Nansen's 1896 two-year trans-Arctic Ocean voyage provided the observations that pack ice motion was always at a large angle to the surface wind (up to 45° *cum sol*). Nansen provided the hint that the Coriolis force must be an important factor. Ekman (1905) obtained the analytic solution for a balance between Coriolis, pressure gradient, and viscous forces. Ekman's solution yielded a logarithmic spiral velocity profile in which the surface effect decayed exponentially away from the surface. Thus, the solution introduced the concept of a thin layer, wherein viscous effects are important. It implies that the geostrophic balance is a good approximation a short distance away from the surface, where viscous forces are negligible. Since the PBL is thin, the pressure field can be assumed to be impressed on the layer—it is the same throughout. These concepts are a key part of Prandtl's (1904) complete boundary layer theory.

Ekman's solution successfully explained the pack ice drift. However, the predicted logarithmic velocity spiral is seldom, if ever, seen. Nevertheless, it is an important starting point for PBL solutions in the atmosphere and the ocean. The spiral in the atmosphere is shown in Fig. 1.1. The velocity profile is frequently plotted in $U-V$ coordinates as the locus of velocity vectors at various heights (or depths) in the PBL.

The continuous velocity profile for linked atmospheric–oceanic PBLs is shown in Fig. 1.2. In the 1960s Ekman's solution was found to be unstable to infinitesimal perturbations but stable to finite perturbations. The predicted velocity profiles for most flow situations now contain large, organized eddies and vary considerably on horizontal scales comparable to the PBL height, with modified mean hodographs which are only qualitatively similar to Ekman's solution (Brown, 1980). One very important consequence of this flow solution is that point profiles, such as those taken with a radiosonde or dropsonde, cannot be expected to measure the average velocity profile. These profiles will vary from point to point within the large eddies (Fig. 1.3). Similar variations can be expected in the ocean (OPBL) (where the organized large eddies are called Langmuir circulations).

The velocity profile in the PBL can be expected to vary with surface roughness. The extraordinary smoothness and uniformity of the pack ice make this variation a small effect over ice regions. Over the ocean the surface

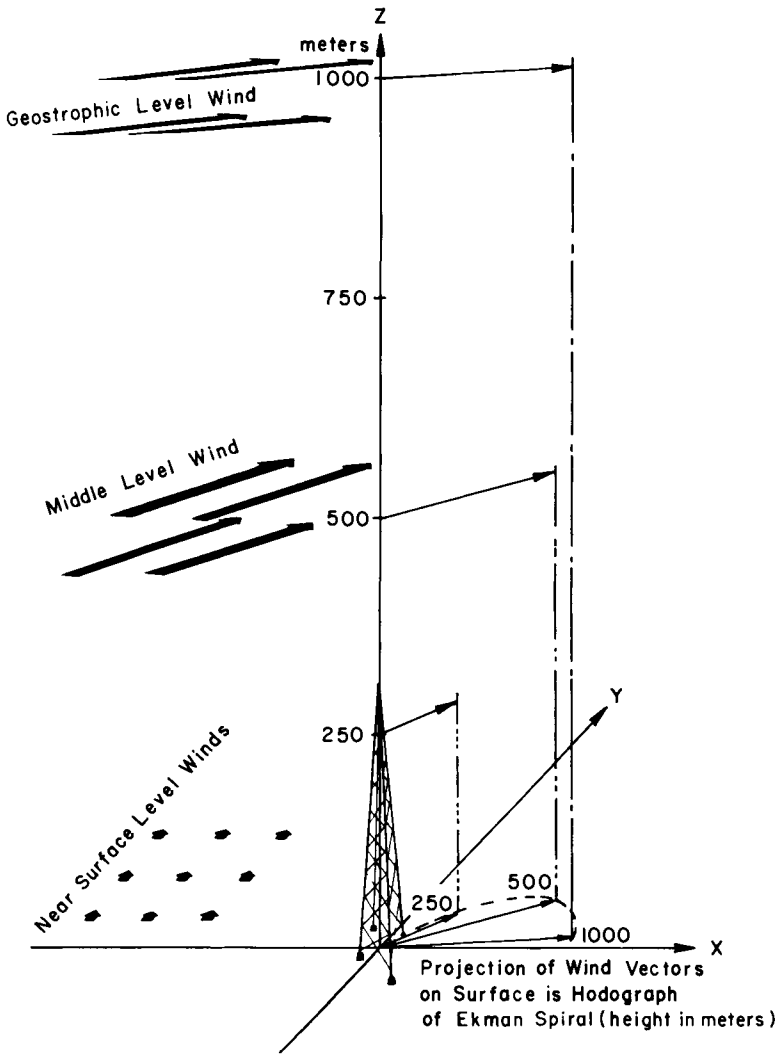

Figure 1.1 Sketch of winds in the atmospheric PBL.

wave field variation must be related to the wind speed to account for the feedback in increased roughness with wind. In addition, the dynamics of the PBL have been found to be quite sensitive to variations in the layer stratification. In the atmosphere this stratification changes mainly in proportion to air–surface temperature differences. In the ocean the quantity of fresh water from rivers or melting ice, or increased brine from freezing, can affect the

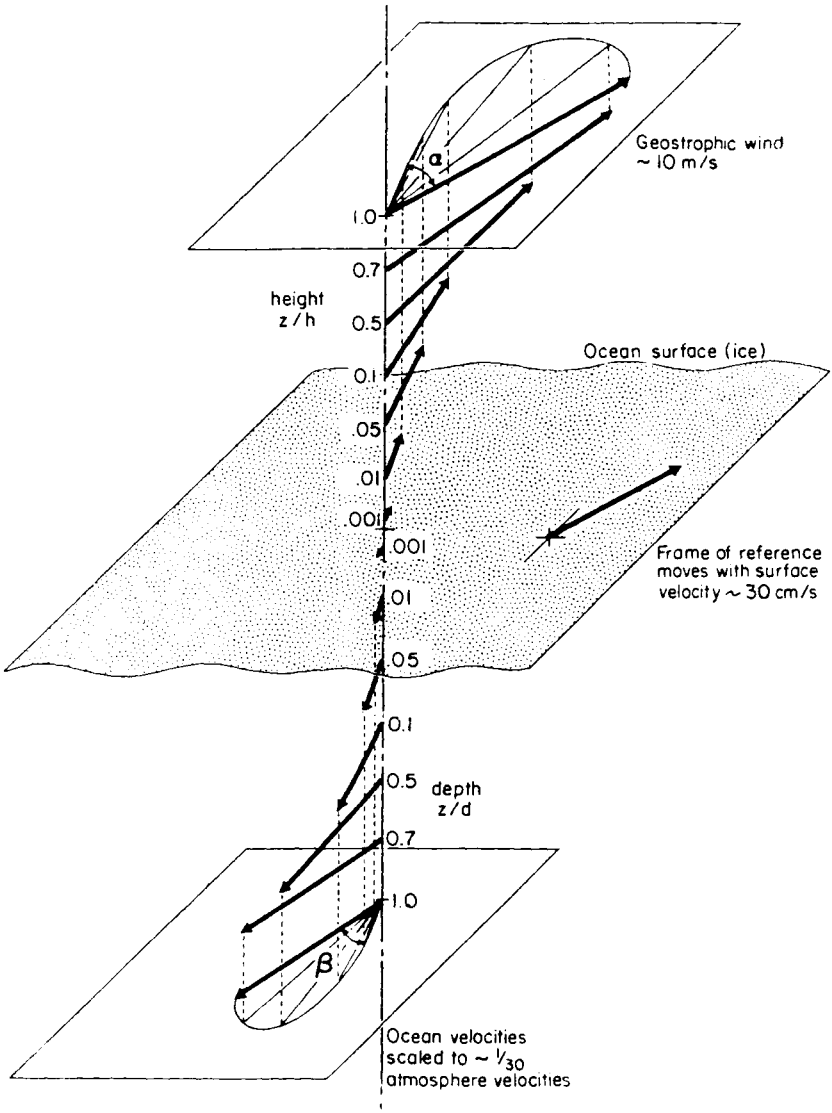

Figure 1.2 Linked-PBL Ekman spiral velocities.

boundary layer stratification (see Chapter 6). Finally, the PBL is frequently topped by an inversion (the OPBL is "bottomed" by a pycnocline), which may be imposed by large-scale dynamics but interacts with the flow within the boundary layer significantly.

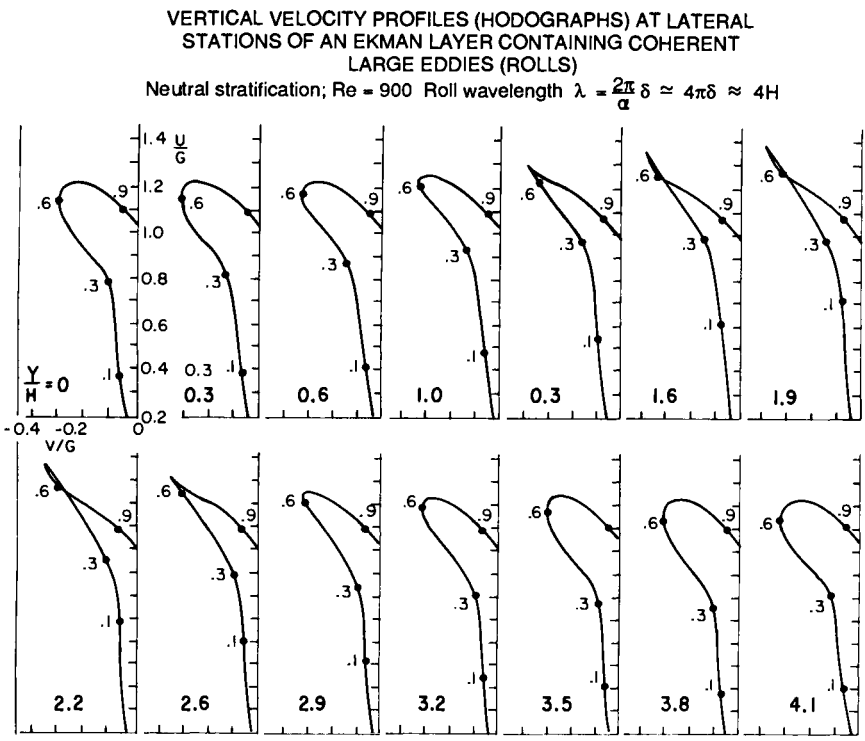

Figure 1.3 Lateral variation of PBL horizontal velocities. One cycle of the large eddies occurs in a lateral distance equal to four times the PBL height. Heights of velocity (u, v) are given at z/H levels.

The problems of the variable roughness, variable stratification, PBL instability with consequent large eddies, baroclinicity in the layer, and inversion have all been addressed in observational experiments and theory. There are experimental data from the MIZ in which the PBL experiences an abrupt change in surface boundary conditions as flow moves from over ice to over water (Guest and Davidson, 1987). The interaction in the vicinity of the MIZ must include both ocean and pack ice models, as well as something in between for the broken ice in the MIZ. Based on history, the polar oceans, which include open ocean and pack ice, offer great challenges and opportunities for modeling the PBL flow and the consequent air–sea interaction.

1. The Ekman layer solution

Within the Ekman layer, wind turning takes place between the gradient (or free-stream) wind and the surface wind. Surface patterns of convergence or vorticity may emerge. These may be forced synoptically by large-scale cli-

mate and weather processes or, from below, by changes in the air–sea–ice boundary condition. Modeling of this layer is a contemporary challenge for atmospheric scientists. The classical Ekman solution, modified with finite-perturbation secondary flows, is a one-dimensional equilibrium model of the flow above a point. It is a good approximation to the extent that the PBL is in equilibrium. The equations are pertinent to the oceanic Ekman layer with a simple change of coordinates. To obtain this solution, one starts with the Navier–Stokes equations:

$$\partial \mathbf{u}/\partial t + \mathbf{u} \cdot \nabla \mathbf{u} = f\mathbf{k} \times \mathbf{u} + (1/\rho)\,\nabla p + g\mathbf{k} + \nu\,\nabla^2 \mathbf{u} \tag{1.1}$$

which are approximated for the boundary layer as

$$-fv + (1/\rho)\,\partial p/\partial x - \nu\,\partial^2 u/\partial z^2 = 0 \tag{1.2}$$

$$fu + (1/\rho)\,\partial p/\partial y - \nu\,\partial^2 v/\partial z^2 = 0 \tag{1.3}$$

Density can usually be considered constant in the boundary layer. The flow is assumed steady and horizontally homogeneous. Most significantly for geophysical applications, the viscosity, ν, must be replaced by an eddy viscosity, K (see Table 1.1 for a list of parameters). This embodies the far-reaching assumption that the turbulent eddies transport momentum and heat, not unlike the molecules in kinetic theory. This works well for small-scale, well-mixed turbulence. However, it is invalid for large-scale turbulence because a continuum does not exist. The large-scale turbulent eddies must be included explicitly. This has been done analytically (Brown, 1970; Mourad and Brown, 1990) and numerically (Sykes *et al.*, 1988).

Turbulence in the PBL spans scales from millimeters to kilometers. One compromise is to calculate the large-scale turbulent eddies explicitly and approximate the smaller-scale (hopefully uniform) turbulence with an eddy viscosity scheme which accounts for the sub-grid-scale turbulence. In certain conditions, this can be done analytically when the large eddies are organized finite perturbations. In this case, the nonlinear term for the Reynolds stress due to the large eddies, $\overline{v_2 w_2}$, is added to Eqs. (1.2) and (1.3):

$$-fv + (1/\rho)\,\partial p/\partial x - K\,\partial^2 u/\partial z^2 = v_2 w_2 \tag{1.4}$$

$$fu + (1/\rho)\,\partial p/\partial y - K\,d^2 v/dz^2 = 0 \tag{1.5}$$

The solution to Eqs. (1.4) and (1.5) is Ekman's spiral $\mathbf{U}_E$ plus a modification term due to the large eddies, $\mathbf{U}_2(z)$. Written in coordinates aligned with $\mathbf{U}_G$, $\partial p/\partial x = 0$, and

$$u(z) = G(1 - \exp(-z/\delta)\cos z/\delta) + u_2 \tag{1.6}$$

$$v(z) = -G\exp(-z/\delta)\sin z/\delta + v_2 \tag{1.7}$$

Table 1.1 List of Parameters and Short Definitions

C_D	Aerodynamic, or bulk, drag coefficient. Associated with a 10-m height unless subscripted with another height
C_E	Latent heat flux coefficient
C_G	Geostrophic drag coefficient ($=u^*/G$)
C_H	Heat flux coefficient
c_p	Heat capacity at constant pressure
d	Depth of the oceanic PBL
E_0	Latent turbulent heat flux
f	Coriolis parameter [$=2 \times (1/24\text{ h}) \times \sin(\text{latitude})$]
GCM	General circulation model
G	$\lvert U_G \rvert$, geostrophic wind magnitude
H	Height of the atmospheric PBL
H_0	Sensible turbulent heat flux ($=\rho c_p \overline{w'T'}$)
K	Eddy flux coefficient for momentum
K_E	Eddy diffusivity in Ekman layer
K_e	Eddy flux coefficient for sensible heat
K_q	Eddy flux coefficient for latent heat
k	von Karman constant ($=0.4$)
k_e, k_q	Molecular diffusion coefficients
L	Obukhov length, surface layer stratification parameter
L_E	Latent heat of evaporation
PBL	Planetary boundary layer
q	humidity
Q	moisture, liquid water
Re	PBL Reynolds number ($=G\delta/K_E$)
Ri	Richardson number
T_A	Air temperature
T_S	Surface temperature
u^*	The "friction velocity," a surface stress proxy ($=\sqrt{\tau/\rho}$)
U_G	Geostrophic wind ($\equiv G$ in geostrophic coordinates)
V_T	Thermal wind parameter = baroclinicity, in degrees Celsius per 100 km
$\overline{w'\xi'}$	Eddy correlation of turbulent vertical velocity perturbation w' and quantity ξ'; equal to flux of ξ. This is an implied average over time or space
$\overline{w_2 u_2}$	Eddy correlation of large-eddy secondary flow
z_0	Surface roughness parameter.
α	Angle of turning between top and bottom of PBL
β	Angle of turning through oceanic PBL
δ	Scale height of PBL ($=\sqrt{K/f}$)
ρ	Air density
Θ	Potential temperature
Θ_T	Angle between geostrophic and thermal winds
τ	Stress, equal to momentum flux ($=\overline{\rho w' u'}$ in the PBL)
τ_0	Surface stress (at $z = 0$).
ν	Molecular viscosity

where $\delta = \sqrt{2K/f}$, Ekman's depth of frictional resistance, and G is the magnitude of the free-stream or geostrophic flow, $(1/\rho f)(0, -\partial p/\partial y)$. The surface friction velocity is defined as

$$u^* \equiv \sqrt{\tau_0/\rho} \tag{1.8}$$

The surface stress can be related to the geostrophic flow in the geostrophic drag coefficient, u^*/G. Ekman's solution predicts a Newtonian-type surface stress,

$$\tau_0 = \rho K_E \, du/dz|_{z=0} \tag{1.9}$$

Similar comments apply to eddy diffusive modeling of the fluxes of sensible heat H_0 and latent heat E_0 with respect to temperature Θ and moisture Q, in analogy to the molecular flux relations,

$$\tau = \rho\nu \, \partial u/\partial z, \qquad H_0 = -\rho c_p k_h \, \partial\Theta/\partial z, \qquad E_0 = -\rho k_e \, \partial Q/\partial z \tag{1.10}$$

The molecular fluxes take place in a very thin layer and are much less than turbulent fluxes (the ratio $K_E/\nu \approx 10^7$). However, analogous equations for turbulent flow such as Eq. (1.9) are not of much practical value, since the turbulent diffusivity coefficients K_E, K_h, and K_e are difficult to determine. These are expected to be some unknown functions of stratification, surface roughness, wind speed, baroclinicity, or other factors which affect the character of turbulence.

In order to relate the stress to a simultaneously measured surface parameter, it is necessary to consider the surface layer concept.

B. The Atmospheric Surface Layer

When surface observations are made, there is a layer near the surface where the turning and the variation in stress appear insignificant (stress varies less than 10% in the lowest 10–20 m). In this layer, the wind speed varies approximately as the natural logarithm of the height. This behavior can be derived as the limit of the Ekman solution for small z, or from dimensional analysis, assuming that the turbulence, and hence the eddy viscosity, is increasing linearly with height (e.g., Brown, 1973). The wind speed is found to satisfy

$$u = (u^*/k) \ln(z/z_0) \tag{1.11}$$

where z_0 is a roughness parameter, defined as the height where $u = 0$.

The values of k and u^* can be found from Eq. (1.11) by measuring $u(z)$ to obtain a plot of u versus $\ln z$. Then u^* can be found using

$$u^* = kz \frac{\Delta u}{\Delta z} \tag{1.12}$$

In practice, z_0 is very small and measurements near $u = 0$ are poor. Extrapolation is necessary and observed values of z_0 vary by orders of magnitude. The value of k has been found to range from 0.32 to 0.45. Recently, in careful experiments in the atmospheric surface layer, the value of k was confirmed to be nearly constant at 0.4. Once k is known, measurement plots such as Fig. 1.4 can be used to determine u^* from Eq. (1.12) in what is called the profile method.

If u^* is measured with other methods, then z_0 can be calculated from a measurement of u at z using

$$z_0 = z/[\exp(ku/u^*)] \tag{1.13}$$

When stratification is important, a correction to this formula is used:

$$u = u^*/k[\ln(z/z_0) - \psi] \tag{1.14}$$

where ψ is an empirical correction for layer stratification (Paulson, 1970).

1. The flux coefficients

The advantage of a surface layer concept is that extensive measurements are available to parametrize the wind profile, heat flux, stress, and other flux parameters (e.g., CO_2, pollutants). The surface roughness parameter, drag coefficient, heat flux coefficient, and other similar parameters have been obtained for variable surface roughness and layer stratification. They can be determined "directly" from high-frequency measurements with a fast-response sensor. In this case, the variables are separated into a mean and a

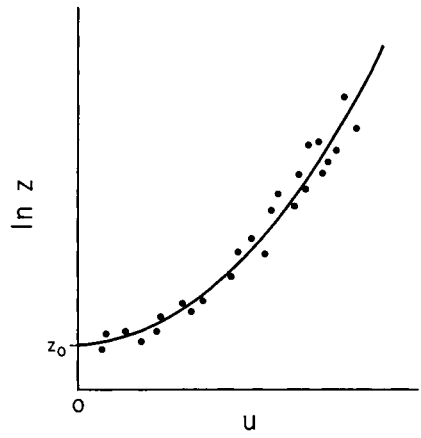

Figure 1.4 Sketch of profile of $u(z)$ method of determining z_0 and u^*.

fluctuation, denoted with a prime. The means of the cross-correlations, $\overline{\rho u' w'}$, $\overline{\rho c_p w' T'}$, $\overline{\rho L_E w' q'}$, are the momentum and sensible and latent heat fluxes. The bulk of these measurements have been made over land, with only a few measurements having been made over pack ice. Only recently have techniques been devised to measure stress from a ship.

Drag coefficients, arrived at by dimensional analysis in the surface layer, are the basic tool of the flux models. Surface stress is generally calculated as a function of the wind speed at a specified low-level height, usually 10 m, according to a "drag coefficient" derived from dimensional analysis,

$$C_D \equiv \tau_0/(\rho U_{10}^2) \tag{1.15}$$

When an atmospheric general circulation model incorporates the surface stress, the lowest-level winds in the model may be used with a bulk coefficient $(\rho U^2 C_D)_Z$ to produce the stress. For many large-scale models, the lowest-level wind is approximately the geostrophic flow above the PBL. Then the drag coefficient is the geostrophic,

$$C_G \equiv [\tau_0/(\rho G^2)]^{1/2} = u^*/G \tag{1.16}$$

If the model has many layers within the PBL, this lowest-level wind may be nearly U_{10}. Otherwise some extrapolation scheme may be employed on higher-level winds to get surface winds, and Eq. (1.15) can be used.

The eddy heat flux coefficient is defined in a similar manner to the drag coefficient, based on dimensional analysis:

$$C_H \equiv H_0/(\rho c_p U_{10}\, \Delta T) \tag{1.17}$$

where H_0 is the turbulent heat flux $(\equiv \rho c_p \overline{w' T'})$ and ΔT is simply the air–surface temperature difference $T_A - T_S$. There is a corresponding latent heat flux,

$$C_E \equiv E_0/(\rho L_E U_{10}\, \Delta q) \tag{1.18}$$

where E_0 is the latent turbulent heat flux $(\equiv \rho L_E \overline{w' q'})$ and Δq is the humidity difference between the air at 10 m and at the surface.

A common problem for heat flux parametrization and stratification corrections to stress is the difficulty in obtaining a good stratification parameter. The classical molecular parameter is the Richardson number:

$$\mathrm{Ri} = \frac{g\, d\Theta/dz}{\Theta(dU/dz)^2} \tag{1.19}$$

This is a local parameter, but another version may be substituted for bulk parametrization:

$$\mathrm{Ri} = \frac{g\, \Delta\Theta\, \Delta Z}{\Theta(\Delta U)^2} \tag{1.20}$$

Here, $\Delta\Theta$, ΔZ, and ΔU are measured across the PBL height ΔZ. However, these values are often difficult to acquire.

The Monin–Obukhov length is a parameter based on dimensional analysis,

$$L = \frac{-u^{*3}}{kg} \frac{(\rho c_p T_0)}{H_0} \tag{1.21}$$

This scale is commonly used but has the liability of involving a term, u^*, which has a large error associated with it (Blanc, 1987) and cubing it. Nevertheless, it has been used quite successfully in organizing surface layer data with respect to stratification in cases where surface stress and heat flux are well measured.

Finally, for most ocean applications, the most accessible stratification parameter is simply the air–surface temperature difference, $T_A - T_S$. This will be used in the summary graphs, with T_A referenced to 10 m.

Because climate studies that include the dynamics of polar oceans are generally pursued using a GCM, air–sea interaction studies are often directed toward furnishing parametrizations of the physical processes which are sub-grid scale to GCMs (less than 100–400 km). In addition to the flux coefficients and ice coverage characteristics, parametrizations are needed for cloudiness and cloud types, albedo, and radiative transfer effects.

C. Methods of Stress Measurement

1. Stress from near-surface observations

Initially, surface stress measurements were derived from tower measurements, seldom higher than 10 m, using the profile method. They had errors of several hundred percent associated with intrinsic measurement errors and the method of calculation (e.g., Blanc, 1987). Field experiments took place in the most uniform areas available: the Australian outback, Kansas wheat fields, and pack ice. Using these techniques, one could estimate the drag coefficient over pack ice at 1×10^{-3}. However, these measurements were inevitably made on the smoothest of floes, and it was expected that contributions from ridges and areas of rougher ice would increase the drag.

As measurement techniques improved, the capability to measure the eddy flux directly produced "direct" stress measurements according to the eddy correlation formula,

$$\tau = \rho \overline{u'w'} \tag{1.22}$$

Sonic anemometers provide these data and have even been deployed on the pack ice. However, stable alignment is crucial to this measurement, and additional difficulties associated with the measurements suggest that large

errors are generally associated with these measurements (Blanc, 1987). Nevertheless, the drag coefficients established with respect to surface measurements form the basis of flux parametrizations. Excellent summaries of these measurements have been given by Macklin (1983), Overland (1985), and McBean (1986). The Overland paper emphasizes the importance of the inversion height in the stress parametrization.

Finally, a technique for inferring stress from the turbulence spectra in the inertial subrange has evolved. This relies on the hypothesis that the inertial subrange is a universal characteristic of the turbulent energy cascade in the dissipation regime. The stress (momentum flux) is a boundary condition for the spectral density and is therefore related to the dissipation, which can be found from high-frequency velocity measurements. A hot film produces voltage variations proportional to the high-frequency velocity fluctuations. Again, there is evidence (Blanc, 1987) that intrinsic errors in the dissipation method are comparable to those in the eddy correlation method. However, recent results suggest that this technique can yield errors less than 30% (Guest and Davidson, 1987).

a. Aircraft observations The first measurements from an aircraft flying in the PBL over pack ice were those taken during the Arctic Ice Dynamics Joint Experiment (AIDJEX) [with the National Center for Atmospheric Research (NCAR) Electra]. These measurements are made with gust probes, which are wedges attached to strain gages that respond to high-frequency wind variations. High-frequency temperature probes (hot wires) are used. The fluxes are calculated using eddy correlation methods. The measurements revealed higher drag coefficients than were observed on the surface using a 26-m tower and the profile method. This was expected because of the integrated effect of the pressure ridges and leads in the higher-level PBL wind profiles. Leads are formed when cracks in the pack ice expose open water. Pressure ridges are formed when the thin ice in a frozen lead is thrust upward by a closing motion of the pack ice. Extensive aircraft measurements have been taken over the ice in the Bering Sea, in the MIZ, and over the adjacent ocean (Walter and Overland, 1984; Overland, 1985; Pease, 1987; Hein and Brown, 1988; Kellner *et al.*, 1987; R. J. Markson, personal communication). In general these result in higher drag coefficients than those obtained at the surface.

2. Momentum integral stress

The profile method accounts for an integrated effect of the surface stress on the surface-layer wind profile. When the entire velocity profile affected by the surface stress is considered, the retarding effect of the surface force can be

related to the integrated momentum loss in the flow across the PBL. Brown (1974) provided a formula for surface stress based on this bulk method:

$$\tau_0/\rho = fh(G^2 - uG)^{1/2} = fhG \sin \alpha = fhu \tan \alpha \tag{1.23}$$

or

$$C_D = fh/u \tan \alpha \tag{1.24}$$

where u is the mean wind speed in the PBL (assuming a well-mixed layer with nearly constant velocity), α the angle of turning between geostrophic and PBL winds, and h the height of the inversion. For a well-mixed layer, measurements are easily made of boundary layer wind speed and direction and of the surface pressure field, which is used to determine G. However, the height of the inversion is not readily available. Some results were obtained during AIDJEX using an acoustic sounder to determine the PBL height. Then

$$C_G = [fh/G \sin \alpha]^{1/2} \tag{1.25}$$

(Fig. 1.5) (Carsey, 1980). The values are high (0.04), and Carsey suggests a coefficient of 0.7 be inserted on the right side of Eq. (1.25).

Pease *et al.* (1983) have used momentum integral techniques to estimate the surface drag of the pack ice acting as a drag plate, and their value of $C_D = 2.8 \times 10^{-3}$ agreed well with surface measurements. They emphasized the importance of the ratio of air/ice drag to ice/water drag for ice drift modeling.

All modeling of the PBL and surface fluxes involves semiempirical formulas which require measurements of the fluxes in conjunction with mean flow parameters. Radiation measurements, and the interaction with clouds, are difficult to sort out over the pack ice. The polar regions are relatively uncomplicated PBL domains (the oceans and pack ice are relatively smooth surfaces, there is a lessened diurnal cycle, and there is a strong Coriolis force). However, the measurement programs present a challenge because of the harsh environment.

III. Major Air–Sea Interaction Polar Experiments

A. The Arctic Ice Dynamics Joint Experiment (AIDJEX)

AIDJEX was the first experiment which involved multiple stations acquiring synoptic data in the Arctic. From March 1975 until early May 1976, four camps surrounded by eight data buoys were operated in the central Beaufort Sea, producing a significant increase in our understanding of ice dynamics. There was a corresponding increase in oceanographic and atmospheric data

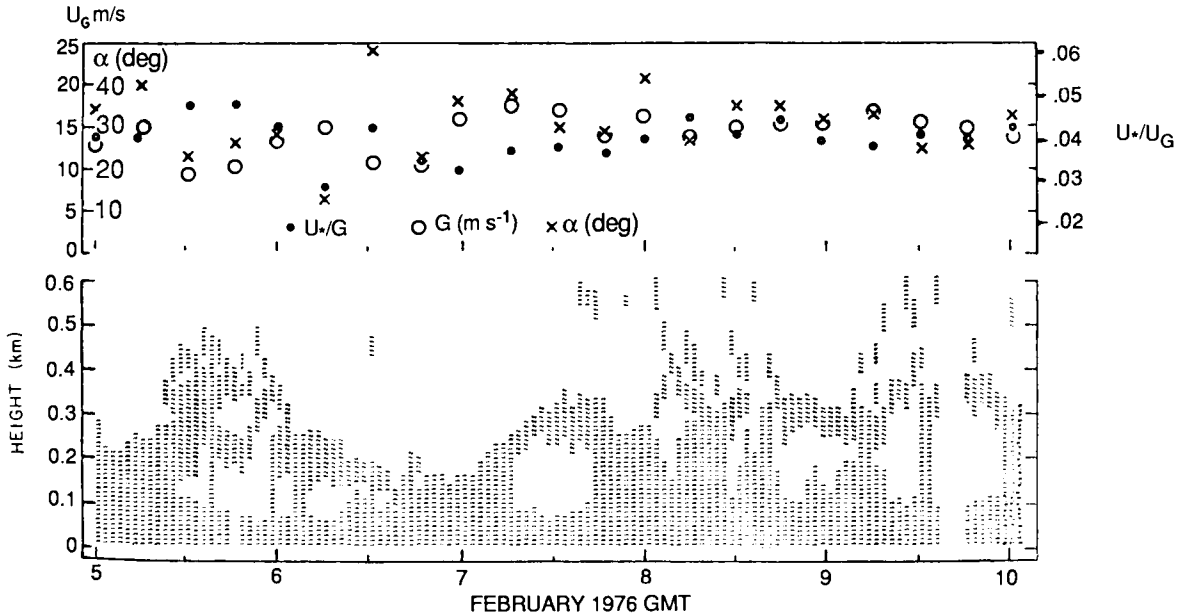

Figure 1.5 Time series of acoustic radar data; $G \equiv U_G$, α, and C_G from Eq. (1.25). Adapted from AIDJEX data (Carsey, 1980).

from this experiment. Two facets of Arctic pack ice meteorology emerged from this experiment. First, it is very difficult to measure the fluxes or PBL dynamics in the neutral to stably stratified PBL over the pack ice. Second, the uniformity of surface roughness and PBL stratification make the geostrophic drag coefficient an adequate measure of synoptic forcing of the ice-covered ocean.

During AIDJEX there were profile measurements on a 26-m tower periodically during the year. There were several periods of sonic anemometer measurements and some "nearly" inertial range turbulence spectra for applying the dissipation method. Airplanes were flown in the PBL, making gust probe measurements of the high-frequency turbulence. An acoustic sounder provided an almost continuous record of the complicated inversions which occur in the central Arctic and contributed another estimate of surface stress. These results were presented in the symposium text edited by Pritchard (1980).

B. Antarctic Experiments

On scales related to synoptic weather and climatology, Antarctica is approximately a large dome of ice. The annual radiation budget is negative, with positive values for only a short period in summer. There is thus great cooling of the surface air, with the result that gravity, or downslope, winds dominate the airflow. One consequence of this dominance is that as the air becomes colder and more dense, it flows with increasing speed down to the coasts under the gravitational influence. The local air mass above the boundary layer is warmer and independent of the katabatic wind. The result is a strengthening inversion, further separating the boundary layer flow from the free atmosphere. Thus the winds which flow over the near-shore ice are uniquely determined by the katabatic forces, which are intimately related to the topography. These katabatic winds may be important considerations for global climate models. Although they are neglected in current models, these drainage winds have a significant influence on the regional surface heat budget, including that of the surrounding ocean. They reach maximum speeds along ice-stream channels and cause persistent open-water polynyas where these channels meet the ocean (Bromwich and Kurtz, 1984). Other coastal polynyas are formed by persistent synoptic offshore winds in both the Arctic and Antarctic (Pease, 1987). Thus the katabatic winds are an important mechanism in long-term air–sea–ice interaction.

The automatic weather stations project (Andre *et al.*, 1986; Wendler *et al.*, 1986) has placed stations on the ice dome and at several sites on the coast of the Ross and Weddell seas. These stations measure the wind velocity, temperature, and air pressure at 3 m. The data are transmitted to ARGOS-

equipped polar orbiting satellites. When the data are combined with satellite-derived measurements of wind and ice motion, the currently unknown weather regimes over and adjacent to the Antarctic pack ice will be better documented. The correlation between ice motion and wind stress noted by Schwerdtfeger (1979) and Cavalieri and Parkinson (1981) can be further elucidated by this process.

C. The Marginal Ice Zone Experiments (MIZEX)

In the past decade there have been several experiments designed to measure the dynamics of the MIZ. Although meteorological measurements have been limited, some new information on stress values over the broken-up ice of the MIZ has emerged.

A series of flights in the PBL over the Bering Sea MIZ measured drag coefficients and defined the PBL dynamics. The commonly observed roll instabilities (Brown, 1980) were found both in the unstable stratification of the cold air outbreak and over the pack ice in neutral stratification (Walter and Overland, 1984). Figure 1.6 is a NOAA-6 photograph of rolls or typical cloudstreets associated with the secondary flow in the PBL. This picture also shows a small (200 km) polar low developing in the cold northerly flow off the pack ice (top of photo). The horizontal eddies (von Karman vortices) in the wake of Bear Island suggest the remarkable persistence of large eddies in the PBL.

The observations of extremely long-wave phenomena provoked a nonlinear analysis of PBL dynamics which revealed turbulent energy flux from the linear large eddies to longer wavelengths (Mourad and Brown, 1990). A cross section of the vertical velocity in the PBL (Fig. 1.7) shows a mixture of large eddies and very large eddies in the case of neutral stratification.

Flights were also made in the cold air outbreaks during the Arctic Cyclone Experiment (ACE) (Hein and Brown, 1988). Large heat fluxes of 700 W/m^2 have been measured near the ice edge. Similar results were found in flights during MIZEX 1984 over the Greenland Sea (Kellner *et al.*, 1987).

Andreas *et al.* (1984) measured the PBL with wind and temperature soundings at the MIZ and iceward for 150 km and obtained a C_D estimate of 4×10^{-3}. As noted by Bennett and Hunkins (1986), this is higher than any other measurement to that date. They point out that the heat flux from the PBL through cloud-top cooling may exceed the heat flux into the ice. The problem of heat flux magnitudes, and even directions, through the PBL is greatly in need of more measurements. These require simultaneous observations of high-frequency wind and temperature to allow calculation of eddy correlation fluxes, mean surface and air temperatures, and surface roughness.

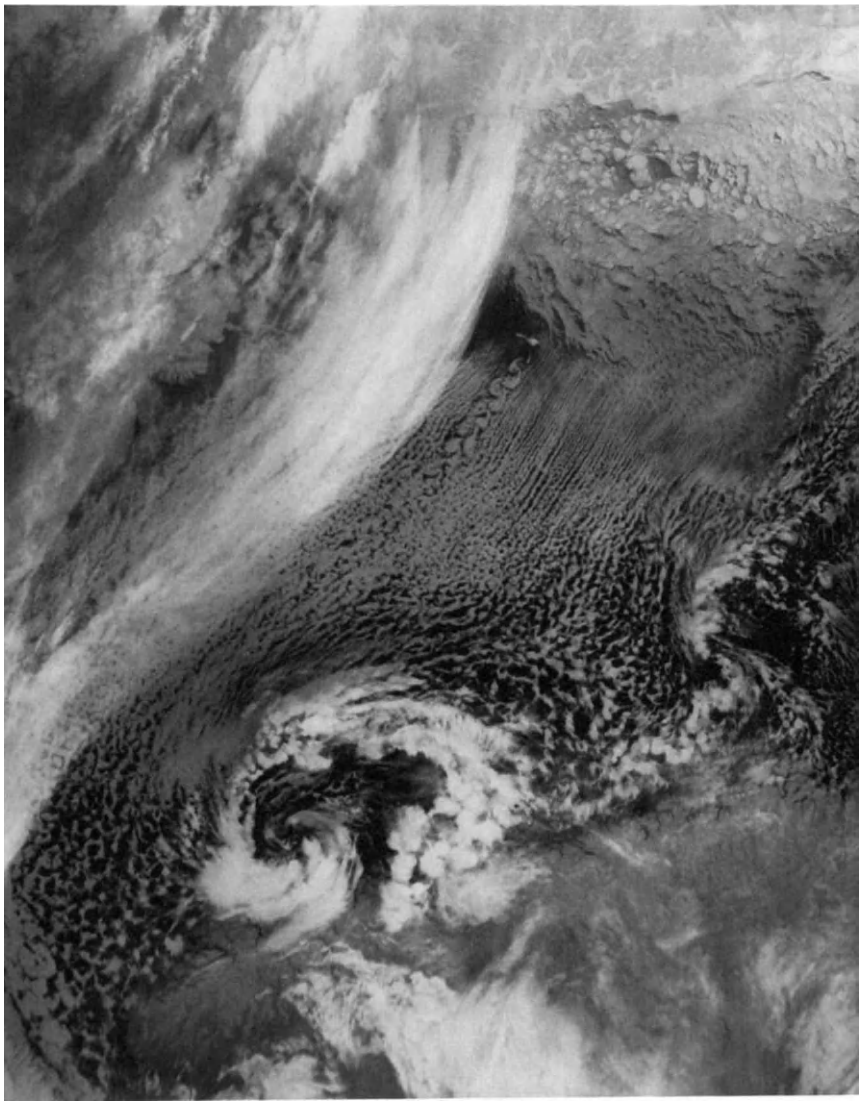

Figure 1.6 NOAA-6 photograph of a cold-air outbreak off the pack ice in the northern Atlantic. Scale is about 1000 × 1000 km. Cloudstreets are about 5 km apart.

Guest and Davidson (1987) and Anderson (1987) made many measurements of C_D over the MIZ and the adjacent ocean. They obtained consistent values over the ocean of $1.2-2.5 \times 10^{-3}$, varying with wind speed. When concentrations of ice were encountered, the drag coefficient rose dramati-

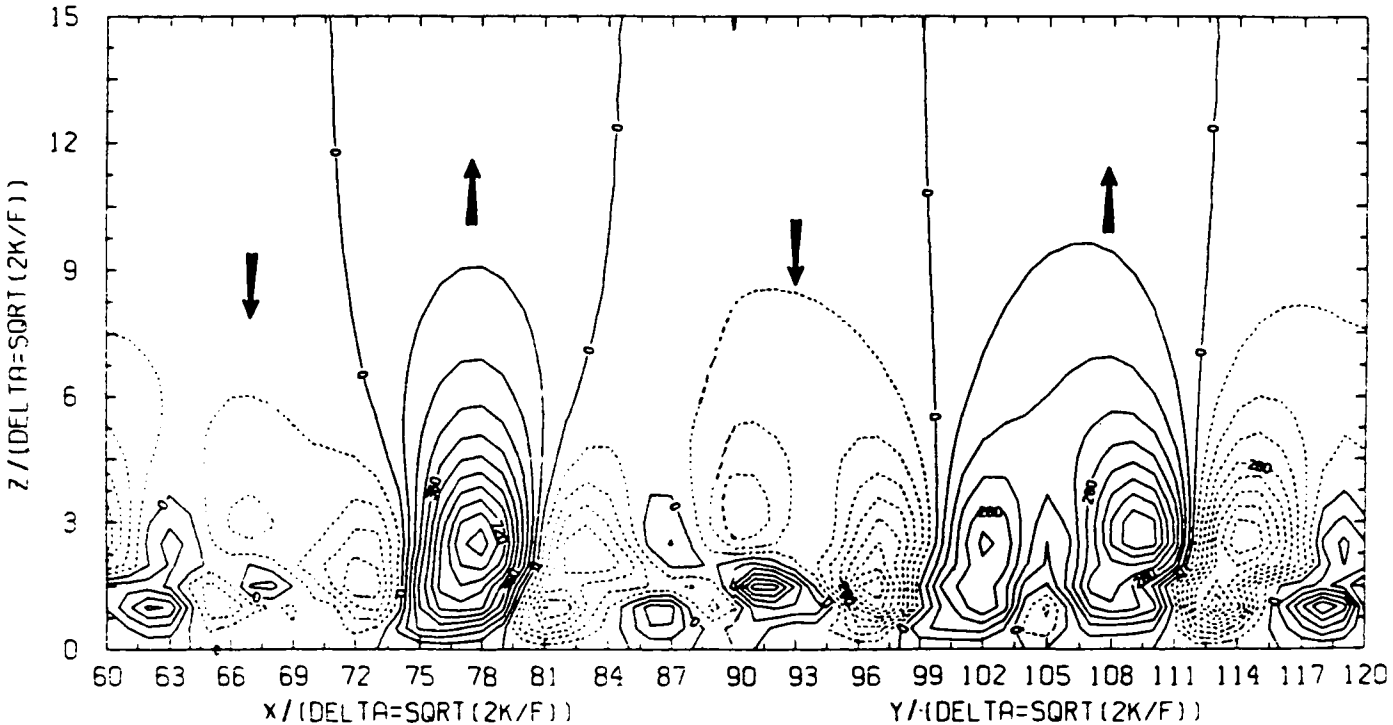

Figure 1.7 Cross section of vertical velocity looking downstream in the PBL. Heights and lateral distance are nondimensionalized with δ.

cally, to 5×10^{-3} in some cases. These data are obtained from summer experiments with air–sea temperature differences no greater than 4°C, in near-neutral stratification, and do not reflect the possible large variations in fluxes due to very unstable stratification associated with cold winter air moving off ice or land and over the ocean. They do demonstrate that there are large variations in drag coefficients due to variations in ice type and concentration.

During the experiments discussed above, strong sea surface temperature fronts (with temperature changes of 4.5°C) were encountered in the near-MIZ area. The PBL stratification change across such fronts will produce local variations in stress and wind vectors, causing both atmospheric and oceanic vertical motion. The amplification of local convergence and vorticity patterns due to ice edge variations such as those shown in Fig. 1.8 can cause dramatic local variations in wind speed, heat flux, clouds, and fog. The corresponding variation in surface stress can produce circulation and eddies in the ocean.

IV. Modeling Methods

All of the long-term surface stress measurements require a manned camp or automatic station and are point measurements from a base camp or ship. Occasional aircraft surveys supplement these point measurements. However, ice and ocean modeling requires fields of fluxes (stress and heat flux) on scales from kilometers to thousands of kilometers. Although numerical modeling of the large-scale free-stream (geostrophic) flow in the atmosphere is quite successful, the PBL representation in these models is generally quite poor. When boundary layer dynamics are described with multiple layers within the PBL, large computational capacity is required, and hence domains for calculation rapidly shrink. There has been progress in numerical modeling of the three-dimensional aspects of the PBL; however, current applications to scales larger than 10 km are not practical. The PBL in the mesoscale regime (a grid size of tens to hundreds of kilometers) can be represented by simpler two-dimensional numerical models which can include greater domains. It is also well approximated by simple one-dimensional equilibrium models incorporating the analytic results of Ekman layer and surface layer dynamics.

The simplest model for the stress is the geostrophic drag coefficient, where $u^*/G = C_G$. This requires only measurements of surface pressure fields to determine G and hence u^*. The most complicated models are numerical representations of the vertical distribution of the turbulence in the PBL. In these models, there are questions of closure, representation of large-scale

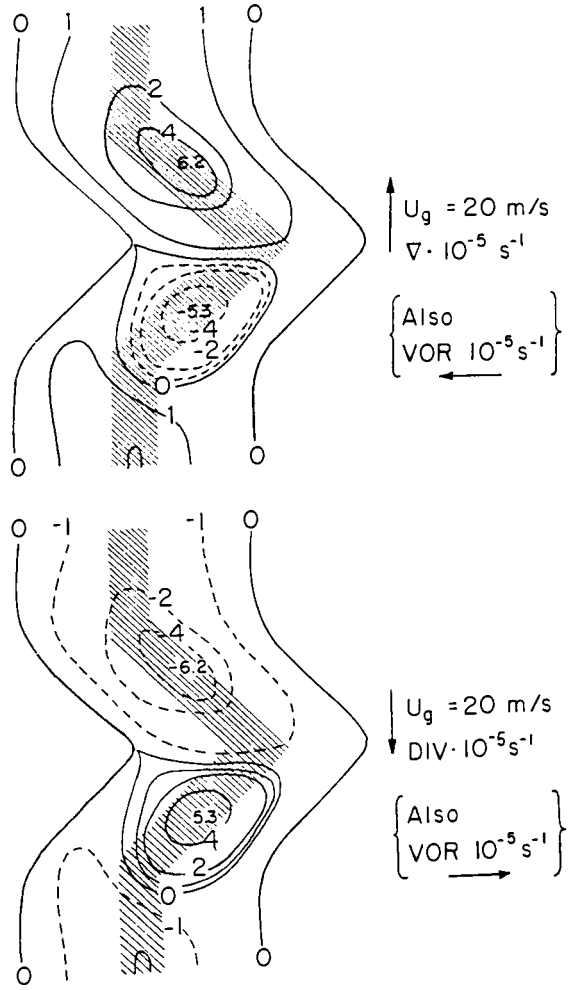

Figure 1.8 Divergence and vorticity (depending on wind direction) at the MIZ (shaded). Ice is on the left. Vorticity is due to U_G at 90° counterclockwise.

eddies, and proper boundary conditions to be resolved. Eventually, they will provide good mesoscale representation of dynamics in the nonequilibrium regions such as the MIZ. In the meantime, semiempirical models such as the integral slab models or similarity models will provide insight into the important mechanisms in the MIZ domain and extrapolation of point data to larger regions. The similarity model remains the most efficient method for representing the PBL and the fluxes in large-scale circulation models.

A. Geostrophic Drag Coefficient

Surface pressures are relatively easy to measure and can be obtained from buoys deployed onto the pack ice. The National Weather Service provides surface pressure analyses at synoptic times (every 6 h). Although these measurements are still sparse in polar regions, they represent the best mesoscale measurements which can be used in models for extrapolation to field values of winds and fluxes. Moritz (1983, 1986) has shown that the NWS surface pressure analysis, incorporating Arctic buoy pressure data, provides good geostrophic winds. For barotropic PBLs, the surface pressures allow calculation of the geostrophic flow. This then constitutes the upper boundary condition on an Ekman layer solution. When the PBL is uniform (i.e., little change in dynamics due to variable stratification, roughness, or wind speed), the free-stream flow can be related to the surface friction velocity. This ratio forms the geostrophic drag coefficient C_G.

There is a high correlation between the geostrophic wind and the ice velocity for the Arctic pack ice motion, as described by Thorndike and Colony (1982). This implies that a fairly constant geostrophic drag coefficient provides a good estimate for the mean stress distribution over the pack ice. Based on the stress required to maintain the observed ice speed, this value is found to be $u^*/G(\text{ice}) = 0.024$. The uniformity of the central Arctic pack ice regions made this a good approximation. Where surface roughness or stratification varies significantly, the changing characteristics of the velocity profile can be accounted for in PBL similarity or numerical modeling.

B. Similarity Modeling

For atmospheric circulation models dealing with mesoscale and large scales, the similarity model for the PBL provides a practical formulization for the relation between the surface fluxes, the 10-m winds, and the geostrophic flow. The product is a geostrophic or surface drag coefficient as a function of stratification throughout the PBL, surface roughness (variable over the ocean), wind magnitude, humidity, and baroclinicity. It includes the assumption of a steady state at each grid point, generally on a 100-km scale.

When the Ekman solution is matched to a surface layer solution, the conditions for matching the velocities and derivatives yield similarity relations between the ratios of the characteristic speeds and scale heights of the two layers. The speed ratio is the geostrophic drag coefficient. It is a function of the ratio of the surface layer height to the Ekman layer height scale λ. This is the basic similarity parameter. Although both the surface layer height and the Ekman layer scale height are not known, their ratio appears to be fairly

constant, and $\lambda = 0.15$ is a good approximation for practical ranges of stratification. The matching of the velocity components can be written

$$kG/u^*(\sin \alpha) = -B \tag{1.26}$$

$$kG/u^*(\cos \alpha = -A' \equiv A + \ln(ku^*/fz_0) \tag{1.27}$$

where B and A are functions of λ and stratification, and A' is a function of λ, stratification, u^*, and surface roughness. In the absence of baroclinicity or secondary flow corrections,

$$u^*/G = (B^2 + A^2)^{1/2} \tag{1.28}$$

However, organized large eddies are often present, and near the MIZ, baroclinicity (thermal wind) is strong. In this case

$$kG/u^*(\sin \alpha + \beta) = -B \tag{1.29}$$

$$kG/u^*(\cos \alpha + \gamma) = -A' \tag{1.30}$$

where

$$\beta \equiv (V_t - U_t + dV_2/dz - dU_2/dz)/2 \tag{1.31}$$

$$\gamma \equiv (V_t + U_t + dV_2/dz + dU_2/dz)/2 \tag{1.32}$$

Here U_t and V_t are the thermal wind components, and U_2 and V_2 are finite-perturbation large eddies parametrized according to Brown (1972).

Both A' and B depend on empirical corrections to the surface layer relation Eq. (1.9) (as given by Paulson, 1970), λ, and z_0. They have been fit with the model with $\lambda = 0.15$ and also with polynomial curves by Arya (1975) (Fig. 1.9).

The variations of β and γ are shown in Fig. 1.10. The drag coefficient for this case is

$$\frac{u^*}{G} = \frac{-(\beta B + \gamma A) + \sqrt{B^2 + A^2 - (A\beta - B\gamma)^2}}{B^2 + A^2} \tag{1.33}$$

When the eddy flux coefficients are matched, the PBL height and the entire boundary layer dynamics can be calculated. Such a model evolved during AIDJEX and has since been used extensively in ice and ocean modeling. When the surface is the ocean, the model accounts for increasing surface roughness with wind speed. The predicted variation of geostrophic drag coefficient with variable roughness and stratification is shown in Fig. 1.11.

Because this is a matched-layer solution, the variable coefficient for unstable stratification reflects the changing characteristics of the Ekman layer organized large eddies. These large eddies are always present for greater than moderate winds (>7 m/s) or unstable stratification. They are a dominant

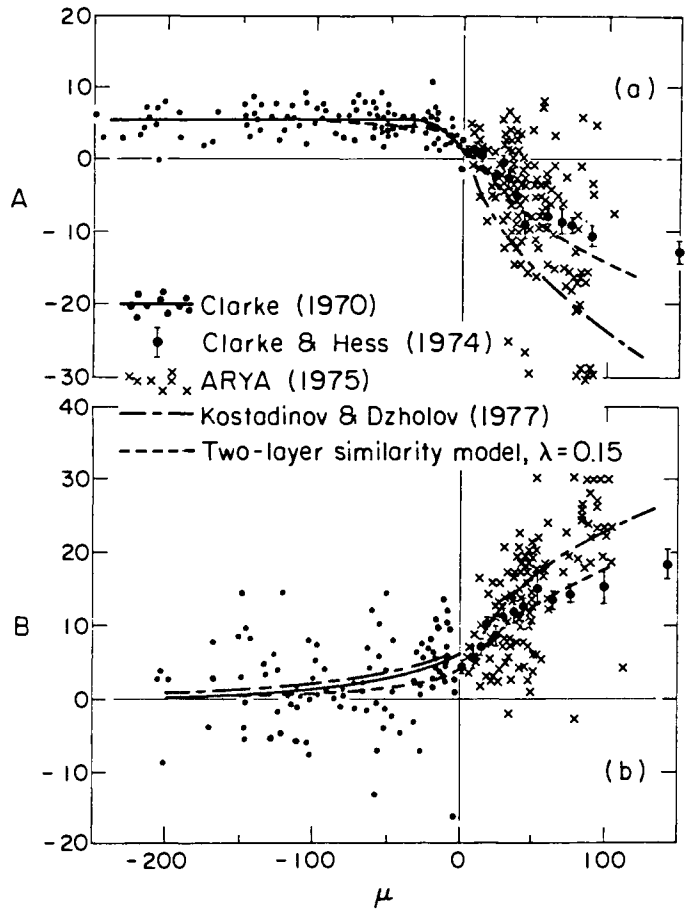

Figure 1.9 Similarity parameters versus stratification parameter $\mu \equiv ku^*/(fL)$. Data points are from Wangara experiment.

feature in the common cold air outbreaks in flow off the pack ice and promote the rapid mixing of this layer. A sketch of the cross section of the PBL and other basic parameters is shown as a function of distance downstream from the ice edge in Fig. 1.12. Although the PBL is evolving in the downstream direction, data indicate that a temporal equilibrium exists for the analysis on the 50–100-km scale so that the similarity model is valid. When the specifics of the flow in the MIZ are needed or either the time dependence or advection is important, numerical methods must be used.

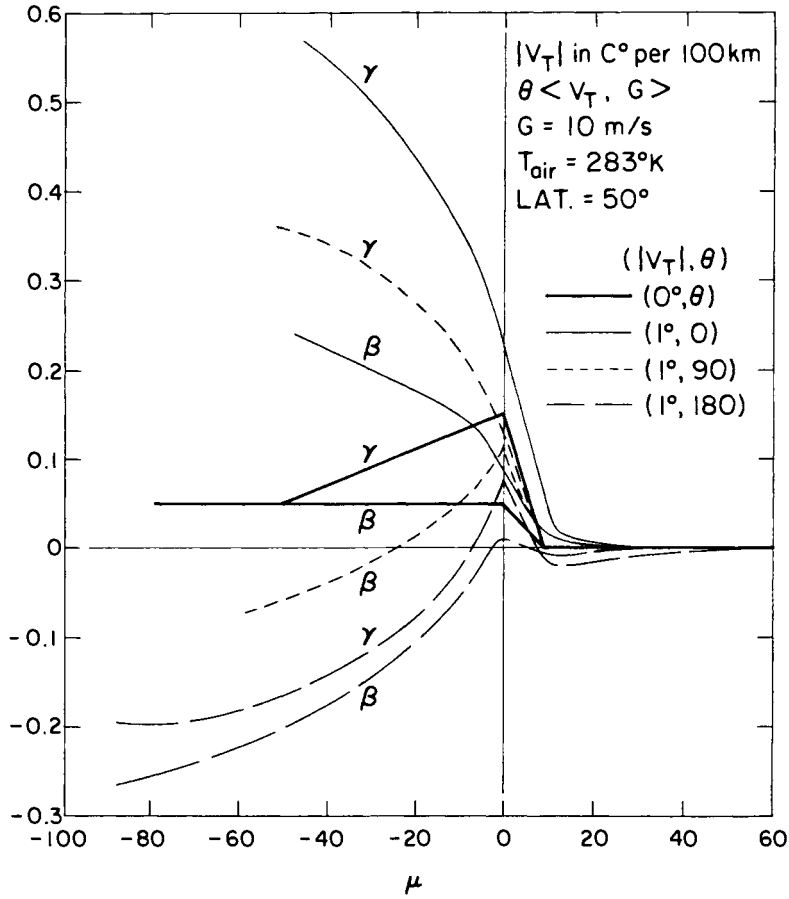

Figure 1.10 Similarity parameters for large eddies and thermal wind as a function of stratification parameter μ at various thermal wind orientations Θ.

C. Numerical Modeling

For the important MIZ case of cold air flowing over warm water, Overland *et al.* (1983) have used a two-dimensional vertically integrated model. The model includes a surface layer, PBL layer, and inversion integrated vertically. It predicts a steady-state wind which varies across the MIZ depending on the prescribed drag and heat flux characteristics of the region. J. E. Overland (personal communication, 1985) has presented a numerical PBL model which employs the turbulent kinetic energy equation to calculate eddy viscosity variation depending on roughness and thermal structure.

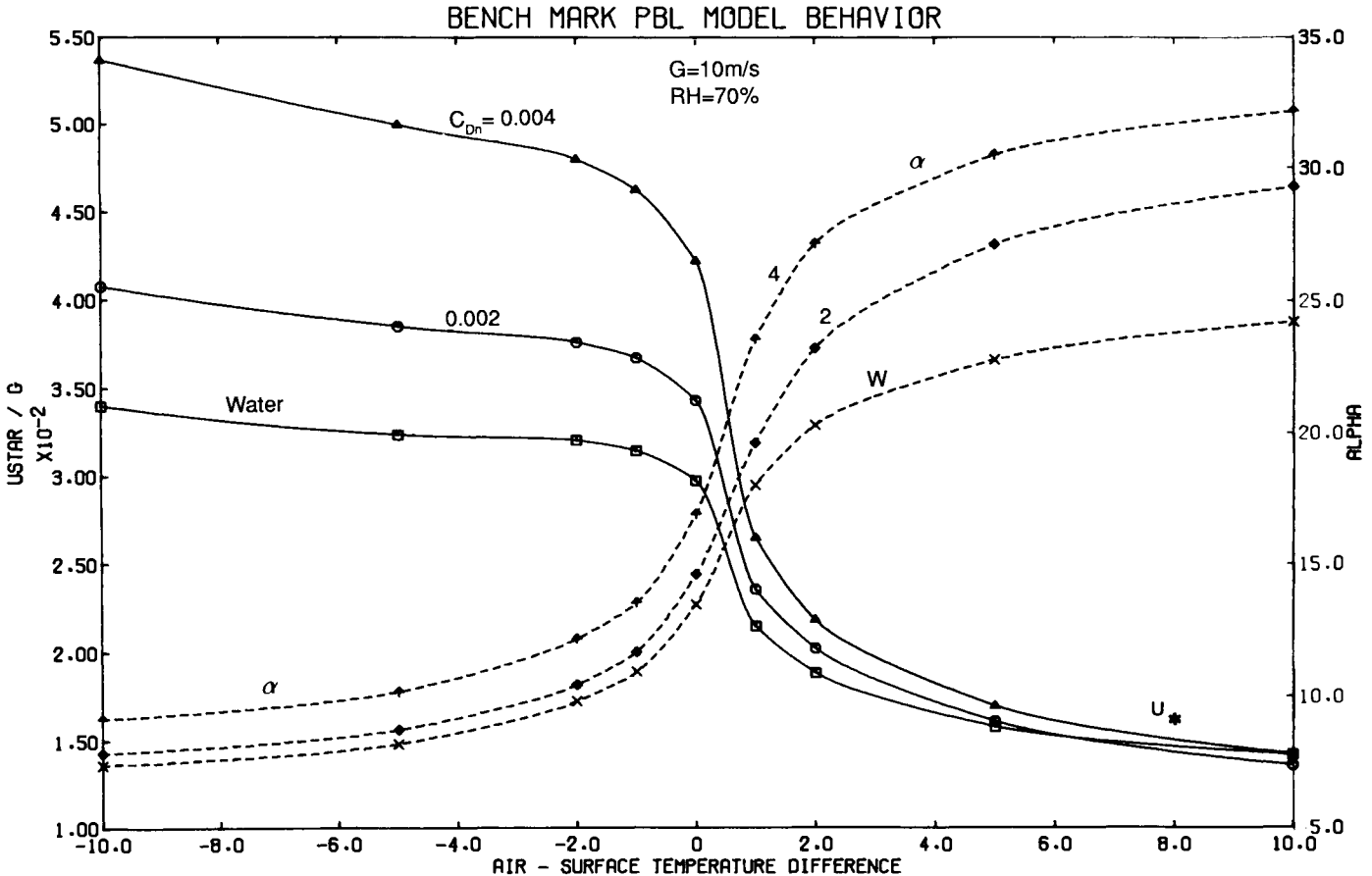

Figure 1.11 Model results for C_G and angle between geostrophic and surface winds at various stratifications and surface roughnesses. Values of $C_{Dn} = 0.002$ and 0.004 correspond to smooth and rough ice. Water has variable roughness but closely corresponds to very smooth ice, $C_{Dn} = 0.001$. $G \equiv U_G = 10$ m/s, relative humidity = 70%, and latitude = 60°.

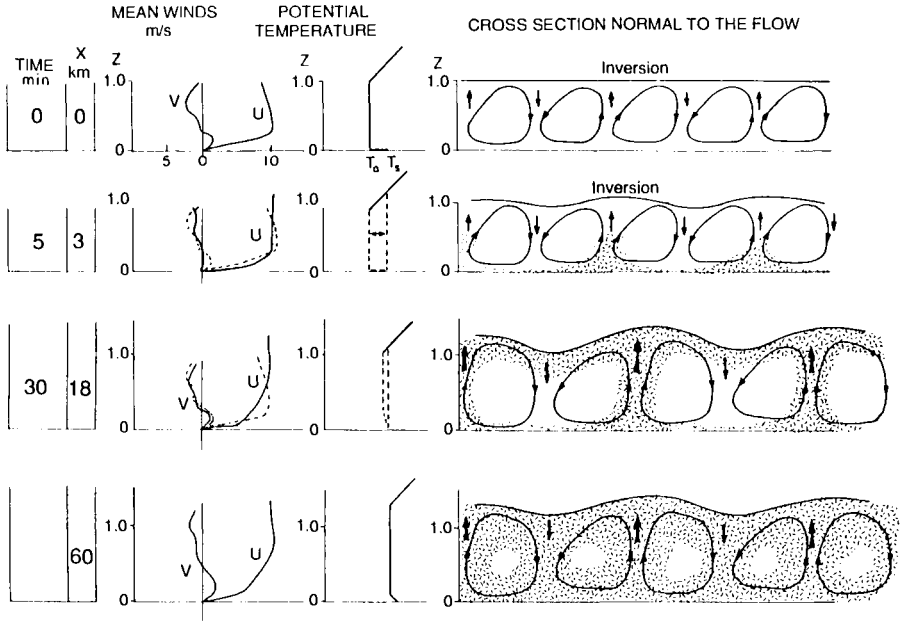

Figure 1.12 Downstream evolution of the PBL in a cold-air outbreak (as in Fig. 1.6). X, Distance from ice edge; Z is nondimensionalized with PBL height. Dashed profiles are point values within large eddies; solid profiles are mean values.

The large eddies obtained in the analytical large-eddy solution have been reproduced in a two-dimensional numerical model. This model is able to show the changing nature of the eddies as surface heating modifies the layer (Sykes *et al.*, 1988). The very large heat flux observed in these events is a possible source of energy for the sudden storms which form in polar oceanic regions. These storms have been the subject of extensive analysis (see the issue of *Tellus,* Vol. 39A, 1987) and are an important feature of high-latitude weather.

V. Remote Sensing

Although they are somewhat remote from the surface, aircraft measurements of fluxes that take place in the PBL have been discussed as surface measurements. Here, we refer to satellite sensing of PBL parameters. In particular, scatterometer measurements are discussed here because they

function as an anemometer over the ocean and provide the basis for future large-scale ocean PBL measurements. The scatterometer is an active microwave sensor which takes two views of the same wave field and determines the wind vector (Brown *et al.*, 1982; Brown, 1986). From these wind fields one can obtain the surface pressure field comparable to National Weather Service analyses (Brown and Levy, 1986) using an inverted version of the similarity model discussed above.

All microwave satellite measurements produce wind speeds with fair accuracy close to the edge of the pack ice, as long as the footprint does not include pack ice. The footprint is typically 25–50 km, so that mesoscale wind fields are determined up to the MIZ. The major correction for stress parametrizations, due to the stratification effect, requires air–sea temperature differences. The sea surface temperature can be measured by satellite. However, air temperatures over the ocean and over the ice must still be determined with *in situ* buoys for the foreseeable future.

The proposed ERS-1 (1990), NSCAT (1995), and EOS (1998) scatterometers will allow complete documentation of weather to the ice edge on a daily basis. The challenge of extending the remotely sensed oceanic wind measurements to the winds over the pack ice may be met by inferring stress from satellite measurements of pack ice drift (and hence winds, by inverting the drag coefficient relation). This capability places more emphasis on establishing good flux coefficients in the polar regions.

Other microwave instruments which measure small-scale roughness of the ocean can be used to infer wind stress magnitude but not direction. One impediment to determining stress and heat fluxes from satellite measurements is the lack of correlating surface data to establish the algorithm. Currently available wind speeds inferred from (SSM/I sensor) microwave radiometers can be used in models to produce heat fluxes and, with ancillary data, air stress vectors over the ocean. The intervention of pack ice eliminates this wave-to-wind correlation, and the stress and heat fluxes over the ice must be determined in other ways.

There has been significant progress in determining pack ice motion from SAR and AVHRR imaging (Emory *et al.*, 1986; Martain and Rothrock, 1986). These sensors and their successors offer potential for determining polar ocean sea and ice temperatures, cloud cover, and ice concentration and motion. These data can then be used to determine surface winds and heat and radiation fluxes.

Meteorology based on satellite data is largely a promise at present. However, the prospects of dramatic increases in data for the polar ocean and pack ice are real and have great implications for capabilities of polar oceanography dynamics and thermodynamics.

VI. Large-Scale Interaction

The interaction between the ocean/ice and the atmosphere on large scales becomes important when season-to-season or climatic variations are considered. Unfortunately, on these scales the data base is sparse or completely absent. Satellite technology may ameloriate this lack in the next decade, but until then most of the analysis is qualitative. Nevertheless, some studies have been made which define the problems and present ideas for future analyses and applications. Other studies present provocative clues of important climate indicators arising from polar air–sea–ice interactions. In general, the success of the large-scale studies depends critically on the correct flux parametrizations and their extrapolation to large scales. Even when these are available, there must be adequate characterization of the large-scale mean flow field.

Significant year-to-year variations in sea ice extent have been observed since early whaling ship excursions. Attempts to correlate these variations with mean atmospheric or oceanic parameters have been limited by the insufficient ice edge record and by the lack of accurate mean atmospheric or oceanic measurements. Recently, the ice edge has been delineated by remote microwave sensors. The ice edge record is expected to be defined routinely and accurately by such sensors in the future. The most likely candidate atmospheric parameter for correlation with ice extent is the sea level pressure field.

Surface pressure maps have long been a basic tool of weather and climate analyses. The National Weather Service routinely produces surface weather maps globally every 6 h on approximately 400-km grids. Although these are produced for polar regions, indications are that there is little skill in these fields for sparsely observed regions (Albright, 1980; Levy and Brown, 1989). The Arctic data buoy project has placed pressure-measuring buoys over the pack ice (1979–1989) and has greatly improved the large-scale pressure fields. Thorndike and Colony (1982) produced space and time statistical studies of Arctic surface pressure fields based on these data. However, the historic pressure fields have questionable merit for anything but very approximate climate effect studies. This is true for even current southern hemisphere fields. Walsh (1986) studied the statistical predictability of Arctic sea ice extent using surface pressure and temperature fields and found only small value in the 1–2-month ice motion prediction. This is no worse than a prediction based on the atmospheric pressure field, and the correlation is often due to persistence. The annual variation in ice extent can be specified only within a fairly wide range in year-to-year and regional differences.

The basic tool for large-scale modeling of the atmosphere in the polar regions is the GCM. These models produce the analyzed surface pressure field at synoptic times and the forecast fields for various intervals. They produce numerical integrations of the equations of motion, the first law of thermodynamics, the equation of continuity, and the perfect gas law. In the atmosphere, the gravitational force and the vertical pressure gradient force are in approximate balance, so that only horizontal equations of motion are integrated. The details of modeling GCM dynamics can be found in Haltiner and Williams (1980). The model physics includes procedures for calculating cloud physics, radiative transfer processes, and transfers of momentum, mass, and heat between the ocean and atmosphere. The polar PBL scale of 100–1000 m is not resolved in most GCMs. Thus the fluxes are parametrized, generally with simple u^*/G and $H_0/(G\,\Delta T)$ relations which may vary with surface characteristics. However, the important variation with layer stratification is not usually included. In fact, these models have poor surface and near-surface temperature fields. Thus, conditions are not well represented in the polar night, where extreme stable stratification exists, and in ocean areas of cold-air outbreaks, where extreme unstable stratification exists.

Sea ice conditions are important to GCMs in several aspects. The albedo effect is significant in radiation calculations, but a single value is generally used for all ice and the entire spectrum. Corrections for solar angle are included empirically. The roughness, ice thickness, snow cover, and thermal properties are expected to be important in flux parametrizations. The internal ice stress and the oceanic stress (Chapters 6 and 7) are important in pack ice motion and ocean currents. However, in general, the sea ice characteristics are set and noninteractive with the atmospheric GCM flow.

Some GCMs have been used in research which specifically addresses the interaction between ocean, ice, and atmosphere (Saltzman, 1978; Hibler, 1980). For instance, the GCM at NASA's Goddard Laboratory for Atmospheric Study has been used in studying ice–climate interactions (Herman, 1986). However, it is apparently not possible to determine the effects of ocean temperature changes, ice edge variations, or other interactive physics in these models without a better base of measurements for comparison and boundary condition updating.

VII. Flux Coefficient Summary

A. Drag Coefficients

A plot of drag coefficients measured over sea ice in various experiments during the past 20 years has apparently shown an "increase of drag coeffi-

cient with time" (Fig. 1.13), although this is evidently a result of measurements being taken over increasingly rough ice, with increasingly unstable stratification, and with better accuracy. In addition, possible effects of baroclinicity and wind speed contribute to uncertainty in measurements.

Overland (1985) made a comprehensive survey of measured drag coefficients over ice and the MIZ. This included over 45 values for C_D and an additional 15 for C_G. It is evident that most measurements are subject to various undocumented effects which produce a wide spread in values. In addition to the intrinsic error discussed by Blanc (1987), there are physical effects that cannot be evaluated because of insufficient data. These include the following.

1. *Stratification:* This has the largest effect on momentum (stress) variations but only recently has been diligently measured as an important parameter. PBL dynamics, particularly the character of the large eddies, changes with stratification. Parametrization suffers from the lack of an obvious or easy-to-measure stratification parameter.
2. *Roughness:* This important character of the surface is only qualitatively available. Rarely is a spectrum of roughness measured, and then not in conjunction with comparably scaled surface flux measurements. The surface roughness parameter z_0 is an artifact of the surface layer approximation, yet it remains the most widely used roughness

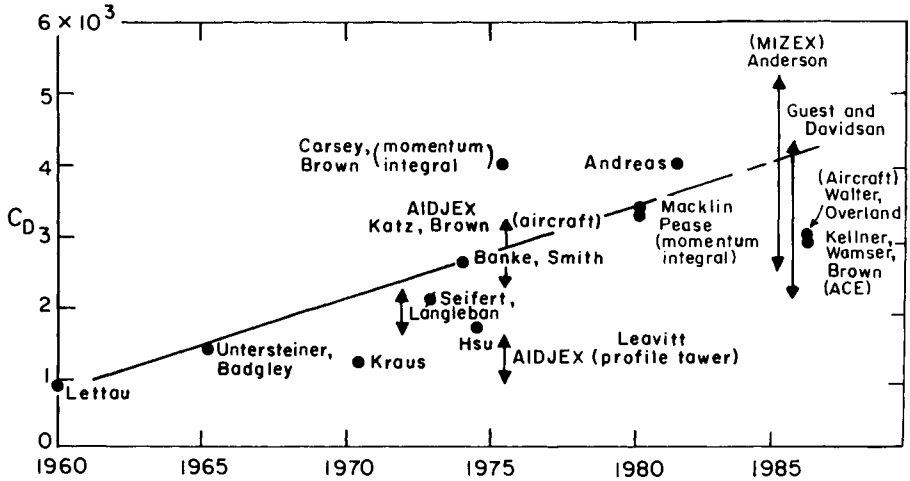

Figure 1.13 Drag coefficients over ice from various experiments. Names given after about 1975 are discussed in the text; prior to 1975, names are given for historical reference only.

parameter. Over the ocean, feedback between roughness and wind speed is a necessary part of any model.

3. *Averaging:* Fluxes depend on averaging correlations which can be locally variable, especially in the MIZ. Aircraft C_D values were generally higher than camp values in the central Arctic, since they included lead and ridge effects which did not appear in smooth-floe camp data. However, aircraft values are often smaller over the MIZ, reflecting spatial averaging compared with the data from locally rough ship environments.
4. *Wind magnitude:* The drag is not necessarily a quadratic function of the wind, and PBL dynamics may change with wind speed. With moderate to high winds the drag coefficient appears to increase linearly with wind speed.
5. *Baroclinicity:* This can influence the geostrophic values when there is a significant horizontal air temperature gradient and the PBL is deep. It will affect the differences in direction between geostrophic and surface stress vectors.
6. *Local nonequilibrium:* Surface measurements taken at a point may be buried in a sublayer of the boundary layer, depending on the stratification, which is representative of conditions no more distant than 100 times the height of the measurement. Also, the presence of large eddies produces error in point or short-term measurements taken through the depth of the PBL.
7. *Inversions:* A temperature inversion represents a cap on the PBL, the stably stratified layer inhibiting mixing between the PBL and the free layer. Such a lid may be imposed by large-scale (synoptic) conditions. Overland (1985) has found this to be a significant parameter.
8. *Latitude:* There is a small effect in PBL dynamics from variation of the Coriolis force. This is minimized when consideration is restricted to the polar regions.
9. *Surface temperature magnitude and humidity:* These have very small effects on stress values and are probably insignificant in polar measurements. However, over and near leads there is significant latent and sensible heat flux. These parameters are needed in these areas.

The result of these caveats is a drag coefficient which has an error bar of about 50–100%. The uncertainty in heat fluxes is about double this. The important stratification and roughness parameters remain qualitative only. Nonetheless, the need for stress and heat flux parametrizations requires a state-of-the-art list. Using the similarity model to extrapolate between measurements yields the basic variations in C_D given in Figs. 1.14 and 1.15. These graphs should be interpreted to give order-of-magnitude estimates and

trends only. The errors will be less in applications to long-time, large-scale averages and uniform-flow domains. For dynamically and thermodynamically active regions, and as scales being considered become smaller, the drag values become more qualitative.

In Fig. 1.14, the geostrophic forcing is 10 m/s and the latitude is 60°. The drag coefficient goes up with increased roughness parameter, more so in unstable stratification due to changing wind profiles. The effect of wind magnitude is shown in Fig. 1.15. Lower winds have higher drag coefficients (but not necessarily higher drag) in unstable stratification and vice versa in stable stratification. In some cases the extrapolated conditions are not often seen. For instance, low winds generally correlate with stable stratification regimes, while strong winds tend toward well-mixed, neutral layers. The trends are as expected; a rougher surface or unstable stratification produces increased turbulence and more efficient momentum flux to the surface. The C_D over the ocean, with variable roughness, is similar to that over a solid surface with $z_0 = 0.02$ cm. When there is high humidity, as over the sea, the curves are shifted to the left by the equivalent of about 0.7°. This is due to the increased buoyancy of the moist parcels. It is evident that the trend in Fig.

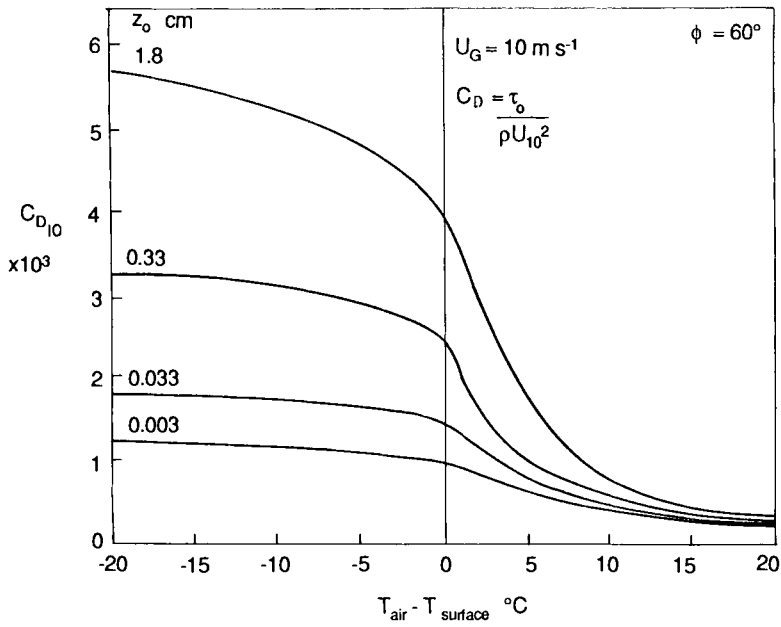

Figure 1.14 Drag coefficient versus stratification for various G ($\equiv U_G$) and z_0 for rough ice.

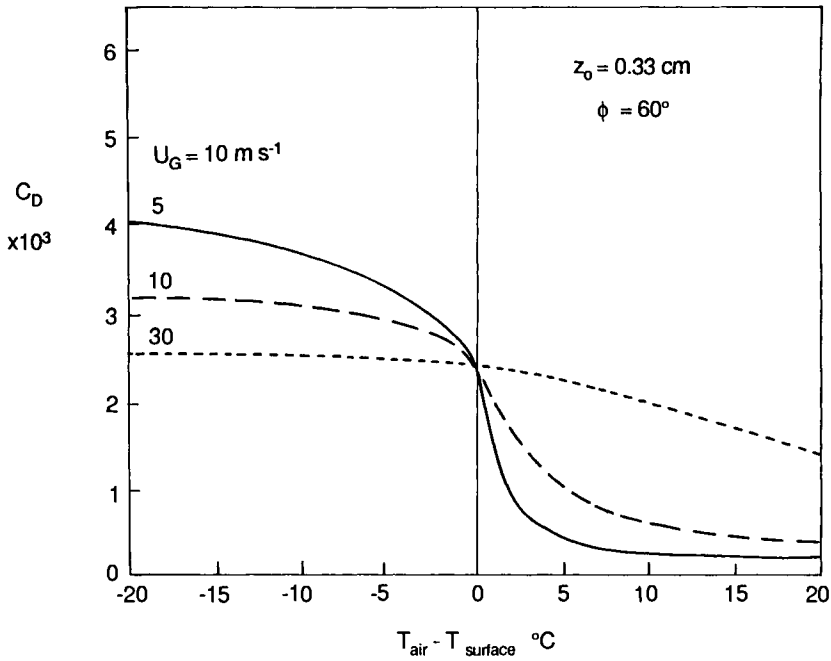

Figure 1.15 Drag coefficient as a function of stratification for various roughnesses.

1.13 is a result of the progress toward measurements with greater z_0 and, in the case of MIZ measurements, moving from right to left in Figs. 1.14 and 1.15 with respect to stratification.

Gross averages of several basic parameters for the various regions of pack ice and MIZ are given in Table 1.2. The ice edge may consist of rafted and broken-up ice alternating with water. The MIZ plates are rough regions, with greater than 90% ice coverage. The ocean PBL which is unaffected by pack ice air can have variable stratification from unstable to stable (Brown and Liu, 1982).

B. Heat Flux Summary

Heat flux parametrization requires good high-frequency wind and temperature measurements, a mean wind, and a reference air–surface temperature difference. The sensible heat flux is

$$H_0 = \rho c_p \overline{w'T'} \equiv -C_H \rho c_p U_{10}(T_a - T_S) \tag{1.34}$$

where H_0 is positive upward and the reference height is 10 m.

Table 1.2 Average Values of Boundary Layer Parameters in Polar Regions for $U_{10} \approx 10$ m/s[a]

Region	Stratification	z_0 (cm)	α (deg)	$\frac{u^*}{G}$	$C_D \times 10^3$	$\frac{U_{10}}{G}$	τ_0 (dyn/cm^2)
Ocean near MIZ	N–U	0.001–0.015	20–5	0.03–0.045	1–2	0.7–0.8	1–2
Ice edge	N–U	10–1	25–10	0.035–0.045	3–5	0.6–0.7	2–4
MIZ plates	N–U	1.0–0.01	20–10	0.03–0.04	2.5–3.5	0.6–0.7	2–2.8
Pack ice (smooth–rough)	S–N	0.001–0.1	30–20	0.02–0.03	1.3–2.3	0.5–0.6	1.0–2.5

[a] Stratification indicates the usual range found in the region: U, unstable; N, neutral; S, stable. Increased roughness, increased wind speed, and unstable stratification (operating independently) increase turbulent mixing, which results in higher values of u^*/G, C_D, U_{10}/G, and τ_0 and a lower value of α.

In addition, turbulent fluxes of sensible and latent heat in polar regions are strongly dependent on the surface characteristics, namely ice thickness and snow cover. They are generally too small to be measured over thick pack ice, significant over thin ice (less than 1 m thick), and up to 2 or 3 orders of magnitude greater over open water (leads and polynyas). In regions covered by thick ice, turbulent fluxes are best estimated using models of ice growth and ice thickness distribution (Maykut, 1978, 1982). In winter, the latent heat flux from thick ice is small [approximately 15–20 W/m^2 downward according to Maykut (1986)]. Sensible heat fluxes from open water and ice with thickness less than 50 cm are large in winter and are directed into the atmosphere. Those from multiyear ice are much smaller in magnitude and oppositely directed.

In winter, sensible and latent heat fluxes are huge (600 W/m^2 and 150 W/m^2, respectively) compared to average fluxes over pack ice. Yet the areal ratio of leads to pack ice is so small (usually less than a few percent) that the heat flux through pack ice may dominate on synoptic scales. However, recent aircraft lidar measurements suggest that the plume from wide (greater than 1 km) leads may reach several kilometers in height and extend hundreds of kilometers downwind (Schnell *et al.*, 1989). These observations indicate that the episodic heat transfer potential from leads needs more investigation. These heat sinks for the ocean must have significant local effects on oceanic circulation and mixing.

In summer, the sensible heat flux is small while the latent flux from open water and melt ponds on the pack ice can be significant. Currently, transfer coefficients must be inferred (extrapolated) either from lower latitude data or from ocean and ice models that yield surface fluxes.

Some heat flux measurements have been made beside an Arctic lead (Andreas *et al.*, 1979). Andreas and Murphy (1986) list $C_H = 2.5 \times 10^{-3}$ and $C_E = 3.0 \times 10^{-3}$ for values downstream from a narrow (less than 50 m) lead in low-wind conditions. The ratio of sensible to latent heat flux, the Bowen ratio,

$$\text{Bo} = (\rho c_p \overline{w'T'} / \rho L_E \overline{w'q'}) \tag{1.35}$$

was about 3 for these special conditions of very cold dry air suddenly exposed to relatively warm water. Andreas and Murphy (1986) have presented a scheme for calculating bulk flux coefficients over leads and polynyas.

Measurements have been made near a polynya in the Canadian archipelago (Smith *et al.*, 1983; den Hartog *et al.*, 1983). The heat flux coefficients depend on stratification and wind speed. Values for $C_H \approx C_E = 2.2 - 1.3 \times 10^{-3}$ as wind speed increases are found for the unstably stratified, very large fetch cases, whereas $C_H = 1.1 \times 10^{-3}$ is found for neutral stratification. In this experiment Bo ≈ 4. The discrepancy in flux coefficients probably results from different stratification and/or roughness characteristics in the experiments. The ratio of latent to sensible heat flux coefficients, C_E/C_H, has not been determined. Evidence over the ocean suggests a value of 1.3 (Friehe and Schmitt, 1976). However, Smith *et al.* (1983) use 1.0. Pease (1987) found surface Bo ≈ 4 in high-wind conditions over the St. Lawrence Island polynya and $C_H = 0.0056$.

The general behavior of the heat flux coefficients is consistent with trends modeled for C_D, taking into account that heat flux coefficients are nondimensionalized with U, compared to U^2 for C_D. As a first approximation the heat flux coefficients are frequently simply taken from the drag coefficient using the ratios from Walter and Overland, 1984,

$$C_H/C_D \approx 0.24 \approx C_E/C_D \tag{1.36}$$

The ratios are dependent on the surface roughness, as suggested in controlled roughness experiments by Owen and Thomson (1963) and over ice by Joffre (1982) and Walter *et al.* (1984). The range for smooth to rough ice appears to be

$$0.1 \leq C_H/C_D \leq 0.3 \tag{1.37}$$

Aircraft measurements have been made over the pack ice; however, the heat flux signal is small and few definitive values have been found. Measurements during AIDJEX suggested a value of $C_H = 0.2 \times 10^{-3}$ over pack ice in neutral to slightly stably stratified conditions.

Over the MIZ and nearby ocean in cold-air outbreaks, the heat fluxes are significant and important in weather and oceanic phenomena. Aircraft measurements are discussed briefly in Walter *et al.* (1984), where extrapolated

surface values are $C_H \approx 0.8 \times 10^{-3}$, Bo = 2.8, and $C_H/C_D \approx 0.24$. The low values of the heat flux coefficient are a consequence of increased roughness greatly increasing the surface stress, with a smaller effect on the heat flux. Aircraft values of $C_H \approx 2-2.8 \times 10^{-3}$ over the MIZ (Kellner *et al.*, 1987) and $0.8-1.3 \times 10^{-3}$ in a cold-air outbreak (Hein and Brown, 1988) have been measured. The variation in heat flux with fetch in the cold-air outbreak can be very strong (Fig. 1.16). These values are hundreds of watts per square meter, compared with average fluxes over the solid pack ice during AIDJEX of less than 10 W/m^2. These and other heat flux measurements were considered in the model parametrization shown in Fig. 1.17. Very few heat flux measurements exist, and the trends shown are based on C_H behaving like C_D in the models.

C. Radiation and Clouds

The polar regions are the heat sink in the earth's radiation balance. Given temperature and optical properties of the surface, radiative fluxes are easily

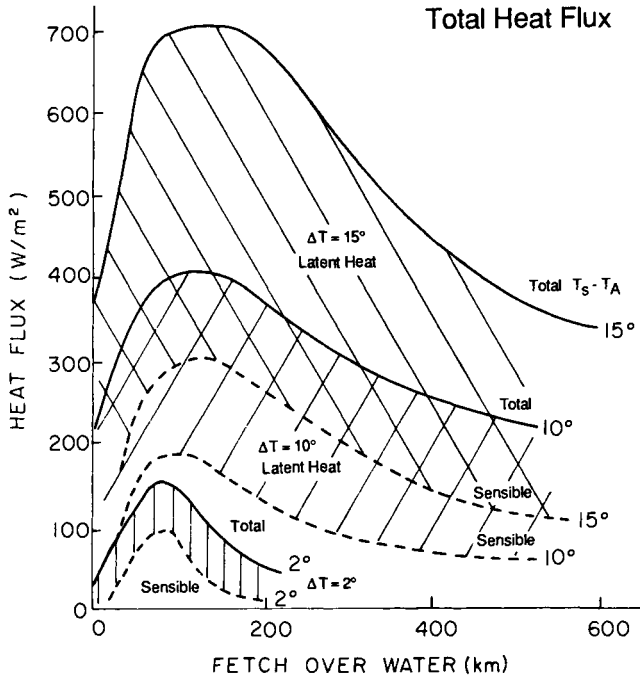

Figure 1.16 Heat fluxes downstream from the ice edge in a cold-air outbreak from the Arctic Cyclone Experiment. (Dashed curves) sensible heat flux; (hatching) latent heat flux; (solid curves) total heat flux.

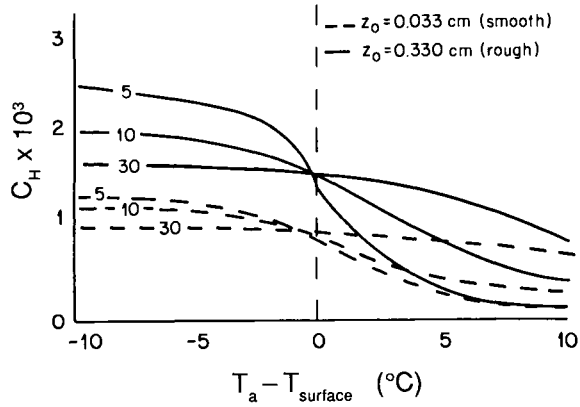

Figure 1.17 Heat flux coefficient versus stratification for $G \equiv U_G = 5$, 10, and 30 m/s and z_0 values corresponding to smooth and rough surfaces.

calculated, including solar zenith angle effects. The optical properties of polar atmospheres and the surface are variable. There is a large difference in albedo between ice and water (Grenfell and Maykut, 1977), and there are significant differences for different types of ice. These are relatively well known, and the problem is mainly one of specifying the surface categories and regional distributions. The effects of snow cover and cloud cover on albedo are not so well known, however. The MIZ dynamics are important in determining the extent of ice cover and rate of change (breakup and freezing) of ocean/ice distribution. The availability of solar irradiance is important to biological production.

The solar and thermal heating rates are very large in polar regions. These terms are well understood and problems arise mainly from cloud or moisture effects on optical properties (Herman, 1986). Maykut (1986) summarized the incoming/outgoing (positive) long-wave radiation (430 – 800 MJ/m^2 per month) for pack ice, as well as the solar short-wave radiation (−500 to −835), and showed that the turbulent heat fluxes (−30 to 40) are not insignificant beside the net radiation (−85 to 210). The typical range of total albedo for the summer season was given by Grenfell and Maykut (1977) and is shown in Table 1.3.

The presence of clouds has an important influence on heat fluxes and light transmission. Stratus clouds reduce solar radiative fluxes by over 50%. At the same time, the IR fluxes below the cloud are increased. The net effect may be small as the albedo and temperature of the stratus clouds may be similar to that of the pack ice. The reflectance from and cooling of the top of the clouds have been measured with aircraft, and the general heat and moisture budgets have been discussed by Curry and Herman (1985) and Curry (1986).

Table 1.3 Total Albedo for Different Ice Types and Cloud Covers, Summer Season[a]

Ice type	Clear	Overcast
Old snow	0.63	0.77
White ice	0.56	0.70
First-year blue ice	0.25	0.32
Mature melt pond	0.22	0.29

[a] After Grenfell and Maykut (1977).

Heat flux and radiation are very important terms in the climatic energy budget. The theory involving turbulent transport mechanisms and the measurements for parametrization schemes are largely unavailable. There are prospects for remote sensing of surface temperatures, pressures, clouds, and winds over water. However, air temperature (or air–surface difference) must still be obtained *in situ*. High-frequency flux measurements will remain rare, with parametrizations dependent on theoretical modeling and extrapolation from measurements at lower latitudes.

VIII. Conclusions

Air–sea interaction meteorology in polar regions has made great progress in the past two decades. Polar regions, with their great uniformity and sharp discontinuity at the ice edge, present relatively straightforward dynamics compared to the PBL over land. The measurement programs in AIDJEX and the MIZEX experiments have provided new knowledge about basic PBL dynamics and flux mechanisms. The drag coefficients have been found to be much larger than originally proposed. The importance of stratification and inversion dynamics has emerged. There is a need for programs to measure the parameters needed to determine these effects quantitatively.

The direction of polar meteorology is currently toward incorporating the great capabilities of satellite data (promised by the Earth Observing System of the 1990s) into well-parametrized surface flux parameters. As scales of interest continually decrease, from 400-km grids to 50-km grids and less, the regional variations in the ocean–pack ice surface will require increasingly accurate measurements for parametrization schemes.

There are exciting prospects for measuring the stress vector over the oceans directly with microwave satellite measurements. Unfortunately, after the success of the short-lived Seasat scatterometer in 1978, there have been

no follow-on satellite scatterometers. This will be remedied when the European Space Agency ERS-1 satellite is launched in 1990.

Meteorology in the polar regions has mixed attributes. It is evident that there is a dearth of measurements and that all modeling schemes rely on semiempirical parametrizations. The theoretical aspects of the modeling are often satisfied better in polar regions than in lower latitudes; however, the measurement environment is considerably worse. The net result is better meteorology and parametrizations in some domains and worse in others. The oceanographer must carefully consider the region of interest, the mitigating effects, and the corresponding error bars on atmospheric parameters.

Acknowledgment

Partial support during research for this chapter was furnished by grant NSF-ATM-8912270.

References

Albright, M. 1980. Geostrophic wind calculations for AIDJEX. *In* "Sea Ice Processes and Models" (R. Pritchard, ed.), pp. 402–409. Univ. of Washington Press, Seattle.

Anderson, R. J. 1987. Wind stress measurements over rough ice during the 1984 Marginal Ice Zone experiment. *J. Geophys. Res.* **92**: 6933–6941.

Andre, J. C., G. Wendler & M. Zephoris. 1986. The IAGO katabatic programme. *Antarct. Clim. Res.* May: 17–18.

Andreas, E. L. & B. Murphy. 1986. Bulk transfer coefficients for heat and momentum over leads and polynyas. *J. Phys. Oceanogr.* **16**: 1875–1883.

Andreas, E. L., C. A. Paulson, R. M. Williams, R. W. Lindsay & J. A. Businger. 1979. The turbulent heat flux from Arctic leads. *Boundary-Layer Meteorol.* **17**: 57–91.

Andreas, E. L., W. B. Tucker III & S. F. Ackley. 1984. Atmospheric boundary-layer modification, drag coefficient, and surface heat flux in the Antarctic Marginal Ice Zone. *J. Geophys. Res.* **89**: 649–661.

Arya, S. P. S. 1975. Geostrophic drag and heat transfer relation for the atmospheric boundary layer. *Q. J. R. Meteorol. Soc.* **101**: 147–161.

Bennett, T. J., Jr. & K. Hunkins. 1986. Atmospheric boundary layer modification in the marginal ice zone. *J. Geophys. Res.* **91**: 13033-13045.

Blanc, R. V. 1987. Accuracy of bulk-method-determined flux stability, and sea surface roughness. *J. Geophys. Res.* **92**: 3867–3876.

Bromwich, D. H. & D. D. Kurtz. 1984. Katabatic wind forcing of the Terra Nova Bay polynya. *J. Geophys. Res.* **89**: 3651–3572.

Brown, R. A. 1970. A secondary flow model for the planetary boundary layer. *J. Atmos. Sci.* **27**: 742–757.

———. 1972. The inflection point instability problem for stratified rotating boundary layers. *J. Atmos. Sci.* **29**: 850–859.

———. 1973. "Analytic Methods in Planetary Boundary Layer Modeling." Wiley, New York.

———. 1974. A simple momentum integral model. *JGR, J. Geophys. Res.* **79**: 4076–4079.

———. 1980. Longitudinal instabilities and secondary flows in the planetary boundary layer: A review. *Rev. Geophys. Space Phys.* **18**: 683–697.

———. 1986. Satellite scatterometer capabilities in air–sea interaction: Review of the status and the possibilities. *J. Geophys. Res.* **91**: 2221–2232.

Brown, R. A. & G. Levy. 1986. A simple objective analysis scheme for scatterometer data. *J. Geophys. Res.* **91**: 5153–5158.

Brown, R. A. & T. Liu. 1982. An operational large-scale marine planetary boundary layer model. *J. Appl. Meteorol.* **21**: 261–269.

Brown, R. A., V. J. Cardone, T. Guymer, J. Hawkins, J. E. Overland, W. J. Pierson, S. Peteherych, J. C. Wilkerson, P. M. Woiceshyn & M. Wurtele. 1982. Surface wind analyses for SEASAT. *J. Geophys. Res.* **87**: 3355–3364.

Budd, W. F. 1975. Antarctic sea-ice variations from satellite remote sensing in relation to climate. *J. Glaciol.* **15**: 417–427.

Carsey, F. D. 1980. The boundary layer height in air stress measurement. *In* "Sea Ice Processes and Models" (R. Pritchard, ed.), pp. 443–452. Univ. of Washington Press, Seattle.

Cavalieri, D. J. & C. L. Parkinson. 1981. Large-scale variations in observed Antarctic sea ice extent and associated atmospheric circulation. *Mon. Weather Rev.* **109**: 2323–2336.

Clark, R. H. 1970. Observational studies in the atmospheric boundary layer. *Q.J.R. Meteorol. Soc.* **96**:91–114.

Clark, R. H. & G. D. Hess. 1974. Geostrophic departure and the functions A and B of Rossby-number similarity theory. *Boundary-Layer Meteorol.* **7**:267–287.

Crane, R. G. 1978. Seasonal variations of sea ice extent in the Davis Strait–Labrador Sea area and relationships with synoptic-scale atmospheric circulation. *Arctic* **31**: 434–447.

———. 1986. Interactions between turbulence, radiation and microphysics in Arctic stratus clouds. *J. Atmos. Sci.* **43**: 90–106.

Curry, J. A. & G. F. Herman. 1985. Relationships between large-scale heat and moisture budgets and the occurrence of Arctic stratus clouds. *Mon. Weather Rev.* **113**:1441–1457.

den Hartog, G., S. D. Smith, R. J. Anderson, D. R. Topham & R. G. Perkin. 1983. An investigation of a polynya in the Canadian archipelago. 3. Surface heat flux. *J. Geophys. Res.* **88**: 2911–2916.

Egorov, K. L., D. L. Laikhtman & V. M. Radikevich. 1974. Ice cover as a link in the ocean–atmosphere system. *Boundary-Layer Meteorol.* **6**: 169–182.

Ekman, V. W. 1905. On the influence of the earth's rotation on ocean currents. *Ark. Mat., Astron. Fys.* **2**: 1–52.

Enory, W. J., A. C. Thomas, M. J. Collins, W. R. Crawford & D. L. Mackas. 1986. An objective method for computing advective surface velocities from sequential IR satellite images. *J. Geophys. Res.* **91**: 12865–12878.

Friehe, C. A. & K. F. Schmitt. 1976. Parameterization of air–sea interface fluxes of sensible heat and moisture by the bulk aerodynamic formulas. *J. Phys. Oceanogr.* **6**: 801–809.

Grenfell, T. & G. Maykut. 1977. The opical properties of ice and snow in the Arctic basin. *J. Glaciol.* **18**: 445–464.

Guest, P. S. & K. L. Davidson. 1987. Wind stress measurements over rough ice during the 1984 MIZ experiment. *J. Geophys. Res.* **92**: 6833–6941.

Haltiner, G. F. & R. T. Williams. 1980. "Numerical Predictions and Dynamic Meteorology." Wiley, New York.

Hein, P. & R. A. Brown. 1988. An analysis of the secondary circulations in the boundary layer flow in cold air outbreaks. *Boundary-Layer Meteorol.* **45**: 177–199.

Herman, G. F. 1986. Atmospheric modelling and air–sea–ice interaction. *In* "Geophysics of Sea Ice" (N. Untersteiner, ed.), pp. 713–754. Plenum, New York.

Herman, G. F. & W. T. Johnson. 1978. The sensitivity of the general circulation to Arctic sea ice boundaries: A numerical experiment. *Mon. Weather Rev.* **106:** 1649–1664.

Hibler, W. D., III. 1980. Modeling a variable thickness sea ice cover. *Mon. Weather Rev.* **108:** 1943–1973.

Joffre, S. M. 1982. Momentum and heat transfers in the surface layer over a frozen sea. *Boundary-Layer Meteorol.* **24:** 211–229.

Kellner, G., C. Wamser & R. A. Brown. 1987. An observation of the planetary boundary layer in the Marginal Ice Zone. *J. Geophys. Res.* **92:** 6955–6965.

Kostadinov & Dzholov. 1977. The universal functions in the resistance and heat exchange laws for the Ekman boundary layer. *Izv. Atmos. Ocean Phys.* **13:** 673–675.

Lemke, P. 1986. Stochastic description of atmosphere–sea ice–ocean interaction. *In* "Geophysics of Sea Ice" (N. Untersteiner, ed.), pp. 785–824. Plenum, New York.

Lemke, P., E. W. Trinkl & K. Hasselmann. 1980. Stochastic dynamic analysis of polar sea ice variability. *J. Phys. Oceanogr.* **10:** 2100–2120.

Levy, G. & R. A. Brown. 1989. Meteorological application of remote sensing over the southern ocean. Reprints from Third International Conference on Southern Hemisphere Meteorology and Oceanography, Nov. 13–17, Buenos Aires, Argentina. American Meteorol. Soc. pp. 286–288.

Macklin, A. 1983. Wind drag coefficient over first-year sea ice in the Bering Sea. *J. Geophys. Res.* **88:** 2845–2952.

Martain, S. & D. A. Rothrock. 1986. Extracting sea ice data from satellite SAR imagery. *IEEE Trans. Geosci. Remote Sensing* **GE-24**(6): 849–854.

Maykut, G. A. 1978. Energy exchange over young sea ice in the central Arctic. *J. Geophys. Res.* **83:** 3646–3658.

———. 1982. Large-scale heat exchange and ice production in the central Arctic. *J. Geophys. Res.* **87:** 7971–7984.

———. 1986. The surface heat and mass balance. *In* "Geophysics of Sea Ice" (N. Untersteiner, ed.), pp. 395–464. Plenum, New York.

McBean, G. A. 1986. The atmospheric boundary layer. *In* "Geophysics of Sea Ice" (N. Untersteiner, ed.), pp. 283–338. Plenum, New York.

Moritz, R. E. 1983. Accuracy of surface geostrophic wind forecasts in the central Arctic. *Mon. Weather Rev.* **111:** 1746–1758.

———. 1986. Accuracy of wind forecasts in the central Arctic. *In* "Geophysics of Sea Ice" (N. Untersteiner, ed.), pp. 1135–1162. Plenum, New York.

Mourad, P. & R. A. Brown. 1990. Multiscale large eddy states in weakly stratified planetary boundary layer. *J. Atmos. Sci.* **47:** 414–438.

Niebauer, J. 1980. Sea ice and temperature variability in the eastern Bering Sea and the relation to the atmospheric fluctuations. *J. Geophys. Res.* **85:** 7507–7516.

Overland, J. E. 1985. Atmospheric boundary layer structure and drag coefficients over sea ice. *J. Geophys. Res.* **90:** 9029–9040.

Overland, J. E. & C. H. Pease. 1982. Cyclone climatology of the Bering Sea and its relation to sea ice extent. *Mon. Weather Rev.* **110:** 5–13.

Overland, J. E., R. M. Reynolds & C. H. Pease. 1983. A model of the atmospheric boundary layer over the MIZ. *J. Geophys. Res.* **88:** 2836–2840.

Owen, P. R. & W. R. Thomson. 1963. Heat transfer across rough surfaces. *J. Fluid Mech.* **15:** 321–334.

Paulson, C. A. 1970. The mathematical representation of wind speed, and temperature profiles in the unstable atmospheric surface layer. *J. Appl. Math.* **9:** 857–861.

Pease, C. H. 1987. The size of wind-driven coastal polynyas. *J. Geophys. Res.* **92:** 7040–7059.

Pease, C. H., S. A. Salo & J. E. Overland. 1983. Drag measurements for first-year sea ice over a shallow sea. *J. Geophys. Res.* **88:** 2853–2862.

Prandtl, L. 1904. Uber flussigkeitsbewegung bei sehr kleiner reibung. *Proc. Int. Math. Congr., 3rd,* Heidelberg.

Pritchard, R. S. (ed.). 1980. "Sea Ice Processes and Models." Univ. of Washington Press, Seattle.

Radok, U. 1979. Polar meteorology and climatology 1975–78. *Rev. Geophys. Space Phys.* **17:** 489–506.

Røed, L. P. & J. J. O'Brien. 1983. A coupled ice–ocean model of upwelling in the MIZ. *J. Geophys. Res.* **88:** 2863–2872.

Rogers, J. C. 1978. Meteorological factors affecting interannual variability of summertime ice extent in the Beaufort Sea. *Mon. Weather Rev.* **106:** 890–897.

Saltzman, B. 1978. A survey of statistical–dynamical models of the terrestrial climate. *Adv. Geophys.* **20:** 184–295.

Schnell, R. C., R. G. Barry, M. W. Miles, E. L. Andreas, L. F. Radke, C. A. Brock, M. B. McCormick & J. L. Moore. 1989. Lidar detection of leads in Arctic sea ice. *Nature (London)* **339:** 530–532.

Schwerdtfeger, W. 1979. Meteorological aspects of the drift of ice from the Weddell Sea toward the mid-latitude westerlies. *J. Geophys. Res.* **84:** 6321–6328.

Schwerdtfeger, W. & S. J. Kachelhoffer. 1973. The frequency of cyclonic vortices over the southern ocean in relation to the extension of the pack ice belt. *Antarct. J. U.S.* **8:** 234.

Smith, S. D., R. J. Anderson, G. D. Hartog, D. R. Topham & R. G. Perkin. 1983. Air investigation of a polynya in the Canadian archipelagos: Structure of turbulence and heat flux. *J. Geophys. Res.* **88:** 2900–2910.

Stearns, C. R. 1984. Antarctic automated weather stations, austral summer 1983–1984. *Antarct. J. U.S.* **19:** 189–190.

Sykes, R. I., W. S. Lewellen & D. S. Henn. 1988. A numerical study of the development of cloud-street spacing. *J. Atmos. Sci.* **45:** 2556–2569.

Thorndike, A. S. & R. Colony. 1982. Sea ice motion in response to geostrophic winds. *J. Geophys. Res.* **87:** 5845–5852.

Vinje, T. E. 1977. Sea ice conditions in the European sector of the marginal seas of the Arctic. 1966–1975. *Arbok, Nor. Polarinst., 1975:* 163–174.

Walker, G. 1974. Arctic conditions and world weather. *Q. J. R. Meteorol. Soc.* **73:** 226–256.

Walsh, J. E. 1978. Temporal and spatial scales of the Arctic circulation. *Mon. Weather Rev.* **106:** 1532–1544.

———. 1986. Diagnostic studies of large-scale air–sea–ice interactions. *In* "Geophysics of Sea Ice" (N. Untersteiner, ed.), pp. 755–784. Plenum, New York.

Walsh, J. E. & C. M. Johnson. 1979. Interannual atmospheric variability and associated fluctuations in Arctic sea ice extent. *J. Geophys. Res.* **84:** 6915–6928.

Walsh, J. E. & J. E. Satler. 1981. Monthly and seasonal variability in the ocean–ice–atmosphere systems of the North Pacific and North Atlantic. *J. Geophys. Res.* **86:** 7425–7445.

Walter, B. A. & J. E. Overland. 1984. Observations of longitudinal rolls in near neutral atmosphere. *Mon. Weather Rev.* **112:** 200–208.

Walter, B. A., J. E. Overland & R. O. Gilmer. 1984. Air–ice drag coefficients for first-year ice derived from aircraft measurements. *J. Geophys. Res.* **89:** 3550–3560.

Wendler, G., Y. Kodama & J. Gosink. 1986. Automatic weather stations in Eastern Antarctica. *Antarctic Journal,* 1985 Review.

2 Sea Ice in the Polar Regions

Anthony J. Gow and Walter B. Tucker III
USA Cold Regions Research and Engineering Laboratory
Hanover, New Hampshire

I. Introduction 47
II. Large-Scale Ice Properties 49
A. Ice Growth and Decay 49
B. Ice Dynamics and Drift 59
C. Morphological Ice Features 65
D. Ice Thickness Distribution 71
E. Ice Extent and Zonation 75
III. Small-Scale Ice Properties 78
A. Ice Growth and Structure: General Considerations 78
B. Salinity of Sea Ice: General Considerations 88
C. Bipolar Comparisons of Sea Ice Salinity 92
D. Crystalline Structure of Polar Sea Ice 97
IV. Summary 116
References 117

I. Introduction

This chapter addresses characteristics of the floating ice covers on the polar oceans. These ice covers give rise to many unique conditions in the polar oceans and atmospheres. Volumetrically, the sea ice cover is almost negligible when compared to the ice contained in the earth's glacial ice masses. However, the sea ice covers an area that encompasses about two-thirds of the total permanent ice cover. Because sea ice is such a thin layer in contrast to the large area that it covers, small changes within the atmosphere or the ocean can cause major changes in the extent and thickness of the ice cover. Such changes, in turn, will have pronounced effects on the ocean and atmosphere through modification of the albedo, the ocean–atmosphere heat and momentum exchanges, and the oceanic salt flux.

Polar Oceanography, Part A: Physical Science

Sea ice in the polar oceans has been under scientific scrutiny for many years. However, research efforts in the past two decades have become considerably more focused on understanding specific aspects of sea ice. These studies have been stimulated by several factors. The identification of the floating ice covers as key elements in the ocean and climate systems, brought about by large-scale computer simulations, has prompted efforts to develop numerical models of sea ice behavior. Interest by several nations in exploring and developing mineral resources in ice-covered waters has stimulated much research dealing with the mechanical behavior of sea ice. The development of airborne and satellite-borne remote sensing instruments capable of all-weather, day-and-night surveillance of the ice cover has also stimulated many studies dealing with the electromagnetic properties of ice. Finally, the desire for commercial and strategic transportation on the surface and beneath the ice cover has resulted in research addressing the morphology and seasonal variations of sea ice extent and thickness. Significant progress in these areas of research has been made possible with the advent of efficient computer systems, state-of-the-art instrumentation, satellite technology, modern icebreakers, and improvements in logistics that enhance field studies.

In this chapter, we have attempted to review our current understanding of sea ice primarily as it pertains to oceanography. Therefore, we have purposely omitted any detailed discussions of mechanical and electromagnetic properties of sea ice. Section II deals with large-scale aspects of floating ice covers, from thermodynamic and dynamic behavior to specific ice features. Characteristics of Arctic and Antarctic sea ice are contrasted. Section III deals with small-scale properties, beginning with the freezing characteristics of seawater and progressing to the crystalline structure and salinity characteristics of sea ice. Again, specific features of the small-scale properties of the Arctic and Antarctic sea ice are compared.

A standard taxonomy for the classification of sea ice based on its stage of growth has been developed by the World Meteorological Organization (1956). Most of this terminology deals with very young ice, however. It is more common to refer to thicker ice (> 50 cm) as simply first-year or multiyear ice. The WMO definition of multiyear ice requires that it have survived two summers. The distinction between multiyear ice and second-year ice (ice that has survived only one summer) is subtle because, in the Arctic at least, one melt season is often sufficient to give the ice a characteristic surface relief appearance of alternating hummocks and melt ponds. Here, unless otherwise noted, we will make only the distinction between first-year ice and other ice that has survived one or more summers, which we will call multiyear ice.

II. Large-Scale Ice Properties

The mass balance of ice within a region is governed by the amounts of ice growth, ice ablation, and ice which drifts into or out of the area. In this section we will discuss large-scale ice growth, ice decay, and ice dynamics as they apply to the Arctic and Antarctic. Characteristic features of sea ice resulting from deformation will be touched upon. Finally, large-scale features of the variations in ice extent and zonation in both areas will be discussed.

A. Ice Growth and Decay

1. General considerations and Arctic implications

Once an initial ice sheet has formed, further ice growth or ablation is controlled by the energy balances at the upper and lower surfaces of the sheet. The balance at the upper surface, where the ice is in contact with the atmosphere, is approximated by

$$(1-\alpha)S - I + L_i - L_e + T_s + T_L + C_u - M = 0 \qquad (2.1)$$

where S is incoming shortwave (solar) radiation, α the albedo of the ice surface, I the flux of shortwave radiation which passes through the thin surface layer into the ice interior, L_i the incoming longwave radiation, L_e the longwave radiation emitted by the ice surface, T_s the sensible heat flux, T_L the latent heat flux, C_u the conducted heat flux at the upper surface, and M the amount of heat loss due to melting or sublimation at the surface. In Eq. (2.1) the signs of individual terms are positive if they represent a gain in energy by the ice surface and negative if they represent a loss.

On the underside of the ice, the energy balance can be represented by

$$Q_f + C_L + F_W = 0 \qquad (2.2)$$

where Q_f is the heat gain or loss due to freezing or melting on the bottom of the ice, C_L the conduction of heat away from the bottom toward the ice surface, and F_w the turbulent heat transfer between the ice and the ocean.

In numerical simulations of thermodynamic processes, Eqs. (2.1) and (2.2) are coupled by the heat conduction terms, C_u and C_L. These terms are considerably more complex than represented here, the primary complexity being introduced by the vertical temperature profile within the ice. If the temperature profile is nonlinear, a thermal diffusion equation must be implemented to calculate further changes in internal ice temperature. Most

large-scale models simplify the problem by using simpler estimates (often linear) of the temperature profile, thus reducing the numerical complexity.

Because major energy gains and losses occur at the ice surface, this balance will be considered first. Figure 2.1 shows average monthly values of the radiative fluxes (S, L_i, and L_e) over ice for the central Arctic basin (Maykut, 1985). In addition to the original estimates of the fluxes, we have shown the net solar radiation $[(1-\alpha)S]$, the net incoming and outgoing longwave radiation ($L_i + L_e$), and the total net radiation (R_{net}). Of the three basic radiative fluxes, the solar radiation clearly shows the largest seasonal variations. It varies from zero during winter months of total darkness to about

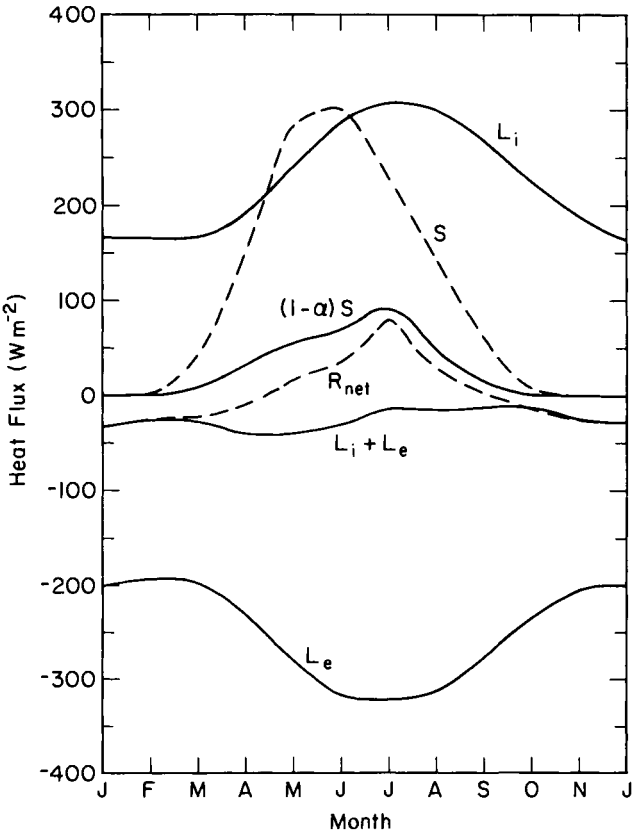

Figure 2.1 Average monthly values of radiative heat fluxes: L_i, Incoming longwave; L_e, outgoing longwave; S, shortwave; $(1-\alpha)S$, net shortwave input at the surface taking into account ice and snow albedo; $L_i + L_e$, net longwave; R_{net}, net radiative flux. Positive indicates a heat gain by the ice and negative indicates loss. From data of Maykut (1985).

300 W m^{-2} during summer solstice when the sun is continuously above the horizon. The pronounced effect of ice and snow albedo can be seen in the $(1 - \alpha)S$ curve. The peak absorption lags that of the incoming shortwave radiation by about a month because the albedo is steadily decreasing as a result of surface melting. The largest influences on the albedo reduction are caused by the loss of the highly reflective snow cover and the increase in the number of surface melt ponds, creating a puddled ice surface.

The incoming longwave radiation (L_i) is produced by the emission of radiation from clouds and atmospheric water vapor. A significant increase during summer is caused by an increase in Arctic cloudiness during summer and a corresponding increase in cloud temperatures, with L_i being proportional to the fourth power of the temperature of the radiating matter (i.e., cloud droplets and water vapor). The longwave radiation emitted by the ice (L_e) is proportional to the fourth power of the surface temperature and is the only radiative flux by which the ice loses energy. A significantly larger loss occurs during summer in response to warming of the ice. It should be noted that αS is also considered to be a flux but is contained within the $(1 - \alpha)S$ term.

As Fig. 2.1 indicates, the net longwave radiation components ($L_i + L_e$) represent a small loss of energy from the ice surface. Inclusion of the solar radiation component shows that the net radiative flux R_{net} is substantially positive in summer and slightly negative during winter. The importance of the radiative fluxes is further emphasized in Fig. 2.2, where R_{net} is contrasted with estimates of the sensible and latent heat fluxes. The sensible heat flux T_s is driven by temperature differences between ice and atmosphere, while the latent heat flux T_L arises from humidity differences. In addition, both depend on surface roughness, wind speed, and stability of the atmospheric boundary layer. The latent heat flux is negligible in winter and slightly negative in summer, when the wet ice surface allows a vapor transfer into the atmosphere. The sensible heat exchange is positive during winter, when a strong temperature inversion generally exists in the lower atmosphere over the central Arctic.

On a monthly basis, the turbulent heat fluxes are small compared to the radiative fluxes. Daily values, particularly of the sensible heat flux, can be large (Maykut, 1985), but frequent reversals of flux direction tend to keep the cumulative totals small. The fluxes are important on an annual basis, however, because the sum of the two turbulent exchanges is 20–50% of the annual net radiation balance (Maykut, 1985). Model simulations by Maykut and Untersteiner (1969) indicate that, without the turbulent heat losses, the surface ablation during summer would be 20–100% larger and would result in a reduction in the equilibrium ice thickness (the thickness of undeformed perennial ice reached after several annual cycles) of about 50%.

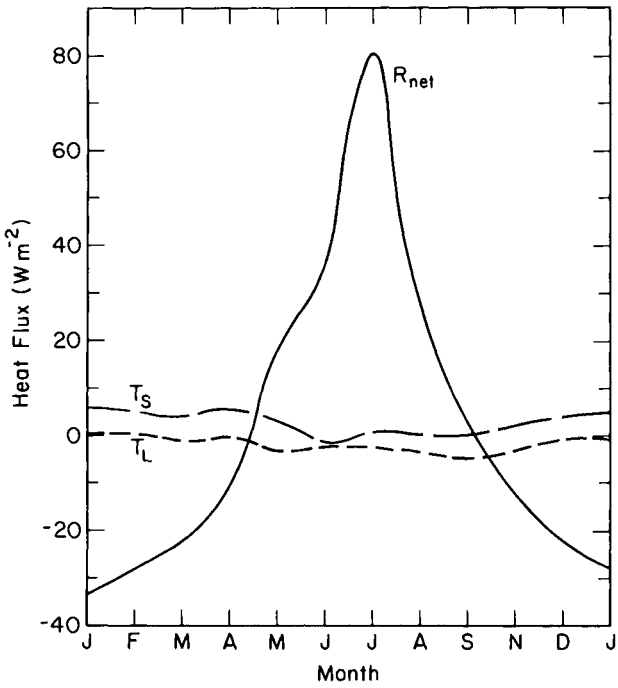

Figure 2.2 Average monthly values of net radiative heat flux R_{net} and sensible, T_s, and latent, T_L, heat fluxes observed over perennial ice (would be different for thin ice). Positive indicates heat gain by the ice and negative indicates loss. From data of Maykut (1985) and Leavitt *et al.* (1978).

There is little doubt, however, that shortwave radiation is primarily responsible for the advanced decay of the ice during summer (Langleben, 1972).

The remaining fluxes in the surface energy balance are the solar radiation passing into the ice interior, I; the conductive heat flux, C_u; and the loss due to melting or sublimation, M. The melting term specifies that excess energy will be used to ablate the ice, and it is this term which is calculated in thermodynamic ice models. The term I is generally a small percentage of the incident solar radiation. As Maykut (1985) explains, however, this term can be more significant for "blue ice," which is characteristic of refrozen melt ponds. The other significant effect of I is that it allows for solar radiation to be directly absorbed by brine pockets in the ice interior, which is a means of internal energy storage that can cause the ice temperature profile to be altered and brine volume to increase.

As mentioned earlier, the conduction of heat in sea ice (represented by C_u) is complicated because the thermal conductivity of sea ice is not a constant.

Instead, it is a function of temperature and salinity and, as such, it typically varies with depth. The conductivity is affected by the presence of brine and air pockets and channels. The brine in these pockets exists in a unique phase equilibrium which depends on its temperature and salinity. If the temperature of the ice decreases, brine in the pockets begins to freeze, releasing latent heat, which in turn acts to warm the ice. The net effect is to retard the cooling of the ice (Maykut, 1985). The opposite occurs when the ice warms. That is, warming causes melting first around the walls of the brine pockets, which requires additional heat, hindering the overall warming of the sheet. The net effect of the brine inclusions is to act as thermal buffers which damp the transport of heat through the ice.

Equation (2.2) describes the energy balance at the ice–water interface. Q_f, the growth term, is again a residual term indicating that if the sum of the oceanic heat flux, F_w, and the lower-boundary conduction term, C_L, is positive the ice will melt. If the sum is negative, the ice will grow, which in turn releases latent heat to be conducted toward the surface. There is generally an upward conduction of heat in the ice, except during the summer (Maykut, 1985). Thus, C_L supplies much of the energy required to balance the substantial long-wave radiation loss at the surface. It should be noted that C_u is equal to the sum of C_L and the latent heat associated with mass changes in the ice surrounding brine pockets. The conductivity flux at the surface (C_u) couples the lower- and upper-surface energy balances and is the sum of the heat input from the ocean, the net annual latent heat released by ice growth, and stored solar energy. Maykut (1985) estimates C_u to be about 8.8 W m^{-2} in perennial ice on an annual basis. In thin ice the heat conducted to the surface is two to three times that of perennial ice.

The oceanic heat flux F_w is a very important component of the energy exchange. This flux is estimated to be 2 W m^{-2} in the central Arctic on an annual basis (Maykut, 1985). The source for this heat in the central Arctic basin is primarily the input of solar radiation directly into the upper layer of the ocean through leads and through very thin ice. In the marginal ice zone of the Fram Strait, where warmer Atlantic waters make up a major component of the surface layer, the oceanic heat flux can be as high as 40 W m^{-2}. It is this northerly influx of oceanic heat which also keeps the Norwegian coast ice free. Maykut and Untersteiner (1971) carried out detailed numerical simulations of the growth and decay of sea ice over many seasonal cycles, examining, in particular, the effects of the various energy fluxes on the equilibrium thickness of perennial ice, which is reached after several annual cycles. Figure 2.3 shows the effects of average annual oceanic heat flux on the equilibrium thickness. The implication is that the radiative and turbulent heat exchanges are balanced so that small changes in the oceanic heat flux can make major differences in the ice thickness. For example, at average

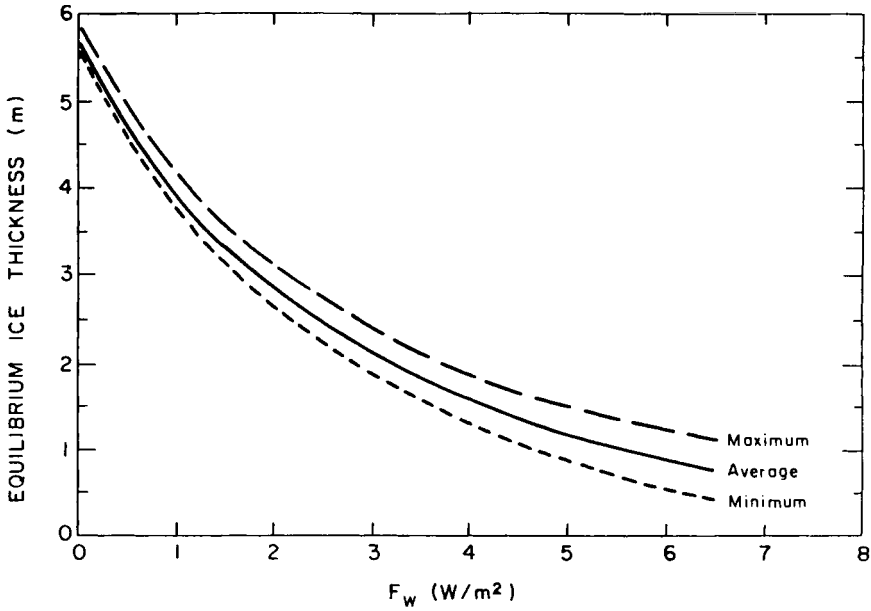

Figure 2.3 Equilibrium thickness of Arctic sea ice as a function of the average annual oceanic heat flux. Reprinted with permission from Maykut (1985). Copyright CRC Press, Inc.

annual oceanic heat flux values exceeding 7 W m^{-2}, the simulations indicate that the Arctic ice cover would disappear in summer. A much more rigorous and detailed discussion of the energy fluxes and thermodynamic modeling is presented in Maykut (1986).

Thus far, the discussion of the thermodynamics of sea ice growth and decay has omitted discussion of a snow cover, except with regard to albedo changes. The existence of a snow cover on sea ice provides additional insulation from the atmosphere. Changes in the thickness of the snow layer can alter not only the growth rate of the ice but also the energy exchanges over it. Maykut (1978) shows that the effects of snow cover on energy exchanges are particularly pronounced for young ice. The simulations of Maykut and Untersteiner (1971) showed, however, that the equilibrium ice thickness in the Arctic is not significantly affected until snow depths reach about 80 cm (Fig. 2.4). Snow, therefore, has two contrasting effects on thick ice: it delays summer ablation by restricting solar radiation input to the ice, and it retards winter growth by insulating the ice from the atmosphere. At snow depths ranging from 30 to 70 cm, the simulations showed that the net effect of snow was to hinder ice growth rather than retard ablation, thus slightly reducing

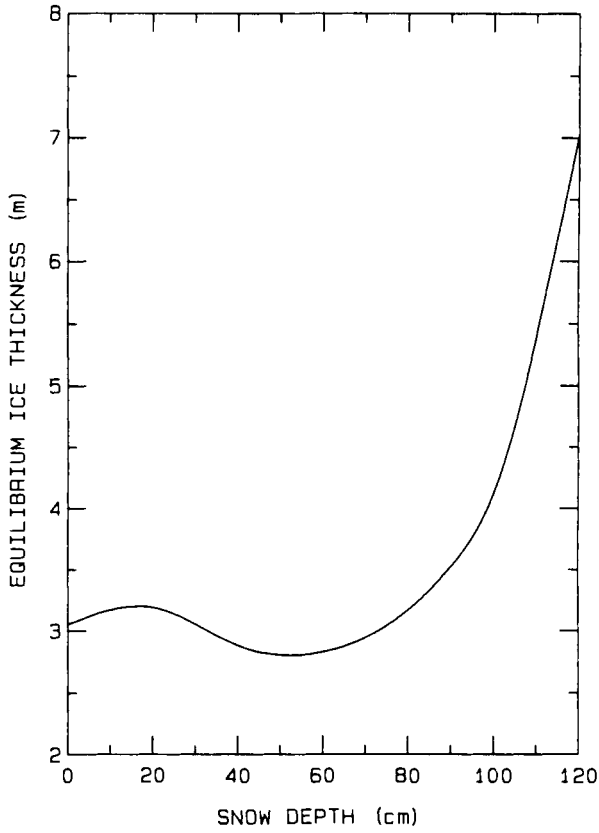

Figure 2.4 Average equilibrium thickness of perennial Arctic sea ice as a function of annual snow depth. Reprinted with permission from Maykut (1985). Copyright CRC Press, Inc.

equilibrium thickness. More than 80 cm of snow, however, acts to delay surface ice ablation until late summer when all the snow has finally melted. At this late date in the annual cycle, however, the shortwave flux has been reduced to the point that minimal ice ablation occurs.

Snow thicknesses on Arctic sea ice appear highly variable. Thicknesses measured on floes in the Fram Strait (Tucker *et al.*, 1987) ranged from 3 to 65 cm on multiyear ice and from 0 to 20 cm on first-year floes. Although these thickness differences furnished a provisional means of distinguishing between first- and multiyear ice, the thicker snow covers on multiyear ice are not enough to alter the equilibrium ice thicknesses significantly, according to the simulations.

In certain areas of the Arctic, however, ice reaches very large thicknesses. Walker and Wadhams (1979) believe that the combination of large snow depths and little or no oceanic heat flux accounts for floes over 6 m thick that may originate in restricted bays and channels of high-latitude islands in the Canadian Archipelago, for example. Using the Maykut and Untersteiner (1971) model, they demonstrated that ice grown under climatic conditions typical of the high Arctic but with zero oceanic heat flux and 1 m annual snowfall would eventually reach a thickness of at least 12 m.

The thermodynamic model calculations of Maykut and Untersteiner (1971) yield many other interesting results. The equilibrium thickness is most affected by parameters which influence the summer melting process. Besides the snow depth and oceanic heat flux, other critical factors include the air temperature, the surface albedo, the incoming radiation, and the turbulent exchanges which are manifested by surface roughness, temperature differences, and wind speed. The simulations indicate that the Arctic ice cover would completely disappear in summer if there were a 3–5°C increase in air temperature, a 25–30% increase in incident solar radiation, or a 15–20% decrease in albedo. A natural occurrence which would increase the incident shortwave radiation seems unlikely because it would almost certainly have to be caused by a dramatic decrease in cloudiness. The increased amounts of open water would, in turn, cause clouds and reduce the incident radiation. The possibility of an air temperature increase or a decrease in albedo is plausible, however. These could possibly be stimulated by large atmospheric CO_2 increases or large volcanic eruptions. These events would also be accompanied by ice–ocean–atmosphere feedback effects such as increased cloudiness, which must be carefully considered before speculating on the demise of the ice cover.

The simulations of Maykut and Untersteiner (1971) showed that the equilibrium thickness of undeformed Arctic sea ice is between 3 and 4 m. This predicted thickness is in general agreement with field observations of older undeformed multiyear ice. Once the equilibrium thickness is reached, the annual cycle shows that about 40–50 cm of ice ablates from the upper surface each summer and a similar amount accretes on the bottom side each winter. A newly accreted ice particle, then, moves upward through the ice sheet at a rate of about 40–50 cm per year until it reaches the surface and melts. In reality, the surface of undeformed multiyear ice during summer also includes pools of surface meltwater, which, early in the summer, may cover 60% of the ice surface (Maykut, 1985). As the snow melts and melt ponds deepen, they occasionally penetrate completely through the ice. Eventually, the melt pond coverage is reduced to 10–30%. Melt pond coverage on smooth first-year ice may be much larger than on multiyear ice. With the onset of winter the ice surface exhibits an undulating appearance consisting

of low-level areas created by the frozen melt ponds and small rounded hummocks. Typical standard deviations of the thickness of undeformed multiyear ice have been found to be about 0.6 m (Ackley *et al.*, 1976; Hibler *et al.*, 1972a).

An important aspect of the energy exchange which has not been discussed is the solar radiation which passes through the ice into the underlying ocean. This energy is critical to biological activity beneath the ice and contributes to the heat balance of the upper ocean. In terms of the surface energy balance [Eq. (2.1)], it is some portion of I which travels completely through the ice into the ocean. I is strongly affected by albedo, in that the lower the albedo, the more shortwave energy is available to pass into and through the ice. As the energy passes through the ice, however, it is reduced by scattering and absorption. These processes are parametrized by an extinction coefficient. Theory and measurements indicate that the amount of shortwave radiation passing through the ice decays exponentially with depth. Perovich *et al.* (1986) indicate that lower albedos and reduced scattering occur as the ice warms, so more energy passes into the ocean. The converse is true during the ice growth season. For more complete treatments of the optical properties of snow and ice, the reader is referred to Grenfell and Maykut (1977) and Perovich *et al.* (1986).

2. Antarctic contrasts

Ice growth and ablation in the Southern Ocean are governed by the same energy fluxes as in the Arctic, but several factors make for considerable differences in the nature of the sea ice in the Antarctic. Whereas the Arctic Ocean lies within a basin nearly surrounded by land masses, Antarctic ice occurs in an open sea which surrounds a continent. Close to the continent, cold katabatic winds can rapidly thicken ice, whereas at the open ocean boundary, marginal ice zone conditions exist. These include warmer air and ocean temperatures and wave action which tends to break up the ice cover into small floes. It appears that the largely unconstrained nature of the ice edge in the Antarctic allows far more vigorous wave action within the ice than occurs in the Arctic.

In general, most of the energy fluxes in the 60–70°S latitude band, where the majority of Antarctic sea ice is found, are similar to the fluxes found in the Arctic. Small differences occur in the shortwave radiation component due to latitude differences, and the turbulent exchanges may be larger because of generally higher wind speeds in the region. The most notable difference is in the oceanic heat flux. Whereas it is generally accepted that the oceanic heat flux in the central Arctic is about 2 W m^{-2}, the average annual flux in many parts of the Southern Ocean (e.g., Weddell Sea) may be as large as 12 W m^{-2} (Gordon *et al.*, 1984). The heat flux is much larger for specific

periods. For example, values approaching 60 W m^{-2} are estimated to be required to account for the massive melt of ice which occurs from mid-November to mid-January (Gordon, 1981). Allison (1981) reports values ranging from 0 to over 50 W m^{-2}, depending on location and time of year, for shorefast ice adjacent to coastal stations. It is thought that for offshore locations much of this heat originates from the flux into the surface layer of warmer water from below the pycnocline (Gordon, 1981). A large amount of heat also results from the absorption of solar radiation in the mixed layer in leads and in the open ocean beyond the ice edge. In dynamic–thermodynamic model simulations of the Weddell Sea ice cover, Hibler and Ackley (1982) obtained generally reasonable agreement with observed ice extent, using only 2 W m^{-2} for the oceanic heat flux. The simulations demonstrated that much of the overall seasonal cycle of ice extent could be accounted for by a wind-driven dynamic–thermodynamic model. However, specific features in some regions of the Weddell Sea (e.g., the Weddell polynya) were not well accounted for, and these can likely be attributed to the large oceanic heat fluxes.

Antarctic sea ice is relatively free of surface melting, as evidenced by the obvious lack of surface melt ponds during summer (Andreas and Ackley, 1982). This is thought to be caused by increased latent heat losses from the ice to the atmosphere induced by lower relative humidities and higher wind speeds. The result is that, unlike the situation in the Arctic, surface layer air temperatures must be significantly above 0°C for melting to begin. Air temperatures are normally less than 0°C over Antarctic sea ice. An important secondary effect is that the surface albedo remains high due to the lack of melt ponds and the persistence of the snow cover. Internal ice warming is retarded because most of the incident shortwave radiation is reflected. Data reported by Wadhams *et al.* (1987) indicate snowfall amounts over Antarctic sea ice that are comparable to those for the Arctic.

Model simulations to determine the thermodynamic equilibrium thickness of Antarctic sea ice have not been conducted. Although the ice drift patterns (discussed later) prevent most Antarctic sea ice from reaching ages greater than 1–2 years, it is fruitful to speculate on the "potential" equilibrium thickness. At certain locations adjacent to the continent where the oceanic heat flux is negligible, air temperatures are lower, and winds are stronger, first-year ice can reach thicknesses approaching 3 m, substantially exceeding the 2-m first-year thickness seen in the Arctic. In a midwinter research cruise which crossed a large part of the Weddell Sea, however, Wadhams *et al.* (1987) found mean thicknesses of undeformed sea ice floes to be about 50–60 cm. Examination of ice cores revealed that many of these floes were composed of rafted pancakes and showed little evidence of new ice growth on the bottom side of the ice (Lange *et al.*, 1988; S. F. Ackley,

personal communication). The implication is that the equilibrium thickness of Antarctic pack ice would be less than that of the Arctic. Congelation growth at significant distances from the coast appears to be substantially retarded by the large oceanic heat flux.

A major component of ice sampled in the Antarctic has proved to be frazil. Observations by Clarke and Ackley (1982), Gow *et al.* (1987a), and Lange *et al.* (1988) have shown that 50–60% of all first-year and multiyear ice floes sampled in the Weddell Sea consisted of frazil. Similar studies of Arctic sea ice (Martin, 1981; Tucker *et al.*, 1987) have found only 5–20% frazil ice. As discussed later, processes dominating frazil ice production are different from those that control the congelation growth of a stable ice sheet. The result is that, by whatever mechanism frazil is generated, it apparently accumulates and consolidates rapidly, making up for the ostensible reduction in congelation growth in the Southern Ocean. Gow *et al.* (1987a) reported occasionally finding undeformed first-year floes in excess of 2 m thick that were composed substantially of frazil ice. Thus it is possible that reasonable thicknesses may accumulate very rapidly through the consolidation of frazil ice. Lange *et al.* (1988) think that a most important mechanism may be the rapid thickening of the ice cover due to the rafting and consolidation of pancake ice. The rafted pancakes composed of frazil permit a reasonably thick ice cover to be established despite the large oceanic heat flux. A similar situation was observed in the Arctic during April 1987 in the southern Barents Sea (A. J. Gow and W. B. Tucker, unpublished results), which has an open sea boundary on its southern periphery. It is not known whether this phenomenon is common in other seas bounding the Arctic Ocean.

B. Ice Dynamics and Drift

1. The momentum balance

In neither the polar oceans nor peripheral seas is the pack ice stationary. Except for areas of landfast ice, the ice is in a state of nearly continuous motion and deformation. This deformation causes the formation of individual ice floes, leads, ridges, and rubbled ice as opposed to a continuous unbroken ice sheet. The movement and subsequent deformation of ice are caused by atmospheric and oceanic stresses acting on the relatively thin ice cover. The force balance for sea ice can be written as

$$m\frac{d\mathbf{u}}{dt} = \mathbf{C} + \boldsymbol{\tau}_w + \boldsymbol{\tau}_a + \mathbf{F} + \mathbf{G} + \mathbf{T} \tag{2.3}$$

where $\mathbf{u}$ is the ice velocity, m the ice mass per unit area, $\mathbf{C}$ the Coriolis force, $\boldsymbol{\tau}_w$ the water stress, $\boldsymbol{\tau}_a$ the air stress, $\mathbf{F}$ the force due to the variation of internal

ice stress, **G** the force due to geostrophic currents, and **T** the force attributed to the tilt of the ocean surface. The implementation of Eqs. (2.1), (2.2), and (2.3) in numerical ice models is discussed in Chapter 7. Here we will discuss aspects of the major components of the ice momentum balance.

Theoretical treatment and observations have verified that the dominant components of the force balance are the air and water stresses, the Coriolis force, and the ice interaction (internal ice stress variation). Hibler (1986) estimates that the air and water stresses typically vary about a value of 0.1 N m^{-2}, whereas the Coriolis force is about half this value. In an analysis of ice station and automatic data buoy drifts in the Arctic basin, Thorndike and Colony (1982) were able to account for 70% of the variance of the ice velocity using the geostrophic wind alone. It has been well known for many years that much of the ice drift far from shore could be explained solely in terms of winds (Nansen, 1902; Zubov, 1943).

The ice interaction **F** is the result of the ability of the ice pack to transmit stresses over considerable distances. The effect of internal ice stresses is made readily apparent to an observer by the fact that in enclosed areas such as bays and fiords the ice does not move under high wind or current forcing. This indicates that **F** is at least as large as the wind and water stress terms. The magnitude of this term is generally calculated as a residual of the force balance. One such example (Fig. 2.5) with the ice interaction, as a calculated residual of other components was measured by Hunkins (1975). It is easily ascertained that **F** may not be ignored except in cases where the ice concentration is so low that the large-scale (covering many floes) ice strength approaches zero and the ice is unable to transmit stress.

The total derivative of ice velocity, du/dt, is composed of a local time derivative of velocity plus a momentum advection term. The local ice acceleration is usually very small and can generally be ignored in numerical simulations of ice drift. The term can be significant during periods of low ice concentration when the ice interaction is minimal, however. McPhee (1980) showed that inertial oscillations which result from changing directions of the ice motion are a significant part of summer sea ice motion. The momentum advection term is almost always negligible because relatively large velocity changes would be required to generate a substantial force (Hibler, 1986).

The force balance diagram (Fig. 2.5) indicates that the geostrophic current and ocean tilt terms (combined as $mg\nabla H$) are relatively small. This is a result of generally small currents beneath the polar pack ice. Hibler and Tucker (1979) demonstrated that the effects of currents in the central Arctic basin are small over time periods of a few days but that long-term effects are important because some of the long-term effects of winds average out the short-term fluctuations. Moritz and Colony (1988) pointed out that currents

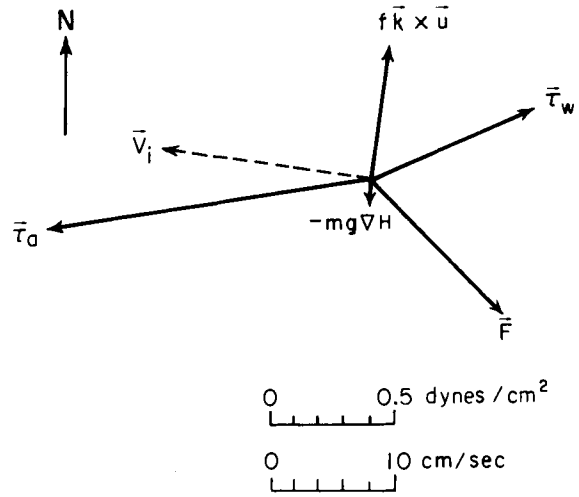

Figure 2.5 Estimate of the force balance on sea ice for winter conditions based on wind and water stress measurements. $\mathbf{V}_i$, Ice velocity; τ_a, air stress; τ_w, water stress; $f\mathbf{k}\times\mathbf{u}$, Coriolis force; $-mg\ \nabla H$, force due to ocean tilt and geostrophic currents; **F**, internal ice stress which is determined as a residual. After Hunkins (1975).

actually dominate the ice drift in the Fram Strait, and Pritchard (1988) has found similar results in the Bering Sea. Currents are particularly important in shallow areas, where barotropic effects may be significant.

2. Ice circulation in the Arctic and the Antarctic

As alluded to previously, the motion of sea ice at some distance from shore is primarily wind driven. This tends to be the general case in both the Arctic and Antarctic. Until recently, techniques for predicting the drift of ice used the forecast geostrophic wind as the sole external parameter. Zubov (1943) established the well-known rule of thumb that the ice drifts parallel to the sea level pressure isobars (usually about 20° to the right of the surface wind in the northern hemisphere) at about 2% of the geostrophic wind speed.

Two dominant features of the ice circulation in the Arctic basin were first described by Gordienko (1958). These are the Beaufort Sea Gyre, a clockwise circulation pattern in the Beaufort Sea, and the Transpolar Drift Stream, a basinwide feature which transports ice from the western to the eastern side of the basin. Both are manifestations of the mean sea level pressure field, which

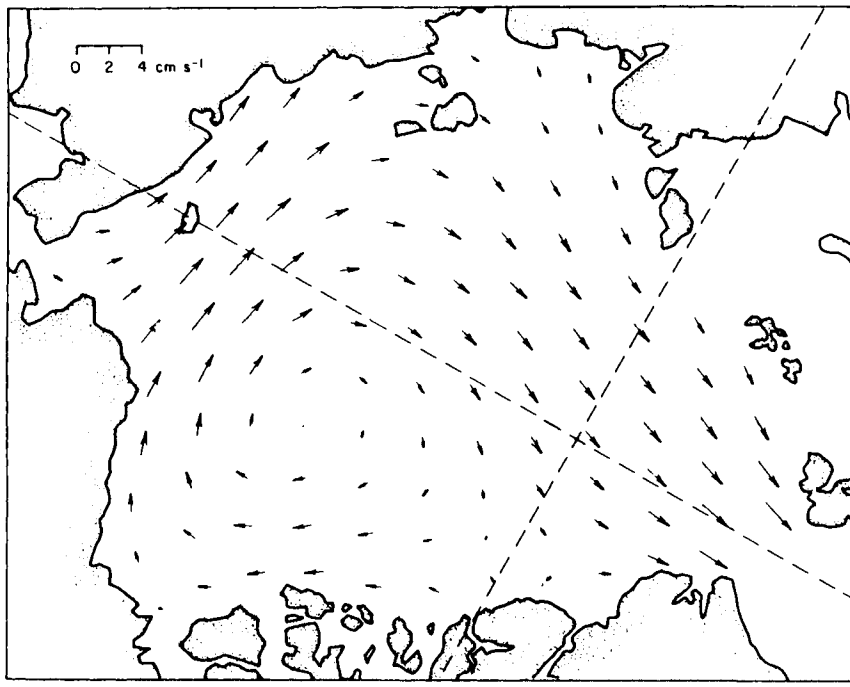

Figure 2.6 Mean field of ice motion interpolated spatially and temporally from manned ice stations and automatic data buoys. After Colony and Thorndike (1984).

indicates a large high-pressure area over the Beaufort Sea and with isobars over the remainder of the basin generally running west to east. Colony and Thorndike (1984), using an analysis of ice station and drifting buoys spanning many years to estimate the mean field of sea ice drift (Fig. 2.6), found that the Beaufort Gyre is much less pronounced than was previously thought. The gyre covers the entire western portion of the basin, including not only the Beaufort but also substantial parts of the Chukchi and East Siberian seas. Further, the Transpolar Drift is not well established, although, as Fig. 2.6 shows, there is still a trend of the ice to drift toward Fram Strait. It must be emphasized that Fig. 2.6 shows the mean motion and that large excursions from this motion frequently occur. Mean velocities are about 2 km day^{-1}, but the standard deviations, which describe the fluctuating component of the velocities, are much larger ($\sim$ 7 km day^{-1}; Colony and Thorndike, 1984). The ice can also remain motionless for weeks at a time, and McLaren *et al.* (1987) have suggested that gyre reversals may be common in the summer.

As a result of this circulation pattern, individual ice floes can remain in the basin for many years. For example, manned ice-island stations have circulated around the basin for decades. Stochastic model calculations by Colony and Thorndike (1985), in which short-term drift observations from buoys were used to predict statistics of drift over long time periods, indicate that ice floe residence times of 5–7 years in the Arctic basin are common. These long residence times result from the fact that there is only one major outflow area for the Arctic basin (the Fram Strait). Relatively little ice leaves the basin through other exits such as the Bering Strait or the Canadian Archipelago. On an annual basis about 10% of the ice cover in the basin flows out through Fram Strait (Maykut, 1985). As southward-flowing ice enters the Fram Strait and Greenland Sea, drift velocities increase to about 15 km day^{-1}. Similar drift rates have been observed in the Bering Sea as the first-year ice is "conveyored" southward to the ice edge, where it melts (Pease, 1980; Reynolds *et al.*, 1985).

Much less is known about the movement of ice in the Southern Ocean (Fig. 2.7). Major features of the drift are the Antarctic Circumpolar Current, which transports ice clockwise around the continent, and the East Wind Drift, which flows in the opposite direction immediately adjacent to the continent. This coastal flow is directed north by protrusions of the continent in the Weddell and Ross seas. The ice contained within the northward flow joins the Circumpolar Current, by which it is transported into warmer water, which eventually melts it.

Figure 2.8, showing tracks of drift buoys that were placed deep in the southern Weddell Sea (Ackley and Holt, 1984), demonstrates the characteristic northward flow along the Antarctic Peninsula. These tracks imply that residence times of sea ice in the Weddell Sea are short relative to those of ice in the central Arctic. All buoys completed their northward journeys in less than a year, emphasizing the extremely short residence times in the Antarctic. Keys (1984) estimates that multiyear ice is limited to about 10–15% of the total area of Antarctic sea ice. This is in sharp contrast to the estimate of 70–80% multiyear ice in the central Arctic basin by Koerner (1973) and the estimate of 75% multiyear ice exiting from the Farm Strait during June and July 1984 (Tucker *et al.*, 1987). It implies that, except for ice which remains in isolated bays and coves, sea ice in the Antarctic rarely exceeds 2 years in age. Because of the generally thinner ice cover in the Antarctic, along with generally higher wind speeds, drift rates could be expected to be somewhat larger than those for Arctic sea ice. Ackley (1981) found that drift rates exceeding 20 km day^{-1} were common in the Weddell Sea, and Keys (1984) reports similarly high rates for the Ross Sea. Mean ice velocities would, of course, be much less because of fluctuations in direction and speed of the wind.

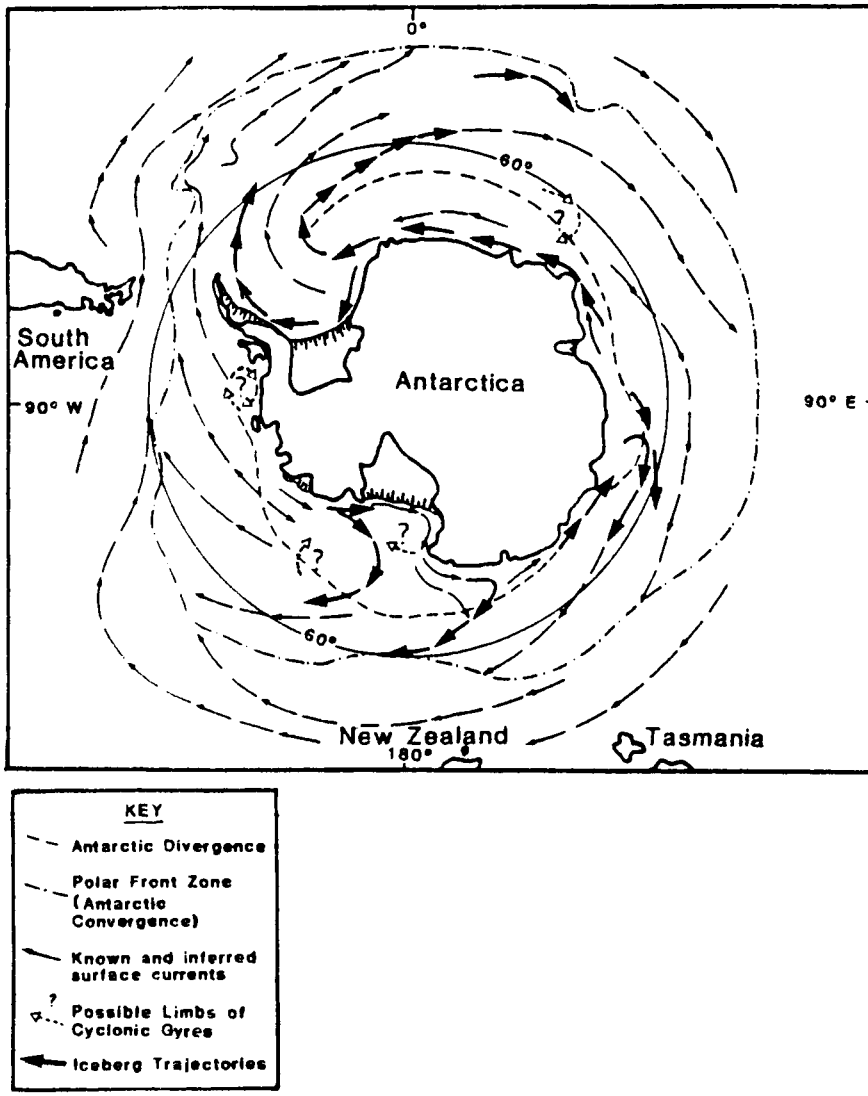

Figure 2.7 Surface circulation and published trajectories of icebergs around Antarctica. After Keys (1984).

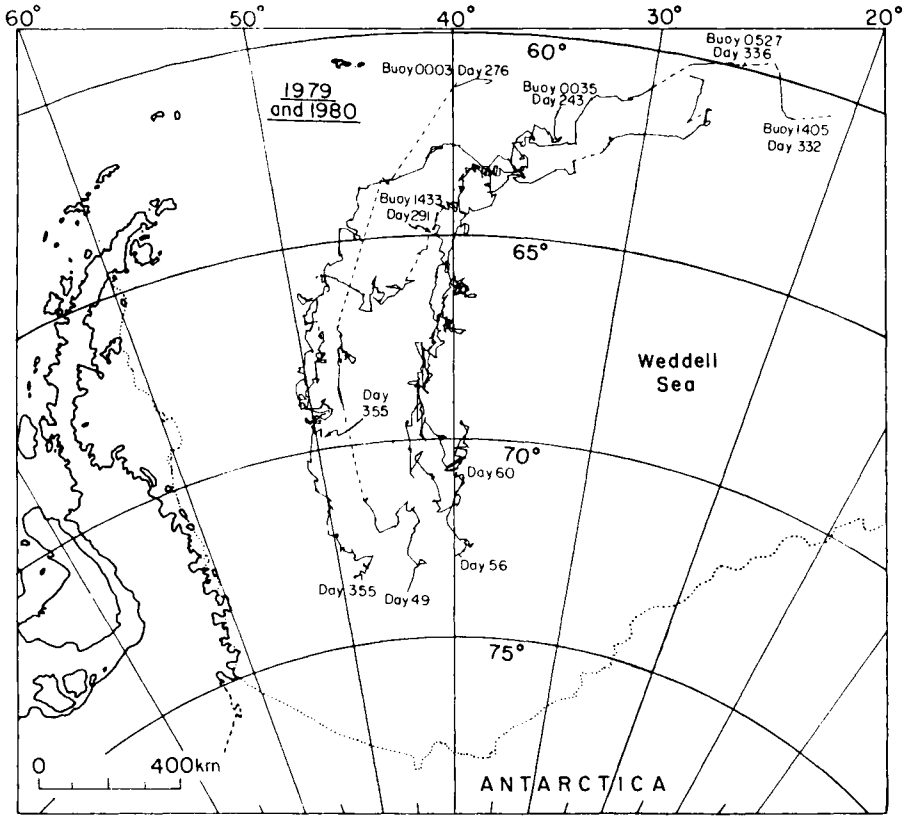

Figure 2.8 Drift tracks of automatic data buoys in the Weddell Sea during 1979 and 1980. After Ackley and Holt (1984).

C. Morphological Ice Features

1. Leads and polynyas

The continuous motion of sea ice combined with ongoing growth and ablation processes causes a variety of ice types to exist within areas on the scale of a few kilometers. Diverging motions cause the ice to pull apart and form leads, allowing the ocean to come into direct contact with the atmosphere. During winter, in the absence of further motion, the leads rapidly refreeze and thicknesses of up to 10 cm can be attained in less than 1 day. Leads are relatively small features, usually tens to hundreds of meters wide and up to several kilometers long. Polynyas are large openings that tend to recur at the

same locations or become semipermanent features. Polynyas can occur adjacent to coastlines, where shearing or divergence of the pack ice acts to move the ice away from the coast. For example, such features occur on the southern side of St. Lawrence Island in the Bering Sea and at locations along the east coast of Greenland. Other polynyas are the result of oceanographic influences such as upwelling. A particularly noteworthy polynya of this nature is the Weddell Polynya, a large area of open water occasionally observed in the eastern Weddell Sea. Leads and polynyas are significant because they are sources of very large heat losses to the atmosphere. During winter, leads and polynyas constitute the major source of new ice production and subsequent salt fluxes to the upper ocean. In summer, when new ice growth is not taking place, small leads often develop into major open-water areas and allow shortwave radiation to be absorbed by the upper ocean, which further stimulates ice ablation. Under such conditions the concept of leads becomes increasingly vague. Leads generally refer to the linear features developing in compact ice, whereas during the melt season there is a changing mixture of floes and interconnected areas of open water rather than leads *per se*. For this reason we usually characterize a summer ice pack by its concentration, the fractional area covered by ice.

The amount of open water in the central Arctic during winter is estimated to be about 1% (Wittmann and Schule, 1966; Maykut, 1985). During summer the amount of open water increases to 10–20%. In marginal ice zones, where divergence and melting are taking place, the percentages of open water can be so large that defining the ice boundary becomes very difficult.

The ice-covered ocean surrounding Antarctica, by virtue of its open ocean boundary, has significantly larger marginal ice zones than the Arctic and therefore is expected to have higher percentages of open water. Zwally *et al.* (1983), using satellite passive-microwave observations, have estimated that the ice concentration over most of the year averages between 60 and 80%. This may be accurate for the outer regions of the pack, but recent field observations indicate that ice concentrations are higher in the interior regions, similar to those in the Arctic pack (S. F. Ackley, personal communication). More open water generally exists in the Antarctic pack ice than in the Arctic because of the relatively larger area of marginal ice zone (MIZ) and greater divergence in the ice produced by a significant northward component in the wind and ice velocity fields.

2. Ice roughness

Although this section deals primarily with large-scale roughness features such as ridges and rubble fields, smaller-scale features are worth pointing out because of their importance for the air and water stress. On the surface, scales of roughness on the order of centimeters result from variations in freeboard

levels of contiguous ice floes of different thicknesses. In the MIZ, the exposed vertical sides of many broken floes, although exhibiting reliefs of only tens of centimeters, give rise to larger wind stress drag coefficients than are observed in the central Arctic, where larger ridges occur. Other small-scale roughness on the surface is caused by the formation of pancake ice with raised edges surrounding each pancake, the fracture and rafting of thin ice, and the densely packed windblown snow features known as sastrugi.

On the bottom side of the ice, differences in floe thickness cause variations in ice draft from a few millimeters to several meters. An important small-scale roughness element is a consequence of ice growth. When seawater freezes, brine is rejected from the growing ice interface, which develops a dendritic structure consisting of platelets of pure ice protruding downward into the seawater. This process is described in detail in Section III. The individual platelets are spaced about a millimeter apart and the roughness created by these small roughness elements contributes to the water stress and the amount of mechanical mixing in the water column. During the melt season, these platelets are completely ablated, leaving a much smoother surface.

The major roughness features of a sea ice pack are caused by the deforming ice and manifested in the form of rubble fields or individual ridges. These features are formed by the compression and shear which result from converging ice, in contrast to divergence, which creates leads. Many ridges are indeed long linear features, sometimes several kilometers in length but only tens of meters wide. However, as Rothrock (1986) points out, ridges frequently overlap due to repeated ridging events, forming piles of rubble which are difficult to characterize quantitatively. Therefore, using only single ridges to define the volume of deformed ice may lead to substantial errors.

It is the thin ice which most often deforms, simply because it has considerably less strength than older first-year or multiyear ice. However, if no thin ice is present and the driving forces are sufficient, thick ice may also deform. This was shown by field investigations by Tucker *et al.* (1984a), who found many pressure ridges containing ice blocks in excess of 1 m thick. Also, there have been numerous unpublished reports of ridges containing blocks 3–4 m thick.

When an ice sheet deforms under compression, the ice blocks, broken by bending and buckling, are piled above and below the surface. The above-surface portion is termed the sail, while the below-surface portion is called the keel. Sail heights and thus keel depths appear to be limited by the thickness of the deforming ice (Tucker *et al.*, 1984a). Pressure ridge modeling by Parmerter and Coon (1972) showed that for ice of a given thickness, strength, and modulus, there is a limiting height to which a ridge can build, and further compression of the ice results in a rubble field stabilizing at the limiting

height. The ridge mass as a whole should tend toward isostatic equilibrium; thus we might expect a general relationship between sail heights and keel depths. Indeed, drillings through ridges indicate that the ratio of keel depth to sail height in first-year ridges is about 4.5 : 1 and in multiyear ridges is about 3.3 : 1 (Kovacs, 1983). The consolidation of the ridge through the freezing of water-filled voids and subsequent isostatic adjustment is partly responsible for the reduction of the keel-to-sail ratio as the ridge ages. Also, ablation during summer tends to round both top and bottom surfaces of ridges.

Ridges and rubble fields are particularly important because they account for a large portion of the total ice mass. Williams *et al.* (1975) estimated that ridges account for about 25% of the total Arctic ice mass, and in heavily ridged regions this amount can reach 50%. Wadhams (1980a) found that about 40% of the total ice cover in the central Beaufort Sea was composed of ridged ice. Quantitative data on ice topography have come from two sources. Airborne laser profiles have provided thousands of kilometers of sea ice surface topography, and upward-looking sonar mounted on submarines has provided the ice bottom relief. Because of the inherent aircraft motion, analysis of the laser data has been restricted to the counting of ridges. The sonar profiles, on the other hand, provide ice draft to a relatively high degree of accuracy. This is particularly useful because isostasy dictates that draft should be about 90% of the thickness, so estimates of the total thickness can be made from draft measurements alone. Rothrock and Thorndike (1980), however, warn that using only ridge counts from sonar profiles to estimate amounts of deformed ice may lead to serious underestimates because much deformed ice is found at scales smaller than would fit the specification of a ridge as defined in a computer algorithm.

Studies using laser and submarine profiles have clearly delineated regional and seasonal variations in ice morphology (Fig. 2.9). Histograms of the mean keel depths for various seasons and regions in the Arctic (Fig. 2.10) indicate that ridging is significantly heavier in some regions. There is little doubt that more ridges are found in spring and winter, and regionally heavier ridging occurs to the north and west of the Canadian Archipelago. The heavier ridging in this region is the result of ice motion toward the shore. Considerable year-to-year variations in ridging have also been observed. For example, Tucker *et al.* (1979) saw significant interannual variations in ridging intensity at Alaskan coastal locations. Similarly, McLaren (1986), in an analysis of two corresponding submarine tracks across the Arctic basin, found more severe ice conditions in 1958 than in 1970. Year-to-year variations are not surprising in that we should expect variability in the environmental parameters which govern ice growth, drift, and decay.

Very few data on deformational features in the Antarctic ice pack exist, although a recent study by Weeks *et al.* (1988) has made use of airborne laser

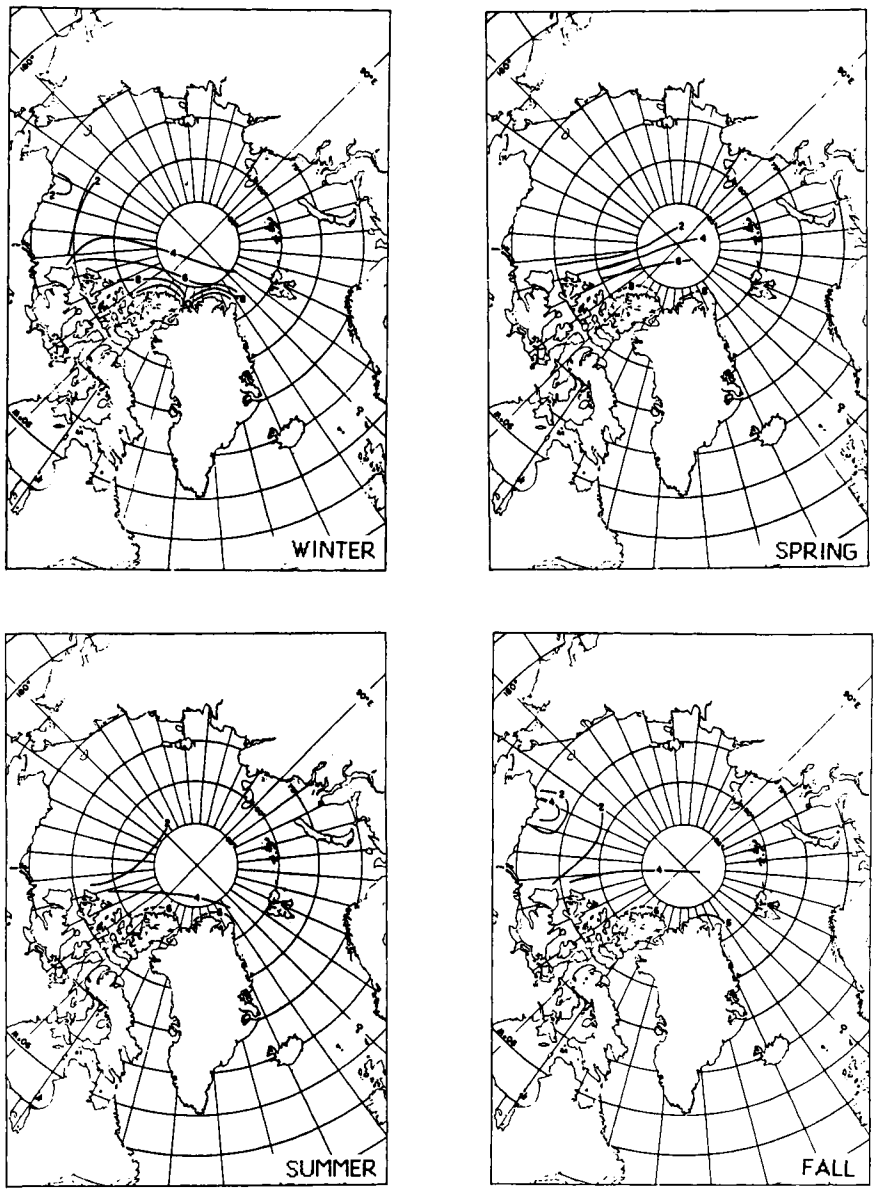

Figure 2.9 Contours of ridge sail frequency (number of ridges per kilometer greater than 1.22 m high) for the four seasons. After Tucker and Westhall (1973).

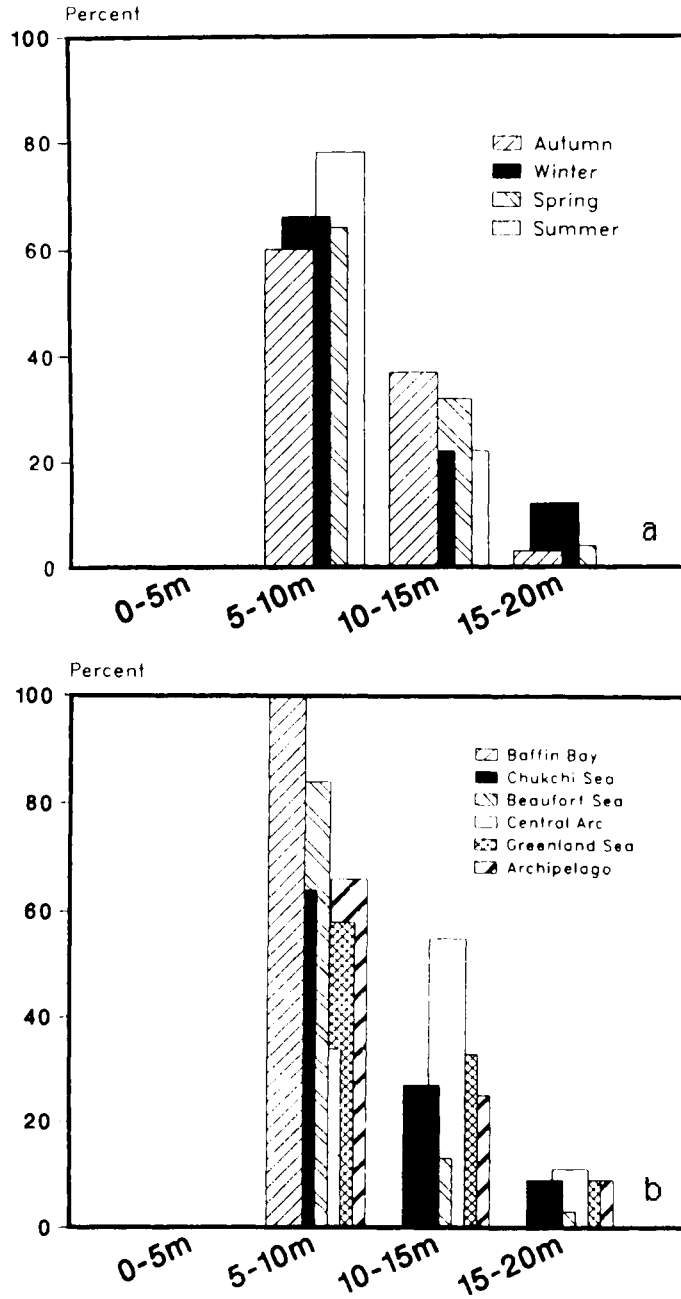

Figure 2.10 Distribution of mean ridge keel depths for (a) the four seasons and (b) various Arctic Ocean subregions. After Bourke and Garrett (1987).

Table 2.1 Ridging Parameters from the Ross Sea Compared to Data from Various Arctic Locations for Winter and Early Spring[a]

Location	Ridges per kilometer	Mean ridge height (m)
Ross Sea		
Coastal	6.8	1.25
Offshore	1.9	1.21
Central Beaufort Sea	2.6	1.47
Beaufort/Chukchi shear zone	4.4	1.51
West Eurasian basin	4.7	1.50
North Greenland	8.2	1.68

[a] Parameters were obtained from laser profilometer data from Weeks *et al.* (1988).

profiles to contrast winter and spring ridging in the Ross Sea with selected Arctic locations. A brief synopsis of the ridging statistics is shown in Table 2.1. The mean ridge height in the Ross Sea is less than at all Arctic locations, and there are fewer ridges in the offshore Ross Sea than for comparable Arctic locations. The less severe ridging statistics for the Ross Sea are clearly a manifestation of the open boundary conditions in the Antarctic and the fact that thinner ice is being ridged. Although no similar data are available for the Weddell Sea, it is suspected that more deformed ice may exist in that region.

Statistical models have been developed to describe the distributions of heights and spacings of ridges (Hibler *et al.*, 1972b, 1974; Wadhams, 1980b, 1981; Wadhams and Horne, 1980; Wadhams and Davy, 1986). A comparison of the distributions is presented by Wadhams (1984). The distributions generally take the form of a negative exponential or lognormal. All have coefficients that can be determined from the mean ridge height or spacing. The models indicate that the height and spacing distributions can be adequately described with only minimal input parameters.

D. Ice Thickness Distribution

Once a sea ice cover is established, its most significant attribute is its thickness. We have discussed the deformation of the pack ice which causes the formation of very thick ridges as well as leads. Subsequent growth in leads produces new ice. Thus the combination of dynamic and thermodynamic processes causes a variety of ice thicknesses to coexist at any given time within a relatively small area (< 1 km). The same processes also cause the

thickness within that area to change constantly. The distribution of ice thicknesses profoundly affects the atmosphere–ocean exchanges of heat, moisture, and momentum. The thickness distribution determines the regional ice strength and thereby affects the future role of ice dynamics within the region. Knowing the distribution of ice thicknesses within a region allows us to couple dynamic and thermodynamic processes and thus to estimate regional-scale quantities such as the heat and moisture exchanges and salt and solar input to the upper ocean (Maykut, 1982). At present, there are no means by which the thickness distribution within a region can be monitored continuously. A theoretical framework for estimating the thickness distribution from data which are available has been developed (Thorndike *et al.*, 1975). This formulation and a two-thickness-level approach developed by Hibler (1979) are especially suited for inclusion in dynamic–thermodynamic sea ice models.

The essence of the preceding discussion has been to point out the importance of the ice thickness distribution and to make note of the fact that for any area the thickness distribution is constantly changing. However, there are large-scale regional differences in mean thicknesses due to such effects as proximity to a coastline or near-continuous divergence. The following discussion briefly examines available data concerning aspects of large-scale ice thickness of the Arctic and Antarctic.

The few submarine sonar profiles that have been analyzed provide information on the variability of thicknesses in the Arctic basin. Thickness can be inferred reasonably well from these profiles of ice draft because, as mentioned earlier, about 90% of the thickness is below sea level. Figure 2.11 shows a probability density function (PDF) plot of ice drafts collected along 400 km of submarine track in April 1976. The ice draft distribution of this transect is bimodal. The small, distinct peak in the 0–1.0-m range is indicative of young first-year ice evident in winter and spring, whereas the larger peak centered at about 3.0 m would indicate undeformed multiyear ice, with a potential contribution from deformed first-year ice. The tail of the distribution is due to deformed multiyear and first-year ice. It is clear that deformed ice constitutes a large portion of the total ice mass represented by this PDF.

Estimates of the mean thickness and standard deviation of the ice within the Arctic basin have also been derived from the submarine data (Hibler, 1979; LeShack, 1983; Bourke and Garrett, 1987). Figure 2.12 shows mean drafts for the summer and winter seasons compiled from data analyzed by Bourke and Garrett (1987). Clearly delineated in these figures are the extremely thick ice areas to the north of Greenland and west of the Canadian Archipelago. Obviously, it is the severe deformation which occurs in these areas that produces such large mean drafts. An artifact in the analysis, caused

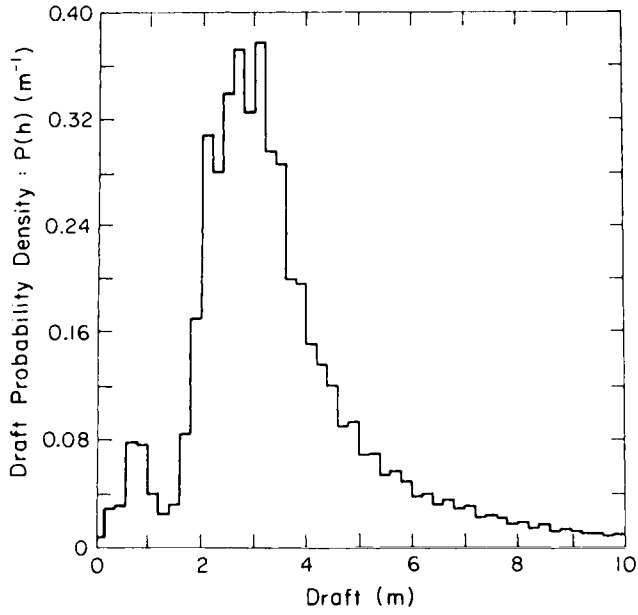

Figure 2.11 Probability density function of ice draft from 400 km of submarine track in the Beaufort Sea. After Hibler (1980); data from Wadhams and Horne (1980).

by the fact that only ice-covered areas were used in the mean-draft calculations (i.e., areas containing open water were deleted), is that the mean draft in the area near the North Pole is larger in summer than winter. Thus in summer, when little thin ice is present, the mean drafts are biased by the surviving deformed and thick ice. Clearly, estimates of mean draft or thickness should be used with caution.

As with other data regarding ice conditions in the Antarctic region, there is a dearth of information on the thickness distribution. The most comprehensive information has evolved from a midwinter cruise across the eastern Weddell Sea (Wadhams *et al.*, 1987). The PDF for the entire cruise, based on over 4400 individual drill holes (Fig. 2.13), has a single mode between 50 and 60 cm as the dominant thickness. Wadhams *et al.* (1987) stated that the PDF seriously underestimates the contribution of ridges and deformed ice to the distribution because they were not often sampled. However, thicknesses of undeformed ice are much less than those of undeformed ice in the Arctic (see, for example, Fig. 2.11). With less ridging and relatively little multiyear ice in the Antarctic, it is safe to assume that ice thickness there will be considerably less than in the Arctic even when the contribution of deformed ice is included. Other thickness data from the Weddell Sea, obtained from

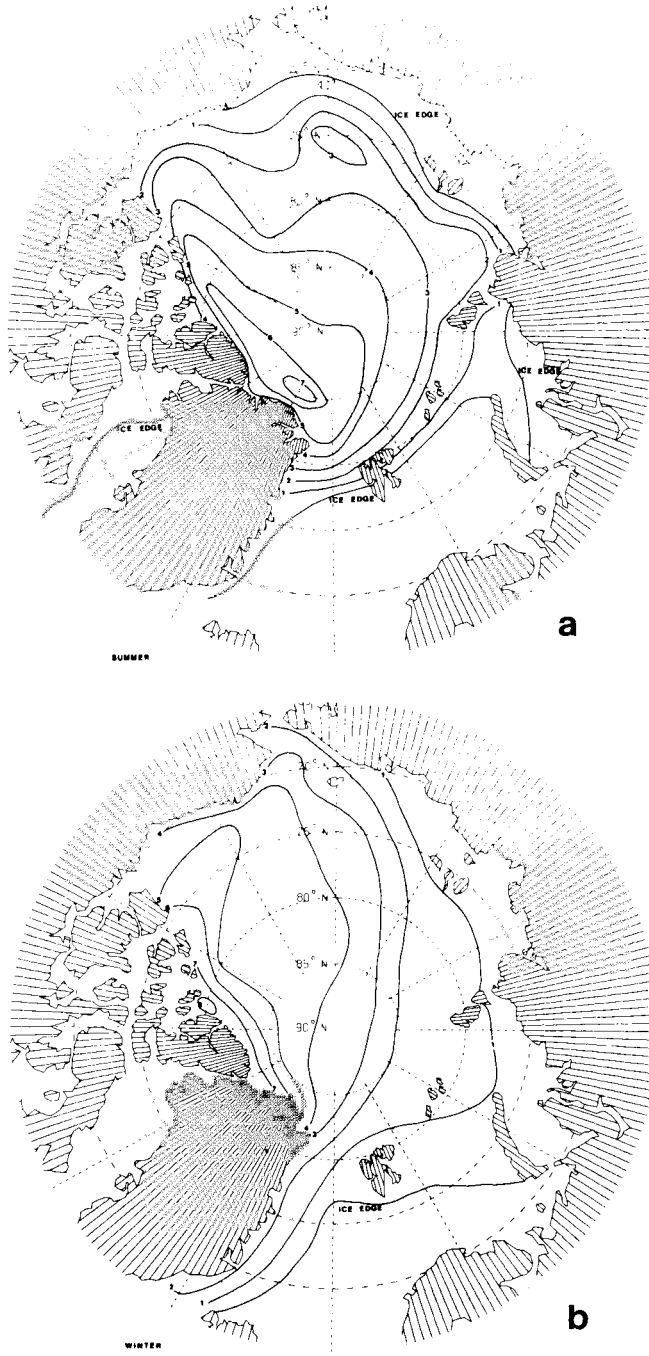

Figure 2.12 Mean ice draft in summer (a) and winter (b) derived from submarine tracks. After Bourke and Garrett (1987).

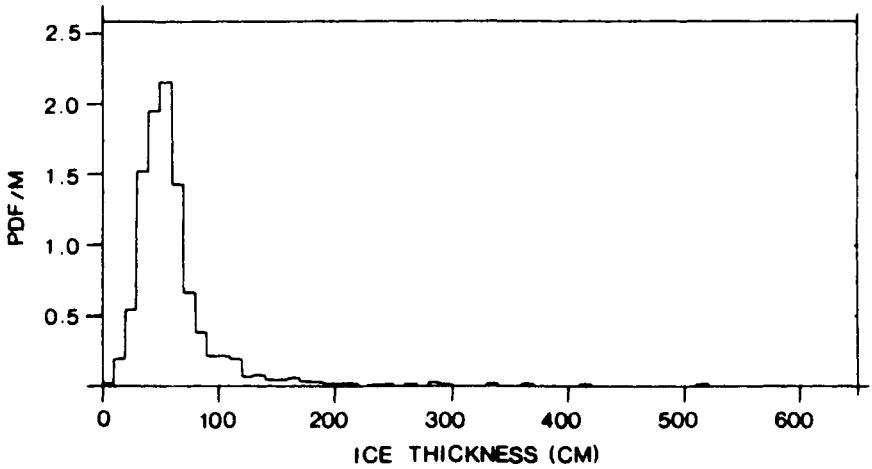

Figure 2.13 Probability density function of ice thickness derived from 4400 drill hole measurements made during winter in the Weddell Sea. After Wadhams *et al.* (1987).

ice-coring investigations (Gow *et al.*, 1987a), indicate that thicknesses of some undeformed floes exceed 4 m. Keys (1984) states that thicker first-year ice is present in the Ross Sea, occasionally reaching thicknesses exceeding 2 m, but time- and space-averaged thicknesses are probably 1–2 m. He also states that multiyear ice is uncommon in the Ross Sea.

E. Ice Extent and Zonation

The most important aspect of the sea ice cover in both the northern and southern hemispheres is the seasonal variability in ice extent. The ice cover experiences large variations in extent because it is an extermely thin layer in comparison to the large area that it covers. Thus, small changes in climate (including seasonal changes) and oceanic heat transport can cause major changes in the extent of the ice cover. Such changes can significantly alter heat and momentum exchanges between the ocean and atmosphere over large areas.

The extent of ice in the Arctic reaches a minimum of about 7×10^6 km^2 in late August or early September (see Fig. B, page xvii). At its maximum in late February or March, the area is doubled, covering about $14-16 \times 10^6$ km^2 (Walsh and Johnson, 1979; Parkinson *et al.*, 1987). During summer, the ice is essentially confined to the Arctic basin with small extensions reaching into the Greenland and Barents seas and the Canadian Archipelago. At its maximum the ice extends far to the south along continental boundaries in many of the adjacent seas. The most southerly extensions of

the ice pack occur in the Labrador Sea and the Sea of Okhotsk, where the ice reaches as far south as 45°N in both seas. As might be reasoned, these areas (as well as the Bering Sea, Baffin Bay, and Davis Strait) contain primarily first-year ice.

In an analysis of the fluctuations of Arctic Sea ice extent, Walsh and Johnson (1979) detected a slight asymmetry in the average rate of advance and retreat of the ice edge. Their findings showed that the growth period proceeded slightly more rapidly than the decay period. In contrast, though using a less extensive data set, Parkinson *et al.* (1987) determined that the growth and decay cycles were nearly symmetric. Walsh and Johnson (1979) and Parkinson *et al.* (1987) both found substantial departures from normal of both monthly and yearly Arctic sea ice extent. These fluctuations indicate the extreme sensitivity of the ice cover to external forcing.

The seasonal variation of ice extent in the Antarctic is far larger than that in the Arctic (see Fig. B, pages xvi–xvii). Minimum extent is reached in February, at which time the total coverage is approximately 4×10^6 km^2, about half of the minimum coverage of Arctic ice. Maximum coverage of about 20×10^6 km^2 occurs in September. The ice cover at maximum extent represents a fivefold increase over the minimum extent and is about 25% larger than the maximum Arctic ice extent. In contrast to the relatively symmetric ice advance and retreat in the northern hemisphere, the spring and summer decay of the Antarctic ice cover occurs much more rapidly than the fall and winter expansion (Zwally *et al.*, 1983). Gordon (1981) suggests that atmospheric heating is not sufficient to account for the rapid decay and implies that the upwelling of warmer deep water may provide a large contribution to the decay process. As in the Arctic, significant monthly and annual departures from normal ice extent have been observed (Zwally *et al.*, 1983).

The differences in seasonal ice extent between the Arctic and Antarctic are due, in large part, to the distribution of the polar land masses. The Antarctic continent is generally contained poleward of 70°S and the sea ice cover forms in the ocean surrounding the continent. The northernmost ice extent occurs in the Weddell Sea, with the maximum extent in other Antarctic oceans generally being confined poleward of 60°S (see Fig. B, page xvi). The seasonal sea ice zone (SSIZ), the area between the minimum and maximum extent, is very large. However, even at maximum extent, the ice cover is confined to a relatively narrow annulus about the continent, its northward progression being hindered by the warmer ocean and atmosphere. The perennial ice zones where the limited amounts of multiyear ice exist are located in the Weddell Sea and adjacent to the continent in other Antarctic seas.

In the Arctic, the area north of 70°N is a landlocked ocean basin which essentially remains ice covered throughout the year. Thus large amounts of multiyear ice exist in the Arctic basin. During winter, cold air flowing from

the adjacent continents allows the ice cover to extend far to the south in some locations, particularly in the Sea of Okhotsk, the Labrador Sea, and the Greenland Sea. In contrast, warm Atlantic water flowing north keeps the southern Barents and Norwegian seas ice free throughout the year. Therefore the land masses serve to direct the atmospheric and oceanic heat flow, which in turn controls ice extent in the SSIZ of the Arctic. In the marginal ice zones, ice conditions and concentrations can vary dramatically as a result of complex interactions between the atmosphere, ice, and ocean. The role of ocean waves in floe breakup is significant for tens of kilometers inside the ice edge. This mechanical breakup greatly expedites the decay of the ice cover in the MIZ.

Shorefast ice zones are located against coastal boundaries. Fast ice is made relatively stable by anchoring itself to the shoreline and to the sea bottom in shallow areas. Pressure ridge keels and multiyear floes which have become grounded in the shallow water also act to stabilize the fast ice. It is in these stable, shallow areas that the largest thicknesses of undeformed first-year ice can accumulate, because the shallow water cools to the freezing point early in the growth season. Widths of the fast-ice zone vary, e.g., from a few kilometers as off Point Barrow, Alaska, to over 100 km on the shallow Siberian shelf. The maximum extent of fast ice in the Antarctic is about 100 km (Keys, 1984). Where rivers are present, the fast ice decays rapidly in the spring when flooding of the ice begins. In some areas of the Canadian Archipelago and in fiords of northern Greenland, fast ice can remain for years and grow to large thicknesses (Walker and Wadhams, 1979). Similarly, fast ice can persist for many years in some bays and coastal indentations of Antarctica — for example, McMurdo Sound, where Gow and Epstein (1972) reported congelation sea ice measuring 15 m thick in an active state of growth.

A shear zone generally is evident between the fast ice and the moving pack ice. This zone consists of extremely deformed ice resulting from shear and pressure of the moving pack against the relatively stable fast ice. The areas of deformed ice tend to become somewhat stable themselves, acting effectively to extend the shear zone tens of kilometers seaward. The coast of Alaska and the western coast of the Canadian Archipelago have very pronounced shear zones, but little is known about the occurrence and extent of shear zones in the Antarctic.

Although we generally think of sea ice in terms of the freezing of surface seawater, it is now believed that large amounts of sea ice are also accreting to the bottoms of Antarctic ice shelves. For example, at Camp J-9, located on the Ross Ice Shelf at a distance of approximately 200 km seaward of the grounding line (boundary separating land ice from the floating ice shelf), Zotikov *et al.* (1980) measured 6 m of coarse-grained congelation ice still

actively accreting to the ice shelf bottom located more than 350 m below sea level. Zotikov *et al.* (1980) estimate that 1–2 cm of sea ice is accreting annually in the vicinity of Camp J-9 and that freezing is occurring over more than 50% of the underside of the Ross Ice Shelf. They infer from additional oceanographic evidence that some distance north of Camp J-9, toward the seaward edge of the Ross Ice Shelf, freezing gives way to bottom melting. Similar situations likely exist under other Antarctic ice shelves, e.g., Filchner–Ronne and Amery, but the areal extent over which freezing is occurring is not known.

III. Small-Scale Ice Properties

A. Ice Growth and Structure: General Considerations

The addition of salt to water depresses the freezing point, T_f, of the seawater according to the approximation $T_f = -0.055S_w$ (Maykut, 1985), where S_w is the salinity per mil of the seawater. Because the great bulk of polar ocean water has a salinity greater than 24.7 per mil, its freezing point is always higher than its temperature of maximum density (Fig. 2.14); surface cooling of this seawater yields an unstable vertical density distribution that leads to

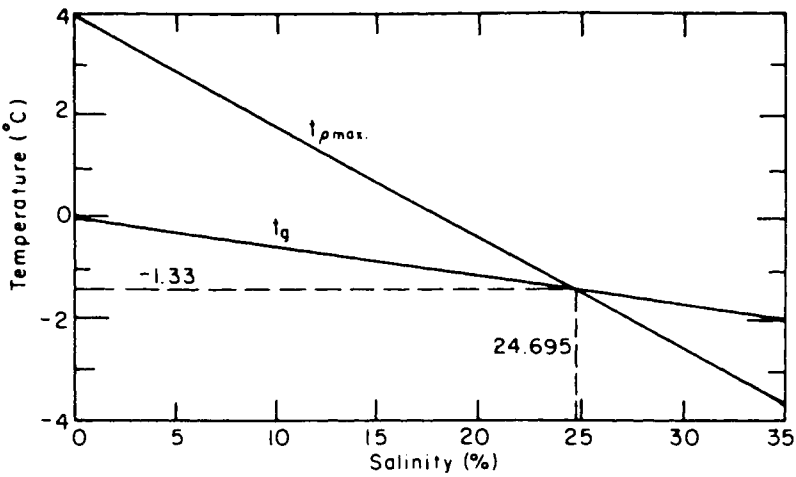

Figure 2.14 Temperature of the density maximum $t_{\rho max}$ and of the freezing point t_g for seawater of different salinities. In normal seawater (salinity >24.7 per mil) a layer of surface water several meters thick must be lowered to its freezing point, or slightly below it, before freezing can begin. After Weeks and Ackley (1982).

convective mixing, which continues until the water reaches the freezing point (Weeks and Ackley, 1982). Density gradients in the upper ocean usually limit the depth to which seawater must be cooled before freezing can begin. Therefore, the density structure of the ocean is a major factor in determining the onset of freezing (Maykut, 1985). Once the entire mixed layer in the upper ocean reaches the freezing point, additional heat loss produces slight supercooling of the water and ice formation begins. The amount of supercooling necessary to initiate ice growth is small, although observations near Greenland have shown a supercooling of as much as 0.2° – 0.4°C to depths of tens of meters (Maykut, 1985).

Sea ice generally contains much less salt than the water from which it froze. Most of this salt is rejected back to the ocean during the freezing process. Further loss of salt occurs during continued growth and aging of the ice by vertical drainage of brine from the ice to the underlying ocean. Normal seawater has a salt concentration of about 34 per mil, and salinities as high as 20 per mil may be found in ice formed during the earliest stages of freezing. By the end of winter, however, the bulk salinity of the ice (1 – 2 m thick) rarely exceeds 6 per mil, which is less than 20% of the salinity of the original seawater.

Initial ice formation occurs at or near the surface of the seawater in the form of small platelets and needles called frazil (Fig. 2.15). Continued freezing results in the production of grease ice, a soupy mixture of seawater and unconsolidated frazil crystals. Under quiescent conditions the frazil crystals quickly freeze together to form a solid, continuous ice cover with thicknesses between 1 and 10 cm. More often, however, wind-induced turbulence in the water inhibits immediate development of a solid cover. Wind and wave action in leads and polynyas drives frazil crystals downwind, where accumulations up to 1 m thick may occur. In the presence of a sustained wave field, pancakes usually form (Fig. 2.16). These circular masses of semiconsolidated frazil, ranging from 0.3 to 3.0 m in diameter, often display irregular raised rims due to constant bumping and pushing up of frazil crystals around their perimeters. Eventually, the pancakes consolidate by freezing together to form a continuous sheet of ice.

Once a continuous ice sheet has formed, the underlying ocean is isolated from the cold air; therefore, latent heat is extracted through the ice sheet by thermal conduction, and the growth rate is now determined by the temperature gradient in the ice and its effective thermal conductivity. Also, once a continuous sheet has formed ice crystals lose a degree of growth freedom. Further crystal growth can proceed, without one grain interfering with the growth of another, only if the grain boundaries are perpendicular to the freezing interface. Direct freezing of seawater to the underside of the ice sheet is called congelation growth and typically yields column-shaped crystals. In

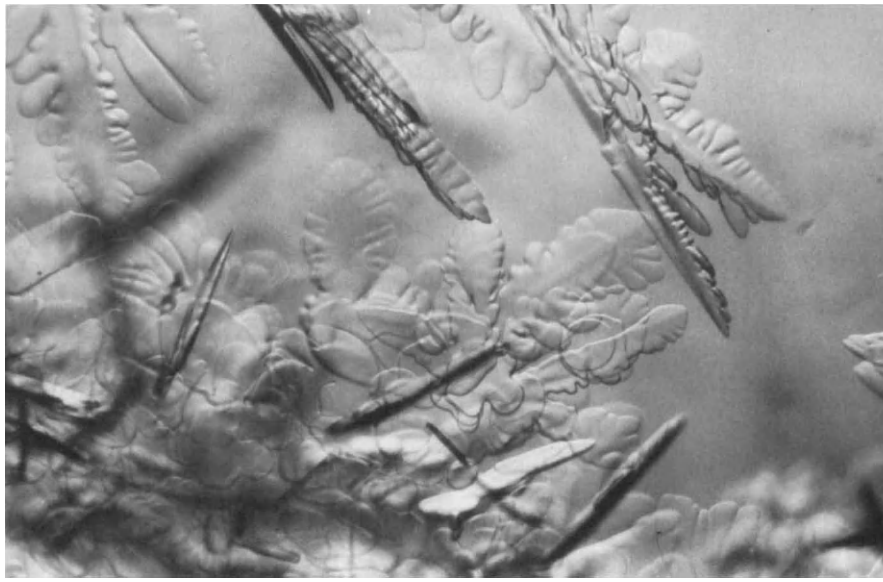

Figure 2.15 Initial stage of ice crystal formation in calm seawater. After Weeks and Ackley (1982).

Figure 2.16 Pancake ice from the Fram Strait. In this instance a sheet of pancake ice was fragmented by wave action to form second-generation pancakes measuring 2–3 m across.

the transition zone between the granular frazil and the onset of columnar congelation ice growth, a process of geometric selection occurs in which crystals in the favored growth direction eliminate crystals in the unfavored orientation. This transition layer is usually 5–10 cm thick (Weeks and Ackley, 1982) and below it congelation ice is found in which there exists a strong vertical crystal elongation parallel to the direction of heat flow. With the onset and full development of congelation growth, the crystals with *c* axes[1] parallel to the ice–water interface quickly begin to eliminate crystals with a less favored orientation. The elimination of the slower-growing crystals proceeds until only crystals with *c* axes substantially parallel to the freezing interface remain.

Within the columnar ice zone a crystal substructure is developed that consists of pure ice plates interspersed with parallel layers of brine inclusions. The overall nature of this substructure, which is best observed in cross section (Fig. 2.17), is the direct result of constitutional supercooling[2], the process by which sea ice incorporates residual brine at the ice–water interface as freezing progresses. Residual brine is the brine that cannot be rejected from the freezing interface, and since brine cannot be incorporated within the ice crystal lattice, it is segregated instead as inclusions between the plates. These plates originate as pure ice dendrites with their tips protruding downward into the seawater beneath the residual brine layer (Fig. 2.18), and it is in the grooves between these dendrites that brine is systematically trapped. Continuation of this process leads to the formation of column-shaped crystals, each crystal consisting of a number of platelike dendrites between which layers of brine pockets are sandwiched (Fig. 2.19). The spacing of these plates (or brine layer separation) varies from a few tenths of a millimeter to about 1 mm, depending on the rate of freezing. With more rapid freezing the plate spacing becomes narrower and the salinity greater. A schematic demonstrating the major changes in the structure of a typical sea ice sheet as outlined above is given in Fig. 2.20. A more detailed and exhaustive account of the overall growth process in sea ice is given in Weeks and Ackley (1982).

[1] The *c* axis is the principal hexagonal axis of the ice crystal; it also corresponds to the optic axis and is widely used as the reference axis for describing crystal structure and for measuring crystal orientation.

[2] Constitutional supercooling is simply compositional supercooling. The process whereby the liquid near the freezing interface can become constitutionally supercooled is due to the different diffusivities of heat and salt in the liquid. Essentially, the heat can be extracted from the liquid faster than the salt can diffuse away, resulting in a supercooled layer at that composition. Such a process has been well documented in connection with solidification from the melt of alloys and impure metals (Tiller *et al.*, 1953). It was subsequently extended to the freezing of salt water by Harrison and Tiller (1963) and Lofgren and Weeks (1967). In the freezing of seawater, constitutional supercooling allows systematic entrapment of brine via the formation of a stable dendritic ice growth interface.

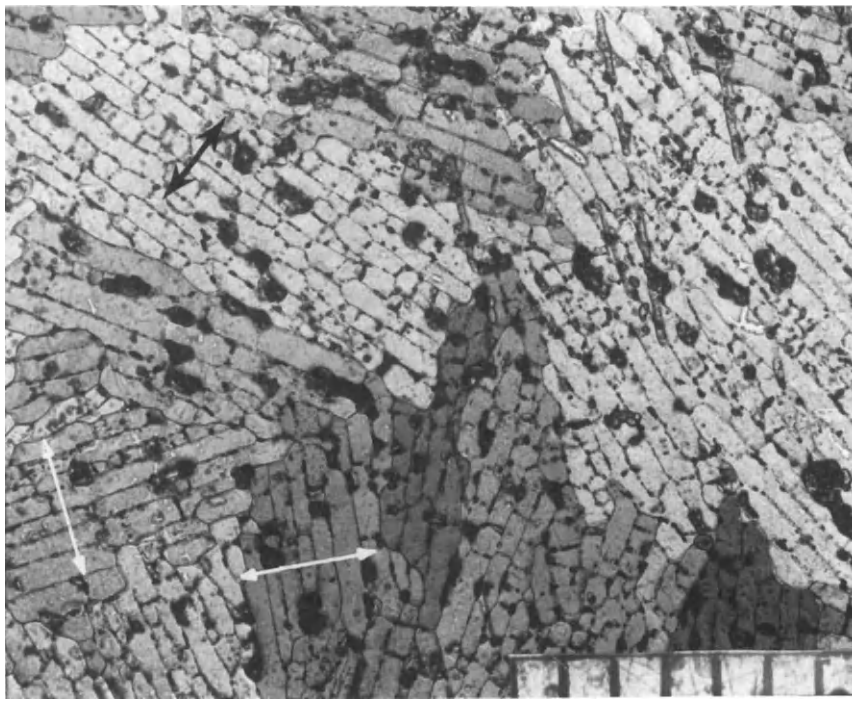

Figure 2.17 Horizontal cross-section photograph of a thin section of sea ice showing the multiplate/brine layer substructure of individual crystals. Arrows indicate *c*-axis orientations in three of the crystals. Scale subdivisions measure 1 mm.

Changes with time in the overall structure of sea ice occur mainly in response to temperature changes in the ice. Brine inclusions are particularly sensitive in this regard; even small changes in thermal regime resulting from daily variations in surface air temperature can cause significant changes in the size, shape, and distribution patterns of the inclusions and the concentration of the entrapped brine. In the case of sea ice subjected to protracted warming, originally disconnected brine inclusions will tend to coalesce into vertical channels that promote migration of the brine. Such a process can lead to substantial redistribution of the brine and eventual drainage and desalination of the ice. Furthermore, desalination and changes in the distribution of the brine are often accompanied by changes in the mechanical properties of the ice, e.g., hardness and strength. The effects of extreme desalination and the resultant increased hardness have been used successfully in the Arctic to differentiate between the two principal ice types—

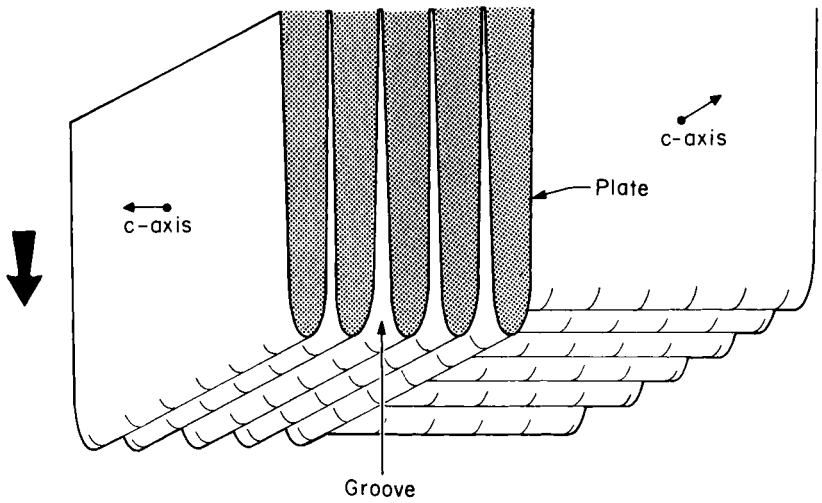

Figure 2.18 Schematic of dendrite and groove structure of two columnar sea ice crystals. Residual brine is trapped in grooves between dendrites (plates), which remain essentially salt free. Large vertical arrow indicates direction of ice growth.

multiyear and first-year sea ice. Physical property changes, particularly those affecting the salinity profile of the ice and the free-water content of the overlying snow, are also responsible for major changes in the electrical properties of the ice, which in turn can have a critical bearing on remote sensing signatures and how they are interpreted (see Chapter 3).

As noted earlier, congelation ice growth invariably leads to the formation of vertically elongated (columnar) crystals with their *c* axes oriented in the horizontal plane. This planar distribution of *c* axes often is tranformed into one in which the *c* axes become aligned in a given direction. Such alignments of *c* axes are commonplace in shorefast sea ice (often extending over areas of many square kilometers) and the direction of the alignment can usually be correlated with the measured or implied direction of current motion at the ice–water interface (Weeks and Gow, 1978, 1980).

In addition to frazil ice, occurring by consolidation of frazil at the top of a sea ice sheet, another type of granular[3] ice is snow ice, which is formed by the

[3] Frazil ice and snow ice are forms of granular ice that originate via different growth mechanisms. The term granular is used to express the textural characteristics of these two kinds of ice. Similarly, the term congelation ice is simply descriptive of the growth mechanism giving rise to columnar-textured crystals. Textural and growth mechanism terms are often used interchangeably.

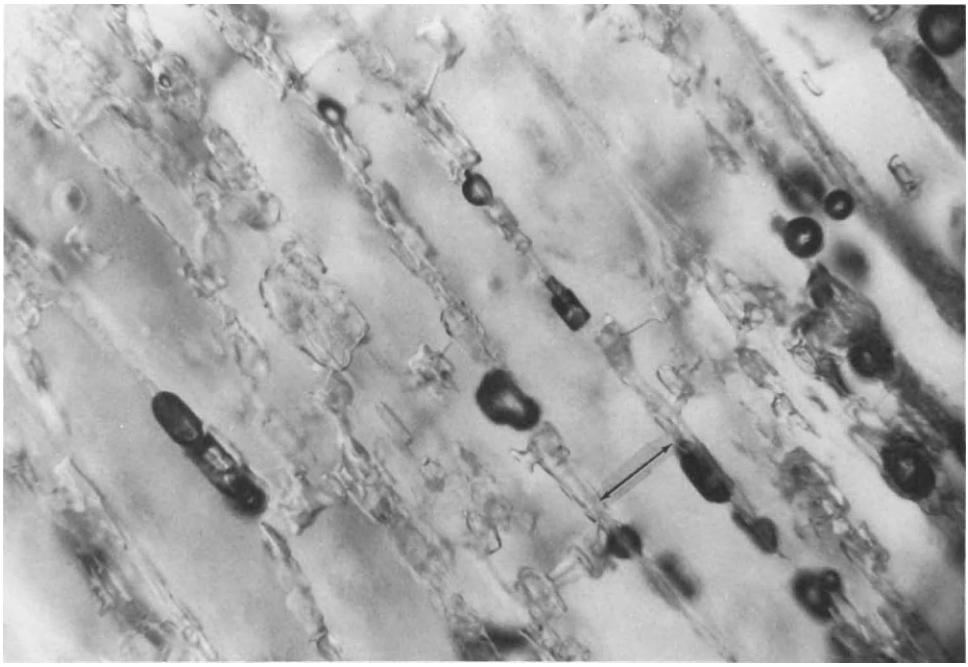

Figure 2.19 Photograph of a thin section of a crystal of sea ice showing individual brine pockets interspersed between the ice plates. The spacing between successive layers of brine pockets (also called the plate spacing) is about 0.6 mm. The *c*-axis direction (arrow) is normal to the platy substructure.

freezing of interstitial water in snow that had been soaked by rain, snow meltwater, or seawater. Naturally, such ice would be restricted to the top of the ice sheet (Fig. 2.20). However, it is often necessary to be able to differentiate snow ice from frazil ice and, occasionally, frazil ice from fine-grained congelation ice (Fig. 2.21). As noted earlier, the formation of sea ice usually begins with the growth of frazil crystals at the surface, but frazil can also form at some depth in the water column beneath a sea ice sheet. By floating upward as either crystals or clumps of crystals, frazil is able to adhere directly to the bottom of an existing ice sheet. Such a process is thought to be responsible, at least in part, for the occurrence of frazil in pack ice in the Weddell Sea (Gow *et al.*, 1982, 1987a). In the Arctic, however, frazil is thought to be mainly the product of turbulent water conditions and thus confined to ice margins, leads, and polynyas. According to Martin (1981), frazil ice accounts for less than 10% of Arctic sea ice, an estimate in general agreement with extensive observations by Weeks and Gow (1978, 1980) of

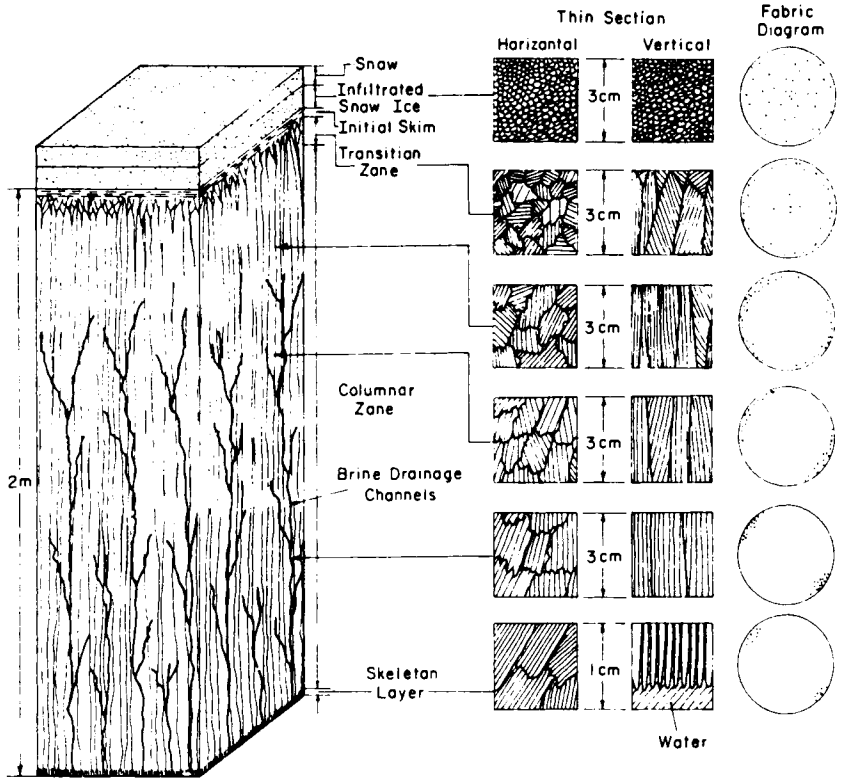

Figure 2.20 Schematic depicting major structural, crystal texture, and *c*-axis fabric elements in a 2-m-thick first-year sea ice sheet. In this schematic the initial skim of frazil ice is overlain in succession by snow ice and snow. The skeleton layer at the bottom of the sheet corresponds to the region of dendritic ice growth. Adapted from Schwarz and Weeks (1977); courtesy of the International Glaciological Society.

shorefast ice along the coasts of the Chukchi and Beaufort Seas and with observations of the structure of ice exiting the Arctic basin through Fram Strait (Tucker *et al.*, 1987; Gow *et al.*, 1987b). In addition, granular ice has been observed in substantial amounts in ridges, where it is thought to originate either by crushing or by growth of frazil in water-filled voids between blocks of ice.

Generally, the various forms of granular ice can all be distinguished from fine-grained columnar ice on the basis of the ice plate/brine layer substructure that characterizes the latter, and differences in texture usually suffice to allow the various granular types to be differentiated. Snow ice, for example, is generally much coarser grained and more bubbly than frazil ice.

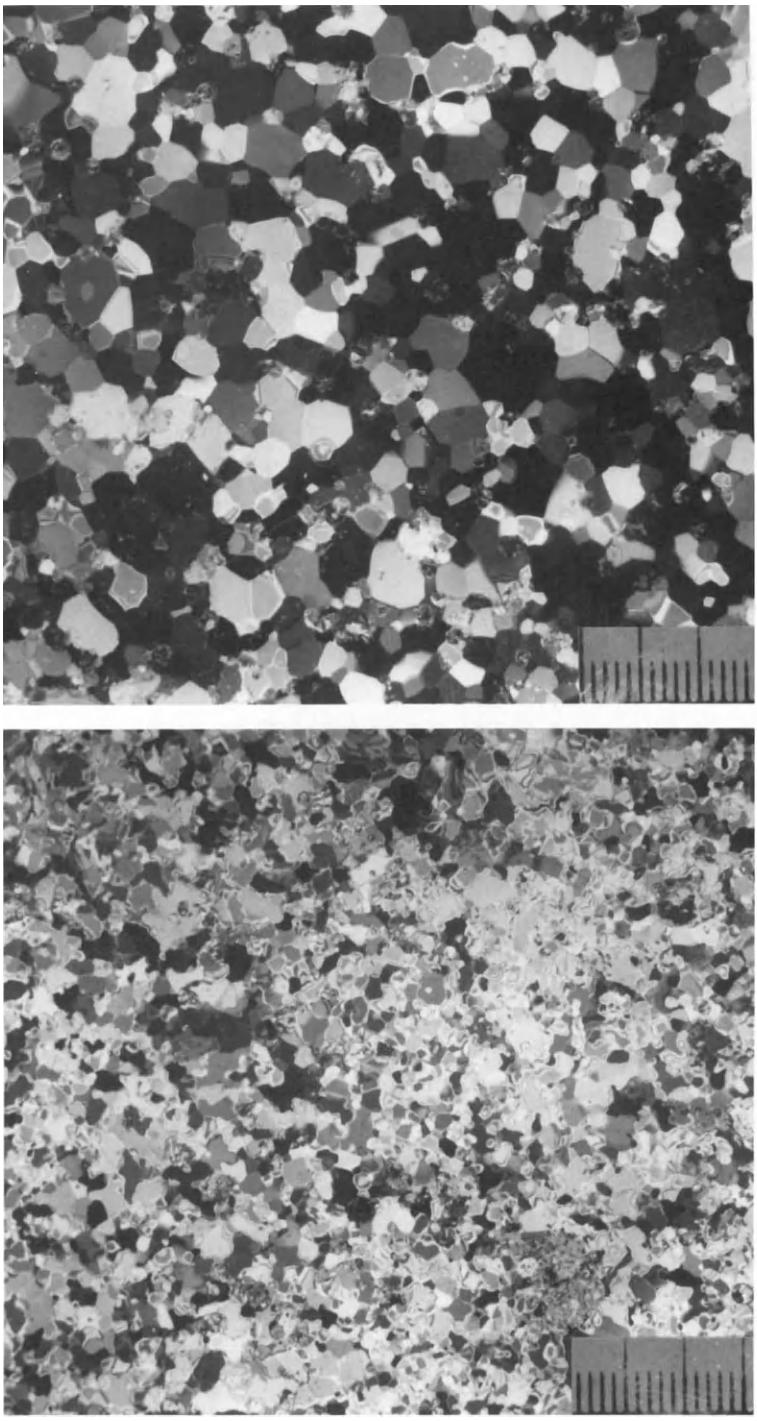
a
b

Principal inclusions occurring in sea ice are brine, salt, and air, with the amounts of each depending on the thermal state of the ice and its age. In addition, varying amounts of lithogenic and biological material may be incorporated into sea ice. Various mechanisms have been invoked to explain entrainment of sediment into both the top and bottom of sea ice sheets. These include turbulent freezing of sediment-laden water, leading to the formation of sediment-rich frazil ice up to 1 m thick; adfreezing of seabed deposits to the bottom of grounded ice sheets; and uplift of sea floor debris to the underside of sea ice by anchor ice crystals. Reviews of the subject are to be found in Osterkamp and Gosink (1984) and Reimnitz *et al.* (1987). Incorporation of biological material, especially algae, into the bottom of sea ice has been documented for both polar regions (see Chapter 9). Differing environmental conditions, leading to the formation of different ice types (e.g., frazil and congelation ice), may help to explain differences among ice algal com-

Figure 2.21 Thin sections photographed between crossed polarizers. (a) Snow ice from the top of an Arctic floe. Note polyhedral shapes of the grains and air bubbles located at the intersection of the grains. (b) Shapeless grains of frazil ice from a depth of 10 cm in Arctic sea ice. (c) Fine-grained congelation ice showing traces of brine layer/plate structure within individual crystals. Smallest scale subdivisions measure 1 mm.

munities. Dieckmann et al. (1986) have also reported on the significance of uprise of platelet ice from depth for biological processes in sea ice forming along the edges of Antarctic ice shelves.

B. Salinity of Sea Ice: General Considerations

The incorporation of salt into sea ice is the singular characteristic feature that distinguishes sea ice from all other forms of floating ice. It is also the single most important parameter in determining the mechanical, electromagnetic, and thermal properties of sea ice. The salt content of sea ice is usually described in terms of a bulk salinity S, where

$$S(\text{per mil}) = \frac{\text{mass of salt}}{\text{mass of ice} + \text{mass of brine}} \times 10^3 \tag{2.4}$$

If ice temperatures are measured simultaneously with salinity, a property known as the brine volume can be calculated (Frankenstein and Garner, 1967; Cox and Weeks, 1983). Brine volume was a commonly used parameter against which temperature-dependent properties of sea ice (e.g., strength) were usually evaluated. However, porosity, which includes air as well as brine volume, is now more widely used. Estimates of the volume of entrapped air require accurate measurements of bulk density, which in the case of freshly formed congelation ice can reach values of 0.92–0.93 Mg m^{-3}. However, in ice that has undergone significant desalination with aging, densities can fall to 0.8 Mg m^{-3} or lower.

The mass of salt initially trapped as brine in the ice depends on both the rate of freezing of the seawater and its salinity. Subsequent changes in the distribution and concentration of salt in sea ice are controlled by phase equilibrium requirements, which dictate that any change in the temperature of the ice must be accompanied by freezing or melting on the walls of brine pockets, leading to reductions or enlargements of the brine pockets and corresponding increases or decreases in the brine volume and brine concentration. With increased warming, as occurs with the onset of summer, individual brine inclusions become larger and ultimately coalesce. In the event of extreme or protracted warming, further coalescence will cause channelization of the brine and result in drainage and desalination of the ice. Some idea of the nature of the changes occurring in sea ice as it ages is given in Fig. 2.22, which shows idealized salinity profiles based on data from several different sources for both first-year and multiyear ice in the Arctic. Important features of these profiles include (a) high salinities at the top and bottom of thinner ice sheets, leading to strongly C-shaped salinity profiles; (b) general weakening of the C-shaped profile accompanied by progressive decrease in bulk salinity with increasing thickness and age of the ice sheet, indicative of downward migration of brine through the ice and its return to the under-

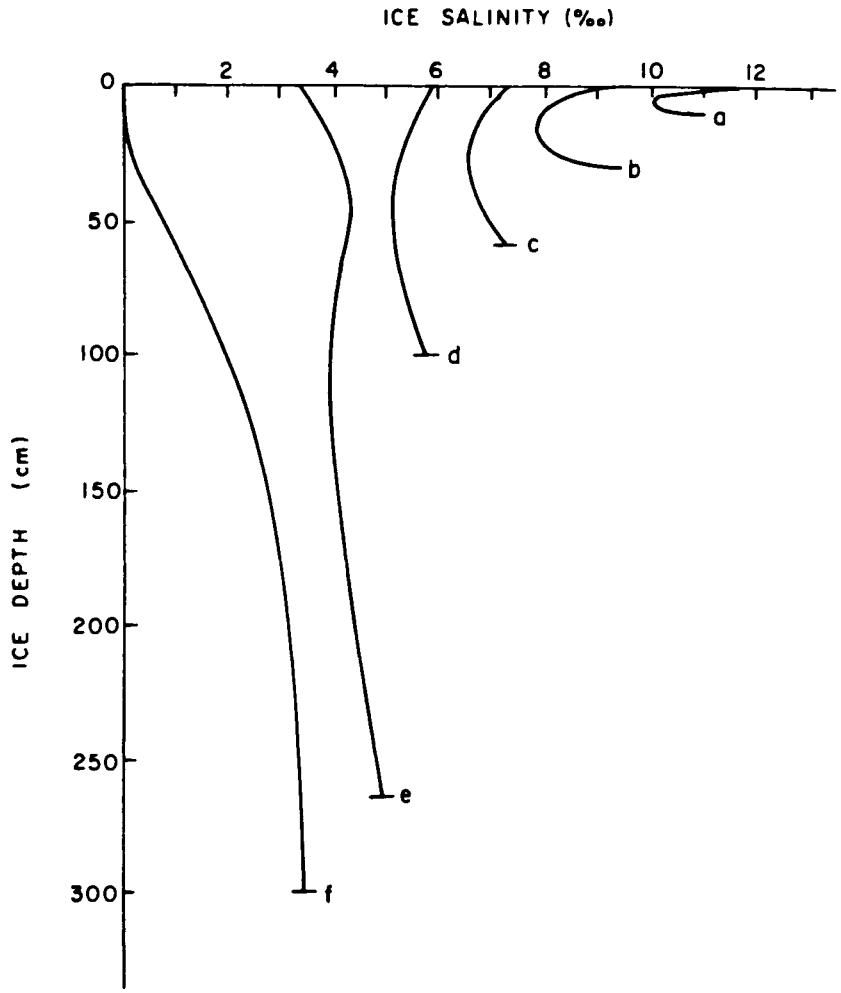

Figure 2.22 Idealized salinity profiles in Arctic sea ice of various thicknesses. Curves a–d represent changes observed in first-year ice. The remaining curves are for two types of profile found in multiyear ice. Curve f represents the salinity profile beneath hummocks and other elevated areas, while curve e typifies the salinity distribution beneath low areas where the surface is close to the freeboard level. Reprinted with permission from Maykut (1985). Copyright CRC Press, Inc.

lying ocean; and (c) virtual desalination of the upper levels of first-year ice during and after its transformation to multiyear ice.

To explain the observed profiles, Untersteiner (1968) described four mechanisms by which brine can be removed from the ice: migration of brine

pockets through ice crystals, brine expulsion, brine drainage, and flushing. The mechanisms can be summarized as follows.

1. Temperature gradients in sea ice lead to the formation of concentration gradients in the brine pockets. Because of phase equilibrium requirements, the ice at the warm end of a brine pocket dissolves while freezing occurs at the cold end, resulting in migration of the brine pocket toward the warm side of the ice. This mechanism is not generally considered to be a significant cause of brine loss.
2. Brine expulsion occurs when a pressure buildup in the brine pocket causes the liquid portion of the inclusion to separate from the vapor bubble. This pressure may become sufficient to cause the surrounding ice to fail along the basal planes of crystals, allowing brine to escape. Brine expulsion upward to the surface is most effective in thin ice when the ice sheet is undergoing rapid cooling. Generally, however, brine expulsion accounts for only a minor amount of the desalination of first-year ice.
3. Gravity drainage is the process whereby brine, under the influence of gravity, drains out of the ice sheet into the underlying seawater. As the ice thickens, its surface gradually rises above sea level in order to maintain isostatic equilibrium, producing a pressure head in the interconnected brine channels which drives the underlying brine out of the ice. Because the density of the brine in equilibrium with the ice is determined by the temperature distribution during the time when the temperature within the ice increases downward, an unstable vertical density distribution exists within the brine channels. This produces convective overturning of the brine within the ice as well as an exchange between the denser brine within the sea ice and the underlying seawater. Cox and Weeks (1975) consider this one of the dominant desalination mechanisms in first-year sea ice, leading to gross weakening of the C-shaped profile that characterizes thinner ice and progressive reduction of the bulk salinity. Actual drainage of brine into the underlying seawater occurs via drainage channels, of the order of 5 mm in diameter, and streamers of brine discharging in this manner can lead to the formation of hollow tubes of ice called "ice stalactites" that can reach lengths of up to 6 m in the Antarctic (Dayton and Martin, 1971).
4. Flushing is a type of gravity drainage that occurs in spring and summer due to the hydrostatic head produced by surface meltwater. This is particularly true of sea ice in the Arctic, where it is thought that flushing is the most effective mechanism of summertime desalination because the time when flushing starts corresponds to the time during the

spring and early summer when major changes in the salinity of the ice, especially in the top 50–100 cm, are observed (Weeks and Ackley, 1982).

The salt rejected initially during the freezing process and later through drainage of brine from the ice passes into the oceanic mixed layer. This is especially important beneath midwinter leads, where rapid ice growth may cause brine plumes to descend into the ocean, giving rise to intense local circulations. Because most of the salt is rejected during growth, the concept of a distribution coefficient becomes important. The distribution coefficient K_{eff} expresses the amount of salt retained by the ice during freezing and is given by

$$K_{\text{eff}} = S_{\text{i}}/S_{\text{w}} \tag{2.5}$$

where S_{i} is the salinity of the ice and S_{w} is the seawater salinity. Cox and Weeks (1975), using radioactive tracers to examine the brine rejection process, were able to determine expressions for K_{eff} as a function of the ice growth velocity. The expressions have been recently slightly modified (Cox and Weeks, 1988) for use in a time-dependent numerical model in which the salinity profile of a growing ice sheet is calculated.

The distribution coefficient can be used to estimate the amount of salt rejected into the oceanic mixed layer. Following Maykut (1982), the flux of salt rejected during growth is given by

$$F = \rho_{\text{i}} f(h)(1 - K_{\text{eff}})S_{\text{w}} \tag{2.6}$$

where ρ_{i} is the ice density and $f(h)$ is the growth rate. Assuming an ice density of 0.92 Mg m^{-3} and determining K_{eff} from the expressions given by Cox and Weeks (1988), we calculate that for an ocean salinity of 33 per mil, fluxes of salt into the mixed layer for growth rates of 10, 5, and 2 cm day^{-1} are 50.3, 29.7, and 13.0 kg m^{-2} mo^{-1}, respectively. Because the growth rate decreases as ice thickness increases, a sustained growth rate of 10 cm day^{-1} is unlikely unless the new ice cover is being continuously advected away. Growth rates of 2–5 cm day^{-1} can be maintained for extended periods, however. These numbers provide for interesting speculation in cases of individual leads. However, when considering salt fluxes over an area or region the role of ice dynamics must be addressed. Maykut (1982) presents model results in which salt fluxes over a large area of the Arctic are calculated using measured ice dynamics and the estimated ice thickness distribution. His results indicate that area-averaged salt fluxes are 1–5 kg m^{-2} mo^{-1} during the ice growth season. The results also indicate that melting during the summer months causes an input of fresh water to the mixed layer which is equivalent to extracting 12–13 kg m^{-2} of salt.

C. Bipolar Comparisons of Sea Ice Salinity

Functional relationships between the average or bulk salinity of Arctic sea ice and its thickness and age were first examined by Cox and Weeks (1974), who found a strong negative correlation between bulk salinity and increasing ice sheet thickness (and age) for cold winter ice and a very weak positive correlation for warm multiyear summer ice (Fig. 2.23). The abrupt change in slope at about 0.4 m for cold ice is consistent with a shift in the dominant desalination mechanism from brine expulsion to gravity drainage. The relationship between salinity (S_i) and thickness (h) in meters of cold ice can be represented by the two best-fit regression lines:

$$S_i = 14.24 - 19.39h \qquad (h < 0.4 \text{ m})$$

and

$$S_i = 7.88 - 1.59h \qquad (h > 0.4 \text{ m})$$

A plot of S_i versus h values for warm ice (Fig. 2.23) shows that the average salinity of warm multiyear ice is lower than that observed for cold ice of similar thickness. A linear regression line for the warm multiyear ice data gives $S_i = 1.57 + 0.18h$. Although a wide range of growth conditions was

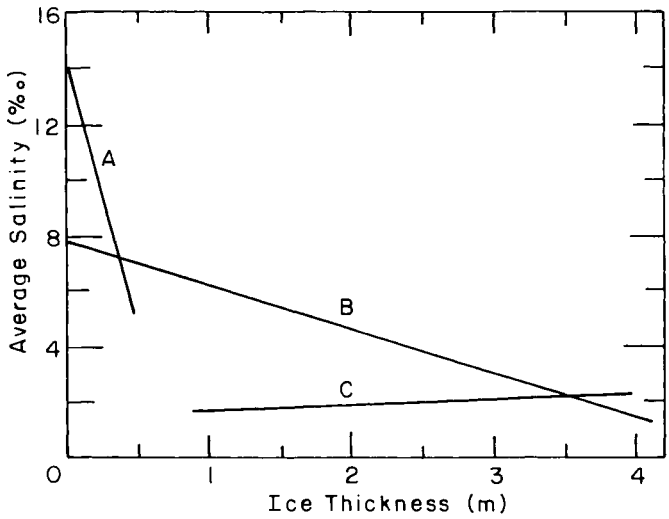

Figure 2.23 Best-fit salinity trend lines for data obtained by Cox and Weeks (1974) for cold ice sampled during the growth season (curves A and B) and for warm multiyear ice sampled during or at the end of the melt season (curve C).

represented, salinity as a function of thickness (and age) displayed relatively little scatter.

From results of the 1984 Marginal Ice Zone Experiment (MIZEX), Tucker *et al.* (1987) and Gow *et al.* (1987b) found a sharp distinction between the bulk salinities of warm first-year and multiyear ice discharging through the Fram Strait from the Arctic basin (Fig. 2.24). For warm multiyear ice the linear regression between salinity S_i and thickness h is $S_i = 1.58 + 0.18h$. Despite some scatter in the data, this least-squares fit is in close agreement with that found by Cox and Weeks (1974) for warm multiyear ice in the Beaufort Sea. On the Ymer-80 expedition, however, where samples were collected in the Greenland and Barents seas, Overgaard *et al.* (1983) found the regression between salinity and thickness to be $S_i = 1.59 + 0.47h$. The slope is more than twice that found by Tucker *et al.* (1987) or Cox and Weeks (1974) and indicates that thicker ice sampled during the Ymer-80 cruise was more saline (≈ 0.8 per mil more saline for 3.0-m ice). However, the differences may not be significant because of the large scatter in the bulk salinities, particularly in the thicker ice categories.

For first-year ice (Fig. 2.24), Tucker *et al.* (1987) obtained $S_i = 3.75 + 0.22h$, while Overgaard *et al.* (1983) found $S_i = 2.15 + 0.19h$. The Ymer-80 sampling took place later in the summer than MIZEX-84, and the lower

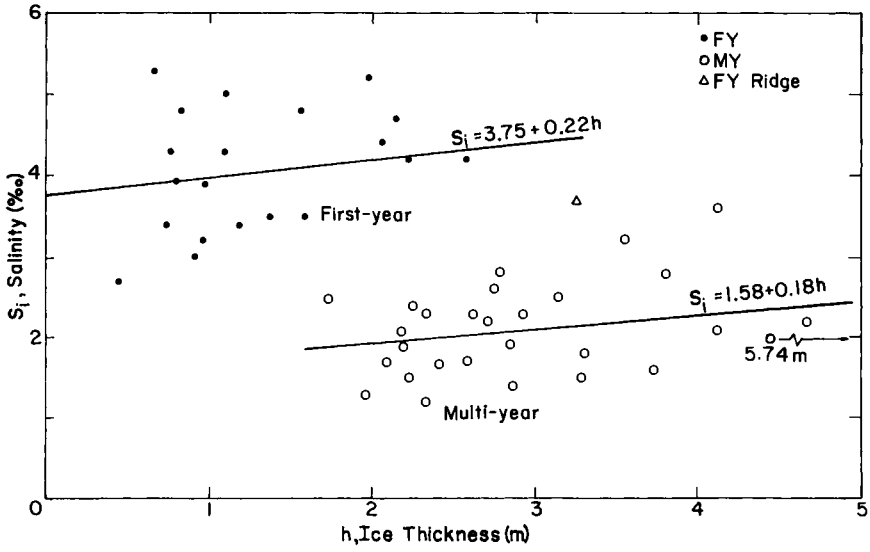

Figure 2.24 Bulk salinity values of ice cores as a function of floe thickness in the Fram Strait. FY, First year; MY, multiyear. After Tucker *et al.* (1987).

salinities observed are in keeping with the trend for salinities to decrease during summer warming. Again, desalination is explained in terms of the very active brine drainage occurring in the ice as it warms.

Tucker *et al.* (1987) also calculated mean salinity profiles of the multiyear and first-year ice cores collected during MIZEX. Separate profiles were calculated for first-year ice cores obtained from June 15 to 28 and July 1 to 9, 1984 in order to examine any possible effects of ongoing brine drainage. Results show that the first-year ice was losing brine for the duration of the field program (Fig. 2.25). The July profile is much less saline (by nearly 2.0

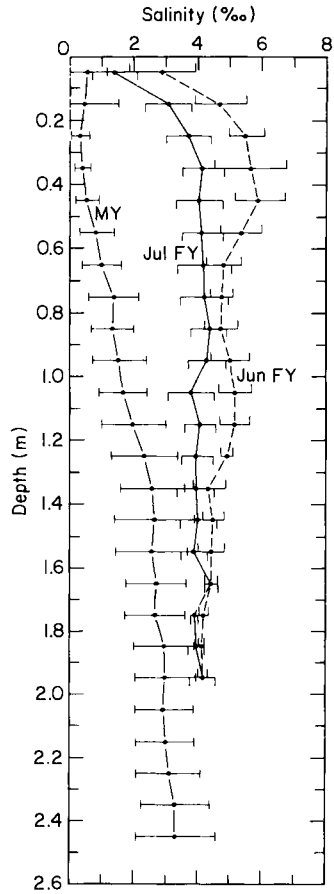

Figure 2.25 Mean salinity profiles from Fram Strait for all multiyear and first-year ice cores analyzed during June and July 1984. After Tucker *et al.* (1987).

per mil at some levels) than the June profile to a depth of 1.5 m, where the profiles begin to converge. All first-year cores had relatively low near-surface salinities, in contrast to normal winter first-year ice, which exhibits a typically C-shaped salinity profile with higher salinities at the top and bottom of the growing ice sheet (Nakawo and Sinha, 1981; Maykut, 1985). The low upper-level salinities are attributed (Tucker *et al.*, 1987) to drainage resulting from warming of the ice prior to sampling. Multiyear ice salinities showed no such temporal dependence when individual mean profiles were calculated for June and July. Extensive desalination during previous summers left the ice nearly free of brine and solid salts, especially in the upper 1.0 m, making further changes difficult to detect.

A comparison of Arctic warm ice data with Antarctic summer sea ice salinity measurements indicates significant differences in their bulk salinities, especially for multiyear sea ice. In the only comparable studies made so far in the Antarctic (Ackley *et al.*, 1980; Gow *et al.*, 1982, 1987a), an average bulk salinity relationship of $S_i = 3.83 + 0.11h$ was obtained for multiyear ice in the Weddell Sea (Fig. 2.26). This relationship yields substantially higher salinities than those found, for example, in Fram Strait ($S_i = 1.58 + 0.18h$). These salinity differences can be attributed mainly to the virtual absence of top surface melting in the Weddell Sea pack (Andreas and Ackley, 1982). This greatly diminishes loss of brine by flushing, a major cause of desalination of sea ice in the Arctic during summer (Untersteiner, 1968). Differences between first-year ice were not as great, with salinities averaging about 0.3–0.5 per mil higher in Weddell Sea ice.

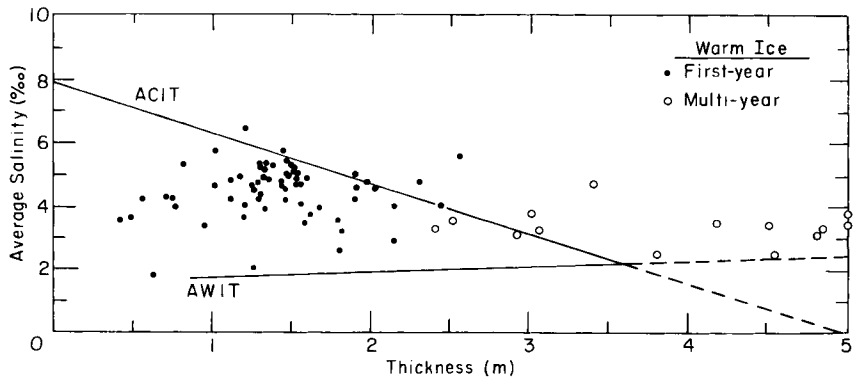

Figure 2.26 Bulk salinities of Weddell Sea ice floes plotted as a function of thickness. Trend lines for Arctic cold ice (ACIT) and Arctic warm (AWIT), after data taken from Cox and Weeks (1974), are included to illustrate the enhanced salinity of warm Antarctic sea ice relative to its Arctic counterpart. After Gow *et al.* (1987a).

Salinity measurements on cold winter-type ice in Antarctica also indicate small but significant departures from those observed in the Arctic (Gow *et al.*, 1982). An example from McMurdo Sound (Fig. 2.27) shows both first-year and multiyear ice to be more saline than their Arctic counterparts. The average salinity of 26 first-year sites was 6 per mil, compared to 4–5 per mil for ice of the same age and thickness in the Arctic. Salinity at the one multiyear site averaged 4.2 per mil, which is more than double the value to be expected in ice of comparable age and thickness (5 m) in the Arctic (Cox and Weeks, 1974). In the case of first-year ice the higher average salinity observed in McMurdo Sound can probably be attributed to faster freezing related to colder winter temperatures than generally prevail at a comparable latitude (78°) in the Arctic.

Salinity variations in sea ice are not limited to changes in the vertical dimension. Tucker *et al.* (1984b), studying small-scale horizontal variations of salinity in a first-year ice sheet in Prudhoe Bay, Alaska, found that substantial horizontal variations also occur over relatively short distances. For six cores spaced 38–76 cm apart, the bulk deviations ranged from 0.2 to 0.8 per mil; an average deviation of 0.4 per mil was found between salinities from the same depth levels. The maximum salinity difference at a given level was 2.0 per mil. These variations in horizontal salinity, which confirmed preliminary observations made earlier by Untersteiner (1968), are attributed by Tucker *et al.* (1984b) to differential drainage of brine related to the irregular distribution of brine drainage channels in the ice.

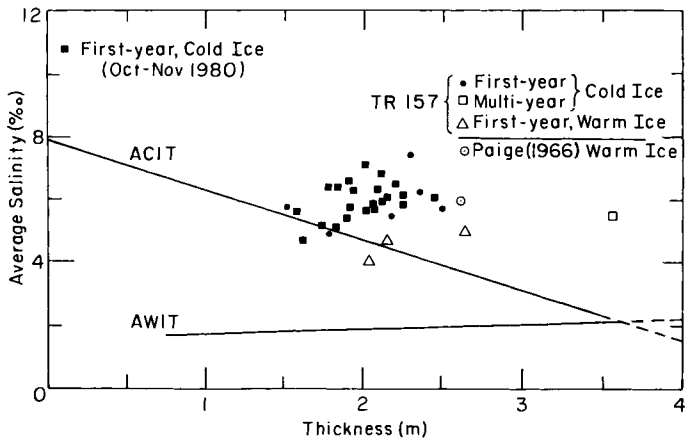

Figure 2.27 Bulk salinities of first-year and multiyear sea ice in McMurdo Sound, Antarctica plotted as a function of thickness. Trend lines for Arctic cold ice (ACIT) and Arctic warm ice (AWIT) are included for comparison. Data indicated by TR 157 were taken from earlier measurements by Hendrickson and Rowland (1965).

D. Crystalline Structure of Polar Sea Ice

As described earlier in this chapter (Section III,A), sea ice has a polycrystalline structure that can occur in several different textures, e.g., granular and columnar, depending on the nature of freezing of the water. These textural variations and the changes associated with thermally activated modification of the ice as it ages have furnished a basis for distinguishing between different ice types, e.g., first-year and multiyear ice. In addition, differences in crystalline texture and the nature and distribution of brine inclusions exert a major effect on the mechanical, optical, and electrical properties of sea ice.

The past 10–15 years have seen a marked resurgence of interest in sea ice research, which can be attributed in part to the discovery of vast oil reserves on the Arctic continental shelf and in part to the increased application of satellite and airborne remote sensing to studies of the polar ocean ice cover. During this period a number of important findings have been made concerning the crystalline structure of sea ice, including (1) the discovery of widespread *c*-axis alignments in shorefast ice and their likely correlation with the direction of the oceanic current at the ice–water interface; (2) the first detailed examination of the crystalline structure of first-year and multiyear ice floes exiting the Arctic basin via Fram Strait, including the assessment of new approaches for distinguishing between first-year and multiyear floes; and (3) the discovery that granular frazil ice is an important, if not major, component of Antarctic pack ice as opposed to columnar congelation ice, which dominates the structure of Arctic pack ice.

1. *c*-Axis orientations in sea ice

Field observations of the growth fabrics of fast and near-fast ice along the coasts of the Beaufort and Chukchi seas show that at depths of more than 60 cm below the upper ice surface, congelation sea ice crystals frequently display striking alignments within the horizontal plane (Gow and Weeks, 1977; Weeks and Gow, 1978; 1980). It had been known (see review by Weeks and Ackley, 1982) that in congelation-type sea ice a dominant horizontal *c*-axis crystal orientation develops rapidly after an initial ice skim has formed. It was not as well known that the *c* axes often become strongly aligned within the horizontal plane. A few isolated observations, mainly on sea ice incorporated into ice islands (Cherepanov, 1964; Smith, 1964) and a single measurement on first-year ice by Peyton (1966), indicated the existence of strong azimuthal alignments of the *c* axes. However, apart from later work by Cherepanov (1971) in the Kara Sea, the regional extent of such alignments and the probable explanation of their origin did not become apparent until the work of Weeks and Gow (1978, 1980), which indicated

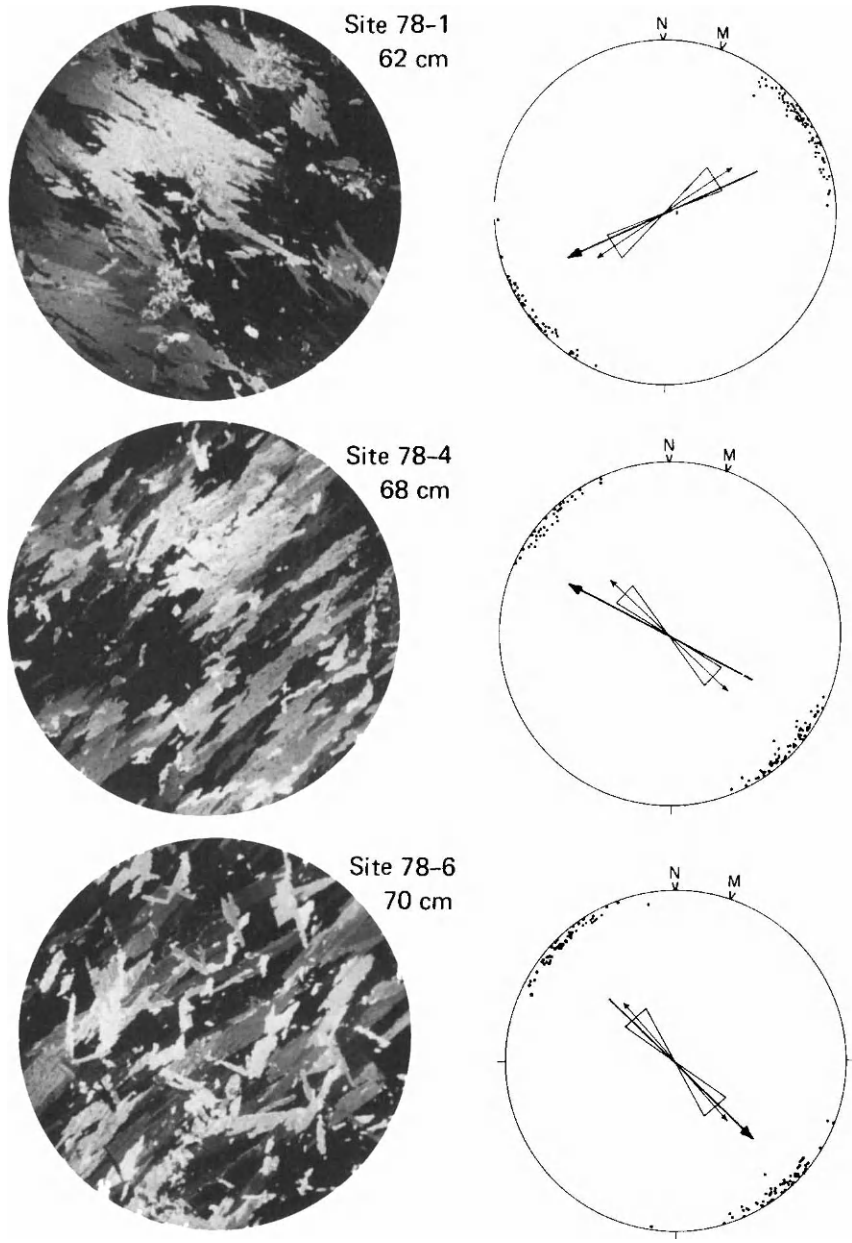

Figure 2.28 Equal area, horizontal projection plots of individual *c*-axis orientations (dots) from three sites in Kotzebue Sound, Alaska, showing strong *c*-axis alignments. The mean direction of *c*-axis alignment at each site is indicated by the double-arrowed line; simultaneously measured current directions beneath the ice are indicated by the single-arrowed lines. Current speeds ranged from 0.06 m s^{-1} at sites 78-1 and 78-4 to 0.02 m s^{-1} at site 78-6.

that the direction of the current at the growing ice–water interface controlled the direction of *c*-axis alignments.

Working along a 1200-km stretch of the north coast of Alaska between the Bering Strait and Barter Island, Weeks and Gow (1980) obtained excellent correlation between *c*-axis alignment directions and current measurements (Fig. 2.28). A similar situation was apparent in a reexamination of Cherepanov's (1971) results from the Kara Sea. Cherepanov did not include current data in his diagram of *c*-axis alignments, but when such information, based on summaries of ocean current data from the U.S. Navy sources, is included, remarkable agreement between the direction of *c*-axis alignments and current direction is obtained (Fig. 2.29). This correlation extends beyond the boundary of the fast ice into the pack ice, indicating that at the time Cherepanov made his observations (March–April 1969) the pack ice was "frozen in" and undergoing little, if any, drift or rotation. Laboratory work by Langhorne (1983), Langhorne and Robinson (1986), and E. Stander

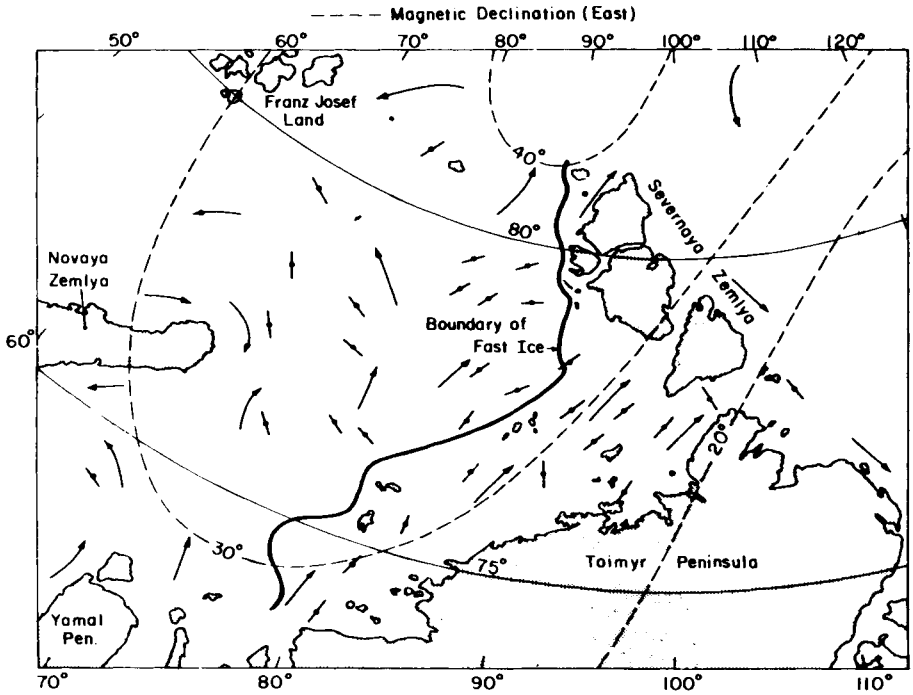

Figure 2.29 The *c*-axis orientations determined by Cherepanov (1971) in sea ice in the Kara Sea region of the USSR. The arrows indicate the estimated direction of the surface currents obtained from U.S. Navy sources. After Weeks and Gow (1980).

(personal communication) confirms this relationship between the direction of *c*-axis alignment and the direction of the prevailing current. Stander and Gidney (1980) have proposed an alternative mechanism based on stress-activated recrystallization to explain *c*-axis alignments, but convincing evidence supporting such a mechanism is lacking.

Weeks and Gow (1978, 1980) postulate that aligned *c* axes are ultimately caused by the current affecting the transfer of impurity (salt) at the growing interface, with crystals with their *c* axes aligned parallel to the current gaining a slight growth advantage. Crystals whose *c* axes are oriented closest to this favored direction (parallel to the current) eventually eliminate less favored neighbors, a situation ultimately leading to the strong *c*-axis alignments observed. As such, *c*-axis alignments can be used to infer the principal current direction at a given location in shorefast ice. The development of strong crystal alignments also results in pronounced anistropy in the mechanical (Richter-Menge and Cox, 1985a) and electrical properties (Campbell and Orange, 1974; Kovacs and Morey, 1978) of shorefast ice.

2. Arctic sea ice structure

Observations over the past 10–15 years of shorefast and near-shorefast ice along the coasts of the Arctic Ocean show that the great bulk of the ice (90% or more) is composed of congelation columnar-textured ice (Weeks and Gow, 1978, 1980; Martin, 1981). During the past few years concerted efforts have been made to evaluate the composition and structure of ice originating in the Arctic basin. As part of MIZEX, the first detailed examination of the structural and physical properties of sea ice exiting the Arctic basin via the Fram Strait was made. The importance of Fram Strait is that it is the major outflow region for Arctic basin ice; according to Maykut (1985), approximately 10% of the ice in the basin is discharged annually through this relatively narrow strait located between the northeast coast of Greenland and Spitzbergen.

Prior to MIZEX very little was known of the structural characteristics of sea ice exiting the Arctic basin, and the discussion that follows is taken largely from results obtained by Tucker *et al.* (1987) and Gow *et al.* (1987b) for a large number of floes in the Fram Strait. Analyses were based mainly on examinations of cores drilled through the entire thickness of each floe. A major objective was to distinguish between first-year and multiyear ice, the identification of which was based largely on differences in their crystalline condition and salinity. Crystalline structure was assessed mainly on the basis of optical thin-section techniques (Weeks and Gow, 1978, 1980).

Identification of multiyear ice from measurements of freeboard or drilled thickness does not always prove reliable because of thickness overlaps be-

tween the thinnest multiyear ice (1.7 – 1.8 m) and the thickest undeformed first-year ice (2.3 m). However, positive identification of multiyear ice can generally be made from observations of the appearance and mechanical condition of the core drilled in the top meter of a floe. Because of the nature of its transformation (by thermal modification of first-year ice during the summer), approximately the top half-meter of multiyear ice becomes very much harder (more resistant to drilling and sawing) and appreciably less opaque than the upper half-meter of first-year ice. The opaque appearance and relative softness of first-year ice are closely linked to an abundance of brine pockets that enlarge, coalesce, and drain during the summer to yield ice with the hardness and transparency characteristics observed in the upper levels of multiyear ice.

Analyses of the crystalline structure of Arctic ice floes have shown that ice textures are predominantly of columnar (congelation) origin in both multiyear and first-year floes. Small amounts of granular ice, mainly frazil ice but including some snow ice, were found in nearly every floe (Fig. 2.30). This is not surprising because the freezing of seawater generally begins with the formation of grease or slush ice. If ridged ice were excluded from the ice composition estimate, the congelation component would amount to 85% of total ice thickness in undeformed floes. Although the granular ice content of undeformed ice floes is somewhat higher (15%) than the 5 – 10% that Martin (1981) reports for Arctic nearshore conditions, it should be noted that Martin restricted his study to thick first-year ice, whereas the Fram Strait (MIZEX-84) investigations spanned a large range of ice thicknesses dominated by multiyear floes. It was also observed that one-third of multiyear ice floes examined for structure in the Fram Strait contained previously de-

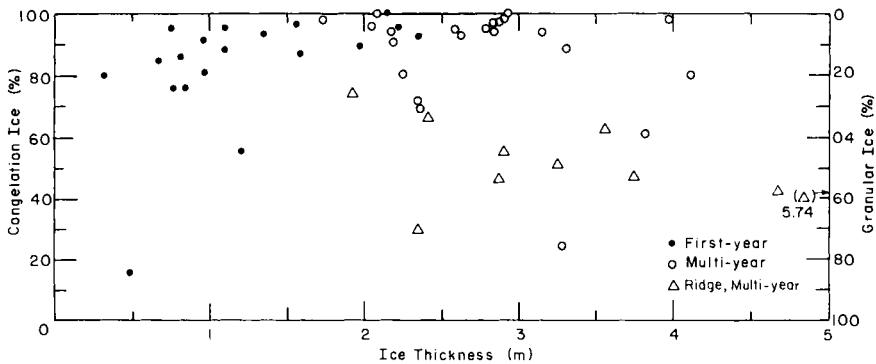

Figure 2.30 Percentages of columnar (congelation) and granular ice as a function of thickness for various ice floe types in the Fram Strait. After Gow *et al.* (1987b).

formed ice, indicating that multiyear floes may be composed of substantial amounts of deformed ice (often occurring as worn-down ridge remnants).

A typical example of first-year ice encountered in the Fram Strait is shown in Fig. 2.31. The floe consisted primarily of columnar ice exhibiting a moderate to strong *c*-axis alignment overlain by a thin (< 10 cm) layer of snow. An approximate 60° change in *c*-axis alignment at about 50 cm depth, suggesting a significant change in the direction of the prevailing current at the ice–water interface, is most probably linked to repositioning of the winter pack in which this piece of ice was growing. The top of the floe featured a thin (2–3 cm) layer of ice derived either from freezing rain or by refreezing of early spring snowmelt. Either process would be consistent with both the desalinated nature of the ice and the elevated temperatures measured at the top of the floe. The bulk salinity of the floe was 4.4 per mil.

A fairly typical example of undeformed multiyear Arctic ice (Fig. 2.32) was found to consist mostly of aligned crystals of columnar ice overlain

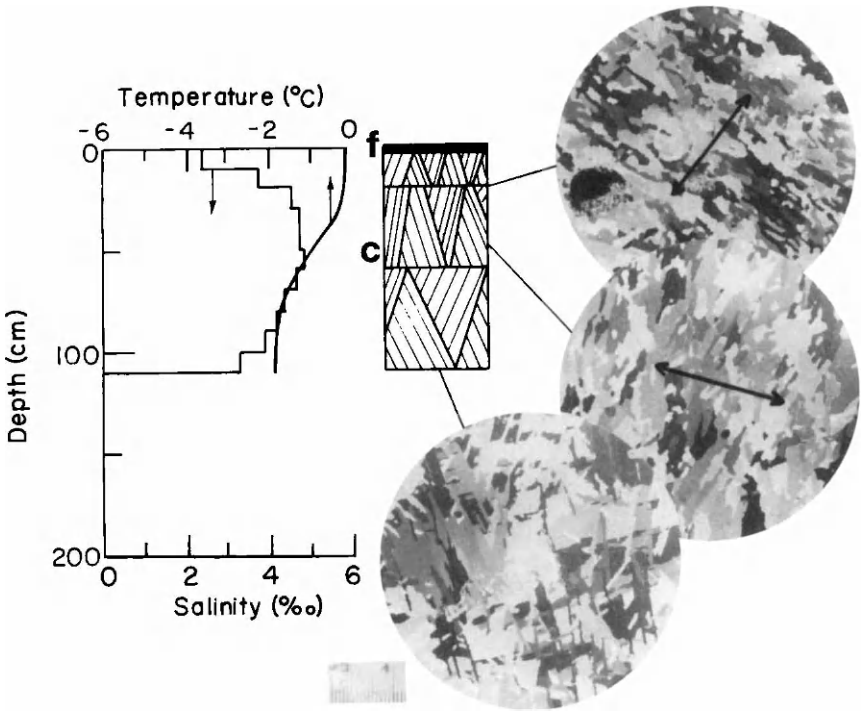

Figure 2.31 Salinity–temperature–structure profiles of an undeformed first-year floe in the Fram Strait. In the vertical structure diagram the symbols f and c designate freshwater ice and columnar ice, respectively. Arrows in horizontal thin section photographs indicate the direction of crystal *c*-axis alignment. After Gow *et al.* (1987b).

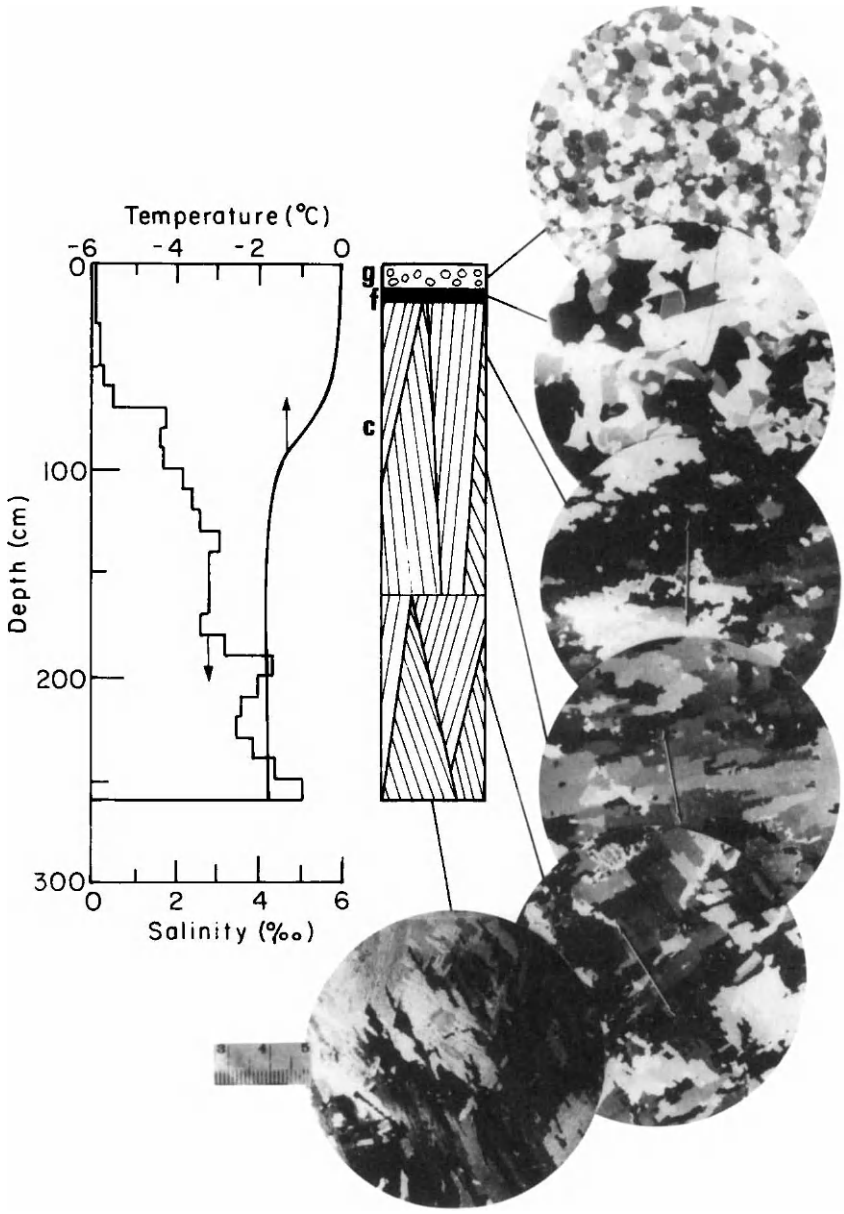

Figure 2.32 Salinity–temperature–structure profiles from an undeformed multiyear ice floe in Fram Strait. The symbols g, f, and c beside the vertical structure diagram designate granular ice, freshwater pond ice, and columnar ice, respectively. Arrows in horizontal thin-section photographs indicate directions of *c*-axis alignment. After Gow *et al.* (1987b).

successively by 7 cm of pond ice, 11 cm of snow ice, and a 25-cm-thick layer of snow. Structure and salinity characteristics indicate a 2-year-old floe that underwent appreciable desalination in the top 70 cm during the summer of 1983. This desalination was accompanied by ponding and subsequent refreezing of the surface water and by very substantial retexturing of the columnar ice to a depth of at least 100 cm. Individual salinities in the top 70 cm did not exceed 0.5 per mil; the overall salinity averaged 2.3 per mil, or only about half of that measured in the first-year floe (Fig. 2.31). A significant salinity surge, beginning at 180 cm depth and yielding salinities in excess of 4 per mil, corresponds closely with the onset of the second winter's ice growth.

Figure 2.33 features a multiyear floe from Fram Strait in which very thick, coarse-grained freshwater pond ice, representing 47% of the floe thickness, is underlain by columnar sea ice. The sharp textural transition from pond ice to columnar ice was also accompanied by a sharp increase in salinity. A very large (80°) change in *c*-axis alignment between 1.0 and 1.5 m implies that the melt pond was underlain by only a thin layer of sea ice at the end of the summer and that the bottom 0.5 – 1.0 m of ice represented growth during the ensuing winter.

Most of the granular ice observed by Tucker *et al.* (1987) in floes in the Fram Strait was associated with frazil crystal formation in old ridges. Such frazil occurred both in the voids between blocks of ice and near the bottoms and on the flanks of ridges. That found on the flanks of keels most likely originates as the frazil present in the water column is accumulated by the sweeping action of the keel as it moves relative to the water column. Only limited amounts of granular ice appear to have been generated by crushing of coarser-grained ice during the ridging process. On average, the multiyear ridges consisted of 40 – 60% frazil ice. Similar findings of high granular ice contents in multiyear ridges have been reported by Richter-Menge and Cox (1985b). The top 1 m of ice in the old ridge fragment featured in Fig. 2.34 consisted of a mixture of tilted blocks of columnar ice with granular ice between the blocks, whereas the lower part of the ridge contained more granular (principally frazil) ice underlain by columnar ice representing recent growth on the flank of the ridge.

Another structure-related feature observed by Tucker *et al.* (1987) in the uppermost layers of Arctic multiyear sea ice is the retextured condition of the ice crystals. This retexturing process is related to the elimination of brine pockets and the rounding off of crystal boundaries induced by elevated air temperatures and increased solar radiation during summer. The depth of retexturing may exceed 100 cm, and the glacial-like, brine-poor ice that results from thermally activated retexturing bears little resemblance to the original columnar-textured sea ice. The extent of the process is illustrated in thin sections of ice from a multiyear floe (Fig. 2.35).

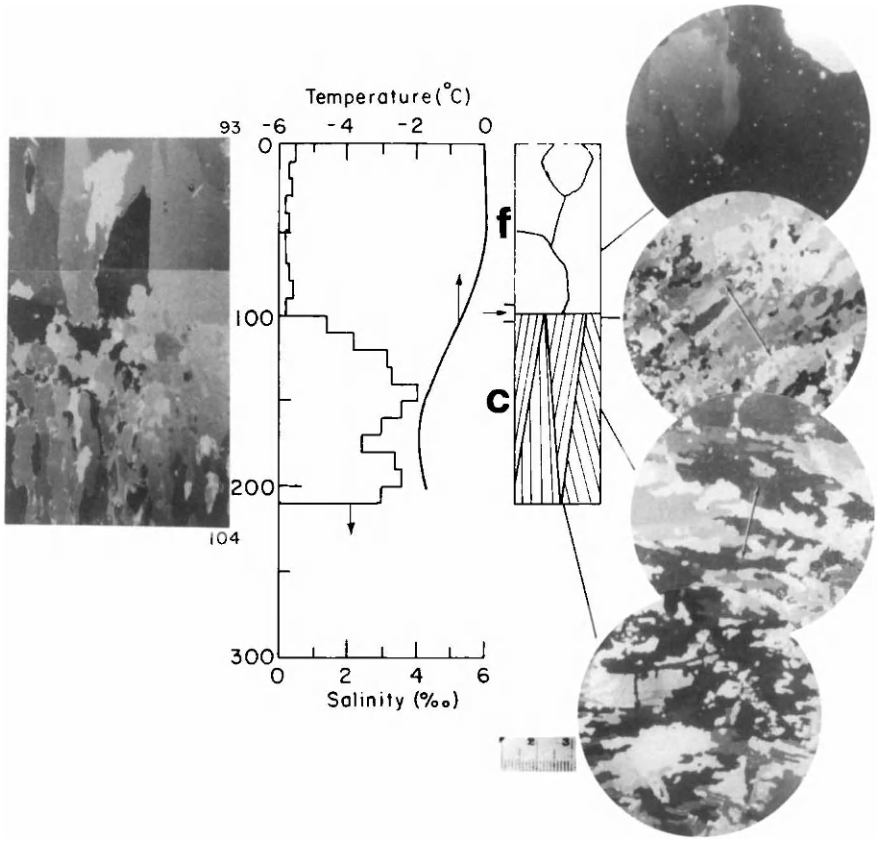

Figure 2.33 Salinity–temperature–structure profiles from a ponded multiyear ice floe in Fram Strait. The symbols f and c designate freshwater pond ice and columnar ice, respectively. The vertical thin-section phtotgraph shows the transition between the ponded and columnar ice at around 100 cm depth. The *c*-axis alignments in horizontal thin-section photographs are also indicated. After Gow *et al.* (1987b).

Most floes examined during MIZEX exhibited evidence of *c*-axis alignments related to growth of ice under the direct influence of oceanic currents. Changes in the direction of alignment at two or more levels in the ice were observed in a number of floes. Such changes have been attributed to alternating episodes of movement and immobilization of a floe and thus constitute a record of a floe's orientation relative to the direction of current motion beneath the ice. Assuming that the *c* axes align on an annually repeating basis, consistent with wintertime growth, such changes in alignment direc-

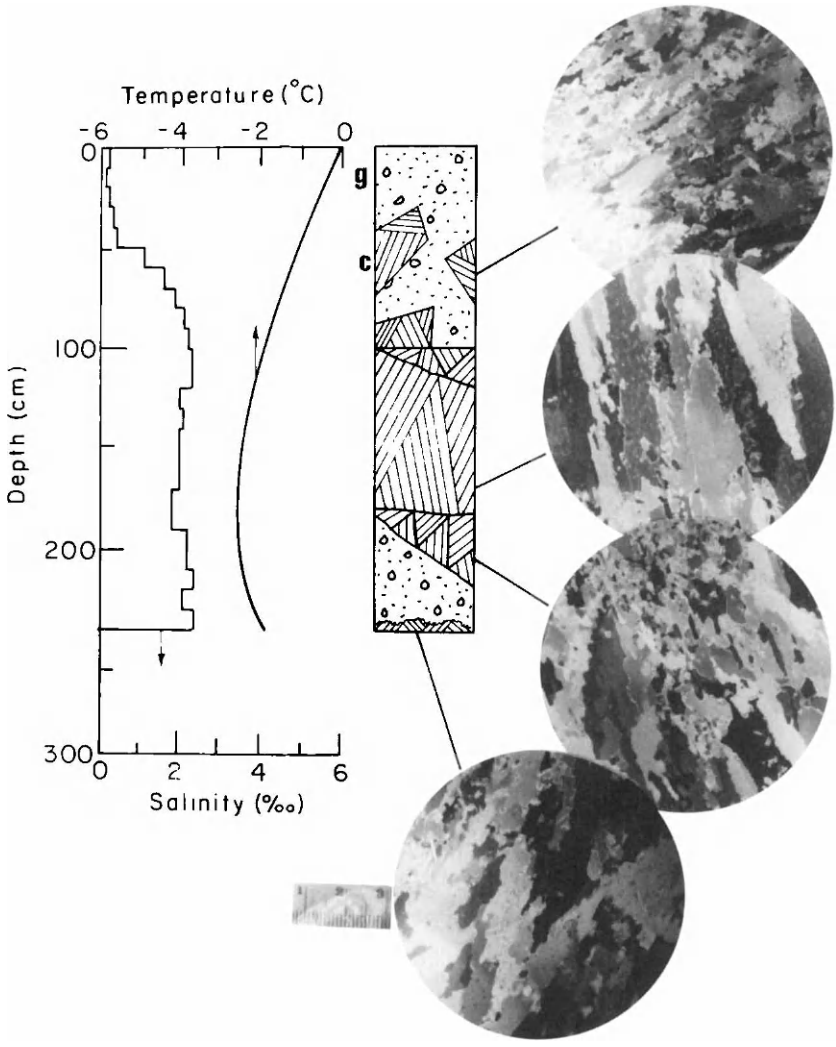

Figure 2.34 Salinity–temperature–structure profiles through old ridged ice in a multiyear floe in Fram Strait. The symbols g and c beside the vertical structure diagram designate granular ice and columnar ice, respectively. After Gow *et al.* (1987b).

tion, together with crystal texture changes and surges in the salinity profile (which often coincide with change of crystal alignment), have been used to estimate the ages of multiyear floes (Gow *et al.*, 1987b).

A winter marginal ice zone experiment was conducted in March and

April 1987. Results of sea ice observations (Perovich *et al.*, 1988) essentially duplicated those obtained in MIZEX.

3. Antarctic sea ice structure

Current knowledge of the dynamics, structure, and related physical properties of Antarctic pack ice stems largely from studies initiated by Ackley in the Weddell Sea (Ackley, 1979a,b, 1981; Ackley *et al.*, 1978, 1980; Gow *et al.*, 1981, 1982, 1987a; Lange *et al.*, 1988). The open, broad-fronted nature of the marginal ice zone in the Weddell Sea contrasts drastically with the largely landlocked situation prevailing in the Arctic basin. This and the fact that the Weddell Sea embayment is backed by a large floating ice shelf, the Filchner–Ronne, appear to have a sufficiently strong impact on near-surface oceanic circulation in the Weddell Sea to cause significant differences in the formational processes and structure of sea ice compared to those of the Arctic basin.

During February and March 1980, 52 first-year and 14 multiyear floes were investigated by Ackley *et al.* (1980) along a 600-nautical-mile transect of the ice edge in the Weddell Sea (Fig. 2.36). In the absence of surface melt features, the higher freeboards of multiyear floes proved the only reliable criterion by which to distinguish these floes from first-year ice in the Weddell Sea.

The most significant result concerning the crystalline structure of Weddell Sea pack ice was the discovery of granular ice, principally frazil, in amounts not observed previously. In many of the ice floes examined structurally in 1980, frazil ice was the dominant component, averaging 72% of the ice thickness of 13 multiyear floes and 37% of 49 first-year floes. The overall average composition, based on the total length of first-year and multiyear cores examined for structure, yielded 54% frazil ice, 39% congelation ice, and 7% admixtures of the two plus snow ice. In general, a higher percentage of congelation ice was found in floes up to 2 m thick (Fig. 2.37). However, every floe thicker than 2 m, except one first-year floe, contained more frazil than congelation ice. Much of this frazil appeared to have been generated during the second year of growth (Fig. 2.38). However, there were cases where multiyear floes were composed entirely of frazil ice (Fig. 2.39).

Interspersed layering of frazil and congelation ice (Fig. 2.40) in many floes shows that frazil formation is episodic. Such structure, especially in thinner floes (< 1.0 m), is consistent with multiple rafting events (overriding of ice sheet fragments one upon the other), and recent studies of winter ice growth in the central Weddell Sea indicate that rafting of frazil-rich pancake ice is an important, if not major, mechanism of frazil ice production at the advancing ice edge (Lange *et al.*, 1988). However, Gow *et al.* (1987a) observed frazil ice occurring in a variety of textures and, at depths of up to 5 m in the thickest

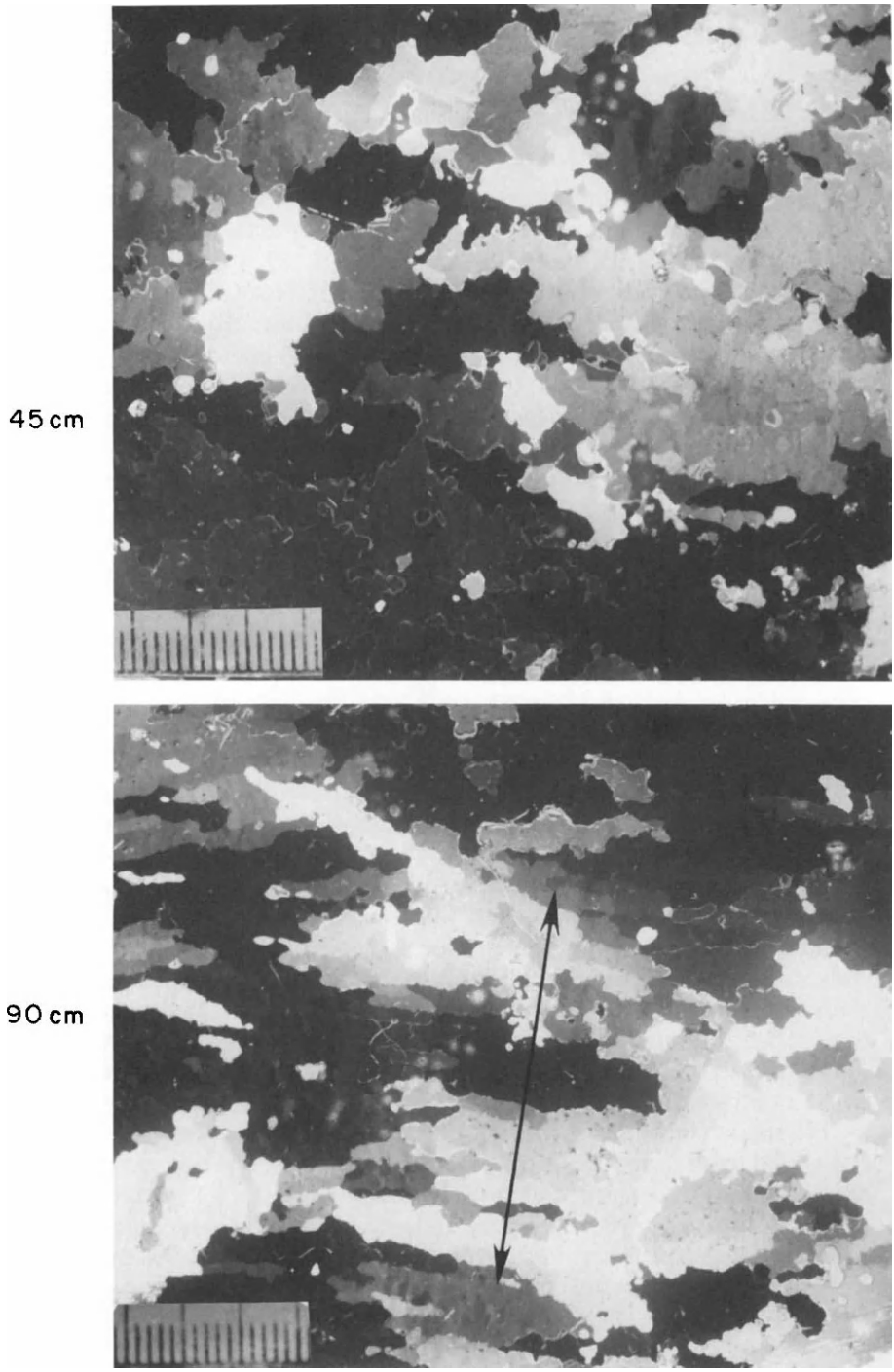

Figure 2.35 Horizontal thin-section photographs demonstrating retexturing of ice in the upper layers of an Arctic multiyear floe. Note in section from 90 cm that the original *c*-axis alignment

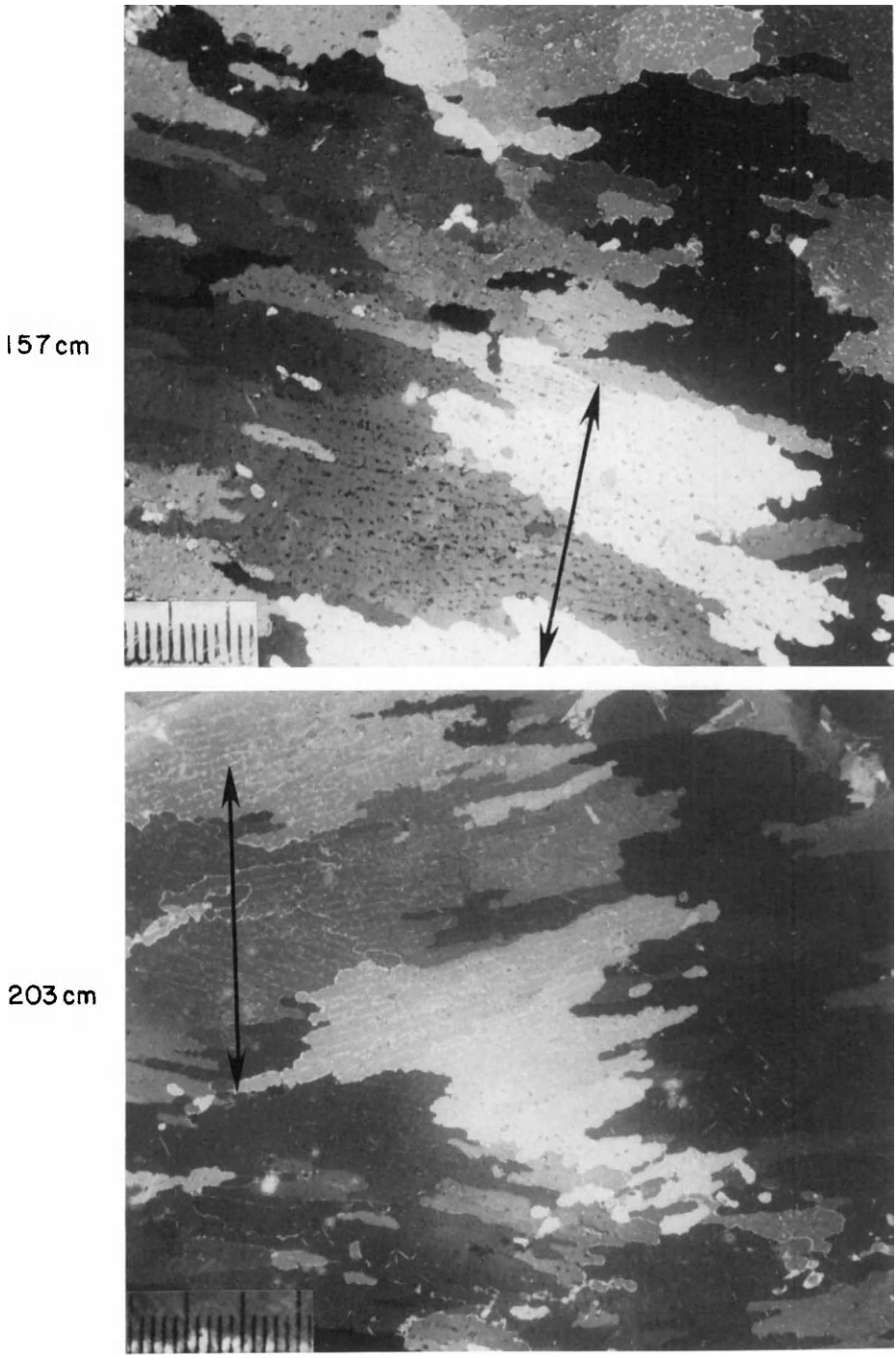

(arrowed) is maintained despite nearly complete loss of brine pocket substructures in contrast to substructures preserved in deeper unretextured ice. After Gow *et al.* (1987b).

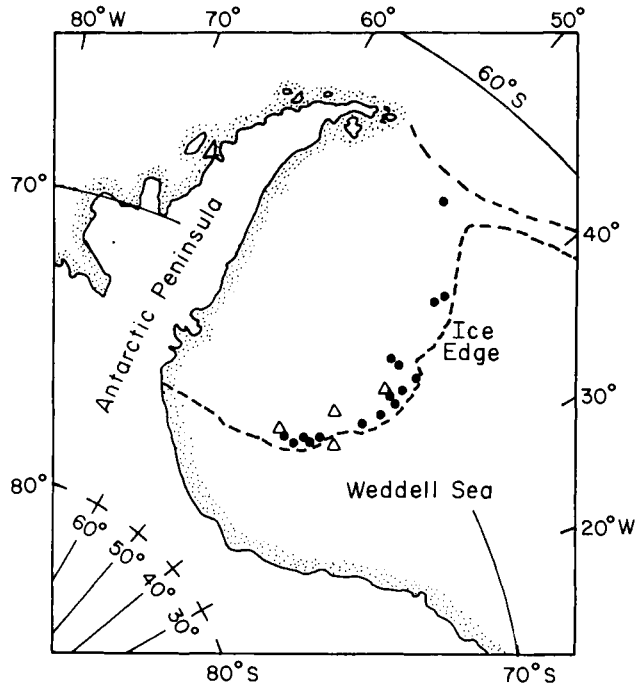

Figure 2.36 Locations of primary sampling sites (circles) visited in 1980 during summertime investigations of the physical and structural properties of pack ice in the Weddell Sea, Antarctica. Triangles indicate locations of data buoys used for monitoring ice drift. After Gow *et al.* (1987a).

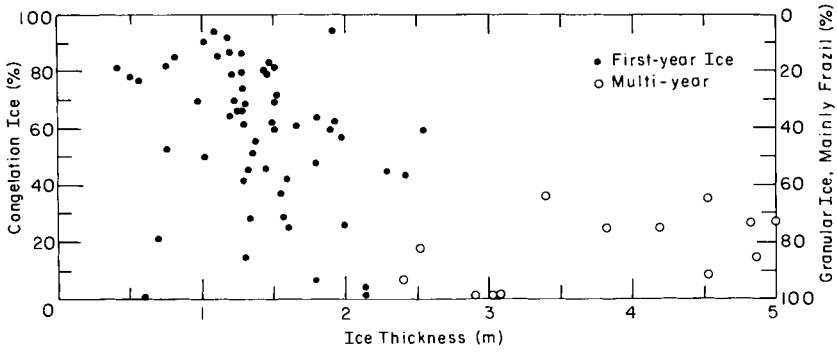

Figure 2.37 Abundances of congelation and granular (principally frazil) ice versus ice thickness in Weddell Sea floes. After Gow *et al.* (1987a).

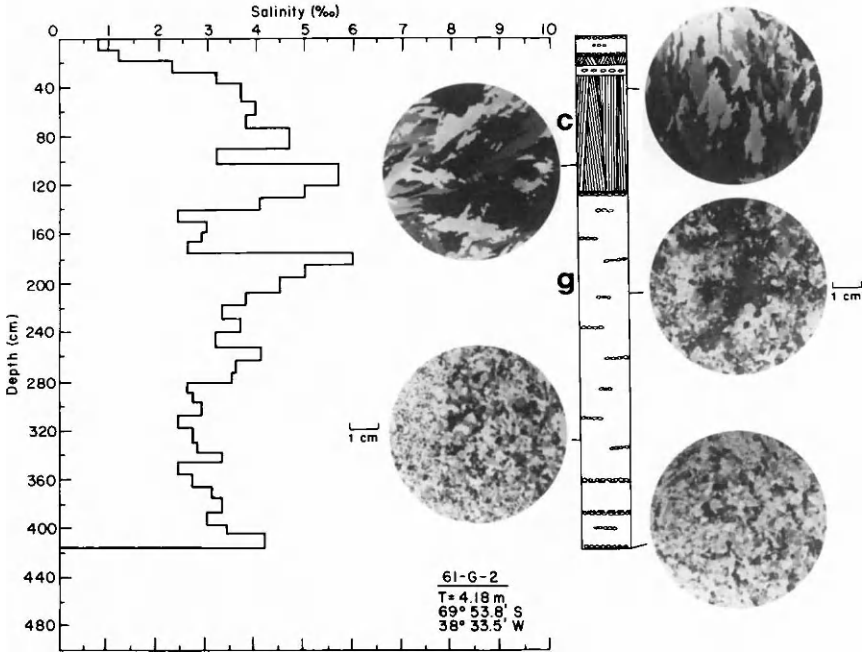

Figure 2.38 Salinity and structure profiles of a 4.18-m-thick multiyear floe in the Weddell Sea. Congelation ice is limited to the top 1.3 m; the underlying frazil ice represents 75% of the total ice thickness. Salinity averaged 3.59 per mil. The first year's growth is interpreted as having ended at the bottom of the congelation ice layer. Symbols g and c at the side of the structure section denote granular (frazil) ice and columnar ice, respectively. After Gow *et al.* (1987a).

floes, indicating that other mechanisms, in addition to surface turbulence and rafting, may contribute to frazil generation in the Weddell Sea. For example, because of its buoyancy, surface-derived frazil is not likely to be transported to depths of 3 m or more, as was observed in some Weddell Sea floes.

Weeks and Ackley (1982), in an attempt to assess the conditions leading to widespread occurrence of frazil ice in the Weddell Sea, described four processes by which frazil may form in polar oceans:

1. Wind- and wave-induced turbulence. This well-known mechanism accounts for substantial frazil growth in leads, polynyas, and the open areas of marginal ice zones. As noted above (Lange *et al.*, 1988), rafting of frazil-rich pancake ice may lead to enhanced thicknesses of frazil ice. In fact, based on their wintertime observations, Lange *et al.* (1988) now believe that it is the rafting of frazil-rich pancake ice that accounts

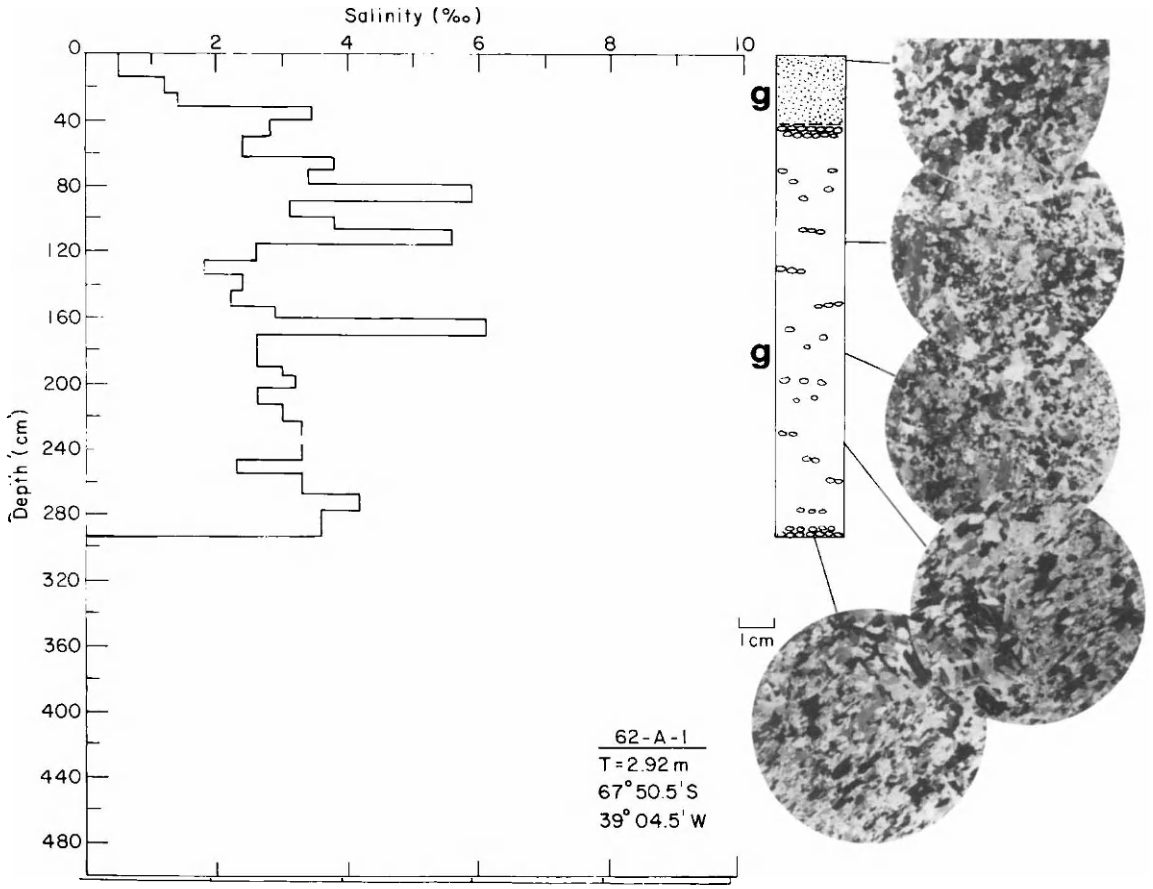

Figure 2.39 Salinity and structure profiles of a 2.92-m-thick multiyear floe from the Weddell Sea. As shown in the vertical structure section, this floe was composed entirely of granular ice which, apart from a 4-cm-thick layer of frazil ice possibly mixed with snow ice in the top 10 cm of the floe, consisted completely of frazil ice of variable grain size and an average salinity of 3.1 per mil. After Gow *et al.* (1987a).

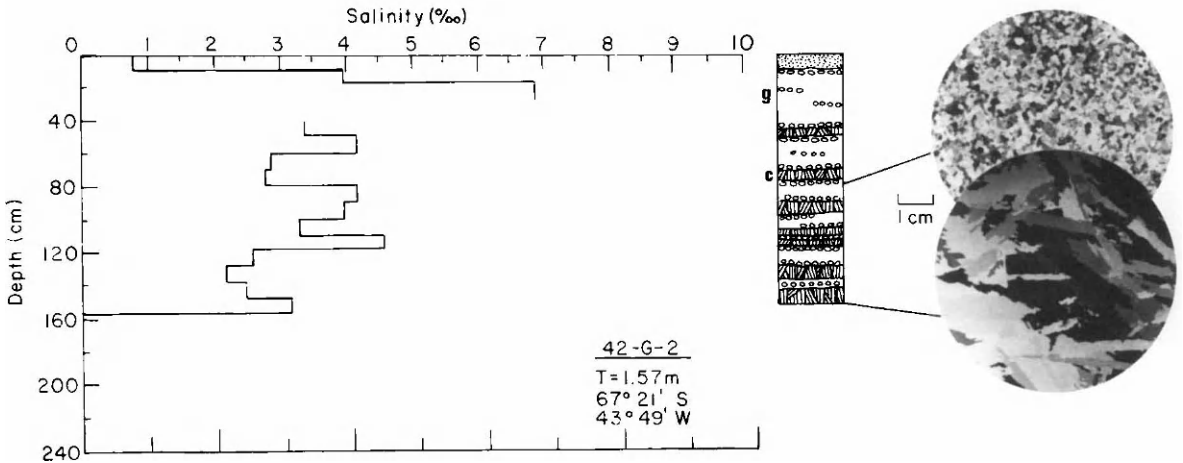

Figure 2.40 Salinity and structure profiles of a 1.57-m-thick first-year floe from the Weddell Sea. As shown in the vertical structure section, there were seven layers of columnar ice (c) interspersed with frazil ice (g), indicating that this floe probably formed by repeated rafting of thin ice. The average salinity of the floe was 3.4 per mil. After Gow *et al.* (1987a).

for the dominance of frazil ice in the Weddell Sea ice pack. Also, Lange *et al.* (1988) obtained frazil/congelation percentages of 57/43, in almost exact agreement with values found by Gow *et al.* (1987a) at the end of the summer.

2. Adiabatic expansion of seawater as it ascends from beneath thick ice shelves. The Weddell Sea is backed by large ice shelves, including the Filchner and Ronne, and higher frazil contents might be expected close to these ice shelves.
3. Contact between two water masses of significantly different salinities; one such case would involve the interaction of seawater with fresh water derived from surface melting. This occurs in limited situations in Antarctica, e.g., beneath an ice shelf in McMurdo Sound (Gow *et al.*, 1965; Gow and Epstein, 1972). A similar process was proposed by Untersteiner and Badgley (1958) to explain the formation of frazil beneath Arctic ice floes. However, this mechanism is not likely to be an important source of frazil in the Weddell Sea because of the lack of surface melting.

   Lange *et al.* (1988) have reported the widespread occurrence of platelet-like ice in layers up to 5 m thick in ice formed along the ice shelf front in the eastern Weddell Sea. They suggest that such ice, as distinct from frazil, originates as a result of the supercooling of meltwater from the bottom of the Filchner Ice Shelf. Similar platelet ice was reported by Dieckmann *et al.* (1986) to form in water 200–270 m deep off the Filchner Ice Shelf. They attribute this growth to freezing from supercooled water streaming out from beneath the shelf. Lewis and Perkin (1985, 1987) have postulated a similar situation existing off the front of the Ross Ice Shelf.
4. Thermohaline convection related to surface freezing. Such freezing results in the formation of cold brine plumes, which, as they descend, could cause frazil to crystallize in the water column underlying the growing ice sheet. This process, given the depth characteristics, textures, and exceptional thicknesses of frazil ice observed by Gow *et al.* (1982, 1987a) in Weddell Sea pack ice, seems attractive because it is not constrained by the problem of crystals having to overcome the buoyancy forces encountered during downward advection of surface-derived crystals.

Large platelike crystals measuring several centimeters long and even larger, loosely bonded waferlike crystals were also observed in bottom ice of several multiyear floes examined by Gow *et al.* (1987a) in the Weddell Sea. Such a platy, waferlike crystal texture appears transitional between those of frazil and congelation ice and is probably equivalent structurally to so-called

underwater ice described by Serikov (1963) for east Antarctic sea ice and by Paige (1966) and Gow *et al.* (1982) for the bottom of sea ice in McMurdo Sound. In McMurdo Sound this kind of platelet ice appeared to be growing in place, unlike that forming at depth in the Weddell Sea as discussed above (Dieckmann *et al.*, 1986; Lange *et al.*, 1988).

In Weddell Sea floes congelation ice was most prevalent in first-year ice, averaging 58% of the ice thickness of 49 floes examined. It was structurally similar to Arctic congelation ice, with *c* axes often showing a preferred alignment (Fig. 2.41).

Virtually nothing is known of the structural characteristics of pack ice in seas bordering other parts of the Antarctic coastline (e.g., the Ross Sea), and observations of shorefast ice have been confined to a few coastal areas including McMurdo Sound, where the winter ice cover is composed predominantly of congelation ice that frequently exhibits aligned *c* axes. As in the Arctic, these alignments appear to be controlled by the direction of the current at the ice–water interface. Much of the bottom ice in McMurdo Sound is also modified by platelet growth extending several tens of centimeters below normal congelation ice (Gow *et al.*, 1982). The formation of platelet crystals appears to be confined to late winter or early spring, indicating that the onset of platelet ice growth is related in some way to changes in the composition or circulation patterns of seawater in McMurdo Sound at that time of the year.

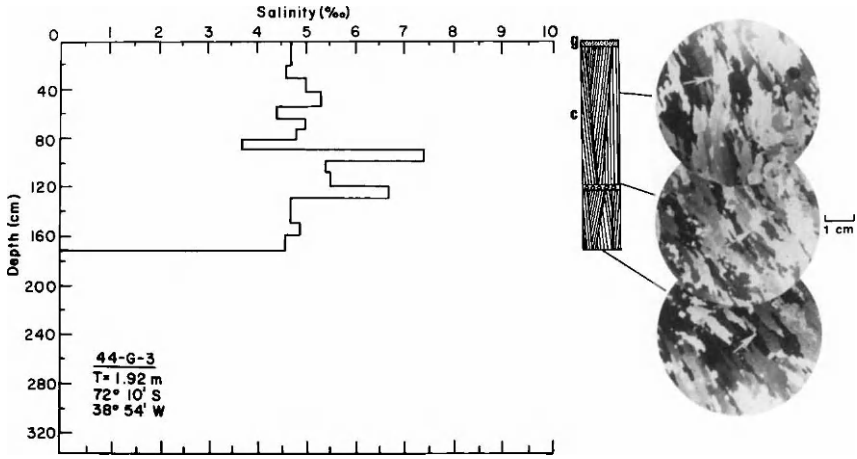

Figure 2.41 Salinity and structure profiles of a 1.92-m-thick first-year floe from the Weddell Sea. Floe is composed of 94% columnar ice exhibiting a near-constant direction of alignment of its *c* axes (arrowed), consistent with growth under near-shore or shelf-fast conditions. The average salinity of this floe was 5.1 per mil. After Gow *et al.* (1987a).

IV. Summary

In our examination of the dynamic and thermodynamic balances of floating sea ice covers, we pointed out the contributions made by individual components of the balance. The heat and momentum balance equations for the ice are the same for both the northern and southern hemispheres, but the magnitudes of the terms are different, and this gives rise to major differences in the sea ice environments. For instance, surface melt features are lacking on Antarctic sea ice because high wind speeds and low relative humidities have enhanced the turbulent heat losses from the ice, significantly raising the melting temperature. The oceanic heat flux in Antarctic seas is considerably larger than that in the Arctic Ocean. Regarding ice dynamics, higher wind speeds and an unconstrained ice edge cause ice velocities to be several times larger than those within the Arctic basin. Within the Arctic basin residence times of ice floes are estimated to be 5–7 years, while Antarctic sea ice rarely survives more than 2 years before it is advected to the ice edge, where it melts. The thickness of Antarctic sea ice appears to be considerably less than that of its Arctic counterpart because of the larger oceanic heat flux and the low survival time of the ice. The most significant contrast, however, is between the extent of ice covers in the northern and southern hemispheres. Whereas the Arctic ice cover nearly doubles its extent in winter, the Antarctic ice cover experiences a fivefold increase in size. At its minimum, the areal extent of Antarctic sea ice is about half that of the Arctic, but at maximum extent it expands to roughly 25% more than the maximum Arctic extent.

The differences in the sea ice environments between the two hemispheres are ultimately a result of the distribution of the polar land masses. The Arctic Ocean is a closed basin surrounded by land, effectively restricting the southward expansion of the ice during winter. With only one major point of egress (Fram Strait), the ice which survives the summer may be held captive in the Arctic basin for a number of years. In contrast, Antarctic sea ice occurs in oceans which surround a continent. Under the influence of generally higher winds, the ice is advected away from the continent toward the open edge, where large oceanic heat fluxes and enhanced wave action ablate the ice. The free exchange of the oceans results in larger oceanic heat fluxes.

In comparing the structural and salinity characteristics of the ice forming in polar oceans it has been shown that major differences exist between the Arctic and the Antarctic that derive directly from differences in land–sea relationships and their effect on ocean–atmosphere interaction and oceanic circulation. Whereas congelation ice, formed by direct freezing of seawater to the bottom of an existing ice sheet, is the dominant crystalline form in Arctic shorefast ice and in most multiyear floes of Arctic pack ice, it is superseded by frazil and platelet ice in the Weddell Sea, a major region of

pack ice formation in Antarctica. Frazil, formed by free nucleation and growth of crystals in the water column, constitutes at least 50% of the ice production in the Weddell Sea. In the Arctic basin, however, frazil represents less than 20% of the total ice production. A number of mechanisms to explain the diverse nature of frazil in Weddell Sea pack ice have been suggested; the most recent observations point to a frazil-rich pancake/rafting process as an important, if not major, generator of frazil. However, the relative importance of this and other mechanisms of frazil ice generation in Antarctic waters needs further evaluation.

Arctic sea ice and Antarctic sea ice also differ significantly in terms of their entrapped salt content or salinity, that of Antarctic sea ice generally exceeding that measured in ice of comparable age and thickness in the Arctic. These differences, which apply to both first-year and multiyear ice, reflect significant differences in seasonal weather patterns in the Arctic and Antarctic. This is especially true of multiyear ice in the Weddell Sea, where, because of the absence of top surface melting during the summer, the ice is able to retain brine that in Arctic sea ice is flushed out by the percolation downward of surface meltwater, the major cause of desalination of Arctic summer ice. The desalination of Arctic sea ice during the summer also leads to significant increases in the hardness and transparency of the ice that allow floes exhibiting these characteristics in freshly drilled cores to be identified immediately as multiyear. By using a combination of structural and salinity characteristics, it has also proved possible to estimate ages of Arctic floes.

Acknowledgments

We gratefully acknowledge the extensive reviews and revisions suggested by Drs. G. A. Maykut, D. K. Perovich, and S. F. Ackley. We are also grateful for the financial support with which this work was performed. Funding was provided by the Office of Naval Research (contract numbers N0001488WM24013 and N0001489WM24004) and by U.S. Army RDTE project number 4A161102AT24, program element 6.11.02A, work units SS-001 and SS-006.

References

Ackley, S. F. 1979a. Drifting buoy measurements in Weddell Sea pack ice. *Antarct. J. U.S.* **16**: 106–108.

———. 1979b. Mass balance aspects of Weddell Sea pack ice. *J. Glaciol.* **24**: 391–405.

———. 1981. Sea-ice atmosphere interactions in the Weddell Sea using drifting buoys. *IAHS Publ.* **131**: 177–191.

Ackley, S. F. & E. T. Holt. 1984. "Sea Ice Data Buoys in the Weddell Sea," CRREL Rep. 84-11. U. S. Army Cold Reg. Res. Eng. Lab., Hanover, New Hampshire.

Ackley, S. F., W. B. Hibler, III, F. K. Kugzruk, A. Kovacs & W. F. Weeks. 1976. "Thickness and

Roughness Variations of Arctic Multi-Year Sea Ice," CRREL Rep. 76-18. U.S. Army Cold Reg. Res. Eng. Lab., Hanover, New Hampshire.

Ackley, S. F., S. Taguchi & K. R. Buck. 1978. "Primary Productivity in Sea Ice of the Weddell Sea Region," CRREL Rep. 78-19. U.S. Army Cold Reg. Res Eng. Lab., Hanover, New Hampshire.

Ackley, S. F., A. J. Gow, K. R. Buck & K. M. Buck. 1980. Sea ice studies in the Weddell Sea aboard USCGS Polar Sea. *Antarct. J. U.S.* **15:** 84–86.

Allison, I. 1981. Antarctic sea ice growth and oceanic heat flux. *IAHS Publ.* **131:** 161–170.

Andreas, E. L. & S. F. Ackley. 1982. On the differences in ablation seasons of the Arctic and Antarctic sea ice. *J. Atmos. Sci.* **39:** 440–447.

Bourke, R. H. & R. P. Garrett. 1987. Sea ice thickness distribution in the Arctic Ocean. *Cold Reg. Sci. Technol.* **13:** 259–280.

Campbell, K. J. & A. J. Orange. 1974. The electrical anisotropy of sea ice in the horizontal plane. *JGR, J. Geophys. Res.* **79:** 5059–5063.

Cherepanov, N. V. 1964. Structure of sea ice of great thickness. *Tr. Arkt. Antarkt. Nauchno Issled. Inst.* **367:** 13–18.

———. 1971. Spatial arrangement of sea ice crystal structure. *Probl. Arkt. Antarkt.* **38:** 176–181.

Clarke, D. B. & S. F. Ackley. 1982. Physical, chemical and biological properties of winter sea ice in the Weddell Sea. *Antarct. J. U.S.* **17:** 107–109.

Colony, R. & A. S. Thorndike. 1984. An estimate of the mean field of Arctic sea ice motion. *J. Geophys. Res.* **89:** 10623–10629.

———. 1985. Sea ice motion as a drunkard's walk. *J. Geophys. Res.* **90:** 965–974.

Cox, G. F. N. & W. F. Weeks. 1974. Salinity variations in sea ice. *J. Glaciol.* **13:** 109–120.

———. 1975. "Brine Drainage and Initial Salt Entrapment in Sodium Chloride Ice," CRREL Res. Rep. 345. U.S. Army Cold Reg. Res. Eng. Lab., Hanover, New Hampshire.

———. 1983. Equations for determining the gas and brine volumes in sea ice samples. *J. Glaciol.* **29:** 306–316.

———. 1988. Numerical simulations of the profile properties of undeformed first-year sea ice during the growth season. *J. Geophys. Res.* **87:** 1971–1984.

Dayton, P. K. & S. Martin. 1971. Observations of ice stalactites in McMurdo Sound, Antarctica. *J. Geophys. Res.* **76:** 1595–1599.

Dieckmann, G., G. Rohardt, H. Hellimer & J. Kipfstul. 1986. The occurrence of ice platelets at 250 m depth near the Filchner Ice Shelf and its significance for sea ice biology. *Deep-Sea Res.* **33:** 141–148.

Frankenstein, G. & R. Garner. 1967. Equations for determining the brine volume of sea ice from −0.5° to −22.9°C. *J. Glaciol.* **6:** 943–944.

Gordienko, P. 1958. Arctic ice drift. *In* "Proceedings of Conference on Arctic Sea Ice," Natl. Acad. Sci., Publ. **598:** 210–222.

Gordon, A. L. 1981. Seasonality of Southern Ocean sea ice. *J. Geophys. Res.* **86:** 4193–4197.

Gordon, A. L., C. T. A. Chen & W. G. Metcalf. 1984. Winter mixed layer entrainment of Weddell deep water. *J. Geophys. Res.* **86:** 4193–4197.

Gow, A. J. & S. Epstein. 1972. On the use of stable isotopes to trace the origin of ice in a floating ice tongue. *J. Geophys. Res.* **77:** 6552–6557.

Gow, A. J. & W. F. Weeks. 1977. "The Internal Structure of Fast Ice Near Narwhal Island, Beaufort Sea, Alaska," CRREL Rep. 77-29. U.S. Army Cold Reg. Res. Eng. Lab., Hanover, New Hampshire.

Gow, A. J., W. F. Weeks, G. Hendrickson & R. Rowland. 1965. New Light on the mode of uplift of the fish and fossiliferous moraines of the McMurdo Ice Shelf, Antarctica. *J. Glaciol.* **5:** 813–828.

Gow, A. J., W. F. Weeks, J. W. Govoni & S. F. Ackley. 1981. Physical and structural characteristics of sea ice in McMurdo Sound. *Antarct. J. U.S.* **16:** 94–95.

Gow, A. J., S. F. Ackley, W. F. Weeks & J. W. Govoni. 1982. Physical and structural characteristics of Antarctic sea ice. *Ann. Glaciol.* **3:** 113–117.

Gow, A. J., S. F. Ackley, K. R. Buck & K. M. Golden. 1987a. "Physical and Structural Characteristics of Weddell Sea Pack Ice," CRREL Rep. 87-14. U.S. Army Cold Reg. Res. Eng. Lab., Hanover, New Hampshire.

Gow, A. J., W. B. Tucker & W. F. Weeks. 1987b. "Physical Properties of Sea Ice in the Fram Strait, June–July 1984," CRREL Rep. 87-16. U.S. Army Cold Reg. Res. Eng. Lab., Hanover, New Hampshire.

Grenfell, T. C. & G. A. Maykut. 1977. The optical properties of ice and snow in the Arctic basin. *J. Glaciol.* **18:** 445–463.

Harrison, J. D. & W. A. Tiller. 1963. Controlled freezing of water. *In* "Ice and Snow Processes, Properties and Applications" (W. D. Kingery, ed.), pp. 8–27. MIT Press, Cambridge, Massachusetts.

Hendrickson, G. & R. Rowland. 1965. "Strength Studies of Antarctic Sea Ice," CRREL Tech. Rep. 157. U.S. Army Cold Reg. Res. Eng. Lab., Hanover, New Hampshire.

Hibler, W. D., III. 1979. A dynamic thermodynamic sea ice model. *J. Phys. Oceanogr* **9:** 815–846.

———. 1980. Sea ice growth, drift and decay. *In* "Dynamics of Snow and Ice Masses" (S. C. Colbeck, ed.), pp. 141–209. Academic Press, New York.

———. 1986. Ice dynamics. *In* "The Geophysics of Sea Ice" (N. Untersteiner, ed.), pp. 577–640. Plenum, New York.

Hibler, W. D., III and S. F. Ackley. 1982. On modeling the Weddell Sea pack ice. *Ann. Glaciol.* **3:** 125–130.

Hibler, W. D., III & W. B. Tucker. 1979. Some results from a linear viscous model of the Arctic ice cover. *J. Glaciol.* **22:** 293–304.

Hibler, W. D., III, S. F. Ackley, W. F. Weeks & A. Kovacs. 1972a. Top and bottom roughness of a multiyear ice floe. *AIDJEX Bull.* **13:** 77–91.

Hibler, W. D., III, W. F. Weeks & S. J. Mock. 1972b. Statistical aspects of sea-ice ridge distributions. *J. Geophys. Res.* **77:** 5954–5970.

Hibler, W. D., III, S. J. Mock & W. B. Tucker. 1974. Classification and variation of sea ice ridging in the western Arctic basin. *JGR, J. Geophys. Res.* **79:** 2735–2743.

Hunkins, K. 1975. The oceanic boundary layer and stress beneath a drifting ice floe. *JGR, J. Geophys. Res.* **80:** 3425–3433.

Keys, J. R. 1984. "Antarctic Marine Environments and Offshore Oil." Comm. Environ., Wellington, N. Z.

Koerner, R. M. 1973. The mass balance of the sea ice of the Arctic Ocean. *J. Glaciol.* **12:** 173–185.

Kovacs, A. 1983. Characteristics of multi-year pressure ridges. *In* "Proceedings of the Seventh International Conference on Port and Ocean Engineering under Arctic Conditions," VTT Symp. No. 37, pp. 173–182. Helsinki, Finland.

Kovacs, A. & R. Morey. 1978. Radar anisotropy of sea ice due to preferred azimuthal orientation of the horizontal *c*-axes of ice crystals. *J. Geophys. Res.* **83:** 6037–6046.

Lange, M. A., S. F. Ackley, P. Wadhams, G. S. Dieckmann & H. Eicken. 1988. Development of sea ice in the Weddell Sea, Antarctica. *Ann. Glaciol.* **12:** 92–96.

Langhorne, P. J. 1983. Laboratory experiments on crystal orientation in NaCl ice. *Ann. Glaciol.* **4:** 163–169.

Langhorne, P. J. & W. H. Robinson. 1986. Alignment of crystals in sea ice due to fluid motion. *Cold Reg. Sci. Technol.* **12:** 197–214.

Langleben, M. P. 1972. The decay of an annual ice cover. *J. Glaciol.* **11:** 337–344.

Leavitt, E., M. Albright & F. Carsey. 1978. Report of the AIDJEX meteorological experiment. *AIDJEX Bull.* **29:** 121–148.

LeShack, L. A. 1983. Arctic Ocean ice deformation chart using sonar data recorded from nuclear submarines. *In* "Proceedings of the Seventh International Conference on Port and Ocean Engineering under Arctic Conditions," VTT Symp. No. 37, pp. 148–157. Helsinki, Finland.

Lewis, E. L. & R. G. Perkin. 1985. The winter oceanography of McMurdo Sound, Antarctica. *Antarct. Res. Ser.* **43:** 145–165.

———. 1987. Ice pumps and their rates. *J. Geophys. Res.* **91:** 756–762.

Lofgren, G. & W. F. Weeks. 1967. "Effect of Growth Parameters on Substructure Spacing in NaCl Ice Crystals," CRREL Res. Rep. 195. U.S. Army Cold Reg. Res. Eng. Lab., Hanover, New Hampshire.

Martin, S. 1981. Frazil ice in rivers and oceans. *Annu. Rev. Fluid Mech.* **13:** 374–397.

Maykut, G. A. 1978. Energy exchange over young sea ice in the central Arctic. *J. Geophys. Res.* **83:** 3646–3658.

———. 1982. Large scale heat exchange and ice production in the central Arctic. *J. Geophys. Res.* **87:** 7971–7984.

———. 1985. The ice environment. *In* "Sea Ice Biota" (R. A. Horner, ed.), pp. 21–82. CRC Press, Boca Raton, Florida.

———. 1986. The surface heat and mass balance. *In* "The Geophysics of Sea Ice" (N. Untersteiner, ed.), pp. 385–463. Plenum, New York.

Maykut, G. A. & N. Untersteiner. 1969. "Numerical Prediction of the Thermodynamic Response of Arctic Sea Ice to Environmental Change," Memo. RM-6093-PR, Rand Corp., pp. 1–173. Santa Monica, California.

———. 1971. Some results from a time-dependent thermodynamic model of sea ice. *J. Geophys. Res.* **76:** 550–1575.

McLaren, A. S. 1986. The under-ice topography of the Arctic basin as recorded in 1958 and 1970: A comparison. *In* "Second Workshop on Ice Penetration Technology," CRREL Sp. Rep. 86–30, pp. 165–191. U.S. Army Cold Reg. Res. Eng. Lab., Hanover, New Hampshire.

McLaren, A. S., M. C. Serreze & R. G. Barry. 1987. Seasonal variations of sea ice motion in the Canada basin and their implications. *Geophys. Res. Lett.* **14:** 1123–1126.

McPhee, M. G. 1980. Analysis of pack ice drift in summer. *In* "Sea Ice Processes and Models" (R. S. Pritchard, ed.), pp. 62–75. Univ. of Washington Press, Seattle.

Moritz, R. E. & R. Colony. 1988. Statistics of sea ice motion, Fram Strait to North Pole. *In* "Proceedings of the Seventh International Conference on Offshore Mechanics and Arctic Engineering" (D. S. Sodhi, C. H. Luk & N. K. Sinha, eds.), Vol. 4, p. 75–82. Am. Soc. Mech. Eng., New York.

Nakawo, M. & N. K. Sinha. 1981. Growth rate and salinity profile of first-year sea ice in the high Arctic. *J. Glaciol.* **27:** 315–330.

Nansen, F. 1902. The oceanography of the North Pole Basin, the Norwegian North Polar Expedition, 1983–1986. *Sci. Res.* **3:** 1–427.

Osterkamp, T. E. & J. P. Gosink. 1984. Observations and analyses of sediment-laden sea ice. *In* "The Alaskan Beaufort Sea: Ecosystems and Environments" (P. W. Barnes, D. M. Schell & E. Reimnitz, eds.), pp. 73–93. Academic Press, Orlando, Florida.

Overgaard, S., P. Wadhams & M. Lepparanta. 1983. Ice properties in the Greenland and Barents Sea during summer. *J. Glaciol.* **29:** 142–164.

Paige, R. A. 1966. "Crystallographic Studies of Sea Ice in McMurdo Sound, Antarctica," Tech. Rep. R494. Naval Civil Eng. Lab., Port Hueneme, California.

Parkinson, C. L., J. C. Comiso, H. J. Zwally, D. J. Cavalieri, P. Gloersen & W. J. Campbell.

1987. Arctic sea ice, 1973–1976: Satellite passive-microwave observations. Natl. Aeronaut. and Space Admin., Washington, D. C. NASA **SP-489**: 1–296.

Parmerter, R. R. & M. D. Coon. 1972. Model of pressure ridge formation in sea ice. *J. Geophys. Res.* **77**: 6565–6575.

Pease, C. H. 1980. Eastern Bering Sea ice processes. *Mon. Weather Rev.* **108**: 2015–1023.

Perovich, D. K., G. A. Maykut & T. C. Grenfell. 1986. Optical properties of ice and snow in the polar oceans. 1. Observations. *In* "Proceedings of the International Society for Optical Engineering, Ocean Optics III (M. Blizard, ed.), SPIE 637, pp. 232–241. ISOE, Bellingham, Washington.

Perovich, D. K., A. J. Gow & W. B. Tucker. 1988. Physical properties of snow and ice in the winter marginal ice zone of Fram Strait. *In* "Proceedings of the 1988 International Geoscience and Remote Sensing Symposium (IGARSS '88)," pp. 1119–1123. Univ. of Edinburgh, Edinburgh, Scotland.

Peyton, H. R. 1966. "Sea Ice Strength," Rep. UAG-182. Univ. of Alaska, Fairbanks.

Pritchard, R. S. 1988. Norton Sound and northeastern Bering Sea ice behavior: 1981–1982. *In* "Proceedings of the Seventh International Conference on Offshore Mechanics and Arctic Engineering" (D. S. Sodhi, C. H. Luk & N. K. Sinha, eds.), Vol. 4, pp. 69–74. Am. Soc. Mech. Eng., New York.

Reimnitz, E., E. W. Kempema & P. W. Barnes. 1987. Anchor ice, seabed freezing, and sediment dynamics in shallow Arctic seas. *J. Geophys. Res.* **92**: 14671–14678.

Reynolds, M., C. H. Pease & J. E. Overland. 1985. Ice drift and regional meteorology in the southern Bering Sea: Results from MIZEX West. *J. Geophys. Res.* **90**: 11967–11981.

Richter-Menge, J. A. & G. F. N. Cox. 1985a. Effect of sample orientation on the compressive strength of multi-year pressure ridge ice samples. *In* "Proceedings of the Conference Arctic '85, Civil Engineering in the Arctic Offshore" (F. L. Bennett & J. L. Machemehl, eds.), pp. 465–475. Am. Soc. Civ. Eng., San Francisco, California.

———. 1985b. Structure, salinity and density of multi-year ice pressure ridges. *In* "Proceedings of the Fourth International Offshore Mechanics and Arctic Engineering Symposium" (J. Chung, ed.), pp. 194–198. Am. Soc. Mech. Eng., New York.

Rothrock, D. A. 1986. Ice thickness distribution—measurement and theory. *In* "The Geophysics of Sea Ice" (N. Untersteiner, ed.), pp. 551–575. Plenum, New York.

Rothrock, D. A. & A. S. Thorndike. 1980. Geometric properties of the underside of sea ice. *JGR, J. Geophys. Res.* **85**: 3955–3963.

Schwarz, J. & W. F. Weeks. 1977. Engineering properties of sea ice. *J. Glaciol.* **19**: 499–530.

Serikov, M. I. 1963. Structure of Antarctic sea ice. *Inf. Byull. Sov. Antarkt. Exped.* **4**: 265–266.

Smith, D. D. 1964. Ice lithologies and structure of ice island Arlis II. *J. Glaciol.* **5**: 17–38.

Stander, E. & G. A. Gidney. 1980. The measurement of finite strain in sea ice by impulse radar techniques. *In* "Proceedings of the Workshop on Sea Ice Field Experiments," C-Core Publ. 80–21, pp. 127–164. Memorial Univ., St. Johns, Newfoundland.

Thorndike, A. S. & R. Colony. 1982. Sea ice motion in response to geostrophic winds. *J. Geophys. Res.* **87**: 5845–5852.

Thorndike, A. S., D. A. Rothrock, G. A. Maykut & R. Colony. 1975. The thickness distribution of sea ice. *JGR, J. Geophys. Res.* **80**: 4501–4513.

Tiller, W. A., K. A. Jackson, J. W. Rutter & B. Chalmers. 1953. The redistribution of solute atoms during the solidification of metals. *Acta Metall.* **1**: 428–437.

Tucker, W. B. & V. H. Westhall. 1973. Arctic sea ice ridge frequency distributions derived from laser profiles. *AIDJEX Bull.* **21**: 171–180.

Tucker, W. B., W. F. Weeks & M. Frank. 1979. Sea ice ridging over the Alaskan continental shelf. *J. Geophys. Res.* **84**: 4885–4897.

Tucker, W. B., D. S. Sodhi & J. W. Govoni. 1984a. Structure of first-year pressure ridge sails in the Alaskan Beaufort Sea. *In* "The Alaskan Beaufort Sea: Ecosystems and Environment"

(P. W. Barnes, D. M. Schell & E. Reimnitz, eds.), pp. 115–135. Academic Press, New York.

Tucker, W. B., A. J. Gow & J. A. Richter. 1984b. On small-scale horizontal variations of salinity in first-year ice. *J. Geophys. Res.* **89**: 6505–6514.

Tucker, W. B., A. J. Gow & W. F. Weeks. 1987. Physical properties of summer sea ice in Fram Strait. *J. Geophys. Res.* **92**: 6787–6803.

Untersteiner, N. 1968. Natural desalination and equilibrium salinity profile of perennial sea ice. *J. Geophys. Res.* **73**: 1251–1257.

Untersteiner, N. & F. Badgley. 1958. Preliminary results of thermal budget studies on Arctic pack ice during summer and autumn. *In* "Proceedings of Conference on Arctic Sea Ice," Natl. Acad. Sci., Publ. **598**: 85–89.

Wadhams, P. 1980a. A comparison of sonar and laser profiles along corresponding tracks in the Arctic Ocean. *In* "Sea Ice Processes and Models" (R. S. Pritchard, ed.), pp. 283–299. Univ. of Washington Press, Seattle.

———. 1980b. Ice characteristics in the seasonal sea ice zone. *Cold Reg. Sci. Technol.* **2**: 37–87.

———. 1981. Sea-ice topography of the Arctic Ocean in the region 70°W to 25°E. *Philos. Trans. R. Soc. London* **302**: 45–85.

———. 1984. Arctic sea ice morphology and its measurement. *In* "Arctic Technology and Policy" (I. Dyer & C. Chryssostomidis, eds.), pp. 179–195. Hemisphere Publ. Corp., Washington, D.C.

Wadhams, P. & T. Davy. 1986. On the spacing and draft distribution for pressure ridge keels. *J. Geophys. Res.* **91**: 10697–10708.

Wadhams, P. & R. J. Horne. 1980. An analysis of ice profiles obtained by submarine sonar in the Beaufort Sea. *J. Glaciol.* **25**: 401–424.

Wadhams, P., M. A. Lange & S. F. Ackley. 1987. The ice thickness distribution across the Atlantic sector of the Antarctic ocean in midwinter. *J. Geophys. Res.* **92**: 14535–14552.

Walker, E. R. & P. Wadhams. 1979. Thick sea-ice floes. *Arctic* **32**: 140–147.

Walsh, J. E. & C. M. Johnson. 1979. An analysis of Arctic sea ice fluctuations, 1957–77. *J. Phys. Oceanogr.* **9**: 580–591.

Weeks, W. F. & S. F. Ackley. 1982. "The Growth, Structure and Properties of Sea Ice," Monogr. 82-1. U. S. Army Cold Reg. Res. Eng. Lab., Hanover, New Hampshire.

Weeks, W. F. & A. J. Gow. 1978. Preferred crystal orientations in the fast ice along the margins of the Arctic Ocean. *J. Geophys. Res.* **83**: 5105–5121.

———. 1980. Crystal alignments in the fast ice of Arctic Alaska. *J. Geophys. Res.* **85**: 1137–1146.

Weeks, W. F., S. F. Ackley & J. Govoni. 1988. Sea ice ridging in the Ross Sea, Antarctica as compared with sites in the Arctic. *J. Geophys. Res.* **94**: 4984–4988.

Williams, E., C. W. M. Swithinbank & G. deQ. Robin. 1975. A submarine study of Arctic pack ice. *J. Glaciol.* **15**: 349–362.

Wittmann, W. & J. J. Schule. 1966. Comments on the mass budget of Arctic pack ice. *In* "Symposium on Arctic Heat Budget and Atmospheric Circulation" (J. O. Fletcher, ed.), RM-5233-NSF, pp. 215–246. Rand Corp., Santa Monica, California.

World Meteorological Organization. 1956. "Abridged Ice Nomenclature," Exec. Comm. Rep. No. 8, pp. 107–116. WMO, Geneva.

Zotikov, I. A., V. S. Zagorodnov & J. V. Raikovsky. 1980. Drilling through the Ross Ice Shelf (Antarctica) confirmed basal freezing. *Science* **207**: 1463–1465.

Zubov, N. N. 1943. "Arctic Ice." Izd. Glavsevmorputi, Moscow.

Zwally, H. J., J. C. Comiso, C. L. Parkinson, W. J. Campbell, F. D. Carsey & P. Gloersen. 1983. Antarctic sea ice, 1973–1976: Satellite passive-microwave observations. Natl. Aeronaut. and Space Admin., Washington, D. C. **NASA SP-459**: 1–206.

3 Remote Sensing of the Polar Oceans

Robert A. Shuchman and Robert G. Onstott
Radar Science Laboratory
Environmental Research Institute of Michigan
Ann Arbor, Michigan

I. Introduction 123
II. Remote Sensing Basics 124
III. Theory of Active and Passive Microwave Imaging of Sea Ice 132
IV. Visible and Infrared Sensors 151
V. Satellite, Aircraft, and Ground-Based Remote Sensing Examples for Polar Oceanography 152
VI. Concluding Remarks 163
References 166

Remote sensing employs the logic of inference to determine how much of what is where from measurements of force fields at locations removed from the materials of interest. The force field then forms the communication link between the material of interest and the remotely located sensor.

I. Introduction

Remote sensing as defined in this chapter refers to the use of active and passive visible, infrared, and microwave techniques to obtain information about the polar oceans without direct *in situ* measurements. Remote sensing can be performed using instruments mounted on ground-based towers, sleds, ships, helicopters, aircraft, and satellites utilizing essentially all regions of the electromagnetic spectrum. From satellite platforms, it offers the potential to study the relatively inaccessible polar regions synoptically using timely sampling intervals.

Polar oceanography includes the study of sea ice as well as ice-free ocean areas. The emphasis in this chapter will be on remote sensing of sea ice rather

Polar Oceanography, Part A: Physical Science

than the liquid ocean, for the remote sensing of the latter is well covered in two books (Stewart, 1985; Apel, 1987). Although visible, infrared, and microwave sensors will be discussed, microwave sensors, with their ability to penetrate clouds, rain, and snow and operate independently of solar illumination conditions, will be highlighted.

In this chapter, we first present some basic remote sensing concepts and introduce sea ice and ocean characteristics obtainable from analysis of data from various remote sensing instruments. The basic concepts are followed by a section dealing with the interaction of electromagnetic energy with various sea ice types, including the effects of snow cover. Following this is a section that illustrates through example that satellite, aircraft, and ground-based remote sensing instruments provide polar oceanographic information. The examples presented are primarily from the Arctic; however, the techniques discussed are equally applicable to the Antarctic region. Included with the examples are discussions of the algorithms utilized to extract the desired geophysical information from the satellite data.

II. Remote Sensing Basics

Active and passive remote sensors operating in the visible, infrared, and microwave regions of the electromagnetic spectrum have been used to provide information pertaining to the polar seas. Active remote sensors such as lasers and radars provide their own source of electromagnetic illumination. The instruments include altimeters, scatterometers, real aperture radars (RARs), and synthetic aperture radars (SARs). Their advantages include operation independent of solar illumination and the optimization of sensor geometry. A disadvantage of active sensors is the power required to operate them.

Passive remote sensors such as radiometers utilize either energy that is emitted from the ocean or sea ice or energy that originates in space and is reflected off the ocean or ice surface. Multispectral scanners (MSSs) such as those on Landsat and Spot satellites, infrared radiometers (PRT-5), and microwave radiometers are all passive instruments. These instruments, with the exception of the infrared and microwave radiometers, are dependent on solar illumination. However, they have lower power requirements than their active counterparts.

Figure 3.1 presents the electromagnetic spectrum from the visible through the microwave region, as well as the regions in which the various optical, infrared, millimeter, and microwave sensors operate. Most optical sensors

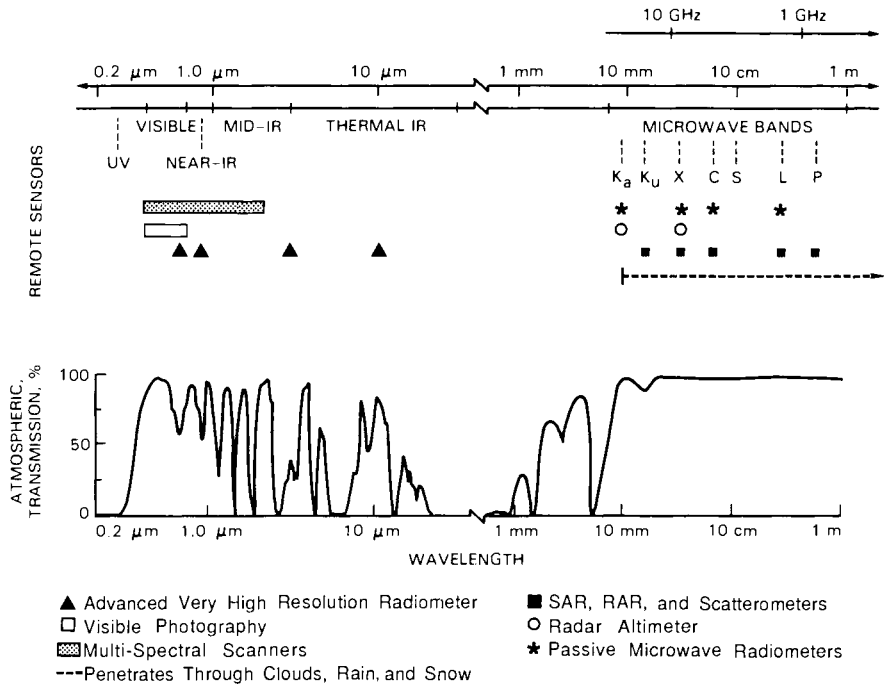

Figure 3.1 Electromagnetic spectrum from the visible through the microwave region. Wavelengths in which various optical and microwave sensors operate are indicated.

take advantage of atmospheric transmission windows, whereas at 10 mm and longer wavelengths the microwave remote sensors are generally unaffected by the atmosphere, rain, or snow.

The resolution (i.e., ability to resolve radiation from two distinct locations on the ground) of a remote sensor is a function of the wavelength utilized, the aperture of the antenna, and the distance to the objects being imaged. In the millimeter and microwave regions of the electromagnetic spectrum the resolution (ρ) of a real aperture system is

$$\rho = (\lambda/D)R \tag{3.1}$$

where D is the antenna dimension, λ the wavelength, and R the distance to the object. Equation (3.1) reveals that real aperture antennas in space produce very large footprints in resolution cells unless very high frequencies or

large antennas are employed. For example, for a typical satellite radiometer with a 3-m-long antenna operating at 1.25 GHz and a range of 850 km, the ground resolution would be approximately 68 km.

A special class of radars termed SAR utilize the motion of the sensor to synthesize a long "antenna," and the resolution obtainable is dramatically improved. SARs have the ability to produce resolutions equal to half the antenna length and thus are powerful tools for the range of polar problems where environmental changes on small scales must be monitored. A complete explanation of the calculation of resolution for RAR and SAR systems can be found in Ulaby *et al.* (1981, 1982).

The resolution of optical sensors, which is referred to as the instantaneous field of view (IFOV), is also a function of wavelength, aperture (in this case the size of the optical lens utilized), and distance to the object. Typical optical or infrared sensors (0.4–14 μm) such as Landsat, Spot, NOAA 9/10, and DMSP operating in a midaltitude orbit in space (850 km) achieve resolutions of 10 m to 1 km, depending on the size of the aperture.

A number of sea ice and ocean parameters and features are of interest to polar scientists. These include sea ice extent, ice concentration, ice type, ice thickness, ice kinematics, floe size distribution, detection of ocean swell and gravity wave propagation into the ice pack, locations of leads and polynyas, sea surface temperature, detection of fronts and eddies, determination of wind speed, indication of phytoplankton biomass, and mapping of internal waves. Table 3.1 is a summary of remote sensors that can be mounted in spaceborne systems to observe the geophysical parameters. For each parameter, a definition is presented along with comments. To bound the problem, the table is constrained to spaceborne systems. Table 3.2 provides specific details on existing and soon to be launched satellites that can provide the information identified in Table 3.1.

It is difficult to select optimum remote sensing instrumentation for polar oceanography. One must consider sensors on the basis of resolution (both spatial and spectral) and coverage (i.e., swath width) and at the same time not ignore the fact that the polar oceans are often cloud covered and, even if not cloud covered, are dark at least half the year. As a result, active and passive microwave sensors are potentially the most useful remote sensing instrumentation for most applications in polar oceanography, particularly if periodic temporal sampling is required.

A notable exception to the use of microwave remote sensing systems for polar oceanography is in the area of biological investigations. At present, visible and infrared passive sensors are used to provide information on chlorophyll distributions and location of upwellings, eddies, and fronts, due to their thermal characteristics.

Table 3.1 Spaceborne Remote Sensors Available for Observing Sea Ice and Ice-Free Ocean Parameters

Parameter	Comments
Ice extent. Sea ice–liquid ocean boundary	*Visual.* High-resolution (10–80 m, MSS) accurate; limited by clouds and darkness. Partial remedy: minimum brightness technique to eliminate clouds (but not darkness). In the case of Landsat or Spot, poor geographic coverage. *Infrared.* Good resolution and positional accuracy; limited by clouds and large atmospheric effects. Partial remedy: minimum brightness technique as above, but problems with atmospheric effects. DMSP and NOAA 9/10 provide IR data. *Passive microwave.* Lower resolution (instantaneous)[a] but useful spatial and temporal resolution (50 km); no effect of darkness and only small effects of atmospheric conditions. Data presently come from SSM/I, which is part of DMSP. *Radar altimeter.* Provides accurate edge information at satellite nadir (i.e., profile mode). *Synthetic aperture radar.* Very high resolution (10–30 m); all weather and seasons; occasional problems with open water/new ice discrimination; high cost of data processing. Only limited data set available from Seasat.
Ice concentration. Amount of ice versus water per given area (total ice concentration). First-year ice/multiyear ice/open water (fraction ice concentration).	*Visual.* Same as ice extent. *Infrared.* Same as ice extent. *Passive microwave.* Similar to ice extent; some unresolved questions about accuracy, especially during freeze-up and melt. *Radar altimeter.* Provide concentration data in profile (10-km) mode. *Synthetic aperture radar.* Same as ice extent, except the small leads are not resolved.
Ice type. Limited to the distinction between first-year (including nilas) and multiyear ice.	*Visual.* No use. *Infrared.* Possible use in relating ice thickness to surface temperature, but rendered operationally uncertain because of overwhelming effect of unknown snow cover. *Passive microwave.* Very useful in principle, but existing algorithms give results at odds with other data. Severe problem with obtaining independent verification (ground truth). *Radar altimeter.* Algorithm to utilize altimeter data does not exist at present. *Synthetic aperture radar.* Research results to date indicate that a SAR system with a higher carrier frequency, *C* band or *X* band, would be effective.
Ice thickness and thickness distribution	No spaceborne system is available at present to sense ice thickness directly.

(continues)

Table 3.1 *(Continued)*

Parameter	Comments
Ice kinematics. Ice movement (i.e., displacement) as well as rotation.	*Visual.* Same as ice extent *Infrared.* Same as visual, except ice floes need to be on the order of 4 km to track with IR. *Passive microwave.* Present resolution of these systems is too coarse to provide any useful kinematic data. *Radar altimeter.* Profile mode not optimum to provide this information. *Synthetic aperture radar.* Same as ice extent; at present the most useful way to provide kinematic information from satellites.
Floe size distributions. Area dimensions of individual ice floes.	*Visual.* Same as ice extent. *Infrared.* Same as visual, except floes must be on the order of 1 km to be observed. *Passive microwave.* Insufficient resolution to be useful at present. *Radar altimeter.* Algorithm does not exist to provide this information. *Synthetic aperture radar.* Same as ice extent; limited to floes 30 m or greater, but at present the best way to obtain information.
Detection of sea and swell gravity waves. Both in ocean and within the pack (wavelengths of 100–600 m).	*Visual.* Landsat/Spot will detect waves if properly illuminated by the sun. *Infrared.* Insufficient resolution. *Passive microwave.* Insufficient resolution to be useful at present. *Radar altimeter.* Provides significant wave height under satellite (profile). *Synthetic aperture radar.* Particularly useful for observing wave propagation into the pack. Some imaging ambiguity of waves and swell in open water.
Location of leads. Open water areas within ice pack (orientation, width, and length).	*Visual.* Same as ice extent. *Infrared.* Same as ice extent. *Passive microwave.* Resolution at present is insufficient to provide useful lead information. *Radar altimeters.* Not optimum to map leads due to profiling mode of operation. *Synthetic aperture radar.* Same as ice extent.
Sea surface temperature. Upper first meter of the ocean.	*Visual.* Not capable of providing quantitative information. *Infrared.* Provides 0.5–1.0°C sea surface temperature data at 1-km resolution. *Passive microwave.* Provides 1°C information, unfortunately on a 50-km resolution grid at present.

	Radar altimeter. Does not provide quantitative temperature information. *Synthetic aperture radar.* Does not provide quantitative temperature information.
Location of fronts and eddies. The fronts and eddies can be either thermal or due to current shear.	*Visual.* Will observe only fronts and eddies that have ocean color changes associated with them. *Infrared.* Will detect thermal fronts. *Passive microwave.* Present resolution prevents detection of fronts and eddies that are 50 km or smaller in diameter. *Radar altimeter.* Not useful due to profiling mode. *Synthetic aperture radar.* Fronts and eddies associated with either temperature or current shear have been visible on the radar images. Imaging mechanism has not been quantified.
Determination of wind speed and direction. Determine wind speed over polynyas, leads, and the open ocean (techniques do not work over ice).	*Visual.* Not useful. *Infrared.* Not useful. *Passive microwave.* Useful for wind speeds greater than 5 m/s. On 50-km grid, and wind speed can be provided to 2-m/s accuracy. Not useful for wind speeds over leads due to resolution. *Radar altimeter.* Can provide 2-m/s wind speed information directly under satellite. *Synthetic aperture radar.* Potentially the best instrument to provide wind speed and direction, due to resolution. Algorithm is still under development.
Biological distribution. Increased biological activity associated with eddies, upwelling, or seasonal changes.	*Visual.* Ratios of various visual bands, optimum technique at present to map pigment distribution. *Infrared.* May provide some information on blooming if associated with thermal activity. *Passive microwave.* Present resolution of system is too coarse to provide useful data. *Radar altimeter.* Not useful. *Synthetic aperture radar.* Useful only if bloom is associated with thermal or current shear.
Detection of internal waves. Wavelengths on the order of 500 m to several kilometers	*Visual.* Same as ice extent. *Infrared.* Limited to observing long internal waves (i.e., 2 km or greater). *Passive microwave.* Resolutions of present systems are inadequate to map internal waves. *Radar altimeter.* Not useful. *Synthetic aperture radar.* At present the most useful system for detecting internal waves in the ice. The transfer function between the SAR signature and internal wave needs to be quantified.

[a] When an algorithm for ice concentration and ice extent is assumed to be infinitely small.

Table 3.2 Satellite Sea Ice Data Sources

Satellite	Sensor	Type	Swath (km)	Resolution	Revisit time/day	Sea ice and ocean parameters measured	Advantage	Disadvantage	Status
Landsat	Multispectral Scanner (MSS)	Passive visible and infrared	186 × 186	30 m	0	Ice edge, ice concentration, floe size distribution, ice motion, chlorophyll concentration, suspended sediment, location of ocean fronts	High-resolution information is easily extracted	Clouds, coverage limited to 81°	Operational
Spot	Multispectral Scanner (MSS)	Passive visible and infrared	60 × 60	10 m	0–2	Ice edge, ice concentration, floe size distribution, ice motion, chlorophyll concentration, suspended sediment, location of ocean fronts	High-resolution information is easily extracted	Clouds, coverage limited to 81°	Operational
DMSP	Optical line Scanner (OLS)	Passive visible and infrared	2900	0.6–3 km	2–12	Meteorology, ice motion, ice edge location, eddy structure, sea surface temperature, ice kinematics	Large swath	Clouds	Operational
DMSP	Special Scanning Microwave Imager (SSM/I)	Passive microwave	750	50–60 km	0–2	Ice type, ice extent, ice concentration, eddy structure, water vapor, and ocean surface winds, sea surface temperature	Penetrates clouds	Resolution, melt and freeze period	Operational
NOAA 9/10	Advanced Very High Resolution Radiometer (AVHRR)	Passive visible and infrared	2500	1–4 km	2–12	See DMSP, OLS	Large swath	Clouds	Operational

GEO-SAT	Radar Altimeter	Active microwave	Nadir profile 7–10	Height 10 cm, spot size 7–10 km	0	Ice edge, ice roughness, gravity wave detection, ice concentration, ocean height topography, geostrophic currents	All weather, minimum data processing	Limited polar coverage, profile only, large spot size	Operational
Japanese MOS-1	Multispectral Electronic Self-Scanning Radiometer (MESSR)	Passive visible and infrared	200	50 m	0	See Landsat, MSS	High-resolution information is easily extracted	Clouds	Operational
Japanese MOS-1	Visible and Thermal Infrared Radiometer (VTIR)	Passive visible and infrared	1500	1–3 km	2–12	See DMSP, OLS	Large swath	Clouds	Operational
Japanese MOS-1	Microwave scanning Radiometer (MSR)	Passive microwave	300	30–40 km	0–1	See DMSP, SSM/I	Penetrates clouds	Resolution, melt and freeze period	Operational
ESA ERS-1	Radar Altimeter	Active microwave	Nadir profile 7–10	Height 10 cm, spot size 7–10 km	0	Ice edge, ice roughness, gravity wave detection, ice concentration, ocean height topography, geostrophic currents	All weather, minimum data processing	Profile only large spot size	Proposed launch late 1990
ESA ERS-1	Synthetic-Aperture Radar (SAR)	Active microwave (*C* band)	80–100	30 m	0	Ice edge location, eddy and ocean front structure, ice type, floe size distribution, ice kinematics, gravity wave propagation, internal wave measurements, ice concentration, surface wind speed, detection of leads, mapping of icebergs	All weather, high resolution	Coverage, data processing	Proposed launch late 1990

III. Theory of Active and Passive Microwave Imaging of Sea Ice

Sea ice type or thickness and age are extremely important parameters to measure and study in the polar oceans. Ice strength is dependent on age and thickness, and the distribution of ice thickness is important in climatic studies. Figure 3.2 is a conceptual illustration of the active microwave return from multiyear and first-year sea ice and open water without wind. Multiyear ice (i.e., ice that has survived a summer melt) can be distinguished from first-year ice by its greater thickness (>2 m versus <2.5 m), its lower salinity ($<2.5‰$ versus $>7.7‰$), and thicker snow cover (>0.2 m versus <0.2 m). The return from multiyear ice is a function of surface and volume scattering, since the low salinity allows penetration into the ice sheets, whereas backscatter from snow-free first-year ice and ocean is dominated by scattering from the surface (i.e., both are high-loss materials).

In order to use satellite and aircraft data to estimate ice types and their respective concentrations, algorithms for use with microwave data have been developed and improved. Major advances have been made in establishing sea ice type and concentration because microwaves penetrate clouds and large areas can be covered repeatedly. Algorithms that differentiate first-year and multiyear ice are not always accurate because radiometric properties change when influenced by melting, wet snow, or water on the ice surface.

Seasonal investigations in the Arctic during the fall freeze-up, late winter, spring, and summer have been conducted to acquire empirical data to describe the microwave properties of sea ice. These data contribute to studies to determine the ability of remote sensing to classify ice types and to character-

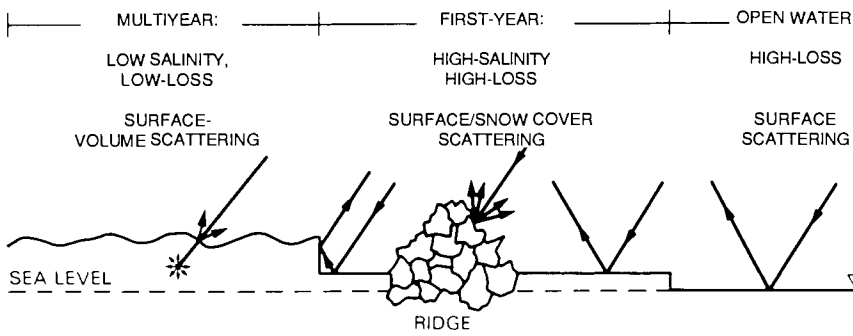

Figure 3.2 Backscatter interactions for multiyear ice, first-year ice, and smooth open water.

ize the physical and electrical parameters which control emission and backscatter levels. A wide range of frequencies, polarizations, and incidence angles have been employed to determine how backscatter and emission levels are influenced, so that sensor parameters may be optimized for extracting the geophysical parameters of greatest interest. Results indicate that many features, including ice types, pressure ridges, other large-scale topographic features, lead (polynya) formations, and icebergs, have unique microwave signatures which may be distinguished using active and passive sensors. Backscatter and emission are influenced by different aspects of the sea ice structure. Through selection of the operating wavelengths, polarization, and viewing angle, one has a measure of control over the depth over which the snow and ice is interrogated and the scattering mechanisms which dominate. These are the tools the scientist has to capture the desired information.

A radar consists of a transmitter and a receiver. The portion of the transmitted energy which returns back to the radar is of great interest because its magnitude is determined by the scattering properties of the area illuminated. By understanding the processes and properties responsible for producing possible microwave signatures (i.e., those of sea ice), we are able to acquire critical geophysical parameters. The average received power (P_r) for a radar may be determined by examining the integral radar equation for distributed targets,

$$P_r = \frac{\lambda^2}{(4\pi)^3} \int_A \frac{P_t G^2 \sigma^\circ}{R^4} \, dA \tag{3.2}$$

where P_t is the power transmitted, G the antenna gain, λ the wavelength, R the range from the radar to the object, A the illuminated area, and σ° is the radar scattering coefficient. The radar scattering coefficient, also called backscatter cross section, is important because it is an absolute measure of scattering behavior. It is a function of frequency, incidence angle, polarization, and the scattering characteristics of the illuminated area.

In contrast to a radar, a radiometer is a passive sensor which measures the intensity of the radiation emitted from the area under observation or reflected from space. Because all bodies emit electromagnetic energy (as expressed by Planck's laws of radiation), the emission T_B can be related to the temperature of the scene T through a quantity called emissivity ϵ. In nature, there is no material which absorbs all incident energy and reradiates this energy (i.e., an idealized blackbody); thus the emissivity is less than one and greater than zero. Using the geometry shown in Fig. 3.3 to indicate the incident and scattered directions, the emissivity may be expressed in terms of a bistatic scattering coefficient σ°, the reflectivity Γ, and the term S to

represent losses due to scattering:

$$\epsilon(\theta_0, \phi_0, P_0) = 1 - \Gamma(\theta, \phi_0, P_0) - \frac{1}{4\pi \cos \theta_0} \times \int S(\theta_0, \phi_0, \theta_s, \phi_s, P_0, P_s) \times [\sigma^\circ(\theta_0, \phi_0, \theta_s, \phi_s, P_0, P_0) + \sigma^\circ(\theta_0, \phi_0, \theta_s, \phi_s, P_0, P_s)] \times d\Omega_s \tag{3.3}$$

where P_0 is the incident polarization, P_s the scattered polarization, (θ_0, ϕ_0) the direction of incident radiation, and (θ_s, ϕ_s) the direction of scattered radiation.

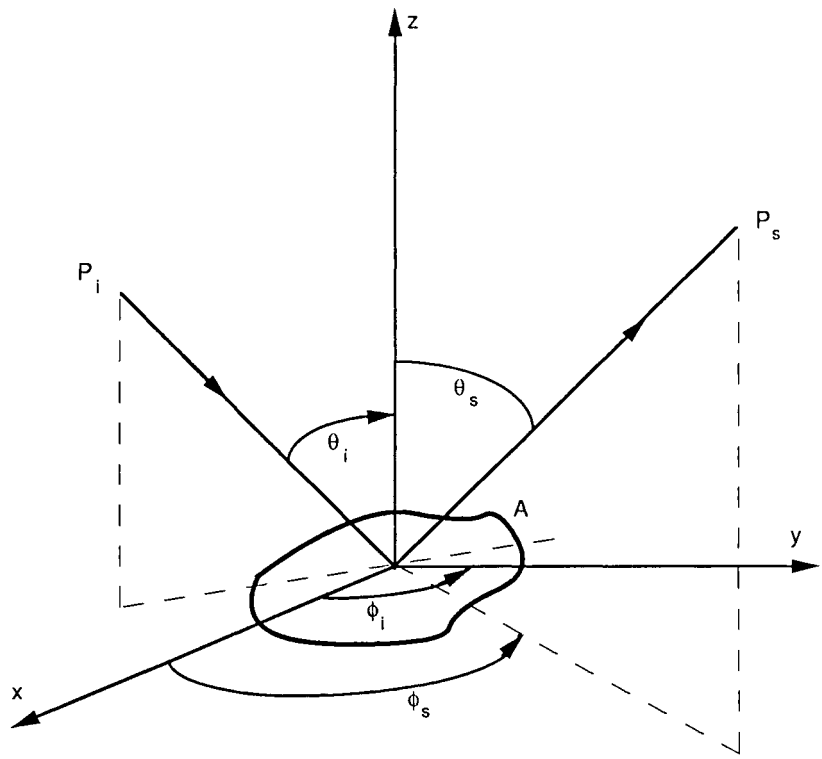

Figure 3.3 Geometry used to indicate the incident and scattered directions for emissivity calculations.

In interpreting active and passive microwave measurements, it is important to recognize that radars typically measure the monostatic scattering cross section. This is measured when the direction of incidence is exactly opposite to the direction of scattering. To calculate emissivity, the description of the bistatic scattering cross section must be complete so that the necessary integration can be performed over all angles.

The way in which sea ice forms, its history, and its age are important in determining its active and passive microwave properties. When ice is young, it may have a surface that is relatively smooth (i.e., formed during undisturbed growth in an open lead) or rough (with rims which are the remains of the pancake ice forms agitated into shapes by wave action). This ice may also exhibit a thin surface layer of brine which may reduce electromagnetic wave propagation to depths of a few millimeters. With a high concentration of brine within its structure, new ice near the freezing point is an extremely lossy material; penetration of electromagnetic energy is limited.

With age, the volume of brine decreases due to salt migration (see Chapter 2). However, first-year ice remains very lossy. During summer the surviving ice experiences melt processes which cause two significant modifications; development of additional surface relief and reduction in the density of the upper portion of the ice sheet. These two characteristics contribute to the difference in the microwave signatures of first-year and multiyear ice. The uppermost portion of the multiyear ice sheet closely governs its microwave signature. It is composed of ice which is almost pure and has very low loss (i.e., significant penetration of microwave energy). Different ice types are more easily distinguished at higher frequencies, and open water is easily distinguished from all sea ice types independent of frequency (Fig. 3.4).

Multiyear ice and first-year ice can be distinguished in the winter independent of frequency (C, X, K_u bands; Fig. 3.4b). However, in the spring and summer (Fig. 3.4c), discriminating first-year from multiyear ice becomes difficult because of the free water in the snow and within the surface of the ice. The free water prevents significant microwave penetration; thus, the volume scattering which distinguishes the multiyear ice return is not present. The only SAR satellite in space operated at L band. It proved to be poor at differentiating the desired ice types. The next scheduled SAR satellite will be launched in 1990 and will operate at C band (5.25 GHz, 6 cm).

The distance an electromagnetic wave travels through a medium before its intensity is reduced by $1/e$ is referred to as the penetration depth and is used to gauge where in a volume scattering may occur. To make this calculation the complex dielectric constant ϵ^* must be known. It is defined by $\epsilon^* = \epsilon_0(\epsilon_r' - j\epsilon_r'')$, where ϵ_0 is the free-space dielectric constant, ϵ_r' the relative dielectric constant, and ϵ_r'' the relative imaginary dielectric constant. The

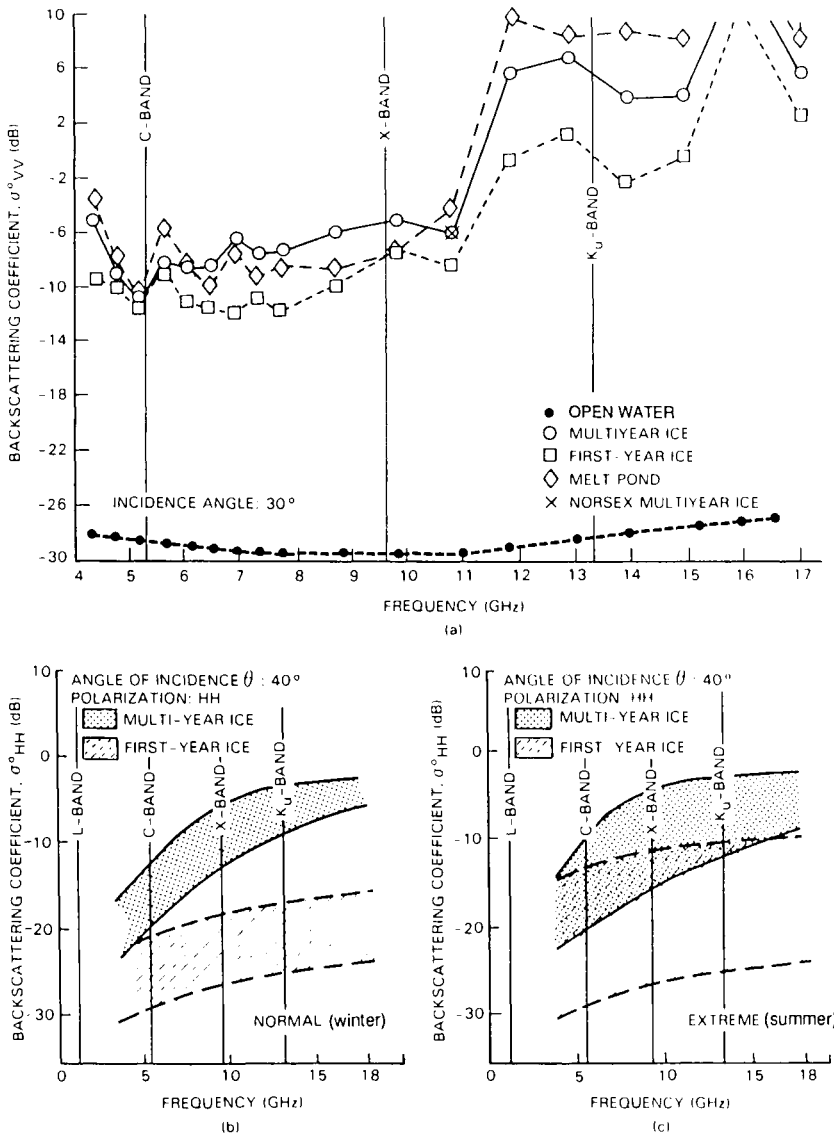

Figure 3.4 Frequency dependence of the backscatter coefficient for first-year and multiyear sea ice at two incidence angles: (a) 30°; (b and c) 40°. Theoretical σ° for multiyear and first-year ice under normal/winter (b) and extreme/summer (c) conditions is also shown. From Earth Observing Report, Volume IIf, SAR Synthetic Aperture Radar. Instrument Panel Report, NASA.

value of ϵ^* is dependent on the density of the ice, the volume of the brine, and the dielectric properties of the ice and brine. The penetration depth δ and loss L are determined by the following:

$$\delta = \frac{1}{2}\left(\frac{2\pi}{\lambda_0}\frac{\mu_r\epsilon_r'}{2}\left\{\left[1+\left(\frac{\epsilon_r''}{\epsilon_r'}\right)^2\right]^{1/2}-1\right\}^{1/2}\right)^{-1} \tag{3.4}$$

and

$$L = 10 \log e^{1/\delta} \quad \text{(dB/m)} \tag{3.5}$$

where λ_0 is the wavelength for free space. At microwave frequencies the relative permeability μ_r is approximately equal to 1. Measurements by Vant *et al.* (1974, 1978) indicate that first-year ice with a salinity of 7–8 per mil at a temperature of −5°C has a penetration depth of 2–4 cm and a loss of about 150 dB/m at *X* band (a wavelength of 3 cm). First-year ice also has few internal scatterers, and these are small compared to a wavelength. In contrast, the upper portion of multiyear ice provides a penetration depth of 60 cm and a significant number of air bubbles with diameters of 1–3 mm. The physical models of first-year and multiyear sea ice which have been useful in the development of theoretical penetration models are shown in Fig. 3.5.

During winter, the microwave signatures of desalinated multiyear ice are clearly different from those of the saline first-year ice. The situation in summer is more complex; this is the time of desalination, of melting snow and ice, and of melt pool formation. In addition, the microwave signatures respond quickly to meteorologically induced melt-and-freeze cycles of the upper surface.

In winter, as during most of the year, the dry snowpack and upper portion of the ice sheet are at temperatures much less than 0°C. Under the dry snow on undulating multiyear ice are flat ice, ice mounds, and depressions filled with frozen meltwater, all with different emissivities (Fig. 3.6). Open water exhibits a large difference between emissivities at the two polarizations (Brewster angle effects) and has an emissivity which increases with increasing frequency. With the dielectric constant of sea ice (i.e., $3.7 - j0.3$ for first-year ice at 10 GHz, $S = 7.5$ per mil, and $T = -5$°C) much lower than that of seawater ($41 - j41$ for 10 GHz, $S = 30$ per mil, and $T = 0$°C), the sea ice has a lower reflectivity. The first-year ice signature is close to unity and is almost independent of polarization and frequency. The multiyear ice signature is not similar to that of either calm water or first-year ice, decreases with increasing frequency, and shows a moderate separation at the different polarizations throughout the entire range of frequencies.

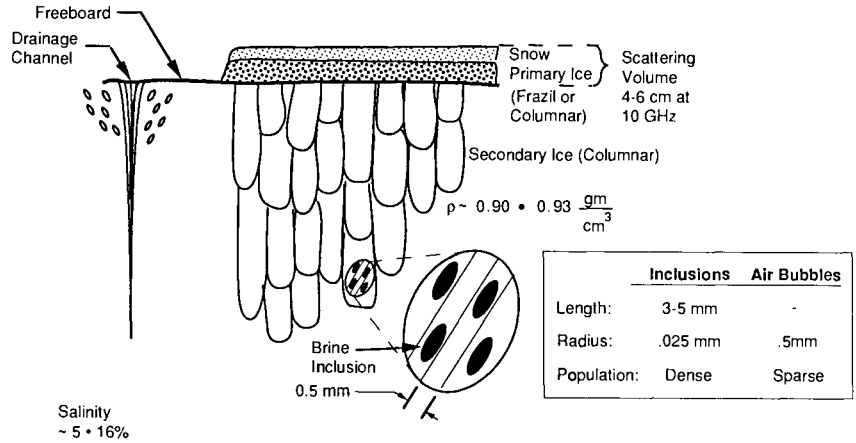

Simplified Cross Section of First-Year Sea Ice

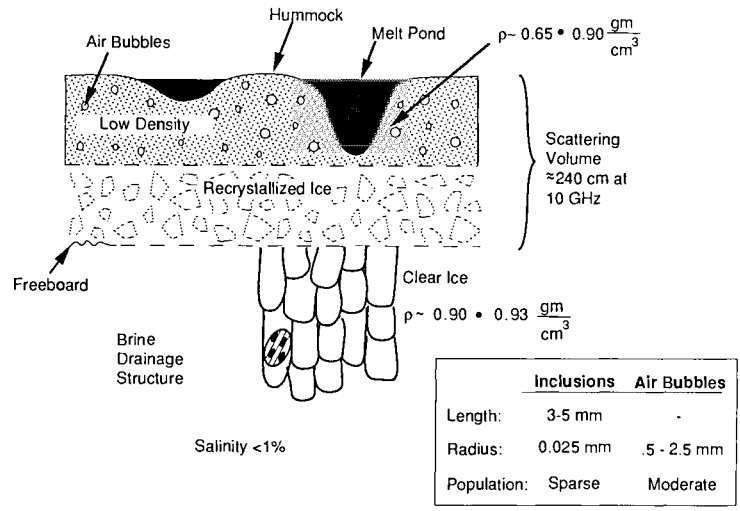

Simplified Cross Section of Multiyear Sea Ice

Figure 3.5 Simplified cross section of first-year and multiyear sea ice.

The active microwave backscatter of first-year and multiyear ice increases linearly with increasing frequency and the radar contrast between these two ice types also improves with increasing frequency. Especially important in the determination of ice concentration, the backscatter levels of water between floes in the ice pack is often considerably lower than those from the

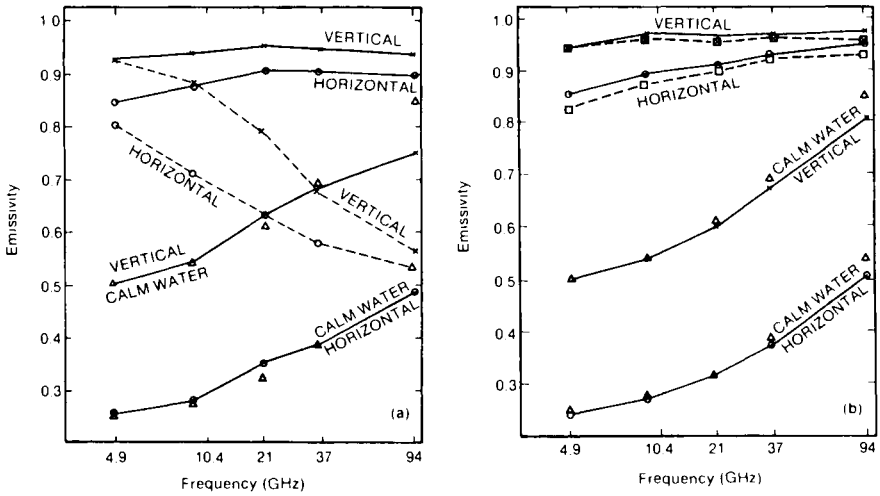

Figure 3.6 Microwave emissivity at 50° incidence angle versus frequency for first-year ice (solid line), multiyear ice (dashed line), and calm water. Triangles indicate theoretical emissivities of calm water. (a) Fall–winter conditions (NORSEX '79). (b) Summer conditions (MIZEX '83). From Matzler *et al.* (1984).

surrounding ice. This is equally true in winter and summer. Radar backscatter cross sections at L, C, X, and K_u bands (Figs. 3.7 and 3.8) illustrate the contrast in ice type and water signatures as a function of frequency and incidence angle.

When temperatures warm during late spring, the interior of the snowpack becomes moist, and moisture from the humid snow layer may collect on the cold ice surface and freeze. The superimposed ice which forms roughens the ice–snow interface. The roughness of this layer increases during the early melt process and eventually becomes the key contributor to the backscatter signatures of thin to medium first-year ice. By midsummer the snowpack has experienced considerable melt. Accumulations of meltwater on multiyear ice and thick first-year ice create slush layers, sometimes many centimeters thick, and drainage of water into depressions contributes to the formation of subsurface melt pools. After midsummer, open water melt pools become common on thick ice; about 50–60% of the snow has melted. A snow–ice crust is in place on elevated multiyear ice surfaces, on thick first-year ice, and on multiyear ice. On thin first-year ice and medium first-year ice the snowpack may have eroded into a 2-cm-thick granular snow–ice layer, and former melt pools may consist of collections of candled ice tips which rise about 1 cm above the freeboard of the thin, saturated ice sheet. Cross-sec-

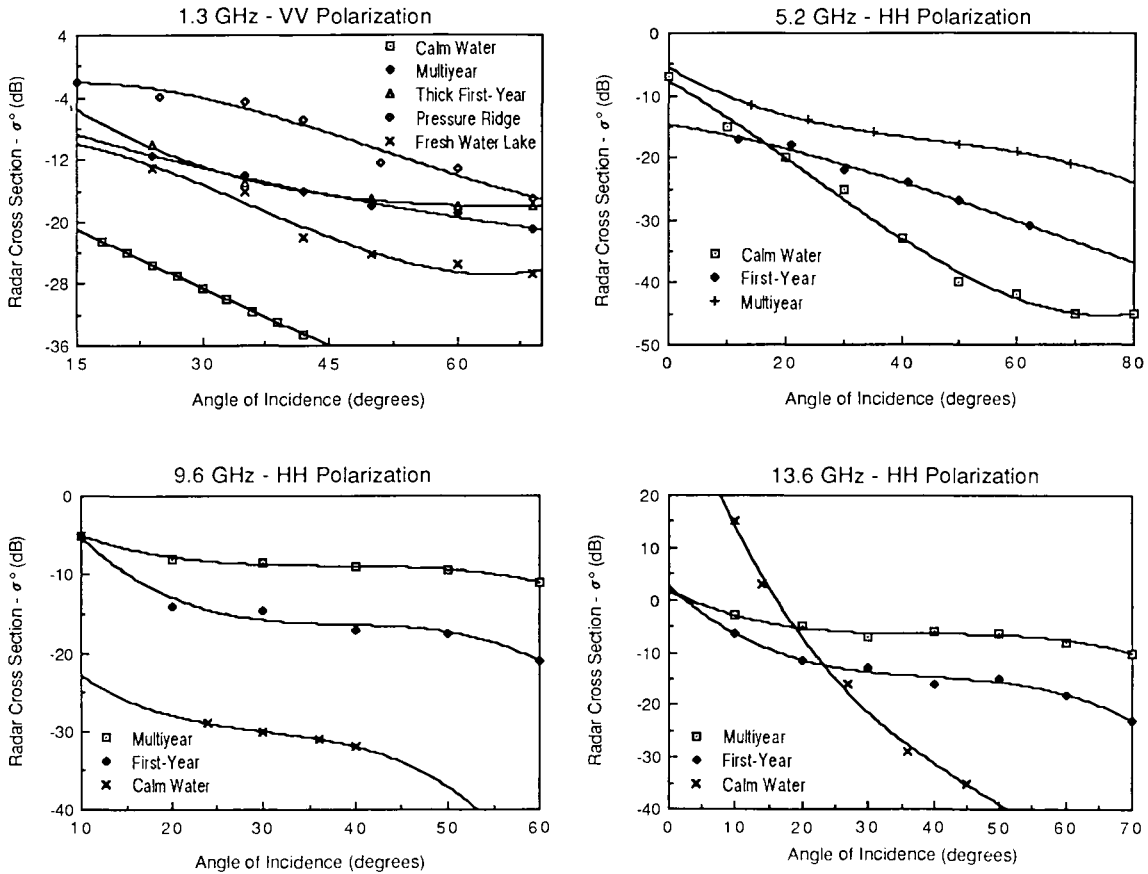

Figure 3.7 Radar backscatter cross sections at L, C, X, and K_u bands during winter, illustrating the contrast in ice type and water signatures as a function of frequency and incidence angle.

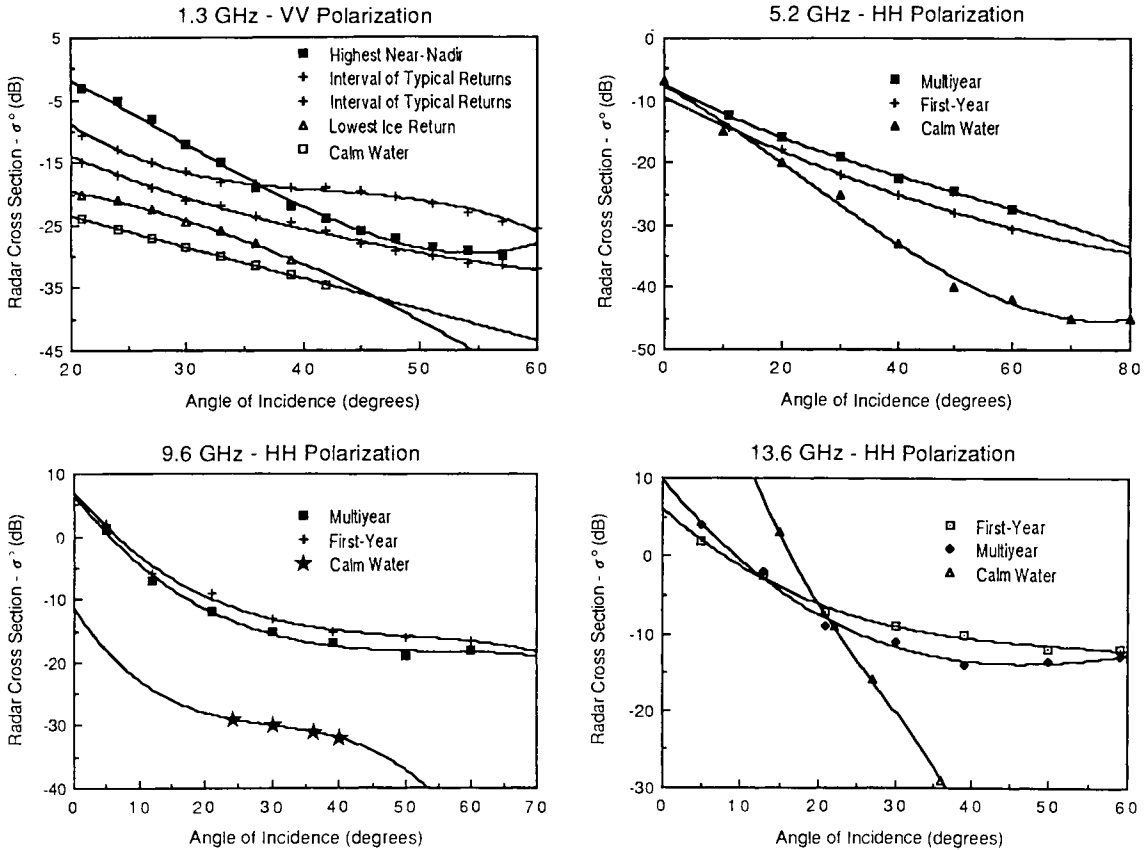

Figure 3.8 Radar backscatter cross sections at L, C, X, and K_u bands during summer, illustrating the contrast in ice type and water signatures as a function of frequency and incidence angle.

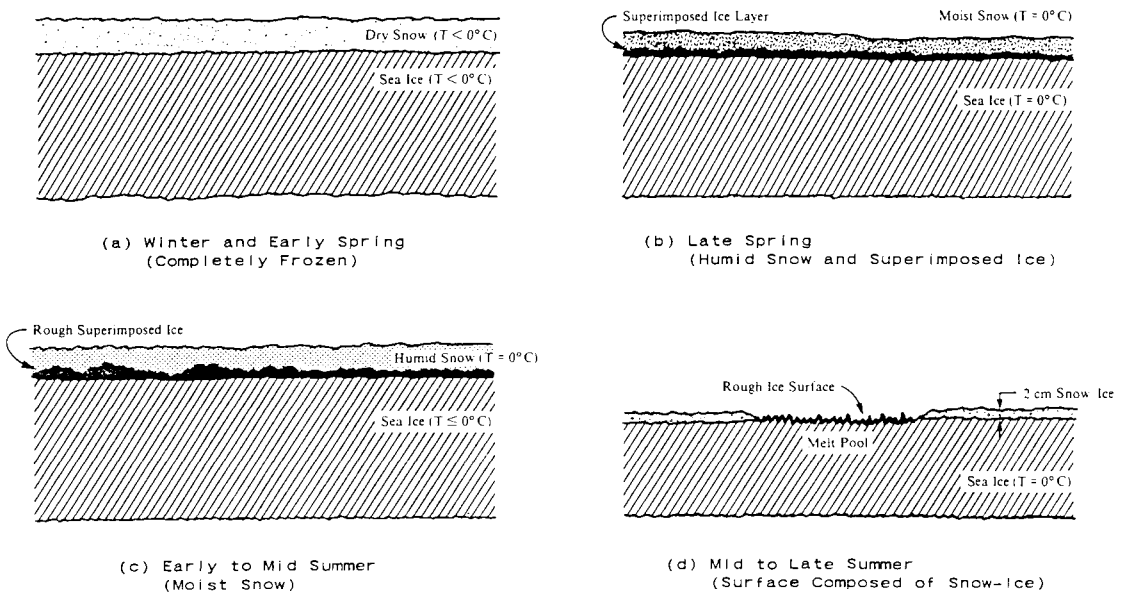

Figure 3.9 Cross-sectional views of first-year sea ice to illustrate the evolution of the ice sheet and snowpack during summer.

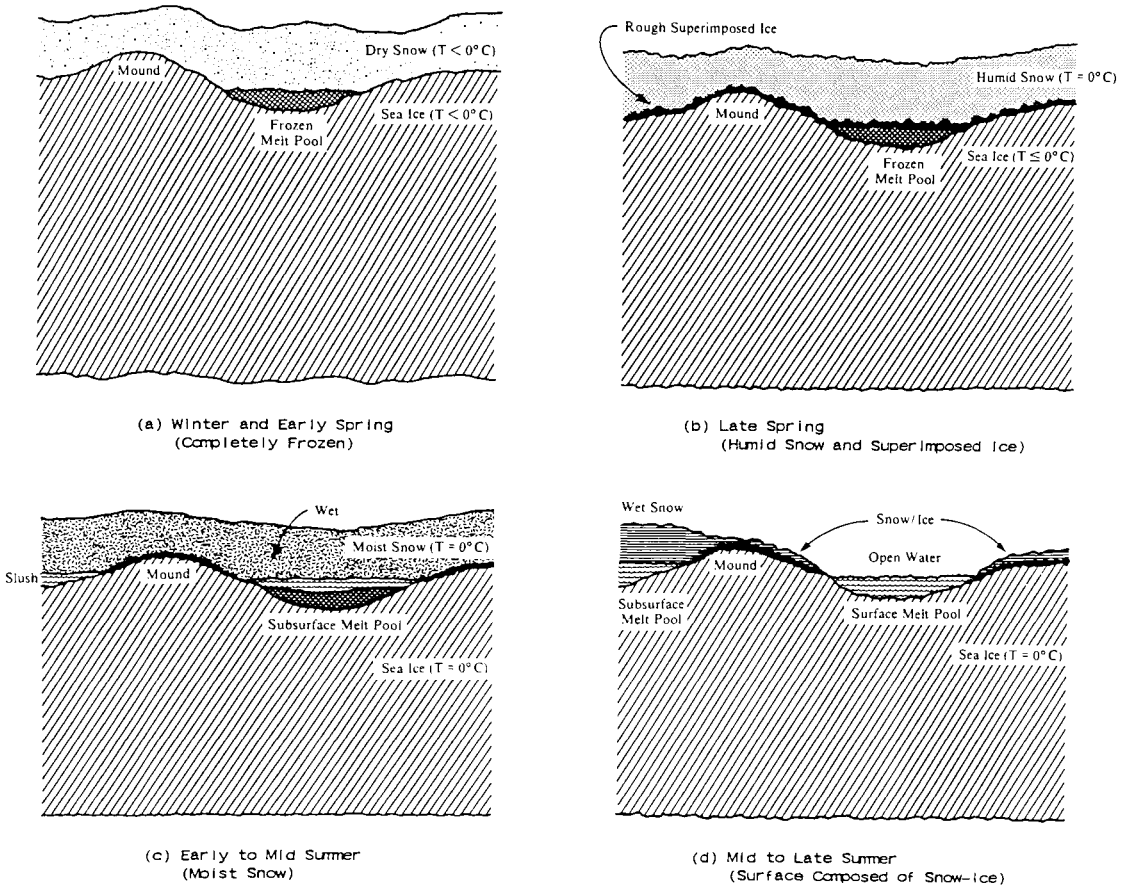

Figure 3.10 Cross-sectional views of multiyear sea ice to illustrate the evolution of the ice sheet and snowpack during summer.

tional views of first-year and multiyear sea ice are provided in Figs. 3.9 and 3.10 to help visualize the evolution of the ice sheet and snowpack during summer.

During the 2 months of summer the mean air temperature stabilizes near 0°C. During this period the microwave signatures of first-year and multiyear ice become very similar. The moist snowpack, warm ice sheet (surface temperatures at about 0°C), and liquid water accumulating at the snow–ice interface greatly limit the ability of microwave signatures to distinguish ice types. Snow-covered multiyear ice and first-year ice share a common emissivity and are represented by an infinitely thick wet snow layer. An emissivity of almost one is obtained at vertical polarization, showing the characteristics of an ideal blackbody.

Radar backscatter during summer is more complex, and discrimination between the major ice types appears possible. During the first part of summer, when the snowpack is moist and at its maximum annual thickness, backscatter signatures for thin and thick ice sheets are very similar if not identical. By midsummer the signature of thin first-year ice is enhanced because the snow layer has thinned to a point where scatter from the ice surface contributes to its backscatter. The distribution of meltwater signatures contributes to their character at this time and is of interest because contrast reversals have been shown to occur between first-year and multiyear ice, the two major summer ice types (Onstott *et al.*, 1987) (Fig. 3.11). By mid- to late summer, the backscatter from multiyear ice becomes greater than that from first-year ice and the contrast between thin and thick ice increases with decreasing frequency. This observation is explained by the fact that the multiyear ice is topographically rougher; has many tilted surfaces; and is complex mixture of ice, snow, and water features which, in total, provide strong surface scatter. The roughness elements on the new snow-free first-year ice are reduced in amplitude because of the continuation of melt, and as surfaces become smoother they produce a weaker backscatter.

Snow on ice plays a variety of roles. On cold multiyear ice, snow with depths greater than 2 m has been shown to be essentially transparent at frequencies below 10 GHz; and on very smooth first-year ice, snow may even dominate the microwave signature (Kim *et al.*, 1985b). In the marginal ice zone (MIZ) the snow thicknesses can become so great that the ice sheet is pushed below sea level, floods with seawater, and acquires a first-year ice signature. Arctic lows may also pass through a region during the spring, and the upper portion of the snowpack may experience melt and refreeze. The snow crystals may enlarge, and a multiyear-like signature may be provided at the highest millimeter-wave frequencies. During early summer the snow layer has a more dominant role. This is illustrated by the critical relationship between frequency and the volumetric liquid water content in the snow and

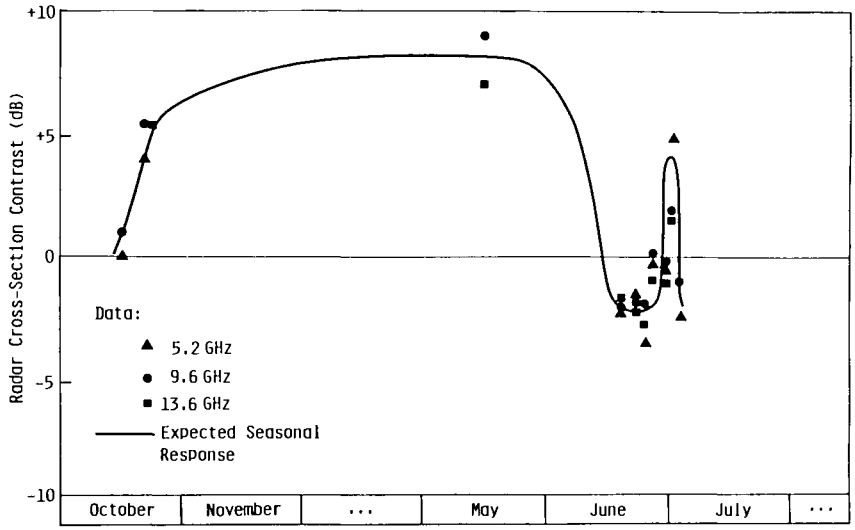

Figure 3.11 Contrast history illustrating contrast reversals which have been shown to occur between first-year and multiyear ice, the two major summer ice types. From Onstott and Gogineni (1985).

penetration depth (Fig. 3.12). The penetration depth is dramatically reduced with even part of a percent of liquid water (a quantity so small that present direct measurement methods provide this value with great difficulty). The penetration depth is further reduced with increasing wetness or increasing frequency. For example, in the Fram Strait region during the summers of 1983 and 1984, the bulk wetness of the snowpack was found to stay at about 5 or 6% (Onstott *et al.*, 1987). The penetration depth at a 30-cm wavelength (note that $\lambda = c/f$, where c is the speed of light and f is frequency) is about 1 m, but at a 6-cm wavelength it is only about 5 cm. Snow thickness prior to melt was about 45 cm on thick ice. As summer progresses, the major role of the snowpack is to provide free water, which accumulates in pools. Typically, there are alternating mounds and pools of ice and water. An important change in the summer microwave signature occurs when the snow becomes completely saturated with water, creating slush. At this point, the emissivity approaches that of open water, and the backscatter signature is increased beyond that of moist snow because of accompanying increases in surface roughness and dielectric constant.

The mean and standard deviation of the brightness temperature of sea ice for a 300 × 300 km region in Fram Strait are shown in Fig. 3.13. Measurements were made at 37 GHz with horizontal polarization using the Nimbus-7 Scanning Multichannel Microwave Radiometer (SMMR) for alter-

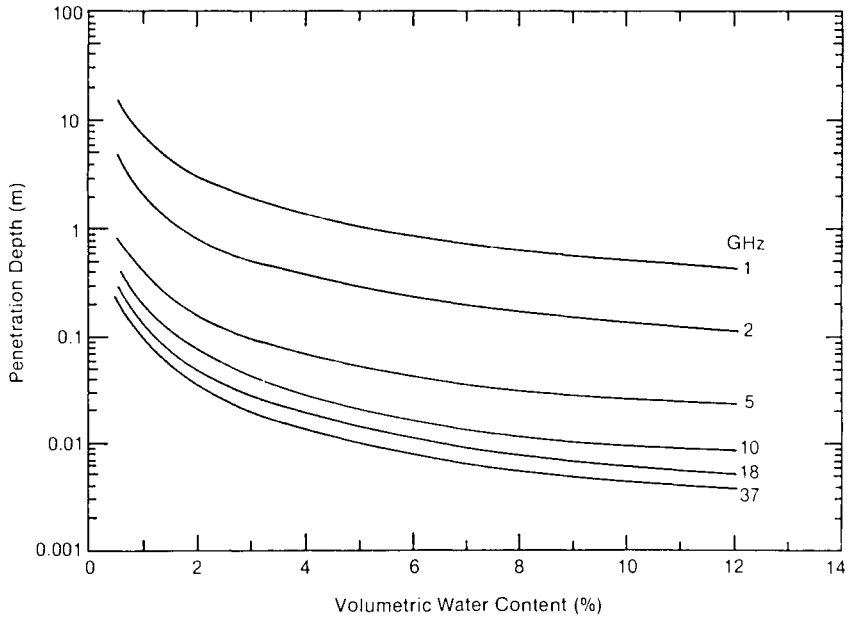

Figure 3.12 Penetration depth for snow with a density of 385 kg/cm^3 for frequencies between 1 and 37 GHz. Calculations are based on experimental data acquired and results published by Matzler (1985), Hallikainen *et al.* (1984), and Tiuri *et al.* (1984).

nate days in a continuous time series record for 1984 (D. J. Cavalieri, unpublished results). During the cold of winter, brightness temperature fluctuations are small and variations are due to changes in ice concentration and in the temperature of the radiative portion of the ice sheets. During the spring warming, brightness temperatures respond accordingly. By late spring, Arctic lows may cause free water to form in the upper portion of the snowpack, inducing brightness temperatures which are almost summerlike. These then decrease below previous spring levels because of increased scattering losses due to enlarged ice crystals in the snowpack. Increases in scattering cause a reduction in the emission and an enhancement in backscatter. The onset of summer, with temperatures stabilizing at about 0°C, is accompanied by a rapid transition to an emissivity that is almost blackbody-like. By midsummer a significant portion of the snowpack has melted and open melt pools are more numerous. During periods of heavy melt followed by "drying" (where the areal extent of surface meltwater is reduced due to draining through cracks, thaw holes, and rotting ice), there may be rapid brightness temperature oscillations. By the beginning of fall, the ice is well drained, a

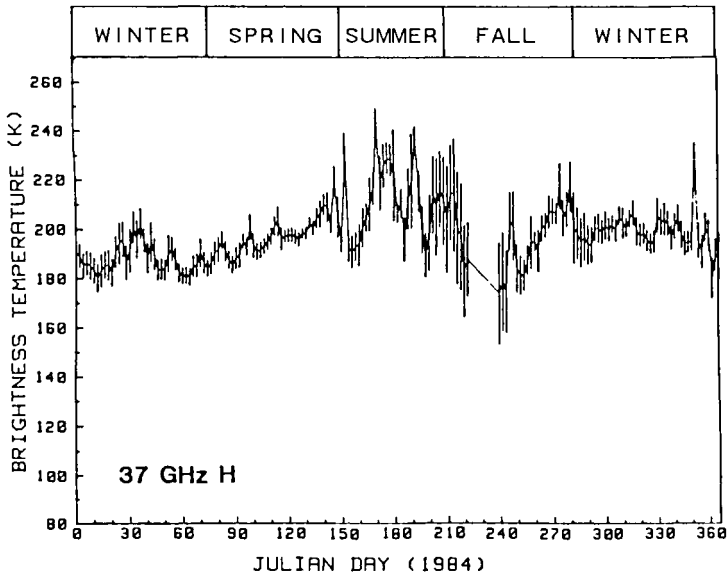

Figure 3.13 Time series of average Nimbus-7 horizontal polarization brightness temperatures at 18 and 37 GHz for a 300 × 300 km region in the Greenland Sea near the MIZEX study area during 1984. The short vertical lines represent 1 standard deviation (D. J. Cavalieri, unpublished).

rapid cooling proceeds, the ice concentration is at a yearly minimum, and the brightness temperature is at its yearly minimum. Within a few weeks brightness temperatures return to their winter levels.

Attempts have been made to explain theoretically the backscatter from sea ice. Models, when successful, prove useful in interpreting the microwave signatures of the many ice forms. Results have been used to refine and focus the measurement of physical and electrical properties in sea ice investigations. A parametric study by Kim *et al.* (1984) allowed an examination of the sensitivity of the microwave signature to changes in key ice sheet parameters, including salinity, temperature, brine volume, density, air bubble size, and surface roughness.

A first attempt to describe the radar backscatter for sea ice was made by Parashar *et al.* (1978). Results were mixed, prompting support for a program which included coincident backscatter measurements and physical property characterizations. A qualitative description of the critical scattering processes by Onstott *et al.* (1979, 1980, and 1982) was based on the results of a series of field investigations. This description provided a basis from which

theoretical formulations were selected for their application in describing backscatter from sea ice. The backscatter and characterization data acquired during these field investigations provided the necessary inputs for model verification.

Backscatter levels for multiyear ice are large and decrease gradually with increasing angle, which suggests that volume scattering is an important contributor. Surface scattering is also expected to be important because returns decrease too rapidly at large angles to be modeled by volume scattering alone. Calculations of the attenuation coefficient and penetration depths for multiyear ice further support this hypothesis. The penetration depth for multiyear ice at 10 GHz with a salinity of 0.5‰ and $T = -5\,^{\circ}\mathrm{C}$ is approximately 60 cm. Ice sheet characterization data show significant numbers of air bubbles (sizes of 1–3 mm) in the upper portion of the ice sheet of a diameter which is within an order of magnitude of the radar wavelength in ice. These bubbles provide the critical source of scatter within the volume. Another source of inhomogeneities is the brine pockets. They are very small compared to a wavelength (about 0.025 mm in radius and 3 mm long) and are not expected to enhance the backscatter.

It is also hypothesized that first-year ice is dominated by surface scatter, with only minor contributions arising from volume scatter. Backscatter data show a rapidly decaying angular response at angles near vertical. Sea ice surfaces are rough, with root-mean-square (rms) values ranging from 0.1 to 1.0 cm. Large attenuation coefficients further strengthen this argument. The scattering volume is small and, as ice characterization measurements show, air bubbles are infrequent and brine inclusions are extremely small. Therefore, surface scattering is the dominant backscatter mechanism.

These hypotheses provide the basis of theoretical and experimental studies of the radar backscatter from sea ice. Results of the application of a combined rough-surface and volume scattering theory to sea ice and snow backscatter were first presented by Fung and Eom (1982). A detailed discussion of the physical and electrical properties of sea ice, the extension of the model to include two ice layers, and a full discussion of the ability of a combined rough-surface and volume scattering theory to model sea ice were later presented by Kim *et al.* (1984).

The surface of homogeneous first-year ice is flat topographically but rough on the small scale. Formulations called the Kirchhoff approximations for rough-surface scattering were selected because of their apparent applicability. These formulations are summarized and derived in Ulaby *et al.* (1982). Predictions for slightly rough surfaces and very rough surfaces were compared to measured microwave signatures of first-year ice data for operation in the frequency range 1–18 GHz (Kim *et al.*, 1985a). The study showed that the physical optics model with an exponential correlation length

to describe the surface roughness statistics provided a reasonable prediction capability. The model includes a fast angular falloff in the small-incidence-angle region and the almost linearly increasing frequency behavior for angles off vertical. In addition, the frequency response was predicted using one set of surface parameters for the frequency range. The expression for the backscatter cross section is

$$\sigma^{\circ}_{pp}(\theta) = 2|R_{pp}|^2 \cos^2\theta\, e^{-k^2\sigma^2\cos^2\theta} \times \sum_{n=1}^{\infty} \frac{(4k^2\sigma^2\cos^2\theta)^n}{n!} \frac{k^2(n/l)}{[4k^2\sin^2\theta + n^2/l^2]^{3/2}} \tag{3.6}$$

where p is the polarization, θ the angle of incidence, R_{pp} the Fresnel reflection coefficient, k the wave number in air, σ the standard deviation of the surface height, and l the surface correlation length derived from the normalized autocorrelation function of the surface roughness profile. An average radius of curvature of the surface which is less than the wavelength and an rms slope which is less than 0.25 are required to satisfy the model assumptions. The role of the dielectric constant can be shown by assuming that the absolute backscatter level is proportional to the square of the Fresnel reflection coefficient.

The passive microwave return from first-year and multiyear sea ice can also be modeled. If a surface can be considered to be specular (i.e., the roughness elements are less than an eighth of the product of the wavelength and the sine of the incidence angle), the emissivity can be expressed as

$$\epsilon(\theta) = 1 - |R_p(\theta)|^2 \tag{3.7}$$

where R_p is the Fresnel reflection coefficient. When the dielectric constant of sea ice ranges between 3 and 4 and surfaces are slightly rough, which is true for a wide range of first-year ice conditions, the expression above produces reasonable estimates. This is, in large part, due to a reasonable insensitivity to small roughness scales.

A key to the modeling of multiyear sea ice is determining how to account for the scattering by the inhomogeneities (i.e., the air bubbles) inside the upper portion of the ice sheet. This may be accomplished by a number of techniques. Radiative transfer theory (Chandrasekhar, 1960) has been attempted and predictions correlate well with measured data. This theory is based on describing the propagation of energy through the medium. By assuming that there is no correlation between the scattered fields, the problem is greatly simplified because intensities can be summed. Another advantage is that multiple scatterings between particles are easily included.

The general theoretical solution may be simplified by neglecting volume–surface interactions to a form that not only produces excellent

agreement with measured data but also improves the understanding of the importance of the surface scatter contribution, the dielectric constant, the density of the ice, and the bubble size. The backscattering cross sections may be described as

$$\sigma^\circ(\theta) = \sigma_s^\circ(\theta) + T^2(\theta)\sigma_v^\circ(\theta') \tag{3.8}$$

where $\sigma_s^\circ(\theta)$ is the contribution due to surface scattering, $T^2(\theta)$ a coefficient which describes the transmission of power into the ice sheet, $\sigma_v^\circ(\theta')$ the backscattering coefficient due to volume scattering within the ice sheet, and θ' the angle of propagation in the ice sheet which results from refraction. If it is further assumed that the air bubbles are spherical and of one size, the volume scattering component is given by

$$\sigma_v^\circ(\theta) = \frac{N\sigma_b \cos\theta'}{2k_e}\left[1 - \frac{1}{L^2(\theta')}\right] \tag{3.9}$$

where N is the number of bubbles, σ_b is the cross section of a single particle, k_e is the volume extinction coefficient, $L(\theta') = \exp[k_e d \sec(\theta')]$, and d is the depth of the low-density ice layer.

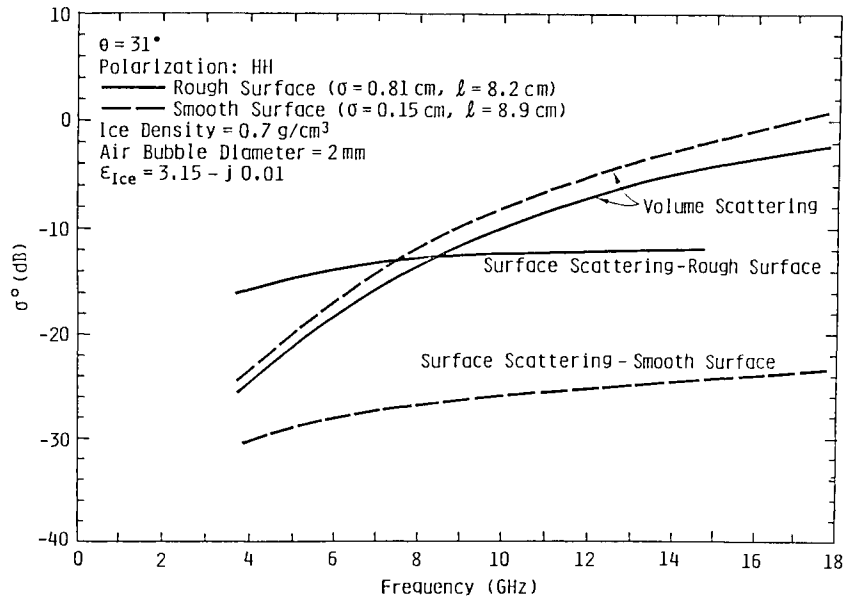

Figure 3.14 Theoretical backscatter response as a function of frequency. Surface and volume scattering contributions are shown separately for rough and smooth surfaces.

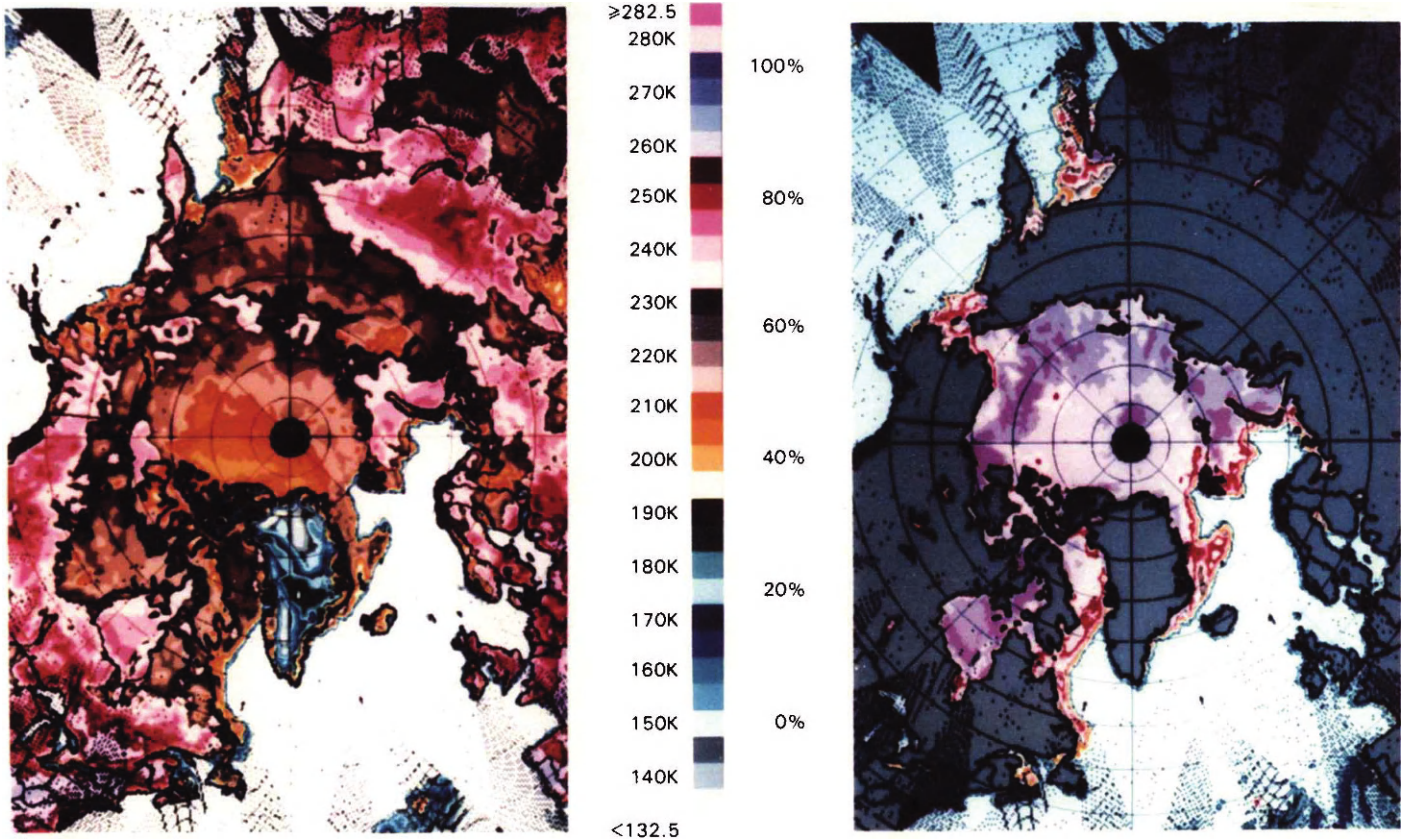

Plate 1 DMSP SSM/I brightness temperatures and resulting sea ice concentration map for the northern hemisphere for January 17, 1988. Data courtesy of Don Cavalieri, NASA Goddard Space Flight Center.

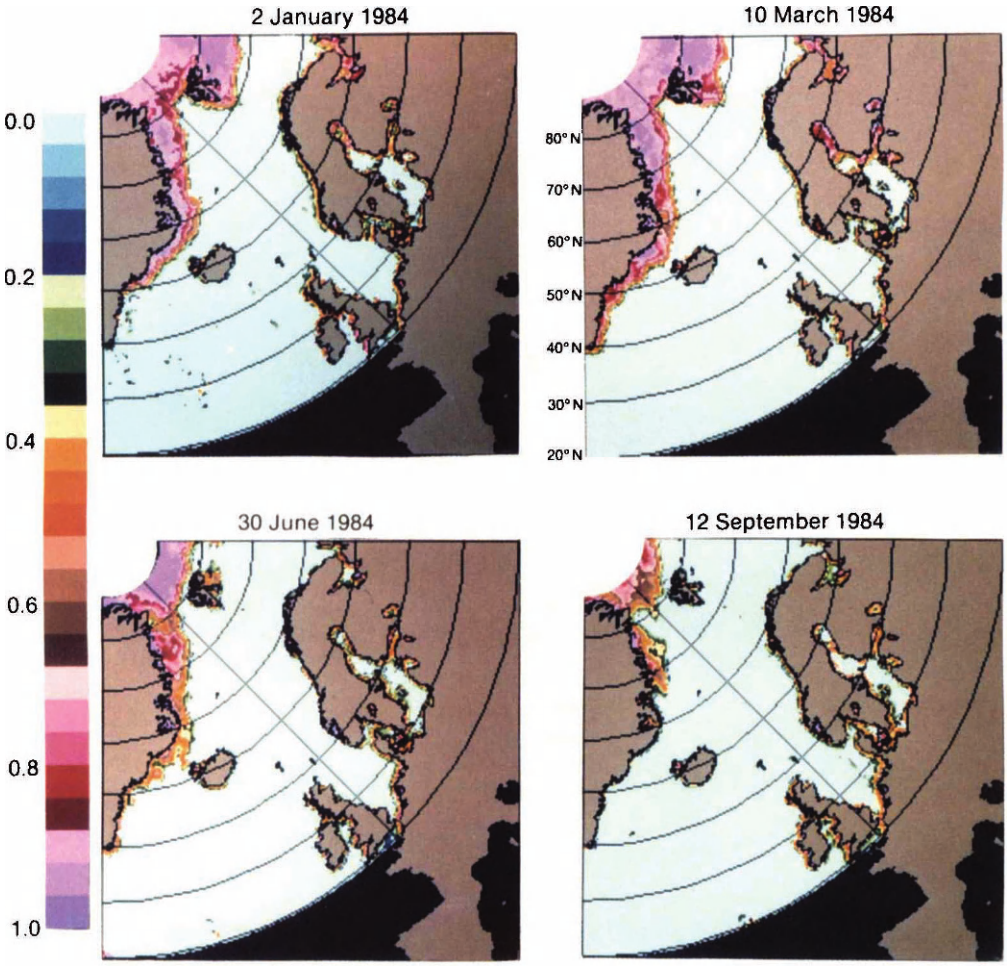

Plate 2 Total ice concentration obtained from Nimbus-7 SMMR for the four seasons over the Greenland Sea and the North Atlantic. Data courtesy of Per Gloersen, NASA Goddard Space Flight Center.

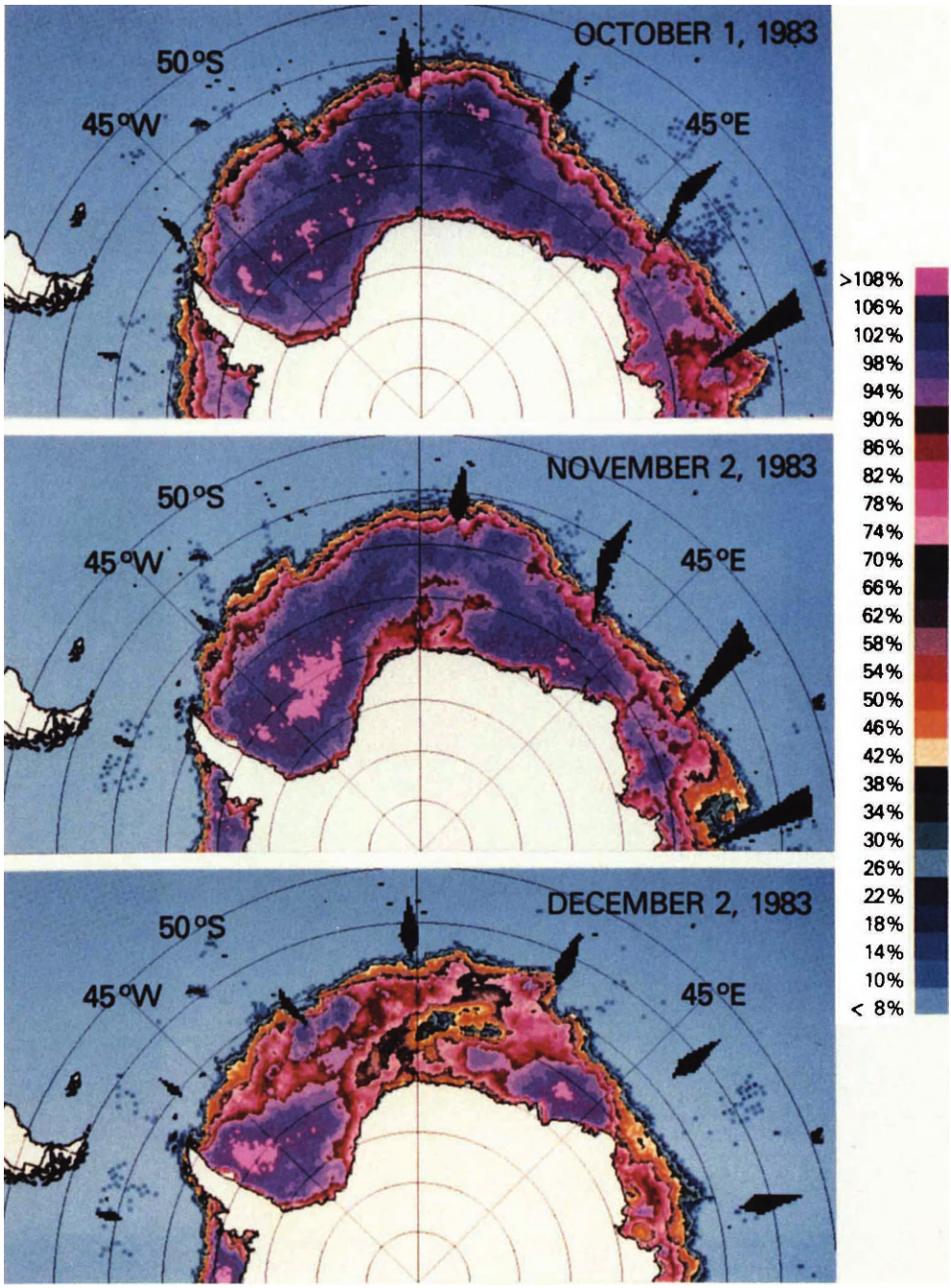

Plate 3 SMMR-derived sea ice concentration maps for the Weddell Sea. From Sullivan *et al.* (1988).

1984 Summer MIZEX

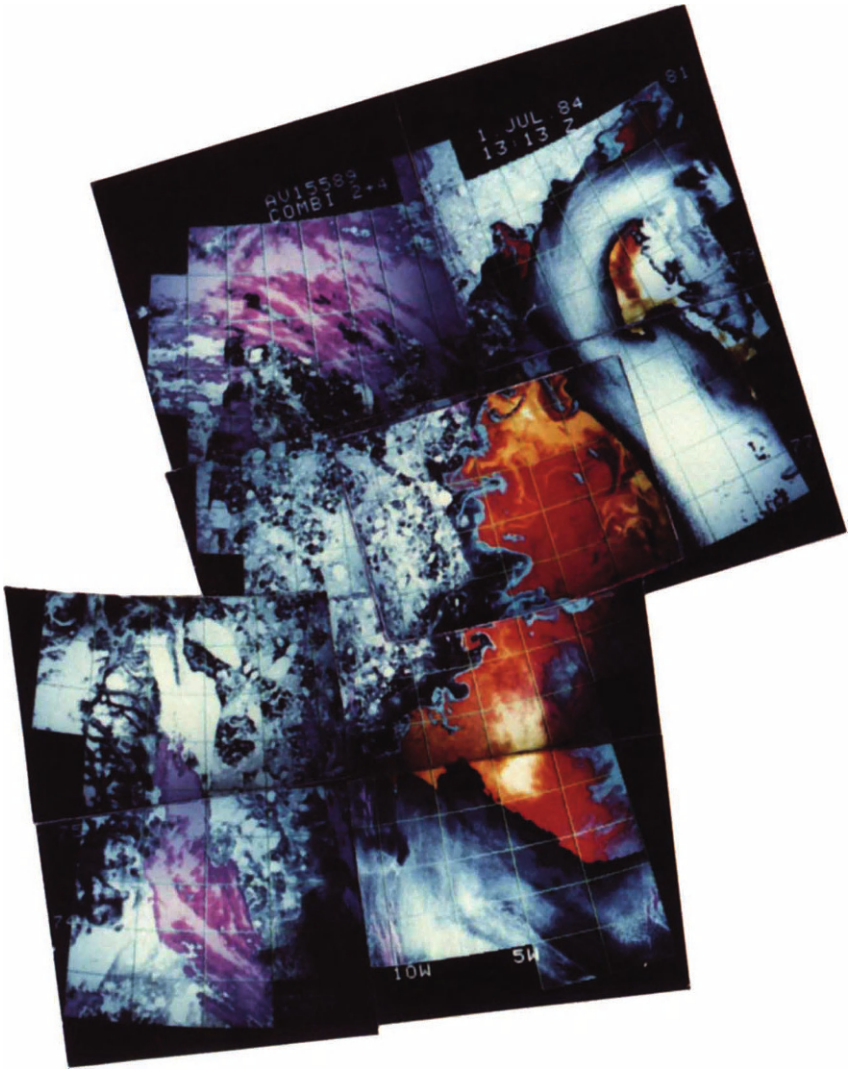

Plate 4 Composite visible and infrared (channels 2 and 4) NOAA AVHRR satellite image of Fram Strait obtained in July 1984. The warm North Atlantic current (yellow and red) can be observed interacting with the cold Arctic water (light blue). The pack ice areas are the white areas superimposed on the dark blue. Cirrus clouds are solid white areas, while the purple areas represent lower level clouds. In actual temperatures, the yellow is approximately 3–4°C, red is 1–2°C, light blue is approximately 0°C, and white and dark blue areas are less than 0°C.

The modeled backscatter cross sections show that the range of returns produced by smooth and rough surfaces is quite large and independent of frequency (Fig. 3.14). A rough surface also acts to reduce the effect of volume scattering. At frequencies of about 5 GHz, volume and surface scattering may contribute equally to the backscatter of multiyear ice. Below 5 GHz, volume scattering decreases rapidly in importance as the frequency is reduced.

In modeling the emissivity of multiyear ice, two approaches have shown promise. A radiative transfer theory, which is an extension of the work described above, combines rough surface and volume scattering effects (Fung and Eom, 1982). Another approach assumes that the snow and ice sheet are a two-layer anisotropic random medium (Lee and Kong, 1985). In this formulation, the dyadic Green's function is obtained and then the first-order backscattering coefficients are calculated using the Born approximation. In both techniques, the emissivity is calculated by determining the difference between one and the total reflectivity, which consists of specular reflectivity and the integral of the bistatic scattering coefficients over the upper hemisphere. The emissivity of multiyear ice has yet to be reduced to a simple expression.

IV. Visible and Infrared Sensors

During the past 10 years, satellites have been used to sense ocean color remotely by measuring the spectral radiance backscattered from the ocean and converting the values into pigment (chlorophyll *a*) concentrations using previously validated algorithms (Gordon *et al.*, 1983). However, the application of the Coastal Zone Color Scanner (CZCS), Landsat, and Spot to polar regions has been slow for a number of reasons. There are many validation problems with these sensors at high solar angles, principally the correction for Rayleigh (air) and aerosol scattering of the atmosphere. Polar regions also have more cloud cover than temperate or tropical regions. Because the sensors are passive and cannot penetrate through clouds, the data are less complete than those from other areas. Large solar zenith angles also reduce the penetration of radiant energy and the absolute amount backscattered. Finally, the presence of ice not only greatly complicates the direct observation of ocean color but also makes interpretation difficult due to the increased amount of reflectance by ice, which obscures the small color signal (Mueller, 1988). The CZCS sensor on board the Nimbus-7 satellite became inoperable in 1986. A more advanced color scanner (SeaWIFS), which will be part of the continuing Landsat series, is to be launched in 1991.

Despite the relatively short period of observation for the CZCS (1979–1986) and the difficulties in collecting, processing, and interpreting any images obtained from polar areas, a number of successful investigations of large-scale ocean color in polar regions have been completed. Maynard and Clark (1987) showed the large-scale distribution of pigments in the vicinity of the Yukon River plume in the Bering Sea and its relationship to a receding ice edge, and Sullivan *et al.* (1988) used CZCS images in conjunction with Advanced Very High Resolution Radiometer (AVHRR) data on ice concentrations to study the spatial extent and variations in phytoplankton blooms in the southern oceans, particularly those associated with the MIZ. A similar study using more advanced color algorithms was conducted by Comiso *et al.* (1990). These studies have provided large-scale coverage of ocean color in regions which are generally inaccessible and have thus extended our understanding of the magnitude of phytoplankton standing stocks in polar regions. Single CZCS images have been used to validate more synoptic trends found in ship-based sampling (Nelson *et al.*, 1987; El-Sayed, 1988).

Because the problem of clouds precludes study with satellite sensors in many polar regions, color sensors have been mounted on airplanes and helicopters which fly at variable altitudes. Although the area observed by aircraft-mounted sensors is much less than that observed by satellites, the aircraft-mounted sensors have the distinct advantage of being more reliable and hence are more applicable to mesoscale oceanographic studies such as those at the ice edge. Such systems can be either active (for example, laser-induced) or passive. Hoge *et al.* (1990) have shown the utility of the active lidar system in waters of the Greenland Sea, and Aiken *et al.* (1988) have investigated a region west of Svalbard using a passive system. However, the integration of aircraft-mounted color sensors into mesoscale oceanographic studies remains to be completed.

V. Satellite, Aircraft, and Ground-Based Remote Sensing Examples for Polar Oceanography

Sea ice is a vital, interactive component of the climate system, affecting and reflecting global changes of the atmosphere and oceans. The presence of sea ice restricts exchanges of heat, mass, momentum, and chemical constituents such as carbon dioxide and other gases between the ocean and the atmosphere, thereby reducing the amount of solar radiation absorbed at the earth's surface. This affects oceanic and atmospheric circulation. Because sea ice forms a layer of insulation between the ocean and the atmosphere, there is 5 to 20 times more heat flux from an open water area than from the same area of solid pack ice.

Since 1973, satellite passive-microwave data have provided excellent information on the large-scale oscillations of sea ice distribution in both the Arctic and the Antarctic. This information serves as useful background for both climate and mesoscale studies. The data obtained by the Electrically Scanning Microwave Radiometer (ESMR) on the NOAA Nimbus-5 satellite from 1973 to 1976 are presented in atlases of the Arctic and Antarctic by Parkinson *et al.* (1987) and Zwally *et al.* (1983), respectively. The data series was continued from 1978 to 1987 utilizing observations from the Nimbus-7 SMMR. Since 1987, the Special Sensor Microwave Imager (SSM/I) of the Defense Meteorological Satellite Program (DMSP) has provided passive microwave data as shown in Plate 1.

Plate 2 is plotted from data from the Nimbus-7 SMMR showing ice concentration (i.e., water versus ice) for the Greenland Sea and part of the North Atlantic as a function of season. The resolution of the SMMR data varies from 18 to 95 km as a function of frequency. The ice derived products which include total ice concentration and multiyear fraction are generally plotted on a 25–50-km grid. The algorithm for calculating the sea ice concentrations and type (multiyear fraction) from multispectral radiances obtained from the SMMR is discussed in detail by Cavalieri *et al.* (1984) and Gloersen and Cavalieri (1986). Briefly, the calculations utilize the vertically (V) polarized radiances obtained at a wavelength of 0.8 cm and the horizontally (H) and vertically polarized radiances at the 1.7 cm wavelength. Ratios of radiance are used to remove the physical temperature of the earth's surface to first order. To generate the concentration values shown in Plate 2, the H and V radiances at 1.7 cm were selected to calculate one of the ratios mentioned above, the polarization ratio (PR), which is used in the calculation of sea ice concentration (Cavalieri *et al.*, 1984). This combination was chosen because it resulted in the algorithm's being less sensitive to the combination of different instrument drifts in the selected channels over the 9-year period. The PR is used principally to distinguish between sea ice and open water because it is relatively insensitive to sea ice type. Another radiance ratio, the spectral gradient ratio (GR), is used to detect the ice type through the wavelength-dependent scattering due to empty brine cells present in the freeboard portion of multiyear ice and absent in first-year ice. The GR is calculated as the ratio of the difference to the sum of the vertical polarizations at the 0.8- and 1.7-cm wavelengths. Limiting the allowable range of GR is also important in reducing the weather effects, which previously led to ambiguous interpretation in the ice margins during storm passages (Gloersen and Cavalieri, 1986).

The accuracies of the calculations of sea ice area (i.e., ice concentration) with the 1.7-cm PR have been estimated (Cavalieri *et al.*, 1984) as about 5% in the central pack and about 9% in the MIZ, where as much as 30% of the ice

may be thin or new and without snow cover (two ice types not taken explicitly into account by the algorithm). The precision or repeatability of the ice coverage calculations is probably better than the accuracy, i.e., closer to the value expected on the basis of instrument noise and drift, 1–2% for a single footprint.

The annual and seasonal variations of the ice distribution of the northern and southern hemispheres have been studied for a number of years with these passive microwave sensors. For example, Gloersen and Campbell (1988), using SMMR data, estimated that the total sea ice extent in the northern hemisphere varies from a minimum of about 8 million km^2 in September to a maximum of about 15 million km^2 in March. Sutherland *et al.* (1989) used SMMR data to observe rapid ice formation and ablation (i.e., 200,000 km^2 in 48 h) in the "Odden" area of the Greenland Sea. The rapid oscillation of the Odden does not appear to be a result of wind-induced ice drift but rather of the rapid formation of thin ice off the main ice edge.

Ice concentration maps produced from SMMR for the Weddell Sea are shown in Plate 3. Color-coded images of ice concentrations derived from SMMR on October 1, November 2, and December 2, 1983, are shown from top to bottom in the figure. The set of images shows qualitatively and quantitatively the state of the ice cover from the time of near-maximum ice extent through the austral spring. The trend of ice decay and the areas most vulnerable to it during various time periods are also evident from the images. The concentration gradient at the MIZ is also observed to be variable, ranging from tens of kilometers to several hundred kilometers (Sullivan *et al.*, 1988).

Thus, one of the most important geophysical parameters that is measurable from space- and airborne sensors is ice concentration (Swift *et al.*, 1985). The determination of the mixture of ice and water (see Hollinger *et al.*, 1984; Svendsen *et al.*, 1983; Comiso, 1983; Carsey, 1985), accomplished by exploiting the large difference in emissivity and/or backscatter intensity between ice and water, was first demonstrated in the early 1970s, when *in situ* observations at manned drifting stations and airborne sensor data were correlated (Vant *et al.*, 1978; Campbell *et al.*, 1978; Gloersen *et al.*, 1973). The contrast in the emission for ice and water is unambiguous. In comparison, radar backscatter may have reduced contrast or even contrast reversals when there are large areas of water (e.g., near the ice edge) and moderate wind speeds, or with viewing angles from vertical to approximately 25°. Within the pack ice, contrasts between open water and sea ice for both active and passive microwave sensors have been generally quite high (Grenfell and Lohanick, 1985).

Algorithms using active- and passive-microwave data are very similar in their nature. At present, algorithms are based on knowing the signature for ice-free ocean and consolidated ice (both first-year and multiyear). Using the

expected signals S for either brightness, temperature, or backscatter intensities of ice and water, ice concentration C is calculated on the basis of linear interpolation as follows:

$$C = (S_o - S_w)/(S_i - S_w) \tag{3.10}$$

where S_o is the observed signal, S_w the mean signal for ice-free water, and S_i the mean signal for consolidated sea ice. At present, algorithms using this technique agree with aerial photography and passive microwave observations to within approximately 10% (Burns *et al.*, 1987).

Satellite radar altimeters have been designed to provide very accurate ocean height information. These data have a resolution on the order of 5 cm and a spot size of approximately 10 km and have been used to provide geoid, gravity wave height, currents, and ocean topography values (Cheney, 1982; Fedor and Brown, 1982). In addition to wave height information (i.e., the two-way time travel of the pulse), the amount of backscatter is analyzed to yield wind information. More recently, Hawkins and Lybannon (1989) have begun to use the U.S. Navy's radar altimeter on the Geosat satellite to provide sea ice information. Potentially, a radar altimeter can provide information about concentration, ice type, and roughness in addition to ice extent.

The return pulse from the radar altimeter has significantly different shapes for the sea ice and the open ocean. Ice, unlike water, tends to produce specular reflection, so a much larger portion of the radiated energy at any angle will reflect off the ice surface at an angle equal to the angle of incidence. In general, the signal strength is much larger than that of the ocean and the shape of the reflected pulse is also modified. Dwyer and Godin (1980), using Seasat altimeter data, developed a semiempirical algorithm for satellite radar altimeters that measures these differences. The algorithm is

$$\text{Ice index} = [(100 + \text{AGC})/(100 \times \text{AASG})] - 10 \tag{3.11}$$

where AGC is the automatic gain control signal and AASG the average altitude/specular gate.

The Geosat ice index is a number that ranges from 0.6 to 0.7 over water and is greater than 1 over ice. Therefore, water–sea ice transitions are evident in the time history of the ice index. Figure 3.15 is a plot of ice index for the Antarctic region with the Geosat satellite radar track as baselines (Hawkins and Lybannon, 1989). The orbital inclination of Geosat (72°) limits the coverage to 72° north and south.

In the past two decades, a series of large Arctic projects have yielded a considerable understanding of the growth, motion, and decay of sea ice in the interior of the Arctic Ocean (Pritchard, 1980). After the Arctic Ice Dynamics Joint Experiment (AIDJEX), attention shifted to the problem of

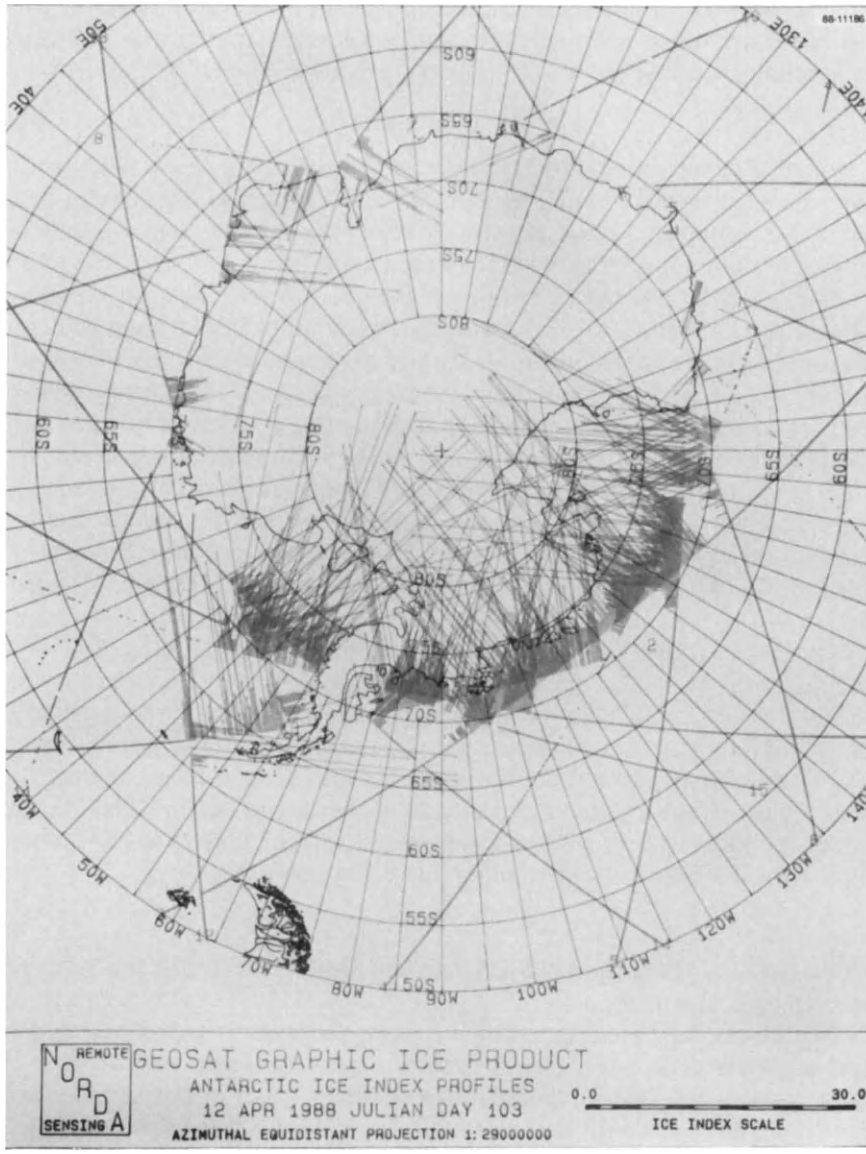

Figure 3.15 Plot of ice index for the Antarctic region with the Geosat satellite track as baselines. An index greater than 1 denotes ice. From Hawkins and Lybannon (1989), copyright © 1989 IEEE.

understanding the processes which occur at the MIZ, the area where the permanent ice pack meets the open ocean. By understanding the interaction between the atmosphere, ocean, and sea ice, the advance and retreat of the ice edge can be determined.

An important area for exchange of heat and mass between the Arctic Ocean and the North Atlantic is the Fram Strait area of the Greenland Sea (see Chapter 4). The Fram Strait area has been the site of three major Marginal Ice Zone Experiments (MIZEXs) conducted in 1983, 1984, and 1987. The warm northward-flowing North Atlantic current, the cold southward-flowing Arctic water, and the pack ice at the MIZ can be observed from AVHRR visible and infrared satellite data at 2-km resolution (Plate 4). Various eddies can also be observed along the ice edge.

Among the objectives of the MIZEX program were studies of the ice edge position, ice kinematics, ice concentration, ice types, locations of eddies, ice physics, ice thickness, ridges, ice floe distribution, leads, and polynyas. A SAR system housed in a CV-580 aircraft was used to provide information about the variables. In addition, the all-weather SAR was used in a real-time mode to guide the research vessels into the eddy regions. For example, a high-resolution SAR mosaic collected on July 5, 1984 (Fig. 3.16) clearly shows the detailed surface structure of an elliptically shaped eddy (E1) on the scale of $\simeq 30$ km. Because winds were light, the sea ice floe size distribution of 50–500 m reflected the upper-ocean circulation. The orbital motion of the eddy was cyclonic, while the spiral motion of ice toward the center indicated an inward frictionally driven radial motion. The ice concentration was more than 80% at the center of the eddy. This implied that there was convergence and that ageostrophic effects are important and must be included in realistic models of these eddies. A second eddy (E2) was seen south of E1. Slicks and bands of ice that indicated internal wave activity were also identified. The area marked "band of 'dead' water" off the ice edge was a distinct meltwater zone. A detailed interpretation of the SAR mosaic describes the location of large individual floes and polynyas, ice concentration estimates, and ice edge and floe size distributions (see Fig. 3.16). Fully automatic algorithms have been developed which can produce sea ice type classification and concentration maps from SAR data (Wackerman *et al.*, 1988). The sea ice type classification algorithm uses local statistics to determine ice type boundaries, and the ice concentration algorithm iteratively decomposes the histogram into ice and water statistical values.

SAR images collected 6 days apart over the same area provide information regarding the dynamic processes in the MIZ. Figure 3.17 shows the analysis of two SAR images collected 6 days apart (June 30 and July 6, 1984) and the transformation of a relatively north–south ice edge to a convoluted,

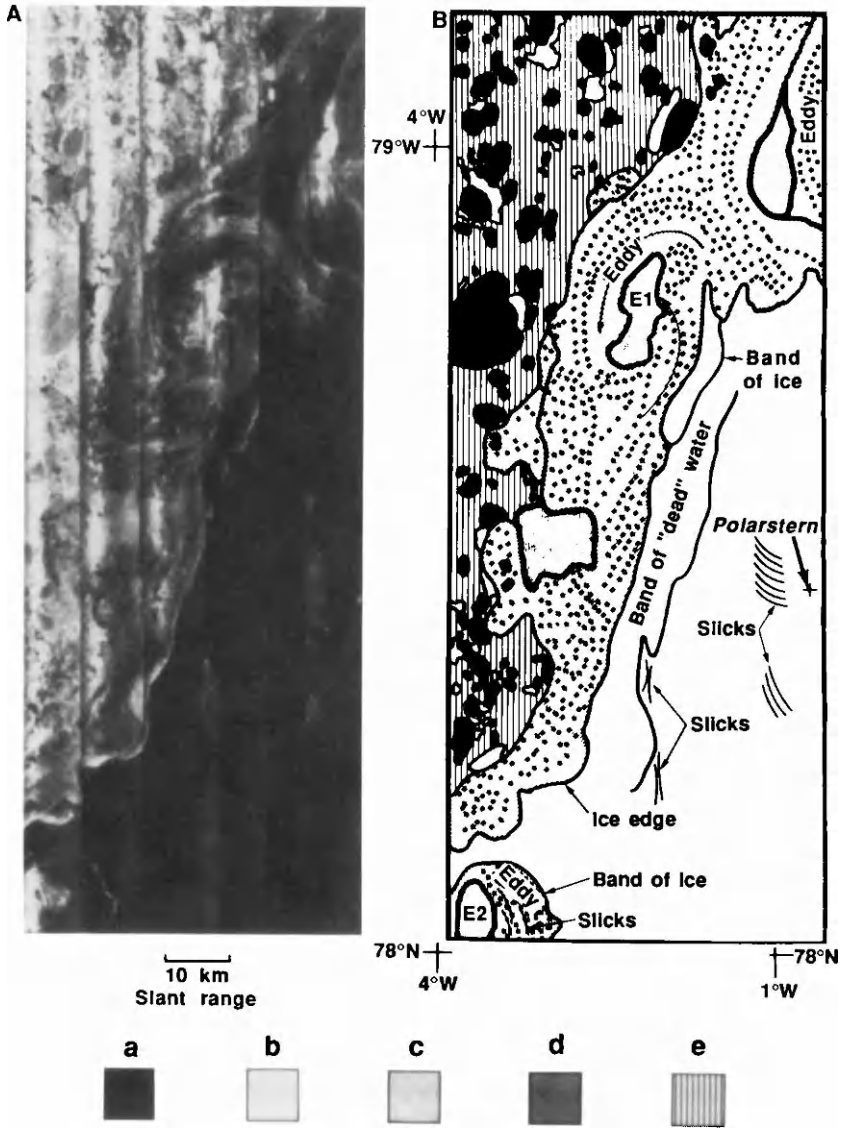

Figure 3.16 *L*-band (1.2 GHz) mosaic (A) collected on July 5, 1984 with the *X-C-L*-band system of the Environmental Research Institute of Michigan/Canadian Center for Remote Sensing. In the radar image, bright zones represent ice and dark zones are ice-free water. The interpretation of this mosaic (B) reveals that large individual floes (a), polynyas and ice-free ocean areas (b), 30% concentration areas with 10–500-m floes (c), 80% ice concentration areas with 10-m to 1.5-km floes (d), and 80% ice concentration areas with 10-m to 6-km floes (e) are clearly delineated in the image. The median floe sizes for areas c, d, and e are 125, 150, and 1000 m, respectively. The dots in area c indicate increased local ice concentration due to surface currents. From Johannessen *et al.* (1987).

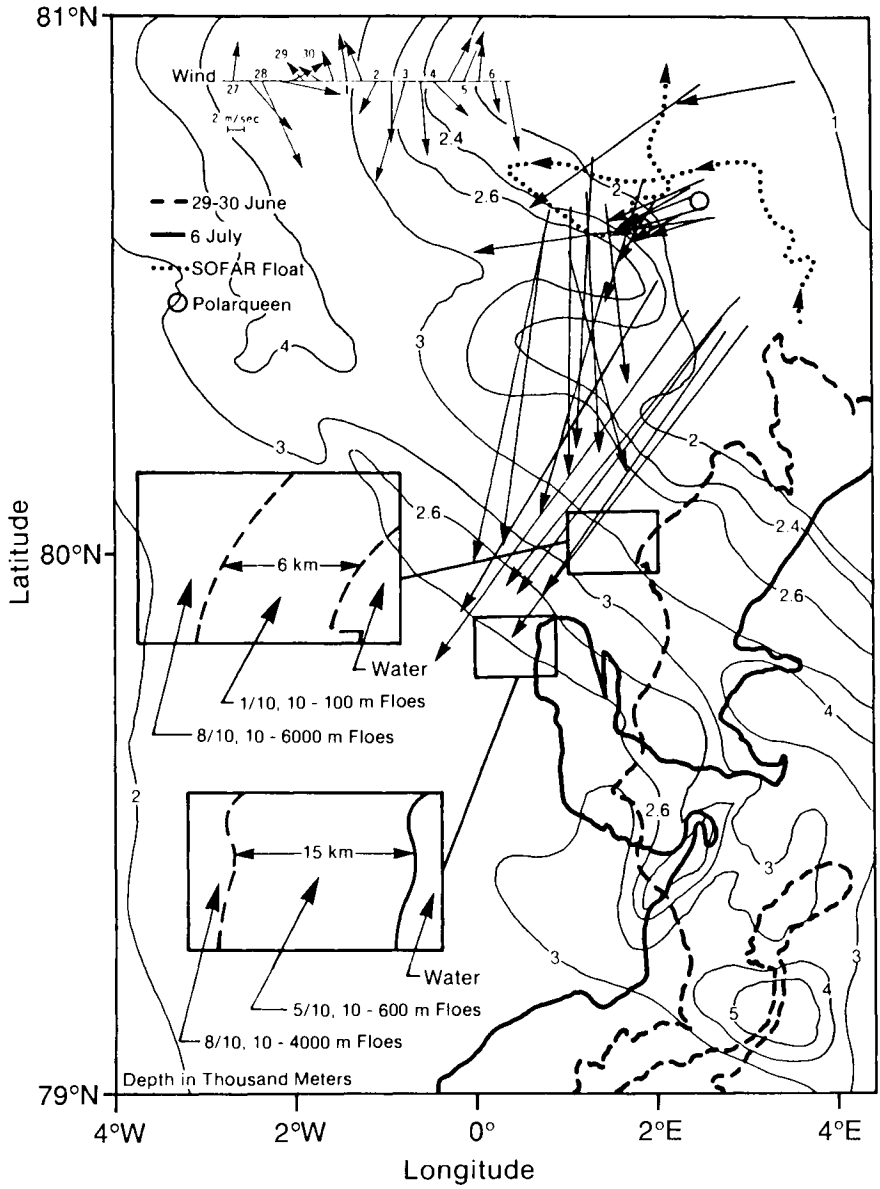

Figure 3.17 Composite sketch of ice edge, concentration, and floe size for 30 June and 6 July 1984 derived from the SAR. Also indicated are the track of a sofar buoy, bathymetry contours, and local surface wind. From Shuchman *et al.* (1987).

meandering ice edge. These meanders result from the complex interactions along the boundary between the rapid southward East Greenland Current, warm northward-flowing Atlantic waters, and highly variable winds. Ice edge meanders may play an important role in the generation of ice–ocean eddies because they provide the initial perturbation in the Ekman transport field that eventually results in eddies. These edge features are composed of ice floes ranging from 50 to 500 m in size, which are the result of gravity wave–ice interaction and eddy-induced floe collisions that break up large floes. Under moderate wind conditions, the ice in these meanders reflects the ocean circulation because the individual ice floes act as Lagrangian drifters moving with the current. This is particularly true in the summer season, when the winds are normally light (less than 4 m/s) and there is no formation of new ice that would freeze floes together.

The sequential images also give ice drift kinematic data. The ice drift vectors were derived by locating the same floe in images on June 29 and July 6. Three regimes of floe drift occurred during this 7-day period. First, the floes at the edge moved fastest, an average distance of 75 km (12.5 cm/s) in a southwesterly direction parallel to the ice edge. Second, floes west of 2°E, at distances greater than 40 km from the edge, moved approximately 45 km (7.5 cm/s) to the south (Shuchman *et al.*, 1987). Finally, in the region near the R/V *Polarqueen,* the ice drift was only 15 km (2.5 cm/s) to the southwest.

The decrease in speed and the change in direction of the ice floe drift across the MIZ result from different forces acting on the ice in the interior and at the edge. The interior, with greater ice concentration and larger floes, is more strongly influenced by internal ice stress than the ice edge, which normally has lower ice concentrations and smaller floe sizes. The wind force also varies across the MIZ because the edge region, with smaller floe size and lower ice concentration, has greater roughness than the interior. The third feature, the region of dramatically reduced ice drift, occurred at precisely the same time and location at which an ocean frontal meander was observed in the dynamic height topography (Manley *et al.*, 1987). Furthermore, the drift of a sound fixing and ranging (sofar) buoy at a depth of 100 m through this anomalous ice drift area showed that this meander was a cyclonic ocean eddy. The location and size of this eddy were such that its circulation was opposed to the general ice drift direction, which reduced the ice drift velocities. Hence, the eddy slowed the ice drift in one region, changed the drift direction in the other region, and possibly augmented the drift to the north.

Surface waves are a major factor determining the structure of the ice in the MIZ. As the waves propagate through the ice field from the open ocean, they are scattered and attenuated by the ice floes. Only the long-period swells propagate more than a few kilometers into the ice; therefore, the breakup by

short waves is most effective near the ice edge. The longest swells from storms can penetrate more than 100 km into the ice and can break up layer floes through flexure for tens of kilometers. The decay coefficient varies approximately as frequency squared, so the shorter waves are damped more quickly (Wadhams *et al.,* 1988). The result is a floe size distribution in which the maximum floe size increases within the pack. Airborne SAR can provide observations of wave penetration into the ice. Lyden *et al.* (1988) utilized SAR data and standard fast Fourier transform (FFT) techniques to observe 230-m-wavelength surface swell, generated by a passing meteorological low several hundred kilometers away, penetrating over 200 km into the pack before significant decay occurred.

In 1978 a free-flying NASA satellite called Seasat was flown in a near-polar orbit and carried a SAR. Although the satellite failed 100 days after launch, more than 150 passes of *L*-band (23.5-cm) SAR data were collected over the Arctic. The resolution of Seasat was 25 m and the swath width was 100 km. Figure 3.18 shows two Seasat 100 × 100 km images of the central ice pack in the Beaufort Sea taken 3 days apart. A kinematic vector image of ice floe motion over the 3-day period is also shown. The velocity vectors resulted from tracking over 750 floes common to both images (Curlander *et al.,* 1985). The vectors show the complexity of motion in an ice field that is the consequence of air stress, ocean surface tilt, water stress, and force transmitted through the ice. The first two stresses are perceived to be essentially constant over the 100-km dimension of the image, whereas the remaining two stresses are known to have spatial variability.

Both ground-based and helicopter-mounted instrumentation can be used to acquire backscatter information. Radars such as the sled-based scatterometer are being transported to the ice floes in the Arctic to couple the accurate measurement of backscatter with scene characterization measurements as well as surface-based passive-microwave measurements. This sled system (Onstott and Shuchman, 1988a) provides data on backscatter from various sea ice forms at frequencies from 0.5 to 10 GHz and relates the sources of scatter to locations within the snow and ice. These *in situ* observations may then be extended to the small scale with helicopter-borne instrumentation such as the *L-C-X*-band scatterometer (Onstott and Shuchman, 1988b) or to the mesoscale with aircraft and satellite sensors. These scatterometers make a powerful contribution to polar research because they provide backscatter values as a function of incidence angle. The measurements at various incidence angles can then be used for validation of backscatter models as well as interpretation of aircraft SAR data, which are typically collected at moderate angles (e.g., 45°), to predict responses of future SAR satellite systems that utilize steep angles of incidence (e.g., 25°) because of power limitations.

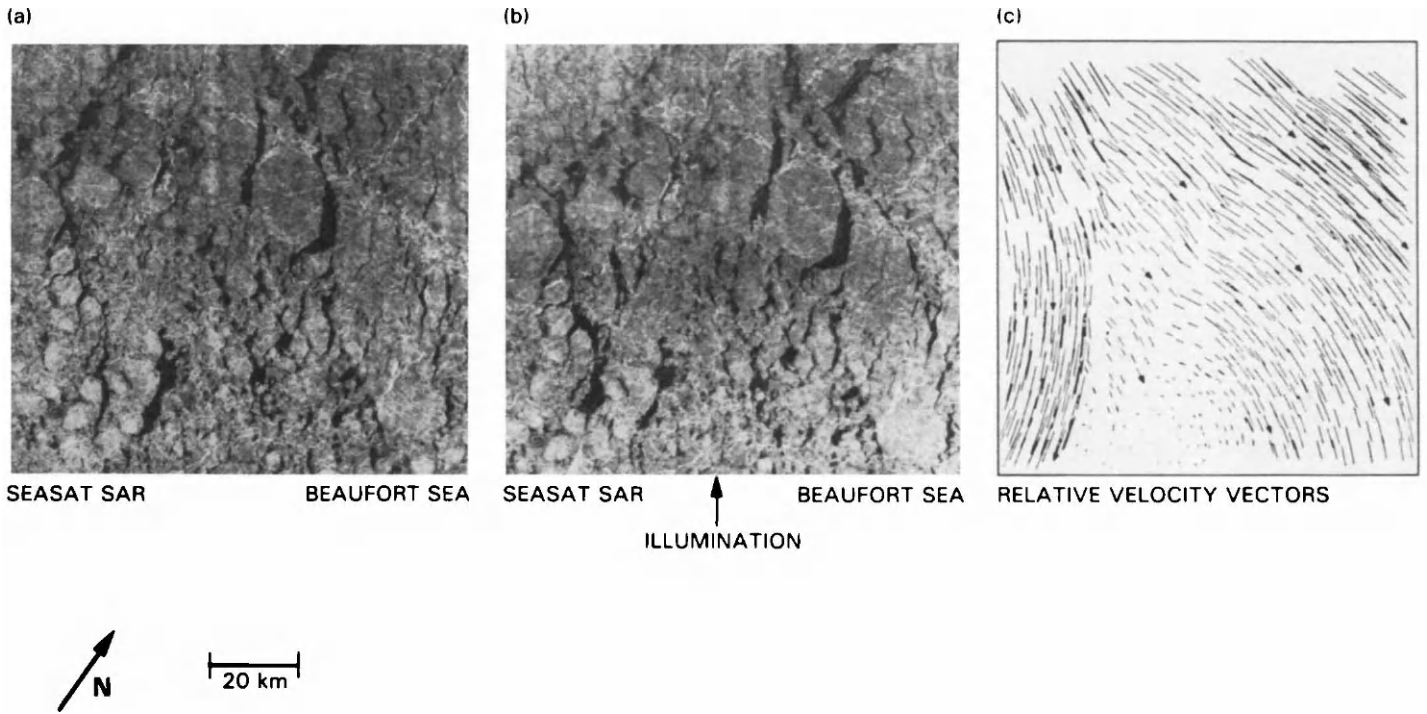

Figure 3.18 Two Seasat 100 × 100 km SAR images taken 3 days apart (while in a 3-day repeat orbit) of the central ice pack in the Beaufort Sea. A kinematic vector image of the ice motion over the 3-day period is also presented. From Curlander *et al.* (1985).

VI. Concluding Remarks

Satellite remote sensing offers the capability of synoptically mapping the Arctic and Antarctic oceans. If microwave sensors are employed, the mapping can be performed independently of weather and solar illumination. Passive-microwave radiometers provide sea ice concentrations with coarse resolution (25–50 km) for both the northern and southern hemispheres. These maps have been obtained on a near-daily basis since 1973. Designs in which the resolution of these passive-microwave systems is improved by an order of magnitude will be implemented within the next decade. Visible and infrared satellite sensors such as Landsat, NOAA AVHRR, and Spot are extremely useful in supplying water mass, biological, and ice information on cloud-free days.

SAR has the greatest potential for providing polar information from space. With its 10–30-m resolution, SAR has been demonstrated to provide observations on ice edge position, ice kinematics, ice concentration, ice types, ice physics, ridges, icebergs, ice flow distribution, leads, polynyas, wave propagation into the pack, locations of eddies and fronts, and determination of wind speed. A number of SARs in polar orbit are planned, beginning with the launch of Earth Resource Satellite-1 (ERS-1) by the European Space Agency (ESA) in 1990. It is thought that by the year 2000 continuous SAR data for both the Arctic and Antarctic will be routinely available.

Radar altimeters provide useful information (10-km resolution) on ice edge extent, ice roughness, gravity waves, significant wave height, wind speed and direction, ocean currents, and ocean surface topography. A series of radar altimeters, which are planned for the coming decades, will increase the availability of altimeter data for the polar regions.

The optical and thermal sensors (AVHRR, OLS, MSS), when weather conditions are favorable (i.e., cloud-free and proper solar illumination), provide excellent high-resolution (10–2000-m) information on sea ice extent, location of fronts and eddies, and mapping of individual water masses including chlorophyll concentration. Kinematics can also be performed if the area remains cloud-free during the required observation period.

Table 3.3 lists the currently planned free-flying satellite systems which can provide information about the Arctic and Antarctic. Not listed are the replacement satellites for the NOAA 9/10 and DMSP series. These replacements are presently scheduled, and thus continuous uninterrupted service should be provided by these satellites.

When selecting a remote sensor for polar oceanography, the trade-off between high resolution and swath width coverage must always be considered. In general, the coarse-resolution sensors (1 km, AVHRR; 50 km, passive microwave) can map a hemisphere over a 1–2-day period. The high-res-

Table 3.3 Earth Observation Missions That Will Provide Polar Information (Planned and Approved)

	Mission	Objectives	Main sensors	Orbit	Launch date	Status of approval
ESA	ERS-1	Ocean-ice monitoring	Synthetic-aperture radar Wind and wave scatterometer Radar altimeter Along-track scanning radiometer Precise range and range rate equipment	780 km alt. sun-synchr.	1990	Approved phase C/D started in 1985
Canada	Radarsat	Ice and land monitoring	Synthetic-aperture radar Wind scatterometer Optical sensor	1000 km alt. sun-synchr.	1994	Approved
Japan	MOS-1	Marine applications	MESSR VTIR MSR	909 km alt. sun-synchr.	1986	Launched
	J-ERS-1	Land applications	Synthetic-aperture radar Visible and near-infrared radiometer	570 km alt. sun-synchr.	1990	Approved

United States: NASA/France	TOPEX/ Poseidon	Ocean circulation	Two-frequency radar altimeter Microwave radiometer Precise positioning	1300 km alt., 63° inclination	1989	Phase B in progress
France	Spot	Land applications	High-resolution (10 m) Visible instruments (×2)	832 km alt. sun-synchr.	Spot-1 in 1986 Spot-2 in 1989	Launched Approved
United States: NOAA + private entity	Landsat 6 and 7	Land applications Ice and ocean	Thematic mapper Multilinear array SeaWifs	700 km alt. sun-synchr.	Landsat 6 in 1989 Landsat 7 in 1991	Under discussion in U.S. Congress
United States: DoD	DMSP	Meteorology Sea ice	High resolution Visible and IR (OLS) Special sensor microwave imager	883 km alt. polar sun-synchr.	May 1986	Launched
United States: NASA	EOS	Meteorology Ice and land monitoring	Radar altimeter Visible Passive micrometer Synthetic-aperture radar	850 km alt. polar sun-synchr.	2000	Under preliminary design

olution sensors (5–100 m; Spot, Landsat, and SAR) provide mesoscale regional coverage (i.e., 300 × 3000 km) daily, but a number of days are needed to assemble a hemispheric map. As satellite sensors become more sophisticated, Spot/Landsat and SAR data should be available with hemispheric coverage daily.

Acknowledgments

This work was supported by the Oceanographer of the Navy, the National Aeronautics and Space Administration (NASA), and the Office of Naval Research (ONR) under contracts N00014-81-C-0692 and N00014-86-C-0469. The Technical Monitor for the Oceanographer of the Navy was R. S. Winokur. The NASA Technical Monitor was R. H. Thomas. The ONR Technical Monitors were C. A. Luther and T. B. Curtin. The authors also acknowledge Laura L. Sutherland for her assistance in the figure preparation and Rita L. Woods for text preparation.

References

Aiken, J., J. W. Nolten, C. C. Trees & J. L. Mueller. 1988. Horizontal and vertical variability of bio-optical fields in the Greenland and Barents seas. *Eos* **69**: 1141 (abstr.).

Apel, J. R. (ed.). 1987. "Principles of Ocean Physics," Int. Geophys. Ser., Vol. 38. Academic Press, Orlando, Florida.

Burns, B. A., D. J. Cavalieri, M. R. Keller, W. J. Campbell, T. C. Grenfell, G. A. Maykut & P. Gloersen. 1987. Multisensor comparison of ice concentration estimates in the marginal ice zone. *J. Geophys. Res.* **92**: 6843–6856.

Campbell, W. J., J. Wayenberg, J. B. Ramseyer, R. O. Ramseier, M. R. Vant, R. Weaver, A. Redmond, L. Arsenault, P. Gloersen, H. J. Zwally, T. T. Wilheit, T. C. Chang, D. Hall, L. Gray, D. C. Meeks, M. L. Bryan, F. T. Barath, C. Elachi, F. Leberl & T. Farr. 1978. Microwave remote sensing of sea ice in the AIDJEX main experiment. *Boundary-Layer Meteorol.* **13**: 309–337.

Carsey, F. D. 1985. Summar Arctic sea ice character from satellite microwave data. *J. Geophys. Res.* **90**: 5015–5034.

Cavalieri, D. J., P. Gloersen & W. J. Campbell. 1984. Determination of sea ice parameters with the Nimbus-7 SMMR. *J. Geophys. Res.* **89**: 5255–5369.

Chandrasekhar, S. 1960. "Radioactive Transfer." Dover, New York.

Cheney, R. E. 1982. Comparison data for Seasat altimetry in the western North Atlantic. *J. Geophys. Res.* **87**: 3247–3253.

Comiso, J. C. 1983. Sea-ice effective microwave emissivities from satellite passive microwave and infrared observations. *J. Geophys. Res.* **88**: 7686–7704.

Comiso, J. C., N. G. Maynard, W. O. Smith, Jr. & C. W. Sullivan. (1990). Satellite ocean color studies of the Antarctic ice edge in summer/autumn. *J. Geophys. Res.* (in press).

Curlander, J. C., B. Holt & K. J. Hussen. 1985. Determination of sea ice motion using digital SAR imagery. *IEEE J. Oceanic Eng.* **OE-10**: 358–367.

Dwyer, R. W. & R. H. Godin. 1980. Determining sea ice boundaries and ice roughness using Geosat-3 altimeter data. *NASA [Contract. Rep.] CR* **NASA-CR-156862.**

Earth Observing Reports. "SAR Synthetic Aperture Radar Instrument Panel Report," Vol. 11F. NASA, Washington, D.C.

El-Sayed, S. Z. 1988. Productivity of the Southern Ocean: A closer look. *Comp. Biochem. Physiol.* **90:** 489–498.

Fedor, L. S. & G. S. Brown. 1982. Waveheight and wind speed measurements from the Seasat radar altimeter. *J. Geophys. Res.* **87:** 3254–3260.

Fung, A. K. & H. J. Eom. 1982. Application of a combined rough surface and volume scattering theory to sea ice and snow backscatter. *IEEE Trans. Geosci. Electron.* **GE-20:** 528–536.

Gloersen, P. & W. J. Campbell. 1988. Variations in the Arctic, Antarctic, and global sea ice cover during 1978–1987 as observed with the Nimbus-7 SMMR. *J. Geophys. Res.* **93:** 10666–10674.

Gloersen, P. & D. J. Cavalieri. 1986. Reduction of weather effects in the calculation of sea ice concentration from microwave radiances. *J. Geophys. Res.* **91:** 3913–3919.

Gloersen, P., W. Nordberg, T. J. Schmuigge, T. T. Wilheit & W. J. Campbell. 1973. Microwave signatures of first-year and multiyear sea ice. *J. Geophys. Res.* **78:** 3564–3572.

Gordon, H. R., D. K. Clark, J. W. Brown, O. B. Brown, R. W. Evans & W. W. Broenkow. 1983. Phytoplankton pigment concentrations in the middle Atlantic Bight: Comparison of ship determinations and CZCS estimates. *Appl. Opt.* **22:** 20–36.

Grenfell, T. C. & A. W. Lohanick. 1985. Temporal variations of the microwave signatures of sea ice during the late spring and early summer near Mould Bay NWT. *J. Geophys. Res.* **90:** 5063–5074.

Hallikainen, M., F. T. Ulaby & M. Abdelrazik. 1984. The dielectric behavior of snow in the 3 to 37 GHz range. *Eur. Space Agency [Spec. Publ.] ESA SP* **ESA SP-215:** 169–174.

Hawkins, J. D. & M. Lybannon. (1989). Geosat altimeter sea ice mapping. *IEEE J. Oceanic Eng.* **14**(2): 139–148.

Hoge, F. E., C. W. Wright, R. N. Swift & J. K. Yungel. (1990). Airborne discrimination between ice and water; application to the laser measurement of chlorophyll-in-water in a marginal ice zone. *J.Geophys. Res.* (submitted for publication).

Hollinger, J. P., B. E. Troy, R. O. Ramseier, K. W. Asmus, M. F. Hartman & C. A. Luther. 1984. Microwave emission from high Arctic sea ice during freeze up. *J. Geophys. Res.* **89:** 8104–8122.

Johannessen, O. M., J. A. Johannessen, E. Svendsen, R. A. Shuchman, W. J. Campbell & E. Josberger, 1987. Ice-edge eddies in the Fram Strait marginal ice zone. *Science* **236:** 427–429.

Kim, Y. S., R. K. Moore & R. G. Onstott. 1984. "Theoretical and Experimental Study of Radar Backscatter from Sea Ice," Rep. RSL TR 168, pp. 331–37. Univ. of Kansas, Lawrence.

Kim, Y. S., R. G. Onstott & R. K. Moore. 1985a. The effect of a snow cover on microwave backscatter from sea ice. *IEEE J. Oceanic Eng.* **OE-9:** 383–388.

Kim, Y. S., R. K. Moore, R. G. Onstott & S. Gogineni. 1985b. Towards identification of optimum radar parameters for sea ice monitoring. *J. Glaciol.* **31:** 214–219.

Lee, J. K. & J. A. Kong. 1985. Passive microwave remote sensing of an anisotropic random medium layer. *IEEE Trans. Geosci. Remote Sens.* **GE-23:** 924–932.

Lyden, J. R., R. A. Schuchman, C. Zago, R. Rottier, P. Wadhams & O. Johannessen. 1988. *Eur. Space Agency [Spec. Publ.] ESA SP* **ESA SP-284:** 1435–1437.

Manley, T. O., J. Z. Villanueva, J. C. Gascard, P. F. Jeannin, K. L. Hunkins & J. van Leer. 1987. Mesoscale oceanographic processes beneath the ice of Fram Strait. *Science* **236:** 432–434.

Matzler, C. 1985. "Interaction of Microwaves with Natural Snow Cover," Treatise No. 152. Inst. Appl. Phys., Univ. of Bern, Bern, Switzerland.

Matzler, C., T. Olaussen & E. Svendsen. 1984. "Microwave and Surface Observations of Water and Ice Carried out from R/V Polarstern in the Marginal Ice Zone North and West of Svalbard," 2nd ed., Geophys. Inst., Div. A., Univ. of Bergen, Bergen, Norway.

Maynard, N. G. & D. K. Clark. 1987. Satellite color observations of spring blooming in Bering Sea shelf waters during the ice edge retreat in 1980. *J. Geophys. Res.* **92:** 7127–7139.

Mueller, J. 1988. Nimbus-7 CZCS: Electronic overshoot due to cloud reflectance. *Appl. Opt.* **27**: 438.

Nelson, D. M., W. O. Smith, Jr., L. I. Gordon & B. H. Huber. 1987. Spring distribution of density, nutrients and phytoplankton biomass in the ice edge zone of the Weddell–Scotia Sea. *J. Geophys. Res.* **92**: 7181–7190.

Onstott, R. G. 1980. Radar backscatter study of sea ice. Ph.D. Diss., Univ. of Kansas, Lawrence.

Onstott, R. G. & S. Gogineni. 1985. Active microwave measurements of Arctic sea ice under summer conditions. *J. Geophys. Res.* **90**: 5035–5044.

Onstott, R. G. & R. A. Shuchman. 1988a. Multifrequency and multipolarization scatterometer for remote sensing. In "Proceedings of Instrumentation and Measurements in the Polar Regions Workshops," pp. 67–80. Monterey, California.

Onstott, R. G. & R. A. Shuchman. 1988b. Active microwave sensors for Arctic applications. *In* "Proceedings of Instrumentation and Measurements in the Polar Regions Workshop," pp. 81–92. Monterey, California.

Onstott, R. G., R. K. Moore & W. F. Weeks. 1979. Surface-based scatterometer results of Arctic sea ice. *IEEE Trans.* Geosci. Electron. **GE-17**, 78–85.

Onstott, R. G., R. K. Moore, S. Gogineni & C. Delker. 1982. Four years of low altitude sea ice broadband backscatter measurements. *IEEE J. Oceanic Eng.* **OE-7**: 44–50.

Onstott, R. G., T. C. Grenfell, C. Matzler, C. A. Luther & E. A. Svendsen. 1987. Evolution of microwave sea ice signatures during early and mid summer in the marginal ice zone. *J. Geophys. Res.* **92**: 6825–6835.

Parashar, S. K., A. K. Fung & R. K. Moore. 1978. A theory of wave scatter from an inhomogeneous medium with a slightly rough boundary and its application to sea ice. *Remote Sens. Environ.* **7**: 35–50.

Parkinson, C. L., J. C. Comiso, H. J. Zwally, D. J. Cavalieri & P. Gloersen. 1987. Arctic sea ice, 1973–1976: Satellite passive-microwave observations. *NASA* [*Spec. Publ.*] *SP* **NASA SP-489**: 1–296.

Pritchard, R. S. (ed.). 1980. "Sea Ice Processes and Models." Univ. of Washington Press, Seattle.

Shuchman, R. A., B. A. Burns, O. M. Johannessen, E. G. Josberger, W. J. Campbell, T. O. Manley & N. Lannelongue. 1987. Remote sensing of the Fram Strait marginal ice zone. *Science* **236**: 429–431.

Stewart, R. H. 1985. "Methods of Satellite Oceanography." Univ. of California Press, Berkeley.

Sullivan, C. W., C. R. McClain, J. C. Comiso & W. O. Smith, Jr. 1988. Phytoplankton standing crops within an Antarctic ice edge assessed by satellite remote sensing. *J. Geophys. Res.* **93**: 12487–12498.

Sutherland, L. L., R. A. Shuchman, P. Gloersen, J. A. Johannessen & O. M. Johannessen. 1989. SAR and passive microwave observations of the Odden during MIZEX '89. *Proc. IGARSS '89 Symp.* 1539–1544.

Svendsen, E., K. Kloster, B. Farelly, O. M. Jahannessen, J. A. Johannessen, W. J. Campbell, P. Gloersen, D. Cavalieri & C. Matzler. 1983. Norwegian remote sensing experiment: Evaluation of the Nimbus-7 scanning multi-channel microwave radiometer for sea ice research. *J. Geophys. Res.* **88**: 2781–2791.

Swift, C. T., L. S. Fedor & R. O. Ramseier. 1985. An algorithm to measure sea ice concentration with microwave radiometers. *J. Geophys. Res.* **90**: 1087–1099.

Tiuri, M., Shivola, E. Nyfors & M. Hallikainen. 1984. The complex dielectric constant of snow at microwave frequencies. *IEEE J. Oceanic Eng.* **OE-9**: 377–382.

Ulaby, F. T., R. K. Moore & A. K. Fung. 1981. "Microwave Remote Sensing," Vol. 1. Addison-Wesley, Reading, Massachusetts.

———. 1982. "Microwave Remote Sensing," Vol. 2. Addison-Wesley, Reading, Massachusetts.

Vant, M. R., R. B. Gray, R. O. Ramseier & V. Makios. 1974. Dielectric properties of fresh sea ice at 10 and 35 GHz. *J. Appl. Phys.* **45:** 4712–4717.

Vant, M. R., R. O. Ramseier & V. Makios. 1978. The complex dielectric constant of sea ice at frequencies in the range 0.1–40 GHz. *J. Appl. Phys.* **49:** 1264–1280.

Wackerman, C. C., R. R. Jentz & R. A. Shuchman. 1988. Sea ice type classification of SAR imagery. *Eur Space Agency* [*Spec. Publ.*] *ESA SP* **ESA SP-284:** 425–428.

Wadhams, P., V. A. Squire, D. J. Goodman, A. M. Cowan & S. C. Moore. 1988. The attenuation nodes of ocean waves in the marginal ice zone. *J. Geophys. Res.* **93:** 6799–6818.

Zwally, H. J., J. C. Comiso, C. L. Parkinson, W. J. Campbell, F. D. Carsey & P. Gloersen. 1983. Antarctic sea ice, 1973–1976: Satellite passive-microwave observations. *NASA* [*Spec. Publ.*] *SP* **NASA SP-459:** 1–206.

4 Large-Scale Physical Oceanography of Polar Oceans

Eddy C. Carmack
Institute of Ocean Sciences
Sidney, British Columbia, Canada

I. Introduction 171
II. Physical Setting 173
A. Bathymetry 173
B. Hydrology 175
C. Ice Cover 176
III. Current Systems 178
A. Arctic Ocean 178
B. Southern Ocean 183
IV. Water Masses 185
A. Arctic Ocean 185
B. Southern Ocean 191
C. Volumetric Comparison 195
V. Thermohaline Circulation 198
A. Arctic Shelf/Estuary Systems 198
B. Halocline Ventilation 202
C. Deep- and Bottom-Water Formation 205
VI. Concluding Remarks 209
References 211

I. Introduction

This chapter attempts a review of large-scale circulation patterns and water mass distributions in the Arctic and southern oceans. This is not easy, for any attempt at synthesis in polar oceanography today is met with an expanding literature that presents both new information and new puzzles at an ever increasing rate. The tack taken here is to rely heavily on past reviews of the subject, to introduce key findings from recent publications, and to combine these in a simple comparison of the two polar regions.

The geographic regions emphasized in this review include the Arctic Ocean between Fram and Bering straits and the Southern Ocean south of the

Polar Oceanography, Part A: Physical Science

Polar Front. For completeness, however, it will be necessary to discuss briefly certain aspects of seas marginal to these two regions, in particular the Greenland Sea between Jan Mayen and Fram Strait.

What defines large-scale oceanography? Normally, we take circulation and water mass systems that are basinwide in extent and time scales of seasonal or longer as constituting the large-scale oceanography. However, when discussing certain systems that influence large-scale patterns, such as polar estuaries and sites of deep-water formation, it will be necessary to touch briefly on smaller structures. The subjects of mesoscale and small-scale physical oceanography are properly reviewed in separate chapters of this book.

A number of review articles discuss various aspects of the large-scale oceanography of polar seas; these are listed here to aid the reader in acquiring a broad view on this subject. The Arctic Ocean is covered in syntheses and reviews by Coachman and Aagaard (1974), Aagaard (1979), Lewis (1982), and Barry (1990). A somewhat different perspective, drawing mainly on Soviet data and literature, can be found in Nikiforov *et al.* (1966), Treshnikov and Baranov (1976), Treshnikov (1977), and Zakharov (1987). The Greenland Sea is reviewed by Trangeled (1974), Johannessen (1986), Swift (1986), and Hopkins (1988). The Southern Ocean is reviewed by Baker (1979a), Gordon (1983), Bryden (1983), and Gordon and Owens (1987), and the structure and dynamics of the Antarctic Circumpolar Current are the subject of thorough discussion by Nowlin and Klinck (1986). A comparison of the two polar oceans is given by Foster (1978). A general review of polar oceanography covering the literature up to about 1982 is given by Carmack (1986).

Regions marginal to the polar seas are generally not covered in the present chapter; however, the interested reader may find the following references useful. The physical oceanography of the Bering Sea is covered in books by Coachman *et al.* (1975), Sayles *et al.* (1979), Hood and Kelly (1975), and Hood and Calder (1981) and in papers by Coachman (1986) and Muench *et al.* (1988). The oceanography of Hudson Bay is discussed by Prinsenberg (1983, 1986). Baffin Bay is described by Bailey (1956), Muench (1971), Coote and Jones (1982), Fissel *et al.* (1982), Lemon and Fissel (1982), Steffen (1986), and Addison (1987). The Labrador Sea is described by Lazier (1973), Clarke and Gascard (1983), Gascard and Clarke (1983), and Clarke and Coote (1988). A description of the Sea of Okhotsk is in Alfultis and Martin (1987). Water masses in Bransfield Strait are discussed by Clowes (1934) and Gordon and Nowlin (1978). Overviews of work carried out during the Marginal Ice Zone Experiment (MIZEX) are in Johannessen (1987) and Muench *et al.* (1987).

II. Physical Setting

A. Bathymetry

The following description of bathymetry is given as a background to discussions of large-scale circulation. More complete information can be found on charts published by Pinther *et al.* (1975) and Heezen *et al.* (1972).

1. Arctic Ocean

The Arctic Mediterranean seas, comprised of the basins lying north of the Greenland–Scotland Ridge, are about 17×10^6 km^2 in area and 17×10^6 km^3 in volume (Fig. 4.1a). The two principal areas of this system are the Greenland/Iceland/Norwegian Sea system and the Arctic Ocean. They are connected by Fram Strait, the wide (600 km), deep (sill depth about 2600 m) passage between Greenland and Spitsbergen.

The Arctic Ocean is roughly divided into the Canadian basin (maximum depth about 3800 m) and the Eurasian basins (maximum depth about 4200 m) by the Lomonosov Ridge (sill depth about 1400 m). The Canadian basin is further divided into the Canada and Makarov basins by the Alpha-Mendeleyev Ridge, and the Eurasian basin is divided into the Nansen and Amundsen basins by the Nansen-Gakkel Ridge.

The continental shelf from Alaska to Greenland is relatively narrow, but from Spitsbergen eastward (the Barents, Kara, Laptev, East Siberian, and Chukchi seas) the shelf is broad, typically from 600 to 800 km. A number of submarine canyons indent the shelf, the largest being the Svataya Anna and Voronin canyons in the Kara Sea.

2. Southern Ocean

The Southern Ocean (Fig. 4.1b) is bounded by the Antarctic continent to the south and the world ocean to the north; the Polar Front forms the boundary between the polar and subpolar water masses. The area of the Southern Ocean south of the Polar Front is about 38×106 km^2, and the volume is about 140×10^6 km^3. The ocean floor around Antarctica has four basins (the Weddell–Enderby, South Indian, Southwest Pacific, and Southeast Pacific basins) with depths exceeding 4500 m, separated by broad submarine ridges and plateaus. The continental shelves surrounding the Southern Ocean are generally quite narrow; the exceptions being the two broad (about 400 km) and deep (about 400 m) shelves of the Weddell and Ross seas. Shelf regions are further characterized by irregular depressions and submarine canyons and by glacial ice shelves which extend seaward from the continent.

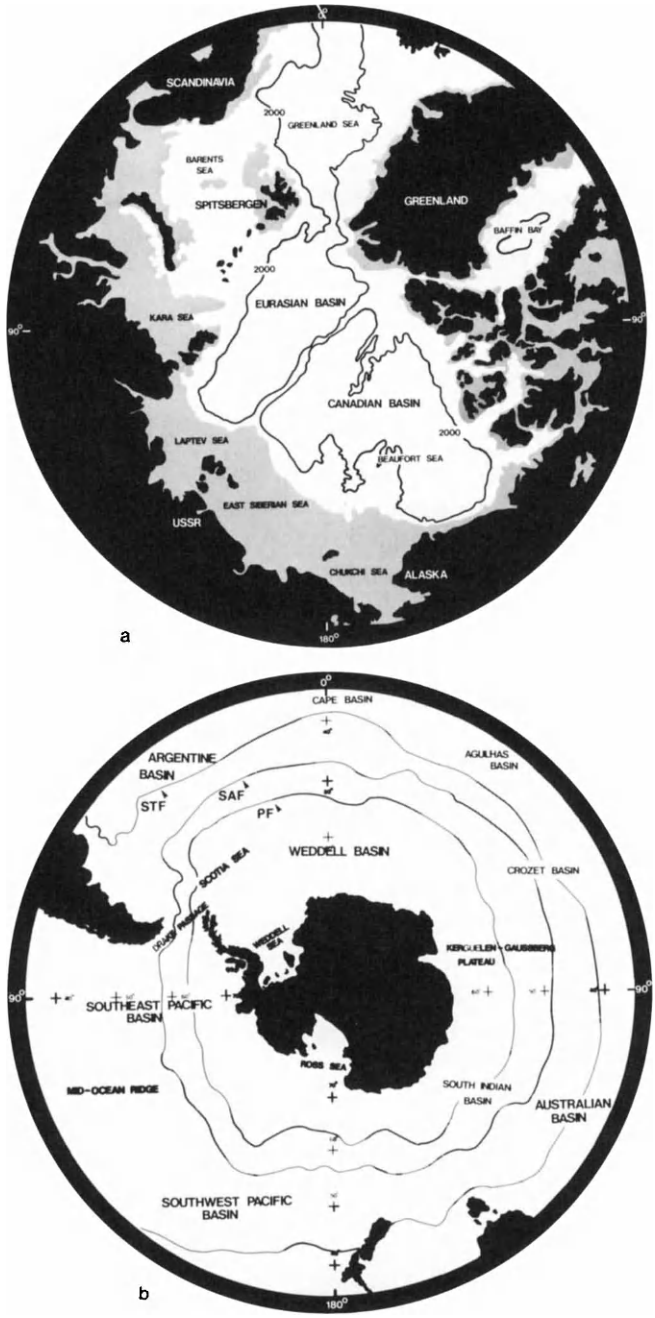

Figure 4.1 Bathymetry and geographic nomenclature for the (a) Arctic Ocean and (b) Southern Ocean.

B. Hydrology

Polar oceans have surface layers freshened by continental inputs (rivers and glacial meltwater) and by sea ice meltwater. An informative schematic of these inputs relative to other parts of the world ocean from Woods (1984) is shown in Fig. 4.2.

1. Arctic Ocean

Discussions on streamflow from major rivers entering the Arctic Ocean are given by a number of authors, including Mackay and Loken (1974), UNESCO (1978), SCOR Working Group 58 (1979), Milliman and Meade (1983), and Treshnikov (1985); according to the latter, the total annual streamflow into the Arctic, including the Arctic Archipelago, is about 3500 $km^3\ yr^{-1}$. The targest inflows come from the Yenisei (603 $km^3\ yr^{-1}$), Ob (530 $km^3\ yr^{-1}$), Lena (520 $km^3\ yr^{-1}$), Pechora (130 $km^3\ yr^{-1}$), Severnay Dvina (110 $km^3\ yr^{-1}$), Kotuy (105 $km^3\ yr^{-1}$), Kolyma (102 $km^3\ yr^{-1}$), Pyasina (86 $km^3\ yr^{-1}$), and Indigirka (57 $km^3\ yr^{-1}$) rivers in the Soviet Union and the Mackenzie River (340 $km^3\ yr^{-1}$) in Canada. An additional 1500–

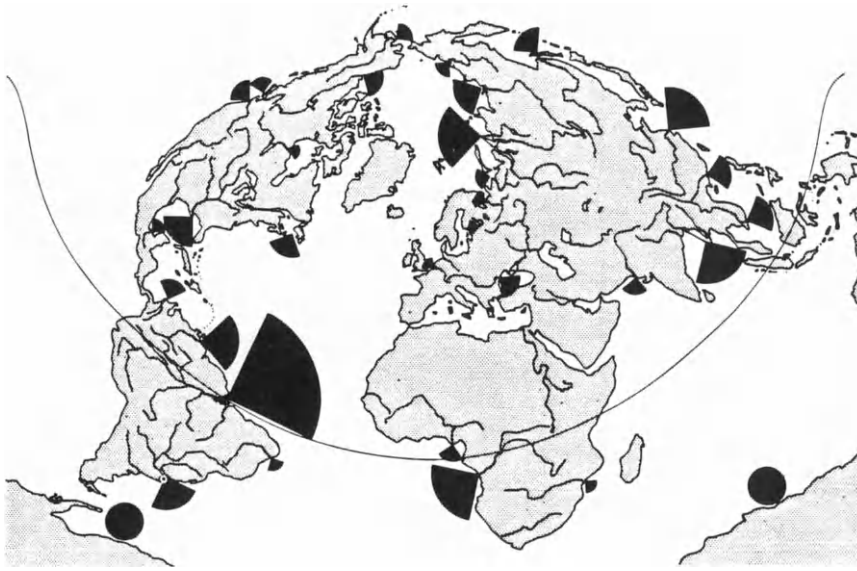

Figure 4.2 Map showing freshwater inputs to the world ocean. The areas of the segments are proportional to the annual volume flow from each river, assuming a spreading depth of 1 m. The iceberg flow from Antarctica is shown schematically as two disks, scaled similarly. From Woods (1984).

2000 $km^3\ yr^{-1}$ enters as a freshwater fraction in the Bering Strait inflow (see Coachman *et al.*, 1975). Aagaard and Coachman (1975) compute the freshwater residence time (defined as stored volume divided by inflow) to be roughly 10 years for the whole Arctic basin, with local values as low as 2 years applying to the southern Eurasian basin.

Significant annual and interannual variations occur in streamflow (Cattle, 1985). The large Soviet rivers Yenisei and Lena exhibit on average about a 40-fold change between low flows in winter and peak flows in June and July; seasonal variability for the Mackenzie River is much less, about 5-fold. Interannual variability is from 5 to 20% of the mean annual flow, depending on the individual rivers.

2. Southern Ocean

In contrast to the Arctic, most of the supply of new fresh water to the southern ocean comes from glaciers by the iceberg calving and melting process, by basal melting under ice shelves, and by wall melting along vertical walls of ice that rim 45% of the Antarctic coastline. Jacobs (1985) has reviewed publications on the mass balance of Antarctica. He notes that on the attrition side, estimates of ice shelf melting range from 0 to 675 $km^3\ yr^{-1}$, while iceberg calving is between 500 and 2,400 $km^3\ yr^{-1}$; he estimates 2,000 $km^3\ yr^{-1}$ to be the average amount of glacial meltwater released to the Southern Ocean.

C. Ice Cover

Sea ice is present over about 7% of the earth's surface at any given time. (It is what one first thinks of when one thinks of polar oceans—at least with today's climate.) Due to the climatic importance of sea ice, determining its basic characteristics (e.g., area, thickness, concentration, and classification) has been the focus of much recent research, and the reader is referred to publications by Ackley (1981), Walsh (1983), Untersteiner (1984), Maykut (1985, 1986), Wadhams (1986), and Lewis (1987).

1. Arctic Ocean

The average extent of sea ice for summer and winter in the Arctic (see Fig. B, page xvii) typically varies from about 7×10^6 km^2 in the boreal summer to 14×10^6 km^2 in the boreal winter (Walsh and Johnson, 1979). The thickness of sea ice is of critical importance because rates of heat exchange, ice growth, and salt rejection depend on ice thickness. In the Arctic the growth of ice starting from open water is typically about 2 m for the first year; after a series of annual melt/thaw cycles the ice tends toward a stable equilibrium thick-

ness of about 3 m. This assumes no mechanical deformation. Observations on the circulation of ice and the occurrence of areas of systematic coastal divergence and convergence are contained in Colony and Thorndike (1980, 1984, 1985).

Interannually, the total areal extent of sea ice in the Arctic varies by about 5° of latitude at all locations where the ice advance is not bounded by land (Walsh and Johnson, 1979). At the winter maximum this amounts to about a 30% variability for individual regions (Johnson, 1980). On the other hand, Carsey (1982) examined ESMR data from the Arctic at the time of minimum ice extent and noted that while regional variations may be large, the total areal coverage varies interannually by only about 2%.

2. Southern Ocean

In the Antarctic a much different sea ice cover prevails. The ice is not constrained by land, and it is predominantly first-year ice with thickness 0.5–2 m. Further, most of the annual variability (the melt/freeze cycle) occurs over deep oceanic areas, rather than over shelves as in the Arctic case.

The average extent of sea ice for summer and winter (see Fig. B, page xvi) in the Antarctic typically varies between 4×10^6 km^2 in the austral summer and 21×10^6 km^2 in the austral winter. Ice compactness is also an important consideration. Zwally *et al.* (1985) found that the amount of open water in Antarctic sea ice, even during winter, is substantial. The presence of leads and polynyas (thin linear and broad nonlinear openings in ice, respectively) is also important; for example, a single polynya, the Weddell Polynya, can occupy a surface area of as much as 0.3×10^6 km^2. In such areas the rapid growth of new ice is possible, and salt rejection takes place as new ice forms (see Comiso and Gordon, 1987). Another factor influencing Antarctic sea ice distributions is the effect of the strong katabatic winds that blow from the continent, forcing sea ice northward and forming and maintaining coastal polynyas (e.g., Bromwich and Kurtz, 1984; Chapter 5). An indication of ice drift in the Southern Ocean is given by iceberg drift tracks published by Tchernia and Jeanin (1984).

Interannually, the areal extent of sea ice in the Antarctic at maximum winter extent (for the period 1973 to 1976) has been observed to vary by about 20%, from 17×10^6 to 21×10^6 km^2 (Zwally *et al.*, 1983). It should be noted that these data are for ice area only (as opposed to ice thickness or volume) and cover the very short time period for which ESMR data are available. Budd (personal communication) has looked at maps of sea ice extent based on aircraft observations in the 1950s compared to modern satellite observations and notes the possibility of a far greater trend toward decreasing ice cover through the past three decades.

III. Current Systems

A. Arctic Ocean

1. Fram Strait exchange

Two main currents exchange water between the Arctic and the world ocean through Fram Strait. The West Spitsbergen Current (WSC) is a northward-flowing extension of the Norwegian-Atlantic current. It flows through Fram Strait off the west coast of Spitsbergen, carrying warm, relatively salty water into the Arctic Ocean. The East Greenland Current (EGC), which lies west of the East Greenland Polar Front, is the main current out of the Arctic Ocean.

Transport estimates for the WSC have been made by various authors. Early estimates based on geostrophic calculations (see Coachman and Aagaard, 1974, for review) yielded values between 2 and 8 Sv (1 Sv = 10^6 m^3 s^{-1}). Aagaard and Greisman (1975) used direct current measurements to obtain estimates of about 7 Sv, and Hanzlick (1983) obtained a transport of 5.6 Sv. Using an inverse technique that finds the minimum barotropic component to ensure mass conservation, Rudels (1987) argued that about 2 Sv of Atlantic water is carried north by the WSC and that about half of this water enters the Arctic Ocean; the rest is thought to recirculate in the vicinity of the strait.

The high temporal variability of WSC transport has been noted. Aagaard (1982) computed transports from current meter and hydrographic data and found variations between 0 and 9 Sv. Hanzlick (1983) analyzed long-term current meter data and demonstrated the lack of significant lateral coherence between moorings. Hanzlick (1983), Quadfasel *et al.* (1987), and Aagaard *et al.* (1987) all emphasize the banded structure of the WSC. Johannessen *et al.* (1987) noted an abundance of eddies in the flow field. Gascard *et al.* (1988) carried out an analysis of surface drifters and sofar floats, deployed at 100–200-m depth, and concluded that the WSC has a tendency to become unstable and generate frequent eddies that follow topographic contours.

The Fram Strait region appears to be a region of pronounced recirculation of Atlantic water, much of it joining the southward-moving East Greenland Current to flow back into the Greenland and Iceland seas. Although this recirculation has long been recognized (see Aagaard and Coachman, 1968b; Carmack, 1973a), the details and dynamics of the return flow have only recently been emphasized (Rudels, 1987; Quadfasel *et al.*, 1987; Gascard *et al.*, 1988). The continuation of the WSC into the Arctic is also complex, as the current appears to split into two or more branches (Perkin and Lewis, 1984; Aagaard *et al.*, 1987; Quadfasel *et al.*, 1987).

Upon entering the Arctic basin, the WSC encounters the southward-

moving pack ice carried by the Transpolar Drift. Here, sensible heat carried by the WSC is used to melt ice, resulting in a cooled and freshened upper layer (Quadfasel *et al.*, 1987; Untersteiner, 1988; Moore and Wallace, 1988). This point of encounter is also a zone of maximum density at the surface. Prior to reaching this point, surface cooling has increased the density of the surface layer; afterward, melting begins to decrease the surface density. The dynamical consequences of a current crossing a density extremum are not clear.

The southward-flowing EGC extends some 2500 km along the Greenland coast. In addition to transporting surface, intermediate, and deep water, the EGC exports sea ice from the Arctic, removing between 4000 and 5000 km^3 of ice each year, an amount approximately equal to the freshwater inflow (Wadhams, 1983; Vinje and Finnekasa, 1986). There are two branches off the mainstream of the EGC: a relatively minor one at about 77°N, which strikes southeast along the Greenland Fracture Zone (see Quadfasel *et al.*, 1987), and a larger one called the Jan Mayen Current that branches eastward at about 73°N to form the southern margin of the Greenland Gyre. The water mass structure of the EGC has been described in detail by Aagaard and Coachman (1968a,b), Paquette *et al.* (1985), Bourke *et al.* (1987), and Foldvik *et al.* (1988).

Transport estimates for the EGC have been published by several investigators. Early estimates, based on either the dynamic method or the water balance, ranged from about 2 to 5 Sv (Jakhelln, 1936; Mosby, 1962; Timofeyev, 1963). Aagaard and Coachman (1968a,b) used direct current measurements from the ice island Arlis II and computed a transport of about 30 Sv. Aagaard and Greisman (1975) assumed zero net transport through Fram Strait and arrived at a transport estimate of about 7 Sv. Foldvik *et al.* (1988) used data from moored current meters and drifting buoys and suggested a reasonable transport for the upper 700 m to be of order 3 Sv. In reconciling the wide range of the above estimates, one must take into account the methods used, the spatial and temporal coverage of the data, and the specific domains and water masses included in the tabulation.

The dynamical forcing of the EGC remains a puzzle. Aagaard (1970) showed that the current could be viewed as a western boundary current resulting from Sverdrup dynamics. Wadhams *et al.* (1979) advanced the idea that the EGC represented the selective withdrawal of a buoyancy-driven boundary current out of the Arctic. Manley and Hunkins (1987) compared current measurements from both sides of the East Greenland Polar Front. They noted that east of the front vertical shear and flows were small and the flow was influenced by the wind. West of the front the shear and currents were much larger, and the fluctuations were not influenced by the wind. Both Foldvik *et al.* (1988), using moored current meter records, and Gascard

et al. (1988), using data from drift buoys and sofar floats, conclude that the EGC is stable and not a source of eddies.

2. Bering Strait exchange

The generally northward flow through the shallow (about 50 m) and narrow (about 85 km) Bering Strait connects the Pacific (Bering Sea) and Arctic (Chukchi Sea) oceans. Early oceanographic measurements were reported by Sverdrup (1929) and Federova and Yankina (1964). Further discussions of transport based on current meter sections across the strait have been given by Coachman and Aagaard (1966, 1981), Coachman *et al.* (1975), and Aagaard *et al.* (1985b). A synthesis of available data by Coachman and Aagaard (1988) reports the following: the long-term mean transport is about 0.8 Sv; there is an annual transport cycle of amplitude 0.6 Sv, with higher flows in summer than in winter, when northerly winds reduce the transport; and there is an interannual variability that is tied to the north–south wind field. Coachman and Aagaard (1981) note that the flow field immediately north of the strait in the southern Chukchi divides into two regimes: a western one with broad, weak flows (less than 0.2 m s^{-1}), and an eastern half with narrow, much stronger flows (almost 0.7 m s^{-1}). Although flow speeds differ, however, the transports within the two regimes are roughly equal.

The background flow through Bering Strait is driven by a mean sea level slope of order 10^{-6} down toward the north (Coachman and Aagaard, 1966). This slope is due to a steric effect related to the lower density of the Pacific relative to the Atlantic (see Weyl, 1968). Wind effects on the transport are described by Aagaard *et al.* (1985b) and Coachman and Aagaard (1988). Westward intensification of the northward flow through Bering Strait and the occurrences of a western boundary current were pointed out by Kinder *et al.* (1986).

The dynamics of flow through Bering Strait have been modeled by Spaulding *et al.* (1987), who carried out sensitivity experiments to show that much of the transport variability comes from the variability of the meridional wind. Overland and Roach (1987) also modeled the flow through Bering Strait and suggest that the maximum flow through the strait is geostrophically limited, as opposed to frictionally or inertially limited. They also note westward intensification of the flow, with the greatest flux coming from the Gulf of Anadyr.

3. Arctic Ocean currents

Two main fields characterize the surface currents of the Arctic Ocean (Fig. 4.3). The first is the Transpolar Drift, in which the surface waters of the Eurasian basin move across the basin toward the North Pole and then on

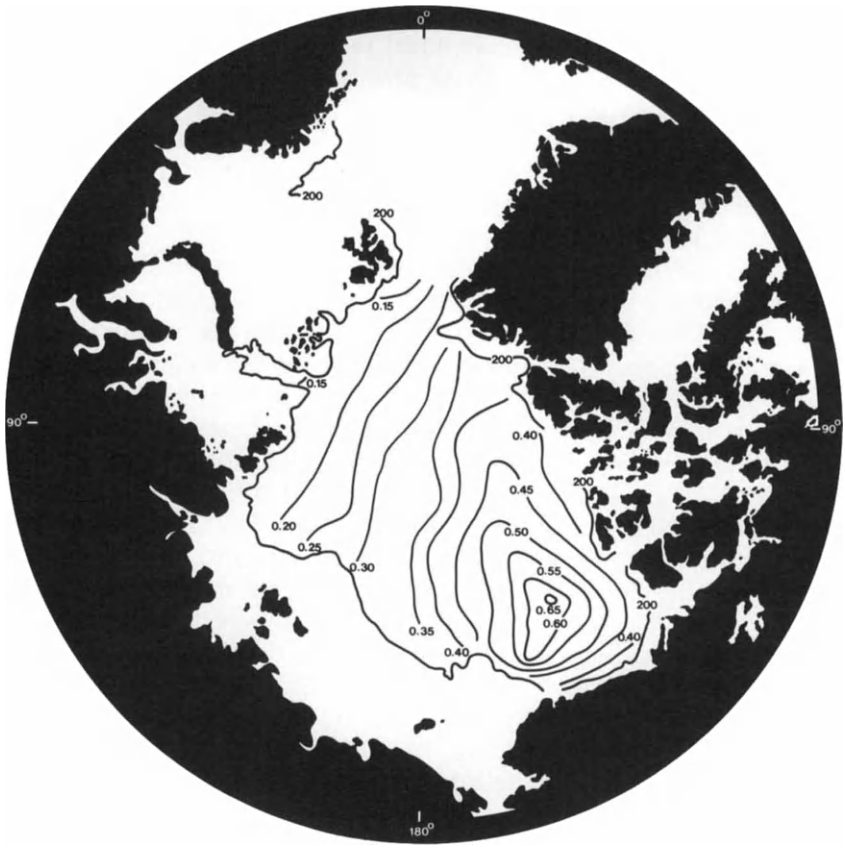

Figure 4.3 Surface currents in the Arctic Ocean (0/1200 dbar). Based on Coachman and Aagaard (1974).

toward Fram Strait; the second is the anticyclonic flow around the Beaufort Gyre in the Canadian basin (see Coachman and Aagaard, 1974; Gorschkov, 1983). Mean current speeds are slow in the central ocean, about 0.02 m s^{-1}, but increase as water exits the basin as part of the EGC (Wadhams *et al.*, 1979; Vinje and Finnekasa, 1986).

A thorough study of the Beaufort Gyre was carried out by Newton (1973). He noted that since the vertical density variation is contained within the pycnocline, the major portion of gyre transport (80%) occurs in the upper 300 m. The total baroclinic transport of the gyre relative to the 500-dbar surface is about 3 Sv, of which 2.3 Sv is surface water and 0.7 Sv is within the Atlantic layer; the gyre is intensified near the Alaskan shelf, presumably due

to topography. Newton also looked at circulation in the Canadian basin in terms of Sverdrup dynamics. He noted that baroclinic transports (about 3 Sv) are much smaller than those predicted by the Sverdrup equation (about 20 Sv) and suggested that the lack of agreement may be due to topographic effects and uncertainties about the efficiency of ice in transmitting wind stress to water. Further discussions of the dynamical forcing of the large-scale circulation by wind stress can be found in the modeling studies of Campbell (1965), Galt (1973), and Semtner (1976, 1987).

There is evidence from at least two areas in the Arctic of shallow, relatively intense boundary currents that flow in a direction opposite to the mean surface drift. The first is in the Nansen basin along the continental slope between Spitsbergen and Franz Josef Land, and the second is along the continental slope in the southern Beaufort Sea. The presence of such an undercurrent in the Nansen basin has long been recognized from property distributions (see Treshnikov, 1977, for example). However, work by Aagaard *et al.* (1981, 1987), Perkin and Lewis (1984), and Quadfasel *et al.* (1987) has added much detail to the description of this flow. As the WSC passes through Fram Strait and subsides, it appears to branch. North of 79°N, where the 200-m and deeper isobaths diverge, the current splits into two main cores. The western or offshore branch follows the western flank of the Yermak Plateau. North of 80°N a portion of this flow again splits off to contribute to the recirculation within the EGC. The eastern or inshore branch of the WSC follows the shelf break around Spitsbergen and into the Arctic Ocean (see Perkin and Lewis, 1984; Quadfasel *et al.*, 1987). During its transit it is cooled and freshened by mixing with overlying waters, thus transforming the original Atlantic water into Arctic intermediate water. The first direct measurements of this flow were made by Aagaard (1989), who noted eastward flow that increased with depth to typical speeds of 0.2–0.3 m s^{-1}.

Although the southern Beaufort Sea is generally thought of as an area of westward (clockwise) water and ice motion, the average subsurface motion above the continental slope is in the opposite direction. Aagaard (1984) called this flow the Beaufort Undercurrent. The presence of the undercurrent is indicated by a subsurface maximum in temperature caused by the eastward flow of water originating in the Bering Sea (see Coachman and Barnes, 1961; Hufford, 1973; Mountain, 1974; Paquette and Bourke, 1974). Aagaard (1984) described the Beaufort Undercurrent as being a topographically steered eastward flow extending seaward of the 50-m isobath out to the base of the continental slope. Speeds are of order 0.1 m s^{-1} and increase with depth down to about 150 m. Transports are of order 1 Sv. The current is probably part of the large-scale circulation of the Canada basin and thus not locally driven.

A possible forcing mechanism for undercurrents in the Arctic has been discussed by Holloway (1987). He argues that the interaction of eddies with longshore variations in topography, together with coastally trapped planetary wave propagation, results in a systematic forcing that acts on the mean flow. Applied to the Arctic, this mechanism predicts an eastward (cyclonic) flow following the basin margins of similar magnitude to the Beaufort Undercurrent.

B. Southern Ocean

A. Antarctic circumpolar current

Surface water flows around Antarctica in a clockwise direction (Fig. 4.4). Many authors have emphasized the zonation inherent in this flow structure (Gordon *et al.*, 1977; Whitworth, 1980; Deacon, 1982; Nowlin and Klinck, 1986). The zone of strong baroclinicity at an average latitude of 53°S is a region of transition of surface water characteristics from subantarctic to antarctic. It is marked by the Antarctic Circumpolar Current (ACC), an intense flow displaying little attenuation with depth. Strong expressions of the ACC are found over the northern slope of the midocean ridge in the southwest Pacific, in Drake Passage and the southwest Indian Ocean immediately below the Agulhas return current.

Recent year-long measurements of the transport of the ACC through Drake Passage (e.g., Nowlin *et al.*, 1977; Bryden and Pillsbury, 1977; Fandry and Pillsbury, 1979; Whitworth, 1983; Whitworth and Peterson, 1985) indicate the mean annual transport to be 134 Sv with an uncertainty of about 10%; the instantaneous flow may vary from the mean by as much as 20% (see Nowlin and Klinck, 1986, for discussion). Heat transports associated with the ACC are discussed by Georgi and Toole (1982).

In a major review of the structure and dynamics of the ACC, Nowlin and Klinck (1986) note that the ACC seems to exist as a banded structure, with multiple narrow jets associated with strong lateral density gradients at the subantarctic and polar fronts. The position of these fronts is highly variable, and excursions of up to 100 km in 10 days have been observed. These meanders can lead to the formation of eddies and current rings (see Joyce *et al.*, 1981; Bryden, 1983). The ACC is thought to be driven mainly by the wind; Baker (1982) showed that a simple Sverdrup balance for waters south of 50°S is consistent with existing data. However, neither the interaction between the wind and thermohaline forcing nor the mechanisms of energy dissipation required to balance the wind are as yet clear. Nowlin and Klinck (1986) note that four braking mechanisms have been proposed: topographic form drag (Munk and Palmen, 1951), thermodynamic effects (Fofonoff,

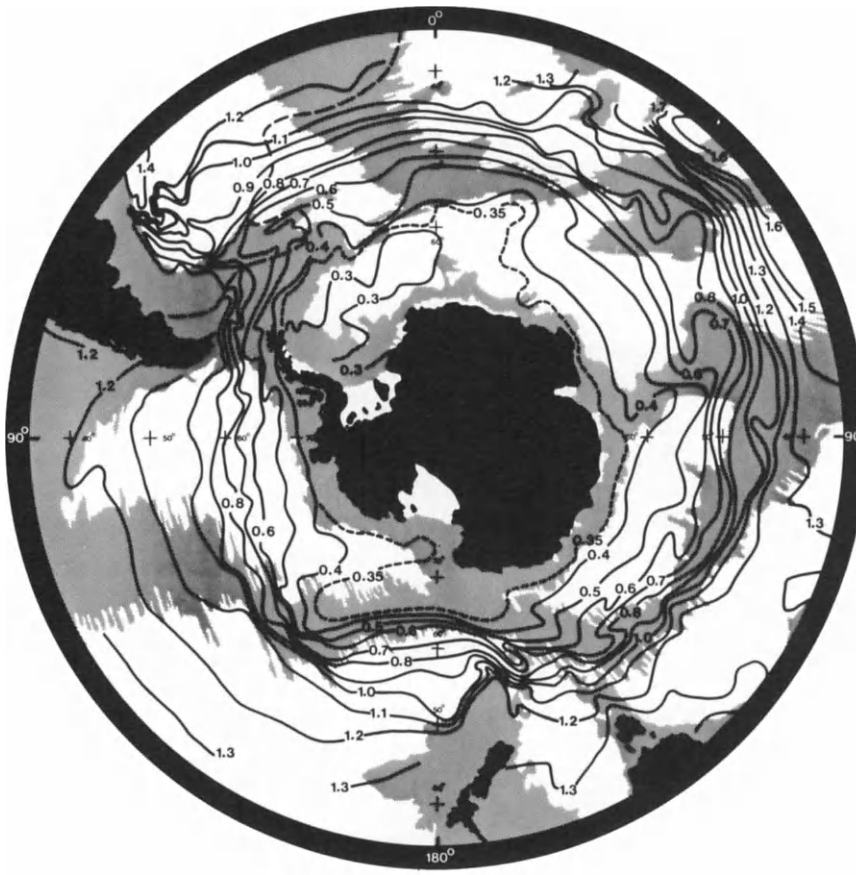

Figure 4.4 Surface currents in the Southern Ocean (0/1000 dbar). Based on Gordon *et al.* (1981b).

1955), partial blocking due to the presence of land masses (Stommel, 1957), and an adverse buoyancy flow resulting from the discharge of freshwater from the continent (Barcilon, 1966, 1967). Theoretical and modeling studies of the ACC are also reviewed by Nowlin and Klinck (1986).

2. Antarctic coastal current

The Antarctic Coastal Current is the name commonly given to the narrow, westward-flowing current that tends to follow the continental margin (Deacon, 1937; Sverdrup, 1953). This flow lies south of the belt of low atmospheric pressure that extends around the continent at roughly 65°S. Current

speeds are roughly 0.1 m s^{-1} (Sverdrup, 1953). The presence of the current indicated by steeply sloping isopycnals, often in the shape of a V, near the continental shelf break (see Gill, 1973; Foster and Carmack, 1976b). This current is not completely circumpolar, but instead becomes part of the clockwise gyres in the Weddell and Ross seas. Within the Weddell Gyre transports of about 8 Sv along the continental margin have been computed by E. Farbach (personal communication) using hydrographic and current meter data.

3. Antarctic gyre systems

The dynamic height anomaly south of the ACC indicates weak baroclinic gyres in the western Weddell basin and north of the Ross Sea. Foster and Carmack (1976a) and Deacon (1976, 1979) described the thermohaline structure of the Weddell Gyre, and Carmack and Foster (1975) utilized short-term current meter measurements and computed the transport associated with the Weddell Gyre to be 97 Sv. Gordon *et al.* (1981a) computed the wind-driven transport of the Weddell Sea using Sverdrup dynamics, balanced by a western boundary current along the Antarctic Peninsula, and obtained a flux of 76 Sv. Deacon (1982) reviewed the physics of the Weddell Gyre in relation to ecological cycles and noted that southward flow along the eastern side of the Weddell Gyre appeared to be a critical factor determining krill cycles.

The northern end of the Weddell Gyre is marked by the Weddell–Scotia Confluence, a complex area in the Scotia Sea northeast of the Antarctic Peninsula. It forms from the convergence of the ACC passing through Drake Passage and the recirculating flow of the Weddell Gyre (Gordon *et al.*, 1977). This region is of considerable biological importance (Deacon and Foster, 1977; Nelson *et al.*, 1987). Foster and Middleton (1984) emphasized the eddy field lying downstream of the confluence.

IV. Water Masses

The purpose here is to define a general temperature/salinity (T/S) classification scheme for both the Arctic and Southern oceans that later will allow a comparison between the two polar regions.

A. Arctic Ocean

The water masses of the Arctic Ocean and adjacent seas are known from contributions by Nansen (1906), Helland-Hansen and Nansen (1909), Killerich (1945), Zubov (1945), Coachman (1961), Coachman and Aagaard

(1974), Swift and Aagaard (1981), and Aagaard *et al.* (1985a). The classification used below follows from the latter two works. The water column is considered to be composed of three main layers: a surface layer, which has densities less than $s_0 = 27.9$; an intermediate layer, which has densities above $s_1 = 32.785$ and is due to an influx of warm, salty water from the Atlantic; and the deep water, which has densities below $s_2 = 37.457$ and is formed by convection (s_0, s_1, and s_2 refer to potential densities relative to the 0-, 1000-, and 2000-dbar surfaces, respectively; see Aagaard *et al.*, 1985a).

1. Arctic surface layer

Three main classes of surface water are recognized. The first is Atlantic Water (AW), which is carried into the system as a branch of the Norwegian–Atlantic Current. It can be defined as water with temperatures above 3°C and salinities greater than 34.9 per mil. The second class of surface water is Polar Water (PW), which is water that has been diluted by admixtures with fresh water; it is generally cold (temperatures below 0°C) and fresh (salinities below 34.4 per mil). It occupies the upper layers of the Arctic down to about 200 m depth and makes up the surface outflow within the East Greenland Current and the Canadian Arctic Archipelago. The third class of surface water is Arctic Surface Water (ASW), which is found mainly in the central gyres of the Greenland and Iceland seas. This water is warmer and more saline than PW, but cooler (0 to 3°C) and fresher (34.4 to 34.9 per mil) than AW. However, this water is notably denser than either PW or AW, indicating that it is not a simple mixture of the two and that large modifications due to air–sea exchanges occur locally. The map of near-surface salinity shows the general distribution of surface water classes (Fig. 4.5).

Polar Water contains additional structure. The top 30–50 m represents the seasonal mixed layer (Solomon, 1973; Morison and Smith, 1981; Lemke and Manley, 1984; Lemke, 1987). In winter this layer tends to be uniform vertically in temperature and salinity. Ice melting in summer results in a pronounced salt stratification; however, this water remains near freezing except for areas that become completely ice free. The lower part of the surface layer contains the main halocline, the layer with low temperatures (less than −1°C) and salinities between about 30.4 and 34.4 per mil, which is arguably the most important feature of the Arctic Ocean (see Section V). This cold, relatively saline layer is thought to be maintained by shelf drainage during winter (Aagaard *et al.*, 1981; Melling and Lewis, 1982). In the Eurasian basin the salinity increases rapidly with depth, reaching 34.9 to 35.0 per mil at about 200 m, while the temperature remains colder than −1.5°C to 150 m and then increases. In the Canadian basin the halocline is deeper, and the salinity increases more slowly with depth. Here, the temperature shows two minima, near the depths with salinities of 31.6 and 33.1 per mil, and a maximum near 32.4 per mil. The minimum near 31.6 per mil is possibly a

Figure 4.5 Salinity distribution at 5 m depth in the Arctic Ocean. Based on Coachman and Aagaard (1974).

remnant of winter cooling. The maximum near 32.4 per mil and the minimum near 33.1 per mil possibly reflect the inflow from the Pacific through Bering Strait. Hence, the Arctic halocline is not a uniform structure, nor is it likely composed of a single water mass. It likely derives from more than one region and is formed by more than one ventilation mechanism (see Jones and Anderson, 1986).

2. The Atlantic layer

To describe water masses occurring in the Arctic Ocean, it is necessary first to consider water mass transformations in the Greenland, Iceland, and Norwegian seas. Swift and Aagaard (1981) identified three varieties of Arctic intermediate water, each with a different T/S signature. They noted that Arctic

Surface Water usually lies above a temperature minimum at 75 to 150 m depth, a temperature maximum at 250 m, and a salinity maximum at about 400 m. To account for these features, the following distinction was made: lower Arctic Intermediate Water (lAIW) lies immediately above deep water, includes the temperature and salinity maxima, and has both temperature and salinity decreasing with depth; upper Arctic Intermediate Water (uAIW) lies in between the temperature minimum and the temperature maximum and has both temperature and salinity increasing with depth; and Polar Intermediate Water (PIW) has somewhat lower salinities than the other two intermediate waters but is largely distinguished by its association with overlying Polar Surface Water.

Within the Arctic Ocean the surface layer overlies the relatively warm and saline water of Atlantic origin, carried into the Arctic through Fram Strait by the WSC. When this water enters the Arctic basin, the initially high temperature and salinity of the water (over 3 °C and 35 per mil in Fram Strait) rapidly decrease as it is cooled by the atmosphere and by mixing with local waters. When the current encounters the ice margin northwest of Spitsbergen, melting further cools and dilutes this water until its T/S properties approximate those of water found within the Atlantic layer throughout the Arctic (Perkin and Lewis, 1984; Aagaard *et al.*, 1987). This water is the Arctic Intermediate Water discussed by Swift and Aagaard (1981) and Aagaard *et al.* (1985a), whose core is identifiable over the entire basin at depths between 200 to 800 m by a temperature maximum and relatively high salinity (Fig. 4.6).

3. Deep waters

The lower portion of the water column is occupied by varieties of cold (<0 °C) deep water. Our basic understanding of the origin of the deep waters has undergone considerable revision in recent years (Aagaard, 1982; Swift *et al.*, 1983; Aagaard *et al.*, 1985a; Rudels, 1987; Swift and Koltermann, 1988). Four basic varieties, each with distinctive T/S characteristics, are presently recognized. Greenland Sea Deep Water (GSDW) is the coldest (about -1.2 °C) and freshest (<34.90 per mil) variety, and Canada Basin Deep Water (CBDW) is the warmest (about -0.5 °C) and most saline (>34.95 per mil). In between are the Norwegian Sea Deep Water (NSDW; -0.9 °C, 34.92 per mil) and Eurasian Basin Deep Water (EBDW; -0.7 °C, 34.94 per mil) varieties. The general distribution of bottom salinities and possible spreading paths are illustrated in Fig. 4.7.

4. Arctic shelf waters

There does not seem to be an available synthesis on the distribution of Arctic shelf waters. However, a number of regional descriptions exist to give a collective view of shelf water distributions. Starting with the Barents Sea and

Figure 4.6 Temperature distribution within the T_{max} core of the Atlantic layer of the Arctic basin. Based on Treshnikov (1977).

proceeding counterclockwise around the basin, the following references are noted: the Barents Sea is discussed by Milligan (1969), Pfirman (1985), and Midttun (1985); the Kara Sea by Hanzlik and Aagaard (1980); the Laptev and East Siberian Seas by Sverdrup (1929) and Codispoti and Richards (1968, 1971); the Chukchi Sea by Paquette and Bourke (1979, 1981) and Coachman *et al.* (1975); the Alaskan Beaufort shelf by Paquette and Bourke (1974), Hufford (1973, 1974, 1975), and Aagaard (1982); the Mackenzie Shelf by Macdonald *et al.* (1987) and Bradstreet *et al.* (1987); and the Canadian Arctic Archipeligo by Bailey (1956), Collin (1963), Sadler (1976), Jones

Figure 4.7 Abyssal salinities and supposed interbasin exchange in the Arctic Ocean.

and Cotte (1980), Melling *et al.* (1984), Rudels (1986b), Prinsenberg and Bennett (1988), and Barry (1989).

Annually, the shelf waters exhibit greater variability in salinity than surface waters in the open ocean, perhaps 2 to 4 per mil on shelves as opposed to 0.5 per mil offshore (Coachman and Aagaard, 1974). Owing to their proximity to river inflow, shelf waters are generally more dilute than their offshore counterparts during summer. However, due to brine water release and possibly the upwelling of saline water onto the shelf, shelf waters may become more saline than offshore waters in winter, reaching salinities of 34.5 per mil or greater (Aagaard *et al.*, 1981; Melling and Lewis, 1982).

B. Southern Ocean

Basic understanding of the waters of the Southern Ocean is founded on classic studies by Brennecke (1921), Wust (1933), Mosby (1934), and Deacon (1937). The importance of zonation with regard to water mass distributions is covered by Gordon *et al.* (1977) and Deacon (1982). Discussions of water mass structure at various locations around the continent are provided in works by Carmack (1977), Reid *et al.* (1977), Sievers and Nowlin (1984), Jacobs *et al.* (1985), and Whitworth and Nowlin (1987). Structural variability is discussed by Gordon (1989).

1. Antarctic surface layer

Antarctic Surface Water (AASW) refers to the cold, relatively low-salinity water in the upper 50–200-m layer north of the continental slope (see Fig. 4.8). It evolves from deep water that has upwelled and been modified by surface exchange processes. Below AASW lies Winter Water (WW), marked by a temperature minimum layer and salinities below about 34.4 per mil. This water results from winter cooling of AASW to the freezing temperature and the addition of brine during ice formation. The upper limit of salinity for WW may be set by the cabbeling instability (see Fofonoff, 1956; Foster and Carmack, 1976a). The WW is most evident immediately north of the continental margin and is deepest and coldest over the upper continental slope (Jacobs *et al.*, 1985). Toole (1981) has modeled the seasonal cycle maintaining the temperature minimum layer.

Two transitional layers separate the surface and deep waters. The first, which dominates near the continent, joins WW and deep water; the second, which occurs farther to the north, joins the T/S characteristic of Antarctic Intermediate Water (AAIW) with deep water.

2. Circumpolar deep water

The greatest volume of water in the Southern Ocean is the Circumpolar Deep Water (CDW). It is characterized by a temperature maximum and oxygen minimum at intermediate depth and a somewhat deeper salinity maximum (Fig. 4.9). Gordon (1971) termed these layers upper and lower CDW, respectively. The CDW is also relatively nutrient rich.

The origin of CDW is North Atlantic Deep Water (NADW) and thus ultimately the Arctic Mediterranean (Reid and Lynn, 1971). However, the work of Callahan (1972), Reid *et al.* (1977), Georgi (1981), Sievers and Nowlin (1984), and Whitworth and Nowlin (1987) clearly shows a complex mixing history as this water moves around the continent. The CDW within the ACC flows from west to east and generally shoals toward the south, reaching its minimum depth below the Antarctic Divergence. Near the con-

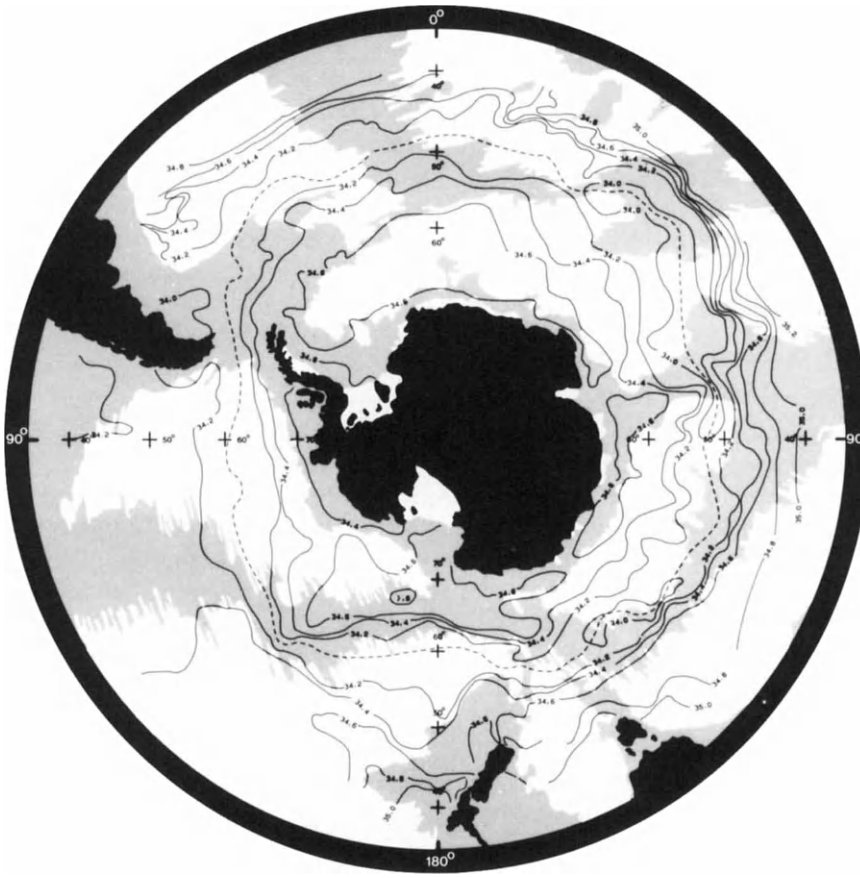

Figure 4.8 Salinity distribution on the shallow S_{min} layer in the Southern Ocean. Based on Gordon *et al.* (1981b).

tinental margin its flow is generally from east to west. Weddell Deep Water (see Gordon, 1982) is a cooler and fresher variety of CDW that has been modified by mixing with continental shelf waters as the CDW circles the continent.

3. Antarctic bottom water

Antarctic Bottom Water (AABW) occupies the lower portion of the water column and is arbitrarily defined by temperatures below 0°C. Two extreme varieties of bottom water are found: the cold, low-salinity Weddell Sea Bottom Water (WSBW), with potential temperature below −0.7°C and

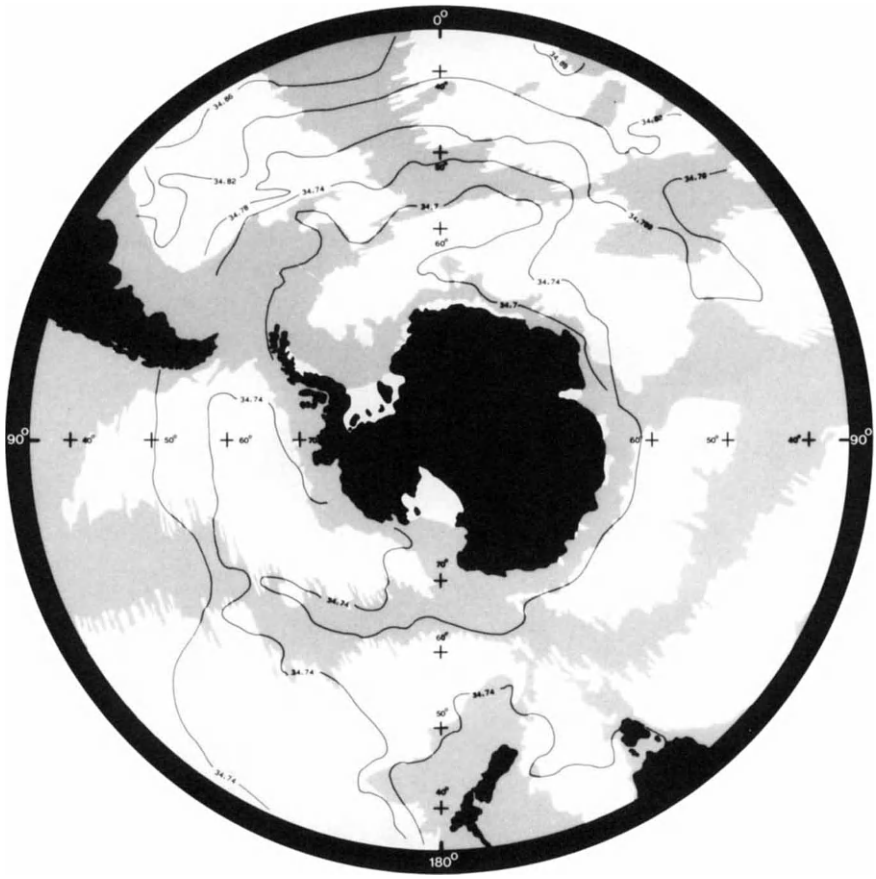

Figure 4.9 Salinity on the density surface near the core of Circumpolar Deep Water in the Southern Ocean. Based on Gordon *et al.* (1981b).

salinities of about 34.64 mil, and the warmer and more saline Ross Sea Bottom Water (RSBW), with potential temperatures of above −0.5 °C and salinities above 34.70 per mil. The densities of AABW within the various basins of the Southern Ocean and paths of spreading are indicated in Fig. 4.10.

4. Antarctic shelf waters

The water mass structure on the continental shelves surrounding Antarctica is highly variable (Gordon, 1974; Carmack, 1977; Jacobs *et al.*, 1985). During summer the surface water above the shelf is somewhat warmed by radia-

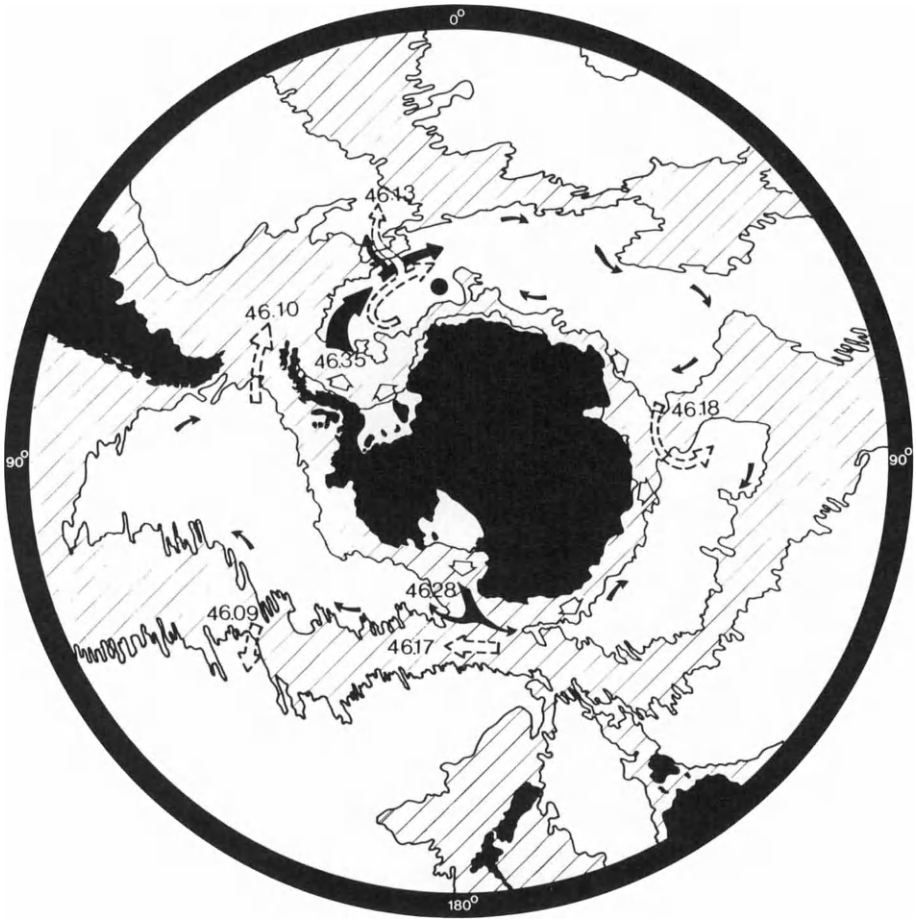

Figure 4.10 Near-bottom potential densities (referenced to 4000 dbar) and supposed interbasin exchange in the Southern Ocean.

tion and diluted by ice melt. Below this seasonal layer, water with temperatures near the freezing point (T_f) covers most of the shelf floor. In relation to shelf drainage and bottom water production, it is convenient to distinguish between Low-Salinity Shelf Water (LSSW) and High-Salinity Shelf Water (HSSW) by the 34.6 per mil isohaline, as this is the approximate threshold required for shelf water to drive deep convection (Mosby, 1934). However, Jacobs *et al.* (1985) argue for the importance of LSSW as an additional mixing component in AABW. Mechanisms that may enhance shelf salinities through brine water production include sea ice formation in leads and polynyas (Foster, 1972b; Szekielda, 1974; Kurtz and Bromwich, 1983) and

freezing at the base of ice shelves (Seabrooke *et al.*, 1971; Gill, 1973). The highest shelf water salinities, up to 35.0 per mil, are found on the broad continental shelves of the Weddell andd Ross seas.

Not all shelf water is cold. Some transects across continental shelves show a mid-depth intrusion of warm water derived from the offshore core of CDW extending southward as far as the glacial ice (Jacobs *et al.*, 1970; Foster and Carmack, 1976b). Jacobs *et al.* (1985) refer to this feature as the Warm Core, although the terms Modified Circumpolar Water and Modified Warm Deep Water have also been used. Here, the name Warm Core Shelf Water (WCSW) is preferred to distinguish its position at mid-depth above continental shelves. Although WCSW is a more or less continuous feature, it does appear to break up into blobs as it mixes with ambient shelf water near its southernmost extension (Foster and Carmack, 1976b).

Ice Shelf Water (ISW) is a shelf water mass unique to the Antarctic. It is marked by temperatures below the freezing temperature at 1 atmosphere (Sverdrup, 1940; Losquinos, 1963; Jacobs *et al.*, 1970). This water attains its unusual properties through cooling at the base of ice shelf because the freezing temperature is depressed by increasing pressure (about $0.00076\,^{\circ}\mathrm{C\,bar^{-1}}$) and temperatures as low as $-2.4\,^{\circ}\mathrm{C}$ have been observed. It is most common in the Weddell and Ross seas. The ISW is important owing both to the relatively high compressibility of cold water and to the fact that vertical motions may lead to frazil ice formation at depth (see Foldvik and Kvinge, 1974; Carmack and Foster, 1975; Jacobs *et al.*, 1979a,b; Foldvik *et al.*, 1985c). Biological consequences of ice formation at depth are noted by Dieckmann *et al.* (1986). For the Ross Sea, Jacobs *et al.* (1985) further distinguish between shallow Ice Shelf Water (SISW) and Deep Ice Shelf Water (DISW). The SISW lies at 50 to 250 m along the Ross Ice Shelf, has salinities below about 34.6 per mil, and likely derives from WCSW coming in contact with the base of the Ross Ice Shelf. The DISW is denser, has salinities above 34.6, and likely derives from the contact of HSSW with the base of the ice shelves, though Jacobs *et al.* (1985) point out that more complex mixing histories are possible.

C. Volumetric Comparison

1. Summary classification

In the following discussion a point on the T/S diagram defines a *water type,* a line is a *water mass,* and, following Montgomery (1958), who spoke of bivariate T/S class intervals, an area on the T/S diagram is a *water class.*

Water classes within the Arctic Mediterranean seas can be defined as follows (Fig. 4.11a): Atlantic Water (AW) has temperatures above 3 °C and salinities above 34.9 per mil; Arctic Surface Water (ASW) has temperatures

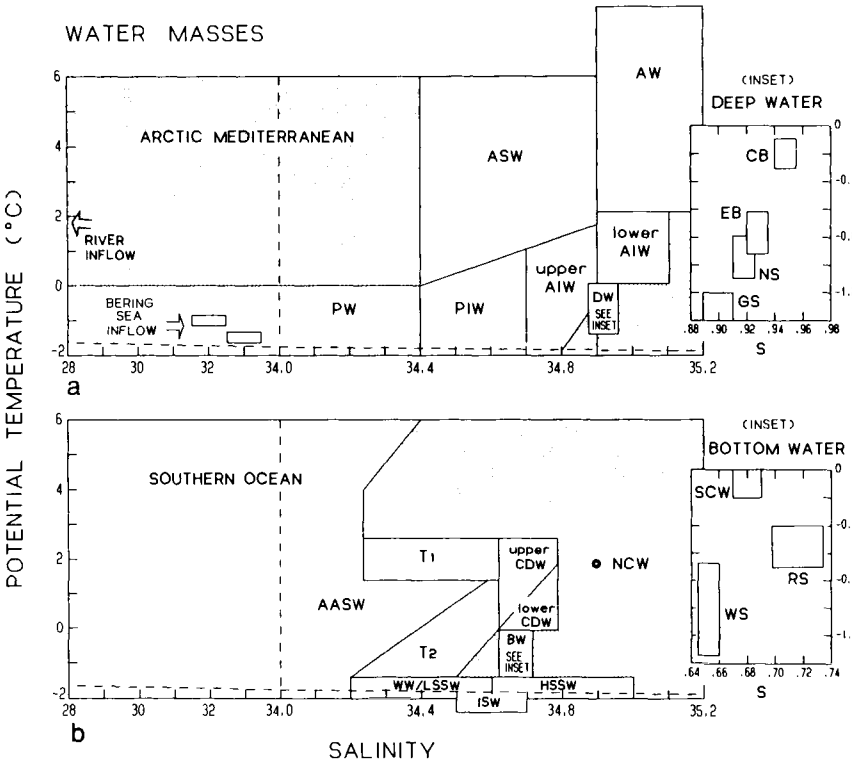

Figure 4.11 Water mass classifications for the (a) Arctic Mediterranean and (b) Southern Ocean.

above 2°C for salinities between 34.7 and 34.9 per mil and temperatures above 0°C for salinities between 34.4 and 34.7 per mil; Polar Water (PW) has salinities below 34.4 per mil; upper Arctic Intermediate Water (uAIW) has temperatures below 2°C and salinities between 34.7 and 34.9 per mil; lower Arctic Intermediate Water (lAIW) has temperatures from 3 to 0°C and salinities between 34.9 and 35.1 per mil; Polar Intermediate Water (PIW) has temperatures below 0°C and salinities between 34.4 and 34.7 per mil; deep water has temperatures below about 0°C and salinities between 34.88 and 34.96 per mil.

Some additional points are noted. The Arctic halocline, with salinities typically between 30.4 and 34.4 per mil, forms the high-salinity end of the PW class. The Arctic thermocline, with salinities above 34.4 per mil and temperatures below 0°C, is contained within the PIW class. The core of the Atlantic layer, with temperatures above 0°C, is contained in the uAIW class.

Finally, the deep waters of the Canadian basin are more saline than those of the Eurasian basin.

Water classes within the oceanic domain of the Southern Ocean can be defined as follows (Fig. 4.11b): CDW has temperatures above 0°C and salinities between about 34.65 to 34.80 per mil; CDW is divided into uCDW and lCDW by a diagonal line passing midway through the CDW bivariate class; AABW has temperatures below 0°C and salinities between 34.64 and 34.74 per mil; WW has temperatures colder than −1°C and salinities between about 34.2 and 34.5 per mil; Antarctic Surface Water has temperatures below about 2°C and relatively low salinities. Two transitional water masses are noted: one that extends horizontally on the T/S curve from uCDW about 2°C and 34.2 per mil, and one that connects upper CDW with WW and about 34.2 per mil.

2. Volume and property comparison

The comparison that follows represents a rough attempt to compare the volumetric distribution of Arctic and Antarctic water masses and their associated properties. The comparison is crude because it is not based on a systematic analysis of both systems but rather on a compilation of spotty information and data. In particular, details for the Arctic Ocean were constructed by simply averaging data at selected stations in the Canadian and Eurasian basins.

A volumetric comparison of the water masses of the two polar oceans is presented in Fig. 4.12. Sources of the information shown here include published volumetric T/S analyses for the Southern Ocean (Carmack, 1974, 1977), the Greenland Sea (Carmack and Aagaard, 1973), and the Iceland Sea (Swift and Aagaard, 1981). A volumetric analysis for the Arctic Ocean has not been published. Instead, the hypsometric curves given by Aagaard *et al.* (1985a) were used to find approximate water mass volumes.

Typical oxygen concentrations within water masses are shown in Fig. 4.13. A major difference apparent here is the much lower values of oxygen in the deep and bottom water of the Southern Ocean. The Southern Ocean contains roughly an order of magnitude more water that the Arctic Mediterranean. However, the overall structure of the two oceans and the relative distributions of surface and deeper waters are quite similar.

Values of silicic acid, taken to be representative of nutrient levels in general, are given in Fig. 4.14. The outstanding difference here is that silicate values in the deep and bottom waters of the Southern Ocean are about an order of magnitude higher than those in the Arctic Mediterranean (see also Chapter 8).

Finally, some estimates of water mass renewal times are shown in Fig. 4.15. Sources of the information shown here include Peterson and Rooth

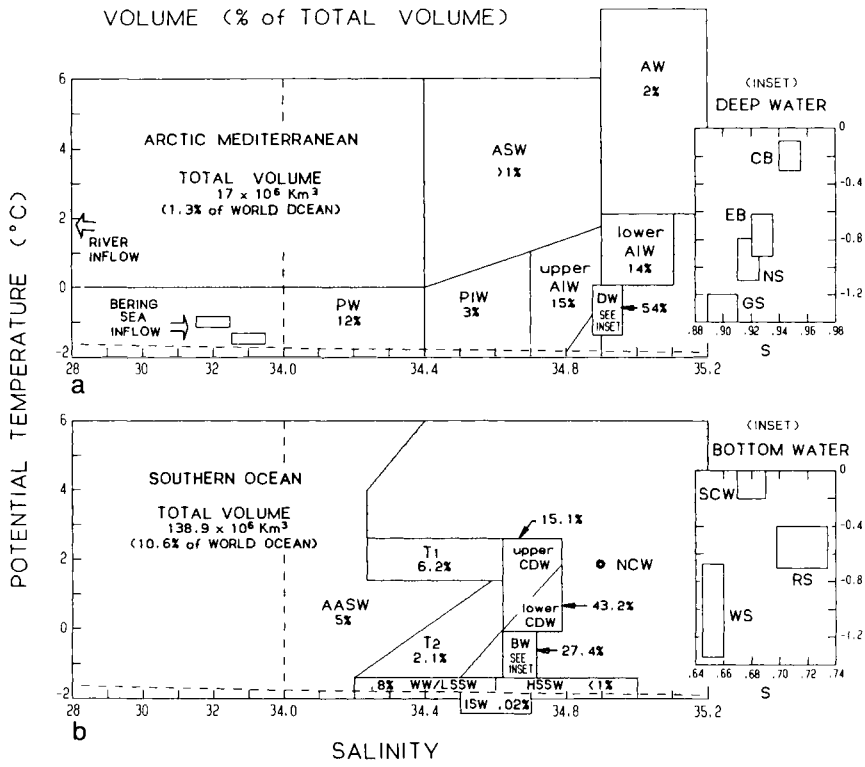

Figure 4.12 Volumetric diagrams for the (a) Arctic Mediterranean and (b) Southern Ocean.

(1976), Bullister and Weiss (1983), Ostlund (1982), Ostlund and Hut (1984), Ostlund *et al.* (1987), and Smethie *et al.* (1986, 1988). With the exception of the very long residence time of CBDW, the waters of the Arctic Ocean are much more rapidly ventilated than those of the Southern Ocean.

V. Thermohaline Circulation

A. Arctic Shelf/Estuary Systems

The estuarine circulation of the Arctic Ocean begins over the broad continental shelves, where a river inflow of about 3,500 $km^3\ yr^{-1}$ is introduced, mainly in summer (Treshnikov, 1985). It is also over the shelves that much fresh water is distilled by the annual freezing and melting cycle: the meltwater helps maintain the low salinity of the Arctic surface layer, while the

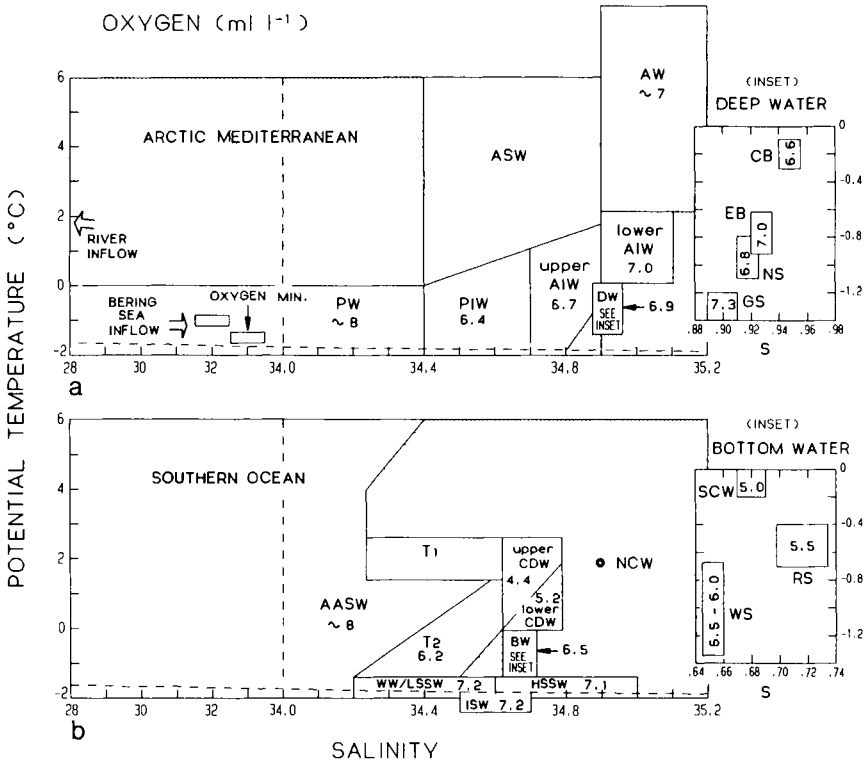

Figure 4.13 Mean oxygen content of water masses in the (a) Arctic Mediterranean and (b) Southern Ocean.

brine enrichment of shelf water by ice formation helps ventilate the halocline (Aagaard *et al.*, 1981; Melling and Lewis, 1982). Hence, during the summer the shelves act as positive estuaries with a net outflow of low-density water at the surface, and during the winter they act as reverse estuaries with a net outflow of high-density water at depth. The term shelf/estuary is here taken to mean shelf regions whose circulation is influenced by density-driven flows. Figure 4.16 shows a schematic of the shelf/estuary circulation for both winter and summer, based largely on data from the Mackenzie Shelf in the Beaufort Sea (Macdonald *et al.*, 1989; Carmack *et al.*, 1989).

Most studies related to fresh water in the Arctic have focused on budgets and basinwide effects (see Aagaard and Griesman, 1975; Ostlund, 1982; Anderson *et al.*, 1983). There is general agreement that the residence time of river inflow within the system is small, about 10 years, and that rivers strongly influence physical and chemical balances. However, budgets thus

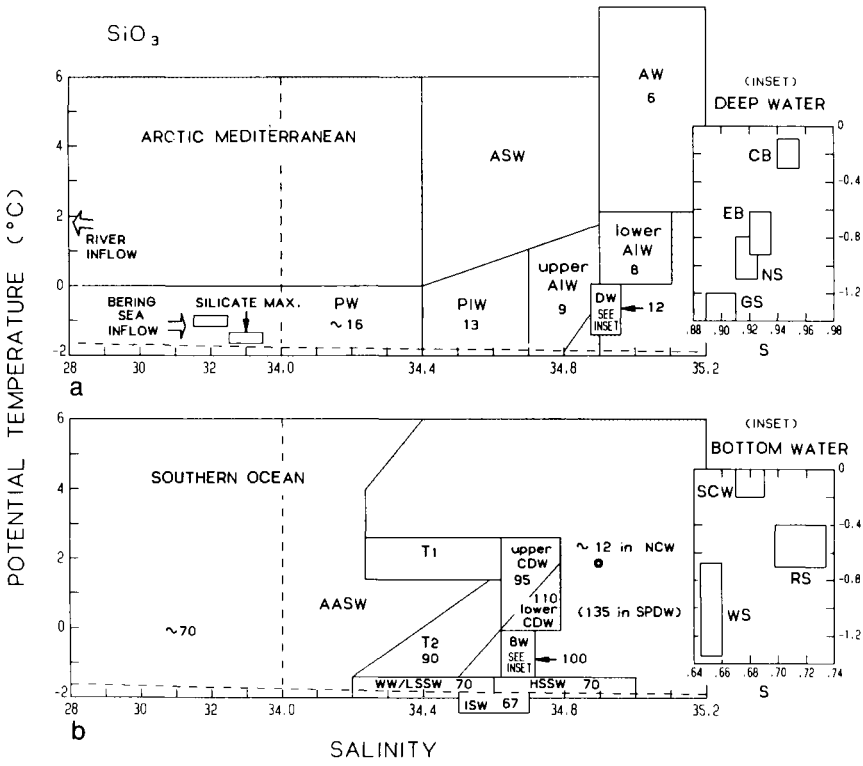

Figure 4.14 Mean silicate content of water masses in the (a) Arctic Mediterranean and (b) Southern Ocean.

far have not taken into account the strong spatial and temporal variability in freshwater distribution that exists within the Arctic. A basic characteristic of the major estuaries is that they extend well over the shelves, as opposed to being internal to bays and the river mouths (see Hanzlik and Aagaard, 1980; Carmack *et al.*, 1989). In fact, the map of near-surface salinity (Fig. 4.5) clearly shows that the complexity of lateral structure in surface waters extends over the whole of the Arctic basin. Details of river water spreading as buoyant plumes under sea ice are presented by Freeman *et al.* (1982) and Ingram and Larouche (1987). A useful view that follows from these citations is that the estuarine structure consists of a superposition of many plumes, each with its own set of characteristics and associated processes.

Only a limited number of models specifically test the influence of a river inflow on water column structure (see review by Cattle, 1985). Stigebrandt

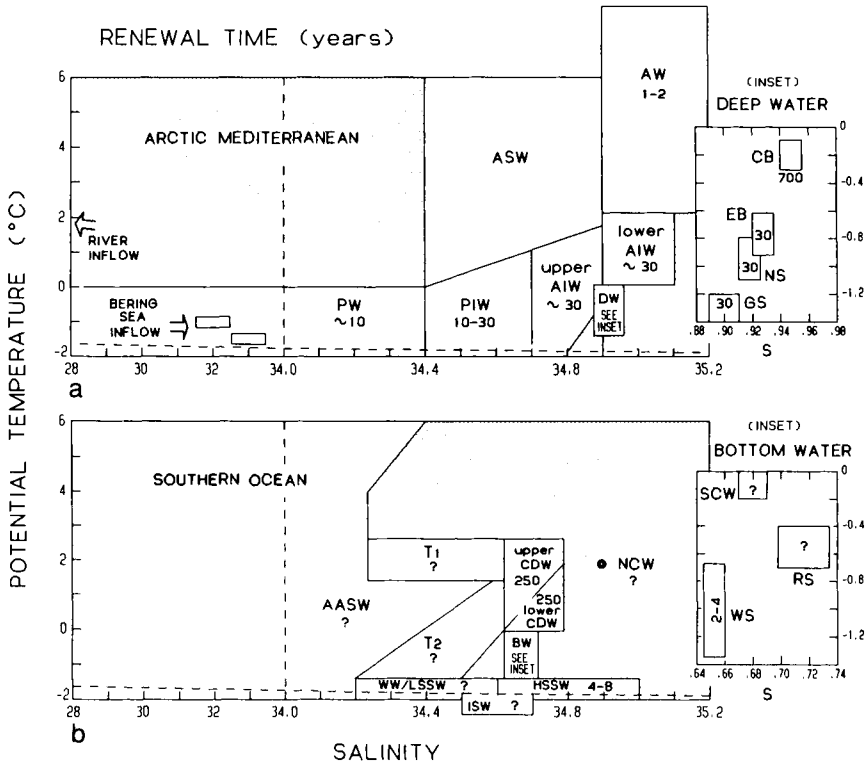

Figure 4.15 Approximate residence times of water masses in the (a) Arctic Mediterranean and (b) Southern Ocean.

(1981) developed a two-layer model with entrainment, driven by specified rates of river inflow and ice melting. Lemke (1987) discussed a one-dimensional mixed-layer model that included the combined effects of river inflow and ice melt. Semtner (1984b) has applied a fully three-dimensional model driven by annual mean river discharges to study climate responses of the Arctic. Killworth and Smith (1984) proposed a $1\frac{1}{2}$-dimensional model of vertical structure which allowed for the lateral insertion of saline plumes and river inflows. Of all efforts so far, this one confronts the problem of halocline formation most directly. Although Killworth and Smith admit that many aspects of the problem remain unsolved, their work demonstrates that the halocline depends on the supply of fresh water, by river and Bering Strait inflow, to the Arctic.

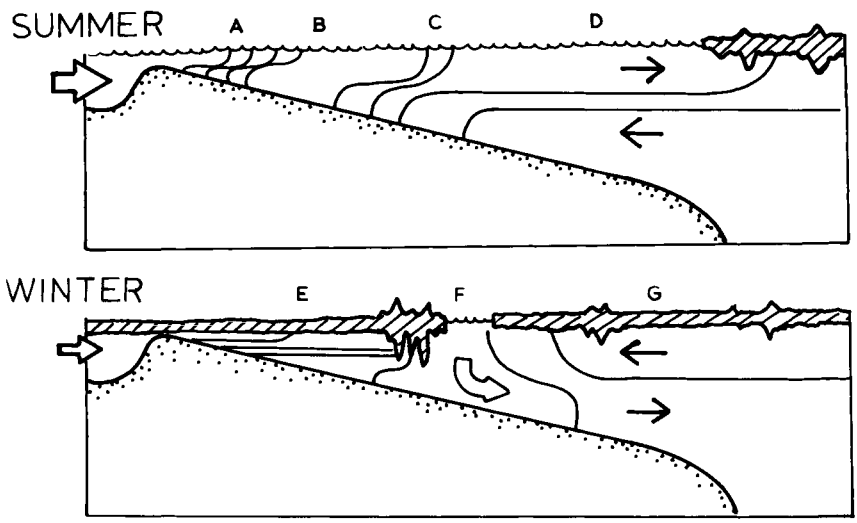

Figure 4.16 Schematic drawing of the seasonal circulation in an Arctic shelf estuary. Here, A denotes the region of the inner plume and salt wedge, B the middle mixed zone, C the outer plume and salt wedge, D the seasonal mixed layer, E the fast-ice zone, F the recurrent flaw lead within the shear zone, and G the pack ice zone.

B. Halocline Ventilation

The occurrence of sea ice is intimately connected with the underlying oceanic structure. Seawater has its temperature of maximum density below the freezing temperature; thus, in a homogeneous ocean the entire water column would have to be cooled to its freezing temperature before ice could form on the surface. In fact, winter convection is limited by polar haloclines, which lie at a depth of 30–60 m in the Arctic and 150–300 m in the southern Ocean.

Nansen (1906) was perhaps the first to note that since temperatures remain low within the halocline, its waters cannot be simple mixtures of Surface and Atlantic waters. Coachman and Barnes (1962) proposed that cold, saline waters draining through submarine canyons adjacent to the Eurasian basin aided halocline formation. A similar process, involving the drainage of water from the Chukchi Sea through Barrow Canyon, was proposed by Garrison and Becker (1976). The hypothesis that the off-shelf drainage of brine water derived from ice growth is largely responsible for halocline ventilation has been discussed by Aagaard *et al.* (1981), Melling and Lewis (1982), Killworth and Smith (1984), and Jones and Anderson (1986). Aagaard *et al.* (1981) calculated the amount of sea ice formation

required in winter to raise the shelf water salinity observed in summer to match that at the base of the halocline offshore as a means of identifying shelf regions that have potential for ventilation; they suggested that the area from Spitsbergen to Svernaya Zemlya supplies the Eurasian basin, while the Chukchi and northern Bering seas and possibly the region north of the Canadian Arctic Archipeligo feed the Canadian basin. Melling and Lewis (1982) suggested the Mackenzie Shelf as a source of halocline waters. They noted that ice production in this region is increased by 60% over thermodynamic ice growth due to divergence of the ice cover, and they also proposed that the upwelling of saline water onto the shelf may augment the observed salinity increase.

Present evidence suggests that more than one mechanism is responsible for the halocline structure. For example, although details vary from region to region, curves of temperature versus salinity (T/S) and stability frequency versus salinity (N/S) for a Beaufort Sea station illustrate some important features (Fig. 4.17b). The surface in summer is marked by low salinities, relatively high temperatures, and a strong seasonal halocline (stability maxima) at salinities between 22 to 30 per mil. At salinities above 34.4 per mil, temperature increases with depth down to the T_{max} of the Atlantic layer, defining the Arctic thermocline, and then decreases into the deep water. Between lies the Arctic halocline, the layer with low temperatures (less than $-1\,^{\circ}C$) and salinities between about 30.4 and 34.4 per mil. Within this layer the temperature is not uniform but instead shows two minima, near 31.6 and 33.1 per mil, and a maximum near 32.4 per mil. The two minima show corresponding minima in stability; the temperature maximum is associated with a maximum in stability. A third stability maximum appears in the vicinity of 34.4 per mil, the boundary between the halocline and the thermocline. Hence, the Arctic halocline is not a uniform structure, nor is it composed of a single water mass. There are three layers of maximum stability separating ice from the Atlantic layer, and two layers down to the shallow T_{max}. Such facts must be taken into account in ice–ocean models.

Figure 4.17a is a schematic of how the Arctic halocline may be maintained by shelf/estuarine processes. (This drawing is based on very sparse information and data and thus should be viewed as highly speculative.) The warm, saline Atlantic water enters the Arctic through Fram Strait via the West Spitsbergen Current, and as it moves north it is cooled by the atmosphere and by mixing with local waters. When the current encounters the sea ice margin northwest of Spitsbergen, ice melting and associated cooling generate a cold, dilute surface layer with T/S properties approximating those found above the Atlantic layer throughout the Arctic (see Quadfasel *et al.*, 1987; Moore and Wallace, 1988). As the flow continues eastward within the basin, contributions are added from first the Soviet shelves, then the Bering

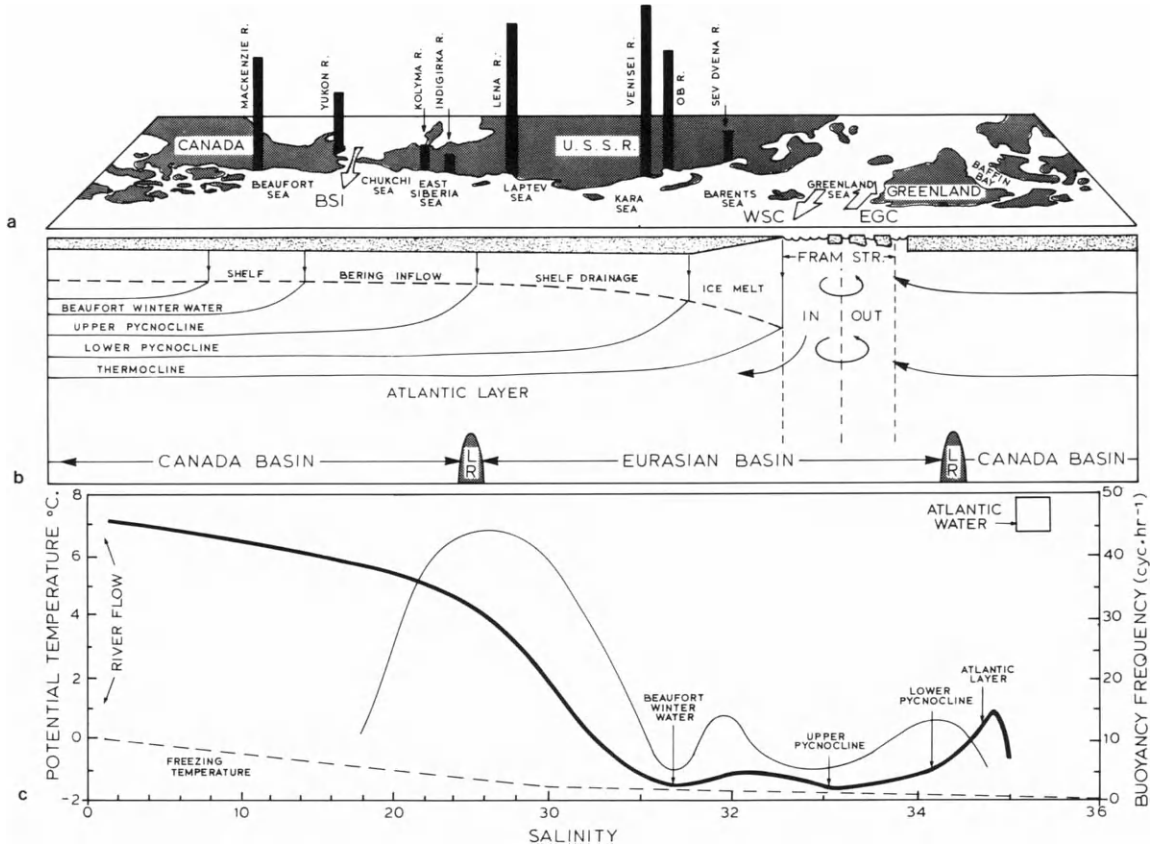

Figure 4.17 Schematic drawing of the circulation and stratification patterns associated with river inflow and halocline ventilation in the Arctic Ocean. (a) Circumterranean view of the Arctic Ocean showing the location of major inflow and outflow currents as well as the inputs from major rivers. (b) Hypothetical section following the shelf break around the Arctic basin and the various strata within the ocean. (c) Correlation diagram for temperature versus salinity and buoyancy frequency versus salinity occurring in the Beaufort Sea.

Sea, and finally the North American shelves (see Aagaard *et al.*, 1981; Jones and Anderson, 1986). The net effect is a kind of "stacking" of layers, one upon the other, to form, ultimately, a thick though heterogeneous halocline.

C. Deep- and Bottom-Water Formation

What is meant by bottom-water formation and rates of production? Solomon (1974) stressed the importance of distinguishing between sinking, which refers to downward vertical motion, and formation, which refers to water mass transformation. He warned that the distinction between the two processes is often ignored in oceanography.

1. Near-boundary and open-ocean convection

Killworth (1983) reviewed deep convection in the world ocean and organized his discussion around two types of convection: near-boundary sinking and open-ocean sinking. The first of these involves the formation on a continental shelf of a dense water mass which subsequently reaches the ocean floor by descending a continental slope. The second occurs far from land, predominately within an oceanic gyre. Killworth (1983) gave what he called the "ingredients" for each type of convection (Fig. 4.18). Near-boundary convection requires (a) a reservoir in which to form dense water, (b) a source or mechanism for dense-water production within the reservoir, (c) a dynamical reason for the reservoir to empty, (d) an appropriate offshore water mass with which to mix, and (e) a dynamical reason to sink to abyssal depths. Polar regions where evidence for near-boundary convection has been detected include the Weddell Sea (Seabrooke *et al.*, 1971; Carmack, 1973b; Foster and Carmack, 1976b; Foster and Middleton, 1980; Foldvik *et al.*, 1985a,b), the Ross Sea (Jacobs *et al.*, 1970), the Adelie Coast (Gordon and Tschernia, 1972), Enderby Land (Jacobs and Georgi, 1977), and off Wilkes Land (Carmack and Killworth, 1978). Observational evidence of near-boundary convection in the Arctic has been published by Garrison and Becker (1976), Melling and Lewis (1982), and Quadfasel *et al.* (1988).

Killworth's ingredients for open-ocean convection require (a) a background cyclonic gyre circulation, (b) preconditioning to create a background of low static stability within the gyre system, (c) intense and rapid surface forcing, (d) a second water mass with which to mix, and (e) a sinking and spreading phase. Polar regions where open-ocean convection is thought to occur include the Greenland Sea (Helland-Hansen and Nansen, 1909; Carmack and Aagaard, 1973, 1974; Killworth, 1979; Rudels, 1989), the Labrador Sea (Lazier, 1973; Clarke and Gascard, 1983; Gascard and Clarke, 1983; Clarke and Coote, 1988), the Weddell Gyre (Gordon, 1978; Carsey, 1980;

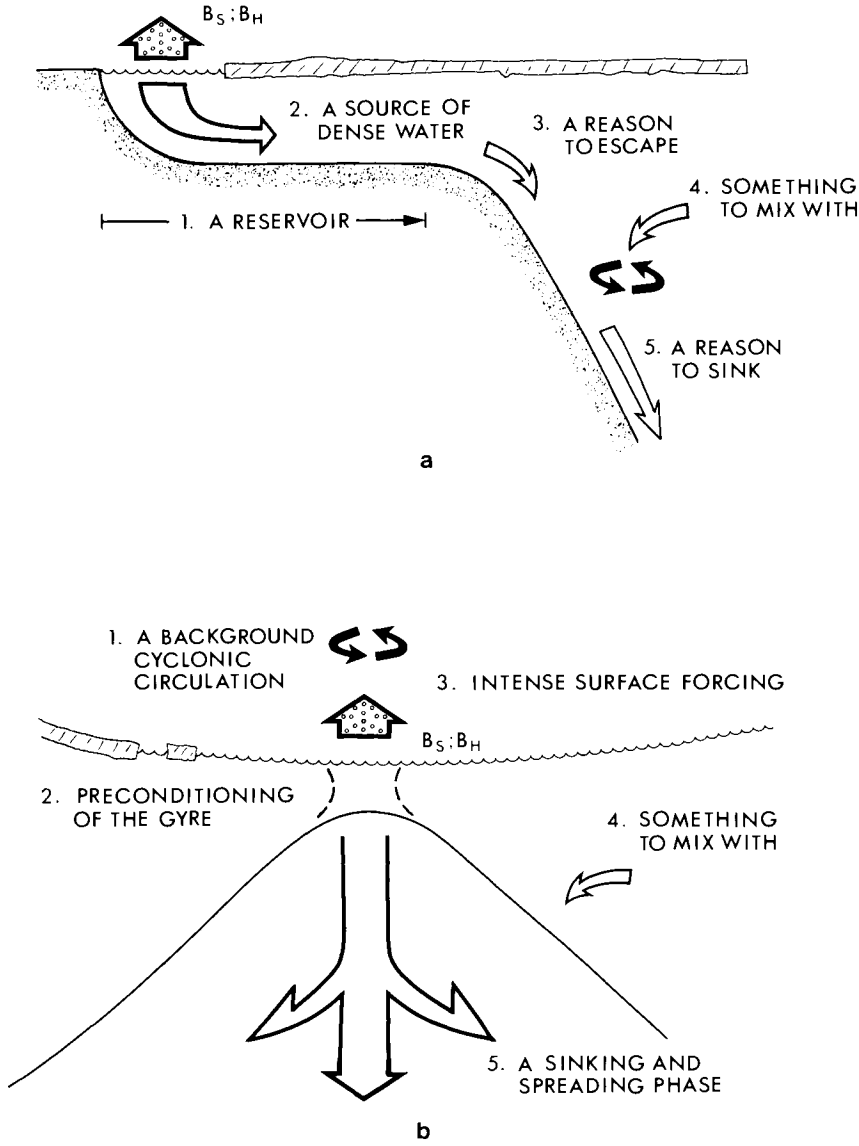

Figure 4.18 Water mass formation by (a) near-boundary and (b) open-ocean convection. Here, B_H and B_S are buoyancy fluxes for heat and salt.

Martinson *et al.*, 1981; Comiso and Gordon, 1987), and within the Bransfield Strait (Gordon and Nowlin, 1978).

2. Northern hemisphere

By far the greatest amount of attention to deep water formation in the Arctic Mediterranean has focused on convection in the Greenland sea. Nansen (1906) and Helland-Hansen and Nansen (1909) identified the Greenland Sea as the main source of deep water in the northern hemisphere and proposed the classic model of mid-gyre convection. Metcalf (1955) proposed that ventilation of the gyre occurred mainly by the sinking of dense water along inclined density surfaces. Mosby (1959) suggested that the renewal process resembled an inverted funnel, with a narrow sinking region feeding the much larger gyre. Worthington (1970) called attention to the Norwegian and Greenland seas acting as a negative estuary to transform subpolar water masses by cooling. Carmack and Aagaard (1973) and later McDougall (1983) proposed the subsurface modification of Atlantic Water (lower Arctic Intermediate Water) by double diffusion. Reid (1979) showed evidence that some properties of the source water to Greenland Sea Deep Water may come from the Mediterranean Sea. Quadfasel and Meincke (1987) noted the possible importance of the marginal ice zone and gyre flank interactions to produce dense water. Hakkinen (1987) suggested that differential upwelling in the vicinity of the ice edge and subsequent cooling may result in convection. Houssais (1988) developed a thermally driven mixed-layer model that simulated deep convection. Rudels (1989) proposed a three-stage model of convection that included frazil ice formation at the sea surface, formation of a surface boundary layer made unstable by brine release, and subsequent sinking to abyssal depths of dense water within a turbulent plume.

Mechanisms for direct ventilation of the abyssal Arctic Ocean have been proposed. Aagaard (1981) called attention to the fact that deep water within the Canadian Basin had higher salinities than deep water within the Eurasian Basin and questioned the classic idea that all deep water within the Arctic Ocean derives from the Greenland Sea. Swift *et al.* (1983) discussed contributions to the Arctic from both the Greenland and Barents seas. The idea of direct ventilation of deep water in the Arctic by near-boundary processes was formalized by Aagaard *et al.* (1985a); this hypothesis has gained some support from geochemical studies by Smethie *et al.* (1988) and Anderson *et al.* (1989). The occurrence of shelf water sufficiently dense to sink to abyssal depths has been observed in the Barents Sea by Midttun (1985). Quadfasel *et al.* (1988) have observed a dense plume descending a deep canyon which leads from Spitsbergen, crossing the Barents shelf into Fram Strait, and eventually entering the Arctic Ocean north of Spitsbergen.

3. Southern hemisphere

In the Southern Ocean most work has focused on the formation of bottom water in the Weddell Sea by near-boundary processes. Brennecke (1921) identified the Weddell Sea as the main source of AABW. Mosby (1934, 1966) stated that the salinity of shelf water must be enhanced by sea ice formation and arrived at a critical shelf water salinity of 34.62 per mil necessary to drive convection and ensure the proper T/S relationship. Fofonoff (1956) argued that the cabbeling instability would influence the T/S properties of water escaping the shelf. Foster (1972a) further examined convection resulting from cabbeling by modeling the response of a fluid to a local (interior) instability. Gill and Turner (1969) noted that the conditions for double diffusion were met above the Antarctic continental slope and that this mechanism could lead to deep convection. Seabrooke *et al.* (1971) proposed that freezing of seawater to the base of the floating ice shelves was responsible for raising the salinity of shelf waters. Gill (1973) gave an illuminating analysis of the bottom-water formation problem that drew together many concerns; he emphasized the importance of the differential compressibility of seawater, discussed freezing and melting at the base of ice shelves, formalized the idea of cross-frontal mixing at the shelf break, and drew attention to the significance of ice divergence in considering the potential for brine water production. Foster and Carmack (1976b) and later Foster and Middleton (1980) supported a mixing model for AABW formation that involved the onshore flow of deep water and its subsequent mixing with shelf water varieties. Variability in bottom-water properties is discussed by Foster and Middleton (1979). The importance of frontal zone dynamics is stressed by Foster *et al.* (1987). Dynamical aspects of near-boundary convection are covered by Killworth (1977), who studied the combined effects of rotation, friction, entrainment, and differential compressibility on the dynamics of sinking plumes.

The possibility of shelf waters being modified by the melting of ice shelves has been discussed by several authors. Carmack and Foster (1975) discussed the distribution of Ice Shelf Water in the Weddell Sea and estimated a melt rate of 0.6 $m^3 s^{-1}$ from the base of the Filchner Ice Shelf. Weiss *et al.* (1979) used oxygen isotope measurements to show that meltwater from glacial ice is indeed a component in bottom water. Foldvik *et al.* (1985c) observed water as cold as $-2°C$ sinking as dense plume along the continental slope of the Weddell Sea. Jacobs (1987) proposed a modification of the mixing model of Foster and Carmack to include additions of Ice Shelf Water.

There is also evidence that open-ocean convection may be important in the Southern Ocean, particularly with regard to the Weddell Gyre (see Wust, 1933). A possible means of deep-water renewal involves chimneys, or deep-

reaching convective features involving intense buoyancy fluxes (Killworth, 1979). Gordon (1978) described one such feature in the Weddell Sea near Maud Rise; within this column of water, about 30 km in diameter and 4000 m deep, the normal sequence of stratification was absent, replaced by cold, low-salinity, and high-oxygen water. Gordon speculated that such features may form in the Weddell polynya region and that these cells may carry sensible heat from the deep layers to the sea surface to help maintain ice-free conditions, a notion that has gained support from subsequent research (Carsey, 1980; Comiso and Gordon, 1987). Gordon (1982) examined changes in the heat content of the Weddell Gyre during the 1970s and suggested these were due to heat loss from the deep water via the chimney mechanism.

Convection within the Weddell Gyre has attracted some theoretical interest. Killworth (1979) looked at the quasi-steady and time-dependent aspects of convection in a rotating fluid. His results suggest that some kind of preconditioning is required to initiate chimney formation. Martinson *et al.* (1981) developed a two-layer model of the Weddell polynya in which wind-induced upwelling initially shallows the pycnocline so that cooling is more effective in driving convection; they also noted that interannual variations in convective activity may follow from changes in freshwater input or in the large-scale circulation. Solomon (1983) developed a pressure-dependent numerical model of bottom-water formation that showed the possibility of sinking along the southern boundary of the Weddell Gyre. Motoi *et al.* (1987) published the results of a one-dimensional mixed-layer model and argued that the occurrence of convection depends on a high near-surface salinity the previous summer.

VI. Concluding Remarks

Despite recent and ongoing work in the Arctic and Antarctic, there is much to learn about the large-scale physical oceanography of these regions. Especially critical here are the interdisciplinary connections with biology and climate.

How does large-scale physical oceanography affect organisms living in and beneath sea ice? (An entire article could be devoted to this question without scratching the surface.) Some interactions are straightforward—e.g., the transport and redistribution of nutrients by current systems, establishment of ambient light climate by turbidity and sea ice fields, seasonal cycles of stratification and mixing due to surface forcing, material exchange at the ice–water interface, and transfer mechanisms operating at marginal ice zones and major frontal systems (see books and review articles by Platt *et al.*, 1982; Horner, 1985; McRoy *et al.*, 1986; Smith, 1987). Others are not so

immediately apparent. For example, how do the polar biota influence the world CO_2 balance? Are alternative large-scale circulation patterns possible which will result in a worldwide shift in nutrient availability? (See Sarmiento and Toggweiler, 1984; Knox and McElroy, 1984; Broecker *et al.*, 1985.)

The relationship between polar oceanography and climate is also critically important. The presence of sea ice influences climate through a number of processes, such as its effect on the earth's radiation budget and on surface heat exchange; the albedo of ice and its attendant snow cover is far greater than that of open water; the insulating effect of ice reduces heat transfer to the atmosphere by one to two orders of magnitude compared to that from open water. Results of general circulation models predict that climate warming due to increases in greenhouse gases will be amplified in polar regions (Manabe and Wetherald, 1980; Kellogg, 1984). The reader wishing to gather more information on the subject is referred to publications by Baker (1979b, 1986), Goody (1980), Polar Group (1980), Barry (1983), Committee on the Role of Polar Regions and Climate Change (1984), Semtner (1984a), and Hall (1988).

Although the presence or absence of sea ice influences climate, it is the distribution of salinity, and specifically the thickness and horizontal extent of polar haloclines, which prevents deep convection and the local flux of heat from underlying water masses that would otherwise block ice formation. A key is understanding the mechanisms by which fresh water from river inflow and ice melt is disposed within the Arctic Ocean. For example, how is the Arctic halocline maintained, what controls its horizontal extent, and by what mechanism is fresh water mixed so deeply within the basin? What would happen to the Arctic halocline if river inflows or the amount of seasonal melting were to change? Are changes in ice conditions likely? Although a completely ice-free Arctic seems unlikely in the near future, it is possible that shelf regions will have longer periods and greater areas of ice-free conditions.

There are also climate-related questions involving the deeper layers of polar regions. For example, do water mass transformation processes in polar regions need to be considered in the light of papers on multiple equilibria in deep circulation (Bryan, 1986; Marotzke *et al.*, 1988)? Are rapid changes, similar to those observed by Gordon (1982) in the Weddell Gyre, possible elsewhere in polar regions, for example, in the deep Arctic?

To punctuate the importance of interdisciplinary thinking with regard to the interaction of large-scale oceanography with biology and climate, a warning by Stafford Beer (1980) seems appropriate:

> Interdisciplinary research often consists of individual disciplinarians standing in a circle, holding hands for mutual comfort, while the problem of interest slips through the middle.

Hopefully, Beer's criticism will not apply to polar oceanographers in the years to come.

References

Aagaard, K. 1970. The wind-driven transports in the Greenland and Norwegian seas. *Deep-Sea Res.* **17**: 281–291.

———. 1979. Polar oceanography. I. Arctic Ocean. *Rev. Geophys. Space Phys.* **17**: 1576–1578.

———. 1981. On the deep circulation in the Arctic Ocean. *Deep-Sea Res.* **28**: 251–268.

———. 1982. Inflow from the Atlantic Ocean to the polar basin. *In* "The Arctic Ocean, the Hydrographic Environment and the Fate of Pollutants" (L. Rey, ed.), pp. 69–82. Comité Arctique International, Monaco.

———. 1984. The Beaufort undercurrent. *In* "The Alaskan Beaufort Sea, Ecosystems and Environments" (P. W. Barnes, D. M. Schell & E. Reimnitz, eds.), pp. 47–71. Academic Press, Orlando, Florida.

———. 1989. A synthesis of the Arctic Ocean circulation. *Rapp. P.-V. Reun., Cons. Int. Explor. Mer* **188**: 11–22.

Aagaard, K. & L. K. Coachman. 1968a. The East Greenland Current north of Denmark Strait. Part I. *Arctic* **21**: 181–200.

———. 1968b. The East Greenland Current north of Denmark Strait. Part II. *Arctic* **21**: 267–290.

———. 1975. Toward an ice-free Arctic Ocean. *Eos* **56**:484–486.

Aagaard, K. & P. Griesman. 1975. Towards new mass and heat budgets for the Arctic Ocean. *J. Geophys. Res.* **80**: 3821–3827.

Aagaard, K., L. K. Coachman & E. C. Carmack. 1981. On the halocline of the Arctic Ocean. *Deep-Sea Res.* **28**: 529–545.

Aagaard, K., J. H. Swift & E. C. Carmack. 1985a. Thermohaline circulation in the Arctic Mediterranean seas. *J. Geophys. Res.* **90**: 4833–4846.

Aagaard, K., A. T. Roach & J. D. Schumacher. 1985b. On the wind-driven variability of the flow through Bering Strait. *J. Geophys. Res.* **90**: 7213–7221.

Aagaard, K., A. Foldvik & S. R. Hillman. 1987. The West Spitzbergen Current: Disposition and water mass transformation. *J. Geophys. Res.* **92**: 3778–3784.

Ackley, S. F. 1981. A review of sea-ice weather relationships in the southern hemisphere. *IAHS Publ.* **131**: 127–159.

Addison, V. G. 1987. The physical oceanography of the northern Baffin Bay–Nares Strait region. M.S. Thesis, Naval Postgraduate School, Monterey, California.

Alfultis, M. A. & S. Martin. 1987. Satellite passive microwave studies of the Sea of Okhotsk ice cover and its relation to oceanic process, 1978–1982. *J. Geophys. Res.* **92**: 13,013-13,028.

Anderson, L. G., D. W. Dyrssen, E. P. Jones & M. G. Lowings. 1983. Inputs and outputs of salt, fresh water, alkalinity, and silica in the Arctic Ocean. *Deep-Sea Res.* **30**: 87–94.

Anderson, L. G., E. P. Jones, K. P. Koltermann, P. Schlosser, J. H. Swift & D. W. R. Wallace. 1989. The first oceanographic section across the Nansen basin in the Arctic Ocean. *Deep-Sea Res.* **36**: 475–482.

Bailey, W. G. 1956. On the origin of the deep Baffin Bay water. *J. Fish. Res. Board Can.* **13**: 313–318.

Baker, J. D. 1979a. Polar oceanography. 2. Southern Ocean. *Rev. Geophys. Space Phys.* **17**: 1578–1585.

———. 1979b. Ocean–atmosphere interaction in high southern latitudes. *Dyn. Atmos. Oceans* **3**: 213–229.

———. 1982. A note on Sverdrup balance in the Southern Ocean. *J. Mar. Res.* **40:** 21–26.
———. 1986. The Arctic's role in climate. *Oceanus* **29:** 41–96.
Barcilon, V. 1966. On the influence of the peripheral Antarctic water discharge on the dynamics of the Circumpolar Current. *J. Mar. Res.* **24:** 269–275.
———. 1967. Further investigation of the influence of the peripheral Antarctic water discharge on the Circumpolar Current. *J. Mar. Res.* **25:** 1–9.
Barry, R. G. 1983. Arctic Ocean ice and climate: Perspectives on a century of polar research. *Ann. Assoc. Am. Geogr.* **73:** 485–503.
———. 1990. Canada's cold seas. *In* "Canada's Cold Environments" (O. Slaymaekr & H. French, eds.) (in press).
Beer, S. 1980. Introduction to autopoiesis. *In* "Autopoiesis and Cognition: The Realization of the Living" (H. R. Maturana and F. J. Varela, eds.), pp. 63–72. Reidel, Boston.
Bourke, R. H., J. L. Newton, R. G. Paquette & M. D. Tunnicliffe. 1987. Circulation and water masses of the East Greenland Shelf. *J. Geophys. Res.* **92:** 6729–6740.
Bradstreet, M. S. W., D. H. Thomson & D. B. Fissel. 1987. "Zooplankton and Bowhead Whale Feeding in the Canadian Beaufort Sea, 1986." Can. Dep. Indian Affairs North. Devel., Ottawa.
Brennecke, W. 1921. Die ozeanographischen Arbeitentder deutschen antarktischen Expedition 1911–12. *Arch. Dsch. Seewarte* **39:** 1–214.
Broecker, W. S., D. M. Peteet & D. Rind. 1985. Does the ocean–atmosphere system have more than one stable mode of operation? *Nature (London)* **315:** 21–26.
Bromwich, D. H. & D. D. Kurtz. 1984. Katabatic wind forcing of the Terra Nova Bay polynya. *J. Geophys. Res.* **89:** 3561–3572.
Bryan, F. 1986. High-latitude salinity effects and interhemispheric thermohaline circulations. *Nature (London)* **323:** 301–304.
Bryden, H. 1983. The Southern Ocean. *In* "Eddies in the Ocean" (A. R. Robinson, ed.), pp. 265–277. Springer-Verlag, New York.
Bryden, H. & R. D. Pillsbury. 1977. Variability of deep flow in the Drake Passage from year-long current measurements. *J. Phys. Oceanogr.* **7:** 803–810.
Bullister, J. L. & R. F. Weiss. 1983. Anthropogenic chlorofluoromethanes in Greenland and Norwegian seas. *Science* **221:** 265–268.
Callahan, J. E. 1972. The structure and circulation of deep water in the Antarctic. *Deep-Sea Res.* **19:** 563–575.
Campbell, W. J. 1965. The wind driven circulation of ice and water in a polar ocean. *JGR, J. Geophys. Res.* **70:** 3279–3301.
Carmack, E. C. 1973a. On the hydrography of the Greenland Sea. Ph.D. Diss., Univ. of Washington, Seattle.
———. 1973b. Silicate and potential temperature in the deep and bottom waters of the western Weddell Sea. *Deep-Sea Res.* **20:** 927–932.
———. 1974. A quantitative characterization of water masses in the Weddell Sea during summer. *Deep-Sea Res.* **21:** 431–443.
———. 1977. Water characteristics of the Southern Ocean south of the Polar Front. *In* "A Voyage of Discovery" (M. V. Angel, ed.), pp. 15–41. Pergamon, Oxford.
———. 1986. Circulation and mixing in ice-covered waters. *In* "The Geophysics of Sea Ice" (N. Untersteiner, ed.), pp. 641–712. Plenum, New York.
Carmack, E. C. & K. Aagaard. 1973. On the deep water of the Greenland Sea. *Deep-Sea Res.* **20:** 687–715.
———. 1974. The formation of bottom water in the Greenland Sea. *Colloq. Int. C. N. R. S.* **215:** 65–82.
Carmack, E. C. & T. D. Foster. 1975. Circulation and distribution of oceanographic properties near the Filchner Ice Shelf. *Deep-Sea Res.* **22:** 77–90.

Carmack, E. C. & P. D. Killworth. 1978. Formation and interleaving of abyssal masses off Wilkes Land, Antarctica. *Deep-Sea Res.* **25:** 357–369.

Carmack, E. C., R. W. Macdonald & J. E. Papadakis. 1989. Water mass structure and boundaries in the Mackenzie shelf/estuary. *J. Geophys. Res.* **94:** 18,043–18,055.

Carsey, F. D. 1980. Microwave observations of the Weddell polynya. *Mon. Weather Rev.* **108:** 2032–2044.

———. 1982. Arctic sea-ice distribution at the end of summer 1973–1976 from satellite microwave data. *J. Geophys. Res.* **87:** 5809–5835.

Cattle, H. 1985. Diverting Soviet rivers: Some possible repercussions for the Arctic Ocean. *Polar Rec.* **22:** 485–498.

Clarke, R. A. & A. R. Coote. 1988. The formation of Labrador Sea water. Part III. The evolution of oxygen and nutrient concentration. *J. Phys. Oceanogr.* **18:** 469–480.

Clarke, R. A. & J.-C. Gascard. 1983. The formation of Labrador Sea water. Part I. Large-scale processes. *J. Phys. Oceanogr.* **13:** 1764–1778.

Clowes, A. J. 1934. Hydrology of the Bransfield Strait. *'Discovery' Rep.* **9:** 1–64.

Coachman, L. K. 1961. On the water masses of the Arctic Ocean. Ph.D. Diss., Univ. of Washington, Seattle.

———. 1986. Circulation, water masses, and fluxes on the southeastern Bering Sea shelf. *Cont. Shelf Res.* **5:** 23–108.

Coachman, L. K. & K. Aagaard. 1966. On the water exchange through Bering Strait. *Limnol. Oceanogr.* **11:** 44–59.

———. 1974. Physical oceanography of Arctic and subarctic seas. *In* "Marine Geology and Oceanography of the Arctic Seas" (Y. Herman, ed.), pp. 1–72. Springer-Verlag, Berlin.

———. 1981. Reevaluation of water transports in the vicinity of Bering Strait. *In* "The Eastern Bering Sea Shelf: Oceanography and Resources" (D. W. Hood & J. A. Calder, eds.), vol. 1, pp. 95–110. Univ. of Washington Press, Seattle.

———. 1988. Transports through Bering Strait: Annual and interannual variability. *J. Geophys. Res.* **93:** 15,535–15,539.

Coachman, L. K. & C. A. Barnes. 1961. The contribution of Bering Sea water to the Arctic Ocean. *Arctic* **14:** 147–161.

———. 1962. Surface water in the Eurasian basin of the Arctic Ocean. *Arctic* **15:** 251–277.

Coachman, L. K., K. Aagaard & R. B. Tripp. 1975. "Bering Strait: The Regional Physical Oceanography." Univ. of Washington Press, Seattle.

Codispoti, L. A. & F. A. Richards. 1968. Micronutrient distribution in the East Siberian and Laptev seas during summer 1963. *Arctic* **21:** 67–83.

———. 1971. Oxygen supersaturation in the Chuckchi and East Siberian seas. *Deep-Sea Res.* **18:** 341–351.

Collin, A. E. 1963. Waters of the Canadian Arctic Archipelago. *In* "Proceedings of the Arctic Basin Symposium," pp. 128–136. Arctic Inst. North Am., Washington D.C.

Colony, R. & A. S. Thorndike. 1980. The horizontal coherency of the motion of summer Arctic sea ice. *J. Phys. Oceanogr.* **10:** 1281–1289.

———. 1984. An estimate of the mean field of Arctic sea ice. *J. Geophys. Res.* **89:** 10623–10629.

———. 1985. Sea ice motion as a drunkard's walk. *J. Geophys. Res.* **90,** 965–974.

Comiso, J. C. & A. L. Gordon. 1987. Recurring polynyas over the Cosmonaut Sea and the Maud Rise. *J. Geophys. Res.* **92:** 2819–2833.

Committee on the Role of Polar Regions and Climate Change. 1984. "The Polar Regions and Climate Change." Polar Research Board, National Academy Press, Washington, D.C.

Coote, A. R. & E. P. Jones. 1982. Nutrient distributions and their relationships to water masses in Baffin Bay. *Can. J. Fish. Aquat. Sci.* **39:** 1210–1214.

Deacon, G. E. R. 1937. The hydrology of the Southern Ocean. *'Discovery' Rep.* **15:** 3–122.

———. 1976. The cyclonic circulation in the Weddell Sea. *Deep-Sea Res.* **23**: 125–126.
———. 1979. The Weddell Gyre. *Deep-Sea Res.* **26**: 981–995.
———. 1982. Physical and biological zonation in the Southern Ocean. *Deep-Sea Res.* **29**: 1–16.
Deacon, G. E. R. & T. D. Foster. 1977. The boundary region between the Weddell Sea and Drake Passage currents. *Deep-Sea Res.* **24**: 505–510.
Dieckmann, G., G. Rohardt, H. Hellmer & J. Kipfstuhl. 1986. The occurrence of ice platelets at 250 m depth near the Filchner Ice Shelf and its significance for sea ice biology. *Deep-Sea Res.* **33**: 141–148.
Fandry, C. G. & R. D. Pillsbury. 1979. On the estimation of absolute geostrophic volume transport applied to the Antarctic Circumpolar Current. *J. Phys. Oceanogr.* **9**: 449–455.
Fedorova, Z. P. & A. S. Yankina. 1964. The passage of Pacific Ocean water through the Bering Strait into the Chukchi Sea. *Deep-Sea Res.* **11**: 427–434.
Fissel, D. B., D. D. Lemon & J. R. Birch. 1982. Major features of the summer near-surface circulation of western Baffin Bay, 1978 and 1979. *Arctic* **35**: 180–200.
Fofonoff, N. P. 1955. A theoretical study of zonally uniform flow. Ph.D. Diss., Brown Univ., Providence, Rhode Island.
———. 1956. Some properties of sea water influencing the formation of Antarctic bottom water. *Deep-Sea Res.* **4**: 32–35.
Foldvik, A. & T. K. Kvinge. 1974. Conditional instability of sea water at the freezing point. *Deep-Sea Res.* **21**: 169–174.
Foldvik, A., T. Gammelsrød & T. Torresen. 1985a. Hydrographic observations from the Weddell Sea during the Norwegian Antarctic Research Expedition 1976/77. *Polar Res.* **3**: 177–193.
———. 1985b. Physical oceanography studies in the Weddell Sea during the Norwegian Antarctic Research Expedition 1978/79. *Polar Res.* **3**: 195–207.
Foldvik, A., T. K. Kvinge & T. Torresen. 1985c. Bottom currents near the continental shelf break in the Weddell Sea. *Antarct. Res. Ser.* **43**: 21–24.
Foldvik, A., K. Aagaard & T. Torresen. 1988. On the velocity field of the East Greenland Current. *Deep-Sea Res.* **35**: 1335–1354.
Foster, T. D. 1972a. An analysis of the cabbeling instability in sea water. *J. Phys. Oceanogr.* **2**: 294–301.
———. 1972b. Haline convection in leads and polynyas. *J. Phys. Oceanogr.* **2**: 462–469.
———. 1978. Polar oceans: Similarities and differences in their physical oceanography. *In* "Polar Research: To the Present and the Future (M. McWhinnie, ed.), pp. 117–140. Westview Press, New Haven, Connecticut.
Foster, T. D. & E. C. Carmack. 1976a. Temperature and salinity structure in the Weddell Sea. *J. Phys. Oceanogr.* **6**: 36–44.
———. 1976b. Frontal zone mixing and Antarctic bottom water formation in the southern Weddell Sea. *Deep-Sea Res.* **23**: 301–317.
Foster, T. D. & J. H. Middleton. 1979. Variability in the bottom water of the Weddell Sea. *Deep-Sea Res.* **26**: 743–762.
———. 1980. Bottom water formation in the Weddell Sea. *Deep-Sea Res.* **27**: 367–382.
———. 1984. The oceanographic structure of the eastern Scotia Sea. I. Physical oceanography. *Deep-Sea Res.* **31**: 529–550.
Foster, T. D., A. Foldvik & J. H. Middleton. 1987. Mixing and bottom water formation in the shelf break region of the southern Weddell Sea. *Deep-Sea Res.* **34**: 1771–1794.
Freeman, N. G., J. C. Roff & R. J. Pett. 1982. Physical, chemical and biological features of river plumes under an ice cover in James and Hudson bays. *Nat. Can. Rev. Ecol. Syst.* **109**: 745–764.

Galt, J. A. 1973. A numerical investigation of Arctic Ocean dynamics. *J. Phys. Oceanogr.* **3**: 379–396.

Garrison, G. R. & P. Becker. 1976. The Barrow Submarine Canyon: A drain for the Chukchi Sea. *JAR, J. Geophys. Res.* **81**: 4445–4453.

Gascard, J.-C. & R. A. Clarke. 1983. The formation of Labrador Sea water, Part II: mesoscale and smaller-scale processes. *J. Phys. Oceanogr.* **13**: 1779–1797.

Gascard, J.-C., C. Kergomard, P. F. Jeannin & M. Fily. 1988. Diagnostic study of the Fram Strait marginal ice zone during summer from Marginal Ice Zone Experiment 83 and 84 Lagrangian observations. *J. Geophys. Res.* **93**: 3613–3641.

Georgi, D. T. 1981. Circulation of bottom waters in the southwestern South Atlantic. *Deep-Sea Res.* **28**: 959–979.

Georgi, D. T. & J. M. Toole. 1982. The Antarctic Circumpolar Current and the oceanic heat and freshwater budgets. *J. Mar. Res.* **40**(Suppl.): 183–197.

Gill, A. E. 1973. Circulation and bottom water production in the Weddell Sea. *Deep-Sea Res.* **28**: 111–140.

Gill, A. E. & J. S. Turner. 1969. Some new ideas about the formation of Antarctic bottom water. *Nature (London)* **224**: 1287–1288.

Goody, R. 1980. Polar processes and world climate (a brief overview). *Mon. Weather Rev.* **108**: 1935–1942.

Gordon, A. L. 1971. Oceanography of Antarctic water. *Antarct. Res. Ser.* **15**: 205–221.

———. 1974. Varieties and variability of Antarctic bottom water. *Colloq. Int. C. N. R. S.* **215**: 33–47.

———. 1978. Deep Antarctic convection west of Maud Rise. *J. Phys. Oceanogr.* **8**: 600–612.

———. 1982. Weddell deep water variability. *J. Mar. Res.* **40**: 199–217.

———. 1983. Polar oceanography. *Rev. Geophys. Space Phys.* **21**: 1124–1131.

———. 1989. Spatial and temporal variability within the Southern Ocean. *In* "Antarctic Variability and Krill Distribution" (D. Sahrhge, ed.), pp. 41–56. Springer-Verlag, Berlin.

Gordon, A. L. & W. D. Nowlin. 1978. The basin waters of the Bransfield Strait. *J. Phys. Oceanogr.* **8**: 258–264.

Gordon, A. L. & W. B. Owens. 1987. Polar oceans. *Rev. Geophys. Space Phys.* **25**: 227–233.

Gordon, A. L. & P. Tchernia. 1972. Waters of the continental margin off Adelie Coast, Antarctica. *Antarc. Res. Ser.* **9**: 59–69.

Gordon, A. L., D. T. Georgi & H. W. Taylor. 1977. Antarctic Polar Front zone in the western Scotia Sea. Summer 1975. *J. Phys. Oceanogr.* **7**: 309–328.

Gordon, A. L., E. Molinelli & T. Baker. 1978. Large-scale relative dynamic topography of the Southern Ocean. *J. Geophys Res.* **83**: 3023–3032.

Gordon, A. L., D. G. Martinson & H. W. Taylor. 1981a. The wind-driven circulation in the Weddell–Enderby basin. *Deep-Sea Res.* **28**: 151–163.

Gordon, A. L., E. Molinelli & T. Baker. 1981b. "Southern Ocean Atlas." Columbia Univ. Press, New York.

Gorschkov, S. G. 1983. "World Ocean Atlas. Arctic Ocean 3." Pergamon, Oxford.

Hakkinen, S. 1987. A coupled dynamic–thermodynamic model of an ice–ocean system in the marginal ice zone. *J. Geophys. Res.* **92**: 9469–9478.

Hall, D. K. 1988. Assessment of polar climate change using satellite technology. *Rev. Geophys. Space Phys.* **26**: 26–39.

Hanzlick, D. J. 1983. The west Spitsbergen Current: Transport, forcing and variability. Ph.D. Diss., Univ. of Washington, Seattle.

Hanzlick, D. J. & A. Aagaard. 1980. Freshwater and Atlantic water in the Kara Sea. *J. Geophys. Res.* **85**: 4937–4942.

Heezen , B., M. Tharp & C. Bently. 1972. "Morphology of the Earth in the Antarctic and

Subantarctic." Antarctic Map Folio Series, No. 16. American Geographic Society, New York.

Helland-Hansen, B. & F. Nansen. 1909. The Norwegian Sea. Its physical oceanography based upon the Norwegian researches 1900–1904. *Rep. Norw. Fish. Mar. Invest., Rep. Technol. Res.* **2**(Pt. 1, No. 2): 1–390.

Holloway, G. 1987. Systematic forcing of large-scale geophysical flows by eddy–topography interaction. *J. Fluid Mech.* **184:** 463–476.

Hood, D. W. & J. A. Calder. 1981. "The Eastern Bering Sea: Oceanography and Resources." U.S. Dept. of Commerce, Washington, D.C.

Hood, D. W. & E. J. Kelly. 1975. "Oceanography of the Bering Sea." Univ. of Alaska Press, Fairbanks.

Hopkins, T. S. 1988. "The GIN Sea: Review of Physical Oceanography and Literature since 1972," SR-124, pp. 1–190. SACLANT Undersea Research Centre, NATO, San Bartolomeo, Italy.

Horner, R. A., ed. 1985. "Sea-Ice Biota." CRC Press, Boca Raton, Florida.

Houssais, M.-N. 1988. Testing a coupled ice–mixed-layer model under subarctic conditions. *J. Phys. Oceanogr.* **18:** 196–210.

Hufford, G. L. 1973. Warm water advection in the southern Beaufort Sea, August–September 1971. *J. Geophys. Res.* **78:** 274–279.

———. 1974. On apparent upwelling in the southern Beaufort Sea. *JGR, J. Geophys. Res.* **79:** 1305–1306.

———. 1975. Some characteristics of the Beaufort Sea shelf current. *JGR, J. Geophys. Res.* **80:** 3465–3468.

Ingram, R. G. & P. Larouche. 1987. Variability of an under-ice river plume in Hudson Bay. *J. Geophys. Res.* **92:** 9541–9548.

Jacobs, S. S. 1985. Oceanographic evidence for land ice/ocean interactions in the Southern Ocean. *In* "Glaciers, Ice Sheets and Sea Level: Effect of CO_2-Induced Climatic Change," pp. 116–128. Report of a workshop, Sept. 13–15, 1984, Seattle, Washington. National Academy Press, Washington, D.C.

———. 1987. Injecting ice-shelf water and air into the deep Antarctic oceans. *Nature (London)* **321:** 196–197.

Jacobs, S. S. & D. T. Georgi. 1977. "Observations on the southwest Indian/Antarctic Ocean. *In* "A Voyage of Discovery" (M. V. Angel, ed.), pp. 43–84. Pergamon, Oxford.

Jacobs, S. S., A. F. Amos & P. M. Bruchhausen. 1970. Ross Sea oceanography and Antarctic bottom water formation. *Deep-Sea Res.* **17:** 935–962.

Jacobs, S. S., A. L. Gordon & A. F. Amos. 1979a. Effect of glacial ice melting on the Antarctic surface water. *Nature (London)* **277:** 469–471.

Jacobs, S. S., A. L. Gordon & J. L. Ardai. 1979b. Circulation and melting beneath the Ross Ice Shelf. *Science* **203:** 439–443.

Jacobs, S. S., R. G. Fairbanks & Y. Horibe. 1985. Origin and evolution of water masses near the Antarctic continental margin: Evidence from $H_2{}^{18}O/H_2{}^{16}O$ ratios in seawater. *Antarct. Res. Ser.* 59–85.

Jakhelln, A. 1936. Oceanographic investigation in East Greenland waters in the summers of 1930–1932. *Skr. Svalb. Ishavet* **6:** 1–79.

Johannessen, J. A., O. M. Johannessen, E. Svendsen, R. Shuchman, T. Manley, W. J. Campbell, E. G. Josberger, S. Sandven, J. C. Gascard, T. Olaussen, K. Davidson & J. Van Leer. 1987. Mesoscale eddies in the Fram Strait marginal ice zone during the 1983 and 1984 marginal ice zone experiments. *J. Geophys. Res.* **92:** 6754–6772.

Johannessen, O. M. 1986. Brief overview of the physical oceanography. *In* "The Nordic Seas" (B. G. Hurdle, ed.), pp. 103–127. Springer-Verlag, New York.

———. 1987. Introduction: Summer Marginal Ice Zone Experiments during 1983 and 1984 in Fram Strait and the Greenland Sea. *J. Geophys. Res.* **92:** 6716–6718.

Johnson, C. M. 1980. Wintertime Arctic sea-ice extremes and the simultaneous atmospheric circulation. *Mon. Weather Rev.* **108:** 1782–1791.

Jones, E. P. & L. G. Anderson. 1986. On the origin of the chemical properties of the Arctic Ocean halocline. *J. Geophys. Res.* **91:** 10,759–10,767.

Jones, E. P. & A. R. Coote. 1980. Nutrient distributions in the Canadian Archipelago: Indicators of summer water-mass and flow characteristics. *Can. J. Fish. Aquat. Sci.* **37:** 589–599.

Joyce, T. M., S. L. Patterson & R. C. Millard, Jr. 1981. Anatomy of a cyclonic ring in the Drake Passage. *Deep-Sea Res.* **28:** 1265–1287.

Kellogg, W. W. 1984. Possible effects of a global warming on Arctic sea ice, precipitation, and carbon balance. *In* "The Potential Effects of Carbon-Dioxide–Induced Climatic Changes in Alaska" (J. H. McBeath, ed.), pp. 59–66. Univ. of Alaska Press, Fairbanks.

Killerich, A. B. 1945. On the hydrography of the Greenland Sea. *Medd. Groenl.* **144:** 1–63.

Killworth, P. D. 1977. Mixing on the Weddell Sea continental slope. *Deep-Sea Res.* **24:** 427–448.

———. 1979. On "chimney" formations in the oceans. *J. Phys. Oceanogr.* **9:** 531–554.

———. 1983. Deep convection in the world ocean. *Rev. Geophys. Space Phys.* **21:** 1–26.

Killworth, P. D. & J. M. Smith. 1984. A one-and-a-half dimensional model for the Arctic halocline. *Deep-Sea Res.* **31:** 271–293.

Kinder, T. H., D. C. Chapman & J. A. Whitehead, Jr. 1986. Westward intensification of the mean circulation on the Bering Sea shelf. *J. Phys. Oceanogr.* **16:** 1217–1229.

Knox, F. & M. B. McElroy. 1984. Changes in atmospheric CO_2 influence of the marine biota at high latitudes. *J. Geophys. Res.* **89:** 4629–4637.

Kurtz, D. D. & D. H. Bromwich. 1983. Satellite observed behavior of the Terra Nova Bay polynya. *J. Geophys. Res.* **88:** 9717–9722.

Lazier, J. R. N. 1973. The renewal of Labrador Sea water. *Deep-Sea Res.* **20:** 341–353.

Lemke, P. 1987. A coupled one-dimensional sea ice–ocean model. *J. Geophys. Res.* **92:** 13,164–13,172.

Lemke, P. & T. O. Manley. 1984. The seasonal variation of the mixed layer and pycnocline under polar ice. *J. Geophys. Res.* **89:** 6494–6504.

Lemon, D. D. & D. B. Fissel. 1982. Seasonal variations in currents and water properties in northwestern Baffin Bay, 1978 and 1979. *Arctic* **35:** 211–218.

Lewis, E. L. 1982. The Arctic Ocean: Water masses and energy exchanges. *In* "The Arctic Ocean, the Hydrographic Environment and the Fate of Pollutants" (L. Rey, ed.), pp. 43–68. Comité Arctique International, Monaco.

———. 1987. Fifty years of progress in understanding sea ice. *J. Glaciol.* **33:** 48–51.

Losquinos, A. J. 1963. Extreme temperatures in the Weddell Sea. *Arbok Univ. Bergen, Mat.-Naturvitensk. Ser.* **23:** 1–19.

Macdonald, R. W., C. S. Wong & P. E. Erickson. 1987. The distribution of nutrients in the southeastern Beaufort Sea: Implications for water circulation and primary production. *J. Geophys. Res.* **92:** 2939–2952.

Macdonald, R. W., E. C. Carmack, F. A. McLaughlin, M. O'Brian & J. E. Papadakis. 1989. Composition and modification of water masses in the Mackenzie shelf/estuary. *J. Geophys. Res.* **94:** 18,057–18,070.

Mackay, D. K. & O. H. Loken. 1974. Arctic hydrology. *In* "Arctic and Alpine Environments" (J. D. Ives & R. G. Barry, eds.), pp. 111–132. Methuen, London.

Manabe, S. & R. T. Wetherald. 1980. On the distribution of climate change resulting from an increase in CO_2 content of the atmosphere. *J. Atmos. Sci.* **37:** 99–118.

Manley, T. O. & K. L. Hunkins. 1987. Current regimes across the East Greenland Polar Front at 78°40′N. latitude during summer, 1984. *J. Geophys. Res.* **92**: 6741–6758.

Marotzke, J., P. Welander & J. Willebrand. 1988. Instability and multiple steady states in a meridional-plane model of the thermohaline circulation. *Tellus* **40**: 162–172.

Martinson, D. G., P. D. Killworth & A. L. Gordon. 1981. A convective model of the Weddell Polynya. *J. Phys. Oceanogr.* **11**: 466–488.

Maykut, G. A. 1985. "An Introduction to Ice in the Polar Oceans," Tech. Rep. APL-UW8510. Univ. of Washington, Seattle.

Maykut, G. A. 1986. The ice environment. *In* "Sea-Ice Biota," (R. A. Horner, ed.), pp. 21–82. CRC Press, Boca Raton, Florida.

McDougall, T. J. 1983. Greenland Sea bottom water formation: A balance between advection and double-diffusion. *Deep-Sea Res.* **30**: 1109–1117.

McRoy, C. P., D. W. Hood, L. K. Coachman, J. J. Walsh & J. J. Goering. 1986. Processes and resources of the Bering Sea shelf (PROBES): The development and accomplishments of the project. *Cont. Shelf Res.* **5**: 5021.

Meier, M. F. 1983. Snow and ice in a changing hydrological world. *Hydrol. Sci. J.* **28**: 3–22.

———. 1985. The ice environment. *In* "Sea-Ice Biota" (R. A. Horner, ed.), pp. 21–82. CRC Press, Boca Raton, Florida.

Melling, H. & E. L. Lewis. 1982. Shelf drainage flows in the Beaufort Sea and their effect on the Arctic Ocean pycnocline. *Deep-Sea Res.* **29**: 967–985.

Melling, H., R. A. Lake, D. R. Topham & D. B. Fissel. 1984. Oceanic thermal structure in the western Canadian Arctic. *Cont. Shelf Res.* **3**: 233–258.

Metcalf, W. G. 1955. On the formation of bottom water in the Norwegian basin. *Eos* **36**: 595–600.

Midttun, L. 1985. Formation of dense bottom water in the Barents Sea. *Deep-Sea Res.* **32**: 1233–1241.

Milligan, D. B. 1969. Oceanographic survey results for the Kara Sea: Summer and fall, 1965. U.S. Navy Hydrographic Office Tech. Rep. 217.

Milliman, J. D. & R. H. Meade. 1983. World-wide delivery of river sediment to the oceans. *J. Geol.* **91**: 1–21.

Mohn, H. 1887. The north ocean, its depths, temperature and circulation. *Norw. North Atl. Exped., 1876–1878* **2**(2).

Montgomery, R. B. 1958. Water characteristics of Atlantic Ocean and of world ocean. *Deep-Sea Res.* **5**: 134–148.

Moore, R. M. & D. W. R. Wallace. 1988. A relationship between heat transfer to sea ice and temperature–salinity properties of Arctic Ocean waters. *J. Geophys. Res.* **93**: 565–571.

Morison, J. H. & J. D. Smith. 1981. Seasonal variations in the upper Arctic Ocean as observed at T-3. *Geophys. Res. Lett.* **8**: 753–756.

Moritz, R. E. 1988. "The Ice Budget of the Greenland Sea," Tech. Rep. APL-UW TR8812. Appl. Phys. Lab., Univ. of Washington, Seattle.

Mosby, H. 1934. The waters of the Atlantic Antarctic Ocean. *Sci. Results Norw. Antarct. Exped. 1927–1928* **1**: 1–131.

———. 1959. Deep water in the Norwegian Sea. *Geophys. Norv.* **21**: 1–62.

———. 1962. Water, salt and heat balance of the North Polar Sea and of the Norwegian Sea. *Geophys. Norv.* **24**: 289–313.

———. 1966. Bottom water formation. *In* "Symposium on Antarctic Oceanography," pp. 47–57. Polar Res. Inst. Sci. Comm. Antarctic Res., Santiago, Chile.

Motoi, T., N. Ono & M. Wakatsuchi. 1987. A mechanism for the formation of the Weddell Polynya in 1974. *J. Phys. Oceanogr.* **17**: 2241–2247.

Mountain, D. G. 1974. Bering Sea water on the North Alaskan shelf. Ph.D. Diss., Univ. of Washington, Seattle.

Muench, R. D. 1971. The physical oceanography of the northern Baffin Bay region. The Baffin Bay–North Water Project. *Arctic Inst. North Am., Sci. Rep.* **1:** 1–150.

Muench, R. D., S. Martin & J. E. Overland. 1987. Preface. *J. Geophys. Res.* **92:** 6715.

Muench, R. D., J. D. Schumacher & S. A. Salo. 1988. Winter currents and hydrographic conditions on the northern central Bering Sea shelf. *J. Geophys. Res.* **93:** 516–526.

Munk, W. H. & E. Palmen. 1951. Note on the dynamics of the Antarctic Circumpolar Current. *Tellus* **3:** 53–55.

Nansen, F. 1906. Northern waters: Captain Roald Amundsen's oceanographic observations in the Arctic seas in 1901. *Skr., Nor. Vidensk.-Akad. [Kl.] I: Mat.-Naturvidensk. Kl.* **1:** 1–145.

Nelson, D. M., W. O. Smith, Jr., L. I. Gordon & B. A. Huber. 1987. Spring distributions of density, nutrients and phytoplankton biomass in the ice-edge zone of the Weddell/Scotia Sea. *J. Geophys. Res.* **92:** 7181–7190.

Newton, J. L. 1973. The Canada basin: Mean circulation and intermediate scale flow features. Ph.D. Diss., Univ. of Washington, Seattle.

Nikiforov, Y. G., Y. V. Belysheva & N. I. Blinov. 1966. The structure of water masses in the eastern part of the Arctic basin. *Oceanology (Engl. Transl.)* **6:** 59–64.

Nowlin, W. D., Jr. & J. M. Klinck. 1986. The physics of Antarctic Circumpolar Current. *Rev. Geophys. Space Phys.* **24:** 469–491.

Nowlin, W. D., Jr., T. Whitworth & R. D. Pillsbury. 1977. Structure and transport of the Antarctic Circumpolar Current at Drake Passage from short-term measurements. *J. Phys. Oceanogr.* **7:** 788–802.

Ostlund, H. G. 1982. The residence time of the fresh water component in the Arctic Ocean. *J. Geophys. Res.* **87:** 2035–2043.

Ostlund, H. G. & G. Hut. 1984. Arctic Ocean water mass balance from isotope data. *J. Geophys. Res.* **89:** 6373–6381.

Ostlund, H. G., G. Possnert & J. H. Swift. 1987. Ventilation rate of the deep Arctic Ocean from carbon 14 data. *J. Geophys. Res.* **92:** 3769–3777.

Overland, J. E. & A. T. Roach. 1987. Northward flow in the Bering and Chukchi seas. *J. Geophys. Res.* **92:** 7097–7105.

Paquette, R. G. & R. H. Bourke. 1974. Observations on the coastal current of Arctic Alaska. *J. Mar. Res.* **32:** 195–207.

———. 1979. Temperature find structure near the sea-ice margin of the Chukchi Sea. *J. Geophys. Res.* **84:** 1155–1164.

———. 1981. Ocean circulation and fronts as related to ice melt-back in the Chukchi Sea. *J. Geophys. Res.* **86:** 4215–4230.

Paquette, R. G., R. H. Bourke, J. F. Newton & W. F. Perdue. 1985. The east Greenland Polar Front in autumn. *J. Geophys. Res.* **90:** 4866–4882.

Perkin, R. G. & E. L. Lewis. 1984. Mixing in the West Spitzbergen Current. *J. Phys. Oceanogr.* **14:** 1315–1325.

Peterson, W. H. & C. G. H. Rooth. 1976. Formation and exchange of deep water in the Greenland and Norwegian seas. *Deep-Sea Res.* **23:** 273–283.

Pfirman, S. L. 1985. Modern sedimentation in the northern Barents Sea: Input dispersal and deposition of suspended sediments from glacial meltwater. Ph.D. Diss., Woods Hole Oceanogr. Inst., Woods Hole, Massachusetts.

Pinther, M., B. C. Heezen & M. Tharp. 1975. "Map of the Arctic Region." American Geographic Society, New York.

Platt, T., W. G. Harrison, B. Irwin, E. Horne & C. Gallegos. 1982. Photosynthesis and photoadaptation of marine phytoplankton in the Arctic. *Deep-Sea Res.* **29:** 1159–1170.

Polar Group. 1980. Polar atmosphere–ice–ocean processes: A review of polar problems in climate research. *Rev. Geophys. Space Phys.* **18:** 525–543.

Prinsenberg, S. J. 1983. Effects of the hydroelectric developments on the oceanographic surface parameters of Hudson Bay. *Atmos. Oceanogr.* **21**: 418–430.

———. 1986. Salinity and temperature distributions of Hudson Bay and James Bay. *In* "Inland Coastal Seas" (I. P. Martini, ed.), pp. 163–186. Am. Elsevier, New York.

Prinsenberg, S. J. & E. B. Bennett. 1988. Mixing and transports in Barrow Strait, the central part of the Northwest Passage. *Cont. Shelf Res.* **7**: 913–935.

Quadfasel, D. & J. Meincke. 1987. Note on the thermal structure of the Greenland Sea gyres. *Deep-Sea Res.* **34**: 1883–1888.

Quadfasel, D., J.-C. Gascard & K.-P. Koltermann. 1987. Large scale oceanography in Fram Strait during the 1984 Marginal Ice Zone Experiment. *J. Geophys. Res.* **92**: 6719–6728.

Quadfasel, D., B. Rudels & K. Kurz. 1988. Outflow of dense water from a Svalbard fjord into Fram Strait. *Deep-Sea Res.* **35**: 1143–1150.

Rahn, K. A. 1981. Atmospheric, riverine and oceanic transport of trace elements to the Arctic Ocean. *Atmos. Environ.* **15**: 1507–1516.

Reid, J. L. 1979. On the contribution of the Mediterranean sea outflow to the Norwegian–Greenland Sea. *Deep-Sea Res.* **26**: 1199–1223.

Reid, J. L. & R. J. Lynn. 1971. On the influence of the Norwegian–Greenland and Weddell seas upon the bottom waters of the Indian and Pacific oceans. *Deep-Sea Res.* **18**: 1063–1088.

Reid, J. L., W. D. Nowlin & W. C. Patzert. 1977. On the characteristics and circulation of the southwestern Atlantic Ocean. *J. Phys. Oceanogr.* **7**: 62–91.

———. 1986a. The theta-S relations in the northern seas: Implications for the deep circulation. *Polar Res.* **4**: 133–159.

Rudels, B. 1986b. The outflow of polar water through the Arctic Archipelago and the oceanographic conditions in Baffin Bay. *Polar Res.* **4**: 161–180.

———. 1987. On the mass balance of the polar ocean with special emphasis on the Fram Strait. *Skr., Nor. Polarinst.* **188**: 1–53.

———. 1989. Haline convection in the Greenland Sea. *Deep-Sea Res.* (in press).

Sadler, H. E. 1976. Water, heat and salt transports through Nares Strait, Ellesmere Island. *J. Fish. Res. Board Can.* **33**: 2286–2295.

Sarmiento, F. & J. R. Toggweiler. 1984. A new model for the role of the oceans in determining atmospheric P-CO_2. *Nature (London)* **308**: 621–624.

Sayles, M. A., K. Aagaard & L. K. Coachman. 1979. "Oceanographic Atlas of the Bering Sea Basin." Univ. of Washington Press, Seattle.

SCOR Working Group 58. 1979. "The Arctic Ocean Heat Budget," Rep. No. 52. Geophys. Inst., Univ. of Bergen, Bergen, Norway.

Seabrooke, J. M., G. L. Hufford & R. B. Elder. 1971. Formation of Antarctic bottom water in the Weddell Sea. *JGR, J. Geophys. Res.* **76**: 2164–2178.

Semtner, A. J. 1976. Numerical simulation of the Arctic Ocean circulation. *J. Phys. Oceanogr.* **6**: 409–425.

———. 1984a. On modeling the seasonal thermodynamic cycle of the sea ice in studies of climatic change. *Clim. Change* **6**: 27–38.

———. 1984b. The climatic response on the Arctic Ocean to Soviet river diversions. *Clim. Change* **6**: 109–130.

———. 1987. Numerical study of sea ice and ocean circulation in the Arctic. *J. Phys. Oceanogr.* **17**: 1077–1099.

Sievers, H. A. & W. D. Nowlin, Jr. 1984. The stratification and water masses at Drake Passage. *J. Geophys. Res.* **89**: 10,489–10,514.

Smethie, W. M., Jr., H. G. Ostlund & H. H. Loosli. 1986. Ventilation of the deep Greenland and Norwegian seas: Evidence from krypton-85, tritium, carbon-14 and argon-39. *Deep-Sea Res.* **33**: 675–703.

Smethie, W. M., Jr., D. W. Chipman, J. H. Swift & K. P. Koltermann. 1988. Chlorofluoromethanes in the Arctic Mediterranean seas: Evidence for formation of bottom water in the Eurasian basin and deep-water exchange through Fram Strait. *Deep-Sea Res.* **35**: 347–369.

Smith, W. O., Jr. 1987. Phytoplankton dynamics in marginal ice zones. *Oceanogr. Mar. Biol.* **25**: 11–38.

Solomon, H. 1973. Wintertime surface layer convection in the Arctic Ocean. *Deep-Sea Res.* **20**: 269–283.

———. 1974. Comments on the Antarctic bottom water problem and high-latitude thermohaline sinking. *JCR, J. Geophys. Res.* **79**: 881–884.

———. 1983. Vertical mixed layer convection in the Weddell Sea. *Atmos.-Ocean* **21**: 187–206.

Spaulding, M., T. Isaji, D. Mendelsohn & A. C. Turner. 1987. The numerical simulation of wind-driven flow through the Bering Strait. *J. Phys. Oceanogr.* **17**: 1799–1816.

Steffen, K. 1986. Ice conditions of an Arctic polynya: North Water in winter. *J. Glaciol.* **32**: 386–390.

Steffen, K. & A. Ohmura. 1985. Heat exchange and surface conditions in the North Water, northern Baffin Bay. *Ann. Glaciol.* **6**: 178–181.

Stigebrandt, A. 1981. A model for the thickness and salinity of the upper layer in the Arctic Ocean and the relationship between the ice thickness and some external parameters. *J. Phys. Oceanogr.* **11**: 1407–1422.

Stommel, H. 1957. A survey of ocean current theory. *Deep-Sea Res.* **4**: 149–184.

Sverdrup, H. U. 1929. The waters on the North-Siberian Shelf. The Norwegian North Polar Expedition with the "Maud" 1918–25. *Sci. Results* **4**: 1–131.

———. 1940. Hydrology. Section 2. Discussion. *Rep. B.A.N.Z. Antarct. Exped. 1921–1931, Ser. A* **3** (Part 2): 89–126.

———. 1953. The currents of the coast of Queen Maud Land. *Nor. Geogr. Tidsskr.* **14**: 239–249.

Swift, J. H. 1986. The Arctic waters. *In* "The Nordic Seas" (B. G. Hurdle, ed.), pp. 129–154. Springer-Verlag, New York.

Swift, J. H. & K. Aagaard. 1981. Seasonal transitions and water mass formation in the Iceland and Greenland seas. *Deep-Sea Res.* **28**: 1107–1129.

Swift, J. H. & K. P. Koltermann. 1988. The origin of Norwegian Sea deep water. *J. Geophys. Res.* **93**: 3563–3569.

Swift, J. H., T. Takahashi & H. D. Livingston. 1983. The contribution of the Greenland and Barents seas to the deep water of the Arctic Ocean. *J. Geophys. Res.* **88**: 5981–5986.

Szekielda, K. H. 1974. The hot spot in the Ross Sea: Upwelling during wintertime. *Tethys* **6**: 105–110.

Tchernia, P. & P. F. Jeanin. 1984. Circulation in Antarctic waters as revealed by iceberg tracks 1972–1983. *Polar Rec.* **22**: 263–269.

Timofeyev, V. T. 1962. The movement of Atlantic water and heat into the Arctic sea basin. *Deep-Sea Res.* **9**: 358–361.

———. 1963. Interaction of the Arctic Ocean waters with Atlantic and Pacific waters. *Okeanologiya (Moscow)* **3**: 569–578. (Engl. trans.).

Toole, J. M. 1981. Sea-ice winter convection and the temperature minimum layer in the Southern Ocean. *J. Geophys. Res.* **86**: 8037–8047.

Trangeled. 1974. Oceanography of the Norwegian and Greenland Seas and adjacent areas. Volume 2: Survey of 1870–1970 literature. SACLANTCEN SM-4, SACLANT, La Spezia, Italy.

Treshnikov, A. F. 1977. Water masses of the Arctic basin. *In* "Polar Oceans" (M. Dunbar, ed.), pp. 17–31. Arctic Inst. North Am., Calgary, Alberta, Canada.

———. 1985. "Atlas Arktiki. Arkt.-Antarkt." Nauchno-Issled. Inst., Moscow.

Treshnikov, A. F. & G. I. Baranov. 1976. Structure of water circulation and dynamics of the water budget of the North Polar region. *Prob. Arktiki Antarkt.* **47:** 93–100.

UNESCO. 1978. "World Water Balance and Water Resources of the Earth," Stud. Rep. Hydrol., No. 25. UNESCO, Paris.

Untersteiner, N. 1984. The cyosphere. *In* "The Global Climate" (J. T. Houghton, ed.), pp. 121–140. Cambridge Univ. Press, London and New York.

———. 1988. On the ice and heat balance in Fram Strait. *J. Geophys. Res.* **93:** 527–531.

Vinje, T. K. & O. Finnekasa. 1986. The ice transport through the Fram Strait. *Skr., Nor. Polarinst.* **186:** 1–39.

Wadhams, P. 1983. Sea-ice thickness distribution in Fram Strait. *Nature (London)* **305:** 108–111.

———. 1986. The ice cover. *In* "The Nordic Seas" (B. G. Hurdle, ed.), pp. 21–84. Springer-Verlag, New York.

Wadhams, P., A. E. Gill & P. F. Linden. 1979. Transect by submarine of the East Greenland Polar Front. *Deep-Sea Res.* **26:** 1311–1327.

Wallace, D. W. R., E. P. Jones & R. M. Moore. 1988. Ventilation of the Arctic Ocean cold halocline: Rates of diapycnal and isopycnal transport, oxygen utilization and primary production inferred using chlorofluoromethane distributions. *Deep-Sea Res.* **34:** 1957–1979.

Walsh, J. E. 1983. The role of sea ice in climatic variability: Theories and evidence. *Atmos.-Oceanogr.* **21:** 229–242.

Walsh, J. E. & C. M. Johnson. 1979. Interannual atmospheric variability and associated fluctuations in Arctic Sea ice extent. *J. Geophys. Res.* **84:** 6915–6928.

Weiss, R. F., H. G. Ostlund & H. Craig. 1979. Geochemical studies of the Weddell Sea. *Deep-Sea Res.* **26:** 1093–1120.

Weyl, P. K. 1968. The role of the oceans in climate change. *Meteorol. Monogr.* **8:** 37–62.

Whitworth, T., III. 1980. Zonation and geostrophic flow of the Antarctic Circumpolar Current at Drake Passage. *Deep-Sea Res.* **27:** 497–508.

Whitworth, T., III. 1983. Monitoring the transport of the Antarctic Circumpolar Current at Drake Passage. *J. Phys. Oceanogr.* **13:** 2045–2057.

Whitworth, T., III & W. D. Nowlin, Jr. 1987. Water masses and currents of the southern Ocean at the Greenwich meridian. *J. Geophys. Res.* **92:** 6462–6476.

Whitworth, T., III & R. G. Peterson. 1985. Volume transport of the Antarctic Circumpolar Current from bottom pressure measurements. *J. Phys. Oceanogr.* **15:** 810.

Woods, J. D. 1984. The upper ocean and air–sea interaction in global climate. *In* "The Global Change" (J. T. Houghton, ed.), pp. 141–187. Cambridge Univ. Press, London and New York.

Worthington, L. V. 1970. The Norwegian Sea as a Mediterranean basin. *Deep-Sea Res.* **17:** 77–84.

Wust, G. 1933. Das Bodenwasser und die Gliederung der atlantischen Tiefsee. *Wiss. Ergeb. Dtsch. Atlanti. Expedi. 'Meteor'* **9:** 1–107.

Zakharov, V. F. 1987. Sea ice and climate. *In* "Interaction Between the Atmosphere and the Oceans and Ice Sheets," pp. 66–89. Arctic and Antarctic Institute, Lenningrad.

Zubov, N. N. 1945. "Arctic Ice." Glavsevmorputi, Moscow.

Zwally, H. J., C. L. Parkinson & J. C. Comiso. 1983. Variability of Antarctic sea ice and CO_2 change. *Science* **220:** 1005–1012.

Zwally, H. J., J. C. Comiso & A. L. Gordon. 1985. Antarctic offshore leads and polynyas and oceanographic effects. *Antarct. Res. Ser.* **43:** 203–226.

5 Mesoscale Phenomena in the Polar Oceans

Robin D. Muench
Science Applications International Corporation
Bellevue, Washington

I. Introduction 223
A. Overview 223
B. Some Scale and Dynamical Considerations 224
C. Large-Scale Distribution of Mesoscale Features 227
II. Frontal Systems 229
A. Overview 229
B. Eastern Arctic Fronts 230
C. Western Arctic Frontal Systems 238
D. Antarctic Frontal Systems 243
E. Frontal Structures in Polar Basins 247
III. Mesoscale Eddies 250
A. Overview 250
B. Eddies in the Eastern Arctic 252
C. Eddies in the Western Arctic 261
D. Eddies in the Antarctic 264
IV. Some Consequences of Mesoscale Processes 269
A. Lateral Fluxes 269
B. Vertical Fluxes 272
V. Polynyas: A Special Case 273
A. Polynyas Defined 273
B. Latent-Heat Polynyas 274
C. Sensible-Heat Polynyas 277
VI. Concluding Comments 279
References 280

I. Introduction

A. Overview

Mesoscale phenomena occur throughout the world's oceans and dominate spatial scales between the basinwide gyres and, at the other extreme, small-scale features such as internal waves. Intrinsic time scales for these phenom-

Polar Oceanography, Part A: Physical Science

ena (i.e., scales which are determined by the internal physics) fall between seasonal and those associated with small-scale processes. Mesoscale phenomena include such physical features as frontal systems and associated currents, boundary currents, current jets, meanders, and eddies. Many of these features share specific dynamic constraints, so it is feasible to consider them under a single heading.

A phenomenological emphasis is present in this chapter, in anticipation of a diverse readership. This approach is intended to be understandable to nonphysical oceanographers while at the same time providing a reasonably comprehensive list of additional references for those wishing to explore further some dynamical aspects of mesoscale processes. Discussion of dynamics is limited primarily to a brief introductory section which reviews some basic concepts necessary for understanding the material presented in later sections. The physical oceanographer interested in pursuing dynamical aspects of the various phenomena discussed will find these aspects treated in detail in the general reference works (Pedlosky, 1982; Gill, 1982) and in the references addressing specific features.

A short section (Section V) is included on the topic of polynyas. These features occur only in the polar regions and are superficially mesoscale based on their length and time scales, if not necessarily their dynamics. They are included because conventional wisdom holds that they may play significant roles in regional oceanographic processes.

For convenience in presentation and discussion, mesoscale phenomena are divided in this chapter into fronts and eddies. This conceptually useful division is artificial, because mesoscale phenomena in fact occupy a continuum from frontal systems through meanders to eddies. It must also be pointed out that mesoscale features in the polar regions are, with the exception of polynyas, generally similar physically and dynamically to those found elsewhere in the world ocean. Discussion of these features as polar oceanographic processes is valid only within the context of a volume dealing specifically with polar oceanography.

The topics treated in this chapter are subjects of intensive ongoing research activity. The motivation for this research can be found in the various, often conflicting, hypotheses which are presented. The goal of this chapter is therefore to define problems and to assess their present level of understanding rather than to present final conclusions.

B. Some Scale and Dynamical Considerations

Oceanic mesoscale features typically have horizontal scales from about 10 to 200 km. The western Arctic Ocean basin contains numerous eddies approximately 10 km in diameter. Meanderlike features with wavelengths from 100

to 200 km have been observed in the winter Labrador Sea marginal ice zone. Permanent fronts such as the East Greenland Polar Front and the Antarctic frontal systems generally exhibit meanders and eddies with length scales falling between these extremes. Vertically, such features can either be restricted to the upper layers of the water column or extend to great depths.

Time scales for mesoscale features are subject to considerably greater uncertainty than the spatial scales, which can be measured directly. Permanent oceanic frontal systems such as the East Greenland Polar Front are affected by processes having time scales from a few days to decades. At the high-frequency end of this spectrum, features with time scales in the 2–10-day range are often found in fronts with fluctuations generated by internal dynamical processes or by external meteorological forcing. Eddy time scales are generally characterized as the periods from eddy formation to final loss of identity through mixing and frictional dissipation. These time scales, which are typically of order several months in the temperate oceans, have been directly observed only in cases where it has been possible to track the eddy from its formation through decay phases. This has not in general been possible in the polar regions. We do, however, suspect that the decay rates may be higher and time scales shorter in ice-covered water than in the open ocean because of frictional interaction with the surface sea ice cover and its contribution to decay of the eddy.

Mesoscale motions are quasi-geostrophic; that is, an approximate balance exists between horizontal pressure gradient and Coriolis forces. Effects of friction, time variability, and latitudinal change in the vertical component of the earth's rotation are assumed to be small relative to the pressure gradient and Coriolis forces. The minimum length scale typifying a mesoscale process can be defined by the internal Rossby radius of deformation. This parameter can be derived from conservation of potential vorticity in the steady case where Coriolis and pressure gradient accelerations are balanced (see Pedlosky, 1982). The radius of deformation is defined for a stratified fluid by

$$a = (g\,\Delta\rho\,h/\rho)^{1/2}/f \tag{5.1}$$

where h is the vertical scale length for the fluid motion, f the vertical component of the earth's rotation rate, g the acceleration due to gravity, and $\Delta\rho/\rho$ a characteristic density difference ratio for the fluid over the vertical scale h. If the fluid is vertically homogeneous, internal oscillations are excluded. The expression for the external radius of deformation is now applied to features which are independent of depth and reduces to

$$a_e = (gh)^{1/2}/f \tag{5.2}$$

For length scales small compared with a, the effects of the earth's rotation on flow are small. If length scales are equal to or greater than a, then rotational

effects become as important as the pressure gradient effects. Typical values of a for a stratified fluid, the "internal" radius of deformation and that most appropriate to mesoscale processes, are 5 – 10 km. Values of a_e, for a homogeneous fluid, are much larger and can be of order 1000 km or more.

Mesoscale oceanic features can exhibit both baroclinic and barotropic behavior. The former are associated with internal density distributions and vary with depth, whereas the latter are invariant with depth. Baroclinic behavior typically dominates such features as the near-surface, highly stratified, localized fronts and eddies which are found along melting ice edges. Associated currents decrease rapidly with increasing depth, and the internal radius of deformation is an appropriate cross-frontal length scale. Eddies and fronts may also exhibit barotropic behavior wherein the associated currents penetrate to the seabed. Barotropic currents tend, through conservation of potential vorticity, to parallel bottom contours. It is this tendency which causes such major mesoscale features as the East Greenland Polar Front to parallel the underlying steep continental slope. Primarily baroclinic features such as eddies are often found embedded within a flow field having a significant barotropic component. Such systems, which can be typified by the East Greenland Current/Polar Front system, can be exceedingly complex.

Mesoscale currents, in particular those associated with energetic frontal systems, frequently exhibit long-period fluctuations (on the order of several days) in speed and/or direction which are not related to the more obvious external forcing mechanisms such as winds. Fluctuations have been observed over a broad range of time scales, but 3 – 5 days seems typical for energetic oceanic frontal systems. These disturbances appear first as meanders. If they continue to grow, they may detach to form discrete eddies. The meanders or eddies propagate at speeds (0.5 m/s or less is typical) which are controlled by the internal dynamics. Wavelengths and amplitudes of the disturbances can become large, of order 100 km or more. These fluctuations can in many cases be explained in terms of a broad class of processes referred to as dynamic instabilities. Such processes reflect a transfer of potential or kinetic energy from the mean internal density or flow fields into fluctuating kinetic energy which manifests itself as oscillations. This can occur via two general mechanisms. One is baroclinic instability, whereby potential energy is transferred from the density field associated with the mean flow into fluctuating kinetic energy. The second is barotropic instability, wherein the energy source is a horizontally sheared mean flow. In either case, under the proper conditions the fluctuations can grow and lead to increasingly energetic fluctuations in the mean flow.

These mechanisms for energy transfer are dealt with by instability theory, which addresses the ability of fluctuating disturbances embedded in a cur-

rent to grow at the expense of the mean flow. The capacity for such growth depends on certain initial conditions, such as vertical and lateral shear of the mean flow field and the associated internal density field, and on external constraints such as the local seafloor topography. A summary mathematical treatment of this theory is beyond the scope of this chapter, and the reader is referred to thorough discussions in Pedlosky (1982) and Gill (1982).

Instability mechanisms have proved consistently difficult to study in the field. The very presence of instabilities will have altered the mean flow from its original unperturbed state. Any attempt to demonstrate that a dynamic instability is responsible for transfer of energy from mean to fluctuating flow is at best difficult, because there is no way to determine the initial, unperturbed flow condition. In past work, a demonstration that the observed fluctuations were successfully predicted by instability theory given an assumed initial mean flow has generally been accepted as strong evidence that the fluctuations were due to dynamic instabilities (e.g., Mysak *et al.*, 1981). Energy balance arguments can provide another form of evidence for instabilities (e.g., Thomson, 1984). A mesoscale cross-stream downgradient heat flux provides evidence that the flow is baroclinically unstable (e.g., Bryden, 1979; Foldvik *et al.*, 1988).

Mechanisms other than instabilities can lead to flow fluctuations. The most obvious involve local meteorological forcing. In many cases, however, these fluctuations remain of uncertain origin. Specific cases will be dealt with in the more detailed discussions below.

C. Large-Scale Distribution of Mesoscale Features

Mesoscale features have been observed in many but not all parts of the polar oceans. This very general statement needs, however, to be qualified. Much of the information from polar regions is based on historical data obtained from large, multidisciplinary expeditions which were concerned primarily with defining large-scale oceanic features. Many of the data are from permanently ice-covered regions, such as the central Arctic Ocean and western Weddell Sea. In these regions the data density is typically too low to allow identification of mesoscale features because the features themselves have spatial scales smaller than the spacing between data points. For example, a strong frontal system 20 km in width would be identified, if at all, only as a region of somewhat increased horizontal gradient if the data points were 50 km apart. This limitation is especially pronounced for much of the historical data from the Antarctic, where oceanographic stations were often spaced at intervals of more than 100 km.

Keeping in mind the above caveat, mesoscale features are most numerous and energetic near the equatorward boundaries of the polar regions. These features decrease in both number and energy toward the poles. The boundaries can be either dynamic, such as ocean fronts, or physical, such as the continental margins.

The most numerous and energetic mesoscale phenomena in the polar regions occur in association with permanent oceanic frontal systems. These systems generally coincide during at least part of the year with the marginal ice zones, which are transition regions between ice-covered and ice-free waters and have width scales on the order of 100 km. Examples are the East Greenland Polar Front, which coincides in summer with the marginal ice zone (MIZ), and the Scotia Front in the southern Scotia Sea, which coincides in austral winter with the marginal ice zone. Both of these frontal systems have associated currents and numerous meanderlike features and eddies.

In the absence of permanent oceanic fronts, the marginal ice zones are typically characterized by frontal activity which is of a more localized and seasonal nature. For example, the summer Chukchi Sea and winter Bering Sea marginal ice zones are associated with strong fronts and current jets. These regions are shallow marginal seas, and the fronts are sustained by local input of meltwater from the sea ice as it melts along the ice edge. Similar fronts occur in the near-surface layers of deep waters in the central Weddell and Ross seas during the summer ice retreat.

Regardless of their origins, frontal systems frequently have associated currents which parallel the fronts and reflect frontal temperature and salinity structures. These currents are at least as wide as the local internal radii of deformation (typically 5–10 km) and are frequently subject to dynamic instabilities which yield the numerous mesoscale eddies which have been observed in the MIZs. Other mechanisms for eddy generation include interactions between barotropic mean currents and the bottom topography and interactions among local winds, the ice edge, and the underlying water. Both the East Greenland and Scotia sea marginal ice zones contain, for example, mesoscale eddies associated at least in part with fronts.

Continental margins and isolated bottom topographic features can serve as loci for mesoscale activity. Coastal current systems are dynamically constrained, in general, to within an internal radius of the coastline. These currents can be as narrow as a few kilometers and have speeds up to several tens of centimeters per second. Interaction between an energetic coastal current and complex coastline configuration may contribute to generation of eddies. Major ocean fronts such as the East Greenland Polar Front interact dynamically with the continental slope and exhibit a wide variety of mesoscale phenomena. Dynamic interactions between the barotropic component

of the mean flow and bottom features lead to mesoscale feature development in both central Fram Strait and Drake Passage.

The central ocean basins in polar regions provide a stark contrast to the mesoscale feature-rich surrounding waters. Little mesoscale activity has been detected in the eastern basin of the Arctic Ocean. In the western basin, activity appears limited to eddies which may originate along the northern Alaskan coastline. The limited data available from the central Weddell Sea suggest that there is little in the way of mesoscale activity there. However, it is impossible to determine the extent to which this apparent lack of mesoscale activity reflects paucity of data, but physical reasoning supports the general absence of such features. The permanent ice cover can be expected to damp upper-layer currents frictionally through internal dissipation, which decreases the current speeds and shear usually associated with mesoscale features. Existing information on boundary currents, such as that along the Antarctic Peninsula in the western Weddell Sea, suggests that these are considerably less energetic than their temperate counterparts, so that less energy is available for generation of mesoscale phenomena. In most cases, however, we simply have insufficient data from the permanently ice-covered regions to quantify mesoscale energy levels.

In summary, the presently known distribution of mesoscale activity in the polar regions suggests that mesoscale features are generated around the energetic boundaries and propagate into the interior basins, decreasing in energy as they migrate away from the boundaries. The data are at present inadequate to fully support or to quantify this hypothesis. The remainder of this chapter describes and discusses specific processes in the various polar ocean regions.

II. Frontal Systems

A. Overview

Frontal systems are among the most obvious of oceanic features and have received considerable attention even in the relatively inaccessable polar seas. Fronts have strong lateral gradients, and frequently vertical gradients as well, in temperature and salinity. The internal density fields reflect these gradients, and the strong ensuing density gradients are typically associated with energetic currents which parallel the fronts. The gradients in water properties across a front can create easily observable surface variations such as color changes or changes in surface wave height. Fronts in the polar regions are often associated with the ice edges. These ice edge fronts are particularly

obvious because the pack ice edge forms a readily observed physical boundary.

Fronts occur usually, but not always, along boundaries between water masses. (The alternative is a "structural front", an example of which occurs on the southeastern Bering Sea shelf.) Regional circulation must maintain the cross-frontal gradients. In other words, water on either side of the front must be continually replenished for the front to persist in the presence of mixing processes which would otherwise dissipate the gradients which define the front. In the polar regions, the primary water masses can be classified in general as two types: those flowing northward from the temperate oceans, and south-flowing waters which have been modified in the polar regions through cooling and (in the upper layers, at least) freshening through addition of low-salinity water from seasonal ice melt. In the northern hemisphere, major frontal systems separate the waters of the North Atlantic from the waters of the Arctic Ocean. In the southern hemisphere, fronts separate the cold waters of the Southern Ocean from the warmer waters of the southern Atlantic, Pacific and Indian oceans. The discussion below is divided regionally, partly for convenience and also because there are some regional differences between fronts, into eastern Arctic, western Arctic, Antarctic, and central polar basin.

B. Eastern Arctic Fronts

The major eastern Arctic polar front is found in the Greenland sea. This front, the East Greenland Polar Front, extends in a southerly direction through Fram Strait, then continues southward along the Greenland continental margin (Fig. 5.1). The front is wedge-shaped in cross section and bounded by the Greenland continental slope, the sea surface, and a sloping interface which either intersects the seabed at about 200 m depth or levels off between 200 and 300 m (Fig. 5.2). It is widest in the north, narrowing toward the south as it impinges on the steep Greenland continental slope south of about 80°N. At its narrowest the front is about 50 km wide, measured in the cross-frontal direction from its surface intersect to the location where it either intersects the seabed or levels off. It marks the boundary between Arctic Ocean Polar Water, which flows southward as part of the East Greenland Current along the Greenland continental margin, and the Atlantic Intermediate Water and Atlantic Water. These Atlantic water types flow northward in the West Spitzbergen Current to the east. Much of this relatively warm water then recirculates cyclonically in Fram Strait and flows southward just east of the Polar Front as the Return Atlantic Current. (See Chapter 4 for a discussion of these water masses.)

The south-flowing Polar Water west of the Greenland Polar Front com-

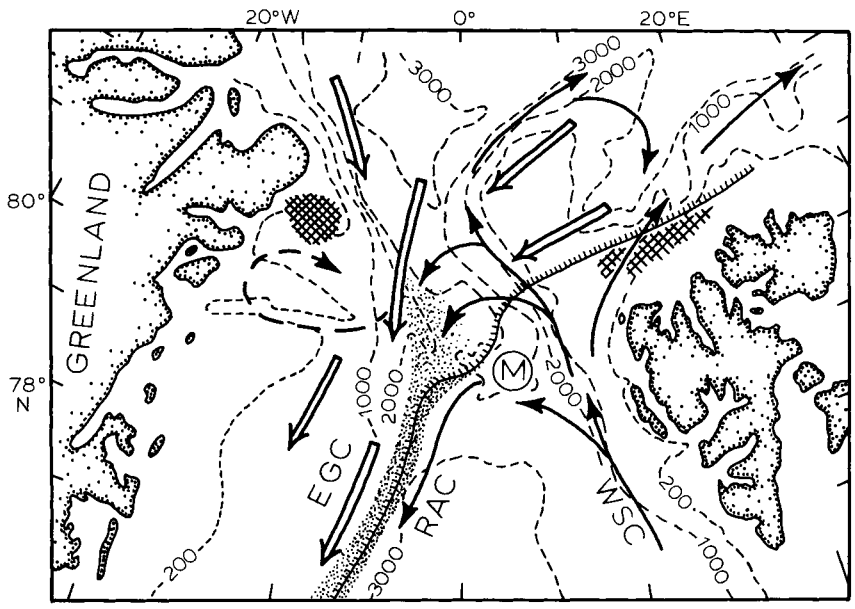

Figure 5.1 Schematic of mean ocean circulation and major frontal structure in the Fram Strait portion of the Greenland Sea. Hollow arrows depict flow of cold Polar Water, and solid arrows depict flow of warmer Atlantic Water. In areas where both water types occur, the Atlantic Water lies beneath the Polar Water. The hachured line indicates a typical summer ice edge location. The East Greenland Polar Front is indicated by the stippled region. Major currents are labeled as follows: WSC, West Spitsbergen Current; EGC, East Greenland Current; and RAC, Return Atlantic Current. Dashed lines are isobaths, with depths in meters, and the circled letter M indicates the Molloy Deep with depths exceeding 5000 m. Crosshatched areas north of Spitsbergen (which is not labeled for lack of space) and off northeast Greenland are sites of polynyas which are discussed in Section V of this chapter.

prises the East Greenland Current. This current has mean southward speeds of 0.1–0.3 m/s, with higher speeds over the Greenland continental slope and lower speeds over the continental shelf to the west (Foldvik *et al.*, 1988). The resulting annual mean southward transport has been computed using 1984–1985 year-long current records to be of order 3×10^6 m^3/s, roughly half of which is barotropic and half baroclinic (Foldvik *et al.*, 1988). Bourke *et al.* (1988) computed a southward baroclinic transport in the combined East Greenland Polar Front and Return Atlantic Current of 3.1×10^6 m^3/s for September 1985, a transport comparable to measured (i.e., barotropic plus baroclinic) value of Foldvik *et al.* (1988) for the East Greenland Current. Different types of observations were used for these transport estimates (Foldvik *et al.* used current and CTD measurements, while Bourke *et al.*

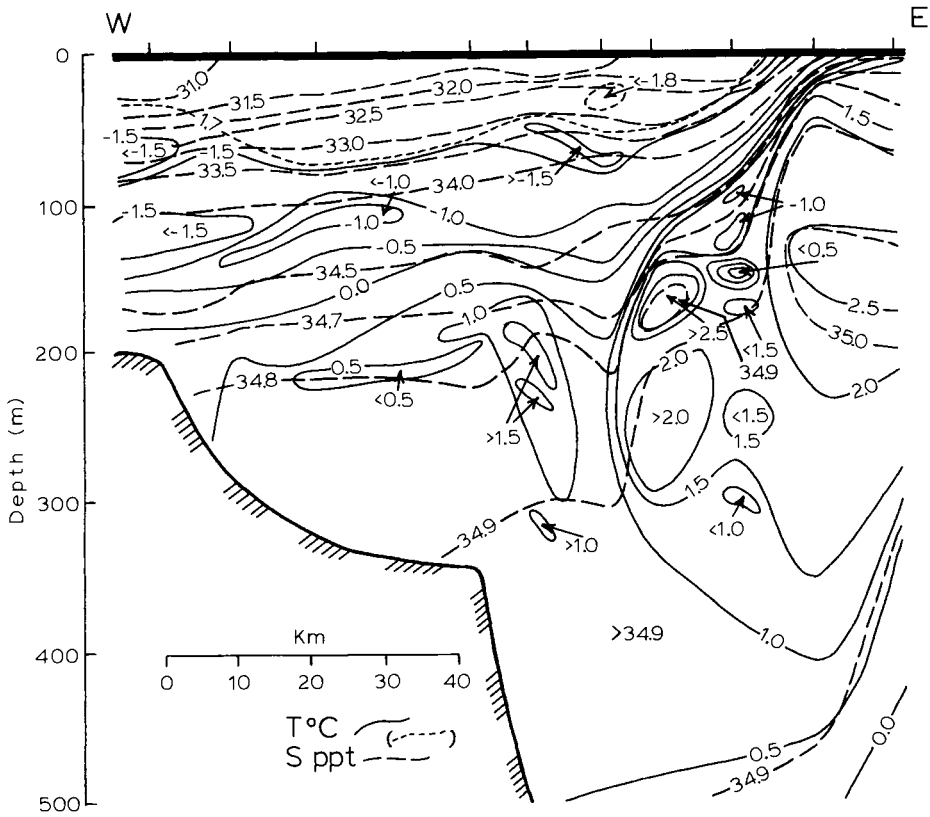

Figure 5.2 Transect showing vertical distributions of temperature (solid contours) and salinity (dashed contours) across the East Greenland Polar Front at about 78°N during autumn 1981. (Supplemental temperature contours at −1.7 and −1.8°C are shown with shorter dashes than the salinity contours.) Note the warm cores (>2–2.5°C) associated with the Return Atlantic Current, the cold layer (<1.7°C) associated with the East Greenland Current, and the fine structure along the front between about 100 and 300 m. The heavy black line at the sea surface indicates that the entire transect was ice-covered, and vertical tick marks at the sea surface show locations of CTD profiles (these conventions are followed for all remaining figures). Adapted from Fig. 5 in Paquette *et al.* (1985); copyright by the American Geophysical Union.

used CTD measurements), and the observations were obtained in different years and seasons. It is therefore difficult to draw conclusions from a comparison other than to speculate that significant year-to-year variability occurs.

Existing data are adequate to characterize the East Greenland Current as a large-scale, buoyancy-forced western boundary current. Wadhams *et al.* (1979) hypothesized, using results from a rotating laboratory-tank model

and theoretical arguments, that the East Greenland Current is a dynamical necessity driven by the buoyancy-forced outflow from the Arctic Ocean in conjunction with a meridional boundary (the Greenland continental margin). The observed southward transport in the East Greenland Current does not show significant seasonal variability, suggesting, in agreement with Wadhams *et al.* (1979), that the flow is driven by large-scale differences in sea level between the Arctic and Atlantic oceans rather than by a seasonal spinup localized to the Greenland Sea gyre (Foldvik *et al.*, 1988). Manley *et al.* (1987a) modeled the East Greenland Current analytically as a frictionless, steady, two-layered geostrophic boundary current having constant potential vorticity. Their computed estimates of transport were of the same order as the observed transports, though their current speeds were too high, probably due to neglect of friction in the model.

Considerably more energetic currents than those found in the East Greenland Current are associated with the East Greenland Polar Front. A narrow near-surface (within a 150-m-thick layer) jet having geostrophic baroclinic speeds exceeding 0.9 m/s has been observed along the front in autumn (Paquette *et al.*, 1985). Vinje and Finnekåsa (1986) showed that southward ice drift is significantly greater along the front than farther west (Fig. 5.3). These features appear to be due at least in part to a greatly improved frictional coupling between surface winds and sea ice within a few kilometers of the ice edge (see Chapter 7 on numerical modeling). Their often highly baroclinic nature and occurrence during summer and autumn suggest that they are due in part also to accumulation of meltwater from ice melting at or near the edge. In addition to such jets, the front is characterized by numerous baroclinic eddies (discussed in Section III of this chapter) which have commanded a large amount of attention during recent research in the region.

Subsurface temperature structures having vertical scales from meters to tens of meters and variations approaching 1 °C have been observed in association with the East Greenland Polar Front (Wadhams *et al.*, 1979; Paquette *et al.*, 1985) (Figs. 5.2 and 5.4). The fine-structure elements can be described as lenses or as along-front filaments of anomalously cool or warm water embedded in the ambient water. They can evolve rapidly; at one autumn 1981 station near the ice edge, a new fine-structure element appeared in the water column between the downcast and upcast—a time interval of about 17 minutes (Fig. 5.4). Manley (1987) has documented similar structures in association with conjoining of the Atlantic and Arctic water types in the West Spitzbergen Current. Such structures have been attributed to warm-core eddies (Paquette *et al.*, 1985) and to internal wave activity (Wadhams *et al.*, 1979), though the data are inadequate to define their origins with certainty. Fine structure of this nature in the vicinity of a front is generally taken

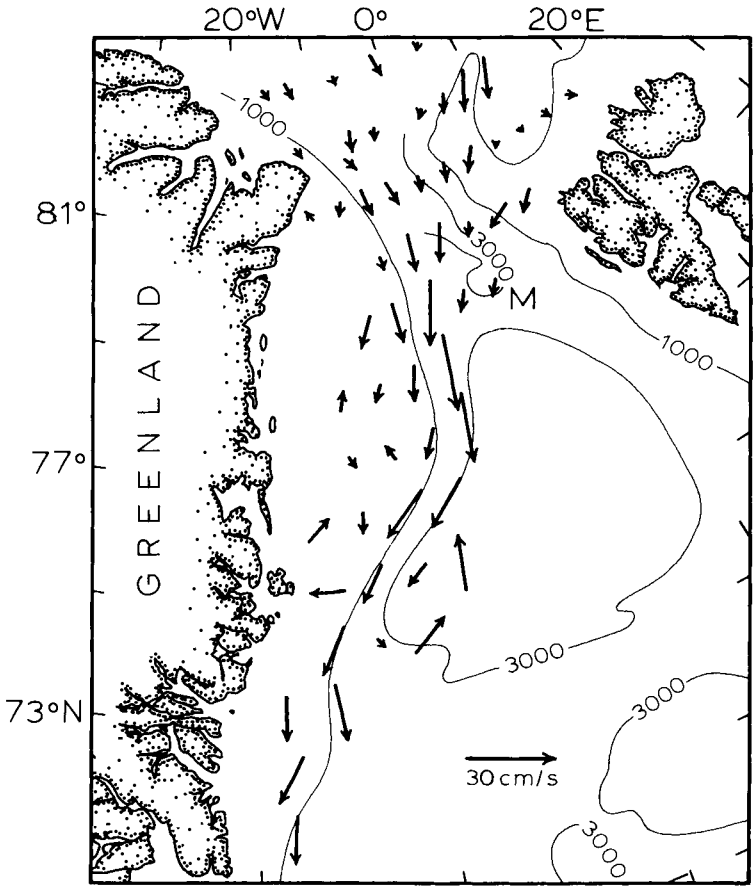

Figure 5.3 Mean ice drift pattern in the Fram Strait region as derived from manned and remotely tracked drift stations during May to August from 1937 through 1984. The ice drift reflects the higher southward current speeds in the Polar Front overlying the shelf break and the relatively sluggish net drift on the Greenland shelf and over the Molloy Deep region (M). Note the general convergence of ice drift onto the shelf break in central Fram Strait. Depths of isobaths are in meters. Adapted from Fig. 9 in Vinje and Finnekåsa (1986).

as evidence for cross-frontal interleaving of different water masses and suggests that enhanced mixing was taking place between the different water masses. The fine structure effectively increases vertical gradients in temperature and can be expected to dissipate through double-diffusive mixing processes: upper portions of the lenses are bounded by salt finger interfaces, while lower portions are bounded by diffusive interfaces. [See Turner (1973) for a discussion of double-diffusive processes.] Although the precise origins

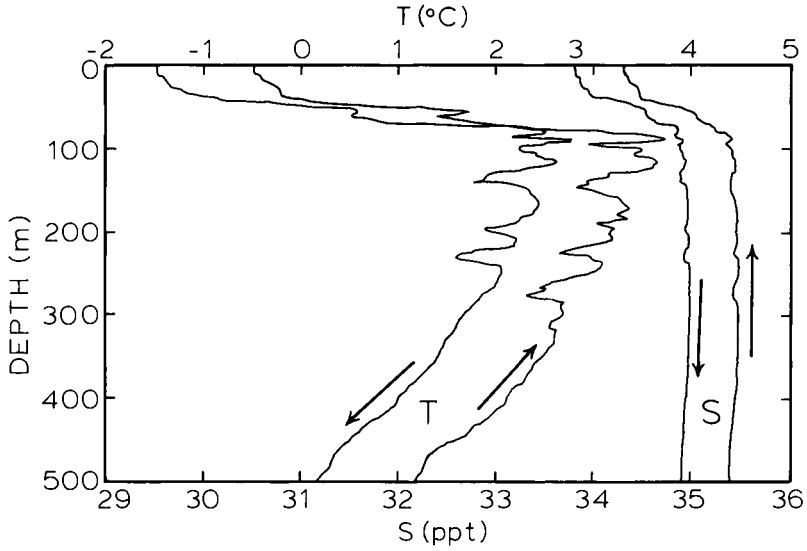

Figure 5.4 Vertical profiles of temperature (T) and salinity (S) illustrating fine structure at a location about 100 km south of the transect shown in Fig. 5.2 and in the eastern portion of the Polar Front. Both downcasts and upcasts are shown, as indicated by arrows, and are offset for clarity (by 1 °C for temperature and by 0.5 per mil for salinity). The total elapsed time required to occupy the cast was 28 minutes. Note the temperature structure which has evolved between 200 and 300 m over a 17-minute period between the down- and upcasts. Reproduced from Fig. 16 in Paquette *et al.* (1985); copyright by the American Geophysical Union.

of the fine structure remain uncertain, there is no doubt that it represents enhanced mixing.

Pack ice is advected southward with the East Greenland Current, west of the East Greenland Polar Front (see, for example, Fig. 5.3). Water east of the front is warmer than to its west, and the front exerts a strong physical control over the location of the pack ice edge. Ice which is advected by eddies, meanders, or off-ice winds seaward (east) of the front melts rapidly in the warmer water. Melt rates as great as 0.5 m/day have been observed in summer in the warmer water just seaward of the mean ice edge (Josberger, 1987). Pack ice is restricted, on the average, to the region west of the front. This physical interaction is sufficiently strong that the seasonal migration of the ice edge is far smaller in the Greenland Sea than in other polar regions—e.g., on the order of 100 km as compared to nearly 1000 km for the combined Bering and Chukchi seas and similar distances in the Antarctic. The ice input rate is adequate to maintain the ice edge at or near the permanent front location even in summer, when melting is maximum. Northward transport of warm water in the upper 100 m of the West Spitsbergen Current at 79 °N is

about 1×10^6 m^3/s. Assuming that the heat supplied by this warm water melts the ice evenly along a 300-km length of ice edge, a southward ice drift of about 0.05 m/s is needed to maintain the location of the edge against melting, consistent with observations (Quadfasel *et al.*, 1987). The rate of ice melting in winter is lower than in summer; therefore the ice edge extends farther seaward. Untersteiner (1988) has suggested that much of the ice melt in Fram Strait actually occurs in its eastern portion, where the south-flowing pack ice meets the warm north-flowing West Spitsbergen Current, and demonstrates an approximate balance between heat required to melt the ice and northward heat flux in the West Spitsbergen Current. He further hypothesizes that much of the ensuing meltwater accompanies the West Spitsbergen Current northward to recirculate back into the Arctic Ocean.

Frontal systems are associated with the seaward edge of the West Spitsbergen Current, as well as with the East Greenland Current (Fig. 5.1). These have not been studied as intensively as the East Greenland Polar Front; nonetheless, sufficient information exists to characterize them and to identify them as sites for mesoscale and small-scale activity similar to that observed in the Polar Front. The West Spitsbergen Current bifurcates into two current filaments in the area west of Spitsbergen (Perkin and Lewis, 1984). Governed by conservation of potential vorticity, the easternmost filament follows the shelf break into the Arctic Ocean, whereas the western filament follows the western flank of the Yermak Plateau northward, though the distance of northward penetration of this western filament has been shown by recent field work (Bourke *et al.*, 1988) to be uncertain. North of about 80°N at least part of this filament detaches from the plateau, presumably to contribute to the cyclonic recirculation of Atlantic Water in Fram Strait (Aagaard *et al.*, 1987). Perkin and Lewis (1984) show that mixing between these filaments and the ambient water is greatly enhanced through intrusive layering which allows both salt fingering and double-diffusive convective mixing to occur, similar to those in the East Greenland Current (see, for example, Fig. 5.4 from the East Greenland Current). These layers are uniform over distances of hundreds of kilometers, which is far greater than the local internal radius of deformation. Perkin and Lewis hypothesized that this was due to generation of multiple fronts, which would allow extension of the layers for distances exceeding the radius of deformation, by eddies or meanders in the mean current. Gammelsrød and Rudels (1983) noted the presence of eddies and meanders, which might contribute to this fine structure, in association with the West Spitsbergen Current. Aagaard *et al.* (1987) showed that a very large upward vertical heat flux (on the order of 200 W/m^2) can occur from the easternmost of the two Atlantic Water cores. There is general agreement that significant modification of northward-flowing Atlantic Water occurs in the region through mixing with ambient water, and it

is clear (although not quantified) that mesoscale processes play a major role in this modification.

A pronounced front separating polar from more temperate waters occurs farther south in the Labrador Sea, where the shelf waters are generally ice-covered from January to June but are ice-free for the rest of the year. Here, cold polar water flows southeastward over the shelf while warmer water flows northward farther offshore.

In winter, the Labrador Sea front is marked by the ice edge as in the Greenland Sea. This ice edge has exhibited regular, wavelike irregularities and well-defined eddies over a broad range of scales (Fig. 5.5). At one extreme were long-wavelength (200–300 km) meanders. Amplitudes of these meanders, whose locations correlate well with local shelf break bathymetric features, exceeded 100 km due to rapid growth of the initial perturbations, which may have been accentuated by baroclinic instability of the mean flow (Ikeda, 1987). These features were transient and had time scales of order a

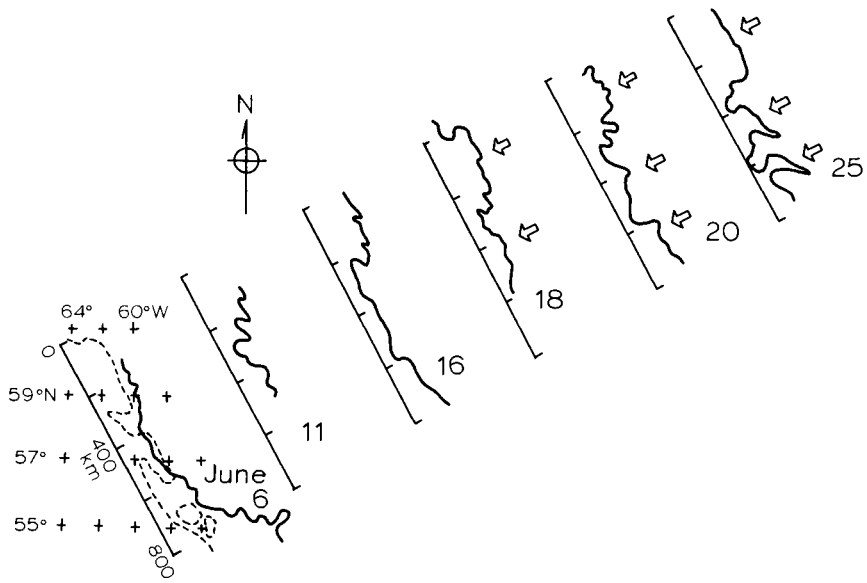

Figure 5.5 Evolution with time of current meanders along the Labrador Sea ice margin from small scale (about 50-km wavelength) to large scale (200–300-km wavelengths). The smaller-scale features persisted throughout the sequence and became superimposed on the larger features. Dashed line on the June 6 plot shows the 200-m isobath, which approximates the shelf break location. Open arrows are for visual reference in feature tracking. Reproduced from Fig. 4 in Ikeda (1987); copyright by the American Meteorological Society.

month interspersed with intervals when the frontal system (as marked by the ice edge) was quite straight.

Shorter-wavelength (30–100-km) meanders were observed along the Labrador Sea winter ice edge by LeBlond (1982), who noted that these propagated southeastward at about 0.2 m/s and were consistent with baroclinic instability of the mean flow (LeBlond, 1982). More recent remote sensing imagery has revealed smaller features (on the order of 20 km in diameter) along the Labrador Sea ice edge (McNutt *et al.*, 1988). The subsurface oceanographic structure of these latter features is unknown. Their origin is uncertain, though their general appearance and size coupled with occurrence along a region of current shear suggest that they are consistent with instabilities in the mean flow, as discussed by Gascard and Clarke (1983).

C. Western Arctic Frontal Systems

Frontal systems in the western Arctic, here meaning the shallow continental shelf portions of the Bering, Chukchi, and Beaufort seas, have considerably different characteristics than those in the eastern Arctic. Fronts in the eastern Arctic are present throughout the year, have more or less invariant geographic locations which are functions of the regional ocean circulation, and exert a strong control over ice edge location. Fronts in the western Arctic, on the other hand, are not always present and vary in location far more than those in the east. There are a number of reasons for these differences. Western Arctic oceanic regions outside the central Arctic Ocean basin are shallow, flat-bottomed continental shelf seas. While fronts are common on continental shelves, major ocean frontal systems associated with high-speed currents tend to be confined to the shelf breaks adjacent to deep ocean regions. No such systems have been observed in the western Arctic. A second reason for the east–west differences in frontal characteristics may be found in the general direction of oceanic water transport. Circulation in the eastern Arctic involves southward flow of Arctic Water and an adjacent northward flow of Atlantic Water within the confines of the same channel—Fram Strait. This circulation maintains strong gradients in water properties. Net flow in the western Arctic is northward with no significant southward counterflow. Lateral property gradients are weaker, and structures are correspondingly less pronounced. Finally, the ice edges migrate meridionally over a far greater distance in the western than in the eastern Arctic, so ice edge–related fronts are correspondingly impermanent.

Several types of fronts occur in the western Arctic. One type is a "structure front," where cross-frontal differences are maintained by differences in tidal and wind mixing rather than by juxtaposition of two different water masses. Water on the shallower side of such a front is typically well mixed vertically

because of tidal and wind mixing over a shallow bottom. On the deeper side of the front, the water column may exhibit two well-mixed layers separated by an interface or by a stratified intermediate layer. The upper layer is mixed by turbulence generated through wind drag or ice motion, and the lower layer is mixed by turbulence generated through currents interacting with the seabed. Such a front has been documented in the southeastern Bering Sea, and a description of this and other oceanic features on the southeastern Bering shelf has been provided by Coachman (1986). These structural fronts may persist year-round, though they are not well documented in winter. Presence of a sea ice cover would be expected to affect the structure both by altering the input of energy available at the surface for mixing and by adding meltwater near the ice edge, which can affect vertical stability.

A second type of western Arctic front is associated with the boundaries of the northward flow which dominates the northern Bering and Chukchi sea region. This flow is driven by the large-scale sea level difference between the North Pacific and Arctic oceans. Though the flow is present throughout the year, associated frontal structures are strongest in summer, when freshwater input and insolation have conditioned the north-flowing water so that it is considerably warmer and less saline than ambient waters. Paquette and Bourke (1974) described the coastal current along the Alaskan Chukchi and Beaufort sea coastlines as a warm, low-salinity, surface-trapped current overlying dense relict bottom water. The seaward boundary of the warm current comprises a front. Ahlnås and Garrison (1984) presented satellite imagery which revealed frequent occurrence of features resembling meanders or offshore-directed jets along the front bordering the seaward edge of the Alaskan coastal current northward from the northern Bering Sea into the Chukchi Sea. They offered no explanation for these features. Similar offshore-directed jets have been observed in other coastal regions, however, and in particular off the California coast. It is hypothesized at present that they result during detachment of meanders or eddies from the coastal current, possibly influenced by the coastline topography (Coastal Transition Zone Group, 1988).

Fronts have been observed seaward of summer baroclinic coastal currents. Wiseman and Rouse (1980) documented such a current along the Alaskan Chukchi coast and hypothesized that it was the major regional circulation feature for the entire Alaskan Chukchi coast. They observed alongshore speeds of order 0.4 m/s, with maxima as great as 0.7 m/s, and a current width of order 3 km, similar to the local internal radius of deformation. These currents responded readily to local winds. Their presence is dependent on a shallow, flat bottom and continental freshwater runoff which sets up and maintains the baroclinic field. [A thorough discussion of the dynamics of coastal and shelf currents is presented by Csanady (1984).]

Such currents would be expected to occur along any of the Arctic coastlines which are bounded by flat continental shelves; however, they have not been documented elsewhere.

The Chukchi Sea coastal current continues, at least in part, along the Beaufort Sea outer continental shelf and slope as the Beaufort Undercurrent (Aagaard, 1984). This current is the dominant circulation feature on the Alaskan Beaufort Sea coast, has eastward speeds of order 0.1 m/s, and persists throughout the year. Presence of a warm core in the current suggest that it plays a significant role in transporting water from the Bering Sea, which is typically 4–5 °C warmer in summer than ambient Arctic Ocean water, eastward and northward into the Arctic Ocean. The dynamics of this flow are uncertain, though Aagaard (1984) speculates that it may be part of the large-scale circulation of the western Arctic Ocean.

A final type of front in the western Arctic, and that which has demanded the most attention recently, is that associated with the marginal ice zone. Such fronts recur at locations in the Bering, Chukchi, and Beaufort seas, migrating zonally on a seasonal basis as they follow the ice edge.

Perhaps the simplest and best documented western Arctic ice edge front is that associated with the Bering Sea winter ice edge. Through the midwinter period the ice distribution remains in a steady state, with new ice forming in the north and ice melting along the southern edge. Mean ice transport within this system has been characterized as a "conveyor belt" (Muench and Ahlnås, 1976; Pease, 1980). Low-salinity meltwater from the ice accumulates along the edge, establishing a frontal system which parallels the ice edge (Fig. 5.6). This front is typically 100–200 km wide on the central shelf, with the greater widths toward the western shelf. The front is two-layered and is bounded to the north and south by vertically homogeneous water. The interface between the two layers surfaces at the seaward, ice edge location. This upper-layer front has associated along-frontal baroclinic currents which occur as one or more parallel cores 20–40 km wide (Fig. 5.6). These cores or jets may represent locations where the ice edge remained stationary for periods of time during which meltwater was added locally. Frontal location is controlled by the balance between the rate at which southward-flowing ice is input from the north and the rate of ice melting along the edge (Muench, 1983; Muench and Schumacher, 1985).

The Bering Sea winter ice edge front is considerably less energetic than the East Greenland Polar Front. Associated mean monthly current speeds in winter 1982–1983 were of order 0.1 m/s in a northwestward along-frontal sense. Lateral shear, spread over the 100–200-km width of the front, was correspondingly small. Variance energy spectra showed that mesoscale energy was present but was not significant relative to other energy in the system (Muench and Schumacher, 1985). The Bering Sea front does not exhibit

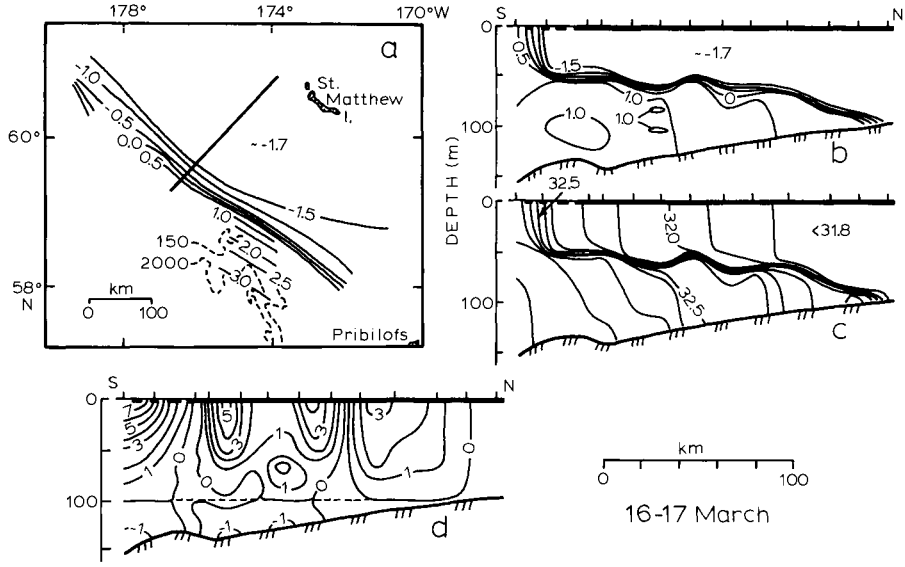

Figure 5.6 Horizontal distribution of surface temperature (degrees Celsius) associated with the Bering Sea winter ice edge front (a) and vertical distributions of temperature (b), salinity (per mil) (c), and along-frontal current speeds (centimeters per second) (d) along a transect normal to the front. Current speeds were computed using the geostrophic approximation referred to a reference level, which is indicated by the horizontal dashed line on transect d; positive speeds are west-northwestward along the front. Data were obtained from February 20 through March 18, 1983, during the Bering Sea Marginal Ice Zone Experiment. Adapted from Figs. 2, 3, and 7 in Muench and Schumacher (1985); copyright by the American Geophysical Union.

meanders or eddylike formations, which are common along the East Greenland Polar Front. Proper conditions for growth of dynamic instabilities which might lead to such features are not present.

As a consequence of the two-layered density stratification characteristic of the Bering Sea front, cyclonic storms transiting the region are effective in autumn, mid- to late winter, and spring at generating near-inertial motions (Lagerloef and Muench, 1987). These motions can be quite energetic, with current speeds exceeding 0.15 m/s, and are coherent over unusually great distances—in excess of 100 km. They probably contribute through interfacial shear-induced turbulence to upward flux of heat from the lower to the upper layer. This additional heat is then available to aid in melting ice. In addition, the lateral shear associated with the inertial currents may contribute to fracturing the ice in the marginal ice zone. The frontal system thus is dependent on the ice edge for its existence and, in turn, exerts a number of physical influences over the ice near the edge.

In spring the ice edge retreats from its location near the Bering shelf break northward through Bering Strait and well into the Chukchi Sea. Spring ice meltback is due both to insolation and to heat derived from northward-flowing North Pacific water. By midsummer, when the edge is at its northernmost location in the Chukchi Sea, meltwater has again established a frontal structure.

The summer ice edge frontal system in the Chukchi Sea consists of upper- and lower-layer fronts (Paquette and Bourke, 1981). The upper-layer front reflects input of meltwater along the ice edge, and the lower-layer front marks the boundary between ambient cold Chukchi Sea water and warmer north-flowing water from the Bering Sea (Fig. 5.7). The frontal structure and overlying ice edge reflect the bottom topography. Embaymentlike features along the ice edge coincide with concentrated warm northward currents which are topographically steered by troughs on the Chukchi shelf (Paquette and Bourke, 1981) (Fig. 5.8). Where mean flow parallels the frontal structure and gradients are weak, lateral interleaving occurs and results in complex

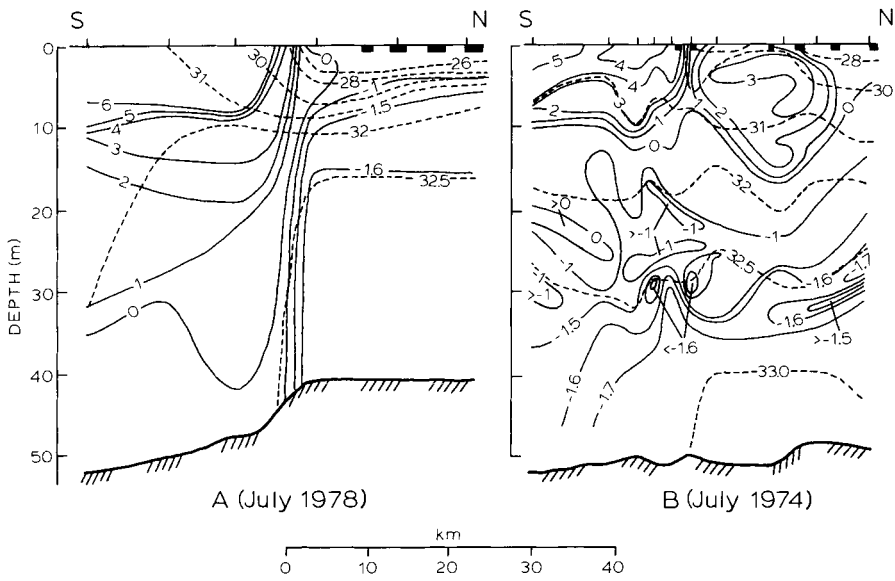

Figure 5.7 Vertical distributions of temperature (solid contours) and salinity (dashed contours) along two transects across the Chukchi Sea summer ice edge front. Approximate locations of these transects, referred to as A and B, are indicated in Fig. 5.8. The left-hand transect illustrates the case of well-defined upper- and lower-layer frontal structures which nearly coincide. The right-hand transect shows complex temperature fine structure resulting from lateral interleaving across the front. Adapted from Figs. 13 and 16 in Paquette and Bourke (1981); copyright by the American Geophysical Union.

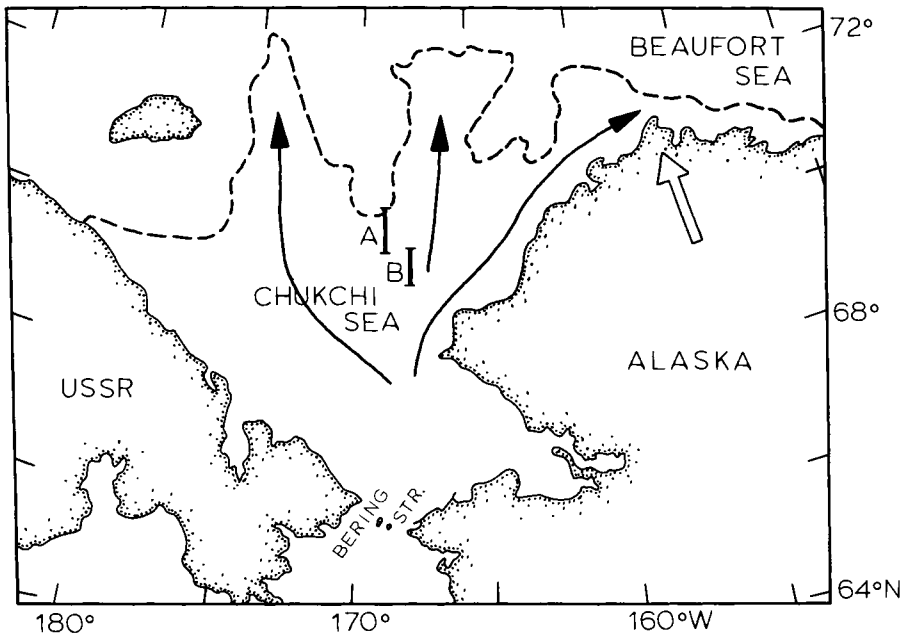

Figure 5.8 Location of Chukchi Sea ice edge on August 22, 1978, derived from a map issued by the Naval Polar Oceanography Center in Suitland, Maryland. The northward "embayments" in the ice edge correspond to topographically steered northward warm current cores (arrows). Heavy solid line segments marked A and B indicate approximate locations of the temperature transects shown in Fig. 5.7. Hollow arrow in northern Alaska indicates site of possible eddy formation as discussed in Section III,C and depicted schematically in Fig. 5.20. Adapted from Paquette and Bourke, (1981); copyright by the American Geophysical Union.

fine structure (Fig. 5.7). Like the fine structure observed in the East Greenland Polar Front, this can be expected to accentuate mixing across the front.

Other variations on these frontal structures have been observed along the Chukchi Sea summer ice edge by Paquette and Bourke (1981), the controlling factors being speed of the north-flowing warm water and its direction relative to the ice edge. Strong currents parallel to the ice edge tend to remove mixing products and lead to a well-defined frontal structure, whereas weaker on-ice flows lead to a more diffuse structure.

D. Antarctic Frontal Systems

We are concerned with conditions in the polar regions, which requires that we put a northern boundary on what is generally referred to as the Southern

Ocean. Most discussions of the Southern Ocean (e.g., Bryden, 1983) extend to considerably lower latitudes (as far north as 40°S) than can be considered truly polar. The Antarctic ocean will be defined here, for consistency with the Arctic case, as generally bounded by the northernmost extent of seasonal pack ice. This is typically 55° – 65°S, with the northernmost extent occurring from the eastern Scotia Sea to the Greenwich meridian (Zwally *et al.*, 1983). The winter ice cover thus lies well south of the core of the Antarctic Circumpolar Current and the Polar Front.

An exception to the above criteria defining "polar" will be made for the Drake Passage, where ice can approach relatively close to the Polar Front in winter. Of the hierarchy of fronts in Drake Passage, the southernmost or Weddell and Scotia fronts are generally impacted by sea ice, being the location during winter of the northern edge of the Antarctic pack ice.

The most energetic, and also the best documented, of the large-scale Antarctic fronts is that associated with the eastward-flowing Antarctic Circumpolar Current through Drake Passage and the Scotia Sea (Figs. 5.9 and 5.10). The frontal system in the Drake Passage – Scotia Sea region is exceedingly complex because the energetic eastward-flowing currents from Drake Passage converge, in a topographically complex area, with the northward-flowing currents from the Weddell Sea. The Polar Front in this region separates the Antarctic Zone water, characterized by an intense minimum temperature region above 200-m depths, from the Subantarctic Zone water, which is nearly isohaline between about 100 and 400 m. In addition to this primary frontal structure, the Antarctic Zone waters of the Weddell and Scotia seas are separated by a region of cold, relatively homogeneous water called the Weddell – Scotia Confluence. The northern and southern boundaries of this confluence are defined by the Scotia and Weddell fronts, respectively (Gordon *et al.*, 1977). There is thus a complex hierarchy of frontal structures in the Drake Passage – Scotia Sea region. Associated with these frontal structures are bands of high-velocity currents (of order 0.35 m/s), of order 50 km wide, which are embedded within the slower, wider eastward flow (Nowlin *et al.*, 1977; Nowlin and Clifford, 1982).

The frontal system in and just east of Drake Passage shows a complex structure of meanders and isolated (possibly detached) eddies, including a semipermanent large S-shaped meander near 45°W (Fig. 5.9). The frontal width has not been well documented, though Gordon *et al.* (1977) note that transitions between the zones occur at distances less than the 50 – 110-km spacing between hydrographic stations. Frontal widths must therefore be of the same order as, or less than, these spacings. The internal Rossby radius of deformation varies from about 17 km in northern Drake Passage to about 8 km near the continent to the south (Inoue, 1985), consistent with narrow frontal structures and reflecting the generally weak vertical stratification

(compared to the East Greenland Polar Front) in the northern portions of the system. The narrow frontal structure persists at least as far east as the Greenwich meridian, where frontal width is about twice the radius of deformation (Whitworth and Nowlin, 1987). The Polar Front is accompanied by temperature- and density-compensating salinity inversions as interleaving layers between about 100 and 400 m (Gordon *et al.*, 1977), similar to the interleaving observed associated with the East Greenland Polar Front, the West Spitsbergen Current, and the Chukchi Sea summer ice edge front.

A detailed set of moored current observations was obtained across Drake Passage during the mid- to late 1970s. Analyses of these current observations suggested that much of the mesoscale variability in currents there is due to baroclinic instability (Inoue, 1985). The combination of high current speeds and weak stratification contributes to these instabilities. The calculated

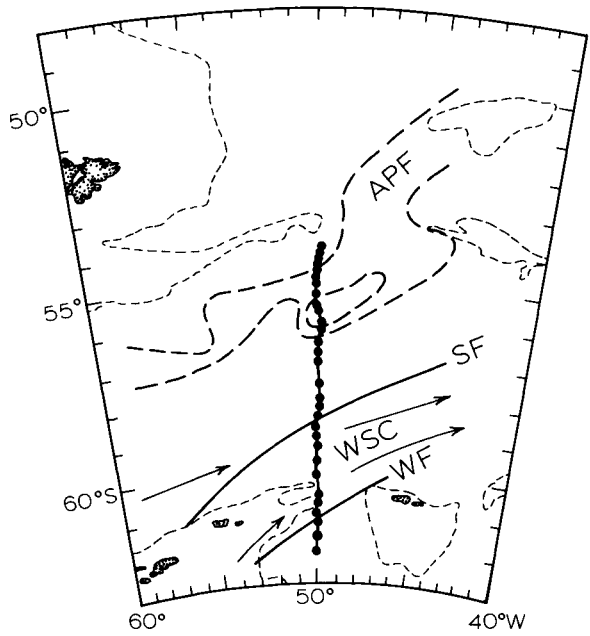

Figure 5.9 Approximate locations of frontal zones in Drake Passage and the northwestern Weddell Sea. The Antarctic Polar Frontal (APF) zone occupies the region between the heavy dashed lines. The Scotia and Weddell fronts are indicated by heavy solid lines labeled SF and WF, respectively, and bracket the Weddell–Scotia Confluence (WSC). The north–south-oriented line with dots indicates the location of the transect shown in Fig. 5.10; dots are station locations. The light dashed line is the 2000-m isobath. Arrows indicate schematically the ocean circulation in the vicinity of the Weddell–Scotia Confluence. Adapted from Figs. 1 and 20 in Gordon *et al.* (1977); copyright by the American Meteorological Society.

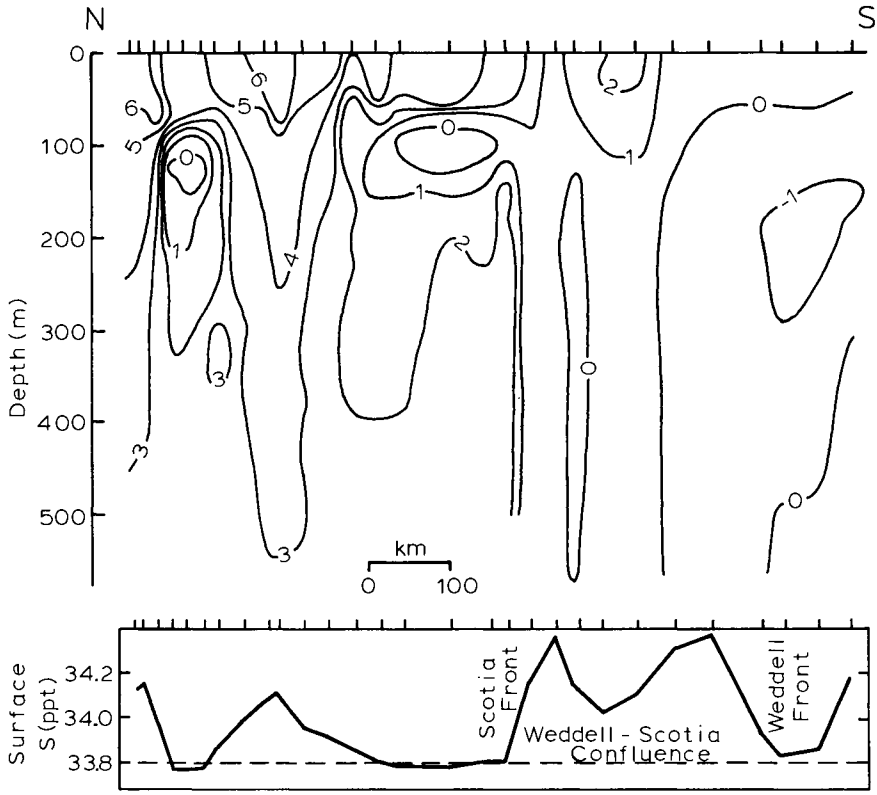

Figure 5.10 Vertical distribution of temperature (degrees Celsius; upper) and surface distribution of salinity (per mil; lower) along a meridional transect from the northwestern Scotia Sea to the northwestern Weddell Sea. Transect location is indicated in Fig. 5.9. Adapted from Fig. 9 in Gordon *et al.* (1977); copyright by the American Meteorological Society.

zonal wavelengths for the most unstable (hence, most rapidly growing) waves varied from nearly 200 km in northern Drake Passage to less than 100 km to the south, consistent with observed scales of variability.

Though considerable effort was put into the current measurements in Drake Passage during the 1970s, there is relatively little information concerning the Weddell–Scotia Confluence and the Weddell Front. The Weddell Front appears to be quite localized zonally, as it originates where the outflow from the Weddell gyre meets the eastward flow from Drake Passage and in the eastern Scotia Sea has degenerated from frontal structure into a field of mesoscale eddies (Foster and Middleton, 1984). At its initial point of

formation, it is about 50 km wide and forms a distinct front between cold Weddell Sea water and the warmer waters to the north (Deacon and Foster, 1977). Nelson *et al.* (1987) noted that the Weddell Front was highly convoluted by mesoscale features in December 1983, when the ice edge coincided with the front.

The Weddell–Scotia Confluence has been hypothesized as the site in winter of vigorous vertical mixing (Deacon and Moorey, 1975; Deacon and Foster, 1977). This hypothesis is based on the observation that surface water density is maximum at the confluence relative to surrounding waters and the waters within the confluence are relatively uniform in the vertical. This lack of vertical stratification persists at least as far east as the Greenwich meridian (Whitworth and Nowlin, 1987). The surface density maximum is probably due to a decrease in upper-layer salinity in the Antarctic Zone water to the south due to addition of meltwater, coupled with a lower salinity in the Circumpolar Current to the north. Unpublished data for the Weddell Front during winter (March) 1988 obtained by the author reveal, however, that considerable stratification was present and suggest that significant vertical mixing was not occurring.

E. Frontal Structures in Polar Basins

Although fronts along the sea ice margins have been heavily documented, relatively little is known concerning fronts beneath the permanently pack ice–covered portions of the polar oceans. This lack of information is due primarily to the extreme logistical difficulty in operating in waters covered by heavy, multiyear pack ice such as that which occupies the central Arctic Ocean basin and the westernmost Weddell Sea. For example, temperature and salinity data from the Arctic Ocean basin have by and large been obtained from drifting ice camps with limited geographic coverage and little control over station locations. There are presently few winter oceanographic data from the western central Weddell Sea gyre and no data whatsoever from the ice-covered westernmost Weddell Sea within about 100 km of the Antarctic Peninsula.

Physical reasoning suggests that energetic frontal structures in the ice-covered central polar ocean basins away from the boundaries are unlikely, since there is no obvious mechanism for maintaining the strong gradients which are required to sustain frontal systems. Nonetheless, a weak north–northeast-oriented density front was detected from a drifting ice camp during spring 1979 within 1.5 latitude of the North Pole by Pounder (1986). This serendipitous discovery occurred during the Lomonosov Ridge Experiment (LOREX). The density difference across the front reflected a horizontal

salinity change of about 1 per mil over a distance of about 50 km. The measured along-frontal currents were compared with the observed density field and found to be in geostrophic equilibrium. The lower-salinity water mass was assumed by Pounder to represent an isolated, small water mass. The mechanism for generation and maintenance of such a feature is uncertain. The front observed by Pounder (1986) occurred in late winter, so local meltwater input would have been insignificant. The low-salinity lens must therefore have persisted since the preceding summer, possibly having been advected eastward via the Transpolar Drift Stream from the western basin. Persistence of such a feature since the previous summer and over such a great distance would imply that mixing processes in the central Arctic Ocean under the ice cover are weak. This case is not isolated, as a similar drop in salinity (about 1 per mil) was observed across a 10-km-wide frontal region from a drifting ice camp about 150 km northeast of Greenland by Hunkins and Manley (1980). McPhee (1980) hypothesized that the latter feature was due to lateral intrusion of an intermediate-density water mass which may have originated on the broad Arctic continental shelf. More complete documentation of such features is needed to provide significant new insight into mesoscale physical processes in the central polar basins.

Lutjeharms and Baker (1980) carried out an analysis of historical hydrographic data from the Southern Ocean, compiling existing data and conducting a structure function analysis to test for mesoscale features. This analysis consisted of constructing the 0/1000 dbar dynamic interval for each station for which data exceeded 1000-m depths, detrending the results, and carrying out statistical analyses of the residuals. The analyses resulted in compilations of "structure functions" which can give, by their spatial correlations, an indication of the horizontal scales of significant features. The results of their analyses for the Scotia, Ross, and Weddell seas indicate that mesoscale features having scales smaller than 100 km, or of the same order as the sample spacing, occur throughout these regions (Fig. 5.11).

In the case of the Weddell Sea the summer marginal ice zone, which migrates seasonally through the western central gyre, provides meltwater input sufficient to generate a weak salinity-controlled upper-layer frontal structure (Husby and Muench, 1988) (Fig. 5.12). This structure did not have significant associated along-frontal currents. A similar structure has been observed in the Ross Sea during the spring period of ice meltback (Smith and Nelson, 1985). These fronts migrate as the ice edge retreats in spring, releasing meltwater to the upper ocean. Their generation mechanisms are therefore similar to those of the western Arctic ice edge fronts. The latter are, however, subject to dynamic constraints imposed by bottom depths of less than 100 m, whereas the shallow Weddell Sea ice edge front observed by

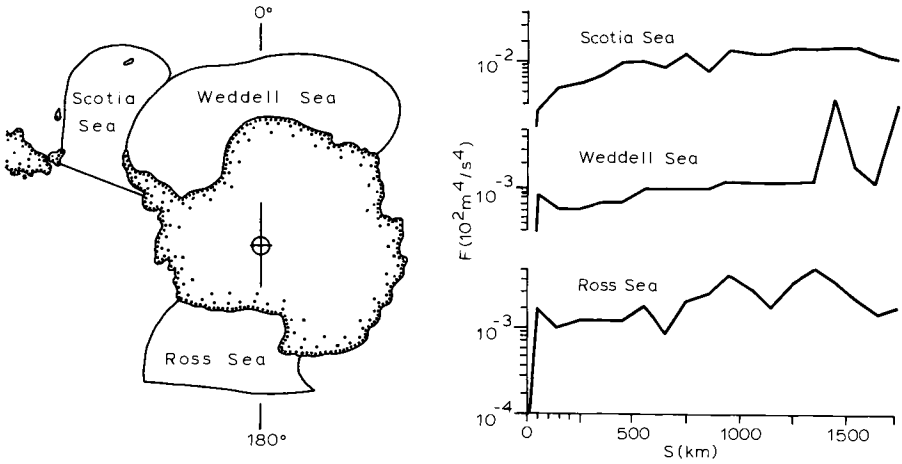

Figure 5.11 Boundaries used in investigating three geographically and dynamically distinct regions of the Southern Ocean for mesoscale features (left) and estimated spatial structure functions (F) plotted versus separation distance (S) for these three regions (right). The dynamic variable used for calculation was the detrended dynamic interval 0/1000 dbar. Curves have been offset on the ordinate to separate them for clarity. Adapted from Fig. 7 in Lutjeharms and Baker (1980); copyright by Pergamon Press.

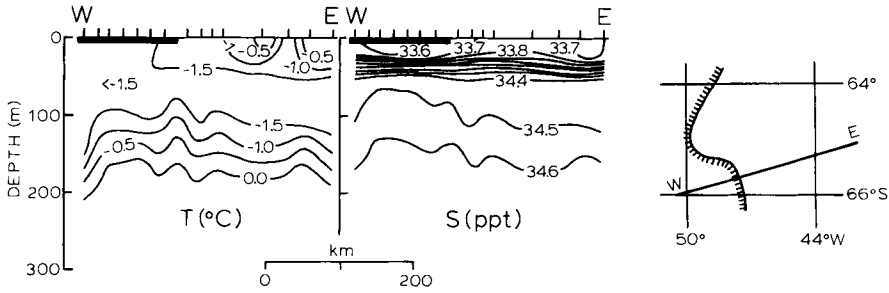

Figure 5.12 Vertical distributions of temperature (degrees Celsius; left) and salinity (per mil; right) along a transect normal to the late summer ice edge in the northwestern Weddell Sea. Approximate location of transect is shown to the right, with the ice edge indicated by the heavy hachured line (ice cover to the left of the line). Derived from Figs. 2 and 3 in Husby and Muench (1988).

Husby and Muench (1988) occurred in a region where bottom depths exceeded 3000 m. Since these fronts are generated and maintained by local ice melt, there is no reason to expect them to persist once early winter freezing has commenced.

III. Mesoscale Eddies

A. Overview

Mesoscale eddies, which are also referred to as synoptic eddies (through analogy with similar features in the atmosphere) or as quasi-geostrophic eddies (referring to their usual dynamics), are closed horizontal circulation features which tend toward circular forms but which may be elliptical or irregular to varying degrees. They rotate about vertical or nearly vertical axes and may either be confined near the surface or extend to depths of several thousand meters. Large oceanic eddies have been observed to persist for years; however, lifetimes are more typically of order weeks or months and are limited by frictional dissipation of the eddy currents and dispersion through mixing of the associated internal density fields. Eddies are energetic features, and rotational current speeds are typically higher than ambient current speeds.

Mesoscale eddies have been found in most parts of the world ocean. The only regions in which rich eddy fields have not been documented are the inaccessible, ice-covered portions of the polar basins. Mesoscale eddies are of considerable interest with respect to large-scale ocean processes, because they can influence ocean "climate" in the same way that atmospheric cyclones affect our weather. They have highly energetic currents which transport, trap, and disperse heat, momentum, and dissolved and suspended matter. Eddies may induce upwelling, and eddy transports contribute to maintenance of shelf mass balances. Eddies contribute substantially to the zonal oceanic heat flux in the Southern Ocean. Eddies also influence the oceanic general circulation through eddy–mean flow and eddy–eddy interactions. In marginal ice zones, eddies may increase transport of ice across the ice edge and hence increase the rate of ice melting by bringing the ice into contact with warmer water, which is normally present seaward of the ice. Recognition of the importance of eddies to oceanic processes led to increased interest, culminating in the Mid Ocean Dynamics Experiments (MODE and POLYMODE) during the 1970s and in a collection of papers dealing exclusively with eddies (Robinson, 1983).

Eddies have proved to be unusually, if not uniquely, difficult to study. Typically migratory, transient, and small when compared to regional-scale

oceanographic sampling schemes, they were overlooked by most early field studies. Only with the advent of modern recording and profiling oceanographic instrumentation and remote sensing from satellites was the pervasive presence of eddies recognized. Remote sensing from satellite- and aircraft-borne sensors has been indispensable in detecting eddies in inaccessible areas such as polar regions. With the recognition of the importance of eddies to the global ocean, analytical and numerical models have been developed and have provided insight into their dynamics.

Even with these recent advances, there is much that we do not know about eddies. Distribution of eddies in the ice-covered basins remains uncertain, since presence of the ice cover prevents use of remote sensing to detect surface thermal signatures which may be associated with them. Pack ice away from the marginal ice zones has sufficient internal friction that it does not respond easily to forcing by currents associated with eddies; therefore, ice motion in the interior pack is generally a poor indicator of underlying eddy motion. Detection of eddies in these regions requires acquisition of temperature, salinity, and current observations through the ice, which is sufficiently costly and time consuming that the data have been quite limited compared with the data for open-ocean or marginal ice zone regions, which are accessible to conventional or icebreaking vessels. Time scales of eddies have proved particularly difficult to estimate, since this requires tracking of a feature from its formation through decay—a process which is difficult in the temperate ocean and virtually impossible in the polar regions.

Eddies require a source of energy for their generation and growth. This source may be a major oceanic boundary current, a coastal current system, a front, a concentrated current jet, or a combination of several such features. Wind forcing and thermohaline convection may also contribute to formation and growth of eddies. The number and energy of eddies in a region are related to the overall energy level of the oceanic system in which they occur. Eddy properties such as vertical extent, sense of rotation, and lifetime will also reflect the source. There are in theory at least five possible mechanisms for generation of eddies in the polar regions: (1 and 2) growth of fluctuations in the mean flow through baroclinic or barotropic instability mechanisms, (3) generation by topographic trapping through conservation of potential vorticity, and (4 and 5) wind–ice or ice–ice interaction along an ice edge. These mechanisms are discussed in greater detail below. Eddies may also be formed elsewhere and advected into the region by the regional circulation. The regional environmental physical parameters which can be expected to influence eddy formation and characteristics differ somewhat between the eastern Arctic, the western Arctic, and the Antarctic. For this reason, and to maintain consistency with Section II above, the following discussion of eddies will be divided into sections dealing with each of these regions.

B. Eddies in the Eastern Arctic

The most extensive and best-documented field of eddies in the Arctic occurs in the Greenland Sea in association with the East Greenland Polar Front and the coincident marginal ice zone. These eddies are particularly evident in the vicinity of Fram Strait — a primary channel for inflow and outflow of water from the Arctic Ocean and the site of strong gradients in temperature, salinity (and hence density), and current speed (Fig. 5.13). These eddies were noted on satellite imagery by Vinje (1977). Wadhams *et al.* (1979) used sound velocity profiles obtained from a submarine to detect warm-water lenses which they interpreted as warm-core eddies originating to the east and migrating into the cold Arctic Water of the East Greenland Current. Johannessen *et al.* (1983) combined temperature, salinity, ice drift buoy, and remote sensing data into a rigorous physical description of eddies in the region north of Spitsbergen. At this location (north of about 82°N; Fig. 5.1) the eddies were primarily cyclonic and had horizontal scales of 10–20 km and associated rotational speeds of about 0.1 m/s. They were limited in vertical extent to the upper mixed layer.

Early recognition of the rich eddy field in Fram Strait, and of its potential importance in regional oceanographic processes, contributed to formulation of the Greenland Sea Marginal Ice Zone Experiment (MIZEX East), which obtained extensive field data on mesoscale processes during the summers of 1983 and 1984 (MIZEX Group, 1986). The eddy-related aspects of these experiments, which included temperature, salinity, currents (from both moored current meters and drifters), and remotely sensed imagery from satellites and aircraft, have been reported by J. A. Johannessen *et al.* (1987), O. M. Johannessen *et al.* (1987), and Manley *et al.* (1987a,b,c).

The MIZEX program focused on the marginal ice zone between about 78° and 81°N and resulted in documentation of eddies which varied in diameter from 20 to 40 km. Rotation speeds were as high as about 0.4 m/s and were usually in a cyclonic sense, so that upward doming of isopycnals occurred in the center of the eddy (Fig. 5.14). Lifetimes were at least 20–30 days, approximately the period during which they were under observation. Many were confined to the near-surface layers, though some extended downward to considerable depths. Several of the eddies appeared to be topographically trapped, in particular, those associated with the Molloy Deep region, as discussed in greater detail below. Others drifted at the mean current speed, so that eddy movement was dominated by advection with the mean flow.

Concurrently with the 1984 summer MIZEX work in Fram Strait, moored current observations were obtained from different depths throughout the water column at three locations along a transect across the East Greenland Polar Front at about 79°N. Foldvik *et al.* (1988) used these data

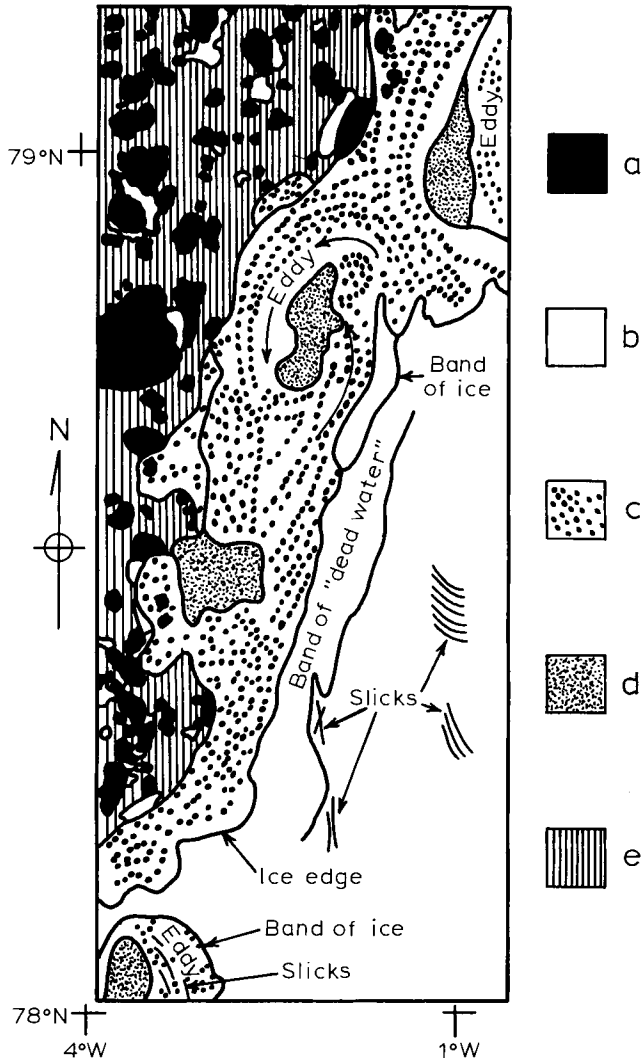

Figure 5.13 Example showing the complex mesoscale structure as reflected in the ice distribution along the summer marginal ice zone in Fram Strait. This figure is an interpretation of a synthetic aperture radar mosaic obtained from an aircraft. The features include large individual floes (a), ice-free areas (b), areas of 3/10 ice cover and floes 10–500 m in diameter (c), areas of 8/10 ice concentration with floes 10 m to 1.5 km in diameter (d), and areas of 8/10 concentration with floes 10 m to 6 km in diameter (e). The dots shown in "c" areas indicate locally increased ice concentration, interpreted as due to surface currents. One complete cyclonic eddy and portions of two additional eddies are included in the field. Adapted from Fig. 1 in O. M. Johannessen *et al.* (1987); copyright by the American Association for the Advancement of Science.

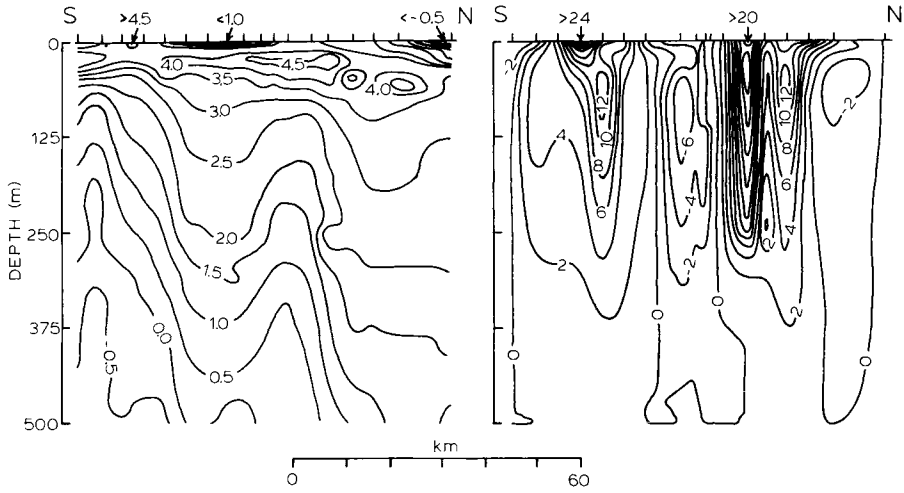

Figure 5.14 Temperature (degrees Celsius; left) and geostrophic velocity (centimeters per second; right) associated with an eddy observed in the Fram Strait marginal ice zone during summer 1984. Transect extended from about 78°20′ to 79°05′N along about 0°20′W longitude. Ice cover was present over most of the section but is not shown here in order to preserve the near-surface features. Adapted from Figs. 4 and 6 in J. A. Johannessen *et al.* (1987); copyright by the American Geophysical Union.

to further characterize the eddy field at this location. They found a rich mesoscale structure, having time scales from a few days to several weeks, in the current records. Much of this structure was interpreted as passage past the moorings of trains of eddies and of widely spaced eddy pairs having length scales of order 10 km. Many of these features at a site east of the Polar Front extended to depths greater than 400 m; in the more strongly stratified East Greenland Current west of the front, they were primarily restricted to the upper Arctic Water layer. Tangential speeds of identifiable eddy features were of order 0.15 m/s, or similar to the local mean flow speed for the East Greenland Current. These speeds were obtained at about 100 m rather than at the surface and as a result are lower than the speeds reported by J. A. Johannessen *et al.* (1987).

Considerable debate exists concerning the origin of mesoscale eddies in the Fram Strait region. Wadhams *et al.* (1979) suggested, based on a simple two-layered, constant-depth model with a vertical western boundary, that the East Greenland Polar Front is dynamically unstable along its entire length and that the observed eddies result from this instability. Griffiths and Linden (1981) hypothesized, based on both rotating-model laboratory experiments and a theoretical model, that the East Greenland Current is unsta-

ble with respect to both barotropic and baroclinic instabilities, the latter mode being dominant. Their predicted wavelength for the most unstable case was 100 km, or more than twice the observed eddy sizes. For the East Greenland Current they assumed a flat bottom, whereas in reality this current overlies the steep Greenland continental slope, which would tend to stabilize the flow with respect to instabilities, through much of Fram Strait. Johannessen *et al.* (1983) concluded, on the basis of a shear-dependent parametrization derived from a simple two-layered model, that eddies north of Spitsbergen result from baroclinic instability. They concluded, using criteria established by Griffiths and Linden (1981), that the flow is barotropically unstable as well. This conclusion is consistent with the observation that the current is in general both vertically and horizontally sheared. J. A. Johannessen *et al.* (1987) concluded from results of the 1984 MIZEX field program that the numerous eddies observed migrating along the marginal ice zone are due to combined barotropic and baroclinic instability of the East Greenland Current along the Polar Front. However, this supposition neglects the stabilizing influence of the steeply sloping shelf break underlying much of western Fram Strait.

In general, instability mechanisms have been the most frequently suggested explanation for the presence of eddies in the Fram Strait region. The East Greenland Polar Front is the site of both vertical and lateral current shear between the southward-flowing East Greenland Current and the Atlantic Water layer (see Section II). A relatively straightforward criterion can be applied in the case of barotropic instability, which can occur only in the presence of an inflection point in the mean horizontal velocity profile (Pedlosky, 1982). Ice edge jets which would cause such inflections were detected in the baroclinic field during autumn 1981 by Paquette *et al.* (1985) and were inferred during summer 1984 from satellite-tracked ice floe motions (MIZEX Group, 1986). Vinje and Finnekåsa (1986) reconstructed an ice edge current jet using a simple model for wind-forced ice and water motion. Such jetlike currents might be augmented by wind-driven ice edge jets as derived from a numerical model by Røed and O'Brien (1983) and observed by Johannessen *et al.* (1983). Existence of such an ice edge current system implies the presence both of inflection points in the horizontal current profile and of significant kinetic energy which might be provided to eddies through instability mechanisms. Sufficient variability exists in the currents within Fram Strait that conditions conducive to instability mechanisms are probably present at various times and locations.

Despite the above physical reasoning, the evidence concerning the contribution of local instability mechanisms to development of the eddy field in Fram Strait remains contradictory. Much of the available data suggests that the flow is dynamically stable. Muench *et al.* (1986) analyzed year-long

current observations from the core of the East Greenland Polar Front at about 78.5°N and demonstrated that mesoscale fluctuating energy actually decreased southward through the system, rather than increasing in a downstream (southward) direction along the mean flow axis as would be expected in the presence of unstable flow. Foldvik *et al.* (1988) carried out more extensive analyses of current observations in the same region and concluded on the basis of negligible downgradient (westward) cross-current eddy heat fluxes that the current was baroclinically stable.

The field evidence suggests also that many of the eddies along the East Greenland Polar Front may form elsewhere and be advected into the region. Manley (1987) suggested, on the basis of water mass analyses applied to observed eddy temperature and salinity characteristics, that the eddies are not locally generated in Fram Strait but develop instead through instability mechanisms along the western flank of the Yermak Plateau, several hundred kilometers to the north. The eddies are then advected southward with the mean flow. Gammelsrød and Rudels (1983) detected eddies in the West Spitsbergen Current which might be advected across Fram Strait by the cyclonic circulation there and entrained into the East Greenland Current. Rudels (1987) estimated that a substantial portion of the West Spitsbergen Current recirculates in Fram Strait, consistent with advection of eddies into the polar frontal zone. Gascard *et al.* (1988) suggested on the basis of drifter data that West Greenland Current eddies originate elsewhere, a probable source being the West Spitsbergen Current.

Numerical modeling efforts have resulted in hypothetical mechanisms for the generation of highly baroclinic upper-layer mesoscale eddies, which are typical of the more heavily stratified waters in the East Greenland Current west of the Polar Front. These models invoke interactions among winds, the ice edge, and the upper ocean or ice–ice interaction to explain the generation of eddies. Killworth and Paldor (1985) demonstrated, using a numerical model applied to an infinite ice edge overlying a passive ocean, that instabilities which lead to eddy formation can occur as a consequence of internal ice dynamics along the edge. Their model leads to eddy sizes in the observed range but involves considerable assumption concerning the ice rheology and neglects the effects of the underlying ocean. Hakkinen (1987) developed a numerical model which demonstrates that ice edge eddies of the proper scales can be generated by interactions among wind, ice, and water along an initially irregular ice edge. These and additional models are discussed in greater detail in Chapter 7. Available field data are, in general, inadequate to test these theories of eddy formation.

Central Fram Strait is the site of a semipermanent mesoscale system which consists of a cyclonic, warm-core eddy and several smaller associated

anticyclonic features. It is present over or near the Molloy Deep, a region west of Spitsbergen centered at about 0°E and between 79° and 80°N and having bottom depths in excess of 5500 m (see Fig. 5.1). Because of the persistence of this feature, its obvious effect in causing seaward bulging of the marginal ice zone, and the considerable speculation in the literature on its origin and nature, it will be focused on here as an example of the variety of processes which can affect such mesoscale systems.

The eddy system associated with the Molloy Deep was first detected, though its nature was not recognized, more than a century ago (Wadhams *et al.*, 1979). It was noted on May 1976 Landsat imagery and through trapping in the eddy field of a satellite-tracked drifting buoy by Vinje (1977) (Fig. 5.15). The drifting buoy also documented a thermal structure which was consistent with the presence of a cyclonic, warm-core eddy (Vinje, 1982). Wadhams *et al.* (1979) detected warmer water within the cold Arctic Water in the region, suggestive of such an eddy. Wadhams and Squire (1983) reported on 1980 oceanographic data which documented a complex circulation pattern within this eddy (Fig. 5.16). Bourke *et al.* (1987b), J. A. Johannessen *et al.* (1987), O. M. Johannessen *et al.* (1987), and Manley *et al.* (1987b) documented the feature during summer 1984 with temperature, salinity, and Lagrangian drifter data. Oceanographic data obtained during

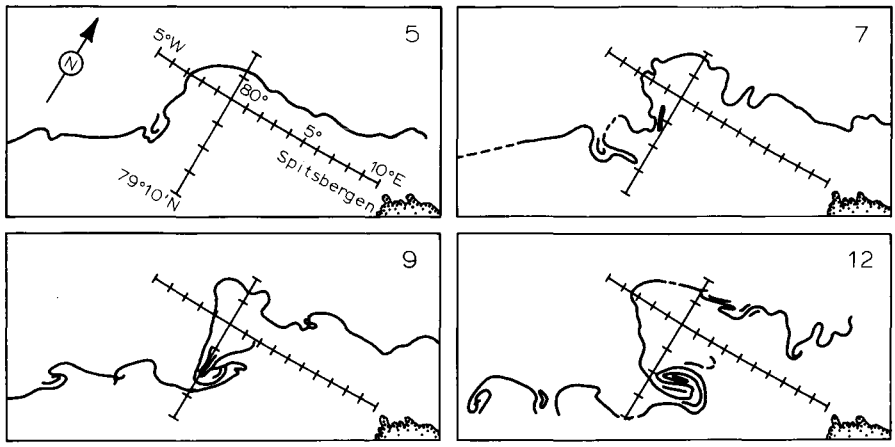

Figure 5.15 Evolution of an ice edge eddy signature in the vicinity of the Molloy Deep in central Fram Strait, as derived from Landsat data obtained on May 5–12, 1976. Dates in May 1976 are shown in the upper right corners of the panels. Note the overall cyclonic nature of the eddy and the evidence on May 9 and May 12 for smaller anticyclonic structures on the northern portion of the eastward-projecting ice tongue which was associated with the eddy. Adapted from Fig. 7 in Vinje and Finnekåsa (1986).

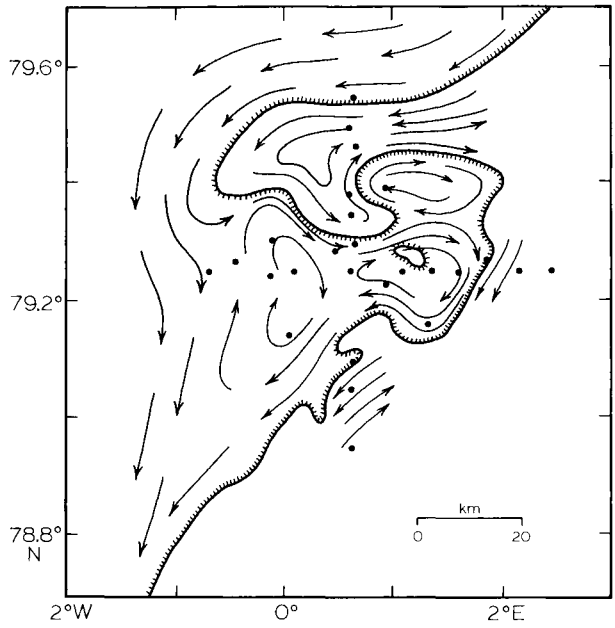

Figure 5.16 Interpretation of surface circulation in the eddy system associated with the Molloy Deep during August 1980. Arrows show the inferred surface drift pattern. Hachured solid line shows the ice edge location. Dots show locations of temperature/salinity (CTD) stations used in computing geostrophic velocities. This interpretation was arrived at using temperature, salinity, ice distribution, and radar-tracked drifter data. Note that, as implied in Fig. 5.15, the overall feature was cyclonic but there were smaller anticyclonic components in its northern and seaward portions. Adapted from Fig. 9 in Wadhams and Squire (1983); copyright by the American Geophysical Union.

this work indicated that the baroclinicity associated with the system extended downward to depths of at least 900 m (Fig. 5.17).

The eddy near the Molloy Deep has horizontal dimensions which have been observed to vary on a year-to-year basis from less than 50 km to greater than 100 km. Near-surface current speeds have been estimated using Lagrangian drift trajectories, direct current measurements, and baroclinic current computations to fall in the range 0.1–0.35 m/s (Vinje and Finnekåsa, 1986; Bourke *et al.*, 1987b; J. A. Johannessen *et al.*, 1987). Because the eddy lies at or near the ice edge in Fram Strait, it has been possible to track its surface development and detailed features using the mobile, loosely packed ice near the edge as a tracer which is readily visible on satellite imagery (Fig. 5.15). The eddy system has an overall cyclonic circulation which tends to be particularly well developed in its southern portions. In the northern part of

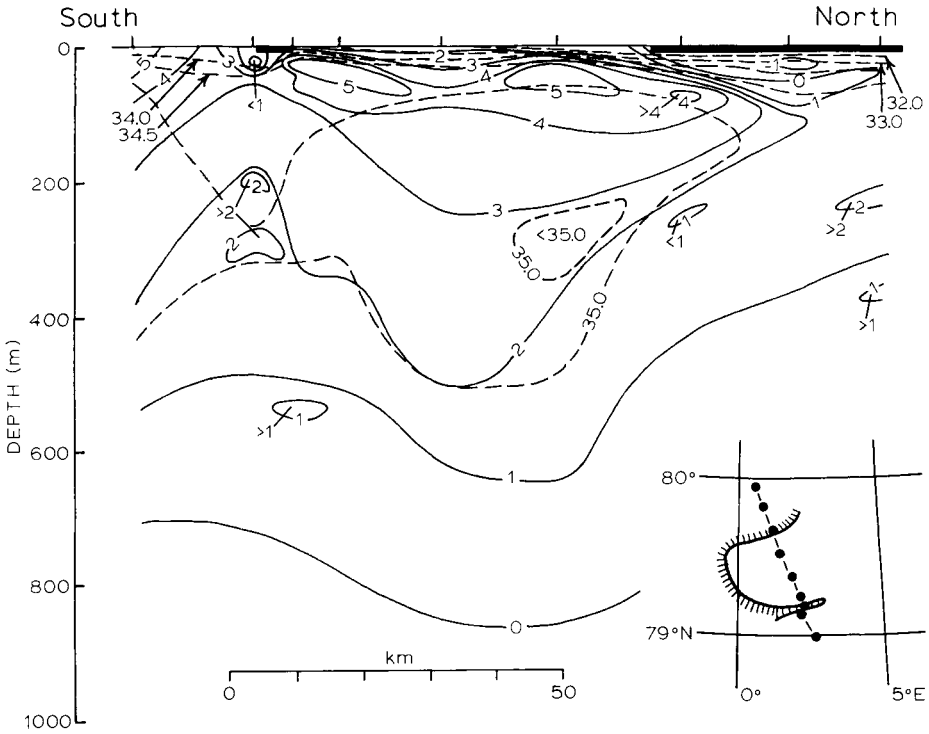

Figure 5.17 Vertical distributions of temperature (solid contours) and salinity (dashed contours) along a transect through the eddy near the Molloy Deep during August 24–25, 1984, showing the warm core and depression of isotherms to at least 900 m. (Inset) The location of the transect is shown as a dash–dot line where the dots are station locations, and the ice edge location is indicated as a hachured line. Derived from Fig. 2 in Bourke *et al.* (1987b); copyright by the American Geophysical Union.

the system, one or more smaller anticyclonic vortices have been observed (Fig. 5.16). Wadhams and Squire (1983) noted that the system appeared to have only a slight eastward drift during their 4-day observation period. Vinje and Finnekåsa (1986) observed an eastward translation by about 10 km over a 4-day period in May 1976. J. A. Johannessen *et al.* (1987) classified the eddy as a bottom-trapped feature, implying that it had a significant barotropic flow component and thereby invoking conservation of potential vorticity.

The eddy near the Molloy Deep was hypothesized by Wadhams and Squire (1983) to be locally generated through a baroclinic instability mechanism. They used a two-layered model, as discussed in Pedlosky (1982), to

derive a wavelength of about 50 km most unstable to baroclinic instability, in agreement with the minimum observed dimensions of the eddy. They also pointed out that the tendencies toward cyclonic and anticyclonic flow patterns shown in Fig. 5.16 are similar to patterns observed by Griffiths and Linden (1982) in a laboratory model for baroclinic instabilities in a buoyancy-driven flow. Their hypothesis failed to account for the apparent lack of downstream propagation by the eddy, which should have occurred according to instability theory as presented in Pedlosky (1982), and for the year-to-year similarity in eddy circulation pattern and location.

Shortcomings in the Wadhams and Squire (1983) hypothesis for generation of the eddy near the Molloy Deep were resolved by Smith *et al.* (1984). They noted that conservation of potential vorticity over the Molloy Deep requires a stationary eddy even in the presence of purely barotropic flow, so baroclinic instability is not necessary for the eddy to occur. They used a nonlinear, time-dependent, two-layer numerical model to derive a circulation pattern which agreed well with the observed eddy (Fig. 5.18). The smaller regions of anticyclonic flow which were observed within the larger cyclonic eddy fit the potential vorticity model in that they coincide with seamounts located within the Molloy Deep. The model of Smith *et al.* predicts that the eddy remains stationary over the deep, as observed, though they point out that under certain conditions it may be possible for small anticyclonic eddies to "spin off" the larger eddy downstream of the deep and be advected away with the mean currents. Such spin-off events have not, however, been observed.

With the exception of possible eddy generation through wind–ice or ice–ice interactions, as predicted by numerical models, the eddies in the Fram Strait region appear to have been generated independently of the

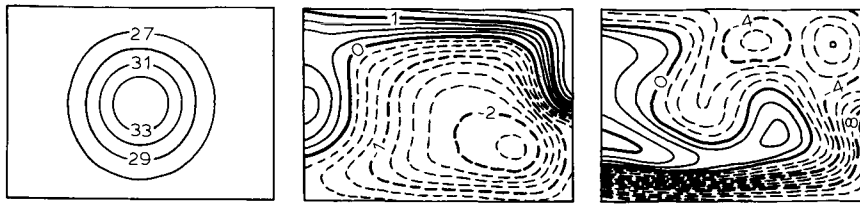

Figure 5.18 Results from a numerical model simulating the flow of a two-layer ocean over a Gaussian-shaped depression 80 km in diameter and 3500 m deep in an ocean of 2500 m depth. (Left) Model topography as depths in meters normalized by 100. (Center) Surface height anomaly, positive up, contour interval 0.25 cm, after a model run of 36 days. (Right) Interface height anomaly, positive up, contour interval 1.0 m, after a model run of the same length. The model flow is driven by inflow through the right (northeast) boundary with a constant speed of 0.1 m/s (after a 10-day spinup). Adapted from Fig. 2 in D. C. Smith *et al.* (1984); copyright by the American Geophysical Union.

presence of the ice edge. The generation and propagation of eddies through the system are a function of the mean ocean circulation and its interactions with locally complex bottom topography. The eddies do not appear to contribute significantly to lateral heat flux across the East Greenland Polar Front, in pronounced contrast to the situation in the Antarctic Ocean, where mesoscale processes are extremely important in driving cross-frontal fluxes (see below). The ice edge interacts with the eddies primarily as a passive tracer, although warm-core eddies may accelerate ice melting along the edge by increasing the rate at which ice is brought into contact with warmer water.

Virtually no observations are available concerning the fates of mesoscale eddies in the MIZs. Presumably those which remain seaward of the ice edge behave similarly to those at lower latitudes, advecting with the mean flow and gradually decaying or perhaps more rapidly being absorbed back into the mean flow. Eddies beneath an ice cover might decay more rapidly, being subject to an additional frictional force in the form of the ice cover. Smith *et al.* (1988) have developed a numerical model for ice–eddy interaction in an MIZ and hypothesize, based on the model results, that along-ice winds can lead to rapid decay of under-ice eddies by a process of erosion. Their results are supported indirectly by observations during summer 1984. The observed easterly along-ice winds would have caused preferential decay of anticyclonic eddies, and 12 of the 14 observed eddies were cyclonic. Decay of an eddy through this mechanism has, however, not been directly observed.

Farther south, in winter, the Labrador Sea marginal ice zone is (as previously noted) subject to apparent dynamic instabilities which result in wavelike fluctuations with scales from about 10 to 200 km. McNutt *et al.* (1988) used synthetic-aperture radar (SAR) data obtained from an aircraft to identify discrete eddies about 10 km in diameter in the marginal ice zone off Labrador. This supplements the earlier work of Ikeda (1987) and LeBlond (1982), who explained the wavelike fluctuations in terms of instabilities but did not have field evidence demonstrating the presence of meanders or eddies. The origin of these features is uncertain, but their scales and the earlier work by LeBlond (1982) and Gascard and Clarke (1983) concerning baroclinic instability in the region suggest that they originate through instability mechanisms. Ikeda (1987) has also demonstrated that these various mesoscale processes contribute significantly to transport of properties across the continental margin off Labrador, which is in marked contrast to the East Greenland Polar Front.

C. Eddies in the Western Arctic

Eddies have not in general been observed on the shallow Bering and Chukchi shelf regions in the western Arctic. Although there may be a low level of mesoscale energy due to instability along, for example, the Bering Sea winter

ice edge front (Muench and Schumacher, 1985), there is apparently inadequate energy in the system for sufficient growth of a meander so that it can detach to form an eddy. There also does not appear to be advection of eddies into these regions. The overall northward transport through the Bering and Chukchi seas dictates that passively advected eddies would have to originate from the south in the Bering Sea. There is no evidence that this occurs.

Although the western Arctic shelf regions are devoid of significant eddy activity, numerous small mesoscale eddies have been observed in the western Arctic Ocean basin seaward of the shelf break. These eddies have horizontal scales of 10–20 km, are primarily anticyclonic, and have their maximum speeds of order 0.3 m/s at depths between 100 and 200 m (Fig. 5.19). They carry, at their cores, water which is significantly warmer than the ambient water. They were first reported by Newton *et al.* (1974) and Hunkins (1974) as a result of observations obtained from a drifting ice camp during the Arctic Ice Dynamics Joint Experiment (AIDJEX). Manley and Hunkins (1985) estimated that these eddies cover as much as 20–30% of the ocean in the region and are a dominant cause of density and velocity variance below the upper mixed layer. More than 90% of the 146 eddies ob-

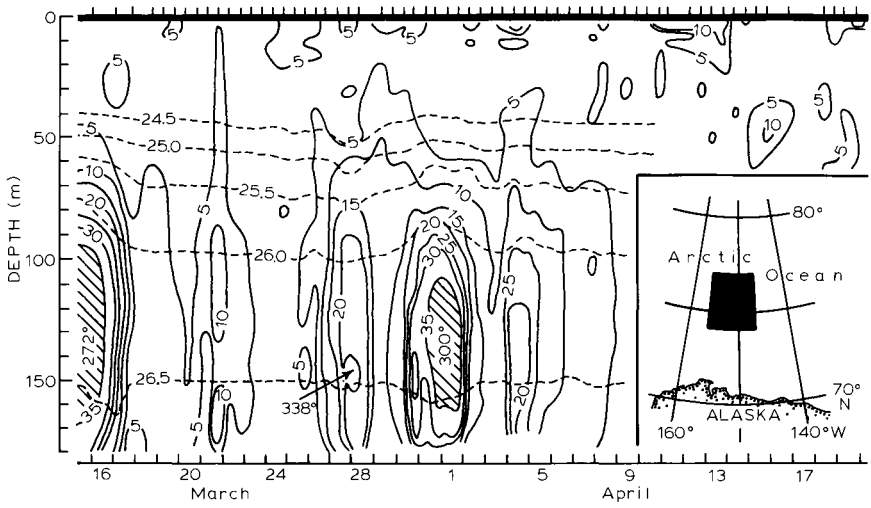

Figure 5.19 Current speed (solid contours, centimeters per second) and sigma-t (dashed contours) as functions of time, obtained from a drifting ice camp in the Arctic Ocean in the region indicated on the inset. Hatched areas represent current speeds greater than 0.35 m/s (35 cm/s), and current directions are given (°T) at identifiable eddy cores. Note the pronounced subsurface maxima in both current speed and density signature and the nearly complete lack of current activity near the surface. Adapted from Fig. 6 in Hunkins (1974); copyright by Pergamon Press.

served contained anomalous water, suggesting that they were generated remotely from the locations where they were observed. These early workers concluded that the eddies were created at the periphery of the western Arctic Ocean basin and advected into its center. Their conclusion was reinforced by Hart and Killworth (1976), who showed with a simple linear theoretical model that these eddies were probably not generated by baroclinic instability in the open ocean but were more likely generated through instability in the shallow peripheral boundary regions.

D'Asaro (1988a,b) classifies these small western Arctic eddies as submesoscale coherent vortices (SCVs), which can be viewed as a subclass of mesoscale eddies. The SCVs have sizes of order 10 km, compact axisymmetric shapes, energetic currents, and an associated strong central vorticity. They are most pronounced below rather than at the surface and usually contain water with different properties than the ambient water. Because of their small sizes and strong curvatures, centripetal forces must be considered, as well as Coriolis and pressure gradient forces, in their internal force balance. To this extent they deviate from the quasi-geostrophic approximation.

The characteristics of many of these arctic SCVs can be explained in terms of a generation mechanism proposed by D'Asaro (1988b) (Fig. 5.20). The vortices are formed from the narrow, intense coastal current which carries

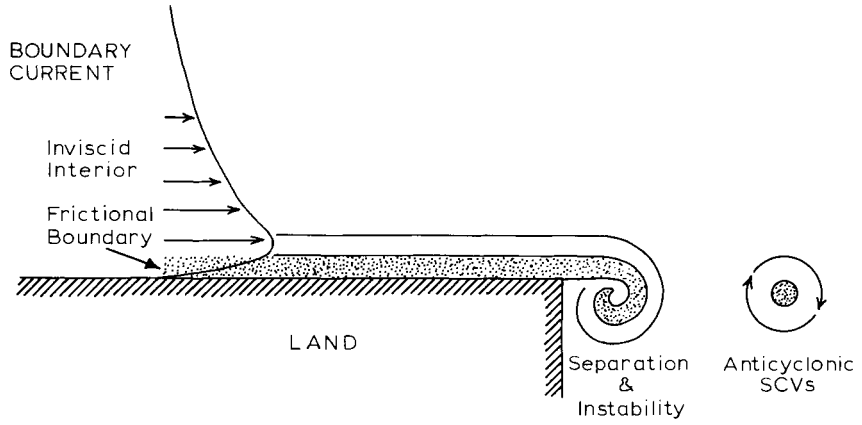

Figure 5.20 Conceptual model by which submesoscale coherent vortices (SCVs) may be generated off the northern coast of Alaska. The frictional boundary layer on the inshore side of the coastally trapped current has a relative vorticity less than $-f$, hence a potential vorticity less than zero, which results in the anticyclonic rotation of the vortices. Vortex core water is derived from the inshore portion of the coastal current. The right-angle bend in the coastline corresponds to the northward-extending point (Point Barrow) indicated by the open arrow in Fig. 5.8. Reproduced from Fig. 5 in D'Asaro (1988b), copyright by the American Geophysical Union.

water from Bering Strait northward along the Alaskan Chukchi Sea coastline. This current is particularly energetic during summer, as the normal northward flow is accentuated in the coastal region by the baroclinic coastal flow driven by continental freshwater runoff (see Wiseman and Rouse, 1980). Frictional torques act to reduce potential vorticity within the bottom boundary layers on the landward side of the coastal flow. The resulting fluid separates from the coastline as it rounds the sharp promontory formed by the northeast Alaska coast, forming discrete anticyclonic vortices which then propagate seaward.

An alternative mechanism by which eddies might form offshore in the Arctic Ocean has been suggested by McWilliams (1988), based on a theoretical model. McWilliams' model allows for geostrophic adjustment of a small oceanic region which has been subjected to diapycnal mixing. In the case of the Beaufort Sea vortices, diapycnal mixing would occur through thermohaline convection consequent to brine rejection accompanying a period of rapid surface ice formation. The vertically mixed region then has a density different from that of the surrounding water. This density differential leads to establishment, through an internal readjustment mechanism, of a baroclinic current vortex. McWilliams does not elaborate on the means by which vertical convection is laterally restricted to suitably small areas—of the same order as the 10-km dimensions of the SCVs. Presumably, ice formation in large leads or systems of leads might have this effect. This mechanism does not, however, explain the warm cores which characterize most of the Beaufort Sea SCVs.

D'Asaro (1988b) showed that the rate of northward transport in the Chukchi Sea coastal jet is consistent, assuming validity of this model, with the observed number of vortices. The vortices serve to carry much of the coastal water well out into the interior Arctic Ocean, decaying presumably partly through internal mixing and dissipation and partly through frictional interaction with the ice cover. (Contrast this northward transport with the eastward subsurface transport of coastal water by the Beaufort Undercurrent as described in Section II of this chapter.) Estimates based on Ou and Gordon's (1986) work suggest that anticyclonic eddies having the observed dimensions (of the same order as the internal radius of deformation) can persist for a year or longer beneath an ice cover. The western Arctic Ocean eddies may therefore retain their identities for long periods of time, particularly in the low-energy ambient environment typical of the region, and may transport coastal water over large parts of the Arctic Ocean.

D. Eddies in the Antarctic

Keeping in mind the caveat that we are restricting our attention to that portion of the Southern Ocean coincident with or south of the winter pack

ice edge, our knowledge of Antarctic eddies is restricted primarily to the Drake Passage–Scotia Sea region and to the eastern central Weddell Sea. These two areas have been the foci of much of the physical oceanographic research carried out in the Antarctic Ocean.

Most observations of eddies in the southern polar region have been in the Drake Passage region. Joyce and Patterson (1977) observed formation of a 30–40-km-diameter cyclonic ring, which subsequently drifted northeastward, along the polar front in Drake Passage. Gordon *et al.* (1977) found a highly convoluted polar front (see Fig. 5.10) but did not observe eddy formation. Peterson *et al.* (1982) documented the formation of a cold-core cyclonic eddy from the Antarctic Polar Front in Drake Passage during early 1979. They showed that zonal currents in Drake Passage are everywhere baroclinically unstable and that high-speed jets adjacent to fronts are barotropically unstable as well. Pillsbury and Bottero (1984) used temperature and current velocity time series data to identify deep (>2500 m) cyclonic eddies. They suggested, based on northward migration, that these eddies resulted from current interaction with the seafloor. They further suggested that such eddies contribute significantly to meridional heat flux and also play a role in dissipating kinetic energy.

Bryden (1983) has provided a useful and succinct summary of the signatures which are associated with baroclinic instability in Drake Passage. First, eddy heat flux is poleward or downgradient. This was confirmed by Sciremammano's (1980) computations, which showed poleward heat fluxes at all the current meter sites in Drake Passage. Second, eddies have an eastward phase propagation of about 0.1 m/s, in general agreement with various observations. Third, there is a vertical phase difference such that deeper velocities precede shallower velocities at a given site. This reflects an upward phase propagation which has been noted in the data by Bryden (1979) and others. Fourth, the instability criteria must be satisfied. For Drake Passage, these criteria specify that the eastward velocity shear and accompanying poleward near-bottom density gradient must balance the generally positive potential vorticity gradient throughout the water column. In other words, instability is a result of interaction between the mean current and the seabed. Finally, poleward velocity and temperature, especially at depth, must be essentially in phase with each other, implying that horizontal flow crosses isotherms.

Mesoscale eddy formation has been observed in the southwestern Scotia Sea in association with the fronts there (see Figs. 5.10 and 5.11). The westernmost portion of these fronts, where the outflowing water from the Weddell Sea has just encountered the eastward current from Drake Passage, is well defined. The fronts lose definition, however, toward the east and take on the characteristics of a broad train of mesoscale eddies (Fig. 5.21). Foster and Middleton (1984) carried out simple statistical analyses of the computed geostrophic currents associated with these eddies. Their statistics showed

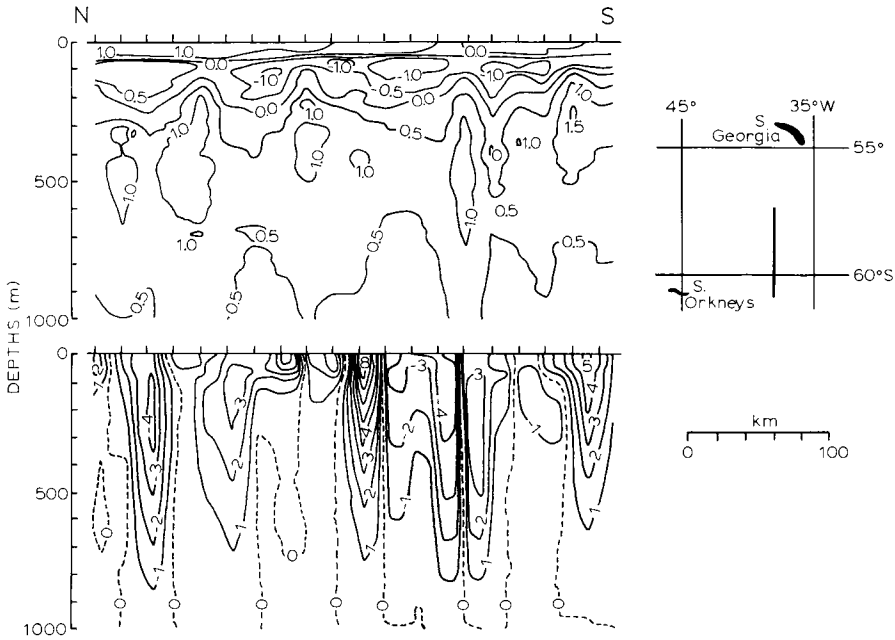

Figure 5.21 Vertical distributions of potential temperature (degrees Celsius; upper) and easterly components of geostrophic velocity (centimeters per second) computed relative to the 1000-dbar level (lower) along a meridional transect crossing the Weddell–Scotia Confluence. Note the deep current and potential temperature signatures associated with apparent mesoscale eddy activity. Approximate location of the transect is shown to the right. Adapted from Figs. 3 and 10 in Foster and Middleton (1984); copyright by Pergamon Press.

that the eddies had maximum scales of about 75 km and that both eddy energy and the lateral width of the eddy field increased in the downstream direction. They then hypothesized, based on their statistics, that the eddies resulted either from baroclinic instability or from shear instabilities generated by the speed differences across the front. Invocation of the baroclinic instability mechanism dictates that the eddies also transfer heat in the downgradient sense, i.e., southward, in qualitative agreement with the earlier demonstration by Bryden (1979) that mesoscale processes transferred heat southward in the Drake Passage region.

The results from field work in the Drake Passage–Scotia Sea region differed qualitatively from those which resulted from the Greenland Sea marginal ice zone experiment. Results from Drake Passage have tended to be more quantitative (e.g., computations of eddy heat fluxes), whereas the

Greenland Sea results have been more descriptive (e.g., descriptions of individual features). The former work relied heavily on moored instrumentation, whereas the latter has relied heavily, if not entirely, on remote sensing, shipboard CTD observations, and Lagrangian drift tracks. Of the results from the Greenland Sea, perhaps the most definitive have been the current record–based computations of Foldvik *et al.* (1988), who were able to demonstrate that the East Greenland Polar Front in Fram Strait is baroclinically stable and that cross-frontal eddy heat flux is negligible. The lesson learned here is not a new one; a meaningful field study of mesoscale processes requires acquisition of time series data over a period which is long in comparison with the time scales of the mesoscale features. In the polar regions, as elsewhere, appropriate record lengths must exceed several months.

Observations of mesoscale eddy activity in the central basins south of the Polar Frontal region are limited because most of the data are inadequate to resolve mesoscale features. There are exceptions, however, and a well-developed eddy was observed during austral summer 1977 by Gordon(1978) west of Maud Rise in the eastern Weddell Sea (Fig. 5.22). This feature was about 30 km in diameter, had rotational surface speeds of more than 0.5 m/s, and extended to at least 4000 m. The core of the eddy was considerably more uniform and colder than the surrounding waters.

Gordon (1978) suggested two possible modes of formation for the eastern Weddell Sea eddy. It may have been a remnant, persisting as a cold-core eddy, of a convective event which occurred during the preceding winter. Regional vertical stability is sufficiently low that ice formation can increase upper-layer density to a point where convective mixing occurs. In fact, the regional stability is so low that convection may occur during some years through surface cooling with no ice formation (Motoi *et al.*, 1987). This occurs when the upper-layer stability is particularly small because of high surface salinities resulting from low ice meltwater input.

As a second possibility, such an eddy may be generated initially from baroclinic instability either near the margins of the Weddell gyre or near Maud Rise, a topographic ridge in the eastern Weddell Sea. The eddy would then migrate toward the observed location. The cyclonic rotation causes upward doming at the center of the eddy, reducing the already small vertical stability and facilitating vertical convection with the onset of winter cooling and ice formation. This results in formation of a convective "chimney," discussed further in Section V.

There have been no other well-defined observations of eddies in the Antarctic ocean basins; however, there is limited evidence that such features are present at least in the western Weddell Sea. Foster and Middleton (1979) acquired and analyzed deep-current data from the northern central Weddell gyre and found mesoscale current fluctuations which may have reflected

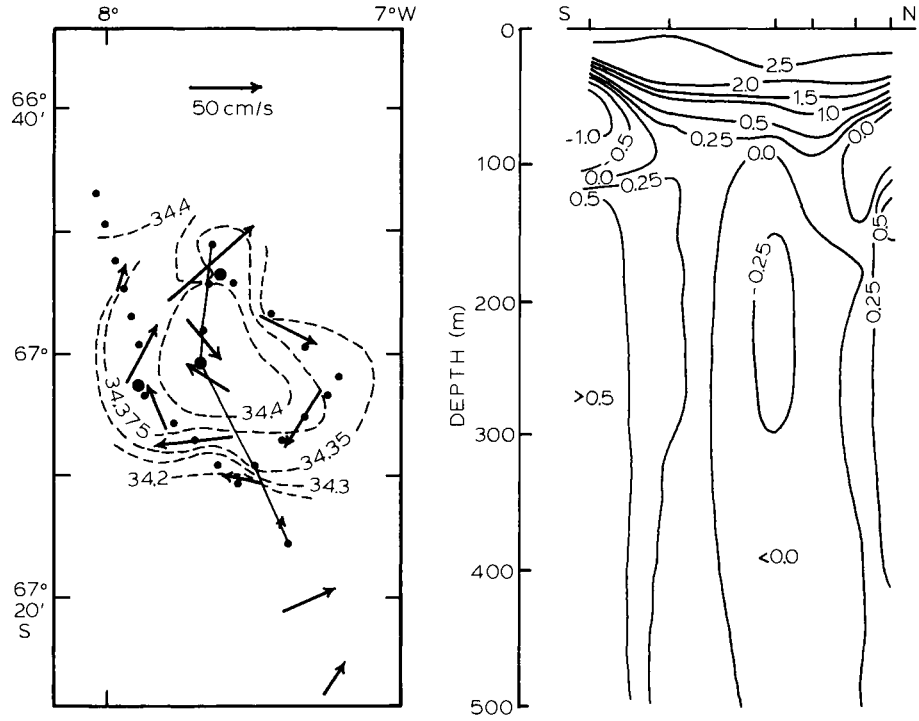

Figure 5.22 Surface salinity (per mil) and currents (centimeters per second) (left) and vertical distribution of temperature (degrees Celsius; right) down to 500 m associated with a deep convective mesoscale eddy which was observed in the central Weddell Gyre during February 1977. Location of the transect is indicated on the left by the solid line. Dashed lines are surface isohalines. Arrows show surface current speeds derived from ship drift. Small dots show locations of XBTs, and large dots are locations for CTD stations. Tick marks at the sea surface on the vertical section indicate station locations. The eddy signature extended downward to at least 4000 m. Adapted from Figs. 3 and 4 in Gordon (1978); copyright by the American Meteorological Society.

eddy activity. Husby and Muench (1988) documented, using temperature and salinity data, a weak baroclinic structure about 200 km east of the end of the Antarctic Peninsula in the northwestern Weddell Sea. This structure was about 100 km across and extended from the surface to at least 1500 m. The structure was consistent with that expected for an anticyclonic eddy, but the origin of this feature is unknown. Bersch (1988) identified a 200-km-wide feature in the central Weddell Sea which had anomalous temperature and salinity properties relative to the surrounding waters. He suggested on the basis of water mass analyses that this feature was a remnant convective cell

which had been advected to its observed location from a formation site farther southeast in the Antarctic Coastal Current. No significant eddylike circulation was detected in association with this feature.

Beyond a certainty that eddies are present and a strong suspicion that they are important in transfer of properties, our knowledge of mesoscale features in the Antarctic regions outside the relatively well-sampled Drake Passage–Scotia Sea region remains poor. Few winter data have been published, though publication of a large data set obtained from the eastern Weddell Sea during winter 1986 is imminent. No data have been obtained through the perennial western Weddell Sea ice cover, in contrast to the Arctic Ocean, where considerable data have been obtained from drifting ice camps.

IV. Some Consequences of Mesoscale Processes

A. Lateral Fluxes

This section will briefly discuss frontal and eddy-associated lateral property fluxes, which have recently been subjects of considerable field and theoretical research in the context of the polar regions. Molecular processes are usually negligible in comparison with those affected by mesoscale motions, with a few exceptions where double diffusion (which has its basis in molecular processes) plays a significant role relative to mesoscale processes.

Perhaps the simplest conceptualization of mesoscale influence on lateral property transfer is a warm-core eddy transporting heat across a front from the warm- to the cold-water side. In the case of a rich eddy field, this mechanism is averaged through the motions of all individual eddies. Because our data concerning the motions and internal temperature structures of eddies are generally incomplete, heat transfer by eddies is often estimated using time series current and temperature data. An excellent example can be found in Foldvik *et al.* (1988), who use current observations from the East Greenland Polar Front to compute lateral heat flux via the eddy correlation technique. They find that turbulent heat flux due to mesoscale motions is significant at only three of nine instruments at different locations and depths across the East Greenland Polar Front near 78.5°N. The significant fluxes occurred in frequency bands longer than 30 days, which are too long to be classified as mesoscale. Their results suggest that mesoscale heat transfer across the East Greenland Polar Front is negligible, at least at the latitude of their observations. This result is consistent with the observation (see Section III) that the East Greenland Polar Front does not appear to be baroclinically unstable.

Mesoscale eddies in the marginal ice zones may transport heat within the ocean upper layers and affect the location of the ice edge by providing

sensible heat for melting ice. Consider, as an example, a cyclonic eddy located across the ice edge and at the same time coincident with the East Greenland Polar Front (see Fig. 5.15). As the eddy impinges on the ice edge, ice is drawn by the eddy current out into open water at the same time that warm water contained in the eddy is advected beneath the ice cover. The net result is to bring ice into contact with warm water so that it can melt more rapidly than if no eddy were present. Ice melt rates approach 2.9×10^{-6} to 5.8×10^{-6} m/s in waters which are above the melting point of about -1 °C, as compared to 1.2×10^{-7} to 2.4×10^{-7} m/s within the pack (Josberger, 1987), so this effect is very pronounced.

Vinje and Finnekåsa (1986) carried out computations based on seaward ice transport by the eddy shown inFig. 5.15, assumed total melting of the ice over a 10-day period, and arrived at a lateral transport of ice lost to melting of about 5.8×10^{-3} m/s. They point out that this is probably a minimum value because it does not reflect off-ice wind transport and acceleration of ice disintegration by such smaller-scale mechanisms as ice banding. J. A. Johannessen *et al.* (1987) estimate that such eddy processes can enhance ice meltback rates along the Greenland Sea marginal ice zone by 1.2×10^{-2} to 2.3×10^{-2} m/s. Manley (1987) carried out a similar computation but noted that assumptions are needed concerning the depth to which heat is extracted from the eddy by melting ice. The sharp vertical density gradients which occur in the marginal ice zones represent a physical barrier which reduces heat transfer from the deeper to the near-surface layers. He also pointed out that the actual ice melt would vary seasonally, as off-ice water temperatures are higher during summer than winter. Manley computed ice retreat rates over a 3-month summer season of 20 to 59 km for heat utilization depths from 20 to 50 m, well under the Johannessen *et al.* minimum value of 1.2×10^{-2} m/s. Presence of warm near-surface filaments associated with eddies might increase the retreat rates by as much as 72% (Manley, 1987), however, bringing Manley's estimates into closer agreement with those of Johannessen *et al.* Manley has pointed out, however, that both his estimates and those of Johannessen *et al.* neglect the finite amount of time when the ice is likely to remain in any single location (i.e., in contact with warm water) as compared with the time required for complete melting. Because ice moves readily in response to local wind forcing, it is likely that ice would frequently be removed from the warm-water environment by winds. The meltback enhancement rates computed by Manley (1987) and J. A. Johannessen *et al.* (1987) are upper limits which assume complete transfer of upper-layer heat into melting the ice cover. Actual rates are probably considerably lower.

Unlike the East Greenland Polar Front, the front underlying the winter ice edge in the Labrador Sea appears to have significant cross-frontal heat transport due to mesoscale activity over a range of size scales. At the large end

of the range were the 100–200-km wavelength meanders described by Ikeda (1987) and illustrated in Fig. 5.5. Assuming that the meanders grow and separate from the mean current to form 70-km-diameter eddies once every 409 days, consistent with observations, water from the eddies penetrates across the entire 150-km-wide shelf and over its 1100-km length. Eddy thickness is assumed to be 400 m. The shoreward heat flux computed using these assumptions is about 70 W/m^2, compared with an estimated sea–air heat flux through 8/10 ice cover of 80 W/m^2 (Ikeda, 1987). It can be assumed that the processes responsible for this lateral heat flux also transport dissolved material such as salt and nutrients, playing a significant role in the material balance of the shelf. Gascard and Clarke (1983) had previously demonstrated that the Labrador Sea frontal structure was baroclinically unstable to wavelengths of order 20 km, consistent with the eddies observed by McNutt *et al.* (1988). Significant cross-frontal heat transfer was therefore occurring on these scales.

Unlike those in the eastern Arctic, marginal ice zone frontal systems on the Bering Sea shelf do not show appreciable meander or eddy formation (Muench and Schumacher, 1985). Hendricks *et al.* (1985) computed a cross-frontal heat for the ice edge front, applying the eddy correlation technique to moored current observations to test for mesoscale transport. They concluded that lateral heat transfer by mesoscale processes was negligible relative to fluxes associated with onshelf advection of heat by the regional northward flow.

The temperature fine structure observed along the summer Chukchi Sea ice edge fronts (Paquette and Bourke, 1979; Bourke, 1983) suggests that widespread interleaving is occurring between the north-flowing warm water and the colder ambient water. Presence of such interleafing is generally accepted evidence that mixing is being enhanced, because the fine structure effectively increases property (in this case, temperature) gradients and also the area of contact between the two different water masses. Despite the qualitative evidence for such processes in the Chukchi Sea, the data are inadequate to quantify the mixing.

Computations of heat or property transport due to mesoscale processes have not been made for other parts of the western Arctic. It is probable, however, that the mesoscale eddies which form perhaps along the coast of Alaska and propagate northward into the western Arctic Ocean basin carry with them significant heat. Presence of the relatively energetic eddy-associated currents would also presumably augment mixing in the subsurface layer, where these eddies are most energetic.

The mesoscale eddies which have been observed in association with fronts surrounding the Antarctic Ocean play a major role in north–south heat transfer. In Drake Passage, in particular, a large southward heat flux reflects

the presence of a baroclinically unstable sheared current. Bryden (1979) demonstrated that extrapolation of the Drake Passage eddy heat fluxes to the entire circumpolar region could provide sufficient poleward heat transport to balance the loss of heat to the atmosphere south of the polar front. DeSzoeke (1978) and Jennings (1980) used observed temperature–salinity and temperature–silica relationships to demonstrate that eddy fluxes are important in the overall salt and silica budgets for the Antarctic Ocean. Bryden (1983) argues that dissipation of energy through eddy formation and decay to smaller scales is adequate to balance the energy input by large-scale wind forcing. The pervasive importance to the Southern Ocean of eddies along the polar front provides a strong contrast to the East Greenland Polar Front, where mesoscale features appear to be primarily passive remnants which do not contribute substantially to cross-frontal transport.

B. Vertical Fluxes

Mesoscale processes can affect vertical fluxes through both advection and mixing processes. Advection can occur as upwelling or downwelling, which may be associated with fronts and eddies, coastal regions, bottom topographic features, and the marginal ice zones. Vertical mixing can be either forced as turbulence generated by winds, moving ice, or currents, or free and due to some combination of surface cooling and brine rejection as ice is formed.

One of the more intriguing and potentially significant mesoscale vertical motions is that associated with convective "chimneys." These are mesoscale areas over which vertical convection, driven by a combination of surface cooling and ice formation, can occur to great depths. An example of such a feature in the eastern Weddell Sea is shown in Fig. 5.22. Killworth (1979) provided an excellent discussion of these features. He demonstrated that for a chimney to occur the water column must be preconditioned to reduce its vertical stability. Cyclonic mesoscale eddies have lateral length scales similar to those of chimneys, show greatly reduced vertical stratification in the top 300 m, and can therefore act as preconditioners. The winter marginal ice zones in the Greenland Sea and at many locations in the Antarctic are sites of both intense mesoscale eddy activity and winter cooling and/or ice formation. These areas are therefore most likely to be sites of chimney formation. These chimneys may help to explain the presence of bottom water in the Greenland Sea, since the associated deep convection can, under the proper conditions, extend to the seafloor.

The ice edge presents a physical discontinuity, and resulting wind-driven upwelling along this discontinuity has been proposed as a mechanism for upward transport. In the case of a fixed ice edge, along-ice wind stress with

the ice edge to the left of the ice edge looking downstream (in the northern hemisphere, and in the opposite sense in the southern hemisphere) would provide an off-ice Ekman transport in the upper ocean layer. This off-ice transport would then have to be replaced, to satisfy volume continuity, by upwelling of deeper water by analogy with the coastal upwelling situation. Such upwelling has been hypothesized as important to ice edge primary productivity because it can transport nutrient-rich deep water to the upper layers (see W. O. Smith, 1987).

Limited field observations have been interpreted as indicating ice edge upwelling in both the Greenland Sea (Buckley *et al.*, 1979) and the Bering Sea (Alexander and Niebauer, 1981). The vast majority of ice edge data do not, however, demonstrate upwelling. Actual ice edges are not fixed but drift under the influence of local winds. Surface roughness varies in a complex fashion across the marginal ice zone such that wind drag is less on the solid pack and open water than on the broken ice near the edge. Early upwelling theories did not take this variation into account. Results from numerical models (see Chapter 7) suggest that for upwelling to occur, stringent conditions must be met in terms of wind direction relative to ice edge orientation and air–ice–ocean drag coefficients. These conditions may only infrequently be satisfied. Finally, an ice edge under the influence of local winds will generally move in response to the wind. The discontinuity presented by the ice edge is no longer stationary and may generate propagating internal waves rather than lead to upwelling (Muench *et al.*, 1983). It seems probable that vertical mixing processes associated with winds, current shear, and convection consequent to cooling and ice formation are responsible for greater vertical transport along the marginal ice zones than upwelling.

V. Polynyas: A Special Case

A. Polynyas Defined

At certain predictable locations throughout the polar regions, there are oceanic regions which remain either partially or totally ice free at times and under climatologic conditions where we would expect the waters to be ice covered. These ice-free areas are called polynyas. They appear in winter, when air temperatures are well below the freezing point for seawater, and they are surrounded by water which is ice covered. They are of interest for a number of reasons encompassing both physics and biology. For example, many polynyas, particularly those bordering Arctic and Antarctic lee coastlines during winter, are sites of active brine formation. This brine may affect the local density structure and current field and may also influence the

large-scale characteristics of a water mass as it is mixed and advected beyond the polynya region. Transfer of heat and water vapor from the open water surface can lead to local climatologic modifications, and the open water can serve as a locus for biological activity at all trophic levels.

Polynyas can form via two different physical mechanisms. First, ice may form within the regions and be continually removed by winds, currents, or both. Second, oceanic heat may enter the region in sufficient quantities to prevent ice formation locally. The first mechanism leads to "latent-heat" polynyas and the second to "sensible-heat" polynyas. These two types occur in different types of area, have somewhat different effects on the surrounding environment, and are described separately below.

B. Latent-Heat Polynyas

In the simplest of these cases, the polynya is maintained by winds or currents in combination with a physical feature such as a coastline or channel constriction. The winds or currents remove the ice as it is formed, while the physical feature prevents existing ice from entering the region. The latent heat of fusion of the continually forming ice is released into the atmosphere and removed by the wind. This is illustrated schematically in Fig. 5.23 for the

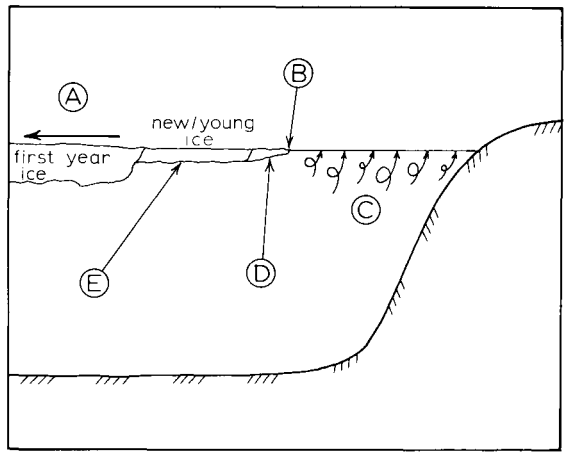

Figure 5.23 Conceptual model for a wind-driven, coastal polynya in the case where water is at the freezing point and air is below freezing. Diagram is coded as follows: (A) first-year sea ice is driven offshore by a cold wind, (B) polynya width stabilizes when ice production balances transport out of region, (C) frazil ice is produced in the turbulent boundary layer and floats to the surface, (D) frazil ice is swept rapidly downwind and collects along the leeward floes, and (E) frazil ice solidifies into area of new ice, which then hardens and thickens to form young ice floes. Adapted from Fig. 1 in Pease (1987); copyright by the American Geophysical Union.

case of a coastal polynya. The size of the open water area depends on the interrelation between air temperature and off-coastal wind speed. If both air temperature and wind speed are sufficiently low, the polynya will freeze over as ice forms more rapidly than it can be removed. A model developed by Pease (1987) demonstrates that the size of the open water area is in fact a stronger function of air temperature than of wind speed. Colder air produces a smaller polynya for a given wind speed. Higher wind speeds remove ice more quickly but also cause ice to form more rapidly, so the effect is in part self-canceling. Once even a thin layer of ice has formed over a polynya, mechanical breaking of ice by surface waves ceases and ice can be removed only by melting and the skin friction component of wind drag. Thus, the energy balance favors a continuing ice cover. Pease's model has been extended by Ou (1988) through addition of more realistic surface ice drift speeds. Ou's results suggest that polynya formation is in equilibrium with synoptic and longer-period meteorological forcing but not with fluctuations whose periods are short compared with the transit time of ice across the polynya.

Coastal polynyas in the northern Bering Sea appear to be due solely to the north–northeasterly winter winds sweeping ice away from lee coastlines as it is formed (Fig. 5.24) and are well described by Pease's (1987) and Ou's (1988) models. The shelf waters are cooled to the freezing point by midwinter, and there is no oceanic heat source to prevent ice formation. Rather than being continually ice free, the polynya opens up during periods of northerly winds and closes when winds are southerly and advect ice into the region, or when the surface radiation balance is strongly upward (rapid cooling) during periods of clear skies and low wind speeds so that ice forms a relatively stationary cover. The resulting pulsewise ice formation events show up in the water column as spikes in the salinity, caused by brine rejection from ice during the freezing events. Peaks in the local ocean currents occur due to the local baroclinic field generated by the elevated salinity during these events (Schumacher *et al.*, 1983). Removal of ice from the polynya as it is formed allows a very large net over-winter ice formation within the polynya area; Schumacher *et al.* (1983) have estimated a net overwinter ice formation of about 5 m for the St. Lawrence Island polyna and Pease (1980) calculated that the Bering Sea ice cover may be regenerated in this manner between two and six times. The brine rejected by this considerable ice formation here and at other locations may contribute significantly to maintenance of the Arctic Ocean halocline (Aagaard *et al.*, 1981).

A latent-heat polynya has been observed overlying the shallow bank just off the extreme northeastern Greenland coast (Wadhams, 1981; Vinje and Finnekåsa, 1986). This area is characterized through the winter by a thin ice cover, which by April has typically become open water. Winter and early

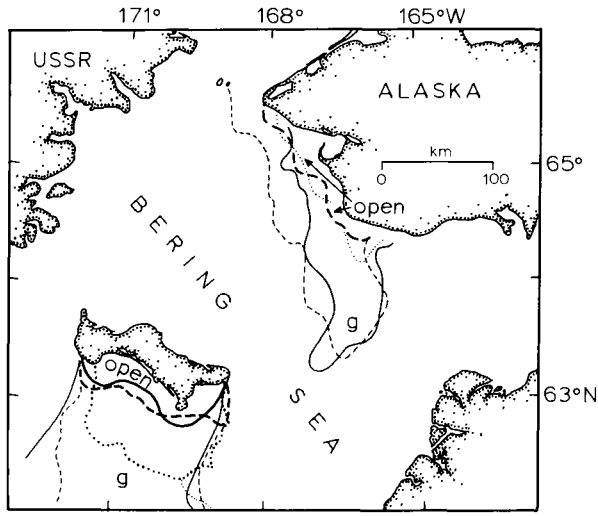

Figure 5.24 Example showing two representative coastal polynyas in the northern Bering Sea during February 1976, as derived from NOAA AVHRR satellite imagery. Heavy contours indicate actual boundaries of open water areas (also labeled "open"); lighter contours indicate transitions between gray ice (g) and lighter gray-white or white ice. Dashed lines show distributions on February 25; dotted lines, February 26; and solid lines, February 27. Adapted from the figure on p. 124 in McNutt (1981).

spring winds are northerly and, in conjunction with local currents, remove ice from the coastal region. Recent summer oceanographic data presented by Bourke *et al.* (1987a) suggest that warm water from east of the Polar Front may at times be present in the polynya region below the stably stratified surface layer.

The Canadian Arctic Archipelago contains a large number of polynyas (Fig. 5.25). The largest is the North Water, which is normally present throughout the winter in northern Baffin Bay and appears to be due in large part to mechanical removal of sea ice as it forms. Northerly winter winds attain high speeds by channeling through steep-sided valleys (Ito, 1982), and currents through the channels from the Arctic Ocean are southward, providing an efficient combination of mechanisms which can sweep newly formed ice away to the south (Muench, 1971; Muench and Sadler, 1973). At the same time, the narrow constriction formed by the channel to the north causes formation there of a structural archlike blockage of the sea ice which prevents existing ice from flowing southward into the polynya region. Past work which was based on summertime oceanographic data suggested that there was no oceanic heat source adequate to prevent ice formation

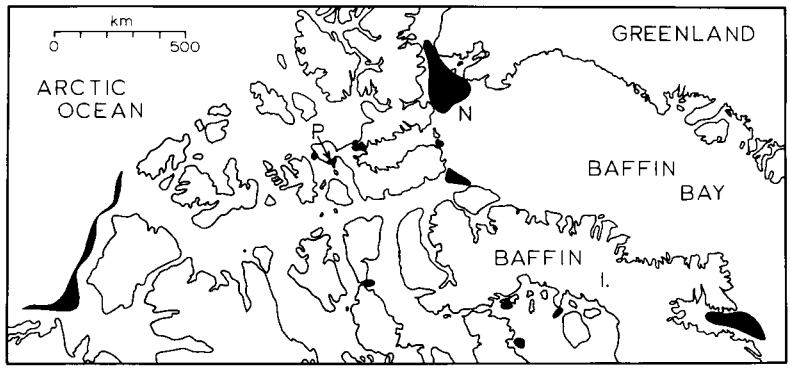

Figure 5.25 Locations of polynyas in the Canadian Arctic Archipelago. N, North Water polynya; P, Penny Strait polynya. Adapted from Fig. 1 in Topham *et al.* (1983); copyright by the American Geophysical Union.

(Muench, 1971). Recent remotely sensed data have revealed elevated-temperature cells in the open water, interpreted by Steffen (1985a,b) to mean that wind-driven upwelling provides heat from the deeper oceanic layers to the surface and so prevents ice formation and contributes to maintenance of the open water area. Resolution of the relative importance of these mechanisms awaits acquisition of winter data from the region.

The Terra Nova Bay polynya in the Antarctic is maintained by strong offshore winds which remove ice to seaward from the region more rapidly than it can be formed or advected into the region (Bromwich and Kurtz, 1984; Kurtz and Bromwich, 1985). A seaward-extending ice tongue blocks westward flow of ice into Terra Nova Bay. Locally wind-generated currents and surface waves combine to prevent the ice, estimated by Bromwich and Kurtz (1984) to form at 2.3×10^{-6} m/s, from consolidating within the polynya. Cavalieri and Martin (1985) have observed similar features along the Antarctic Wilkes Land coast in satellite imagery. Zwally *et al.* (1985) have computed brine rejection estimates based on ice formation within such Antarctic coastal polynas, and their computations demonstrate that salinity of Antarctic continental shelf water is significantly increased through this mechanism.

C. Sensible-Heat Polynyas

In a sensible-heat polynya, sufficient oceanic heat is made available to the water surface to prevent ice from forming. This upward heat transfer can occur through vertical mixing of heat from deeper water or through upward

advection of heat by such mechanisms as wind-driven upwelling. Unlike mechanically generated polynyas, sensible-heat polynyas are not sites of large net winter ice production and consequent brine addition to the underlying water column. A secondary mechanism for maintaining a sensible-heat polynya is the shift in radiation balance caused by the presence of clouds enhanced by the open water area as a moisture source.

A sensible-heat polynya occurs in winter in the "Whaler's Bay" region along the north of Spitzbergen. The regional oceanography is dominated by vigorous mixing between warm Atlantic Water flowing northward in the West Spitzbergen Current and colder ambient waters (see Fig. 5.1). Aagaard *et al.* (1987) have computed a heat loss from the 100–200-m warm-water layer of more than 200 W/m^2, a large heat loss which, if provided directly to the upper layer, can contribute significantly to preventing ice formation. Perkin and Lewis (1984) computed an order of magnitude smaller upward heat flux in the same region for ice-covered conditions. Presence or absence of an ice cover in this region is hypothesized by Aagaard *et al.* (1987) to contribute to observed variability in regional water temperature and salinity characteristics.

One of the smaller polynyas in the Canadian Archipelago—the Penny Strait polynya (Fig. 5.25)—was intensively studied with respect to oceanographic and meteorological processes (Topham *et al.*, 1983; S. D. Smith *et al.*, 1983; den Hartog *et al.*, 1983). It was found that surface water temperatures were as much as 0.2°C above freezing despite extreme temperature differences between the atmosphere and the ocean. The elevated surface water temperatures, which prevent ice formation, are due to advection and upward mixing of warmer water from depths greater than 50 m. This warm water originated from the warm Atlantic Water layer of the Arctic Ocean (Melling *et al.*, 1984). Like the St. Lawrence Island polynya in the Bering Sea, this feature was not steady state but varied in size, expanding during periods of spring tidal currents which mixed heat upward more vigorously and also when air temperatures were higher. Air temperature was found to play a major role in determining the size of the polynya, and the open water has been observed to vanish under the prolonged influence of low air temperatures.

A prominent polynya has been observed in the central Sea of Okhotsk in satellite imagery by Alfultis and Martin (1987). They interpreted summer oceanographic data to mean that upwelling or vertical mixing associated with a submarine bank provides oceanic heat to maintain the polynya. A separate polynya which occurs along the northern coastline of the Sea of Okhotsk is mechanical in origin and similar to those occurring in the northern Bering Sea. Alfultis and Martin estimate that significant quantities of

dense shelf water are produced through cooling and brine rejection in this coastal polynya.

It is necessary in the interest of completeness to discuss briefly the Weddell Sea polynya, though this feature when present was a regional rather than a mesoscale feature, because it is the most dramatic example of a sensible-heat polynya. Detected by satellite imagery, the Weddell Polynya appeared in the eastern Weddell Sea during several winters in the late 1970s and appears to have been due to upward transport of oceanic heat sufficient to prevent ice formation. This has been verified by numerical models (Martinson *et al.*, 1981; Parkinson, 1983) and is consistent with what is known of the regional oceanography (Gordon and Huber, 1984). The Weddell Polynya is presumed to be possible because of the very low vertical water column stability which typifies much of the Southern Ocean and allows vertical mixing to transport heat from deeper layers to the surface. It is likely that formation of convective chimneys, discussed in Section IV,B, played a role in its formation. Two smaller polynyas were observed in the same general region in winter 1980 in satellite imagery and were attributed to vertical mixing in concert with localized upward doming of the pycnocline (Comiso and Gordon, 1987).

VI. Concluding Comments

The foregoing chapter provides a very much summarized description and discussion of oceanic mesoscale processes as observed in the polar regions. Some materials have been intentionally omitted, based on a subjective judgment that they were of less importance than other topics. The material presented is treated in greater or lesser detail depending, again, on a subjective appraisal of significance. It is intended that the literature citations provide additional points of reference for the interested reader.

Mesoscale processes have served as a focal point for polar oceanographic exploration from the mid-1970s to the late 1980s. This focus, which provided guidance in planning such programs as the International Southern Ocean Studies (ISOS) and the Arctic Marginal Ice Zone Experiments (MIZEX), anticipated the significant roles which mesoscale processes play in polar oceanographic processes. Results from these programs have aided in quantifying these roles.

Despite recent advances in our knowledge, there is still a great deal of uncertainty concerning polar mesoscale processes. For example, formation processes for eddies and fronts remain uncertain. Our knowledge, even at a purely descriptive level, of mesoscale features in the ice-covered polar basins

remains very limited. Little information is available concerning winter convective processes which may be associated with mesoscale features. Only in a few cases do we have quantitative estimates of the effects of mesoscale phenomena on the surrounding ocean. Programs under way or being planned will address these and related problems.

Acknowledgments

Thanks are extended to Drs. Eddy Carmack, Eric D'Asaro, Miles McPhee, Humphrey Melling, Gary Lagerloef, and Joe Niebauer for providing helpful critical suggestions during preparation of this chapter. This work has been funded through Office of Naval Research Contract No. N00014-82-C-0064 with Science Applications International Corporation and National Science Foundation Grants DPP-8420646 and DPP-8715979 to Science Applications International Corporation.

References

Aagaard, K. 1984. The Beaufort undercurrent. *In* "The Alaskan Beaufort Sea: Ecosystems and Environments" (P. Barnes, D. Schell & E. Reimnitz, eds.), pp. 47–71. Academic Press.

Aagaard, K., L. K. Coachman & E. Carmack. 1981. On the halocline of the Arctic Ocean. *Deep-Sea Res.* **28:** 529–545.

Aagaard, K., A. Foldvik & S. R. Hillman. 1987. The West Spitsbergen Current: Disposition and water mass transformation. *J. Geophys. Res.* **92:** 3778–3784.

Ahlnås, K. & G. R. Garrison. 1984. Satellite and oceanographic observations of the warm coastal current in the Chukchi Sea. *Arctic* **37:** 244–254.

Alexander, V. & H. J. Niebauer. 1981. Oceanography of the eastern Bering Sea ice edge zone in spring. *Limnol. Oceanogr.* **26:** 1111–1125.

Alfultis, M. A. & S. Martin. 1987. Satellite passive microwave studies of the Sea of Okhotsk ice cover and its relation to oceanic processes, 1978–1982. *J. Geophys. Res.* **92:** 13,013–13,028.

Bersch, M. 1988. On deep convection in the Weddell Gyre. *Deep-Sea Res.* **35:**1269–1296.

Bourke, R. H. 1983. Currents, fronts and fine structure in the marginal ice zone of the Chukchi Sea. *Polar Rec.* **21:** 569–575.

Bourke, R. H., J. L. Newton, R. G. Paquette & M. D. Tunnicliffe. 1987a. Circulation and water masses of the East Greenland Shelf. *J. Geophys. Res.* **92:** 6729–6740.

Bourke, R. H., M. D. Tunnicliffe, J. L. Newton, R. G. Paquette & T. O. Manley. 1987b. Eddy near the Molloy Deep revisted. *J. Geophys. Res.* **92:** 6773–6776.

Bourke, R. H., A. M. Weigel & R. G. Paquette. 1988. The westward turning branch of the West Spitsbergen Current. *J. Geophys. Res.* **93:** 14,065–14,077.

Bromwich, D. H. & D. D. Kurtz. 1984. Katabatic wind forcing of the Terra Nova Bay polynya. *J. Geophys. Res.* **89:** 3561–3572.

Bryden, H. L. 1979. Poleward heat flux and conversion of available potential energy in Drake Passage. *J. Mar. Res.* **37:** 1–22.

———. 1983. The Southern Ocean. *In* "Eddies in Marine Science" (A. R. Robinson, ed.), pp. 265–277. Springer-Verlag, New York.

Buckley, J. R., T. Gammelsrød, J. A. Johannessen, O. M. Johannessen & L. P. Røed. 1979. Upwelling: Oceanic structure at the edge of the Arctic ice pack in winter. *Science* **203:** 165–167.

Cavalieri, D. J. & S. Martin. 1985. A passive microwave study of polynyas along the Antarctic Wilkes Land coast. *Antarct. Res. Ser.* **43:** 227–252.

Coachman, L. K. 1986. Circulation, water masses, and fluxes on the southeastern Bering Sea shelf. *Cont. Shelf Res.* **5:** 23–108.

Coastal Transition Zone Group. 1988. The coastal transition zone program. *Eos* **69:** 698–707.

Comiso, J. C. & A. L. Gordon. 1987. Recurring polynyas over the Cosmonaut Sea and the Maud Rise. *J. Geophys. Res.* **92:** 2819–2833.

Csanady, G. T. 1984. "Circulation in the Coastal Ocean." Reidel, Boston, Massachusetts.

D'Asaro, E. A. 1988a. Observations of small eddies in the Beaufort Sea. *J. Geophys. Res.* **93:** 6669–6684.

———. 1988b. Generation of submesoscale vortices: A new mechanism. *J. Geophys. Res.* **93:** 6685–6693.

Deacon, G. E. R. & T. D. Foster. 1977. The boundary region between the Weddell Sea and Drake Passage currents. *Deep-Sea Res.* **24:** 505–510.

Deacon, G. E. R. & J. A. Morrey. 1975. The boundary region between currents from the Weddell Sea and Drake Passage. *Deep-Sea Res.* **22:** 265–268.

den Hartog, G., S. D. Smith, R. J. Anderson, D. R. Topham & R. G. Perkin. 1983. An investigation of a polynya in the Canadian Archipelago, 3, surface heat flux. *J. Geophys. Res.* **88:** 2911–2916.

DeSzoeke, R. A. 1978. Inferred eddy salt fluxes in the Drake Passage. *Eos* **59:** 1120 (abstr.).

Foldvik, A., K. Aagaard & T. Torresen. 1988. On the velocity field of the East Greenland Current. *Deep-Sea Res.* **35:** 1335–1354.

Foster, T. D. & J. H. Middleton. 1979. Variability in the bottom water of the Weddell Sea. *Deep-Sea Res.* **26:** 743–762.

———. 1984. The oceanographic structure of the eastern Scotia Sea—I. Physical oceanography. *Deep-Sea Res.* **31:** 529–550.

Gammelsrød, T. & B. Rudels. 1983. Hydrographic and current measurements in the Fram Strait, August 1981. *Polar Res.* **1:** 115–126.

Gascard, J. C. & R. A. Clarke. 1983. The formation of Labrador Sea water. Part II: Mesoscale and smaller-scale processes. *J. Phys. Oceanogr.* **13:** 1779–1797.

Gascard, J. C., C. Kergomard, P.-F. Jeannin & M. Fily. 1988. Diagnostic study of the Fram Strait marginal ice zone during summer from 1983 and 1984 Marginal Ice Zone Experiment Lagrangian observations. *J. Geophys. Res.* **93:** 3613–3641.

Gill, A. E. 1982. "Atmosphere–Ocean Dynamics." Academic Press, New York.

Gordon, A. L. 1978. Deep Antarctic convection west of Maud Rise. *J. Phys. Oceanogr.* **8:** 600–612.

Gordon, A. L. & B. A. Huber. 1984. Thermohaline stratification below the Southern Ocean sea ice. *J. Geophys. Res.* **89:** 641–648.

Gordon, A. L., D. T. Georgi & H. W. Taylor. 1977. Antarctic Polar Front zone in the western Scotia Sea—summer 1975. *J. Phys. Oceanogr.* **7:** 309–328.

Griffiths, R. W. & P. F. Linden. 1981. The stability of buoyancy-driven coastal currents. *Dyn. Atmos. Oceans* **5:** 281–306.

———. 1982. Laboratory experiments on fronts. 1. Density-driven boundary currents. *Geophys. Astrophys. Fluid Dyn.* **19:** 159–187.

Hakkinen, S. 1987. Feedback between ice flow, barotropic flow, and baroclinic flow in the presence of bottom topography. *J. Geophys. Res.* **92:** 3807–3820.

Hart, J. E. & P. D. Killworth. 1976. On open ocean baroclinic instability in the Arctic. *Deep-Sea Res.* **23**: 637–645.

Hendricks, P. J., R. D. Muench & G. R. Stegen. 1985. A heat balance for the Bering Sea ice edge. *J. Phys. Oceanogr.* **15**: 1747–1758.

Hunkins, K. L. 1974. Subsurface eddies of the Arctic Ocean. *Deep-Sea Res.* **21**: 1017–1033.

Hunkins, K. L. & T. O. Manley. 1980. Oceanographic measurements at the Fram I ice station. *Eos* **61**: 278 (abstr.).

Husby, D. M. & R. D. Muench. 1988. Hydrographic observations in the northwestern Weddell Sea marginal ice zone during March 1986. *NOAA Tech. Memo.* **NOAA-TM-NMFS-SWFC-106**, 1–33.

Ikeda, M. 1987. Modeling interpretation of mesoscale meanders of the ice edge off the Labrador coast observed in NOAA satellite imagery. *J. Phys. Oceanogr.* **17**: 1468–1483.

Inoue, M. 1985. Modal decomposition of the low-frequency currents and baroclinic instability at Drake Passage. *J. Phys. Oceanogr.* **15**: 1157–1181.

Ito, H. 1982. Wind through a channel-surface: Wind measurements in Smith Sound and Jones Sound in the northern Baffin Bay. *J. Appl. Meteorol.* **21**: 1053–1062.

Jennings, J. C., Jr. 1980. Meridional flux of silica in the Drake Passage. *Eos* **61**: 263 (abstr.).

Johannessen, J. A., O. M. Johannessen, S. Svendsen, R. Shuchman, T. O. Manley, W. J. Campbell, E. G. Josberger, S. Sandven, J. C. Gascard, T. Olaussen, K. Davidson & J. van Leer. 1987. Mesoscale eddies in the Fram Strait marginal ice zone during the 1983 and 1984 Marginal Ice Zone Experiments. *J. Geophys. Res.* **92**: 6754–6772.

Johannessen, O. M., J. A. Johannessen, J. Morison, B. A. Farrelly & E. A. S. Svendsen. 1983. Oceanographic conditions in the marginal ice zone north of Svalbard in early fall 1979 with an emphasis on mesoscale processes. *J. Geophys. Res.* **88**: 2755–2769.

Johannessen, O. M., J. A. Johannessen, E. Svendsen, R. A. Shuchman, W. J. Campbell & E. G. Josberger. 1987. Ice edge eddies in the Fram Strait marginal ice zone. *Science* **236**: 427–429.

Josberger, E. G. 1987. Bottom ablation and heat transfer coefficients from the 1983 Marginal Ice Zone Experiments. *J. Geophys. Res.* **92**: 7012–7016.

Joyce, T. M. & S. L. Patterson. 1977. Cyclonic ring formation at the Polar Front in Drake Passage. *Nature (London)* **265**: 131–133.

Killworth, P. D. 1979. On "chimney" formations in the ocean. *J. Phys. Oceanogr.* **9**: 531–554.

Killworth, P. D. & N. Paldor. 1985. A model of sea-ice front instabilities. *J. Geophys. Res.* **90**: 883–888.

Kurtz, D. D. & D. H. Bromwich. 1985. A recurring, atmospherically forced polynya in Terra Nova Bay. *Antarct. Res. Ser.* **43**: 177–201.

Lagerloef, G. S. E. & R. D. Muench. 1987. Near-inertial current oscillations in the vicinity of the Bering Sea marginal ice zone. *J. Geophys. Res.* **92**: 11,789–11,802.

LeBlond, P. H. 1982. Satellite observations of Labrador Current undulations. *Atmos. Oceans* **20**: 129–142.

Lutjeharms, J. R. E. & D. J. Baker, Jr. 1980. A statistical analysis of the meso-scale dynamics of the Southern Ocean. *Deep-Sea Res.* **27**: 145–159.

Manley, T. O. 1987. Effects of sub-ice mesoscale features within the marginal ice zone of Fram Strait. *J. Geophys. Res.* **92**: 3944–3960.

Manley, T. O. & K. L. Hunkins. 1985. Mesoscale eddies of the Arctic Ocean. *J. Geophys. Res.* **90**: 4911–4930.

Manley, T. O., K. L. Hunkins & R. D. Muench. 1987a. Current regimes across the East Greenland Polar Front at 78°40′ north latitude during summer 1984. *J. Geophys. Res.* **92**: 6741–6753.

Manley, T. O., J. Z. Villanueva, J.-C. Gascard, P. F. Jeannin, K. L. Hunkins & J. van Leer. 1987b. Mesoscale oceanographic processes beneath the ice of Fram Strait. *Science* **236:** 432–434.

Manley, T. O., R. A. Shuchman & B. A. Burns. 1987c. Use of synthetic aperture radar–derived kinematics in mapping mesoscale ocean structure within the marginal ice zone. *J. Geophys. Res.* **92:** 6837–6842.

Martinson, D. G., P. D. Killworth & A. L. Gordon. 1981. A convective model for the Weddell Polynya. *J. Phys. Oceanogr.* **11:** 466–488.

McNutt, L. 1981. Ice conditions in the eastern Bering Sea from NOAA and Landsat imagery: Winter conditions 1974, 1976, 1977, 1979. *NOAA Tech. Memo.* **ERL-PMEL-24,** 1–179.

McNutt, L., S. Argus, F. Carsey, B. Holt, J. Crawford, C. L. Tang, A. L. Gray & C. Livingstone. 1988. LIMEX '87, the Labrador Ice Margin Experiment, March 1987. *Eos* **69:** 634–643.

McPhee, M. 1980. Heat transfer across the salinity-stabilized pycnocline of the Arctic Ocean. *In* "Proceedings of the Second International Symposium on Stratified Flows" (T. Carsons & T. McClimans, eds.). pp. 527–537. Tapir, Trondheim.

McWilliams, J. C. 1988. Vortex generation through balanced adjustment. *J. Phys. Oceanogr.* **18:** 1178–1192.

Melling, H., R. A. Lake, D. R. Topham & D. B. Fissel. 1984. Oceanic thermal structure in the western Canadian Arctic. *Cont. Shelf Res.* **3:** 233–258.

MIZEX Group. 1986. MIZEX East 83/84: The summer marginal ice zone experiment in the Fram Strait/Greenland Sea. *Eos* **67:** 513–517.

Motoi, T., N. Ono & M. Wakatsuchi. 1987. A mechanism for the formation of the Weddell Polynya in 1974. *J. Phys. Oceanogr.* **17:** 2241–2247.

Muench, R. D. 1971. "The Physical Oceanography of the Northern Baffin Bay Region," Baffin Bay–North Water Project Rep. 1. Arctic Inst. North Am., Montreal.

———. 1983. Mesoscale oceanographic features associated with the central Bering Sea ice edge: February–March 1981. *J. Geophys. Res.* **88:** 2715–2722.

Muench, R. D. & K. Ahlnås. 1976. Ice movement and distribution in the Bering Sea from March to June 1974. *JGR, J. Geophys. Res.* **81:** 4467–4476.

Muench, R. D. & H. E. Sadler. 1973. Physical oceanographic observations in Baffin Bay and Davis Strait. *Arctic* **26:** 73–76.

Muench, R. D. & J. D. Schumacher. 1985. On the Bering Sea ice edge front. *J. Geophys. Res.* **90:** 3185–3197.

Muench, R. D., P. H. LeBlond & L. E. Hachmeister. 1983. On some possible interactions between internal waves and sea ice in the marginal ice zone. *J. Geophys. Res.* **88:** 2819–2816.

Muench, R. D., G. S. E. Langerloef & J. T. Gunn. 1986. "1984–85 Current Observations in the East Greenland Current: A Preliminary Description," CRREL Spec. Rep. 86-3, pp. 41–53. U.S. Army Cold Reg. Res. Eng. Lab., Hanover, New Hampshire.

Mysak, L. A., R. D. Muench & J. D. Schumacher. 1981. Baroclinic instability in a downstream varying channel: Shelikof Strait, Alaska. *J. Phys. Oceanogr.* **11:** 950–969.

Nelson, D. M., W. O. Smith, L. I. Gordon & B. A. Huber. 1987. Spring distributions of density, nutrients, and phytoplankton biomass in the ice edge zone of the Weddell–Scotia Sea. *J. Geophys. Res.* **92:** 7181–7190.

Newton, J. L., K. Aagaard & L. K. Coachman. 1974. Baroclinic eddies in the Arctic Ocean. *Deep-Sea Res.* **21:** 707–719.

Nowlin, W. D., Jr. & M. Clifford. 1982. The kinematic and thermohaline zonation of the Antarctic Circumpolar Current at Drake Passage. *J. Mar. Res.* **40:** 481–507.

Nowlin, W. D., Jr., T. Whitworth, III & R. D. Pillsbury. 1977. Structure and transport of the Antarctic Circumpolar Current at Drake Passage from short-term measurements. *J. Phys. Oceanogr.* 7: 788–802.

Ou, H.-W. 1988. A time-dependent model of a coastal polynya. *J. Phys. Oceanogr.* **18:** 584–590.

Ou, H.-W. & A. L. Gordon. 1986. Spin-down of baroclinic eddies under sea ice. *J. Geophys. Res.* **91:** 7623–7630.

Paquette, R. G. & R. H. Bourke. 1974. Observations on the coastal current of Arctic Alaska. *J. Mar Res.* **32:** 195–207.

———. 1979. Temperature fine structure near the sea-ice margin of the Chukchi Sea. *J. Geophys. Res.* **84:** 1155–1164.

———. 1981. Ocean circulation and fronts as related to ice melt-back in the Chukchi Sea. *J. Geophys. Res.* **86:** 4215–4230.

Paquette, R. G., R. H. Bourke, J. L. Newton & W. Perdue. 1985. The East Greenland Polar Front in autumn. *J. Geophys. Res.* **90:** 4866–4882.

Parkinson, C. L. 1983. On the development and cause of the Weddell Polynya in a sea ice simulation. *J. Phys. Oceanogr.* **13:** 501–511.

Patterson, S. L. & H. A. Sievers. 1980. The Weddell–Scotia confluence. *J. Phys. Oceanogr.* **10:** 1584–1610.

Pease, C. H. 1980. Eastern Bering Sea ice processes. *Mon. Weather Rev.* **108:** 2015–2023.

———. 1987. The size of wind-driven coastal polynyas. *J. Geophys. Res.* **92:**7049–7059.

Pedlosky, J. 1982. "Geophysical Fluid Dynamics." Springer-Verlag, New York.

Perkin, R. G. & E. L. Lewis. 1984. Mixing in the West Spitsbergen Current. *J. Phys. Oceanogr.* **14:** 1315–1325.

Peterson, R. G., W. D. Nowlin, Jr. & T. Whitworth, III. 1982. Generation and evolution of a cyclonic ring at Drake Passage in early 1979. *J. Phys. Oceanogr.* **12:** 712–719.

Pillsbury, R. D. & J. S. Bottero. 1984. Observations of current rings in the Antarctic zone at Drake Passage. *J. Mar. Res.* **42:** 853–874.

Pounder, E. R. 1986. Physical oceanography near the North Pole. *J. Geophys. Res.* **91:** 11,763–11,773.

Quadfasel, D., J.-C. Gascard & K.-P. Koltermann. 1987. Large-scale oceanography in Fram Strait during the 1984 Marginal Ice Zone Experiment. *J. Geophys. Res.* **92:** 6719–6728.

Robinson, A. R. (ed.). 1983. "Eddies in Marine Science." Springer-Verlag, New York.

Røed, L. P. & J. J. O'Brien. 1983. A coupled ice–ocean model of upwelling in the marginal ice zone. *J. Geophys. Res.* **88:** 2863–2872.

Rudels, B. 1987. On the mass balance of the polar ocean, with special emphasis on Fram Strait. *Skr., Nor. Polarinst.* **88:** 1–53.

Schumacher, J. D., K. Aagaard, C. H. Pease & R. B. Tripp. 1983. Effects of a shelf polynya on flow and water properties in the northern Bering Sea. *J. Geophys. Res.* **88:** 2723–2732.

Sciremammano, F., Jr. 1980. The nature of poleward heat flux due to low-frequency current fluctuations in Drake Passage. *J. Phys. Oceanogr.* **10:** 843–852.

Smith, D. C., IV, J. H. Morison, J. A. Johannessen & N. Untersteiner. 1984. Topographic generation of an eddy at the edge of the East Greenland Current. *J. Geophys. Res.* **89:** 8205–8208.

Smith, D. C., IV, A. A. Bird & W. P. Budgell. 1988. A numerical study of mesoscale ocean eddy interaction with a marginal ice zone. *J. Geophys. Res.* **93:** 12,461–12,473.

Smith, S. D., R. J. Anderson, G. den Hartog, D. R. Topham & R. G. Perkin. 1983. An investigation of a polynya in the Canadian Archipelago. 2. Structure of turbulence and sensible heat flux. *J. Geophys. Res.* **88:** 2900–2910.

Smith, W. O. 1987. Phytoplankton dynamics in marginal ice zones. *Oceanogr. Mar. Biol.* **25:** 11–38.

Smith, W. O. & D. M. Nelson. 1985. Phytoplankton bloom produced by a receding ice edge in the Ross Sea: Spatial coherence with the density field. *Science* **227:** 163–166.

Steffen, K. 1985a. "Surface Temperature and Sea Ice of an Arctic Polynya: North Water in Winter," Zh. Geogr. Schr. 19. Geographisches Institut der Eidg, Technischen Hochschule, Zurich.

———. 1985b. Warm water cells in the North Water, northern Baffin Bay during winter. *J. Geophys. Res.* **90:** 9129–9136.

Thomson, R. E. 1984. A cyclonic eddy over the continental margin of Vancouver Island: Evidence for baroclinic instability. *J. Phys. Oceanogr.* **14:** 1326–1348.

Topham, D. R., R. G. Perkin, S. D. Smith, R. J. Anderson & G. den Hartog. 1983. An investigation of a polynya in the Canadian Archipelago. 1. Introduction and oceanography. *J. Geophys. Res.* **88:** 2888–2899.

Turner, J. S. 1973. "Buoyancy Effects in Fluids." Cambridge Univ. Press, London and New York.

Untersteiner, N. 1988. On the ice and heat balance in Fram Strait. *J. Geophys. Res.* **93:** 527–531.

Vinje, T. 1977. "Sea Ice Studies in the Spitsbergen–Greenland Area," Landsat Rep. E77-10206. Natl. Tech. Inf. Serv., Springfield, Virginia.

———. 1982. The drift pattern of sea ice in the Arctic with particular reference to the Atalntic approach. *In* "The Arctic Ocean" (L. Rey & B. Stonehouse, eds.), pp. 83–96. Macmillan, London.

Vinje, T. & O. Finnekåsa. 1986. The ice transport through Fram Strait. *Skr., Nor. Polarinst.* **186:** 1–39.

Wadhams, P. 1981. The ice cover in the Greenland and Norwegian seas. *Rev. Geophys.* **19:** 345–393.

Wadhams, P. & V. A. Squire. 1983. An ice–water vortex at the edge of the East Greenland Current. *J. Geophys. Res.* **88:** 2770–2780.

Wadhams, P., A. E. Gill & P. F. Linden. 1979. Transects by submarine of the East Greenland Polar Front. *Deep-Sea Res.* **26:** 1311–1327.

Whitworth, T., III & W. D. Nowlin, Jr. 1987. Water masses and currents of the Southern Ocean at the Greenwich meridian. *J. Geophys. Res.* **92:** 6462–6476.

Wiseman, W. J., Jr. & L. J. Rouse, Jr. 1980. A coastal jet in the Chukchi Sea. *Arctic* **33:** 21–29.

Zwally, H. J., J. C. Comiso, C. L. Parkinson, W. J. Campbell, F. D. Carsey & P. Gloersen. 1983. "Antarctic Sea Ice, 1973–1976: Satellite Passive-Microwave Observations," NASA Spec. Publ. 459. NASA, Washington, D.C.

Zwally, H. J., J. C. Comiso & A. L. Gordon. 1985. Antarctic offshore leads and polynyas and oceanographic effects. *Antarct. Res. Ser.* **43:** 203–226.

6 Small-Scale Processes

Miles G. McPhee
McPhee Research Company
Naches, Washington

I. Introduction 287
II. Fundamental Physics 290
A. Conservation Equations 291
B. Reynolds Stress 292
C. Rotation and Geostrophy 293
D. Fluid Properties 295
III. Turbulent Exchange: Processes and Scales 296
A. Turbulence 296
B. Scales Governing RBL Turbulence 298
C. A Heuristic Model for Turbulent Flux in the RBL 302
IV. Some Measurements from the Under-Ice Boundary Layer 310
V. Drag Coefficients and Under-Ice Roughness 314
A. Surface Layer Profile Measurements 316
B. Direct Measurements of Reynolds Stress 317
C. Momentum Integral Methods 318
D. Combination Methods 318
E. The Force Balance Method 318
F. A Comparison of Roughness Lengths 321
VI. Heat and Mass Flux at the Ice/Ocean Interface 322
VII. Internal Wave Drag 327
VIII. Summary 330
References 331

I. Introduction

The direct interaction between polar oceans and the atmosphere occurs across a relatively thin boundary layer, which differs from the upper part of the rest of the world ocean in that its properties and physics are affected directly by a layer of ice which may reach several meters in thickness. The small-scale oceanic processes which affect air–sea–ice interaction in polar

Polar Oceanography, Part A: Physical Science

regions are the subject of this chapter. The main thrust is describing the physical processes that control the exchange of heat, mass, and momentum near the surface when sea ice is present. The problems addressed, which are pertinent in most respects to all upper-ocean physics, tax the best observational and theoretical tools we have. Oceanographic measurements in polar oceans are expensive and often difficult. Remote sensing is hampered by long polar nights and persistent cloudiness. Quantitative theoretical treatment requires a thorough understanding of turbulent boundary layer dynamics, influenced by rotation, buoyancy, and sea ice. Despite the difficulties, there has been heightened interest and much progress in recent years, driven by both increased operational needs and recognition of the role that polar and subpolar oceans play in long-term climate fluctuations, especially ventilation of the deep ocean.

The story begins nearly a century ago with F. Nansen and the drift of the research vessel *Fram* in the ice pack of the Eurasian basin of the Arctic Ocean. Nansen observed that the ice consistently veered 20° to 40° to the right of the surface wind. He correctly surmised that the veering resulted from the Coriolis force (i.e., the apparent deflection of an object moving in a rotating reference frame) acting differentially at various levels in the shear flow beneath the ice. Nansen interested V. Ekman in the problem, and in a remarkable paper published in 1905, Ekman developed the mathematics of a sheared fluid on a rotating surface, discovering elegantly simple spirals in theoretical profiles of mean current and turbulent stress. His theory predicted that surface current should be 45° to the right *(cum sole)* of surface stress, which explained qualitatively Nansen's observations. He also showed how large, circular motions superimposed on the mean drift (inertial oscillations) could develop in the upper ocean and further suggested that the eddy viscosity relating current shear to turbulent stress depended on surface stress. In the last two areas, Ekman was far ahead of his time, and it was not until the latter half of the century that observations (and, in some respects, theory) caught up with him.

Ekman's paradigm failed to account for a thin region near the ice/ocean interface where strong shear develops parallel to the direction of interfacial stress. By considering data from Soviet Polar Drift stations, Shuleikin (1938) patched the ice to the Ekman solution via a thin surface layer and worked out the intricate force balance that determines ice response to wind in the absence of internal stress gradients. Reed and Campbell (1962) later incorporated these concepts into their ice modeling work, modifying them somewhat by letting the eddy viscosity of the lower, Ekman layer depend on the interfacial stress.

Strong inferential evidence for Ekman dynamics was found in the rightward (leftward in the southern hemisphere) deflection of ice drift and surface currents, but there was no unequivocal example of an Ekman spiral in

upper-ocean currents until Hunkins (1966) presented measurements made from Arctic Drift Station Alpha during the summer of 1958 (Fig. 6.1). Hunkins interpreted his measurements as including three more or less separate currents: (1) a geostrophic current, $\mathbf{V}_g$, associated with slope of the sea surface and not dependent on the recent, local wind; (2) the Ekman spiral up through the boundary layer, culminating in $\mathbf{V}_0$; and (3) a thin (less than 2 m) layer of intense shear, indicated by the relative velocity, $\mathbf{V}_2$. These three elements are present in nearly all current measurements made from drifting ice, provided the currents are averaged long enough that inertial effects are not dominant.

During the 1960s and 1970s, advancing technology and increased interest in high-latitude oceanography led to greater understanding of ice/ocean interaction. This was accompanied by a gradual shift in attitude from treating the ice as a barrier preventing oceanic access to appreciating its potential as an amazingly stable platform for conducting high-resolution experiments

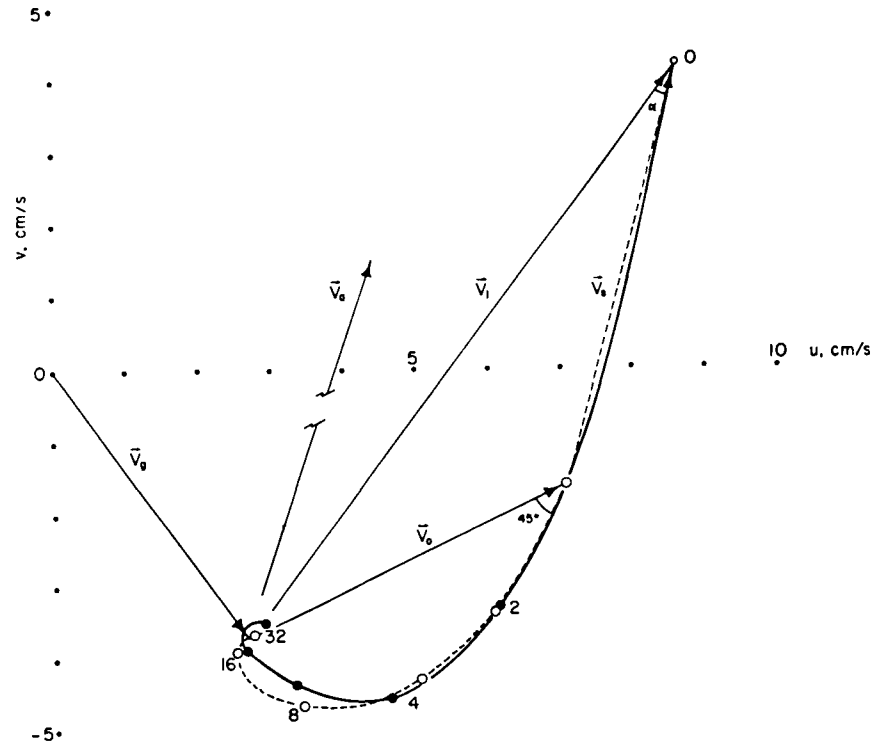

Figure 6.1 Vector average of nine current profiles taken over a 2-month period at drift station Alpha (filled circles), shown with Ekman current spiral for eddy viscosity of 23.8 $cm^2 s^{-1}$ (open circles). Reprinted with permission from Hunkins (1966); copyright by Pergamon Press.

in the boundary layer and pycnocline. Neshyba *et al.* (1971) reported, in unprecedented detail, small-scale step structure in the thermocline under drifting ice island T-3. Pilot studies of the Arctic Ice Dynamics Joint Experiment (AIDJEX) in 1971 and 1972 included the elegant turbulence experiments of Smith (Smith, 1974; McPhee and Smith, 1976). The year-long AIDJEX Main Experiment (1975–1976) provided unsurpassed time series of upper-ocean currents and temperature/salinity profiles at multiple stations in the central Arctic (Hunkins, 1980). At the same time, rapid advances in atmospheric planetary boundary layer theory, aided by computer modeling, were providing a broader context for interpreting the measurements.

After AIDJEX, emphasis shifted toward the complicated interactions that occur near the lateral boundaries of the sea ice, i.e., the marginal ice zone (MIZ). Large, multidisciplinary experiments such as MIZEX West in the Bering Sea and the series of MIZEX East experiments in the Greenland Sea MIZ examined the interplay between thermodynamics and dynamics as the ice encounters relatively warm water. Interest in high Arctic upper-ocean processes, especially the internal wave climate, has revived, as witnessed by the Arctic Internal Wave Experiment (AIWEX 85) and the planned Co-ordinated Eastern Arctic Experiment (CEAREX) operations in the eastern Arctic. These projects have spawned significant improvements in measurement technology, including sophisticated velocity/temperature/conductivity profilers (Morison *et al.*, 1987; Villanueva and van Leer, 1987), acoustic Doppler profilers (Pinkel *et al.*, 1986), and direct turbulent heat flux measurements (McPhee, 1986a). A recent transect of the mixed layer in the Weddell Sea (Gordon, 1987) has revealed fascinating contrasts with the relatively well-documented Arctic mixed layer that call out for further study.

It would be difficult to summarize adequately all of this work, even the most recent, in a short chapter. The intent is rather to provide the reader with a general view of our current understanding of small-scale processes near the ice/ocean interface. As such, the chapter necessarily reflects some of my personal views, which a properly skeptical reader will recognize. In some cases (specifically, Section III,C), what I call "simple" might justifiably be called anything but; however, the description is related to alternatives, mainly numerical modeling, and I have tried to identify the underlying concepts, which, in the main, are quite simple.

II. Fundamental Physics

This section presents a brief synopsis of the fundamental fluid equations pertinent to understanding upper-ocean transfer processes. For a reader not familiar with the fluid equations or elementary vector and tensor notation, a

number of standard textbooks treat the concepts well. Gill (1982, Chapters 3 and 4) presents an especially clear and useful development of the state equations, conservation equations, and equation of motion.

A. Conservation Equations

The equations that govern fluid behavior may be stated in relatively compact form. Let ϵ be an arbitrary property of the fluid, say density, internal energy (or equivalently in our case, heat content), or concentration of salt or some other contaminant such as frazil ice crystals, or a vector quantity such as momentum. Consider a fixed, infinitesimal control volume in the fluid. Within the volume, the local rate of change of ϵ will depend on a source of the property, Q_ϵ, less the net flux, $\mathbf{F}_\epsilon$, integrated over the surface of the control volume. By Gauss's theorem

$$\partial\epsilon/\partial t = Q_\epsilon - \nabla \cdot \mathbf{F}_\epsilon \tag{6.1}$$

For scalars, the source term Q_ϵ is associated mainly with phase changes; e.g., if frazil crystals form in supercooled water, heat and salt are released locally, so local internal energy and salinity increase. In most situations, the source term for scalars will be small.

The flux vector (or tensor when ϵ is momentum) $\mathbf{F}_\epsilon$ may comprise several elements, examples being the advective flux $\epsilon\mathbf{u}$, where $\mathbf{u}$ is the local velocity vector; a molecular diffusion term $-\rho k_\epsilon \nabla\epsilon$, where k_ϵ is the molecular diffusivity coefficient; or, when ϵ is internal energy, a radiative flux associated with insolation. By far the most important element for the rotational boundary layer (RBL) is the advective term, so as a first approximation the flux vector may be written

$$\mathbf{F}_\epsilon \cong \epsilon\mathbf{u} \tag{6.2}$$

but note that there may be special circumstances where other terms are important, pertinent examples being solar heating when ice concentration is low (radiative flux divergence) and molecular viscosity effects in a thin layer near the ice/ocean interface.

For dynamical purposes, most oceanic flows may be treated as incompressible, meaning that density ρ following fluid parcels does not change (i.e., the material derivative is zero). This leads directly to the continuity equation

$$\nabla \cdot \mathbf{u} = -(1/\rho)\,(d\rho/dt) = 0 \tag{6.3}$$

If Eq. (6.2) (advective flux) and Eq. (6.3) (continuity) are incorporated into Eq. (6.1), the general conservation equation may be written

$$\partial\epsilon/\partial t + \mathbf{u} \cdot \nabla\epsilon = Q_\epsilon \tag{6.4}$$

Substituting salinity ρS for ϵ, the conservation of salt is expressed as

$$\partial S/\partial t + \mathbf{u} \cdot \nabla S = Q_S/\rho \tag{6.5}$$

where Q_S is a salinity source within the fluid (e.g., from nucleation of frazil crystals).

Provided divergence of radiative flux is incorporated into a source term Q_h, which may also include latent heat associated with phase change, we can write a similar equation for temperature:

$$\partial T/\partial t + \mathbf{u} \cdot \nabla T = Q_h/\rho c_p \tag{6.6}$$

where c_p is the specific heat at constant pressure. Specific heat varies with temperature, salinity, and pressure (see Gill, 1982, Table A3.1); however, the variation is relatively small, and here we use a constant value of 3980 J kg^{-1} K^{-1}.

Now substitute vector momentum $\rho\mathbf{u}$ for ϵ in Eq. (6.4). We have

$$\partial \mathbf{u}/\partial t + \mathbf{u} \cdot \nabla \mathbf{u} = Q_f/\rho \tag{6.7}$$

In this interpretation, the source term is the vector sum of the negative gradient of pressure in the fluid, $-\nabla p$, and gravity, $-g\mathbf{k}$, where $\mathbf{k}$ is the vertical unit vector. Thus we arrive at Euler's equation

$$\partial \mathbf{u}/\partial t + \mathbf{u} \cdot \nabla \mathbf{u} = -(1/\rho)\,\nabla p - g\mathbf{k} \tag{6.8}$$

This is, of course, a highly simplified derivation of Newton's second law for fluids. Batchelor (1970, Chapter 3) treats the subject in detail.

B. Reynolds Stress

Ignoring molecular effects in the conservation equations is not the same as assuming that the fluid is frictionless. When ice moves in response to wind, it encounters drag from the water, which indicates a net downward momentum flux. Unless the forcing is very small, we know that in the bulk of the RBL molecular transfer processes can account for only a minute fraction of the total momentum flux. The remainder occurs in a way that can best be shown by manipulating the advective term in the momentum equation. Suppose that the flow velocity consists of rapid variations superimposed on an underlying "mean" signal that changes relatively slowly in response to the large-scale forcing. Over some area large compared with the scale of the small, frequent fluctuations, we may express the local instantaneous flow as

$$\mathbf{u} = \langle \mathbf{u} \rangle + \mathbf{u}' \tag{6.9}$$

where the angle brackets indicate the mean over the area and $\mathbf{u}'$ is the

deviation from the mean ($\langle \mathbf{u}' \rangle = 0$). With the continuity condition, Eq. (6.3), and the well-known rule for the average of products,

$$\langle u_i u_j \rangle = \langle u_i \rangle \langle u_j \rangle + \langle u_i' u_j' \rangle \tag{6.10}$$

the average of the advective term [the second term on the left of Eq. (6.8)] can be expressed in component form as

$$\langle u_i \frac{\partial u_j}{\partial x_i} \mathbf{e}_j \rangle = \left(\langle u_i \rangle \frac{\partial \langle u_j \rangle}{\partial x_i} + \frac{\partial \langle u_i' u_j' \rangle}{\partial x_i} \right) \mathbf{e}_j \tag{6.11}$$

where $\mathbf{e}_j$ is the unit vector in the j direction ($j = 1, 2, 3$; repeated indices imply summation; and by convention $\mathbf{e}_3$ is the vertical unit vector $\mathbf{k}$).

Unless otherwise noted, from here on $\mathbf{u}$ written without angle brackets represents the underlying mean flow velocity. The Euler equation becomes

$$\partial \mathbf{u}/\partial t + \mathbf{u} \cdot \nabla \mathbf{u} = -(1/\rho) \nabla p - g\mathbf{k} + \nabla \cdot \boldsymbol{\tau} \tag{6.12}$$

where the components of the symmetric tensor $\boldsymbol{\tau}$ are

$$\tau_{ij} = -\langle u_i' u_j' \rangle \tag{6.13}$$

which is the kinematic Reynolds stress. Reynolds stress is most often associated with more or less chaotic deviations called turbulence, but internal waves (which are not in general turbulent) can also transport momentum by correlation of velocity deviations.

If ϵ is a scalar property, we may similarly write the general scalar conservation equation [Eq. (6.4)] as

$$\partial \epsilon/\partial t + \mathbf{u} \cdot \nabla \epsilon = Q_\epsilon - \nabla \cdot \langle \epsilon' \mathbf{u}' \rangle \tag{6.14}$$

where unprimed quantities again refer to underlying mean values.

C. Rotation and Geostrophy

The acceleration of a fluid parcel moving with velocity $\mathbf{u}$ relative to a frame of reference that is rotating about some axis with angular velocity $\boldsymbol{\Omega}$ includes two terms that are not present in an inertial reference frame. One of these is a centripetal acceleration, which is usually incorporated into the apparent gravity g. The other term is the Coriolis acceleration $2\,\boldsymbol{\Omega} \times \mathbf{u}$ and is often of central importance in geophysical flows. A special symbol f (the Coriolis parameter) denotes twice the vertical component of rotation,

$$f = 2\Omega_3 = 2\Omega \sin \Phi \tag{6.15}$$

where Φ is the latitude (north positive) and Ω the angular rotation speed of the earth, $7.292 \times 10^{-5}\ \mathrm{s}^{-1}$.

If we ignore the vertical component of the Coriolis term, the Euler equation in a fixed-to-earth (rotating) frame is

$$d\mathbf{u}/dt + f\mathbf{k} \times \mathbf{u} = -(1/\rho)\,\nabla p - g\mathbf{k} + \nabla \cdot \boldsymbol{\tau} \tag{6.16}$$

The *geostrophic current* is defined by

$$f\mathbf{k} \times \mathbf{u}_g \equiv -(1/\rho)\,\nabla p \tag{6.17}$$

Neglecting variation in air pressure, the surface geostrophic flow can be expressed in terms of the gradient of sea surface elevation η,

$$f\mathbf{k} \times \mathbf{u}_g = -g\,\nabla\eta \tag{6.18}$$

From Eq. (6.16), the geostrophic flow coincides with the actual flow only in a steady state with no advective flux or Reynolds stress. It is often convenient to consider flow relative to the surface geostrophic flow, e.g., wind-driven currents with respect to a relatively slowly changing geostrophic flow. With the approximation that the material derivative of $\mathbf{u}_g$ is zero, we may write Eq. (6.16) as

$$d\mathbf{u}_r/dt + f\mathbf{k} \times \mathbf{u}_r = \nabla \cdot \boldsymbol{\tau} \tag{6.19}$$

where $\mathbf{u}_r = \mathbf{u} - \mathbf{u}_g$.

Equation (6.19) provides a simple relation between kinematic stress at the surface (or ice/ocean interface) and net volume transport relative to the underlying geostrophic flow. Since our primary concern is mean horizontal current, it is convenient to express two-dimensional (horizontal) vectors as complex numbers, that is, $\hat{u} = u + iv$, where u and v are velocity components in the x and y directions and $i = \sqrt{-1}$. This has the advantage of simplifying notation and calculation (using straightforward complex arithmetic) and will be used extensively in the following sections. When a normally complex quantity $\hat{A}$ is written without the caret, scalar magnitude is implied, that is, $\hat{A} = Ae^{i\theta}$, where θ is the counterclockwise angle from the real axis, $\theta = \tan^{-1} \mathrm{Im}(\hat{A})/\mathrm{Re}(\hat{A})$. Note that complex multiplication and division implies both scaling and rotation

$$\begin{aligned} \hat{A}\hat{B} &= AB\,e^{i(\theta_A + \theta_B)} \\ \hat{A}/\hat{B} &= (A/B)e^{i(\theta_A - \theta_B)} \end{aligned} \tag{6.20}$$

For a horizontally homogeneous system (i.e., no horizontal gradients), Eq. (6.19) becomes in complex notation

$$d\hat{u}_r/dt + if\hat{u}_r = \partial\hat{\tau}/\partial z \tag{6.21}$$

where $\hat{\tau}$ is the horizontal traction vector component of the Reynolds stress tensor,

$$\hat{\tau} = -(\langle u'w' \rangle + i\langle v'w' \rangle) \tag{6.22}$$

We suppose that at some level the Reynolds stress driven by surface momentum flux decreases to zero, so integrating Eq. (6.21) from the maximum depth of frictional influence, H, we have

$$\frac{d\hat{M}}{dt} + if\hat{M} = \hat{\tau}(z=0) = \hat{\tau}_0$$
$$\hat{M} = \int_{-H}^{0} \hat{u}_r \, dz \tag{6.23}$$

This equation allows a steady-state balance in which the integrated transport is equal to the surface stress divided by f, directed 90° *cum sole* (clockwise in the northern hemisphere) to the stress direction.

Suppose a system obeying Eq. (6.23), initially at rest, is subjected to a step-function wind stress in the imaginary (y) direction, $\hat{\tau} = i\tau$, at $t = 0$. The solution for $t > 0$ is

$$\hat{M}(t) = \frac{\tau}{f}(1 - e^{-ift}) = \frac{\tau}{f}[1 - \cos(ft) + i\sin(ft)] \tag{6.24}$$

The locus of solutions of Eq. (6.24) in the complex plane is a circle of radius τ/f centered at τ/f on the real axis; thus the transport vector traces a clockwise circle about its mean value in one inertial period, $2\pi/f$, which is 12 h at the pole. A trajectory traced out by the mean transport shows a series of cycloidal scallops, called inertial oscillations. This may seem highly idealized, but in fact we often find large circular motions superimposed on a relatively small mean translation in ice drift trajectories (e.g., Hunkins, 1967; McPhee, 1978), which persist for up to 8 or 10 inertial periods and are clearly related to abrupt changes in wind forcing.

D. Fluid Properties

Density of seawater depends on pressure, temperature, and dissolved salts, indicated by practical salinity S. Formulas for calculating density from T, p, and S are given by Gill (1982, Appendix 3), along with tables for quick reference.

It is often relative changes in density that are important dynamically, and then it is convenient to relate the changes directly to changes in temperature and salinity via expansion coefficients:

$$\Delta\rho/\rho = -\beta_T \Delta T + \beta_S \Delta S \tag{6.25}$$

β_S has a weak dependence on temperature but for polar waters can be approximated by the constant value 0.81×10^{-3} (Gill, 1982; Table A3.1). β_T varies with both temperature and salinity (see, e.g., Table 3.1 of Neumann and Pierson, 1966). Two points are worth noting. First, for salinities above

about 25 ppt, the thermal expansion coefficient is positive for all temperatures above freezing. Thus seawater does not exhibit a density maximum like that found at about 4°C in fresh water. Second, at temperatures near freezing, β_T is about an order of magnitude smaller than at moderate (15°C) temperatures, so that at low temperatures the density is controlled mainly by changes in salinity.

The UNESCO formula for the freezing temperature of saline water in degrees Celsius is given by Gill (1982):

$$T_f(S, p) = -0.0575S + 1.710523 \times 10^{-3} S^{3/2} - 2.154996 \times 10^{-4} S^2 - 7.73 \times 10^{-3} p \qquad (6.26)$$

where S is salinity in parts per thousand and p is pressure in bars. A straight-line fit to Eq. (6.26) yields $T_f = -0.054S$ at surface pressure. Note that the freezing point is depressed by about 0.008° for every 10-m increase in depth. Thus water which is at its *in situ* freezing temperature at depth will be supercooled if brought to higher levels.

III. Turbulent Exchange: Processes and Scales

In this section, a relatively simple conceptual view of turbulence in the under-ice RBL is constructed, using the fundamentals of Section II along with basic scaling principles. We review the mixing-length hypothesis, discuss what controls the scales of the turbulence, and relate the concepts in a heuristic model of turbulent exchange.

A. Turbulence

When inertial forces in a fluid become large compared with viscous forces (i.e., as the Reynolds number increases), the fluid behavior becomes highly nonlinear (chaotic) and a deterministic description of turbulent flow is virtually impossible. We resort instead to characterizing the statistics of the turbulent flow and seek to relate turbulent fluxes implicit in the statistics to mean flow quantities. Much research and an extensive literature exist on turbulence in rotating planetary boundary layers (see, e.g., Friehe, 1987; Price *et al.*, 1987; Wyngaard, 1985; Mellor and Yamada, 1982), although, with the exception of the atmospheric surface layer, data are still relatively sparse. Characteristics of turbulence in the ice/ocean boundary layer are described by McPhee and Smith (1976) and reviewed by McPhee (1986b). Although the general topic and its various theoretical underpinnings are far too vast to attempt to summarize here, there are some surprisingly simple ideas that explain much (but certainly not all!) about the behavior of the ice/ocean RBL, even in relatively complex situations like the marginal ice

zone. The intent of this section is not to present a comprehensive review but rather to equip the reader with some useful tools for treating small-scale processes.

There is no generally accepted definition of turbulence, but Tennekes and Lumley (1972) list several characteristics of a turbulent flow which identify it as such: (1) turbulence is irregular and seemingly random; (2) it is highly diffusive; (3) it is always highly rotational; and (4) it is essentially dissipative, meaning that the energy transfer in turbulence is always toward increasing internal energy (and entropy) of the fluid at the expense of the flow's overall kinetic or potential energy. Turbulence accomplishes diffusion much more efficiently than is possible by molecular processes alone. Ultimately, energy is dissipated at molecular scales by molecular processes; the main impact of turbulence is to involve many more molecules.

Picture a turbulent disturbance centered at some level in a flow with a positive vertical gradient of some arbitrary property ϵ. As it overturns, the eddy (which is highly diffusive) will distribute an excess of ϵ below the plane and a deficit above. The net result is a downward flux of ϵ. The mixing-length hypothesis (see, e.g., Hinze, 1975, Chapter 5) is simply that this flux should depend on three quantities: (1) the gradient of ϵ; (2) a velocity scale u_ϵ proportional to the eddy velocity in the direction of the gradient; and (3) a length scale λ characteristic of the distance over which the most energetic eddies transport the fluid, such that the smaller eddies can "keep up" in diffusing away deviations of ϵ from the local ambient value. The simplest expression for vertical flux is

$$F_\epsilon = -ku_\epsilon \lambda \, \partial\epsilon/\partial z \tag{6.27}$$

where k is von Karman's constant, equal to 0.4.

By analogy with molecular diffusivity (which is proportional in an ideal gas to the product of the root-mean-square velocity of the molecules and their mean free path) we may define an "eddy diffusivity"

$$K_\epsilon = ku_\epsilon \lambda \tag{6.28}$$

From Section II,B, when a flow with rapid fluctuations about some mean value is averaged in an ensemble sense, Reynolds flux terms appear in the conservation equations. Equation (6.27) provides a link between the turbulent Reynolds fluxes and the mean flow properties. Our main concern is vertical flux, and we have for temperature, salinity, and horizontal momentum:

$$\langle w'T' \rangle = -K_T \, \partial T/\partial z \tag{6.29}$$

$$\langle w'S' \rangle = -K_S \, \partial S/\partial z \tag{6.30}$$

$$\hat{\tau} = -(\langle u'w' \rangle + i\langle v'w' \rangle) = K_m \, \partial\hat{u}/\partial z \tag{6.31}$$

In the context of the mixing-length hypothesis, the different eddy diffusivities imply different length scales; e.g., under certain circumstances, momentum is "diffused" much more effectively (by pressure terms in the covariance equations) than is a scalar like salt, which requires direct diffusion at the molecular level. However, in the absence of density gradients and far enough from solid boundaries, we expect the eddy diffusivities to be roughly equivalent. In such cases, the "Reynolds analogy" is often invoked, which treats all the eddy diffusivities as equal.

The mixing-length hypothesis is only one way of addressing the "closure" problem of turbulence, i.e., relating the Reynolds flux terms to mean flow properties. Another is "second-order" closure, in which ensemble-averaged equations for the covariance equations are solved simultaneously with the mean equations. A useful strategy is to solve numerically the full set of equations, closed at second order, and then use the solutions to derive much simpler equations for closure at the mean (first-order) level. Mellor and Yamada (1982) describe a hierarchy of closure schemes, developed within one basic theoretical framework, that has been used successfully to model many different types of turbulent flow, including the under-ice RBL (Mellor *et al.*, 1986).

A different approach is the so-called large-eddy-simulation (LES) model, which solves the time-dependent, three-dimensional equations for grid scales small enough (within the inertial subrange of the turbulence spectrum) to resolve the large, energy-containing eddies explicitly (e.g., Deardorff, 1972; Moeng, 1984). To learn about the ensemble statistics of the large eddies, LES model output is essentially treated as a substitute for actual measurements. The computing power required for LES models is formidable, but as supercomputers become more accessible, LES models may provide useful answers for some difficult problems, e.g., how drag is affected by various scales of under-ice topographic relief.

B. Scales Governing RBL Turbulence

Certain scaling principles seem to describe turbulent mixing in the ice–ocean RBL reasonably well. The first is that the local turbulent velocity scale u_ϵ in Eq. (6.27) is proportional to the square root of the horizontal turbulent shear stress. Here we define the *friction velocity* scale as a vector rather than a scalar.

$$\hat{u}_* = \frac{\hat{\tau}}{\sqrt{\tau}} = -\frac{(\langle u'w' \rangle + i\langle v'w' \rangle)}{(\langle u'w' \rangle^2 + \langle v'w' \rangle^2)^{1/4}} \tag{6.32}$$

The friction velocity at the ice/ocean interface is

$$\hat{u}_{*0} = \hat{\tau}_0 / \sqrt{\tau_0} \tag{6.33}$$

In the RBL, stress decreases from its surface value to zero at depth; thus an obvious scale for kinematic stress is $u_{*0}\hat{u}_{*0}$.

The length scale for vertical exchange depends on several factors, and describing it correctly is the crux of the mixing-length problem. In a steady, horizontally homogeneous RBL the scale is governed in varying degrees by the distance from the surface, the "planetary" length, u_*/f and the Obukhov length associated with gravitational effects on turbulent overturn.

For a neutrally stratified turbulent flow in the vicinity of the "wall," i.e., the ice/ocean or air/ocean interface, the length scale depends on the distance from the wall

$$\lambda = |z| \qquad \text{(surface layer)} \tag{6.34}$$

Much is known about this flow regime (see, e.g., Hinze, 1975, Chapter 7), which includes the lower tens of meters of the atmospheric boundary layer and most turbulent flows important in engineering problems. Variation in turbulent stress across the region of validity of Eq. (6.34) is small, and it is often a fairly good approximation to set $u_* = \text{constant} = u_{*0}$, which results in the "law of the wall"

$$\frac{\hat{u}}{\hat{u}_{*0}} = \frac{1}{k}\ln|z| + C = \frac{1}{k}\ln\frac{|z|}{z_0} \tag{6.35}$$

where $C\,[= -\ln(z_0)/k]$ is an integration constant; z_0 is called the *roughness length;* and $\hat{u}$ is the velocity relative to the interface, which varies logarithmically with distance from the interface in the direction of stress. Equation (6.35) is valid only in the region where the mixing length varies with z and where stress is nearly constant. The region is commonly called the *surface layer* and comprises roughly one-tenth of the entire RBL depth.

As the distance from the interface increases, the scale of the eddies does not continue to grow without bound. In the outer, "free-turbulence" region beyond the surface layer, we find from both measurements and dimensional analysis (see also the stability analysis arguments of Stern, 1975, Chapter 8) that the turbulent length scale for the neutral RBL is approximately

$$\lambda_N = \xi_N u_*/f \qquad \text{(outer layer)} \tag{6.36}$$

where ξ_N is a constant, approximately equal to 0.05 (McPhee, 1981). If the eddy scale increases linearly near the interface, the extent of the surface layer is of order $\xi_N u_{*0}/f$.

The third major factor affecting the length scale of turbulence in the RBL is buoyancy, i.e., the gravitational force that tends to retard (or enhance, if unstable) vertical motion when a density gradient is present. When variations in density are small relative to mean density, as is the case in the RBL, the small fluctuations are important dynamically only when they occur in

combination with gravity (the Boussinesq approximation). It is then convenient to define a buoyancy flux

$$\langle b'w' \rangle = (g/\rho) \langle \rho'w' \rangle \tag{6.37}$$

where $\langle \rho'w' \rangle$ is the Reynolds mass flux. [Although it violates the literal sense of the word, the convention adopted here is that buoyancy flux and turbulent mass flux are in the same direction; many authors prefer a minus sign in Eq. (6.37).]

There are two main sources of buoyancy flux in the ice-covered RBL: melting or freezing at the ice/ocean interface and turbulent entrainment at the mixed-layer/pycnocline interface. The buoyancy flux may be expressed in terms of (kinematic) heat and salt flux using Eq. (6.25):

$$\langle b'w' \rangle = g(\beta_S \langle w'S' \rangle - \beta_T \langle w'T' \rangle) \tag{6.38}$$

Because of the disparity in expansion coefficients at low temperatures, buoyancy flux in polar waters is controlled mainly by salinity, even though the thermodynamic forcing is usually heat flux associated with temperature gradients. The reason for this is that sea ice excludes all but a small fraction of the salt in seawater as it freezes; hence freezing is associated with downward buoyancy flux and melting with upward buoyancy flux, even though the buoyancy due to heat flux is in the opposite sense.

Obukhov (1946, see English translation, 1971) examined the effect of buoyancy on surface layer dynamics by considering the turbulent kinetic energy budget (see, e.g., Tennekes and Lumley, 1972); however, a simpler heuristic argument adapted from Businger and Arya (1974) serves our purpose here. Consider again an overturning eddy in a density gradient. A parcel of fluid with vertical velocity w' will convert its kinetic energy to potential energy after it has traveled a vertical distance λ when

$$-g\delta\rho\lambda \cong -g \frac{\partial \rho}{\partial z} \lambda^2 \propto \rho \langle w'^2 \rangle \propto \rho u_*^2 \tag{6.39}$$

Since

$$\partial \rho / \partial z = -\langle \rho'w' \rangle / K = -\langle \rho'w' \rangle / k\lambda u_* \tag{6.40}$$

we have

$$\lambda = R_c \rho u_*^3 / kg \langle \rho'w' \rangle = R_c L \qquad \text{(highly stable)} \tag{6.41}$$

where L, equal to $u_*^3/(k\langle w'b' \rangle)$, is the Obukhov length, and the proportionality constant R_c has been shown by Zilitinkevich (1975) to be the critical flux Richardson number (the ratio of buoyancy to shear production terms in the turbulent kinetic energy equation). The argument is that the length scale of

turbulence in a highly stratified flow adjusts so that the kinetic energy is roughly in balance with the potential energy gained as eddies overturn.

In summary, there are three length scales that affect vertical turbulent exchange in a steady, horizontally homogeneous RBL: (1) the distance from the ice/ocean (or air/ocean) interface, (2) some fraction of the planetary length scale, u_*/f; and (3) the Obukhov length, which is proportional to the vertical distance a fluid parcel must travel in a stratified fluid in order to convert its kinetic energy to potential energy. The smallest of these length scales will usually determine the turbulence characteristics. A schematic of the turbulence regime is shown in Fig. 6.2. At the surface, there are turbulent stress and buoyancy flux. In the surface layer, the size of the largest and most energetic eddies is controlled by the distance from the surface and, to a lesser extent, by buoyancy effects. The eddies grow until they reach some limiting

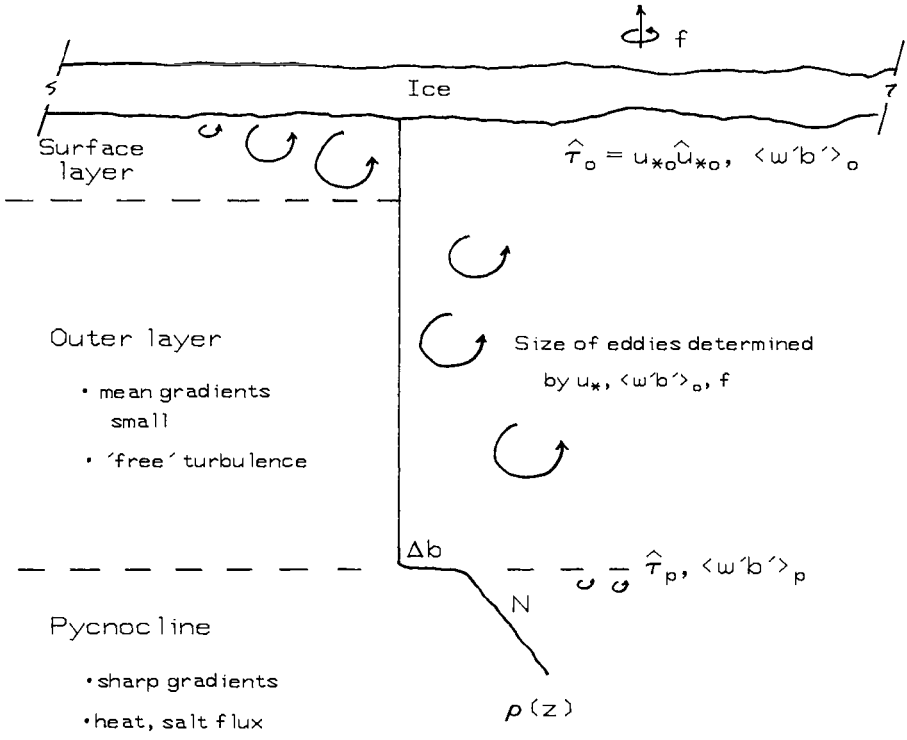

Figure 6.2 Schematic showing the breakdown of the upper-ocean system into three zones: (1) surface layer, eddy size dependent mainly on distance from interface; (2) outer (mixed) layer, eddy size dependent on u_*/f and surface buoyancy flux; and (3) pycnocline, eddy size dependent on stress and buoyancy flux at the interface between the mixed layer and the underlying density gradient.

size in the outer layer determined by the rotation, stress, and surface buoyancy flux. The vertical exchange scale of the largest eddies will be comparable to the surface layer thickness, and they will extend through the boundary layer to some level determined either by Coriolis-induced attenuation of the turbulent stress or by encountering a preexisting density gradient (pycnocline). If there is turbulent stress at the base of the mixed layer (τ_p), then an eddy flux of heat and salt may occur there ($\langle b'w' \rangle_p$), but gravitational forces associated with a sharp jump in buoyancy across the interface (Δb) and the underlying density gradient (characterized by the Brunt – Väisälä frequency N) will dramatically reduce the size of the eddies.

C. A Heuristic Model for Turbulent Flux in the RBL

A useful tool in fluid dynamics is the concept of similarity, in which a whole class of flows is reduced to one set of equations by nondimensionalizing with carefully chosen scales. A familiar example is wind-tunnel testing of scale airplane models, but the idea is also often applied in rotational boundary layer studies. A method called "Rossby number similarity" has been developed for describing geostrophic wind drag in the neutrally stratified atmosphere (e.g., Blackadar and Tennekes, 1968), in which the scales for stress, velocity, and vertical displacement are u_*^2, u_*, and u_*/f, respectively. We used this nondimensionalization to compare mean flow and turbulence data from the 1972 AIDJEX with atmospheric boundary layer models quite successfully (McPhee and Smith, 1976), even though the actual length scales of the two boundary layers differ by a factor of about 30.

The planetary depth scale of Rossby similarity, u_*/f, and the velocity scale u_* apply only with neutral stratification. When there is positive or negative surface buoyancy flux, the depth scale contracts or expands, with opposing changes in the velocity scale. Compare a case with very rapid melting (analogous to strong radiational cooling in the atmosphere) to one with similar surface stress but little or no buoyancy. In the former, stabilizing buoyancy flux at the surface decreases the vertical exchange scale, so that mixing of heat, salt, and momentum is confined to a thinner layer. The mixed layer shoals, and since momentum is trapped near the surface, currents (including ice velocity) increase. In earlier work (McPhee, 1981, 1983), I proposed a generalization of Rossby similarity for turbulent stress and scalar flux, which includes buoyancy effects and is outlined as follows.

Define the nondimensional variables $\zeta = z/H$ and $\hat{T} = \hat{\tau}/u_{*0}\hat{u}_{*0}$, where H is a characteristic length scale for the RBL and, as before, $u_{*0}\hat{u}_{*0}$ is the vector scale for turbulent stress. The nondimensional, steady-state version of Eq. (6.21) is

$$i\hat{U} = \partial\hat{T}/\partial\zeta \tag{6.42}$$

where $\hat{U}$ is nondimensional velocity,

$$\hat{U} = \frac{fH}{u_{*0}} \cdot \frac{\hat{u}}{\hat{u}_{*0}} \tag{6.43}$$

First-order closure in nondimensional variables is

$$\hat{T} = K_* \, \partial \hat{U} / \partial \zeta \tag{6.44}$$

where

$$K_* = K/fH^2 \tag{6.45}$$

so that differentiation of Eq. (6.42) leads to a second-order, ordinary differential equation for turbulent stress:

$$(i/K_*)\hat{T} = d^2\hat{T}/d\zeta^2 \tag{6.46}$$

To find the depth scale H we consider a combination of the maximum exchange scales given by Eqs. (6.36) for the neutral RBL and (6.41) for the highly stable RBL. A simple function which satisfies the two limits is

$$\lambda_m = \xi_N u_{*0} \eta_*^2 / f \tag{6.47}$$

where

$$\eta_* = \left(1 + \frac{\xi_N u_{*0}}{f} \cdot \frac{1}{R_c L}\right)^{-1/2} \tag{6.48}$$

The nondimensional eddy viscosity is

$$K_* = k u_{*0} \lambda_m / fH^2 = k \xi_N \tag{6.49}$$

in which the last equality comes from the stipulation that the nondimensional eddy viscosity is the same for all solutions, including neutral. Thus

$$H = u_{*0} \eta_* / f \tag{6.50}$$

Since we are considering turbulent stress, variation of K within the surface layer is relatively unimportant (see, e.g., Fig. 1 of McPhee, 1981), and as a first-order approximation we assume that eddy viscosity through the entire boundary layer is constant, $K_* = k\xi_N$. The solution of Eq. (6.46) with boundary conditions $\hat{T}(0) = 1$ and $\hat{T}(-\infty) = 0$ is

$$\hat{T} = e^{\hat{\delta}\zeta} \tag{6.51}$$

where

$$\hat{\delta} = (i/K_*)^{1/2} \tag{6.52}$$

This remarkably simple expression for momentum flux in the boundary layer contains many features found both in boundary layer data and in more

sophisticated numerical models (see the comparison in McPhee, 1987). With increasing depth, the complex exponential both rotates *(cum sole)* and diminishes the magnitude of the horizontal stress vector. An important consequence of the extended similarity theory is that, since profiles of momentum flux are similar for all neutral and stably stratified RBLs, it can predict how deep turbulence will penetrate (and thus mix conserved properties) under varying conditions of surface stress and surface buoyancy flux. We refer to this depth as the dynamic RBL depth, to distinguish it from the mixed-layer depth (which may reflect, say, previous conditions of much different surface forcing). For the neutral atmospheric planetary boundary layer (PBL), estimates of the nondimensional dynamic boundary layer depth vary from around 0.25 to 0.6. Using observations of freshening of the upper ocean during the melt season at the AIDJEX camps, I found the nondimensional dynamic depth to be about 0.4 (McPhee, 1986b). Using this value, the dynamic boundary layer depth for high latitudes ($f = 1.4 \times 10^{-4}$ s^{-1}) is plotted for u_{*_0} ranging from 0.5 to 1.5 cm s^{-1} (stress ranging from

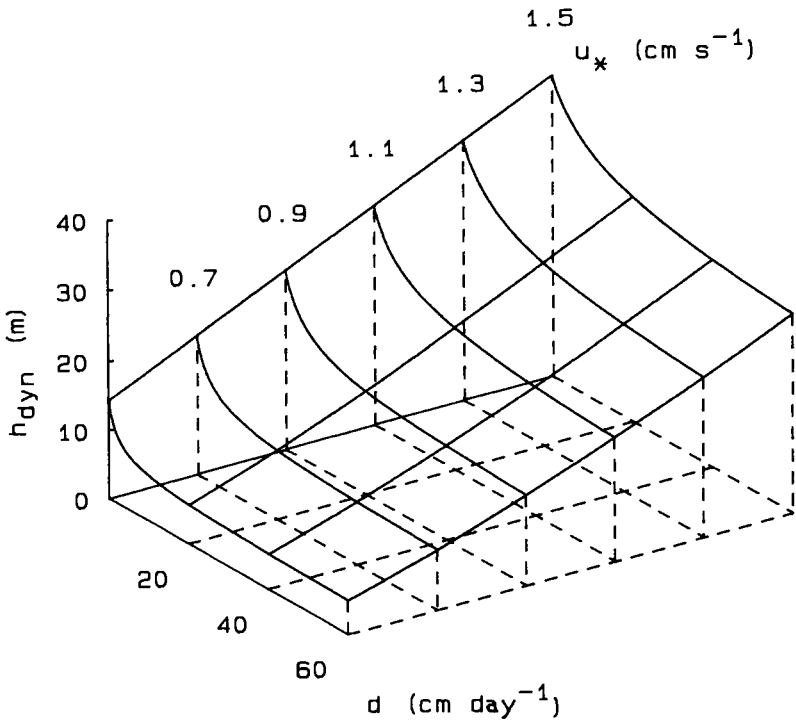

Figure 6.3 Perspective view of dimensional dynamic boundary layer depth, i.e., the maximum depth of active turbulent mixing, for melt rates ranging from 0 to 60 cm day^{-1} and stress ranging from 0.03 to 0.23 Pa.

0.025 to 0.23 Pa) and ice melt rates from 0 to 60 cm day^{-1} in Fig. 6.3. The depth of frictional influence decreases rapidly with melt rate, especially with small to moderate turbulent stress.

The heuristic arguments may be extended to include a pycnocline as follows. Consider the stress profile in an idealized system comprising a well-mixed layer with eddy viscosity K overlying a stable pycnocline, with turbulence characterized by a much smaller eddy viscosity K_p as sketched in Fig. 6.2. To simplify matters, we ignore the buoyancy jump Δb but note that it is straightforward (but algebraically messy) to reinstate it.

We have introduced a new physical length scale: the mixed-layer depth $-z_p$. When the layer is thin relative to the dynamic boundary layer depth ($z_p > z_{dyn}$), turbulence may be intense at the mixed-layer/pycnocline interface, but its exchange scale will be substantially reduced by the density gradient. This will affect both the current structure (and ice drift) of the system and the rate at which denser water is entrained into the mixed layer from below. On the other hand, if the existing mixed-layer depth is greater than the dynamic depth and if there is positive surface buoyancy flux, a new, shallower mixed layer will begin to form at z_{dyn}. During the melt season, the polar mixed layer thus progresses through a series of steps in salinity and temperature structure as the interplay between wind and melt rate dictates how the layer shoals or deepens (see McPhee, 1986b).

With the same RBL scales as before, the nondimensional stress profile is obtained by matching stress and velocity (which is proportional to the derivative of stress) at the nondimensional pycnocline level ζ_p (see McPhee, 1986b, 1988)

$$\hat{T}(\zeta) = \begin{cases} 2\hat{A}\sinh(\hat{\delta}\zeta) + e^{-\hat{\delta}\zeta}, & \zeta \geq \zeta_p \\ \hat{T}_p\, e^{\hat{\gamma}(\zeta-\zeta_p)}, & \zeta < \zeta_p \end{cases}$$

$$\hat{A} = \frac{(\hat{\gamma}+\hat{\delta})e^{-\hat{\delta}\zeta_p}}{2[\cosh(\hat{\delta}\zeta_p) - \hat{\gamma}\sinh(\hat{\delta}\zeta_p)]} \tag{6.53}$$

where $\hat{\gamma} = (i/K_{*p})^{1/2}$, K_{*p} is the eddy viscosity in the upper part of the pycnocline, and $\hat{T}_p$ is nondimensional stress at ζ_p.

When the system is entraining (i.e., actively mixing at z_p), the key to estimating flux is the length scale of turbulence for K_{*p}. We assume that stratification is always sufficient to force turbulence to scale with the local Obukhov length

$$K_p = k u_{*p} R_c L_p \tag{6.54}$$

where

$$L_p = u_{*p}^3 / k\langle b'w'\rangle_p \tag{6.55}$$

and

$$u_{*_p}\hat{u}_{*_p} = \hat{T}_p u_{*_0}\hat{u}_{*_0} \tag{6.56}$$

Assuming the eddy diffusivity for scalar flux is proportional to eddy viscosity, the buoyancy flux may be written in terms of mean quantities

$$\langle b'w' \rangle_p = -\alpha K_p \left.\frac{\partial b}{\partial z}\right|_p = \alpha N^2 K_p \tag{6.57}$$

where α is the ratio of scalar eddy diffusivity to eddy viscosity (the inverse turbulent Prandtl number) and N the buoyancy frequency in the upper pycnocline. Substituting into Eq. (6.54) and nondimensionalizing, we have

$$K_{*_p} = \frac{fK_p}{(u_{*_0}\eta_*)^2} = \sqrt{\frac{R_c}{\alpha}}\,\frac{f}{N}\,\frac{T_p}{\eta_*^2} \tag{6.58}$$

Combining Eqs. (6.58) and (6.53) provides an implicit equation for the one unknown, T_p, which can be solved by iteration.

The ratio α varies from unity (or possibly higher) in fully developed turbulence to quite small values in very stable flows (see Turner, 1973, Figure 5.13). I was able to simulate summer AIDJEX data reasonably well with a constant value of 0.1 (McPhee, 1986b). When the mixed layer is very shallow, α is probably larger (McPhee, 1987).

When the surface buoyancy flux is negative (freezing), the Obukhov length is negative, and η_* is larger than unity. An *ad hoc* extension of the similarity model to unstable conditions allows the turbulent exchange scale to grow with increasing η_*, following Eq. (6.48), until it reaches $|z_p|$. Unlike situations where a large expanse of ice can overrun warm water and melt very rapidly, freezing rates are limited by heat conduction through the ice, which slows rapidly as ice thickness increases. We thus expect surface buoyancy flux due to freezing to have a relatively small impact on RBL dynamics; however, an exception may occur if an expanse of water exposed to cold temperature is continually swept clear of newly formed ice by the wind.

Mean profiles of velocity, temperature, and salinity are obtained by integrating their respective flux profiles. Nondimensional velocity, for example, is found by integrating Eq. (6.53) through the layers shown schematically in Fig. 6.2. Below the dynamic depth, $\hat{U}$ is zero, so in the pycnocline

$$\hat{U}(\zeta) = -i\hat{\gamma}\hat{T}_p e^{\hat{\lambda}(\zeta-\zeta_p)}, \qquad \zeta < \zeta_p \tag{6.59}$$

In the well-mixed outer (Ekman) layer

$$\hat{U}(\zeta) = \hat{U}(\zeta_p) - i\hat{\delta}[2\hat{A}\cosh(\hat{\delta}\zeta) - e^{-\hat{\delta}\zeta}], \qquad \zeta_p \leq \zeta \leq \zeta_{sl} \tag{6.60}$$

where $-\zeta_{sl}$ is the nondimensional depth of the surface layer. For the mean velocity profile, variation of eddy viscosity in the surface layer is important,

since much of the shear takes place in the logarithmic layer near the interface. We define the surface layer depth by the level at which the distance from the surface is equal to the limiting exchange scale λ_m [Eq. (47)]. For smaller distances, the exchange scale is equal to the depth, so the nondimensional surface layer extends to

$$\zeta_{sl} = -\eta_* \xi_N \tag{6.61}$$

in which the eddy viscosity is

$$K_* = -k\zeta/\eta_* \tag{6.62}$$

For $|\zeta|$ small, nondimensional stress can be expressed by a Taylor series expansion

$$\hat{T} = 1 + \hat{\delta}\zeta \tag{6.63}$$

so that

$$\hat{U}(\zeta) = \hat{U}(\zeta_{sl}) - \frac{\eta_*}{k}\int_{\zeta_{sl}}^{\zeta}\left(\frac{1}{\zeta'} + \hat{\delta}\right)d\zeta', \qquad \zeta > \zeta_{sl} \tag{6.64}$$

The integrand is ill behaved as ζ approaches zero, so the upper limit of integration is taken as the nondimensional surface roughness

$$\zeta_0 = -fz_0/(u_{*0}\eta_*) \tag{6.65}$$

and surface velocity is given by

$$\hat{U}_0 = \hat{U}(\zeta_{sl}) + \frac{\eta_*}{k}\left[\ln\left(\frac{\zeta_{sl}}{\zeta_0}\right) + \hat{\delta}\zeta_{sl}\right] \tag{6.66}$$

Equation (6.66) is a generalized drag law for sea ice, which expresses the surface velocity relative to the undisturbed geostrophic flow as a function of the friction velocity at the interface, the buoyancy flux at the interface, the depth of the mixed layer, and the strength of stratification below the mixed layer.

To recapitulate, the equations for stress and velocity as a function of depth in the steady RBL are solved by matching stress and velocity at the base of the mixed layer to derive an implicit equation for T_p, the nondimensional stress magnitude at ζ_p, which is solved by iteration. Velocity is obtained by integrating the stress divided by eddy viscosity through three separate layers representing the pycnocline, the mixed (Ekman) layer, and the logarithmic surface layer. Profiles of temperature and salinity may be obtained in a completely analogous way, except that a laminar/transition sublayer adjacent to the ice/ocean interface must also be considered, as discussed in Section VI.

The calculations are simplified if stratification can be ignored. If the mixed layer is deep and melting or freezing is slow (a situation that pertains to the central Arctic much of the year), then nondimensional stress is given by Eq. (6.51) and surface velocity is

$$\hat{U}_0 = -i\hat{\delta}(1 - \hat{\delta}\xi_N) + \frac{1}{k}\left(\ln \frac{\xi_N u_{*0}}{f z_0} - \hat{\delta}\xi_N\right) \tag{6.67}$$

Grouping terms, we have the Rossby similarity drag law expressed in complex form:

$$\hat{U}_0 = \frac{\hat{u}_0}{\hat{u}_{*0}} = \frac{1}{k}([\ln \mathrm{Ro}_* - A] - iB) \tag{6.68}$$

where $\hat{u}_0$ is the surface (ice) drift velocity relative to the surface geostrophic flow, $\mathrm{Ro}_* = u_{*0}/fz_0$ is the "surface friction Rossby number," and

$$\begin{aligned} A &= \left(1 - \ln \xi_N - \sqrt{\frac{k}{2\xi_N}} + \sqrt{\frac{\xi_N}{2k}}\right) \cong 2.2 \\ B &= \sqrt{\frac{k}{2\xi_N}} + \sqrt{\frac{\xi_N}{2k}} \cong 2.3 \end{aligned} \tag{6.69}$$

Various effects of rotation and buoyancy on the turbulent stress and mean velocity of the boundary layer are demonstrated in Fig. 6.4, for a fixed interfacial kinematic stress of 1 $cm^2\ s^{-2}$ directed along the y axis, with $z_0 =$ 0.06 m. For case (a) there is no stratification in the water column, the mixed layer is at its freezing temperature, and there is no melting. Both stress and velocity spiral clockwise downward, with velocity leading by 45° in the neutral Ekman layer below the surface layer (which extends down about 3.7 m). At the interface, the surface current (which is ice velocity) is 13.5 cm s^{-1}, directed 23° to the right. Case (b) is like case (a) except that a pycnocline with constant density gradient ($N = 0.02\ s^{-1}$) is imposed below 15 m. Stress is confined mainly to the mixed layer. Below the surface layer, currents are relatively uniform at right angles to the surface stress, down to the pycnocline, at which there is large shear in both speed and direction. Surface velocity is slightly retarded relative to the neutral RBL and directed a few degrees farther to the right. The level of stress at 15 m suggests that active entrainment is occurring. Case (c) is like case (b) except that the mixed-layer temperature is set to 3°C, which gives rise to a melt rate (see Section VI) of about 27 cm day^{-1}. The ice drifts about 25% faster and 6° farther to the right. Note also that current structure in the mixed layer is much less "slablike," as buoyancy reduces the vertical scale of the RBL, in effect pushing the pycnocline deeper in nondimensional coordinates.

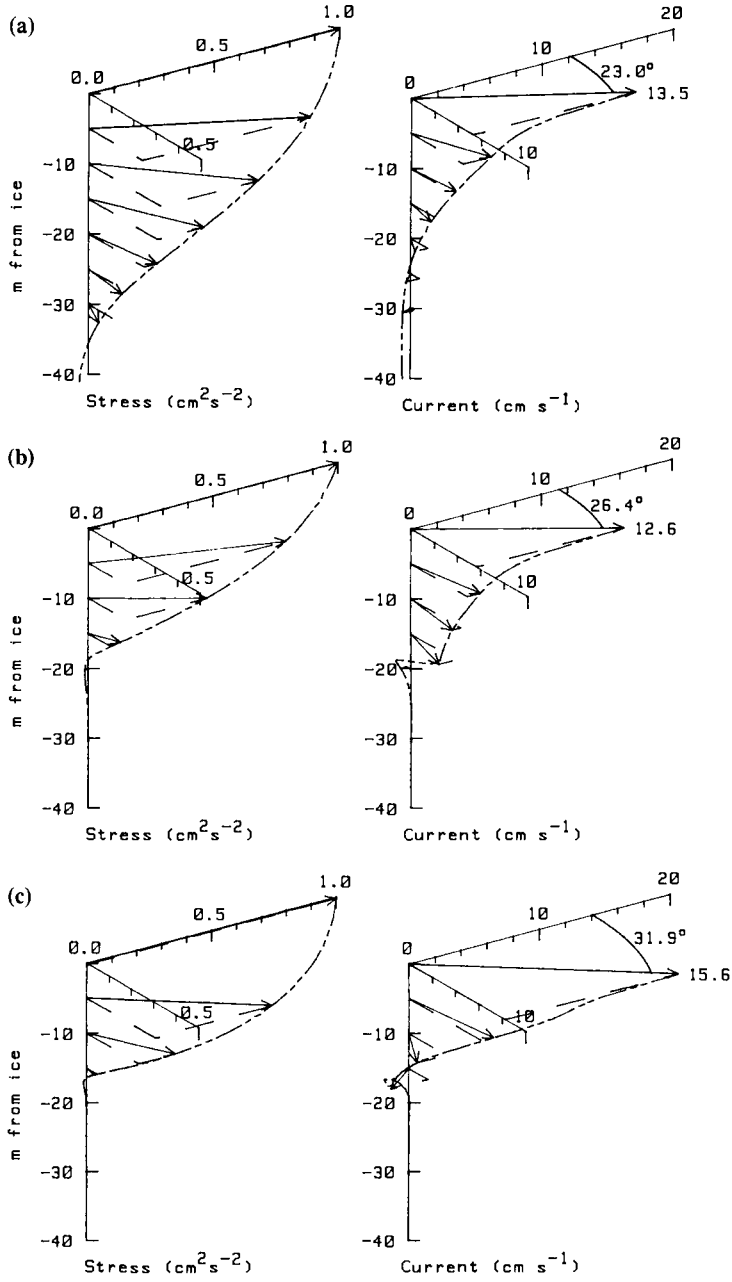

Figure 6.4 Implicit-analytical model hodographs of Reynolds stress and mean current for (a) no surface buoyancy flux (the mixed layer is at its freezing temperature), no pycnocline; (b) no surface buoyancy, pycnocline at 15 m; (c) mixed-layer temperature set to 3°C, pycnocline at 15 m. Numbers at surface indicate surface speed in centimeters per second and boundary layer turning angle.

IV. Some Measurements from the Under-Ice Boundary Layer

A sample of measurements from under-ice RBL studies helps illustrate some of the concepts developed in the previous section. Figure 6.5, from the 1972 AIDJEX Pilot Study (McPhee and Smith, 1976), provides another good example of spiral-like structure in mean currents, this time from a composite average of 5 h of data during a particular storm. Currents are drawn relative to flow measured by an instrument cluster 32 m below the ice/ocean interface, which was near the base of the mixed layer, with the x axis aligned along the direction of shear between the ice and the 2-m level. Note that the integrated volume transport through the boundary layer is almost all in the y direction, i.e., at right angles to the interfacial stress. We found that this integral implied a stress of about 0.29 Pa [see Eq. (6.23)], whereas direct turbulence measurements indicated local turbulent stress at the interface to be about 0.1 Pa, and argued that the difference was due mainly to pressure gradients associated with under-ice topography, i.e., form drag on ridge

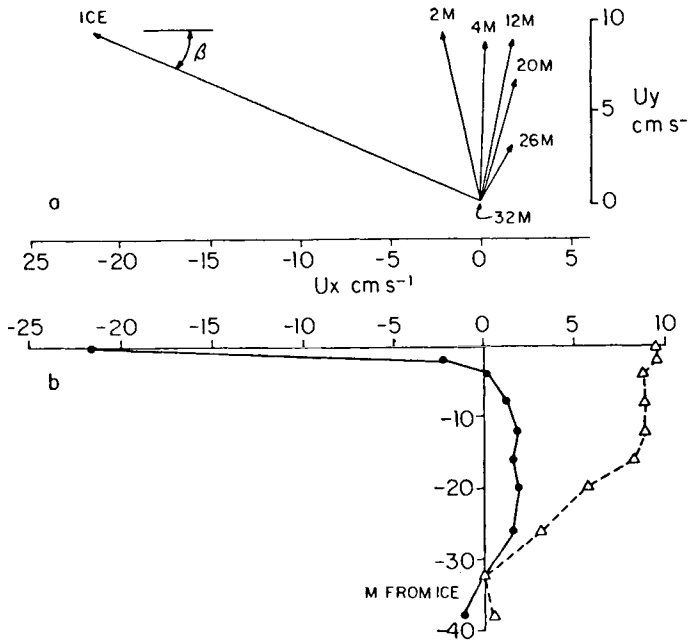

Figure 6.5 Mean current hodograph and profiles relative to 32 m below the ice during a storm at AIDJEX 72 Pilot Study. In a frame of reference drifting with the ice, the relative current at 32 m was within 2 cm s^{-1} of the apparent bottom velocity. Reprinted with permission from McPhee (1986b); copyright by Plenum Press.

keels. Profiles of the diagonal components of the Reynolds stress tensor, scaled by u_* and u_*/f, where u_* was estimated from turbulent stress measurements, are shown in Fig. 6.6. The sum of the three components is twice the turbulent kinetic energy per unit mass. The measurements are shown with results from two numerical models of the neutrally stable atmospheric boundary layer: the second-order closure model of Wyngaard *et al.* (1974) and averaged results from the LES model of Deardorff (1972).

Similar measurements in the marginal ice zone of the Greenland Sea are shown in Fig. 6.7, from McPhee *et al.* (1987). Here, velocity vectors averaged over 3.5 days are drawn relative to drifting ice (measurement reference frame), along with the average results of a time-dependent, numerical model based on the scaling concepts introduced in Section III. During this time, the mixed-layer depth varied between 10 and 20 m. Observed and modeled velocity hodographs differ in some details, but their overall similarity is striking. The relatively shallow pycnocline exerts strong influence on the mean velocity structure, as can be seen by comparison with Fig. 6.5, for which the mixed-layer depth was 30–35 m.

Figure 6.8 shows the measured and modeled Reynolds stress vectors for the same period. Contrary to the turbulence model, measured turbulent

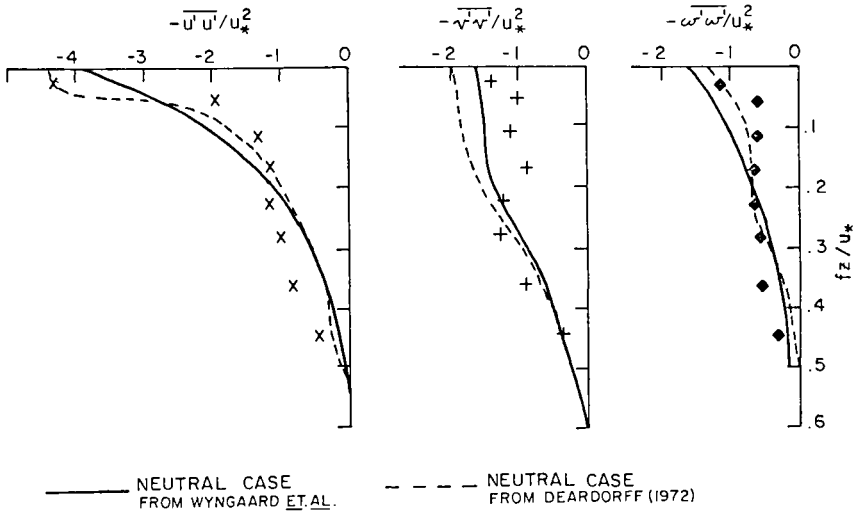

Figure 6.6 Profiles of the diagonal components of Reynolds stress at eight depths ranging from 2 to 32 m in the boundary layer for the same period as Fig. 6.5, nondimensionalized by u_* as determined from near-surface stress measurements. Curves are corresponding predictions from the atmospheric models of Wyngaard *et al.* (1974) and Deardorff (1972). Reprinted with permission from McPhee and Smith (1976); copyright by the American Meteorogical Society.

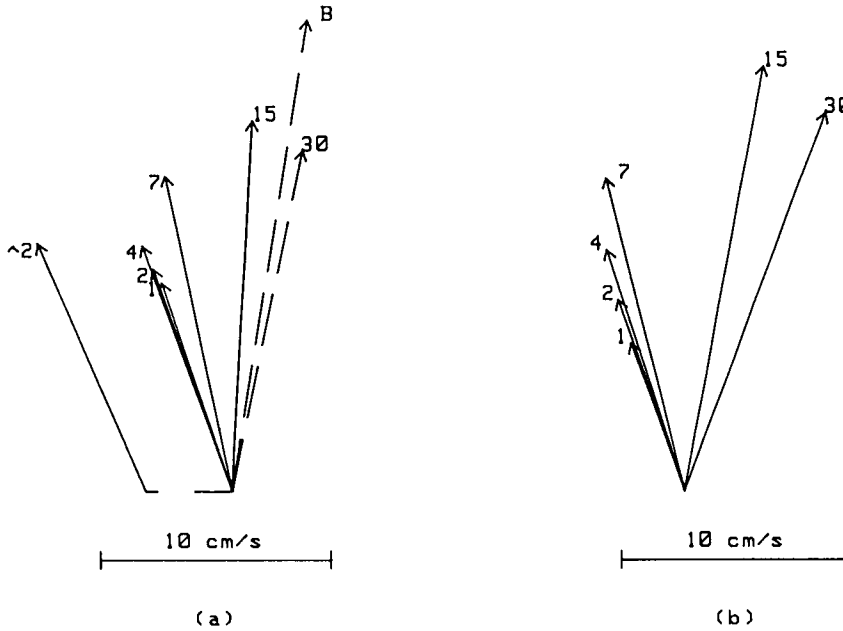

Figure 6.7 (a) Average current hodograph from an 84-h storm during MIZEX 84 in the Greenland Sea. North is up. Numbers indicate depth from the ice underside, with the vector labeled "^2" from a cluster about 100 m away from the main turbulence mast. Vectors labeled "30" and "B" are, respectively, the average 30-m velocity from a profiling system and the apparent bottom velocity from satellite navigation. (b) Averaged results from a time-dependent numerical model forced by observed wind stress, transformed into the drifting reference frame. Reprinted from McPhee *et al.* (1987); copyright by the American Geophysical Union.

stress decreases as the ice/ocean interface is approached. We argued that this resulted from the nonuniform nature of roughness elements on the ice underside, with larger elements contributing to the Reynolds stress observed in the middle and outer regions of the mixed layer but not to the stress measured near the interface under smooth ice. As discussed in the next section, resolving how total drag is partitioned into skin friction, overall turbulent stress, and form drag warrants additional research.

A surprisingly different RBL is shown in Fig. 6.9, from data taken with a frame of equally spaced turbulence clusters under ice near the center of the AIWEX camp in April 1985. The upper cluster on the frame was positioned 2 m below the interface, and data were gathered for about 2 h during a steady drift. The velocity hodograph on the left shows near-surface currents roughly comparable to the MIZEX measurements of Fig. 6.7, but stress magnitudes

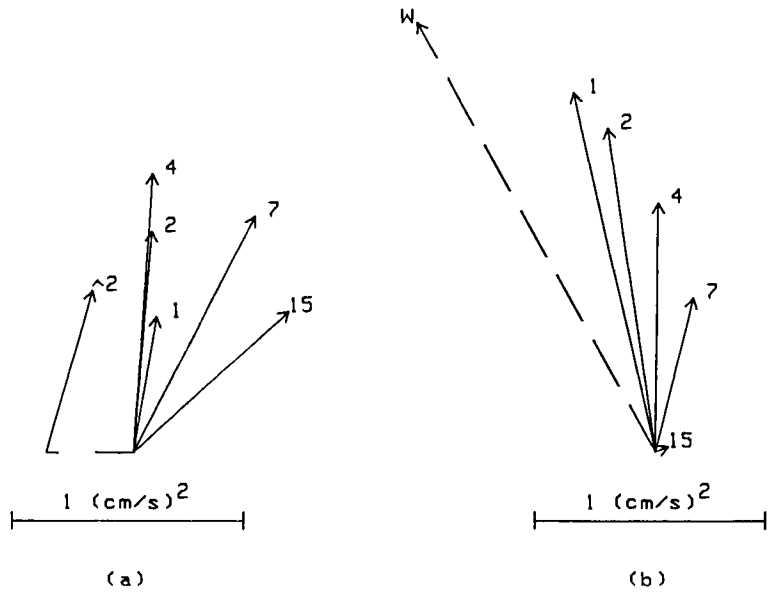

Figure 6.8 As in Fig. 6.7, except (a) measured Reynolds stress and (b) modeled turbulent stress. Reprinted McPhee *et al.* (1987); copyright by the American Geophysical Union.

(right-hand hodograph) are at least five times smaller than at the MIZEX site (Fig. 6.8). The mixed layer was 20–25 m thick and very close to neutrally stable at AIWEX; so I estimated the interfacial friction velocity u_{*0} by fitting (in a least root-mean-square sense) the measured stress at each level, nondimensionalized by interfacial stress, to the simple exponential given by Eq. (6.51). The stress hodograph drawn is the result, with surface stress aligned with the relative current at 2 m. Despite the short averaging time and small magnitudes (of order 0.01-Pa actual stress), the measurements fit the simple exponential quite well.

The stress at the interface is so small that a Reynolds number based on u_{*0} and z_0 [derived from Eq. (6.35)] fell within a range for which the surface is considered hydraulically smooth (see Hinze, 1975, Chapter 7). Under these conditions, the RBL no longer depends on surface roughness, and we may replace the logarithmic part of the surface layer velocity in Eq. (6.66) (with $\eta_* = 1$) by Hinze's empirical result, namely

$$U_s = 2.44 \ln (u_{*0}|z_{sl}|/\nu) + 4.9 \tag{6.70}$$

where ν is kinematic molecular viscosity and

$$z_{sl} = -u_{*0}\xi_N/f \tag{6.71}$$

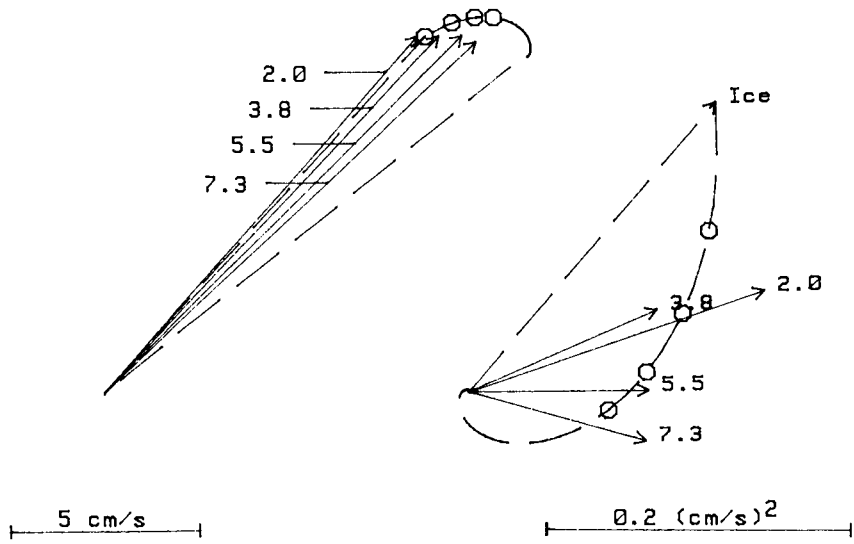

Figure 6.9 Hodographs of mean current and stress measured relative to the ice during AIWEX 85 in the Beaufort Sea. The theoretical curves are from a simple exponential stress model fitted to the observations, with velocity obtained by assuming the surface to be hydraulically smooth.

The model velocity hodograph constructed in Fig. 6.9 thus depends only on u_{*0}, and the measurements are remarkably close to an ideal, hydraulically smooth, rotating boundary layer.

Finally, direct measurements of vertical turbulent heat flux ($\langle w'T' \rangle$) in the RBL are shown in Fig. 6.10, from McPhee *et al.* (1987). During the MIZEX 84 drift, the ice crossed an abrupt mixed-layer temperature front, after which bottom melting increased rapidly. Figure 6.10 shows the average heat flux from all turbulence clusters within the mixed layer, along with a melt rate derived from once-daily measurements of bottom elevation at several sites surrounding the turbulence experiment. The heat flux and melt rate scales are equivalent if we assume that all of the upward heat flux melts ice, where the latent heat of melting is adjusted for brine volume (see Section VI). The dashed curve marked by crosses is from a simple model based on mixed-layer temperature and salinity and u_{*0}, described in Section VI.

V. Drag Coefficients and Under-Ice Roughness

Much of the previous discussion of RBL dynamics may seem esoteric to a reader who simply wants to know: what is the drag of the ocean on drifting

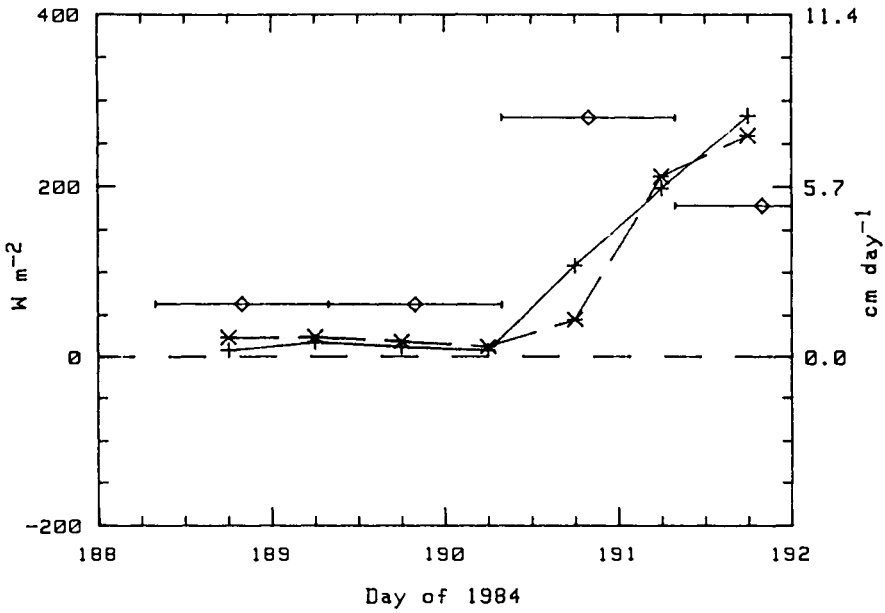

Figure 6.10 Vertical turbulent heat flux in watts per square meter during the MIZEX 84 drift of Fig. 6.7. Solid curve marked "+" is the average of all $\langle w'T' \rangle$ determinations in the mixed layer; dashed curve marked "X" is from the heat flux model described in Section VI; solid bars with diamonds are daily average bottom melt rates in centimeters per day, from ablation stakes surrounding the turbulence mast. Reprinted from McPhee *et al.* (1987); copyright by the American Geophysical Union.

sea ice? But, like the proverbial one-armed economist, an oceanographer who answers quickly risks oversimplifying a complex set of problems. First, there are a number of differing meanings and concepts concerning under-ice drag, so precise definition is difficult; and second, there are factors such as buoyancy and internal wave drag that, for ice with given roughness and velocity, can drastically modify momentum flux to the ocean. There have been several determinations of interfacial stress, drag coefficients, and under-ice surface roughness for drifting sea ice. In this section, the methods and results are discussed and compared in a common context.

Since actual shear stress on the ice undersurface is rarely, if ever, measured directly, its value is inferred from other measurements. We thus require some "model" of how measurable quantities are related to the actual stress, and often uncertainty in our theoretical methods is at least as important as the accuracy or statistical significance of our measurements. Several methods for determining ice/ocean stress have been used, including (1) profiles of mean current in the "logarithmic" layer, (2) direct measurements

of turbulent (Reynolds) stress, (3) measurements of total transport in the RBL (momentum integral method); (4) combining turbulent stress measurements with mean velocity measurements; and (5) inferring stress indirectly as a residual in the balance of forces acting on the ice.

Before describing the methods, it is pertinent to discuss what comprises "interfacial stress." Three potentially major contributors to the total momentum flux between ice and ocean have been identified from observations: "skin friction" arising from turbulence associated with shear in the boundary layer, "form drag" on objects (like pressure ridge keels) that protrude well beyond the general roughness elements characteristic of the under-ice surface, and momentum flux out of the ice/RBL system in the internal wave field. The last, discussed in Section VII, is important only when there is strong stratification near the surface, which is rare except in marginal ice zones. Of the five methods mentioned above, only the last includes a measure of internal-wave stress.

The distinction between skin friction and form drag is meaningful under conditions which seem to typify much of the perennial Arctic ice pack, where reasonably flat and uniform floes are bounded by pressure ridges separated by distances which are large compared with the size of the ridges. Using the analogy implied by the planetary (u_{*0}/f) length scaling, we may view flow in the RBL under pack ice with pressure ridge keels every few hundred meters as a scale model of mid-latitude atmospheric flow over fairly uniform terrain punctuated every few kilometers by low hills. In the latter, the flow will be disturbed in the vicinity of the hills and a net pressure on each hill will add to the downward momentum flux, increasing the total drag on the atmosphere. However, if we measured turbulent stress in the surface layer somewhere on the flat between hills, we would not detect the form drag stress. A similar situation often applies to sea ice, but when the larger roughness features are closely spaced, disturbances from each blend with the others and the distinction between turbulent skin friction and form drag blurs. Measurements near the interface may then show less of the actual turbulent flux than is apparent farther into the boundary layer at the same location. We suggested (McPhee *et al.*, 1987) that this was the reason for the increase in stress observed in the first few meters under the MIZEX floe.

A. Surface Layer Profile Measurements

Surface layer profile techniques follow directly from the law of the wall, Eq. (6.35). If current speed relative to the ice is measured at two levels, z_1 and z_2, in the surface layer, stress is calculated from

$$u_{*0} = k(u_2 - u_1)/\ln(z_2/z_1) \tag{6.72}$$

and surface roughness is

$$z_0 = \exp\left(\frac{u_2 \ln|z_1| - u_1 \ln|z_2|}{u_2 - u_1}\right) \tag{6.73}$$

The drag coefficient applicable to relative current measured at a particular level in the flow, $z = h$, is related to surface roughness by

$$c_h = \left(\frac{1}{k} \ln \frac{|h|}{z_0}\right)^{-2} \tag{6.74}$$

Untersteiner and Badgley (1965), Johannessen (1970), Ling and Untersteiner (1974), and Pease *et al.* (1983) cite either drag coefficients or surface roughness lengths calculated by the "log profile" method. Although easily applied, the technique has several drawbacks. First, the disparity in scales makes the surface layer in the ocean roughly 30 times thinner than the atmospheric surface layer, so the assumption of constant stress out to realistic measurement levels is suspect. It turns out that this is not as restrictive as it might seem, since the relative speed profile remains approximately logarithmic for some distance past the surface layer. On the other hand, since measurements are made at the edge or beyond the surface layer, stability effects need to be considered carefully. Unless properly accounted for, a melt rate as low as a couple of centimeters per day can have a significant impact on stress estimated from the mean profile out to 5 m. Also, since the method is confined to measurements in or near the surface layer, it fails to include any estimate of form drag effects.

B. Direct Measurements of Reynolds Stress

With the proper equipment, we can measure turbulent fluctuations in the flow under the ice and, from a statistical treatment, estimate the momentum flux at a given level directly. Interfacial stress is inferred from the Reynolds stress. Examples of Reynolds stress measurements are given by Smith (1974), McPhee and Smith (1976), Langleben (1980, 1982), McPhee *et al.* (1987), and McPhee (1989).

Langleben used a three-axis ultrasonic current meter to measure mean and turbulent velocities 1 m below the ice at AIDJEX station Caribou, located on a floe in the multiyear pack over the Canadian basin. He later measured stress 1 m below undeformed first-year ice in Barrow Strait, Northwest Territories. In both cases, he found quite small values for the drag coefficients (in fact, the measurements in Barrow Strait imply a hydraulically smooth surface), which again pose the surface layer dilemma: if the measurements are close enough to be considered within the constant-stress

layer, they are probably too close to pick up turbulence generated by larger but sparser roughness elements (see, e.g., the MIZEX stress hodograph in Fig. 6.8).

C. Momentum Integral Methods

A distinctly different approach uses Eq. (6.23) to estimate the total stress including form drag by integrating the volume transport through the boundary layer from a level at which stress is assumed to be zero. For currents averaged over an inertial cycle, the time derivative is often negligible. While the method in principle includes the contribution from keel form drag (Hunkins, 1975), it is valid only if averaged over an area that encompasses features responsible for the form drag. In other words, profiles from a single location may be unduly influenced by local under-ice topography. I cited an example from AIDJEX 72 (McPhee, 1974) in which surface stress calculated from simultaneous current meter profiles, spaced about 110 m apart, varied by a factor of $2\frac{1}{2}$, despite similar surface layer behavior and roughly the same amount of RBL turning. The difference came in the shape of the cross-stress profiles and in the choice of reference level.

D. Combination Methods

If stress and velocity are measured at more than one level in the RBL, the added information may be used to refine the estimate of interfacial stress. McPhee and Smith (1976) showed that stress in the near-surface RBL measured during AIDJEX 72 was affected by a local pressure gradient most likely associated with topographic relief. By combining Reynolds stress measurements and the momentum integral of mean velocity between instrument levels, we were able to estimate the magnitude of the pressure gradient term in the momentum equation and adjust our surface stress estimate accordingly.

A variant on this scheme is to formulate a model of RBL stress [such as Eq. (6.51)] and then determine u_{*0} by fitting observations so as to minimize rms errors, as demonstrated earlier in analyzing the "smooth" RBL of Fig. 6.9.

E. The Force Balance Method

The last method, which can in principle be applied without any measurements from the oceanic RBL at all, consists of deducing the average under-ice stress as a residual in the ice force balance. Expressed in its complex,

steady-state form, the balance is

$$i\rho_i h_i f(\hat{u}_i - \hat{u}_g) = \hat{\tau}_a - \hat{\tau}_0 + \hat{F}_i \tag{6.75}$$

where ρ_i, h_i, and $\hat{u}_i$ are, respectively, ice density, thickness, and velocity; $\hat{\tau}_a$ is tangential air stress; and $\hat{F}_i$ is the sum of forces internal to the ice, usually expressed as the gradient of internal ice stress. The term involving the geostrophic velocity $\hat{u}_g$ comes from the slope of the sea surface, via Eq. (6.18). The internal force term is very difficult to monitor directly, so the best way of applying the technique is to identify situations in which the internal stress must be small, e.g., when ice is thin or divergent, or when inertial oscillation is prominent. Sea surface tilt is also often difficult to measure directly, especially in coastal areas or near frontal regions, so in those cases an accurate measure of relative current just below the RBL is necessary.

Using the force balance method to amass statistics on interfacial stress and relative ice drift for the four AIDJEX stations during the melt season of 1975 (when internal ice forces were small), I found (McPhee, 1979) that the stress/velocity relation was like that predicted by Rossby similarity theory. Of the various drag laws proposed in the literature, only those that incorporated u_*/f scaling agreed with the AIDJEX free drift results (McPhee, 1982). Using a 10-m wind drag coefficient of 0.0027, based on integration of pilot balloon profiles at the AIDJEX sites, and estimating the average ice thickness to be 2.7 m, I found that the surface roughness appropriate for Rossby similarity [see Eq. (6.68)] was about 10 cm, which contrasts sharply with the value of about 0.2 cm inferred from the drag coefficient reported for AIDJEX station Caribou by Langleben (1980), based on direct stress measurements 1 m below the ice.

Pease *et al.* (1983) used an interesting variation on the force balance theme to estimate both air and water drag coefficients directly from measured surface wind, measured current in the under-ice surface layer, ice velocity, and estimates of geostrophic current. They obtained results similar to those from a current profile analysis done at the same site. Expressed in complex notation, the method is as follows. Let $\hat{u}_0 = \hat{u}_i - \hat{u}_g$ again be the ice velocity relative to geostrophic flow, and use quadratic formulas for air and water stress. If $\hat{F}_i$ is negligible, Eq. (6.75) becomes

$$i\rho_i h_i f\hat{u}_0 = \rho_a c_a u_a \hat{u}_a - \rho c_w u_w \hat{u}_w \tag{6.76}$$

where $\hat{u}_a$ and $\hat{u}_w$ are wind and current relative to the drifting ice. Given accurate measurement of all the velocities and ice thickness, the real and imaginary components of Eq. (6.76) determine the two unknowns c_a and c_w. As Pease *et al.* (1983) point out, if the term on the left side of Eq. (6.76) is small, the force balance is mainly between the two terms on the right, which

are nearly collinear. In this situation, small errors in h_i or $\hat{u}_0$ unduly influence the calculated magnitudes of c_a and c_w, but even so, the method provides a robust estimate of the ratio of the two drag coefficients.

Intuitively, estimates of drag coefficients improve as the Coriolis turning increases, and it is natural to consider the method in the context of the entire boundary layer. It is often convenient to express free drift as a complex ratio of ice velocity (relative to geostrophic flow) to surface wind:

$$\hat{u}_0/\hat{u}_a = re^{-i\theta} \tag{6.77}$$

where θ is the rightward deflection angle with respect to surface wind direction. For the AIDJEX free-drift period (summer 1975), the average ratio for all camps was 0.020 (2%!) with about 47° deflection (McPhee, 1980). During this time the average drift speed (corrected for small geostrophic currents) was about 0.13 m s^{-1}, and from current measurements near the ice we found that the average turning angle in the RBL was about 24°. With this information, it is possible to estimate the surface wind drag coefficient and the geostrophic water drag coefficient, c_g, as a function of ice thickness. We express the wind and water stress in terms of $\hat{u}_0$, so that the steady force balance is

$$i\rho_i h_i f\hat{u}_0 = (\rho_a c_a/r^2)\, u_0\hat{u}_0 e^{i\theta} - \rho c_g u_o\hat{u}_0 e^{i\beta} \tag{6.78}$$

where β is the RBL turning angle. We again decompose the complex equation into components, with the real part expressing the ratio of water and air drag coefficients:

$$c_g/c_a = (\rho_a/\rho r^2)\cos\theta/\cos\beta \tag{6.79}$$

and the imaginary part furnishing the magnitude,

$$c_a = (r^2\rho_i f h_i/\rho_a u_0)(\sin\theta - \cos\theta\tan\beta)^{-1} \tag{6.80}$$

Equation (6.80) implies that for given ice speed, wind drift ratio, and RBL turning (all of which can be readily measured with remote buoys), the drag coefficients are proportional to ice thickness. Unfortunately, mean ice thickness is often quite difficult to estimate, especially over an area large enough to represent the regional force balance. If mean ice thickness in the AIDJEX region is assumed to have been between 3 and 4 m, the corresponding 10-m wind drag coefficient ranges between 0.0021 and 0.0029, with the geostrophic water drag ranging from 0.0049 to 0.0068. These values coincide with the range of independent estimates of air and water drag made for the AIDJEX region. If one or the other of the drag coefficients is known with some confidence, the computation may be inverted to estimate mean ice thickness.

F. A Comparison of Roughness Lengths

Table 6.1 lists a number of independent determinations of under-ice drag, here expressed in terms of the surface roughness length z_0. A number of the cited works report drag coefficients, either referenced to relative current velocity at a particular level or as a "geostrophic" drag. These have been converted to equivalent z_0 values using Eq. (6.74) where a particular level is given [2 m was taken as the reference level for Smith's (1974) drag coeffi-

Table 6.1 Representative Estimates of Undersurface Roughness Length[a]

Source	Location	Method	Reported	z_0 (cm)
Ling and Untersteiner (1974) (after Untersteiner and Badgley, 1965)	Beaufort Sea (Arlis 2)	1	z_0	0.82–1.9
Johannessen (1970)	Gulf of St. Lawrence	1	z_0	3.2
		1	z_0	9.4
	Gulf of St. Lawrence	1	z_0	3.0
	North Pole	1	z_0	0.2
Smith (1974)	Beaufort Sea (Camp 200)	2	c_s	0.13–0.70
McPhee (1974)	Canada Basin (AIDJEX 72)	3	c_g	1.9
Hunkins (1975)	Canada Basin (AIDJEX 72)	3	Stress, u_0	1.1
McPhee and Smith (1976)	Canada Basin (AIDJEX 72)	4	Ro.	0.08
McPhee (1979)	Canada Basin (AIDJEX 75)	5	z_0	10
Langleben (1980)	Canada Basin (AIDJEX 75)	2	c_1	0.2
Langleben (1982)	Barrow Strait NWT (fast ice)	2	c_1	0.0017
Pease *et al.* (1983)	Bering Sea	1	z_0	8.0
	Bering Sea	5	$c_{1.1}$	5.7–7.4
McPhee (1989)	Greenland Sea (MIZEX)	4	z_0	5.5–7.7
	Beaufort (AIWEX)	4	z_0	Smooth
	Beaufort (PRUDEX)	4	z_0	0.45–0.63
Martinson and Wamser (1990)	Weddell Sea (WWSP-86)	5	c_g	0.06

[a] Method refers to technique used for determining stress: (1) log profile, (2) direct Reynolds stress, (3) momentum integral, (4) combination of direct stress and mean current measurements, or (5) force balance residual. Conversion of drag coefficients to roughness length is described in the text.

cients], or using the rear component of Eq. (6.68) for studies including the entire RBL.

It is difficult to generalize from the results of Table 6.1. The surface layer and direct turbulence measurements do not include the effect of form drag on large pressure ridge keels, yet Johannessen's (1970) second case and my MIZEX example produce very large roughness lengths. The comparison between AIDJEX 72 momentum integral determinations [Hunkins (1975), 1.1 cm; McPhee (1974), 1.9 cm] and the AIDJEX 1975 force balance (10 cm) is interesting because they come from roughly the same geographic region during different years. My force balance estimate is based on a fairly large wind drag coefficient (0.0027) but is consistent with the range of drag coefficients found in the previous subsection for mean ice thickness ranging from 3 to 4 m. In principle, both the momentum integral and force balance methods should account for most of the form drag effect, so the observed increase is probably indicative of a significant increase in ice roughness. It is also interesting that the "marginal ice zone" cases (the second Gulf of St. Lawrence example and the Bering and Greenland Sea examples) are uniformly large. This may be due to processes that tend to break up floes in some more or less similar fashion.

The range of roughness lengths found in Table 6.1 emphasizes the need for more research, both theoretical and observational, on the partition of total drag between skin friction and form drag and on what routine observations can be made to estimate regional values of under-ice roughness.

VI. Heat and Mass Flux at the Ice/Ocean Interface

In the previous sections, momentum flux between the ice and underlying RBL was described in detail. The question asked was essentially: given stress at the interface, what is the velocity of the ice relative to undisturbed water below the boundary layer and how is momentum distributed in the RBL? The inverse question — given relative velocity, what is stress at the ice/ocean interface and how is it distributed? — is just as relevant and is answered in much the same way.

To understand the system fully, we must ask similar questions about fluxes of temperature and salinity and other scalar properties. If we specify the heat and salt flux at the interface (essentially, the ice growth rate), then we should be able to use our knowledge of the dynamics of the RBL to predict changes in its mean temperature and salinity structure. In many practical problems, however, the question is posed in its inverse form: given surface momentum flux and temperature and salinity of the RBL, what is the heat flux (melt rate) at the interface? Stated another way: if an expanse of sea ice is

drifting over a mixed layer that is above freezing, how long will the ice last and how fast will it cool the mixed layer? It appears from recent measurements that the answer is highly dependent on what occurs in a thin layer near the interface and thus has no direct analog in the momentum flux/mean velocity question.

An idealized view of the heat and salt balances at the ice/ocean interface is given in Fig. 6.11, adapted from Mellor *et al.* (1986). We draw an infinitesimal control volume which follows the migrating interface, either up or down according to whether the ice is melting or freezing. From isostasy

$$w = -(\rho_i/\rho)\,\dot{d} = w_0 + w_i \tag{6.81}$$

where $\dot{d}$ is the ice growth rate and ρ_i is ice density. The interface vertical velocity is the sum of w_0, which is due to bottom melting, and w_i, the "percolation" velocity due to water that migrates to the interface from melting in the interior or at the surface of the ice column. The latter is often the

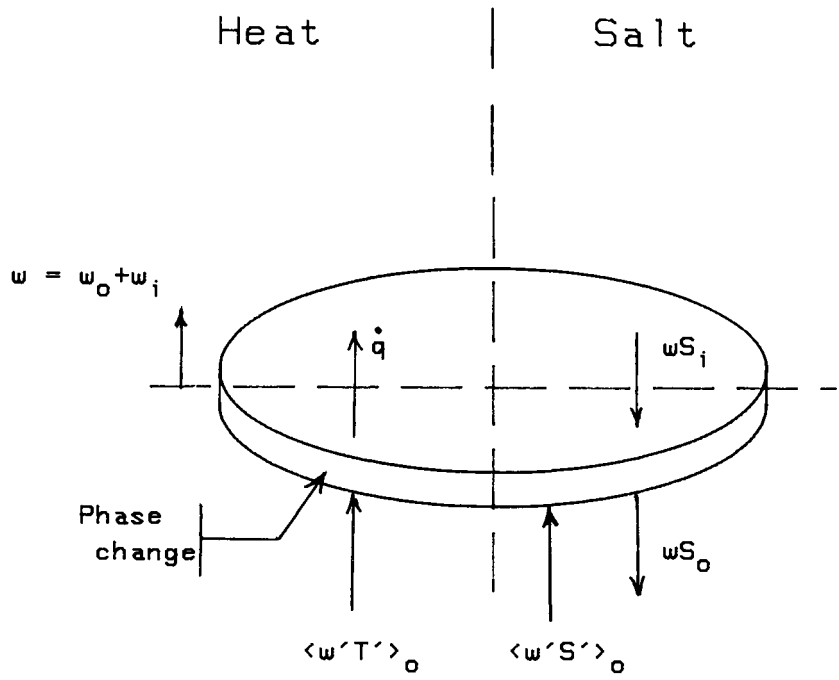

Figure 6.11 Schematic of an infinitesimal control volume following the ice undersurface with vertical velocity w. The heat balance is dominated by conduction through the ice $\dot{q}$; heat flux from the ocean, $\langle w'T'\rangle_0$; and the phase change associated with the bottom melt velocity, w_0. w_i is a "percolation" velocity from melt at the surface and within the ice. The salt budget is a balance between advection and turbulent flux.

major source of buoyancy when ice is compact, and the mixed-layer temperature remains near freezing. We treat it here as uniformly distributed, although it probably occurs in separated drainage channels and at floe boundaries. High melt rates occur when ice overruns warm water (Josberger, 1987); then w may come almost entirely from bottom melting.

The salt balance is shown on the right of Fig. 6.11. If w is positive (melting), fluid with salinity S_i advects into the control volume from above, much saltier fluid with salinity S_0 advects out, and the imbalance is compensated by the upward turbulent flux from the fully turbulent part of the boundary layer

$$\langle w'S' \rangle_0 = w(S_0 - S_i) \tag{6.82}$$

The heat balance is dominated by (a) conduction of heat through the ice, (b) the phase change if bottom freezing or melting occurs, and (c) turbulent heat flux from the ocean. Since sea ice is a mixture of pure ice and brine, its effective latent heat of fusion varies with brine volume, which is a function of temperature and salinity of the ice (Maykut, 1985). For ice that is near the freezing point of typical seawater, this relation is approximately

$$L_S \cong L_0(1 - 0.03S_i) \tag{6.83}$$

where L_0 is the latent heat of pure ice. Neglecting small changes in enthalpy associated with temperature changes in the control volume, the first-law heat balance is

$$\langle w'T' \rangle_0 = w_0 Q_L + \dot{q} \tag{6.84}$$

where

$$\dot{q} = -\frac{k_c}{\rho c_p} \frac{\partial T}{\partial z}\bigg|_{ice} \tag{6.85}$$

is the heat conduction through the ice (k_c is the thermal conductivity and c_p the specific heat of seawater) and Q_L is the latent heat of fusion (adjusted for brine volume) divided by specific heat, with units of temperature. Water at the immediate interface is at its freezing temperature, related to salinity at the interface by the linear approximation to Eq. (6.32): $T_0 = -mS_0$.

If we assume that the percolation velocity is known (or can be calculated with a model of ice thermodynamics), the fundamental problem of heat and mass transfer at the ice/ocean interface is to relate the bottom ablation rate to mean properties at some level in the fluid. This is a formidable theoretical problem and has been addressed (with widely varying results) by, among others, Josberger (1983), Ikeda (1986), and Mellor *et al.* (1986). McPhee *et al.* (1987) developed a framework for comparing the various approaches, which is briefly recapped here.

Expressing flux as an exchange coefficient times the mean gradient, with Eqs. (6.84) and (6.85), and then integrating from some level z to the surface, the nondimensional changes in temperature and salinity from z to the surface are given by

$$\frac{u_{*0}[T(z) - T_0]}{(w_0 Q_L + \dot{q})} = \Phi_T = \int_z^0 \frac{u_{*0}\, dz'}{\mathcal{K}_h} \tag{6.86}$$

and

$$\frac{u_{*0}[S(z) - S_0]}{(w_0 + w_i)(S_0 - S_i)} = \Phi_S = \int_z^0 \frac{u_{*0}\, dz'}{\mathcal{K}_S} \tag{6.87}$$

where $\mathcal{K}_h$ and $\mathcal{K}_S$ are heat and salt diffusivities, including both turbulent and molecular effects, and u_{*0} is the magnitude of the friction velocity at the interface. Using the freezing-line approximation, Eqs. (6.53) and (6.54) may be combined to obtain a quadratic equation for S_0

$$mS_0^2 + [T_q + (1 + c_1)c_2 - mS_i]S_0 - (T_q + c_2 S_q) = 0 \tag{6.88}$$

where

$$\begin{aligned} c_1 &= \Phi_S w_i / u_{*0}, \qquad c_2 = \Phi_T Q_L / \Phi_S \\ T_q &= T(z) - (\Phi_T / u_{*0})\, \dot{q} \\ S_q &= S(z) + c_1 S_i \end{aligned} \tag{6.89}$$

and thus for the bottom ablation velocity

$$w_0 = \frac{S(z) - S_0}{\Phi_S (S_0 - S_i)}\, u_{*0} - w_i \tag{6.90}$$

McPhee *et al.* (1987) reviewed several approaches to specifying the nondimensional functions Φ_T and Φ_S and found, using heat flux, turbulent stress, and mean T and S measured at 2 m depth during MIZEX 84, that molecular effects dominate the change in T and S across the boundary layer. We suggested that the nondimensional functions can be expressed as a sum of a contribution across the transition/laminar sublayer plus a much smaller contribution across the fully turbulent part of the boundary layer. Standard engineering practice (e.g., Incropera and DeWitt, 1985) and laboratory studies of Yaglom and Kader (1974) indicate an appropriate form of the nondimensional functions for the sublayer region to be

$$\Phi_{T,S} = b \left(\frac{u_{*0} z_0}{\nu} \right)^{1/2} \left(\frac{\nu}{\alpha_{T,S}} \right)^{2/3} + \Phi_{\text{turb}} \tag{6.91}$$

where ν, α_T, and α_S are, respectively, molecular kinematic viscosity, heat

diffusivity, and salt diffusivity. Representative values (Mellor *et al.*, 1986) in square meters per second are $\nu = 1.8 \times 10^{-6}$, $\alpha_T = 1.3 \times 10^{-7}$, and $\alpha_S = 7.4 \times 10^{-10}$. For the MIZEX data, McPhee *et al.* (1987) found the constant in Eq. (6.91) to be $b = 1.6$, about half the laboratory value.

Estimating the turbulent contribution to the nondimensional flux profiles, Φ_{turb} in Eq. (6.91), requires a model for turbulent exchange. A problem often encountered in sea ice studies, especially near the ice margins, is to estimate the bottom melt rate of ice drifting in water above the freezing temperature as a function of interfacial stress, mixed-layer temperature, and mixed-layer salinity. This can be accomplished with a straightforward extension of the similarity concepts discussed in Section III,C. We ignore the pycnocline and assume the Reynolds analogy in the mixed layer. Following closely the derivation of the nondimensional velocity profile in Section III,C (see also McPhee *et al.*, 1987), we have

$$\begin{aligned}\Phi_{\text{turb}} &= \frac{T_{\text{ml}} - T(z_0)}{\langle w'T' \rangle_0 / u_{*0}} = \frac{S_{\text{ml}} - S(z_0)}{\langle w'S' \rangle_0 / u_{*0}} \\ &= \frac{1}{k\xi_{\text{N}}} \int_{-\infty}^{\zeta_{\text{sl}}} e^{a\zeta}\, d\zeta + \frac{\eta_*}{k} \int_{\zeta_{\text{sl}}}^{\zeta_0} \frac{e^{a\zeta}}{\zeta}\, d\zeta\end{aligned} \tag{6.92}$$

where

$$a = \text{Re}(\delta) = 1/\sqrt{2k\xi_{\text{N}}} \tag{6.93}$$

If the integrals are approximated by using a Taylor series expansion for the exponential, and with $|\zeta_{\text{sl}}| \gg \zeta_0$, the result is

$$\Phi_{\text{turb}} = \left(\sqrt{\frac{2}{k\xi_{\text{N}}}} - \eta_* \sqrt{\frac{\xi_{\text{N}}}{2k}} \right) + \frac{\eta_*}{k} \left(\ln \frac{u_{*0}\xi_{\text{N}}\eta_*^2}{fz_0} - \eta_* \sqrt{\frac{\xi_{\text{N}}}{k}} \right) \tag{6.94}$$

where the first term in parentheses is the contribution of the outer layer and the second is from the fully turbulent part of the surface layer. For typical values under sea ice ($u_{*0} = 0.01$ m s^{-1}, $z_0 = 0.05$ m) and with $\eta_* = 1$, Φ_{turb} evaluates to

$$\Phi_{\text{turb}} = 9.6 + 10.1 = 19.7 \tag{6.95}$$

with surface and outer layers contributing about equally. By contrast, the nondimensional changes across the laminar/transition sublayer, given by the first term on the right of Eq. (6.91) with $b = 1.6$, are 153 and 4823 for temperature and salinity, respectively. In other words, the fully turbulent part of the boundary layer contributes less than 12% of the total temperature change and less than 0.5% of the salinity change. Thus a "mixed" layer can exist, even with high surface fluxes, because most of the change in scalar properties occurs across a very thin layer adjacent to the surface.

Steps in using the heat and mass flux model are as follows: (1) specify ice characteristics (w_i, $\dot{q}$, S_i) and forcing environment (u_{*0}, T_{ml}, S_{ml}), (2) evaluate Φ_T and Φ_S using Eq. (6.91) with an initial estimate for η_*, (3) solve the quadratic Eq. (6.88) for S_0 and use this to obtain w_0, and (4) calculate the buoyancy flux from total melt velocity for a refined estimate of η_* and iterate if the change in η_* is significant. This procedure was used to calculate the melt rate of 27 cm day^{-1} in Fig. 6.4c for $u_{*0} = 1$ cm s^{-1}, $T_{ml} = 3$°C, and $S_{ml} =$ 32 ppt ($S_i = 4$ ppt, $w_i = \dot{q} = 0$), demonstrating the effect of high surface buoyancy flux on the stress and velocity profiles.

The MIZEX heat and mass balance studies showed that even with highly turbulent flow near the hydraulically rough ice undersurface, the rate of heat and mass transfer is controlled by molecular processes in a thin layer near the immediate interface. In practical terms, this means that ice can last much longer in water several degrees above freezing than was anticipated using models which neglected the sublayer (Josberger, 1983; Ikeda, 1986). At the immediate ice edge, there is some evidence (Josberger, 1987) that transfer rates are somewhat higher than implied by the "universal" functions of Eq. (6.91); a possible source of higher heat flux there may be enhanced stirring by surface gravity waves.

Figure 6.10 shows results predicted using the model developed in McPhee *et al.* (1987) for drift in above-freezing water compared with actual measurements of heat flux and bottom melt (see also Fig. 18 of Morison *et al.*, 1987).

VII. Internal Wave Drag

Because of the restoring force exerted by gravity, vertical displacement in a stratified fluid is often accompanied by internal waves, which, unlike turbulent processes, are capable of transporting momentum and energy away from the ice/upper-ocean system. In contrast to the open ocean, the ice-covered RBL often has a ready source for internal waves in the form of pressure ridge keels drifting at speeds comparable to internal-wave phase speeds. It has long been speculated that drag from internal waves could be a significant factor in the ice force balance. However, the Arctic Ocean is also noted for the low intensity of its deep internal-wave field (Morison, 1986; Levine *et al.*, 1985); thus we can surmise that, overall, the ice cover probably diminishes rather than enhances internal wave generation.

By extrapolating Ekman's (1906) laboratory studies of "dead-water" drag on a model ship hull to pressure ridge keels, Hunkins (1974) found that for normal ice velocities and 35–50-m-thick mixed layers, internal-wave drag implied by the laboratory model results would be small. Rigby (1974) also

examined internal-wave generation by pressure ridge keels and concluded that the effect was small for typical central Arctic conditions. On the other hand, a set of modern tow tank experiments (Hachmeister and Rigby, 1980; Muench and Hachmeister, 1984) showed that for key parameters typical of the marginal ice zone, internal-wave drag on their model pressure ridges was as great as form drag.

During the last week of the 1984 summer MIZEX project in the Greenland Sea, the behavior of the ice/upper ocean system suggested that internal waves played an important role in RBL dynamics. Figure 6.12a, from Morison *et al.* (1987), shows wind forcing, relative ice speed, and drag coefficient

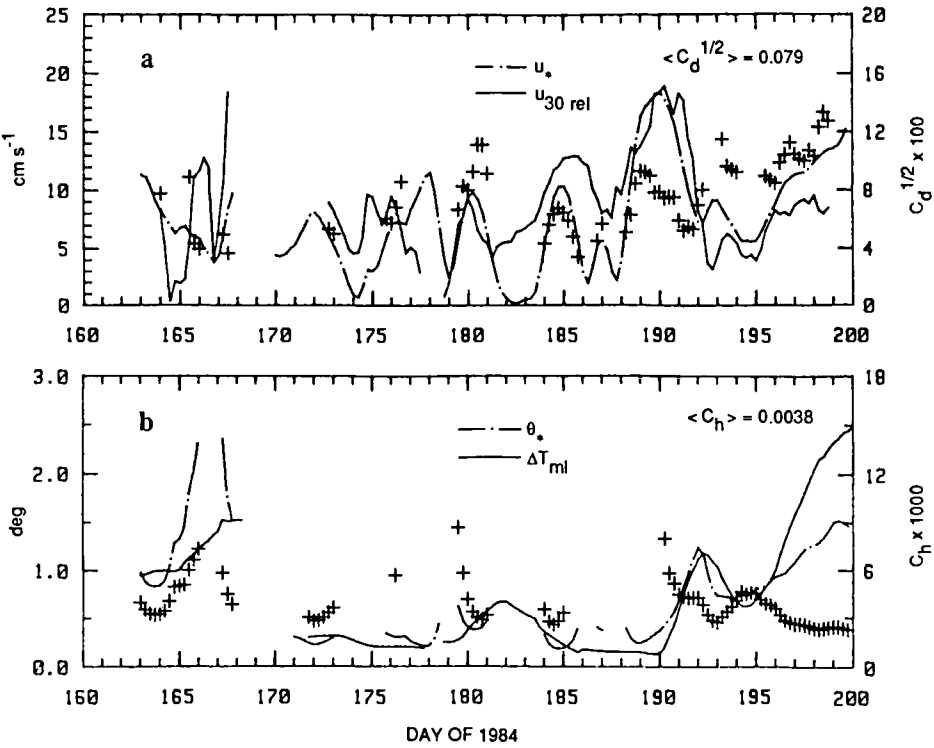

Figure 6.12 (a) Friction velocity determined from wind stress; ice speed relative to 30-m depth; and their ratio, the square root of drag coefficient (+), plotted against time for the entire MIZEX 84 drift in the Greenland Sea. (b) Forcing temperature θ_* (heat flux divided by u_*); elevation of mixed-layer temperature above freezing, ΔT_{ml}; and their ratio, the heat exchange coefficient (+). Reprinted from Morison *et al.* (1987); copyright by the American Geophysical Union.

for the entire drift, where u_* is derived from the wind stress modified by Coriolis acceleration of the ice. Figure 6.12b shows thermal forcing, mixed-layer temperature, and heat transfer coefficient for the entire MIZEX 84 drift. The heat transfer scale θ_* is kinematic heat flux (proportional to bottom melt rate) divided by u_*, and c_h is θ_* divided by mixed-layer temperature. During the last few days, ice was melting in water well above freezing, with stable stratification almost to the interface—conditions for which we would expect strong buoyancy effects. Nevertheless, the drag coefficient was larger than at any other time, while the heat transfer coefficient was smaller. If turbulence had been the only transfer mechanism, buoyancy should have acted to decrease both coefficients, with the largest effect on momentum. Morison *et al.* (1987) argued that momentum flux into the internal-wave field could account for the otherwise peculiar behavior and showed that internal waves with the proper characteristics for significant downward radiation of momentum and energy were present in data from instrument clusters in the upper part of the RBL.

For most practical problems, the length and time scales of internal waves that provide much vertical momentum flux are too small to resolve individually. A parametrization of internal-wave drag on sea ice has been suggested by McPhee and Kantha (1989), based on a two-layer, inviscid theory similar to that described by Gill (1982). Without repeating the complete derivation, our results for one Fourier component of under-ice waviness, characterized by wave number k (which should not be confused with von Karman's constant) and amplitude h_0, expressed the additional drag from internal-wave generation as the product of two factors. The first is the drag that would be encountered if the pycnocline density gradient, characterized by buoyancy frequency N, extended to the ice/ocean interface:

$$c_{wd} = \tfrac{1}{2}k_x^2 h_0^2 \left[(k_c^2/k_x^2) - 1\right]^{1/2} \tag{6.96}$$

where $k_c = N/u_r$ is a critical wave number above which the solutions are evanescent and k_x is the wave number component in the direction of ice motion. This is multiplied by an attenuation factor which takes into account the mixed-layer depth H and the strength of the buoyancy jump at the base of the mixed layer, Δb:

$$\Gamma = \left(\sinh^2(kH)\left\{\left[\coth(kH) - \frac{k\,\Delta b}{u_r^2 k_x^2}\right]^2 + \frac{N^2}{u_r^2 k_x^2} - 1\right\}\right)^{-1} \tag{6.97}$$

The kinematic internal-wave stress is

$$\hat{\tau}_{IW} = -\Gamma c_{wd}\, u_0 \hat{u}_0 \tag{6.98}$$

and acts in addition to the normal RBL turbulent and form drag stress.

The attenuation factor decreases rapidly with increasing mixed-layer depth, so that for H much greater than about 10 m the drag is small. In the central Arctic, the mixed layer is rarely as shallow as 10 m, so internal-wave drag is not often a factor in ice drift. But in the marginal ice zone, rapid melting sometimes leads to extreme stratification and substantial increased drag. This not only slows the ice but also reduces the RBL capacity for turbulent mixing, which both reduces heat flux (bottom melting) and slows mixed-layer deepening.

In McPhee and Kantha (1989), we applied the parametrization in an ice/RBL numerical model, with drag calculated by integrating a plausible spectrum of under-ice roughness over two-dimensional wave number space. We found that a spectrum with a peak wave number of 0.06 m^{-1} (100 m wavelength) and root-mean-square amplitude of 2.0 m produced about the observed amount of increased drag and decreased heat flux. The model also predicted significantly less mixed-layer deepening than a similar model without internal-wave drag, again in agreement with observations. We obtained similar results when we replaced the under-ice waviness spectrum with a single wave number disturbance with the same wavelength and amplitude reduced to 1.4 m. The latter reduces computation significantly.

VIII. Summary

In order to understand (and model) ice motion and thermodynamics, mixed-layer evolution, how physics affects biological processes, and air–ice–sea interaction in general, it is necessary to describe properly what controls fluxes of momentum, heat, salt, and other quantities near the ice/ocean boundary. My experience has been that the problem is usually approached in one of two ways: (1) express the fluxes in terms of bulk exchange coefficients and search for ways of simplifying the physics to specification of a few empirical "constants," or (2) use a computer to solve a numerical model of the conservation equations at multiple levels, in essence relegating the empiricism to smaller and smaller scales, where our knowledge is greatly enhanced by laboratory studies. In some sense, this chapter documents an attempt to strike a middle course, in which we ask: what is the simplest conceptual view of the exchange process that can still account for the important features of the observational base and the results of sophisticated numerical models?

Perhaps the most common question associated with small-scale processes is how much drag the ocean exerts on drifting ice. Studies during the past couple of decades have shown that this is by no means a simple question, nor is it one that we can consider answered. A number of important factors affect

the drag, among which are under-ice roughness, both small and large scale; buoyancy flux at the ice/ocean interface and at the base of the mixed layer; and pressure–displacement correlations in internal waves generated by ridge keels. Similar considerations apply to heat and salt flux between ice and ocean, except that even with very rough ice it appears that much of the gradient in these scalars occurs in a thin layer near the interface where molecular effects are important, often dominant.

Not all of these factors operate all the time. If the mixed layer is deep, internal waves are unlikely to play much role in the ice force balance, and the effect of buoyancy flux at the base of the mixed layer will be minimal. If the mixed layer is near its freezing temperature and the ice is more than a few centimeters thick, it is unlikely that surface buoyancy flux will be of overriding importance in RBL dynamics. Thus, for much of the ice pack in winter, we can probably do an adequate job of describing momentum flux with an expression like Eq. (6.51) and ice velocity relative to the ocean with a Rossby similarity drag law [Eq. (6.68)] (although the question of what value to use for z_0 remains). But the interesting dynamics, thermodynamics, and biology are often associated with areas where many of the factors come into play simultaneously: rapid melting or freezing, changes in upper-ocean stratification, even large modification of under-ice roughness. To adequately model air–sea–ice interaction in these situations most likely requires treating small-scale exchange processes as realistically as possible.

References

Batchelor, G. K. 1970. "An Introduction to Fluid Mechanics." Cambridge Univ. Press, London.

Blackadar, A. K. & H. Tennekes. 1968. Asymptotic similarity in neutral planetary boundary layers. *J. Atmos. Sci.* **25**: 1015–1019.

Businger, J. A. & S. P. Arya. 1974. The height of the mixed layer in a stably stratified planetary boundary layer. *Adv. Geophys.* **18**: 73–92.

Deardorff, J. W. 1972. Numerical investigation of neutral and unstable planetary boundary layers. *J. Atmos. Sci.* **29**: 91–115.

Ekman, V. W. 1905. On the influence of the earth's rotation on ocean currents. *Ark. Mat., Astron. Syst.* **2**: 1–52.

———. 1906. On dead water. *In* "Scientific Results, Norwegian North Polar Expedition 1893–1896" (F. Nansen, ed.), Vol. 5, pp 1–15. Christiania, Norway.

Friehe, C. A. 1987. Review of atmospheric boundary layer research, 1983–1986. *Rev. Geophys.* **25**: 387–392.

Gill, A. E. 1982. "Atmosphere–Ocean Dynamics." Academic Press, New York.

Gordon, A. L. 1987. Mixed layer under Southern Ocean sea ice. *Eos* **68**: 1768 (abstr.).

Hachmeister, L. E. & F. A. Rigby. 1980. Laboratory studies of stratified flow interaction with topography. *In* "Proceedings of the Second International Symposium on Stratified Flows" (T. Carstens & T. McClimans, eds.), pp. 623–635. Tapir, Trondheim.

Hinze, J. O. 1975. "Turbulence." McGraw-Hill, New York.

Hunkins, K. 1966. Ekman drift currents in the Arctic Ocean. *Deep-Sea Res.* **13:** 607–620.

———. 1967. Inertial oscillations of Fletcher's Ice Island (T-3). *JGR, J. Geophys. Res.* **72:** 1165–1174.

———. 1974. An estimate of internal wave drag on pack ice. *AIDJEX Bull.* **26:** 141–152.

———. 1975. The oceanic boundary layer and stress beneath a drifting ice floe. *JGR, J. Geophys. Res.* **80:** 3425–3433.

———. 1980. Review of the AIDJEX oceanographic program. *In* "Sea Ice Processes and Models" (R. S. Pritchard, ed.), pp. 34–35. Univ. of Washington Press, Seattle.

Ikeda, M. 1986. A mixed layer beneath melting sea ice in the marginal ice zone using a one-dimensional turbulent closure model. *J. Geophys. Res.* **91:** 5054–5060.

Incropera, F. P. & D. P. DeWitt. 1985. "Fundamentals of Heat and Mass Transfer." Wiley, New York.

Johannessen, O. M. 1970. Note on some vertical profiles below ice floes in the Gulf of St. Lawrence and near the North Pole. *JGR, J. Geophys. Res.* **75:** 2857–2861.

Josberger, E. G. 1983. Sea ice melting in the marginal ice zone. *J. Geophys. Res.* **88:** 2841–2844.

———. 1987. Bottom ablation and heat transfer coefficients from the 1983 Marginal Ice Zone experiments. *J. Geophys. Res.* **92:** 7012–7016.

Langleben, M. P. 1980. Water drag coefficient at AIDJEX, station Caribou. *In* "Sea Ice Processes and Models" (R. S. Pritchard, ed.), pp. 464–471. Univ. of Washington Press, Seattle.

———. 1982. Water drag coefficient of first-year sea ice. *J. Geophys. Res.* **87:** 573–578.

Levine, M. D., C. A. Paulson & J. H. Morison. 1985. Internal waves in the Arctic Ocean: Comparison with lower-latitude observations. *J. Phys. Oceanogr.* **15:** 800–809.

Ling, C.-H. & N. Untersteiner. 1974. On the calculation of the roughness parameter of sea ice. *JGR, J. Geophys. Res.* **79:** 4112–4114.

Martinson, D. G. & C. Wamser. 1990. Ice drift and momentum exchange in winter Antarctic pack ice. *J. Geophys. Res.* (in press).

Maykut, G. A. 1985. "An Introduction to Ice in the Polar Regions," Tech. Rep. APL-UW 8510. Univ. of Washington, Seattle.

McPhee, M. G. 1974. An experimental investigation of the boundary layer under pack ice. Ph.D. Diss., Univ. of Washington, Seattle.

———. 1978. A simulation of inertial oscillation in drifting pack ice. *Dyn. Atmos. Oceans* **2:** 107–122.

———. 1979. The effect of the oceanic boundary layer on the mean drift of sea ice: Application of a simple model. *J. Phys. Oceanogr.* **9:** 388–400.

———. 1980. An analysis of pack ice drift in summer. *In* "Sea Ice Processes and Models" (R. S. Pritchard, ed.), pp. 62–75. Univ. of Washington Press, Seattle.

———. 1981. An analytic similarity theory for the planetary boundary layer stabilized by surface buoyance. *Boundary-Layer Meteorol.* **21:** 325–339.

———. 1982. "Sea Ice Drag Laws and Simple Boundary Layer Concepts, Including Application to Rapid Melting," CRREL Rep. 82-4. U.S. Army Cold Reg. Res. Eng. Lab., Hanover, New Hampshire.

———. 1983. Turbulent heat and momentum transfer in the oceanic boundary layer under melting pack ice. *J. Geophys. Res.* **88:** 2827–2835.

———. 1986a. Medium resolution turbulence clusters for upper ocean measurements under sea ice. *In* "Proceedings of the IEEE Third Working Conference on Current Measurement" (G. Appell & W. E. Woodward, eds.), pp. 163–168. Inst. Electr. Electron. Eng., New York.

———. 1986b. The upper ocean. *In* "The Geophysics of Sea Ice" (N. Untersteiner, ed.), pp. 339–394. Plenum, New York.

———. 1987. A time-dependent model for turbulent transfer in a stratified oceanic boundary layer. *J. Geophys. Res.* **92**: 6977–6986.

———. 1988. Analysis and prediction of short-term ice drift. *Trans. ASME: J Offshore Mech. Arctic Eng.* **110**: 94–100.

———. 1989. Inferring ice/ocean surface roughness from horizontal current measurements. *Trans. ASME: J. Offshore Mech. Arctic Eng.* **111**: 155–159.

McPhee, M. G. & L. H. Kantha. 1989. Generation of internal waves by sea ice. *J. Geophys. Res.* **94**: 3287–3302.

McPhee, M. G. & J. D. Smith. 1976. Measurements of the turbulent boundary layer under pack ice. *J. Phys. Oceanogr.* **6**: 696–711.

McPhee, M. G., G. A. Maykut & J. H. Morison. 1987. Dynamics and thermodynamics of the ice/upper ocean system in the marginal ice zone of the Greenland Sea. *J. Geophys. Res.* **92**: 7013–7031.

Mellor, G. & T. Yamada. 1982. Development of a turbulence closure model for geophysical fluid problems. *Rev. Geophys. Space Phys.* **20**: 851–875.

Mellor, G., M. G. McPhee & M. Steele. 1986. Ice–seawater turbulent boundary layer interaction with melting or freezing. *J. Phys. Oceanogr.* **16**: 1829–1846.

Moeng. C.-H. 1984. A large-eddy-simulation model for the study of planetary boundary-layer turbulence. *J. Atmos. Sci.* **41**: 2052–2062.

Morison, J. H. 1986. Internal waves in the Arctic Ocean: A review *In* "The Geophysics of Sea Ice" (N. Untersteiner, ed.), pp. 1163–1183. Plenum, New York.

Morison, J. H., M. G. McPhee & G. A. Maykut. 1987. Boundary layer, upper ocean, and ice observations in the Greenland Sea marginal ice zone. *J. Geophys. Res.* **92**: 6987–7011.

Muench, R. D. & L. E. Hachmeister. 1984. "Internal Wave Forces on Ice Keels in the Marginal Ice Zone: Some Preliminary Laboratory Results," CRREL Spec. Rep. 84-7, pp. 83–90. U.S. Army Cold Reg. Res. Eng. Lab., Hanover, New Hampshire.

Neshyba, S., V. T. Neal & W. Denner. 1971. Temperature and conductivity measurements under Ice Island T-3. *J. Geophys. Res.* **76**: 8107–8120.

Neumann, G. & W. J. Pierson, Jr. 1966. "Principles of Physical Oceanography." Prentice-Hall, Englewood Cliffs, New Jersey.

Obukhov, A. M. 1971. Turbulence in an atmosphere with a non-uniform temperature. *Boundary-Layer Meteorol.* **2**: 7–29.

Pease, C. H., S. A. Salo & J. E. Overland. 1983. Drag measurements for first-year sea ice over a shallow sea. *J. Geophys. Res.* **88**: 2853–2862.

Pinkel, R., S. Beck & J. H. Morison. 1986. Doppler acoustic velocity profiling in the Arctic. *In* "Proceedings of the IEEE Third Working Conference on Current Measurement" (G. Appell & W. E. Woodward, eds.), pp. 163–168. Inst. Electr. Electron. Eng., New York.

Price, J. F., E. A. Terray & R. A. Weller. 1987. Upper ocean dynamics. *Rev. Geophys.* **25**: 193–203.

Reed, R. J. & W. J. Campbell. 1962. The equilibrium drift of Ice Station Alpha. *J. Geophys. Res.* **67**: 281–297.

Rigby, F. A. 1974. Theoretical calculations of internal wave drag on sea ice. *AIDJEX Bull.* **26**: 129–140.

Shuleikin, V. V. 1938. The drift of ice-fields. *C. R. (Dokl.) Acad. Sci., URSS* **19**: 589–594.

Smith, J. D. 1974. Turbulent structure of the surface boundary layer in an ice-covered ocean. *Rapp. P.-V. Reun., Cons. Int. Explor. Mer* **167**: 53–65.

Stern, M. E. 1975. "Ocean Circulation Physics." Academic Press, New York.

Tennekes, H. & J. L. Lumley. 1972. "A First Course in Turbulence." MIT Press, Cambridge, Massachusetts.

Turner, J. S. 1973. "Buoyancy Effects in Fluids." Cambridge Univ. Press, London.

Untersteiner, N. & F. Badgley. 1965. The roughness parameters of sea ice. *J. Geophys. Res.* **70:** 4573–4577.

Villanueva, J. Z. & J. C. van Leer. 1987. Anatomy of the East Greenland Polar Front as observed by cyclesondes. *Eos* **68:** 1754 (abstr.).

Wyngaard, J. C. 1985. Structure of the planetary boundary layer and implications for its modeling. *J. Clim. Appl. Meteorol.* **24:** 1131–1142.

Wyngaard, J. C., O. R. Cote & K. S. Rao. 1974. Modeling the atmospheric boundary layer. *Adv. Geophys.* **18A:** 193–212.

Yaglom, A. M. & B. A. Kader. 1974. Heat and mass transfer between a rough wall and turbulent fluid flow at high Reynolds and Peclet numbers. *J. Fluid Mech.* **62:** 601–623.

Zilitinkevich, S. S. 1975. Resistance laws and prediction equations for the depth of the planetary boundary layer. *J. Atmos. Sci.* **32:** 741–752.

7 Models and Their Applications to Polar Oceanography

Sirpa Häkkinen
NASA Goddard Space Flight Center
Greenbelt, Maryland

I. Ice Models 335
A. Introduction 335
B. Dynamic Ice Models 337
C. Thermodynamic Ice Models 342
D. Dynamic-Thermodynamic Ice Models 351
II. Ocean Models 357
A. Introduction 357
B. Large-Scale Ocean Circulation Models 358
C. Process Studies 360
III. Coupled Ice-Ocean Models 362
A. Introduction 362
B. Large-Scale Fully Coupled Ice-Ocean Models 363
C. Mesoscale Ice-Ocean Models 365
D. Other Ice-Ocean Models 375
IV. Concluding Remarks 380
References 381

I. Ice Models

A. Introduction

Ice cover has a major influence on the heat exchange in the polar regions because the ice cover reduced the surface heat loss by two orders of magnitude compared with that from open water. This insulating effect of the ice cover is strongly related to the climate we now experience. We know that there have been fluctuations in the world's climate in the past which have also been reflected in the ice cover. It is fair to say that sea ice cover can act as an indicator of climate fluctuations, which is one of the reasons we seek to model and predict the behavior of the ice cover. Understanding ice dynamics

Polar Oceanography, Part A: Physical Science

is as important as understanding the thermodynamics; that is, we need to know how to describe wind- and current-driven ice motion. We also want to be able to predict ice drift so that we can manage natural resources in the Arctic and assist shipping in ice-covered waters.

The first efforts in analyzing ice motion are described in Zubov (1945), whose work on wind-driven ice drift and on ice growth was fundamental in understanding ice dynamics and thermodynamics. However, it was not until the development of computers that the governing equations could be used to solve the sea ice motion. The assumption of a continuum makes ice much more amenable to numerical modeling; that is, by assuming the ice field to behave like a continuous medium, one can describe the ice motion in terms of a smooth differentiable velocity field.

The first numerical model for the ice drift in the Arctic was reported by Campbell (1965). His aim was to describe the mean ice motion in the Arctic basin based on the climatological mean pressure field. With better atmospheric data, the ice models have been extended to explore the monthly and seasonal ice motion (Hibler, 1974; Hibler and Tucker 1977, 1979) and used for operational ice forecasting in the Baltic (Lepparanta, 1981).

While the first dynamical models for sea ice were being developed, the first efforts to describe the thermodynamics of ice and its seasonal growth and ablation were also being made (Untersteiner, 1961, 1964). The model by Untersteiner described the evolution of the mean ice thickness in the Arctic under the influence of the surface heat flux, oceanic heat flux, and conductive heat flux. This thermodynamic model was refined later with the explicit inclusion of snow cover (Maykut and Untersteiner, 1969, 1971). The model was further developed by Semtner (1976a), who modified it to be suitable for climate modeling. Besides the prediction of the annual cycle of the average ice thickness in the Arctic, Pease (1975) used the Maykut–Untersteiner model without snow cover (1969) with considerable success to preduct ice extent in the Antarctic along a transect from 70°S to 58°S at 155°E. The thermodynamic model of Semtner (1976a) was extended by Washington *et al.* (1976) to two dimensions to simulate the seasonal change of the Arctic and Antarctic sea ice cover.

To model the climate, Bryan (1969) and Bryan *et al.* (1975) have developed a thermodynamic ice model coupled with an atmospheric model, where sea ice is transported passively with the ocean currents. Their model is driven by annual mean forcing instead of daily or monthly means, and it considers the ice thicknss to be determined by surface heat imbalance of the atmospheric heat flux and conductive flux throught ice and of snowfall and evaporation. Grid cells with ice cover do not include any leads in the ice pack.

The first fully dynamic–thermodynamic ice models were developed by Parkinson and Washington (1979) and by Hibler (1979). These models were

used to study the large-scale seasonal sea ice variability in the Arctic and the Antarctic and to predict the ice drift, ice thickness, and ice concentration. The models are driven by realistic forcing by observed winds, air temperatures, and radiative fluxes. Parkinson (1983) and Hibler and Ackley (1983) also applied these models to a specific case study of the Weddell Polynya, which was discovered by a satellite microwave radiometer (Zwally and Gloersen, 1977; Carsey, 1980). A long-term, 30-year simulation of the Arctic ice cover has been done by Walsh *et al.* (1985).

B. Dynamic Ice Models

Before a discussion of the details and specifics of evolution of dynamic ice models, the dynamic equations for ice motion, on which the discussion is based, are presented. Since the assumption of a continuum is applied to ice and ice motion, the evolution of an ice field can be described with two momentum equations (for horizontal components) and continuity equations for ice concentration A and ice mass ρD, where D is ice thickness h_i multiplied by ice concentration. A is also called ice compactness or fractional area of ice. The governing equations are expressed as follows.
Momentum equations:

$$\rho_i D\, du/dt = \rho_i D(fv - gh_x) + A(\tau_{xw} - \tau_{xb}) + \rho_i D\tau_{xi} \tag{7.1}$$

$$\rho_i D\, dv/dt = \rho_i D(-fu - gh_y) + A(\tau_{yw} - \tau_{yb}) + \rho_i D\tau_{yi} \tag{7.2}$$

Continuity equations:

$$dA/dt + (uA)_x + (v\mathrm{A})y = 0 \tag{7.3}$$

$$dD/dt + (uD)_x + (v\mathrm{D})y = 0 \tag{7.4}$$

where ρ_i is the ice density (910 kg m^{-3}), u and v are the x and y components of ice velocity, f is the Coriolis parameter, g is gravitational acceleration (9.8 m s^{-2}), h is sea surface height, τ_{xw} and τ_{yw} are the x and y components of the wind stress, τ_{xb} and τ_{yb} are the x and y components of the interfacial (ice–ocean) stress, and τ_{xi} and τ_{yi} are the x and y components of the ice internal stress.

The different terms in the momentum equations (7.1) and (7.2) are the inertial acceleration, Coriolis force, acceleration due to sea surface tilt, wind stress, ice–ocean interfacial stress, and ice internal stress, respectively. The wind stress and the ice–ocean stress have been based on a linear drag law:

$$\tau_{xw} = b(U_g \cos\phi - V_g \sin\phi) \tag{7.5}$$

$$\tau_{yw} = b(U_g \sin\phi + V_g \cos\phi) \tag{7.6}$$

$$\tau_{yb} = d[(u - U_w)\cos\theta - (v - V_w)\sin\theta] \tag{7.7}$$

$$\tau_{yb} = d[(u - U_w)\sin\theta + (v - V_w)\cos\theta] \tag{7.8}$$

where b and d are constant drag coefficients, U_g and V_g are geostrophic wind velocities, U_w and V_w are the long-term geostrophic currents, and ϕ and θ are Ekman angles in the air and water, respectively. In current models, the quadratic form for τ_w and τ_b is preferred,

$$\tau_w = \rho_a C_{aw} W^2 \tag{7.9}$$

$$\tau_b = \rho_i C_{wi}(u - U_w)^2 \tag{7.10}$$

The earliest ice models by Nikiforov (1957) and Doronin (1970) explored the ice drift as a simple balance between wind stress, bottom (ice–ocean interface) stress, and Coriolis force, Eqs. (7.1) and (7.2). This balance of forces is often called the "free drift" and gives a good approximation away from boundaries and in divergent conditions. Of course, this force balance is considerably altered when ice floes are packed together, as during convergence and ridging. Ridging is pronounced near coastlines, where the movement of ice is severely inhibited by land, land-fast ice, or grounded ridges in shallow water. Ridging is a manifestation of the ice internal stresses, the last term in Eqs. (7.1) and (7.2).

Formulation of the ice constitutive law has been a topic of discussion as long as there have been numerical ice models. The different stress laws considered for ice are viscous, elastic, viscous–plastic, and elastic–plastic. The evolution of considerations related to the constitutive law will be discussed in the order in which they were introduced, which also represents the evolution toward more sophisticated models.

Campbell (1965) used a constant-viscosity stress law in his ice model, considering ice to be a Newtonian fluid. The stress tensor for a two-dimensional constant-viscosity "fluid" can be expressed as

$$\sigma_{ij} = 2\eta(\dot{\epsilon}_{ij} - \delta_{ij}\dot{\epsilon}_{kk}/2) \tag{7.11}$$

where $\dot{\epsilon}_{ij}$ is the strain rate tensor, defined as

$$\dot{\epsilon}_{ij} = (\partial u_i/\partial x_j + \partial u_j/\partial x_i)/2 \tag{7.12}$$

(i and j correspond to the x and y components). Now the stress force per unit area can be computed, e.g., for the i component:

$$\tau_i = \partial\sigma_{ij}/\partial x_j = \eta\,\nabla^2 u_i \tag{7.13}$$

where repeated indices mean summation.

Using the mean annual geostrophic wind field, Campbell (1965) simulated the mean ice drift in the Arctic. The solution did not include either continuity equation, (7.3) or (7.4); thus ice concentration was considered

uniform in the Arctic. The simulated drift pattern captures the large-scale Beaufort Sea gyre; however, the Transpolar Drift Stream is only partially developed when compared with observational mean ice drift charts (Fig. 7.1, adapted from Gordienko, 1958). The convergence shown by the streamlines at the center of the gyre (Fig. 7.2) gives ice accumulation rates that are too high compared with the observational arguments of ice equilibrium thickness. Nevertheless, the results of this model were promising enough to warrant further studies of the predictability of sea ice motion assuming a continuum description for the varying sea ice field.

When better meteorological data became available and it was possible to study the synoptic variability of ice drift, the simulations revealed that low ice concentrations correspond to low viscosity and high ice concentrations indicate high viscosity. Hibler and Tucker (1977, 1979) determined the viscosities empirically in their ice model, in which the viscous ice stress also included a bulk viscosity according to Glen (1970):

$$\sigma_{ij} = 2\eta\dot{\epsilon}_{ij} + (\zeta - \eta)\dot{\epsilon}_{kk}\delta_{ij} \tag{7.14}$$

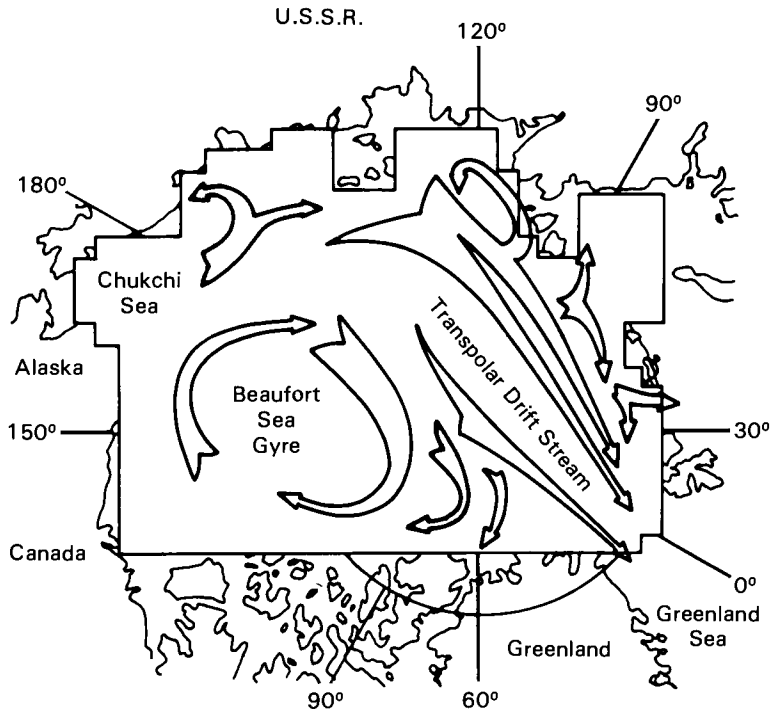

Figure 7.1 Annual mean ice drift in the Arctic. Adapted from Gordienko (1958).

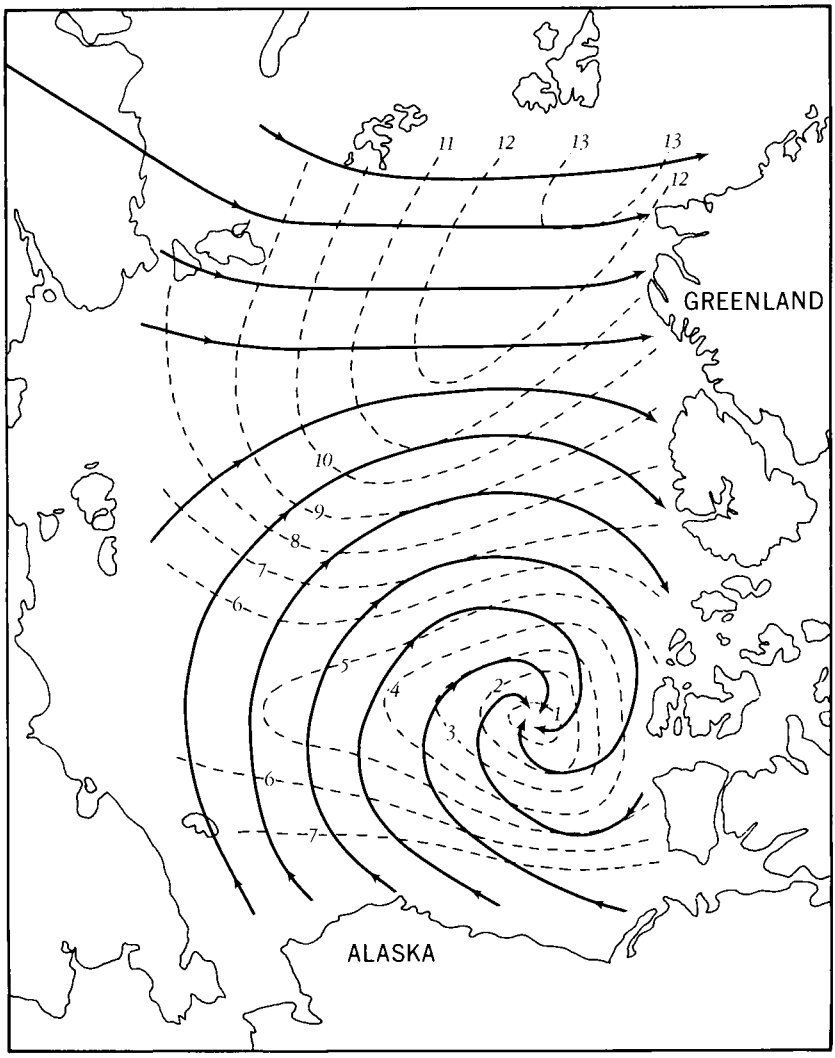

Figure 7.2 Streamlines (solid lines) and isotachs (dashed lines) in centimeters per second from the Arctic ice model of Campbell (1965); copyright by American Geophysical Union.

The empirical search for a best fit requires smaller viscosity values during summer than winter. Besides the seasonal variation in viscosity, it appears from the calculations of Hibler and Tucker that for the best fit with observations viscosity has to vary spatially, with smaller values near the coast and larger values in the central ice field. This seasonal and spatial variability can

be achieved by describing viscosity as a linear function of ice compactness, as suggested by Nikiforov (1957): Near the coastlines and in the summer season, the ice pack has a considerable amount of open water between the individual floes due to the coastal shear zones and melting, respectively. This empirical dependence on the ice concentration has been included in most later constitutive laws.

The early modeling experiments and an extensive field experiment, the Arctic Ice Dynamics Joint Experiment (AIDJEX) in the early 1970s, prompted a search for alternative constitutive equations for sea ice. The new form was expected to take into account small-scale characteristics of the ice field, such as the fact that ice cannot support tension but can resist compression. An example of a stress law in which this property is not accounted for is the bulk viscosity form of Glen (1970), which gives the same stress independent of the convergence or divergence of the ice field. Also, field experiments suggested that the ice field can support varying strain-rate states under fairly uniform forcing (Hibler *et al.*, 1974), which advocated the use of the plastic laws (Coon *et al.*, 1974); Pritchard, 1975; Pritchard *et al.*, 1975). The essence of plastic laws is the form of yield curve, which is a function of stress invariants (or principal stresses), with points along the curve representing plastic yielding under constant stress. Several yield curve shapes have been chosen; e.g., a teardrop curve was used by the AIDJEX modelers and an ellipse by Hibler (1977). Because of the inability of the ice field to support tension, the yield curve has to be confined to the negative principal stress quadrant.

Whether or not a rigid plastic law is superior in describing ice stresses in a model, it did lead to a quite complicated formulation in order to solve the ice dynamical equations. This was one of the main reasons why Hibler (1977) reformulated the plastic law into a viscous form in which the bulk and shear viscosities simulate the plastic behavior in a stochastic sense. This viscous law derived from a plastic yield curve is

$$\sigma_{ij} = 2\eta(\dot{\epsilon}_{ij}, P) + [\zeta(\dot{\epsilon}_{ij}, P) - \eta(\dot{\epsilon}_{ij}, P)]\dot{\epsilon}_{kk}\delta_{ij} - P\delta_{ij}/2 \qquad (7.15)$$

(Hibler, 1977), where η and ζ are nonlinear shear and bulk viscosities depending on pressure P and strain rate ϵ_{ij}. The pressure term is introduced because the yield curve is not centered at the origin of the principal axis plane. The pressure depends strongly on ice thickness (i.e., thicker ice resists convergence more strongly than does thinner ice) and ice concentration. The form Hibler chose is

$$P = P^* D \exp[-C(1 - A)] \qquad (7.16)$$

where P^* is called the ice strength. There is an order of magnitude difference between observations and numerical simulations for the value of P^*. The

constant C has some large value, such as 20, to produce a rapid decrease in viscosity for ice concentrations less than 85%. Comparison with drifting buoys shows that the model with a viscous–plastic stress law predicts the observed ice drift in the main Arctic basin rather well. However, it is to be expected that away from convergence regions the precise form of the stress law is probably unimportant.

As in the development of the viscous–plastic constitutive law, a considerable amount of empiricism is involved. This approach is taken even further by using the Reiner–Rivlin formulation, which is a generalization to variable-viscosity fluids as in Smith (1983) and Häkkinen (1987c). In the latter, the bulk and shear viscosities are chosen on empirical grounds in accordance with observations. This constitutive law includes plastic properties of ice without explicitly invoking the plastic deformation principles; e.g., the ice gives strong resistance to convergence but no resistance to divergence. This type of constitutive law has been further developed by Overland and Pease (1988), who applied it to coastal ice processes. They assumed the ice strength to depend quadratically, instead of linearly, on the ice thickness, which seemed to improve the results greatly.

C. Thermodynamic Ice Models

Sea ice occupies the Arctic basin year-round and consists of ice of varying ages, from frazil ice to multiyear ice. Correspondingly, the ice thickness distribution has a wide range, from a few centimeters to several meters. From field observations, the equilibrium ice thickness is estimated to be about 3 m in the Arctic. This is not due solely to thermodynamic effects; the ice transport out of the Arctic is a major contributor, as 7–10% of the ice cover is transported out through the Fram Strait annually (estimate based on the transport values given by Moritz, 1988). The Antarctic sea ice is quite different in nature; it is mainly seasonal with a maximum thickness of 1.5 m and an average of 0.5 m.

The prediction of sea ice growth and melt is complicated by the existence of snow cover, which is also thickest during the ice growth season. The ice accumulation in the Arctic is further affected by the salinity of the ice and the brine pockets left in the ice during accretion. The early attempts to describe the ice growth and melt merely developed empirical formulas based on observed surface temperatures. Although it was known that the surface fluxes and heat conduction are necessary elements of heat balance in the ice, it was not until the 1950s and 1960s, with better observational information on the variability in the surface fluxes and sea ice thickness, that this knowledge was put to use to predict seasonal sea ice growth in the Arctic (Untersteiner, 1961, 1964). In the following we concentrate on the thermody-

namics of ice based on the model of Maykut and Untersteiner (1969, 1971). This model contains all the important components affecting ice growth and melt, including snow cover. Most later thermodynamic ice models have been based on their formulation.

Maykut and Untersteiner (1969, 1971) (hereafter referred to as M & U) consider the snow–ice system shown in Fig. 7.3. which also shows all the relevant fluxes. Their equations apply to a horizontally uniform slab of ice and therefore are a function of only the vertical coordinate. The turbulent and radiative fluxes acting on the top surface of this snow–ice system are specified, as is the oceanic heat flux, which is the least known flux component, acting at the bottom of the ice. The heat input by the atmospheric and oceanic heat fluxes is transported in the snow and ice by conduction.

The surface heat balance components are the solar short-wave radiation modified by the surface reflectance or albedo α, $(1-\alpha)F_r$; the long-wave radiation from the atmosphere and clouds, F_d; and the outgoing long-wave radiation determined by the surface temperature, $F_u = \epsilon_L \sigma T_0^4$ (ϵ_L is the

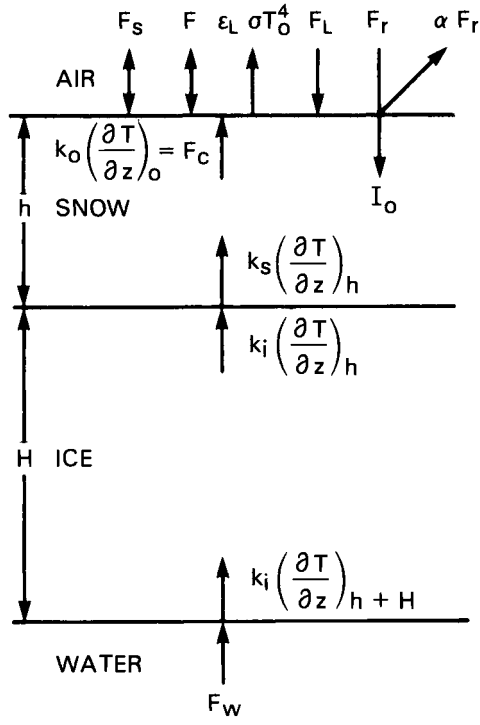

Figure 7.3 Fluxes at the different interfaces of a snow–ice–water system. Adapted from Maykut and Untersteiner (1971).

long-wave emissivity and σ is the Stefan–Boltzmann constant). Since the heat exchange occurs over a finite depth, an additional flux of absorbed solar radiation (I_0) is taken into account in the melting season. This energy is not available to melt the ice at the surface, but it is transformed into an internal heat source. The albedo of the snow–ice cover plays a very important role in the Arctic heat budget. Unfortunately, the value of the albedo is difficult to assess because it changes during seasons; in the late winter, with extensive snow cover, it is quite high (0.64–0.66), but with the progress of the melting season the snow cover disappears and melt ponds form, giving rise to a much lower albedo, as low as 0.45. Most of these melt ponds eventually drain into the ocean.

Another difficulty in solving the ice heat budget lies in determining the flux of absorbed solar radiation (I_0). This flux has a complex dependence on the physical characteristics of the incident radiation and of the snow–ice surface, but for modeling purposes M & U chose I_0 to be 17% of the net short-wave radiation at the surface (Fletcher, 1965). Inside the snow–ice cover the penetration of this energy is modeled by a simple exponential decay. The governing equation of the thermodynamics of the snow–ice system is the diffusion equation for the temperature (T) in the snow and ice layers:

$$(\rho c)_s \, \partial T/\partial t = K_s \, \partial^2 T/\partial z^2 + \kappa_s I_0 \exp(-\kappa_s z) \tag{7.17}$$

$$(\rho c)_i \, \partial T/\partial t = K_i \, \partial^2 T/\partial z^2 + \kappa_i I_0 \exp[-\kappa_i (z - h) - k_s h] \tag{7.18}$$

where ρ is the density, c the specific heat, κ the bulk extinction coefficient, K the thermal conductivity, and indices s and i refer to snow and ice, respectively. It is assumed that K_s and κ_s are constant, but in the ice the corresponding quantities can vary along with the ice density because of brine pockets trapped during ice accretion. Untersteiner (1961) introduced approximate formulas to describe the effects of the brine pockets on the density, specific heat, and conductivity of ice:

$$(\rho c)_i = (\rho c)_{i,f} + \gamma S(z)/(T - 273)^2 \tag{7.19}$$

$$K_i = K_{i,f} + \beta S(z)/(T - 273) \tag{7.20}$$

where the subscript f refers to the corresponding quantity for pure ice, $S(z)$ is salinity at depth z, and γ and β are specified constants. It should be noted that c_i and K_i increase considerably during the summer melt season, when heat can be stored in brine pockets left in the ice, thus increasing the thermal inertia of ice.

The boundary conditions can now be expressed by setting the heat flux to be continuous at different interfaces. At the surface of the snow or ice, if snow

cover has disappeared (thus a generic index 0), the condition is

$$K_0(\partial T/\partial z)_0 - I_0 = -(1-\alpha)F_r - F_d + F_u - F_s - F_l - Q_{ab} \quad (7.21)$$

where F_s and F_l are the sensible and latent heat fluxes and Q_{ab} is the heat required for ablation; Q_{ab} is zero if T_0 is below 273 K and otherwise is equal to the rate of ablation of the snow and ice thickness multiplied by the latent heat of fusion. At the two other interfaces the simple balance of fluxes is

$$K_s(\partial T/\partial z) = K_i(\partial T/\partial z)$$
evaluated at $z = h$ (snow–ice interface) (7.22)

$$K_i(\partial T/\partial z) = F_w + q\, d(h+H)/dt$$
evaluated at $z = h + H$ (ice–ocean interface) (7.23)

where F_w is the oceanic heat flux, and the last term can represent either accretion or ablation.

The simulation with this one-dimensional model of Maykut and Untersteiner (1971) was done using the monthly Arctic heat budget from Fletcher (1965), which consists of monthly averages of the turbulent heat flux and snowfall, incoming long-wave radiation and solar radiance, and the constant oceanic heat flux of 2 W/m^2. The outgoing long-wave radiation is specified from the predicted surface temperature. The albedo varies monthly and is lowest (0.64) for melting ice. This model was quite successful in predicting the equilibrium temperature and thickness of sea ice. The simulated seasonal cycle is shown in Fig. 7.4. The behavior of the isotherms in the ice is quite similar to the pattern observed at IGY station Alpha (Untersteiner, 1961) in that the maximum winter ice temperatures are more than or equal to -18°C, with the early autumn temperatures being about -0.5°C. The predicted equilibrium thickness is 288 cm (with a maximum of 314 cm and a minimum of 271 cm), which is difficult to assess observationally because of pressure ridges, but the result does compare favorably with results from IGY station Alpha. The main discrepancies of this model appear to be the too-warm early autumn temperatures (by 0.25 °C) and too little ice ablation. These differences could come from several sources: freezing of the melt ponds, underestimation of I_0, or uncertainties in the ice salinity profile. The overall agreement between the model results and the station Alpha observations may be fortuitous, because the M & U model does not include the effect of leads or the divergence due to ice transport through Fram Strait. Furthermore, the model simulation also shows that the snow–ice system is very sensitive to changes in the surface albedo; lowering the average albedo from 0.6 to 0.45 would result in rapid (on the order of a few years) vanishing of the pack ice in the Arctic.

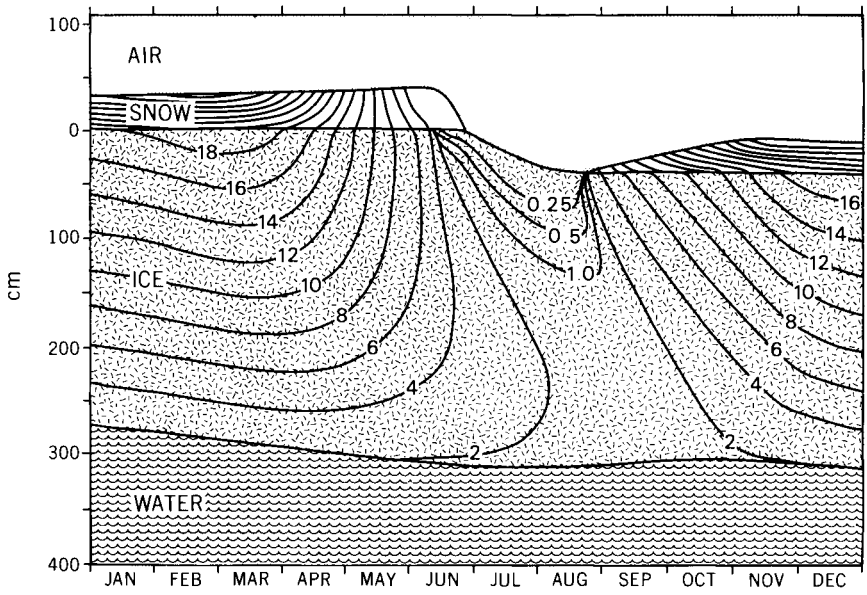

Figure 7.4 Equilibrium temperature and thickness for sea ice. Isotherms are labeled in negative degrees Celsius. From Maykut and Untersteiner (1971); copyright by American Geophysical Union.

The M & U model gives a fine-resolution (10-cm) temperature distribution as a function of the vertical coordinate in the snow and ice. To apply this model to large scales such as the entire Arctic basin is not presently feasible. A simplification was provided by Semtner (1976a), who replaced the M & U fine-resolution temperature profile with one with a cruder resolution. A schematic view of the layered system with one snow layer and two ice layers is shown in Fig. 7.5. Below the ice there is a 30-m-thick oceanic mixed layer which has a constant (most of the time) temperature of $-2\,^{\circ}\mathrm{C}$. The numerical solutions for the temperatures at the surface (T_s), in the snow (T_0), at the top of the ice layer (T_1), and at the center of the different ice layers (T_n, n ice layers) are derived in terms of the interfacial heat fluxes. The conductive flux $F = K\,\partial T/\partial z$ across each layer can be differentiated and expressed (the snow and total ice thicknesses are h_s and h_i, respectively) as follows.

At the interfaces inside the ice, for $\Delta z = h_i/n$.

$$F_k = K_i(T_{k-1} - T_k)/\Delta z, \qquad k = 1, \ldots, n-1 \tag{7.24}$$

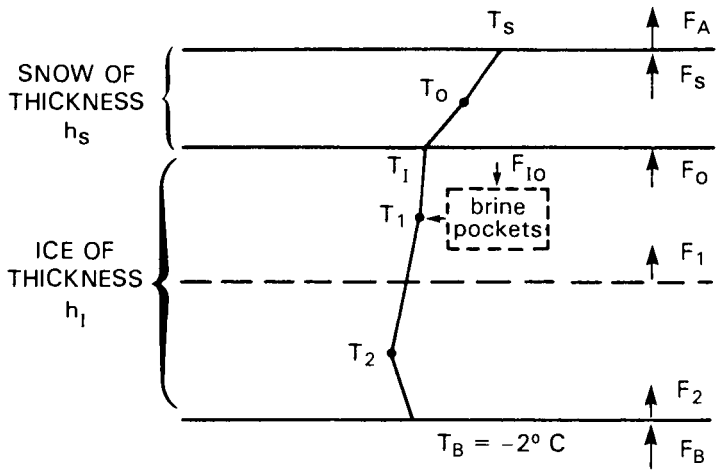

Figure 7.5 Three-layer snow–ice system adapted from Semtner (1976a).

At the bottom of the ice,

$$F_n - K_i(T_b - T_n)/0.5\,\Delta z, \qquad T_b = -2°C = \text{constant water temperature} \tag{7.25}$$

At the top of the snow,

$$F_s = K_s(T_0 - T_s)/0.5h_s = F_a \qquad \text{at the snow–ice interface} \tag{7.26}$$

$$F_0 = K_i(T_1 - T_i)/0.5\,\Delta z = K_s(T_i - T_0)/0.5h_s \tag{7.27}$$

Without any snow cover $T_s = T_i$, and the surface flux balance is

$$F_0 = K_i(T_1 - T_s)/0.5\,\Delta z = F_a - I_0 \tag{7.28}$$

The surface temperature T_s is solved from either Eq. (7.27) or Eq. (7.28), but these equations are fourth order in T_s due to the upward long-wave radiation. Fortunately, T_s can be expressed in terms of the previous (time step) surface temperature (T_p) plus a change in T, which facilitates the use of a Taylor series expansion to approximate T_s^4 at the new time step. With these fluxes the diffusion equation can be solved in each layer in case of full snow cover (no snow melt) and with ice accretion in the bottom:

In the snow:

$$\Delta T_0 = \Delta t(F_0 - F_a)/h_s(\rho c)_s \qquad (T_s < 0°C) \tag{7.29}$$

In the ice:

$$\Delta T_k = \Delta t(F_k - F_{k-1})/\Delta z(\rho c)_i, \qquad k = 1, \ldots, n \qquad (7.30)$$

For the more complicated boundary conditions the reader is referred to the original paper.

This model, like the previous model, is forced by specifying the monthly average turbulent heat flux and precipitation (snowfall), solar irradiance, and incoming long-wave radiation (Fletcher, 1965). Also, the albedos are taken to be the same as those in Maykut and Untersteiner (1971). The simulation of the snow and ice temperatures and ice thickness even with a coarse three-layer system (Fig. 7.6) appears to give excellent agreement with the M & U model. The maximum discrepancy in ice thickness is 22 cm, and most of the discrepancy occurs later in the melt season and in the beginning of the growth period, which reflects the fact that the three-layer system stores more heat in the brine pockets than does the M & U model. Whereas the M & U model simulation had to be terminated if the ice cover disappeared in response to a decrease in the albedo or to an increase in the oceanic heat flux, the Semtner model will produce multiyear cycles of the ice thickness. Seasonally modulated multiyear cycles result with the same seasonal forcing from year to year because of the different conductivities of snow and ice. Totally open water may also appear once during the cycle.

This Semtner model was used by Washington *et al.* (1976) to simulate the seasonal variability of the Arctic and Antarctic sea ice cover. However, there are some differences; the fluxes of sensible heat, latent heat, and incoming long-wave and solar radiation are calculated from atmospheric parameters instead of being specified. The model contains a snow layer and only one ice layer, below which there is a 30-m-thick mixed layer. A uniform heat flux is assumed inside snow and ice, implying immediate adjustment of the temperature field to the external forcing; i.e., the surface, snow, and ice temperatures are calculated directly from flux balances as in Semtner (1976a). Resulting ice thickness distributions for the Arctic and Antarctic are shown in Fig. 7.7 (Washington *et al.*, 1976). The zero-ice-thickness line representing the ice extent correlates reasonably with the observed one in the Arctic, although the Greenland–Barents Sea ice cover has some serious problems because of the absence of advection of the warm Atlantic waters to the north.

The Antarctic simulation suffers from excessive ice production everywhere around the continent (Fig. 7.7). The model results did improve considerably with the use of an oceanic heat flux that was six times larger and the inclusion of an additional variable representing open leads, so that excess heat in the leads was used to melt ice laterally and not to decrease ice thickness. Besides the expected sensitivity to the oceanic heat flux, the findings on the effect of albedo and cloudiness agree with those of the previous

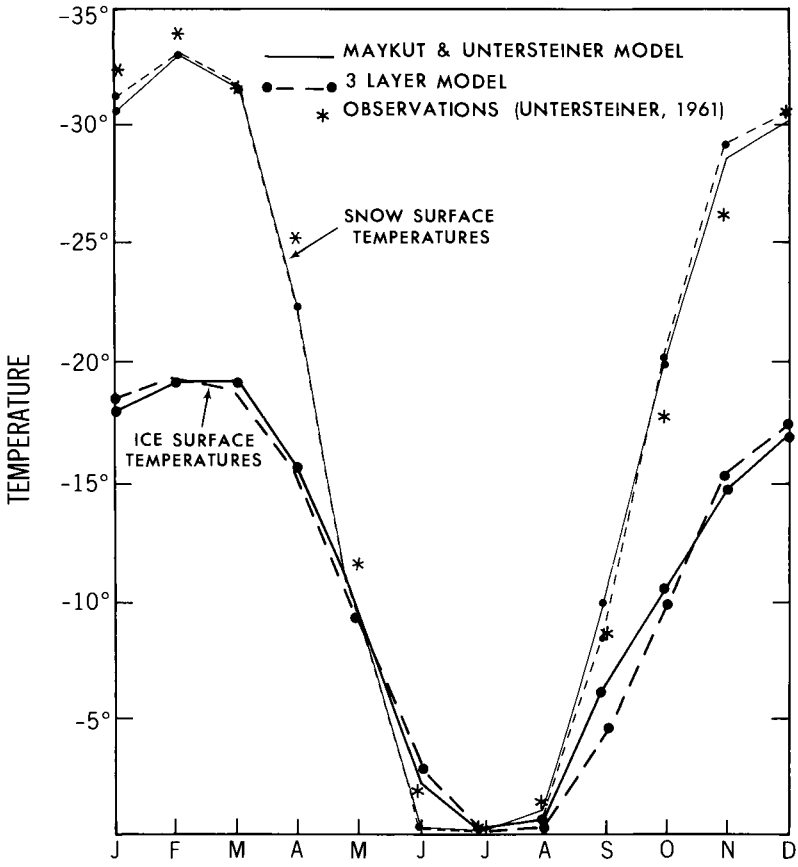

Figure 7.6 Temperatures at the snow surface and the ice surface, as predicted by a three-layer model (dashed lines) and by Maykut and Untersteiner model (solid lines). From Semtner (1976a); copyright by American Meteorological Society.

two 1-dimensional models. As their major conclusion, Washington *et al.* state that thermodynamics alone is capable of simulating the main features of the ice distribution in the polar regions.

The models discussed above and a model by Welander (1977) are used to study the ice growth and melt considering only the ice thickness variation. This point of view is convenient when the focus is on climate change. However, when studying the marginal ice zones (MIZs), in which the pack ice changes to open ocean, the assumption of predominantly vertical ice melt/growth (in ice thickness) is not well founded because of the less compact ice cover. Because of the large amounts of open water surrounding the ice floes,

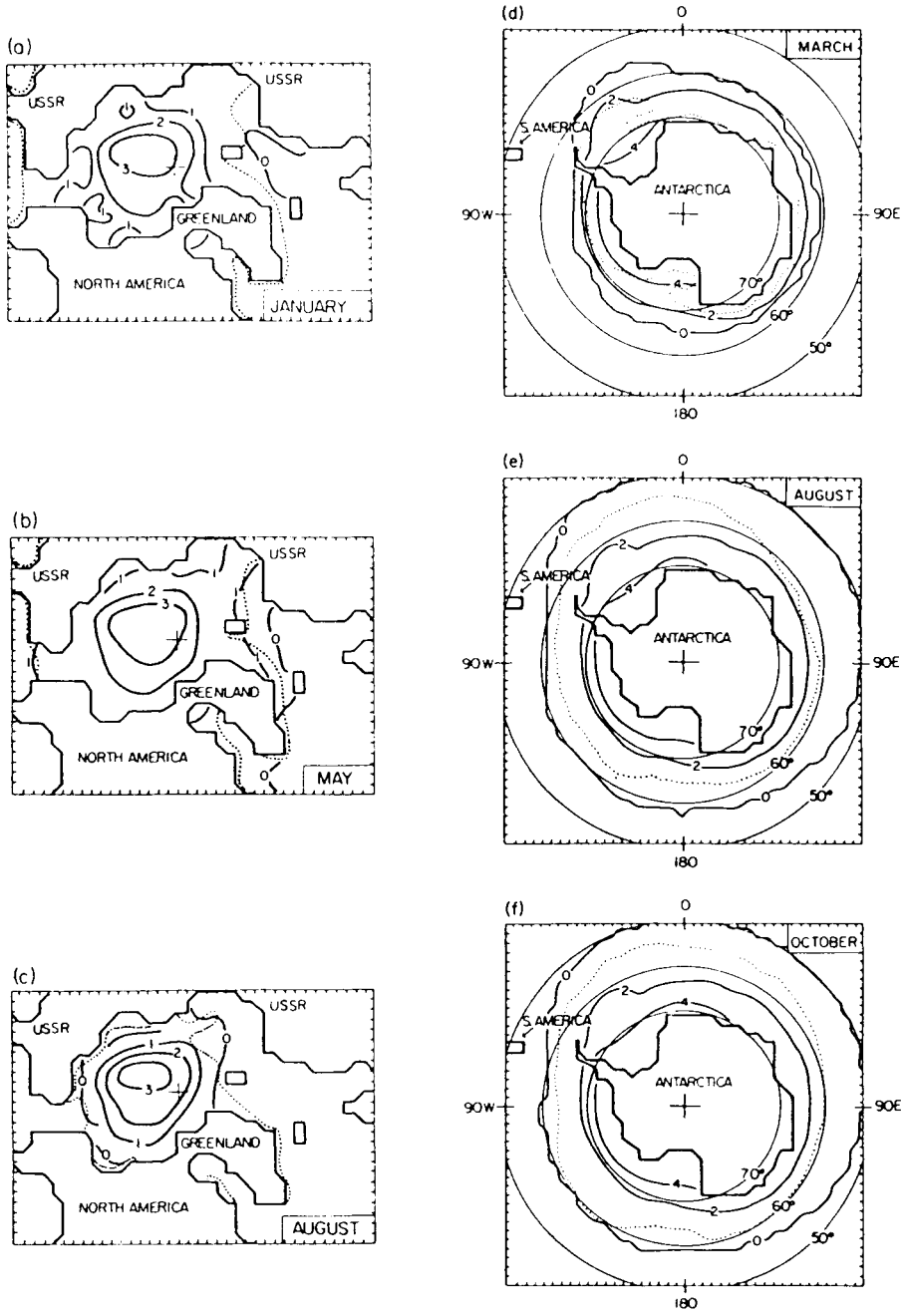

Figure 7.7 Computed (solid lines) and observed (dashed lines) Arctic and Antarctic ice thickness (meters) and limits for various months. From Washington *et al.* (1976); copyright by American Meteorological Society.

the absorption of short-wave radiation is enhanced, and warming of the mixed layer will effectively contribute to lateral ice melt. Røed (1984) proposed a model appropriate for the MIZ, in which the ice can be produced or melted only in the lateral direction. This model predicts ice concentration and mixed-layer temperature. The driving force is imposed through the temperature difference between the deep water and the atmosphere [Fig. 7.8a; adapted from Røed (1984)], and the mixed-layer thickness is a parameter in the model. Using the notation for different fluxes as in Fig. 7.5, the equations predicting the mixed-layer temperature (T) and ice concentration (A) are

$$\rho c_p h \, dT/dt = A(F_w - F_{wi}) + (1 - A)(F_w - F_{wa}) \tag{7.31}$$

$$Q_i D_0 \, dA/dt = A(F_{ai} - F_{wi}) + (1 - A)(F_{aw} - F_{wa}) \tag{7.32}$$

(Røed, 1984), where changes in the mixed layer and ice heat content are determined by the imbalance of the interfacial fluxes [fluxes are multiplied by A in ice-covered regions and by $(1 - A)$ in ice-free areas], Q_i is the heat of fusion for sea ice, and D_0 is a constant ice thickness. The fluxes are parametrized using a transfer coefficient multiplying the interfacial temperature differences. The model needs three different heat transfer coefficients, one each for the atmosphere, ice, and water. These coefficients are bulk parameters which may not represent actual turbulent fluxes realistically, but they allow the evaluation of various feedbacks between the air, ice, and ocean in a systematic way. The results of this model identify three different regimes, of which two have an ice-free steady state and one has an ice cover with an ice concentration less than 100%, as shown in Fig. 7.8b. The time scales of freezing and melting are 2 and 6.5 days, respectively, but these values depend solely on the heat transfer coefficients used. An essential conclusion of this work is that the thermodynamic effects and dynamics occur on the same time scales and hence interact strongly.

D. Dynamic–Thermodynamic Ice Models

After the fundamental dynamic and thermodynamic models had been laid out, it was time to investigate how the seasonal and interannual ice drift, concentration, and thickness fields in the polar oceans change when the thermodynamic effects are allowed to interact with the ice dynamics. Parkinson and Washington (1979) extended the model of Washington *et al.* (1976) to include ice dynamics. Their model contains four layers (ice, snow, ocean, and atmosphere), of which only ice is dynamically active. The ocean is assigned a constant dynamic topography, i.e., sea surface tilt, and geostrophic currents, which are used in the ice–ocean interfacial stress. The continuity equations in the form of Eqs. (7.3) and (7.4) are not used, but

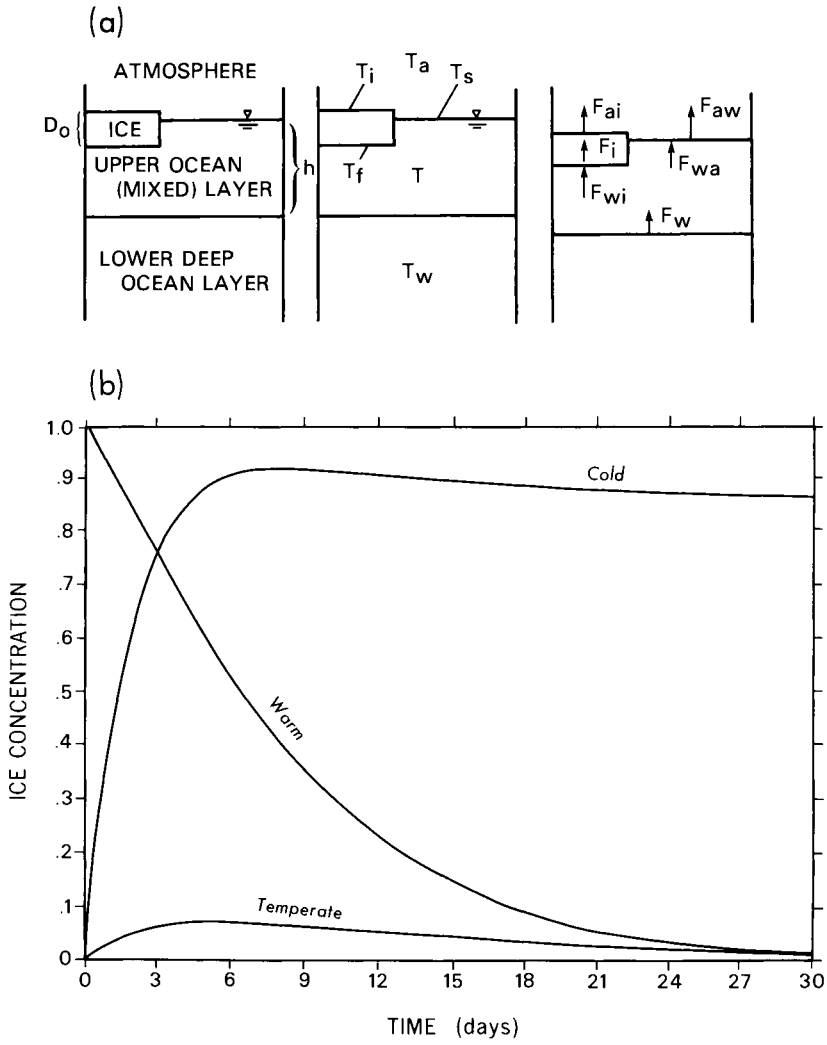

Figure 7.8 (a) Schematic view of the ice–ocean system used by Røed (1984). (b) Evolution of the ice concentration toward a steady state for different temperature regimes. From Røed (1984); copyright by American Meteorological Society.

merely a simple advection of ice volume and areal coverage is applied. The dynamic and thermal forcings are determined by atmospheric parameters given by climatological monthly means and by a specified oceanic heat flux as in Washington *et al.* (1976). The temperature of the slab ocean is deter-

mined from the net fluxes at the surface, so that if the ocean temperature is at the freezing point, the excess heat loss is converted to ice growth. The model results are not too different from the ones shown in Fig. 7.7. Maximum ice thickness still occurs in the center of the Arctic basin. In the Antarctic the ice thickness is similar, but the maximum has decreased from 2 m to 1.2 m due to a larger oceanic heat flux (25 W m^{-2}). The model predicts a uniform ice cover with 97% concentration during winter in the Arctic. During the austral winter the model produces several areas of lower ice concentration (90%) within a solid pack ice which as an ice concentration of 97%.

Hibler studied the Arctic ice cover with his dynamic–thermodynamic models (Hibler, 1979, 1980, 1985; Hibler and Walsh, 1982). The dynamics of these models includes the viscous–plastic stress law. Snow cover is not included. Thermodynamics is introduced in the ice system by addition of source and sink terms on the right-hand side of the continuity equations, Eqs. (7.3) and (7.4), to take into account ice melt and growth. These source terms are expressed as

$$\begin{aligned}
&\mathrm{SD} = Af(h_i) + (1-A)f(0), && h_i = D/A && \text{[in Eq. (7.4)]} && (7.33)\\
&\mathrm{SA} = (1-A)f(0)/h_0 && \text{if } f(0) > 0 \text{ (freezing)} && \text{[in Eq. (7.3)]} && (7.34)\\
&\quad = 0 && f(0) < 0 &&&&\\
&\quad = 0 && \mathrm{SD} > 0 &&&&\\
&\quad = \mathrm{SD}/2h_i && \mathrm{SD} < 0 \text{ (melting)} &&&&
\end{aligned}$$

where D and h_i are an average and a "true" ice thickness, respectively, f is the growth/melt rate of ice of thickness h_i with minimum ice thickness h_0 (= 0.5 m). The function f was given by the seasonal ice growth/melt estimates of Thorndike *et al.* (1975), which are for the central Arctic basin (Hibler, 1979). In the later papers the growth rate f is calculated using Semtner's model with a motionless oceanic mixed layer. An additional mechanical source term for the mean thickness results from limiting A to be less than 1.

The results from this and a thermodynamics-only model forced by atmospheric data for 1973–1975 (Hibler and Walsh, 1982) are shown in Fig. 7.9. The input data are daily instead of monthly means as in Parkinson and Washington (1979). Figure 7.9 shows a clear distinction between a purely thermodynamically driven model and a one coupled with dynamics. First, the high ice thicknesses created in the center of the gyre are forced to drift toward Fram Strait with the Transpolar Drift Stream. The highest thicknesses are found north of Greenland, where the ice is pushed toward the coast, which is also observed in submarine data (Hibler, 1979). Even though the agreement with observations is relatively good in most areas, the northern Atlantic simulation is inaccurate and predicts too much ice. This is due to thermodynamics related to the warm Atlantic water inflow, which is not

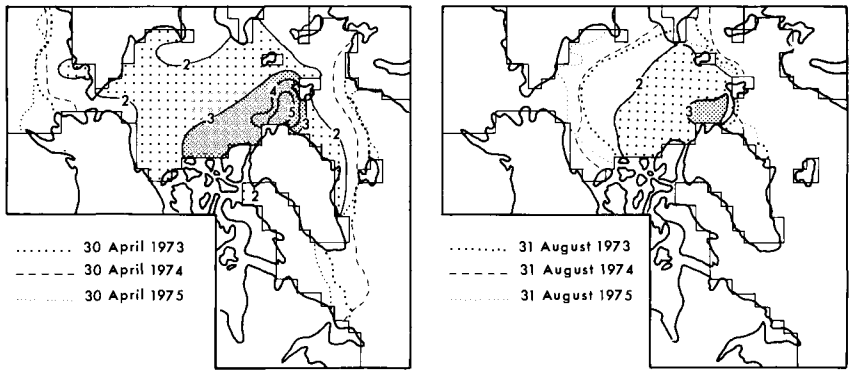

(a) SIMULATED (dynamic & thermodynamic)

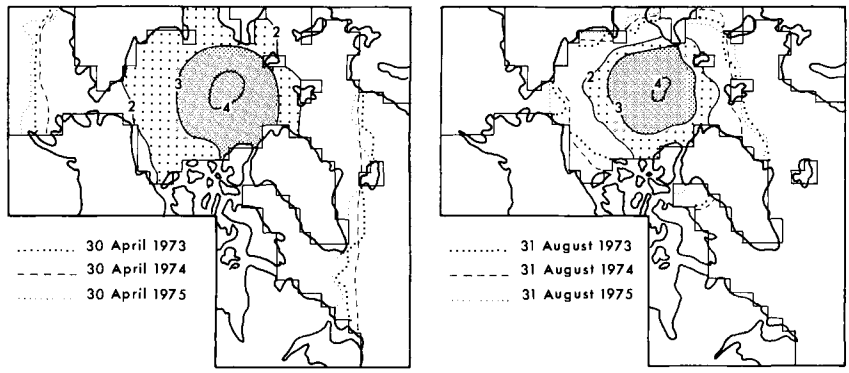

(b) SIMULATED (thermodynamic only)

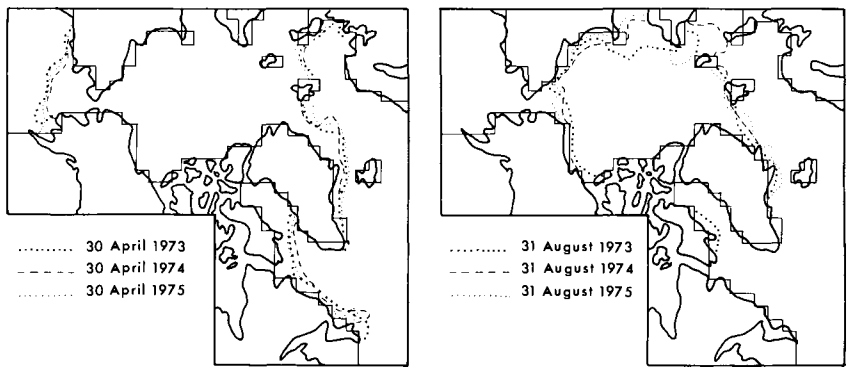

(c) OBSERVED

Figure 7.9 Positions of simulated (a and b) and observed (c) ice edge at the end of April and August, 1973–1975. Contours of ice thickness in (a) and (b) are in meters. From Hibler and Walsh (1982); copyright by American Meteorological Society.

included in the model. In the Beaufort Sea the summer melt is too strong compared with observations, which the authors attribute to neglecting snow cover. Snow cover would delay the onset of the summer melt by reflecting more of the solar energy.

An interesting case study was performed by Parkinson (1983), who investigated the development of the Weddell Polynya. This polynya has been seen in passive-microwave imagery (Zwally and Gloersen, 1977; Carsey, 1980; Comiso and Gordon, 1987) during 1974–1976. Again, the input meteorological data are monthly means which are interpolated to the model time steps. The oceanic heat flux is constant spatially, the "standard" case using 25 W m^{-2}. The "standard" calculation results are shown in Fig. 7.10. The polynya forms at about the right time and place and is considered to be a direct response to the wind field and heat flux determined by the wind field. Low wind speeds in the center of a low-pressure system slow down ice production by reducing heat flux. The reduction in ice production is necessary to form areas of low ice concentration because the wind-driven advection is weak in removing ice over a distance of 1000 km.

Hibler and Ackley (1983) have simulated the Weddell Sea pack ice. Using daily atmospheric data from 1979, they conclude that the advance of the ice pack is driven mainly by thermodynamics, whereas the retreat and decay depends mostly on lead generation and ice advection. The rapid decay is due to warming of the mixed layer by absorption of solar radiation in the leads. They also predict the presence of substantial amounts of open water in winter.

A long-term simulation of the Arctic ice cover has been performed by Walsh *et al.* (1985) for the period 1951–1980. This simulation uses Hibler's dynamic–thermodynamic ice model (1979, 1980) with the explicit inclusion of snow cover, which can accumulate according to prescribed rates (Maykut and Untersteiner, 1971). The forcing of this model includes geostrophic winds calculated daily using a sea level pressure data set from the National Center for Atmospheric Research (NCAR) together with a daily air temperature data set, generated from monthly climatological air temperatures modulated by monthly air temperature anomalies (e.g., Hansen *et al.*, 1983).

The simulation shows considerable variation in the ice thickness and concentration as well as in the ice drift on seasonal and interannual scales. The outflow of ice through Fram Strait is mainly wind driven in the model, the climatological ocean currents providing a small contribution to the ice drift. The simulated outflow of ice varies by a factor of 2 to 3 in successive years. Although there is strong interannual variability in subsections of the Arctic in ice thickness and concentration, the total simulated ice mass has only a weak interannual variability and shows no trends (Fig. 7.11). The total ice mass varies seasonally by a factor of 2. The study also points out that the

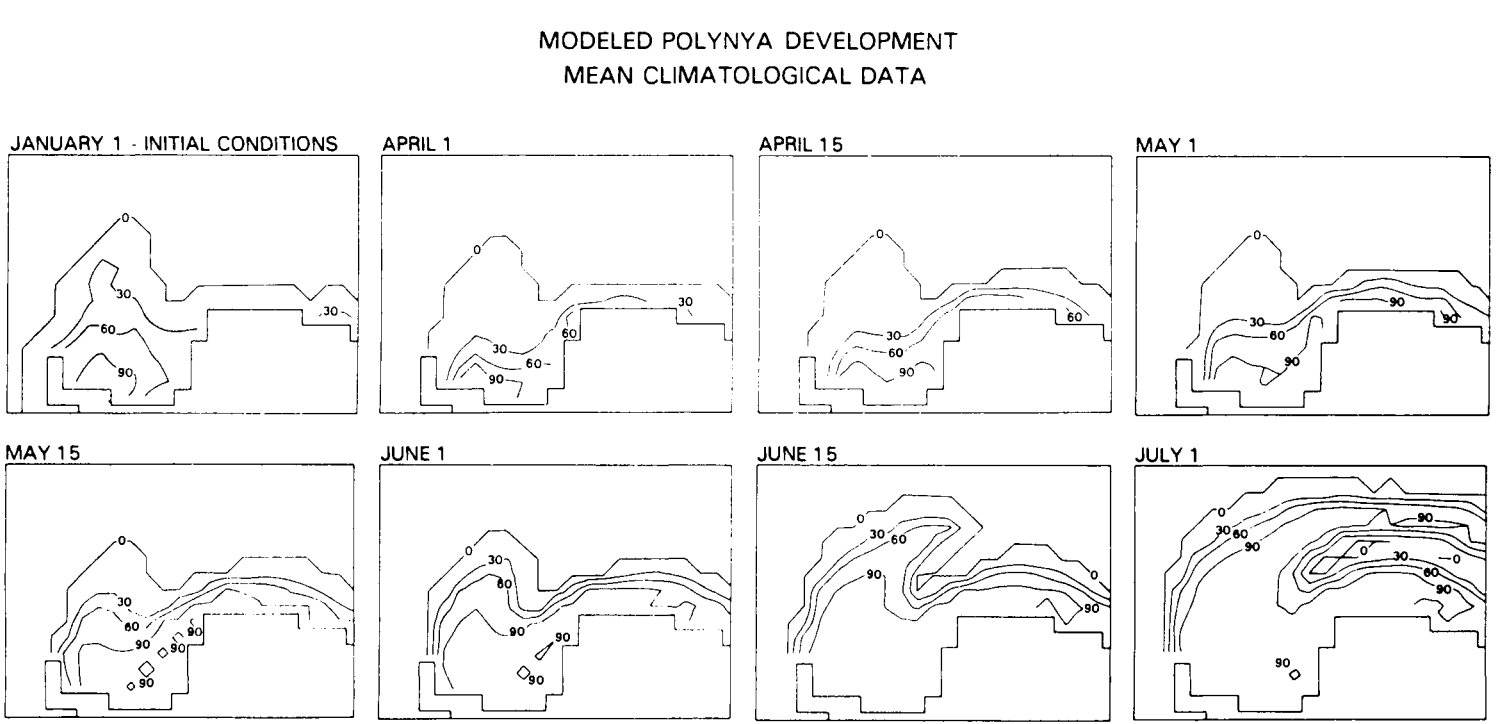

Figure 7.10 Development of the simulated Weddell Polynya. Contours of the ice concentrations are percentages. From Parkinson (1983); copyright by American Meteorological Society.

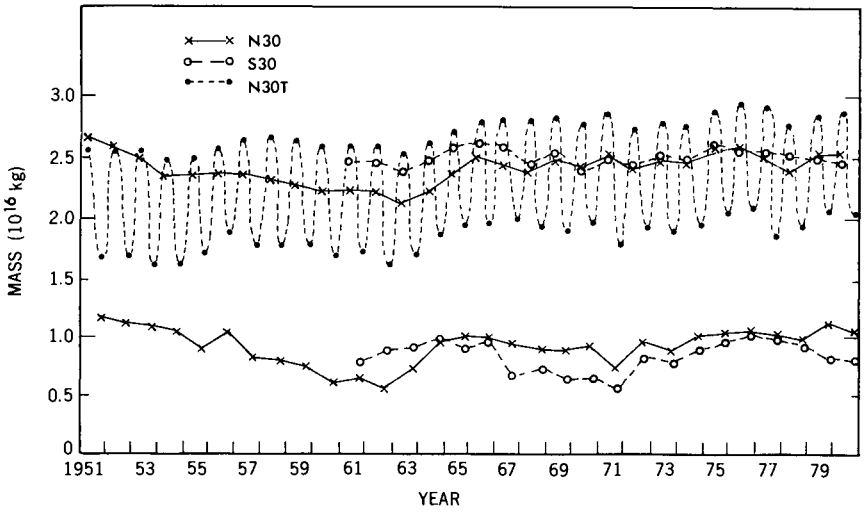

Figure 7.11 Time series of the simulated total ice mass. Simulation denoted by N30 uses a full dynamic–thermodynamic model forced by air temperature data given by Hansen *et al.* (1983); only annual maxima and minima are shown. N30T gives the seasonal cycle simulated by a thermodynamics-only model. From Walsh *et al.* (1985); copyright by American Geophysical Union.

normal seasonal cycle is basically determined by thermodynamics, but ice thickness anomalies, which occur nearly everywhere in the Arctic, are caused by dynamical processes during the cooling season. Changes in the surface heat fluxes driving thermodynamic anomalies influence mostly the ice margins during melting periods.

II. Ocean Models

A. Introduction

The Arctic Ocean is a complex system in which inflows of the Atlantic and Pacific waters, outflow of the Arctic surface water, river runoff, ice growth and melt on the shelves accompanied by salt flux, and surface momentum and heat budget form a delicate balance. Changes in this balance affect the thermohaline circulation of the world oceans. The stratification in the Arctic is weak but stable due to a strong halocline, below which there is a maximum in the temperature profile at around 500 m, signaling the warm Atlantic water at mid-depth.

Polar ocean modeling efforts have been aimed at a diversity of problems, ranging from general circulation (Galt's barotropic ocean model, 1973) and

the maintenance of the Arctic halocline at large scales (Semtner, 1976b) to such smaller-scale ("mesoscale") processes as deep water production through cabbeling (Foster, 1972a), mixing on the continental slopes around the Antarctic (Killworth, 1974, 1977), and haline convection initiated by freezing in the leads (Foster, 1972b). All of these studies have considered only the oceanic effects, and the existence of ice is simply taken into account through surface forcing, i.e., through the momentum, heat, and salt fluxes.

B. Large-Scale Ocean Circulation Models

The stratification at high latitudes is quite weak compared with that in the rest of the world's oceans, and therefore one expects the barotropic circulation to be strong. Barotropic flow is also influenced strongly by bottom topography; conservation of potential vorticity forces the flow to follow f/H contours. Furthermore, at high latitudes the β effect is neglibible, but the strong topographic variations can replace the planetary waveguide with a topographic waveguide. This is demonstrated in Galt's (1973) barotropic ocean model for the Arctic. The model forcing consists of surface stress predicted from Campbell's (1965) ice model using mean annual winds. Also inflows and outflows through boundaries are specified at several locations, of which Fram Strait is the most important. The simulations by Galt (1973) show that the location of the Beaufort Gyre and the intense currents along the Alaskan coast in the Beaufort Gyre are due to a topographic β effect: the topographic Rossby waves are responsible for developing and maintaining the current pattern. The Lomonosov Ridge, by acting as a waveguide to the Rossby waves, in turn limits the Beaufort Gyre to the Canadian basin. Whereas the circulation in the Canadian basin is mainly wind driven, the inflow–outflow forcing dominates wind effects in the Eurasian basin. Galt showed that, in order to achieve a realistic flow pattern, a reduction of the variability of the bathymetry was necessary. This reduction simulates the effects of baroclinicity which tend to reduce topographic influence on the flow.

The Arctic Ocean has a strong halocline, which is much shallower than the thermocline. Obviously, the consideration of halocline maintenance in the Arctic must include the whole ocean, in which the different components of the forcing are distributed. As an example, all around the periphery of the Arctic Ocean strong seasonal ice growth takes place, filling the shelves with cold and very saline water, which may descend to deeper parts of the ocean basin. Most of the river runoff is distributed around the Siberian coast, and the extent to which this river runoff counteracts the freezing effects is unclear.

To tackle the complex problem of Arctic Ocean dynamics and thermodynamics, Semtner (1976b) used a multilevel general circulation model, with 14 vertical levels and 110-km grid resolution. The governing equations for the model—the horizontal and vertical momentum equations [Eqs. (7.35) and (7.36)], continuity equation [Eq. (7.37)], equation for salt and heat [Eq. 7.38)], and equation of state [Eq. 7.39)]—are

$$\frac{\partial v}{\partial t} + v\,\nabla_h v + w\frac{\partial v}{\partial z} + f(k \times v) = -\nabla_h \frac{p}{\rho_0} + K\frac{\partial^2 v}{\partial z^2} + A_m\,\nabla_h^2 v \quad (7.35)$$

$$\partial p/\partial z = -\rho g \qquad \text{(inertial and viscous terms neglected)} \quad (7.36)$$

$$\nabla_h v + \partial w/\partial z = 0 \quad (7.37)$$

$$\frac{\partial(T, S)}{\partial z} + v\,\nabla_h(T, S) + w\frac{\partial(T, S)}{\partial z} = K\frac{\partial^2(T, S)}{\partial z^2} + A_h\,\nabla_h^2(T, S) \quad (7.38)$$

$$\rho = \rho(T, S, z) \quad (7.39)$$

where v, w, T, S, and ρ are horizontal velocity, vertical velocity, pressure temperature, salinity, and density, respectively. If the stratification becomes unstable, convective adjustment is employed to a level at which stratification becomes stable. The uniform temperature of the convective column is determined from conservation of heat. The model also contains bathymetry resolving the Lomonosov Ridge, which separates the Arctic Ocean into the Canadian and Eurasian basins. The wind stress is computed from the geostrophic velocities based on mean annual atmospheric pressure using a rather high drag coefficient, which is assumed to be a compromise between fully ice-covered ocean and open-ocean values. The thermal boundary conditions are chosen to obey flux conditions such that a large negative heat flux (80 W m^{-2}) is assigned to ice-free areas and a small value (2 W m^{-2}), as in Untersteiner and Maykut (1971), is assigned to areas with surface temperature less than -2°C (ice-covered region). Inflows of the Atlantic and Pacific waters are included, as well as the river runoff.

Semtner (1976b) studied several cases in which many of the observed features of the Arctic Ocean circulation were simulated fairly successfully. These model simulations primarily were aimed at studying the equilibrium fields, which were achieved in 15 years for the salinity and in 40 years for the temperature. He focused on three case studies with different wind stresses, of which case I has the strongest stress. Figure 7.12 shows the simulated surface currents at the 20-m level in terms of the dynamic pressure field in the three cases. All three cases are similar in that they contain a closed Beaufort Gyre circulation and a Transpolar Drift Stream. The most realistic current pattern of case I has velocities that are 50% too large. Because of the model's sensitiv-

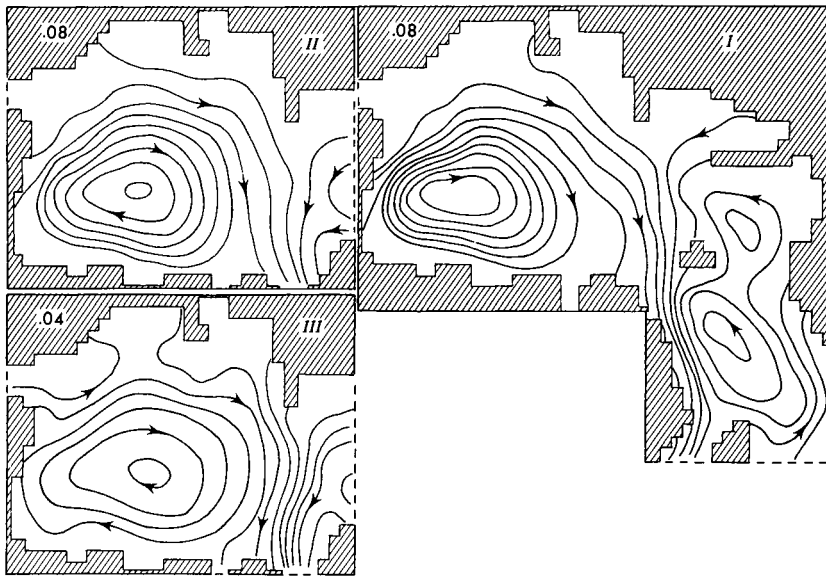

Figure 7.12 Predicted pressure fields at 20 m from the 14-level Arctic Ocean model. Contour interval in dynamic meters is shown at the top of the figure in each case. From Semtner (1976b); copyright by American Meteorological Society.

ity to horizontal viscosity, the horizontal currents and salinity and temperature fields are out of phase, compared to observations, with changing wind stress: Either the current field is reasonable and salinity and temperature fields are less realistic, or vice versa. In the case where the currents are too weak, the salinity profile displays a realistic halocline in the upper water column and the temperature profile has a maximum at 500 m. In general, the vertical advection (wind stress curl) dominates the salt balance in the center of the Canadian basin and thus determines the halocline depth. The lateral salinity field shows the major observed features, such as the low-salinity regions due to river runoff around the Siberian coast and in the Mackenzie River delta. Since the model is forced with annual mean fluxes, it cannot show the influence of the seasonal ice cover variation and the resulting salt flux.

C. Process Studies

Before coupled ice–ocean models are discussed, several process studies focusing solely on high-latitude oceanic phenomena will be reviewed. These processes are driven by winds and/or surface buoyancy fluxes, especially the

salinity component of buoyancy flux mimicking the salt flux during ice formation, or by instabilities due to an unstable vertical distribution of temperature or salinity or both (while the initial stratification is stable).

Foster (1972a) studied cabbeling instability as applicable to the Southern Ocean conditions. Cabbeling is defined as a nonlinear mixing process in which the parent constituents have different temperatures and salinities but nearly same density, leading to an end product with higher density. Foster studied a two-layer system in which a cold surface layer lies on top of more saline, warmer deep water. The problem involves solving u- and (full) w-momentum equations [Eqs. (7.35) and (7.36)] and the conduction and salt diffusion equations [Eq. (7.38)] and continuity equation [Eq. (7.37)] together with the nonlinear equation of state

$$\rho = \rho_0(1 - \alpha T - \beta T^2 + \gamma S) \tag{7.40}$$

in x–z space using Fourier transforms. Since the study is concerned with only spontaneous instabilities, there is no forcing at the top or bottom surfaces; i.e., there are no tangential stresses and no heat or salt fluxes across the boundaries. This two-layer system evolves by forming a higher-density layer at the interface of the two original layers. When this new layer becomes thick enough, convection will start and extend to the bottom below the stable upper layer. Convection is expected to be limited by the rate of mixing at the interface. The study considers only turbulent mixing as an initiator for cabbeling. The effects of molecular diffusivity have been neglected, and therefore cabbeling is likely to be delayed due to the slow molecular diffusion.

Killworth (1973) studied bottom-water formation around Antarctica using a two-dimensional channel with sloping sidewalls to describe the dynamics involved, i.e., basically the up- or downwelling along the continental slope. The main assumption of the model is that the dense water forms on the shelf; thus one has to find the processes responsible for driving this water mass into the deep ocean. The surface forcing contains a wind stress and buoyancy flux due to ice formation at a rate of 2 m/year. The results show that a fluid parcel, which has a southward component (with easterly winds), becomes heavier when traveling across the channel and being exposed to the surface salinity flux. Eventually, the water mass entering the southern wall has to sink, but to remove the dense water from the shelf slope the winds must be strong enough to give rise to advection that can force the density surfaces to tilt. This means that the wind forcing has to overcome convection in the southern portion of channel, which is continuously driven by the salt flux. A quantitative analysis shows that to reproduce the observed rate of Antarctic bottom-water production, one has to assume that the entire coast of the Antarctic participates in the production.

To understand the observed gradients in the salinity along the Weddell Sea and Ross Sea shelves, Killworth (1974) constructed a two-dimensional, two-level model. In this study the barotropic flow is neglected, which allows considerable simplification in solving the two-level baroclinic system; without any topography the vertically averaged transport has to vanish. The Weddell Sea is assumed to be a square box attached to a channel ("the circumpolar current region") with cyclic boundary conditions. The model is forced only by brine formation, which decreases northward and is zero in the channel region.

The gradient in the surface salt flux gives rise to the most saline water mass in the southern portion of the "Weddell Sea" and induces by geostrophy an eastward flow in the upper layer, compensated by a westward flow in the lower level. By continuity there must be downwelling on the eastern side and upwelling on the western side of the basin, which leads to an east–west density gradient. The densest water mass is generated at the southern portion and moves northward along the coast in the lower level. To set up the system of boundary fluxes by diffusive effects took about 30 model years, but still, after the long adjustment time, the model predicted too small northward fluxes compared with observed values. This discrepancy may be related to the surface buoyancy flux, which was chosen to be constant in the east–west direction. Strong salt fluxes (more ice production) nearer the western boundary could reduce the discrepancy.

These two models of Killworth show the bottom water forming from one parent water mass which is modified with surface salt flux, but observations show that the bottom water must be a mixture of at least two water masses in the region. Also, if the surface wind forcing is not as strong as depicted in Killworth (1973), it will be extremely difficult to make the dense water sink down the slope, because by geostrophy it is confined to move along the shelf. Only frictional forces (formation of bottom boundary layer) can allow the salty shelf water to sink along the slope, but this may well be too slow to account for the bottom-water formation rates, as shown by Killworth (1977) using plume models containing turbulent entrainment of surrounding waters. Killworth suggested the inclusion of pressure-dependent coefficients in the nonlinear equation of state, which will provide internal energy for the plume by giving increasing buoyancy force for a sinking and sufficiently cold fluid parcel.

III. Coupled Ice–Ocean Models

A. Introduction

Earlier modeling efforts to predict the large-scale sea ice edge in the Greenland and Barents seas failed to produce realistic results; thus it became

obvious in subsequent efforts to use an ocean model which included not only dynamics but also thermodynamics. Major improvements in this respect have been provided by Hibler and Bryan (1984, 1987) and Semtner (1987), who have constructed large-scale ice–ocean models focusing on the seasonal behavior of the Arctic ice cover and circulation.

The Greenland Sea ice margin may, for most part, be determined by large-scale dynamics, but it is actually a region with energetic mesoscale variability, e.g., where the ice edge meanders and moves over several tens of kilometers within a few days. Beginning at the end of the 1970s, increased interest in the marginal ice zones of the Greenland and Bering seas prompted the development of a number of models investigating wind-driven ice edge phenomena such as upwelling, eddies, and fronts. These mesoscale phenomena are important for mixing and water mass formation as well as for increased productivity at the ice edge (see Chapters 5 and 9).

The first attempts to model ice edge upwelling assumed a barotropic ocean (Gammelsrød *et al.*, 1975), a continuous stratified ocean (analytic model of Clarke, 1978), and a multilevel ocean (Niebauer, 1981) with ice cover as a simple boundary condition. The models that included stratification predicted upwelling similar to coastal upwelling (ice on the left from the wind direction), with an effective scale of twice the Rossby radius of deformation. Including a dynamic ice medium in the ocean models changes some of these results, as discussed in Section III,B.

B. Large-Scale Fully Coupled Ice–Ocean Models

The first large-scale fully coupled ice–ocean model, by Hibler and Bryan (1984, 1987), combines the previously discussed fully dynamic–thermodynamic ice model of Hibler (1979) and the Bryan–Cox multilevel (14-level) ocean model (Bryan, 1969). The ice model provides both dynamic forcing through surface stress and thermodynamic forcing through salt and heat fluxes to the ocean model. The input data of the model consist of the geostrophic wind field derived from the First Global GARP (Global Atmospheric Research Program) Experiment (FGGE) (in 1979) daily varying sea level pressures, monthly climatological air temperatures and humidities, and a radiation budget as discussed in Hibler (1980). Also, seasonally varying river runoff was specified at the boundaries, so that the annual mean runoff is the same as that in Semtner (1976b). Climatological salinity and temperature data were used to force (weakly) the ocean model so that the long-term model climatology relaxes toward observed values. The daily varying surface forcing, either directly by the atmosphere or through the ice–ocean interaction, has a considerable influence on the upper-ocean behavior.

This study provides two main results. First, oceanic currents greatly increase the ice drift in the East Greenland Current, accounting for about 50%

of the total drift rate. Second, the ice margin is simulated well in the Greenland and Barents seas, when compared with the observed average ice edge location (Fig. 7.13). The heat flux from the deeper ocean to the mixed layer (convection) prevents ice formation there even in midwinter. The model shows that the Barents Sea ice edge is very sensitive to the advection of heat and salt, because meltwater tends to limit mixing in the upper ocean by increasing stratification. This allows the mixed layer to cool rapidly and thus advance the ice edge. Some of the discrepancy between the full model prediction and the observed ice edge has been attributed to the use of the FGGE winds, which do not represent climatological mean winds.

The study by Semtner (1987) is somewhat similar to the previous one, with a multilevel ocean model coupled to an ice model. The essential difference is that the relaxation of the oceanic temperature and salinity is removed, allowing interannual/climatological simulations in which the oce-

Figure 7.13 Simulated and observed 50% concentration limits for the coupled ice-ocean model and ice-only model. The observed limits are given at end of the month from U.S. Navy Fleet Weather charts. From Hibler and Bryan (1987); copyright by American Meteorological Society.

anic state can be very different from the present state. Also, Semtner applies simplified ice dynamics by using a bulk viscosity as the only internal sink for ice energy. The thermodynamics of the ice is described by his three-level model of snow-covered ice, as discussed earlier (Semtner, 1976a). The forcing of the model is provided by the 30-year mean monthly values for winds, air temperature, and humidity as in Walsh *et al.* (1985). Besides specified river runoff, the mass fluxes through the Bering Strait and Faroe–Shetland channel are included in the model.

After 20 years of simulation, the model reaches a quasi-equilibrium with an ice margin and ice thickness distribution similar to that of Hibler and Bryan; the simulated ice thickness distribution is shown in Fig. 7.14a. But the most noticeable feature in these results is that the ice thickness is nearly half of the observed value, even though in a one-dimensional case the same ice model predicted a very realistic value for the equilibrium ice thickness. The important difference in this simulation is the ice transport and divergence of the ice field, which gives rise to open water and new thin-ice production in winter. The observed percentage of thin (less than 1 m) ice in the Arctic is about 20–25% (Bourke and Garrett, 1987). The error in estimating the conductive flux through thin ice when using average ice quantities can be nearly 100%, as shown later by the simulations of Mellor and Kantha (1989).

Returning to the Semtner results, Fig. 7.14b shows the ice growth values for January. The major ice growth areas are in the coastal shelves around the Arctic and give rise to increased salinities at the coast with respect to the central basin, where salinities remain at nearly their summer values. In contrast, even in winter the Greenland Sea ice edge is controlled by ice melt by the heat from the deep ocean via convection. Furthermore, this oceanic heat flux also governs the minimum ice extent in the main Arctic basin.

Two additional applications of this model show that the river runoff, which affects the stratification and thus the heat flux to the bottom of the ice, has only localized effects on the ice cover. This suggests that the possible Soviet river diversions will have a minimal impact on the Arctic ice cover. However, an increase of 2° in the surface air temperature, such as might result from doubling of the atmospheric level of CO_2, would result in the disappearance of the Arctic ice cover by the end of the melting season. This would lead to considerable feedback with the atmosphere, and it will be one of the major research topics for the future.

C. Mesoscale Ice–Ocean Models

Marginal ice zones are areas where pack ice changes to open water on scales on the order of 100 km in and out from the ice edge. This is the region where most of the ice meanders, eddies, upwelling, and fronts are to be found

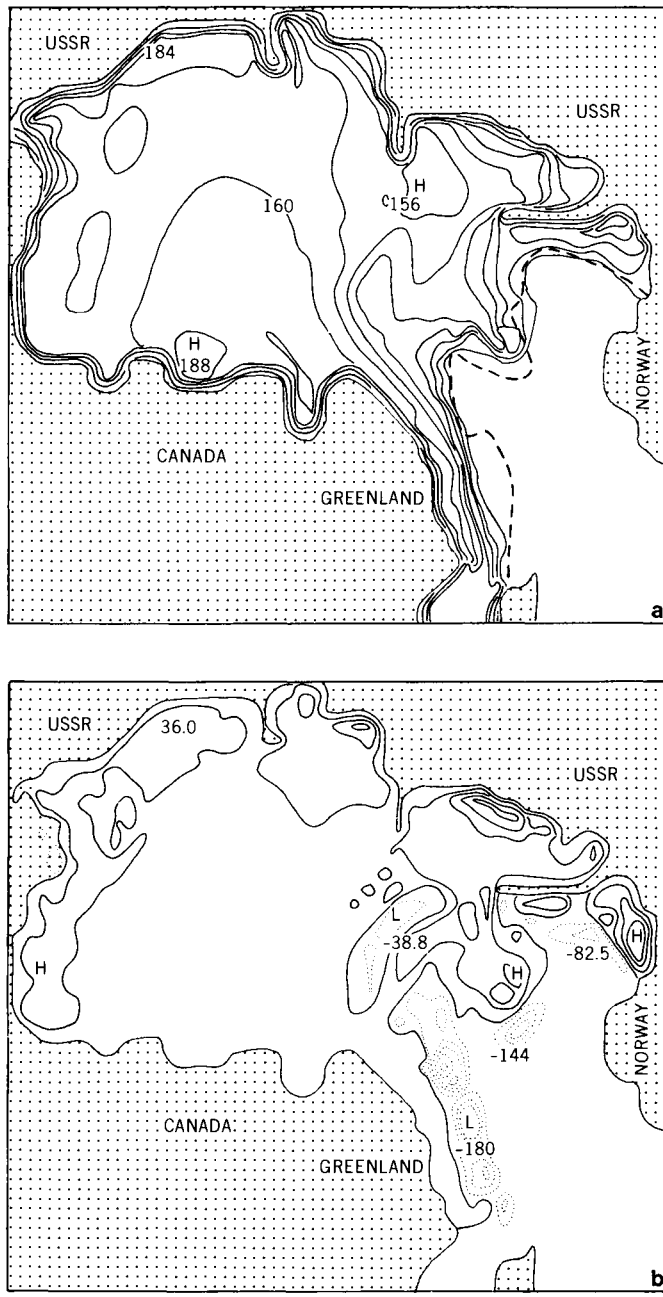

Figure 7.14 (a) Simulated January ice thickness (20-cm contour interval) with observed ice edge shown dashed. (b) Ice growth during January (20-cm contour interval). From Semtner (1987); copyright by American Meteorological Society.

(Johannessen *et al.*, 1983). Røed and O'Brien (1983) took the ice edge upwelling into consideration in their coupled ice–ocean model in which a dynamic ice medium is coupled to a reduced-gravity ocean, the simplest representation of a stratified ocean. The oceanic governing equations which are to be coupled with Eqs. (7.1)–(7.3) are for linear ocean dynamics:

$$u_t = fv - g^* h_x + [(1 - A)\tau_{aw,x} - A\tau_{wi,x}]/\rho H + A_h \nabla^2 u \tag{7.41}$$

$$v_t = fu - g^* h_y + [(1 - A)\tau_{aw,y} - A\tau_{wi,y}]/\rho H + A_h \nabla^2 v \tag{7.42}$$

$$h_t + H(u_x + v_y) = 0 \tag{7.43}$$

where g^* is the reduced gravity [$= g(\rho_2 - \rho_1)/\rho$, where $\rho_2 - \rho_1$ is the density difference between the upper and the lower layer], H is the upper-layer thickness, h is the pycnocline anomaly, and u and v are the oceanic velocity components. Wind and interfacial stresses, τ_{aw} and τ_{wi}, are defined in Section I,B.

To illustrate the up- and downwelling dynamics at the ice edge, it is assumed in the following that the ice edge and winds are parallel to the y axis and that there is no variation in the ocean or in the ice cover in the y direction (no y derivatives). The Ekman transport in the x direction in the open ocean will be determined simply by the wind stress, but in a partially ice-covered area it is

$$u_e = [(1 - A)\tau_{aw,y} + A\tau_{wi,y}]/\rho H f \tag{7.44}$$

For upwelling to occur there has to be a divergence in the surface stress, which implies that τ_{wi} and τ_{aw} must be considerably different in magnitude. Observations have shown that indeed there is a factor of 2–3 (as much as 5) difference in the surface drag coefficients over open water and a partially ice-covered region in marginal ice zones (Macklin, 1983); the increased surface roughness is caused by the abundance of open water between the ice floes, increased even further by a multiyear ice component in the MIZ. Assuming a free drift ice momentum balance, this translates to

$$\tau_{wi} = (2-3)\tau_{aw} \tag{7.45}$$

Thus the forcing of ice edge upwelling results from the difference in the momentum transfer from the atmosphere to the open ocean and the ice-covered ocean. This is quite different from earlier theories, in which divergence was produced with the ice cover acting as a rigid nonmoving boundary.

In the coupled dynamic model, the width of the upwelling zone is basically determined by the gradient of ice concentration (area of surface stress divergence) and ice edge advection. If the ice edge does not move and the ice concentration is a step function, the effective width of the upwelling zone is

twice the Rossby radius of deformation [$R_d = (g^* H^{1/2}/f$], which is the smallest baroclinic scale of motion in the ocean. If the ice edge moves considerably during the wind event, the upwelling is weak and extends over the distance of the ice edge advection.

The model of Røed and O'Brien was extended to two dimensions by Häkkinen (1986), which also allowed variability along the ice edge. The influence of ice cover variability as a source of eddies when the ice–ocean system is forced by winds was investigated. One example considered as an initial ice cover configuration is shown in Fig. 7.15a. Now, not only the divergence across the ice edge but also the variability in the Ekman transport along the ice edge comes into play by creating upwelling and downwelling areas as the ice edge moves mainly along the "mean" ice edge direction (Fig. 7.15b). It is necessary for the wavelength of the along-ice-edge disturbance to be large enough so that the ocean can resolve the variability. Resolution is limited by the Rossby radius of deformation and the advection distance of the ice. If the along-ice-edge variation has scales less than the Rossby radius of deformation or the ice advects the distance in less than two to three inertial cycles, the only influence of the disturbance in the ocean is excitation of inertial waves.

Ice charts show ice meanders in numerous locations along the Greenland Sea ice edge, besides the well-known Molley Deep vortex, all of which are present in successive charts and are seen every year (reported in the Yearbook published by the Danish Meteorological Institute). These meanders share the common feature that they are all located in an area with strong variations in the bottom topography. To investigate the effects of topography on the coupled ice–ocean system, Häkkinen (1987a) used a two-layer ocean with a moving lower layer and variable topography. The study shows the importance of the barotropic flow over variable topography in generating its own disturbances in the ice cover (ice meanders) which can propagate downstream. But aside from their surface appearance as eddies, there is no oceanic baroclinic variability under these features. If winds are turned on, the variations in the topography enhance the baroclinic signal (up- or downwelling), which can have local maxima in the pycnocline anomaly, i.e., eddies.

It is well known that the Greenland Sea MIZ is a source region for the densest water mass in the world ocean, but the formation process, suggested to occur in convective "chimney"-like regions (Killworth 1979) which extend to the bottom, has been elusive so far. The winter MIZEX experiment does reveal narrow chimneys near the ice edge, but the CTD casts extended to only about 300 m, and hence it is difficult to ascertain whether these chimneys represent the Greenland Sea bottom-water formation events (MIZEX Group, 1989).

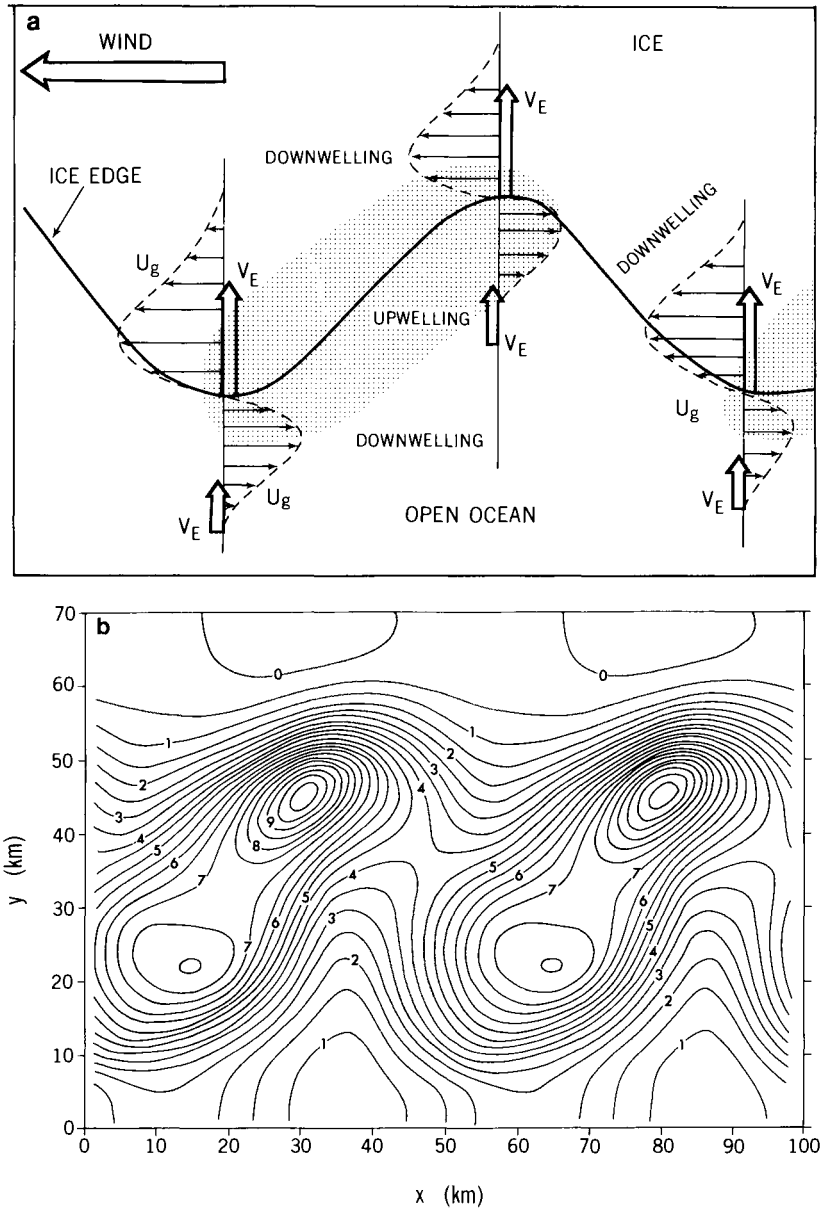

Figure 7.15 (a) Schematic diagram of the dynamics when upwelling-favorable winds are imposed on a wavy ice edge. (b) Pycnocline anomaly (in meters) for upwelling-favorable winds with an initial ice cover as in (a). From Häkkinen (1986); copyright by American Geophysical Union.

To explore the processes that can create conditions favorable to deep convection, Häkkinen (1987b, 1988) added thermodynamics to a one-dimensional coupled ice–ocean model in which the upper layer is actually the mixed layer. The source and sink terms for ice concentration are as in Røed (1984), without any heat conduction through ice. The ice is divided into two categories, thin and thick, which have their own concentrations. With this choice, the thick multiyear ice is allowed only to melt but the thin ice can be created or melted.

Inclusion of thermodynamics in the ocean model requires specification of the rate of heat and salt exchange between the mixed layer and the lower layer. The model uses Kraus–Turner parametrization for mixing, which is a function of the friction velocity (or wind stress), the surface buoyancy flux, and the density difference across the pycnocline and to the thickness of the mixed layer (Niiler and Kraus, 1977). Thus, conditions favorable to upwelling at the ice edge increase mixing by reducing the mixed-layer thickness. Also, adding a strong surface heat loss (e.g., 500 W m^{-2}) typical of strong wind events results in a great reduction in the density difference, further driving mixing. Figure 7.16 shows the time evolution of the different variables. The salinity increase is strongest in the area affected by ice edge upwelling left in the wake of the receding ice edge. The simulation shows that upwelling can allow the convection to penetrate to the bottom of the Atlantic layer in about 9 days. Deeper convection will take a couple of additional days, as it has to overcome much weaker stratification than that at the pycnocline. The model also shows that this area affected by ice edge upwelling does not freeze because the mixing brings continually warmer water to the mixed layer. Mixing under the newly formed ice is much slower, and it is unlikely that this area is a source of bottom water; instead, it is likely to represent the formation of intermediate water masses.

The models of the MIZ described above have a very simple vertical structure and basically focus on the system away from land boundaries. With improved vertical resolution and including a coastal boundary, Ikeda (1985) studied processes at an ice-covered shelf applicable to the Labrador coast. He uses a Hibler-type ice model, including a plastic rheology for the ice. With an air–ice drag coefficient that is twice the air–water drag coefficient, winds parallel to the shoreline, and ice on the right, the model produced upwelling at the ice edge by inducing stronger Ekman transport underneath the ice than in the open ocean. At the coast the same winds induce downwelling, giving rise to a nearly closed cross-shelf circulation (Fig. 7.17), which confines the ice to the shelf. The results also indicate that the ice movement and velocities are very sensitive to the offshore wind component, which determines how strongly ice is packed toward the coast or pulled away from the coast and thus strongly influences the ice momentum balance by increasing

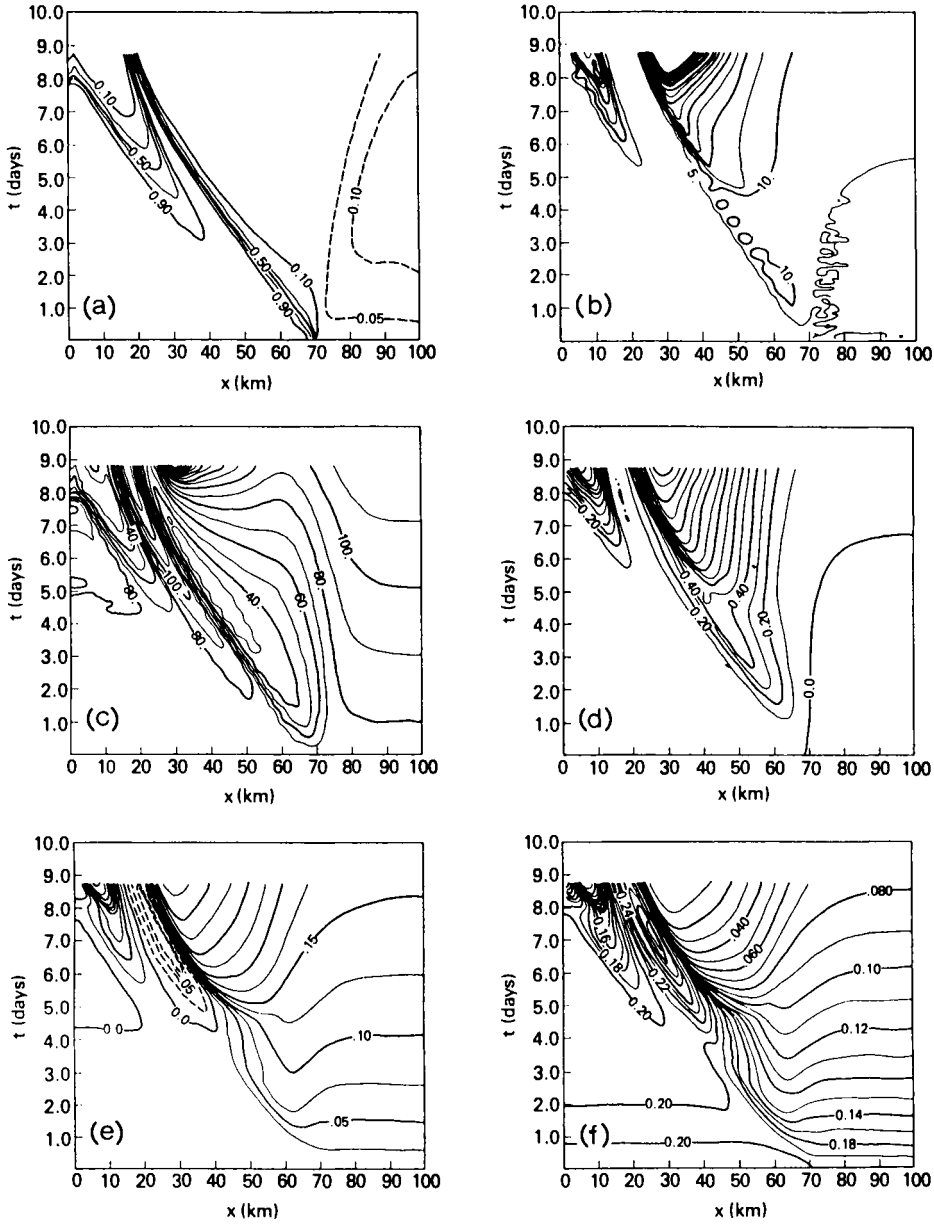

Figure 7.16 Evolution of a dynamic–thermodynamic ice–ocean system in which the ocean is described as a one-dimensional mixed-layer model. Wind forcing is favorable to upwelling; the surface heat loss is specified. (a) Multiyear ice concentration (solid lines) and thin-ice concentration (dashed lines). (b) Entrainment rate at the bottom of the mixed layer (meters per day). (c) Depth of the mixed layer (meters). (d) Increase of the mixed-layer salinity (per mil). (e) Increase of the mixed layer temperature (degrees Celsius). (f) Density difference across the pycnocline (σ_t units). From Häkkinen (1988); copyright by American Geophysical Union.

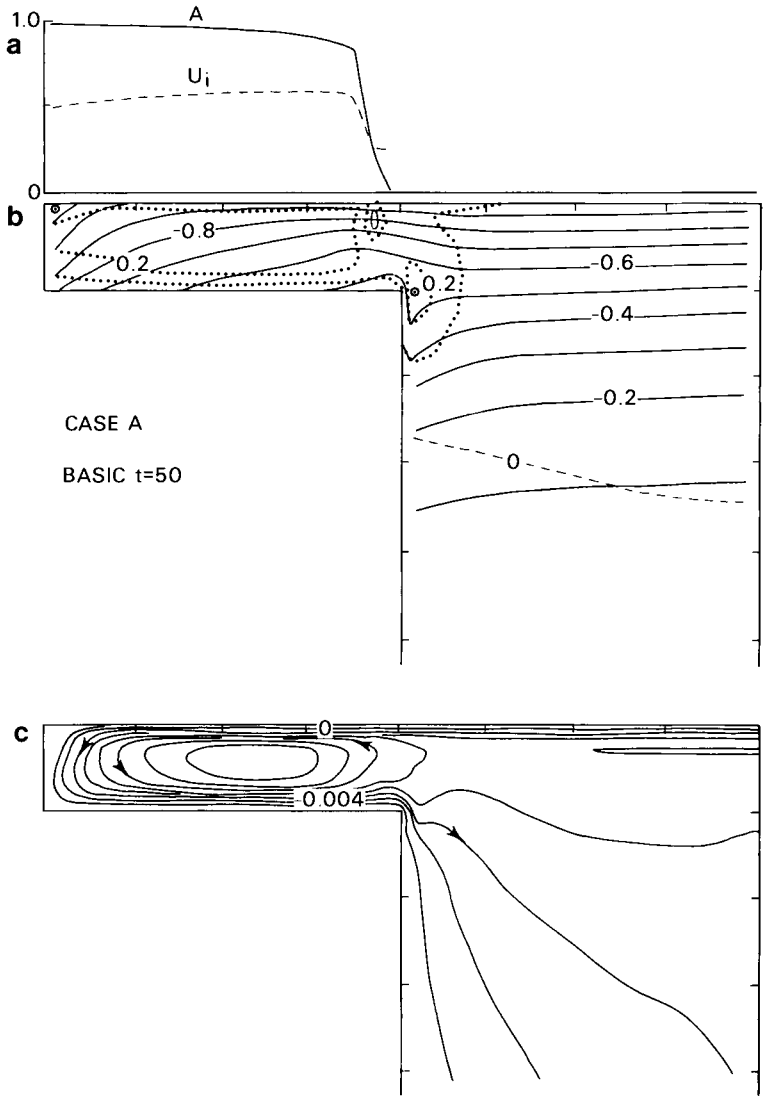

Figure 7.17 Ice conditions and flow structures from a coupled ice–multilevel ocean model with one solid boundary. (a) Ice concentration. (b) Isopycnals (solid lines) and oceanic along shore velocity, with positive values outward from the page (dotted lines). (c) Across-shore stream function. From Ikeda (1985); copyright by American Geophysical Union.

dimensions (with three vertical levels) and thermodynamics has been included (Ikeda, 1988). Choosing the two lowest layers to be warm, with alongshore winds and ice on the right, forces warm water to upwell at the ice edge and thus considerably reduces ice formation, as was the case in Häkkinen's results (1987b, 1988).

These dynamic–thermodynamic models reflect the importance of mixing processes for the ice–ocean system for controlling both the large- and small-scale ice edge variation and convection in the ocean, which could be initiated by vigorous ice edge upwelling. These models have more or less relied on bulk parametrizations for mixing, but this can lead to serious deficiencies. For instance, it is not well established how strong the influence of the buoyancy-induced turbulence is in the formula of Kraus and Turner. To reduce these deficiencies, a Mellor–Yamada second-moment turbulence closure model (Mellor, 1985) has been introduced to couple the ocean model with an ice model (Ikeda, 1985: one-dimensional model in the z direction; McPhee *et al.*, 1986: two-dimensional; Mellor and Kantha, 1989: one-dimensional; Kantha and Mellor, 1989a: two-dimensional). The interfacial stresses are also predicted on the basis of the turbulence parametrizations; i.e., the ice–water drag is variable, instead of a constant, depending on the surface stress and momentum exchange between the ice and ocean.

As an example of the application of a coupled ice–ocean model with turbulence closure coupled to a viscous–plastic ice dynamics model (Hibler's) and a Semtner-like snow–ice three-level thermodynamic model, we focus on the Bering Sea ice edge simulations by Kantha and Mellor (1989a). This model describes the transition from ice-covered ocean to open ocean, separated by the ice edge front and the two-layered circulation underneath the ice cover. The solution of the primitive equations involves solving the second-moment closure for turbulent mixing. The closure scheme has several parameters which are determined by laboratory experiments. The salt and heat exchanges across the ice–ocean interface are computed from the law of the wall, assuming a turbulent boundary layer over a rough surface. The scheme uses the Yaglom and Kader formulation (1974) for heat and mass transfer over a rough wall, which gives different salt and heat resistance coefficients. This effect can give rise to supercooling of the upper ocean in freezing conditions. This particular version of the model also includes double diffusion.

The model inputs are vertically uniform temperature (warm waters, 2.5°C) and salinity, which are kept constant at the inflow side (the Pacific), where mass flux is specified. The winds blow from right to left, i.e., from the north (Fig. 7.18). The model incorporates typical wintertime temperatures and cloudiness in the Bering Sea to compute the surface heat fluxes. The results (Fig. 7.18) show the influence of the ice melt in the water column; ice

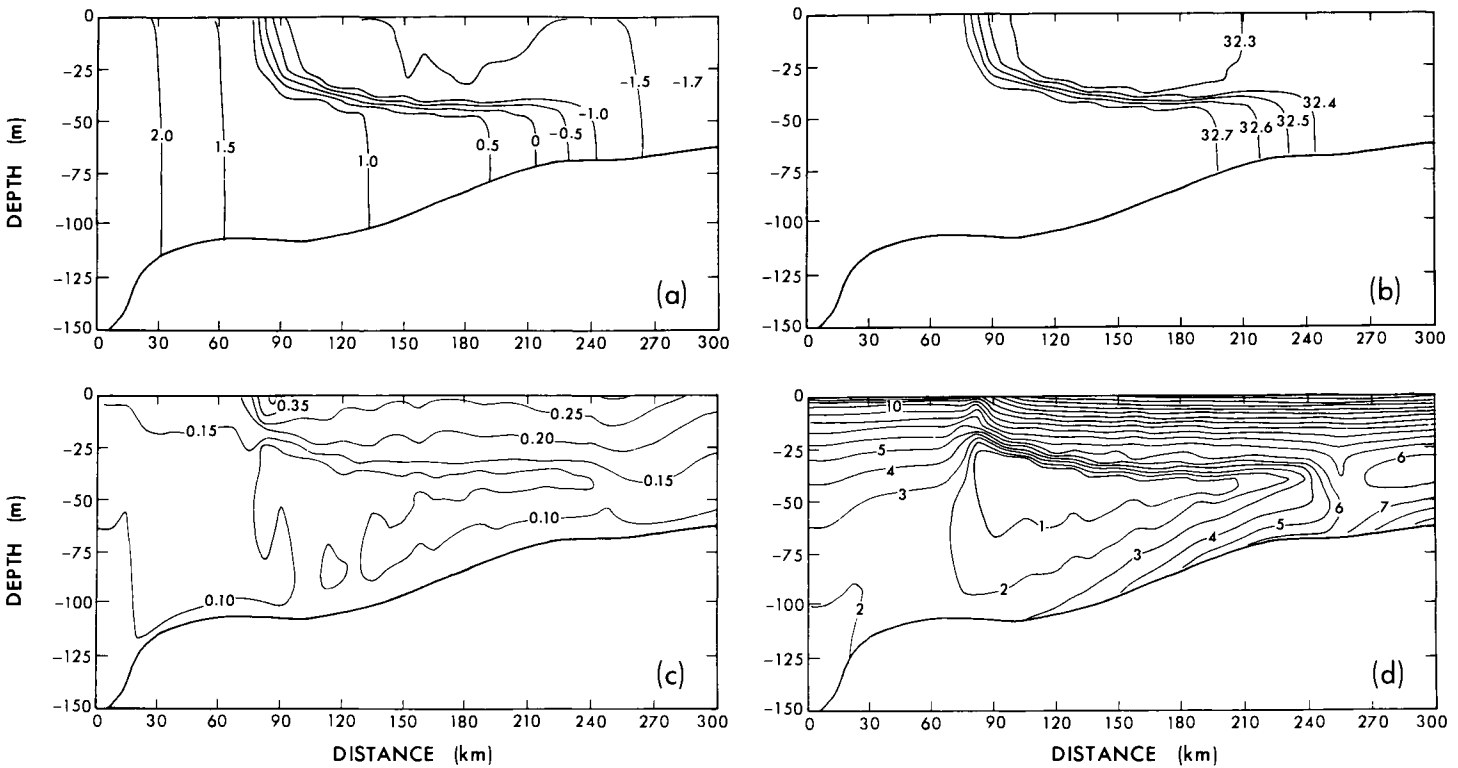

Figure 7.18 Simulation of the Bering Sea marginal ice zone showing model-predicted (a) temperatures, (b) salinities, (c) velocities along the ice edge, and (d) turbulent kinetic energy (in centimeters squared per second squared). Wind direction is to the left, and the specified oceanic net transport is toward the right. From Kantha and Mellor (1989a); copyright by American Geophysical Union.

melt creates a new mixed layer which is cooled not only by the surface heat loss but also by the ice melt itself. When strong stratification is induced, the lowest portion of the ocean becomes insulated from cooling. These results compare well with the wintertime measurements of salinity and temperature by Hendricks *et al.* (1986). The frontal formation at the ice edge generates a strong ice edge jet both in the ice and in the upper ocean.

D. Other Ice–Ocean Models

This section is devoted to other interesting models which do not fit under the earlier headings. These models take advantage of simplifying the problem to one dimension (horizontal or vertical) and removing upper-ocean dynamics (except mixing), which enables economical studies of the long-term evolution of the system, studies of the parameter ranges, and sensitivity analyses.

After Gordon (1978) found a very narrow (15–20 km) hydrographic feature with nearly uniform salinity and temperature below the summer mixed layer in the Weddell Sea, Killworth studied possible mechanisms and necessary surface forcing to produce these features, which he termed "chimneys" (1979). He found that, given strong enough surface heat loss, not only the region of the chimney but also all other hydrographic sections in the vicinity would overturn. He concluded that there must be some preconditioning mechanism which selected that particular area to overturn. As the foremost candidate for preconditioning, he suggested baroclinic instability, which occurs on the same spatial scales. Cyclonic eddies resulting from the instability would bring the pycnocline nearer to the surface than the surroundings, thus giving rise to enchanced mixing.

The model by Killworth (1979) was revised by Martinson *et al.* (1981) to study the deep convection in the large polynyas occurring in the Weddell Sea. Their model consists of a two-level ocean in which the depth of the upper layer is an external parameter. The model is forced by surface heat loss and mass flux (precipitation). Ice thickness is also predicted, given the conductive flux through the ice (and precipitation). The heat exchange processes between water and ice and across the pycnocline are parametrized using constant exchange coefficients. Martinson *et al.* set out to test the hypothesis that surface cooling and salt rejection from ice formation decrease the temperature and increase the salinity, thus creating a static instability and homogenizing the water column. Homogenization will necessarily bring warm water to the surface, which will melt the ice and further prevent its formation. Using observed heat flux and precipitation, they found that the overturning process will repeat itself from year to year, with some variation in the starting time depending mainly on the ice onset. This cycle is not very sensitive to the variations in the surface cooling and heating, which result in differences of a few weeks in ice onset and overturning. But the variations in

the precipitation rate on a seasonal scale are of crucial importance. If the precipitation is not large enough to balance the salinity increase in the upper layer due to overturning, the system will evolve toward a steady seasonal cycle without seasonal ice cover. On the other hand, if the precipitation is larger than the critical value, the system does not overturn seasonally but stays in a two-layer state with an ever-freshening upper layer.

The model is extremely sensitive to upper-layer thickness. For observed layer thicknesses of about 200 m (or thinner), the overturning process could occur every winter. Increasing the layer thickness by 100 m leads to a system which is stable against the buoyancy fluxes and contains a stable ice cover through the winter. Together, the variations in the mixed-layer depth and precipitation determine the conditions that maintain the yearly cycle of overturning; i.e., the thinner the upper layer is, the less precipation is needed to balance out the salinity increase. One may note that overturning occurs in this model always after the onset of ice cover toward the end of the cooling season. Thus, this model predicts deep-water formation which is limited to a narrow period compared to the total length of the cooling season.

One-dimensional predictions of the stratification in the Arctic are given by Stigebrandt (1981) and Killworth and Smith (1984). These authors stress the influence of positive buoyancy flux caused by river runoff and the Bering Strait inflow to the Arctic, of which the latter is more important in maintaining the upper Arctic salinity profile. This source water helps balance the outflow of polar water through Fram Strait. Moreover, the model of Stigebrandt, which also predicts the ice thickness, shows that a decrease in river runoff of as much as 50% will have a minimal effect on the ice thickness as well as on the open water area in the Arctic. The same conclusion is given by the general circulation models of Semtner (1976b, 1987).

The ice–ocean models of Pollard *et al.* (1983), Lemke (1987), and Mellor and Kantha (1989) are purely thermodynamic and include mixing via bulk parametrization or calculate it explicity in the upper ocean. The main focus of Pollard *et al.* (1983) is to provide a simple ice–ocean model that can predict sea surface temperatures which can be used in connection with atmospheric general circulation models. Their model uses a modified Kraus–Turner formula to parametrize entrainment/detrainment. Monthly climatological atmospheric data are used to predict the ice thickness and mixed-layer thickness, but the heat exchange between the ice and ocean is specified. The sea surface temperature (SST) and mixed-layer depth are predicted along a section across the Pacific. Generally, the model gives realistic sea ice thicknesses and extent, whether one uses a fixed- or variable-depth mixed layer. Model results are in surprisingly good agreement with observations, considering that advective effects are totaly absent. The SST predictions are fair for a fixed-slab mixed layer, giving temperatures that are

1–2°C too high in the mid-Pacific (away from the equator); but essential differences also appear at the high latitudes, where the model with a variable-depth mixed layer performs better. Of course, one could anticipate that the winter convection has to influence both the SSTs and the layer depth.

Lemke (1987) pursues a coupled ice–ocean model similar to that of Pollard *et al.* (1983); the entrainment is determined using a bulk formula of Kraus and Turner, which acts between the mixed layer and the lower ocean with an exponential profile for temperature and salinity. The advective effects are taken into account as net heat and salt sources by specifying first the divergence/convergence of the horizontal transports. The model computes explicitly the heat flux to the bottom of the ice. The atmospheric forcing consists of climatological data, which are given once a day at 1° resolution.

The model predicts the seasonal equilibrium response of ice thickness, mixed-layer depth, and mixed-layer temperature and salinity. Figure 7.19a clearly displays the effect of ice formation and brine rejection on the system; the maximum salinity occurs with the maximum ice thickness. The ice melt begins with the surface heat gain and not with increased oceanic heat flux to the bottom of the ice. No seasonal overturning of the ocean occurs in the standard simulation. The main difference between the fixed- and variable-depth mixed-layer simulations in this model is that freezing is slowed down by convection in the fall, which deepens and brings warm water into the mixed layer. The mixed-layer heat content and inertia are thus very important for the onset of the ice cover. Furthermore, Lemke investigated how to initiate large polynyas such as the Weddell Polynya. He first experimented with resetting the mixed-layer depth to 40 m, which is much shallower than it would be during the yearly cycle, for a short period of 50 days. This was done to simulate the effect of the warm cyclonic eddies found in the Weddell Sea. The influence of this short event is drastic, not only for the ongoing season but also for several years afterward. The changes included disappearance of the ice cover for a couple of years as well as major changes in the mixed-layer salinity, temperature, and depth (Fig. 7.19b). After several years the heat balance between surface heat flux and upwelling and the salt balance between precipitation and upwelling have been recaptured, and the system is forced back to the regular seasonal cycle. The second experiment designed to create a polynya assumed an ice divergence acting for 40 days in the beginning of freezing season that created open water which led to excess ice formation and associated salt flux. The excess salt forces the system to convect more deeply, which brings warmer and more saline water to the mixed layer and leads to (near) disappearance of the ice cover. Again, the system takes several years to recover from the event and the results are

similar to those in Fig. 7.19b. The disturbance, either warm eddy or ice divergence, is most effective when it occurs early in the freezing season. The necessary conditions for the occurrence of a polynya are that the stratification is very weak and the disturbance is strong, i.e., large displacement of the pycnocline or large ice divergence.

The one-dimensional model of Mellor and Kantha (1989) applies a second-moment turbulence closure scheme to the upper ocean, which is coupled to a three-level snow–ice system similar to that of Maykut and Untersteiner (1971) and Semtner (1976a). The ice concentration and aver-

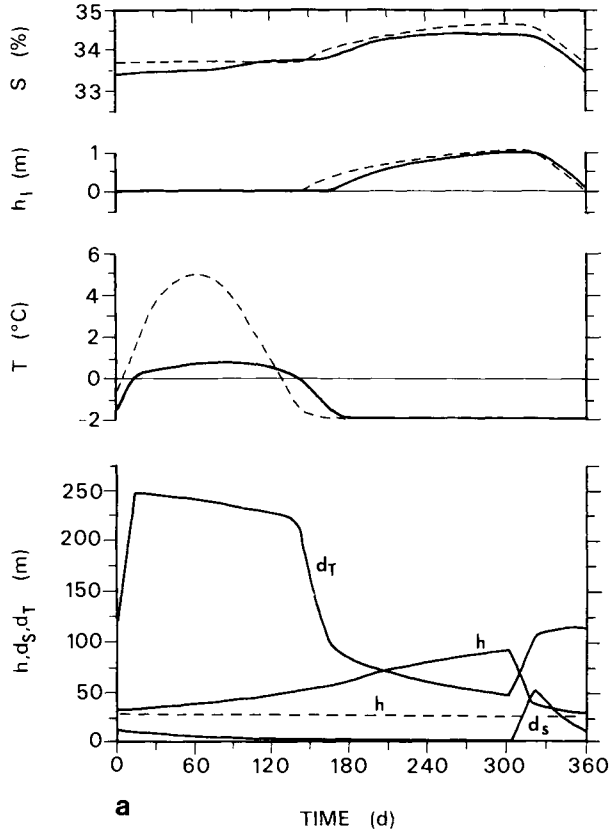

Figure 7.19 (a) Simulated Southern Ocean (64°S) equilibrium seasonal sea ice thickness, mixed-layer temperature T, and depth h (solid lines). Dashed lines are for a simulation with constant mixed-layer thickness. (b) Model results for mixed-layer salinity S, ice thickness h_i, mixed-layer temperature T, and depth h when a 50-day perturbation (at the arrow) in the mixed-layer depth is introduced. From Lemke (1987); copyright by American Geophysical Union.

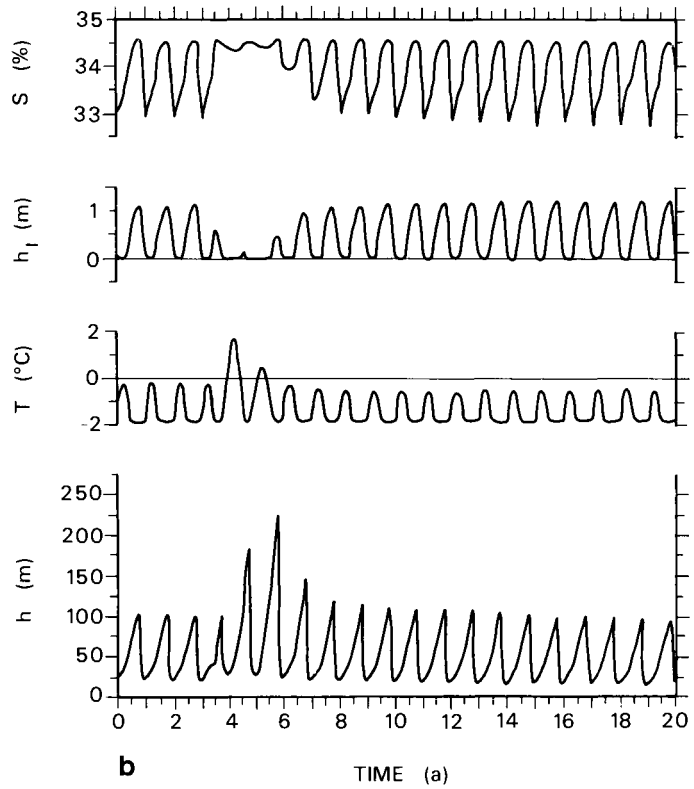

Figure 7.19 *(Continued)*

age thickness are predicted assuming Fletcher's monthly climatology, as well as ice divergence to take into account the net ice transport from the Arctic. This divergence term is very important for the ice mass balance and thus for the equilibrium ice thickness. Mellow and Kantha find that with reasonable divergence values the equilibrium ice thickness is far below the observed value (3 m). However, changing the conductivity of the ice by factor of 1.5 – 2 yields a reasonable equilibrium thickness. This factor can be justified by the fact that there is about 20 – 25% thin ice (less than 1 m thick) even in the mid-Arctic during the cooling season and that conduction is much stronger through this thin-ice portion than through the thicker ice. In the modeling framework of using average values, an apparent increase in mean conductivity is necessary to account for this effect. Another result of their work is that the predicted oceanic heat flux to the bottom of the ice is much lower than the customary constant value used in several early models (0.33 versus 2 W m^{-2}).

IV. Concluding Remarks

The models reviewed here show the complexity of the dynamic and thermodynamic processes in the ice and polar oceans. These two aspects are intertwined in controlling the Arctic ice cover. The dynamics provides the leads (or polynyas) where ice can grow or increases the ice thickness by ridging. Thermodynamic processes give growth and melt at the bottom and top surfaces; the bottom accretion depends on the thickness and on the dynamic and thermodynamic history of the ice. The ice melt in the central Arctic occurs mainly through top ablation by solar radiation. The surface melting and existence of a stable year-round ice cover are very sensitive to the surface albedo. This sensitivity is heightened during the melting season, when melt ponds, whether from snow or ice, can lower the albedo considerably and increase the energy absorption at the surface.

Both winds and ocean currents influence the ice drift, creating a net outflow of ice from the Arctic through Fram Strait, which makes the total ice budget positive. With net ice production, there is an associated positive salt flux from brine rejection, which is compensated in a complex manner by precipitation, ice melt, river runoff, and Bering Sea water inflow. This salt balance is also complicated by the inflow of Atlantic waters and outflow of polar waters through Fram Strait. It is worth noting that the few studies that have explored the model sensitivities to inflows and outflows suggest the importance of the Bering Sea inflow in the salt balance of the Arctic and in maintaining the halocline. This also implies its influence in controlling the ice cover by maintaining a stable stratification. Also common to these models is the result that river runoff is important only locally; thus, the possible diversion of Soviet rivers would not greatly affect the Arctic ice cover.

An interesting feature of the models is the importance of convection in the areas of seasonal ice cover, e.g., in the Greenland and Barents seas and around Antarctica. In the beginning of the cooling season, convection increases the thermal inertia of the upper ocean and thus delays the onset of the ice cover. In the Greenland Sea, convection prohibits ice formation away from the East Greenland Current even in midwinter. Furthermore, in these areas mixing and precipitation form a delicate balance which, if disturbed, takes several years to recover.

It seems imperative that there be further efforts in the future to improve atmospheric modeling and data collection in the polar regions to provide reliable surface forcing data for the ice–ocean models. Data collection for the atmospheric general circulation models (AGCMs) has been improved by the Arctic buoy program (Untersteiner and Thorndike, 1982), which records the ice drift, sea level pressure, and air temperature. To improve the surface

boundary conditions for AGCMS, whether for prediction or analysis, a natural further step is to consider fully coupled, interactive atmosphere–ice–ocean models in which feedback can be included. There have been some steps toward this goal, e.g., by Kantha and Mellor (1989b), who describe an atmospheric boundary layer model for the marginal ice zone.

The ice–ocean models reviewed above have laid the foundation by investigating the basic feedbacks between the ice and the ocean. However, we are still not prepared to give a satisfactory answer to the simple question of why there is an ice cover in the Arctic, i.e., which interface, ice–ocean or atmosphere–ice, is more important in the energy balance responsible for a stable ice cover. In the coming years we should be able to perform longer simulations of fully coupled atmosphere–ice–ocean models. One of the goals is to predict and simulate climate changes, in which the ice and the polar ocean have an important role by being the source regions for the thermohaline circulation and a sink for atmospheric CO_2. The expected doubling of CO_2 in the atmosphere in the coming century will have a profound impact on the polar ice and ocean system, a problem that is bound to occupy polar ocean modelers and other researchers for years to come.

Acknowledgments

I gratefully acknowledge support from the NASA Headquarters Oceanic Processes Branch, from the NOAA Geophysical Fluid Dynamics Laboratory where I was a visiting scientist, and from the Office of Naval Research. The helpful suggestions and comments on the manuscript from Drs. H. J. Niebauer, W. O. Smith, G. L. Mellor, and L. H. Kantha were greatly appreciated. I wish also to thank the GFDL drafting department for figure preparation.

References

Bourke, R. H. & R. P. Garrett. 1987. Sea ice thickness distribution in the Arctic Ocean. *Cold Reg. Sci. Technol.* **13**: 259–280.

Bryan, K. 1969. A numerical method for the study of circulation of the world oceans. *J. Comput. Phys.* **4**: 347–376.

Bryan, K., S. Mamabe & R. C. Pacanowski. 1975. A global ocean–atmosphere climate model. Part II. The oceanic circulation. *J. Phys. Oceanogr.* **5**: 30–46.

Campbell, W. J. 1965. The wind driven circulation of the ice and water in a polar ocean. *J. Geophys. Res.* **70**: 3279–3301.

Carsey, F. 1980. Microwave observations of the Weddell Polynya. *Mon. Weather Rev.* **108**: 2032–2044.

Clarke, A. J. 1978. On wind driven quasi-geostrophic water movement at fast ice edges. *Deep-Sea Res.* **25**: 41–51.

Comiso, J. C. & A. L. Gordon. 1987. Recurring polynyas over the Cosmonaut Sea and Maud Rise. *J. Geophys. Res.* **92**: 2819–2834.

Coon, M. D., G. A. Maykut, R. S. Pritchard & D. A. Rothrock. 1974. Modelling the pack ice as an elastic-plastic material. *AIDJEX Bull.* **24**: 1-105.

Doronin, Y. P. 1970. On a method of calculating the compactness and drift of ice floes. *Tr. Arkt. Antarkt. Nauchno-Issled. Inst.* **291**: 5-17.

Fletcher, J. O. 1965. "The Heat Budget of the Arctic Basin and its Relation to Climate," R-444-PR. Rand Corporation, Santa Monica, California.

Foster, T. D. 1972a. An analysis of the cabbeling instability in sea water. *J. Phys. Oceanogr.* **2**: 294-301.

———. 1972b. Haline convection in polynyas and leads. *J. Phys. Oceanogr.* **2**: 462-469.

Galt, J. A. 1973. A numerical investigation of Arctic Ocean dynamics. *J. Phys. Oceanogr.* **3**: 379-396.

Gammelsrød, T., M. Mork & L. P. Røed. 1975. Upwelling possibilities at an ice-edge: Homogeneous model. *Mar. Sci. Comm.* **1**: 115-145.

Glen, J. W. 1970. Thoughts on a viscous model for sea ice. *AIDJEX Bull.* **2**: 18-27.

Gordienko, P. 1958. Arctic ice drift. *N.A.S.—N.R.C., Publ.* **598**: 210-220.

Gordon, A. L. 1978. Deep Antarctic convection west of Maud Rise. *J. Phys. Oceanogr.* **8**: 600-612.

Häkkinen, S. 1986. Coupled ice-ocean dynamics in the marginal ice zones: Up/downwelling and eddy generation. *J. Geophys. Res.* **91**: 819-832.

———. 1987a. Feedback between the ice flow, barotropic and baroclinic flows in the presence of bottom topography. *J. Geophys. Res.* **92**: 3807-3802.

———. 1987b. A coupled dynamic-thermodynamic model of an ice-ocean system in the marginal ice zone. *J. Geophys. Res.* **92**: 9469-9478.

———. 1987c. A constitutive law for sea ice and some applications. *Math. Modell.* **9**: 81-90.

———. 1988. A note on deep water production via a "chimney" formation in the ice edge regions. *J. Geophys. Res.* **93**: 8279-8282.

Hansen, J., D. Johnson, A. Lacis, S. Lebedeff, P. Lee, D. Rind & G. Russell. 1983. Climatic effects of atmospheric carbon dioxide. *Science* **220**: 873-875.

Hendricks, P. J., R. D. Muench & G. R. Stegen. 1986. A heat balance for the Bering Sea ice edge. *J. Phys. Oceanogr.* **15**: 1747-1758.

Hibler, W. D., III. 1974. Differential sea ice drift. II. Comparison of mesoscale strain measurements to linear drift theory predictions. *J. Glaciol.* **13**: 457-471.

———. 1977. A viscous sea ice law as a stochastic average of plasticity. *JGR, J. Geophys. Res.* **82**: 3932-3938.

———. 1979. A dynamic thermodynamic sea ice model. *J. Phys. Oceanogr.* **9**: 815-846.

———. 1980. Modeling variable thickness sea ice cover. *Mon. Weather Rev.* **108**: 1943-1973.

———. 1985. Modeling sea-ice dynamics. *Adv. Geophys.* **28**: 549-580.

Hibler, W. D., III & S. F. Ackley. 1983. Numerical simulation of the Weddell Sea pack ice. *J. Geophys. Res.* **88**: 2873-2887.

Hibler, W. D., III & K. Bryan. 1984. Oceanic circulation: Its effect on seasonal sea ice simulations. *Science* **224**: 489-492.

———. 1987. A diagnostic ice-ocean model. *J. Phys. Oceanogr.* **17**: 987-1015.

Hibler, W. D., III & W. B. Tucker. 1977. Seasonal variations in apparent sea ice viscosity on the geophysical scale. *Geophys. Res. Lett.* **4**: 87-90.

———. 1979. Some results from a linear viscous model of the Arctic ice cover. *J. Glaciol.* **22**: 293-304.

Hibler, W. D., III & J. E. Walsh. 1982. On modeling seasonal and interannual fluctuations of the Arctic sea ice. *J. Phys. Oceanogr.* **12**: 1514-1523.

Hibler, W. D., III, S. J. Mock & W. B. Tucker III. 1974. Classification and variation of sea ice ridging in the western Arctic basin. *J. Geophys. Res.* **79**: 2735-2743.

Ikeda, M. 1985. A coupled ice–ocean model of a wind driven coastal flow. *J. Geophys. Res.* **90:** 9119–9128.

———. 1988. A three dimensional coupled ice–ocean model of coastal circulation. *J. Geophys. Res.* **93:** 10731–10748.

Johannessen, O. M., J. A. Johannessen, J. Morison, B. A. Farrelly & E. A. S. Svendsen. 1983. The mesoscale oceanographic conditions in the marginal ice zone north of Svalbard in early fall 1979. *J. Geophys. Res.* **88:** 2755–2769.

Kantha, L. H. & G. L. Mellor. 1989a. Application of a two-dimensional coupled ocean–ice model to the Bering Sea marginal ice zone. *J. Geophys. Res.* **94:** 10921–10935.

———. 1989b. A numerical model of the atmospheric boundary layer over a marginal ice zone. *J. Geophys. Res.* **94:** 4959–4970.

Killworth, P. D. 1973. A two-dimensional model for formation of Antarctic bottom water. *Deep-Sea Res.* **20:** 941–971.

———. 1974. A baroclinic model of motions on Antarctic continental shelves. *Deep-Sea Res.* **21:** 815–837.

———. 1977. Mixing on the Weddell Sea continental slope. *Deep-Sea Res.* **24:** 427–448.

———. 1979. On chimney formations in the ocean. *J. Phys. Oceanogr.* **9:** 531–554.

Killworth, P. D. & J. M. Smith. 1984. A one-and-one-half dimensional model for the Arctic halocline. *Deep-Sea Res.* **31:** 271–294.

Lemke, P. 1987. A coupled one-dimensional sea ice–ocean model. *J. Geophys. Res.* **92:** 13164–13172.

Lepparanta, M. 1981. An ice drift model for the Baltic Sea. *Tellus* **33:** 583–596.

Macklin, S. A. 1983. Wind drag coefficient over first-year sea ice in the Bering Sea. *J. Geophys. Res.* **88:** 2845–2852.

Martinson, D. G., P. D. Killworth & A. L. Gordon. 1981. A convective model for the Weddell Polynya. *J. Phys. Oceanogr.* **11:** 466–488.

Maykut, G. A. & N. Untersteiner. 1969. "Numerical Prediction of the Thermodynamic Response of Arctic Sea Ice to Environmental Changes." Rand Corporation, Santa Monica, California.

———. 1971. Some results from a time-dependent thermodynamic model of sea ice. *J. Geophys. Res.* **76:** 1550–1575.

McPhee, M. G., G. L. Mellor & M. Steele. 1986. Ice–seawater turbulent boundary layer interaction with melting or freezing. *J. Phys. Oceanogr.* **16:** 1829–1846.

Mellor, G. L. 1985. Ensemble average, turbulence closure. *Adv. Geophys.* **28:** 345–358.

Mellor, G. L. & L. Kantha. 1989. An ice–ocean coupled model. *J. Geophys. Res.* **94:** 10937–10954.

MIZEX Group. 1989. MIZEX East 1987: The winter marginal ice zone program in the Fram Strait/Greenland Sea. *EOS, Trans. Am. Geophys. Union* **70**(17).

Moritz, R. E. 1988. "The Ice Budget of the Greenland Sea," Tech. Rep. APL-UW TR8812. Univ. of Washington, Seattle.

Niebauer, H. J. 1981. Wind and melt driven circulation in a marginal ice edge frontal system: A numerical model. *Cont. Shelf Res.* **1:** 49–98.

Niiler, P. P. & E. B. Kraus. 1977. One-dimensional models of the upper ocean. *In* "Modelling and Prediction of the Upper Layers of the Ocean (E. B. Kraus, ed.), p. 325. Pergamon, Oxford.

Nikiforov, E. G. 1957. "Variations in Ice Cover Compaction due to its Dynamics," Probl. Arktiki, Vol. 2. Morskoi Trans., Leningrad.

Overland, J. E. & C. H. Pease. 1988. Modeling ice dynamics of coastal seas. *J. Geophys. Res.* **93:** 15619–15637.

Parkinson, C. L. 1983. On the development and cause of the Weddell Polynya in a sea ice simulation. *J. Phys. Oceanogr.* **13:** 501–511.

Parkinson, C. L. & W. M. Washington. 1979. A large scale numerical model of sea ice. *J. Geophys. Res.* **84**: 311–337.

Pease, C. H. 1975. A model for the seasonal ablation and accretion of Antarctic sea ice. *AIDJEX Bull.* **29**: 151–172.

Pollard, D., M. L. Batteen & Y. J. Han. 1983. Development of a simple upper ocean and sea ice model. *J. Phys. Oceanogr.* **13**: 754–768.

Pritchard, R. S. 1975. An elastic plastic constitutive law for sea ice. *J. Appl. Mech.* **42**: 379–384.

Pritchard, R. S., M. D. Coan & M. G. McPhee. 1975. Simulation of sea ice dynamics during AIDJEX. *J. Pressure Vessel Technol.* **99**: 491–497.

Røed, L. P. 1984. A thermodynamic ice–ocean model of the marginal ice zone. *J. Phys. Oceanogr.* **14**: 1921–1929.

Røed, L. P. & J. J. O'Brien. 1983. A coupled ice–ocean model of upwelling in the marginal ice zone. *J. Geophys. Res.* **88**: 2863–2872.

Semtner, A. J. 1976a. A model for the thermodynamic growth of sea ice in numerical investigations of climate. *J. Phys. Oceanogr.* **6**: 379–389.

———. 1976b. Numerical simulation of the Arctic Ocean circulation. *J. Phys. Oceanogr.* **6**: 409–425.

———. 1987. A numerical study of sea ice and ocean circulation in the Arctic. *J. Phys. Oceanogr.* **17**: 1077–1099.

Smith, R. B. 1983. A note on the constitutive law for sea ice. *J. Glaciol.* **29**: 191–195.

Stigebrandt, A. 1981. A model for the thickness and salinity of the upper layer in the Arctic Ocean and relationship between the sea ice thickness and some external parameters. *J. Phys. Oceanogr.* **11**: 1407–1422.

Thorndike, A. S., D. A. Rothrock, G. A. Maykut & R. Colony. 1975. The thickness distribution of sea ice. *JGR, J. Geophys. Res.* **80**: 4501–4513.

Untersteiner, N. 1961. On the mass and heat budget of the Arctic sea ice. *Arch. Meteorol., Geophys. Bioklimatol. Ser. A* **12**: 151–182.

———. 1964. Calculations of temperature regime and heat budget of sea ice in the central Arctic. *J. Geophys. Res.* **69**: 4755–4766.

Untersteiner, N. & A. S. Thorndike. 1982. Arctic data buoy program. *Polar Rec.* **21**: 127–135.

Walsh, J. E., W. D. Hibler, III & B. Ross. 1985. Numerical simulation of northern hemisphere sea ice variability, 1951–1980. *J. Geophys. Res.* **90**: 4847–4865.

Washington, W. M., A. J. Semtner, C. Parkinson & L. Morison. 1976. On the development of a seasonal change sea-ice model. *J. Phys. Oceanogr.* **6**: 679–685.

Welander, P. 1977. Thermal oscillations in a fluid heated from below and cooled to freezing from above. *Dyn. Atmos. Oceans* **1**: 215–223.

Yaglom, A. M. & B. A. Kader. 1974. Heat and mass transfer between a rough wall and turbulent fluid at high Reynolds and Peclet numbers. *J. Fluid Mech.* **62**: 601–623.

Zubov, N. N. 1945. "Arctic Ice," p. 491. (Engl. transl. NTIS No. AD 426972).

Zwally, H. J. & P. Gloersen. 1977. Passive microwave images of the polar regions and research applications. *Polar Rec.* **18**: 431–450.

Index

Advanced Very High Resolution Radiometer (NOAA 9/10), 130
Advection, effect of mesoscale processes on vertical fluxes through, 272–273
Advective term, rotational boundary layer, 291–293
Age, of sea ice, *see* Residence times
Aging, sea ice
  changes during, 88–89
  effect on electromagnetic wave penetration, 135
AIDJEX, *see* Arctic Ice Dynamics Joint Experiment
Airborne laser profiles, sea ice surface topography, 68
Air bubbles, in sea ice, 87–88, 137
Air–sea–ice interactions
  large-scale, 32–33
  marginal ice zone, 4–5
  pack ice, 3–4
  wind stress, 5–6
Air–sea interactions
  AIDJEX, 17–19
  Antarctic experiments, 19–20
  automatic weather stations project, 19–20
  katabatic wind effects, 19
  MIZEX, 20–23
Air–surface temperature difference, 15
Albedo
  for different ice types and cloud covers, table, 42
  effect on radiative fluxes, 41
  sea ice, 49
    Antarctic, 58
    Arctic, 51
Algae, in sea ice, 87–88
Antarctica, *see* Antarctic region
Antarctic Circumpolar Current, 63, 183–184
  frontal system associated with, 244–246
Antarctic Coastal Current, 184–185
Antarctic Polar Frontal zone, 245
Antarctic region
  automatic weather stations project, 19–20
  bottom-water formation, 361
  experiments in, 19–20
  ice index for, 155–156
  katabatic winds, 19
  open water during winter, 66
  satellite passive-microwave data on, 153
  sea ice
    extent of, 76
    growth and decay, 57–59
    morphology, 68–71
    thickness distribution, 73–75
    zonation, 77
Arctic basin, sea ice
  circulation, 61–63
  extent, 75–76
  morphology, 68–71
  residence times for floes, 63
  thickness distribution, 72–73
Arctic Cyclone Experiment, 20
  heat fluxes downstream from ice edge in a cold-air outbreak, 40
Arctic Ice Dynamics Joint Experiment (AIDJEX), 155
  interfacial stress and relative ice drift measurements, 319
  mesoscale eddies in western Arctic Ocean, 262–263
  surface stress measurements, 16

Arctic Ocean
AIDJEX, 16, 155, 262–263, 319
bathymetry, 173
circulation models, large-scale, 358–360
convection in, 207
current systems
Beaufort Gyre, 181–182
Bering Strait exchange, 180
East Greenland Current, 179–180
Fram Strait exchange, 178–180
surface currents, 180–182
Transpolar Drift, 180–181
undercurrents, 182–183
West Spitsbergen Current, 178–179
deep-water formation, 207
eddies
formation offshore, 264
seaward of shelf break, 262–263
geographic nomenclature for, 174
halocline ventilation, 202–205
hydrology, 175–176
ice cover, *see* Sea ice
mesoscale features, 227–229
sea ice, *see* Sea ice
submesoscale coherent vortices, 263–264
volumetric comparison with Southern Ocean, 195–198
water masses, T–S scheme, 185–190
Arctic shelf waters, 188–189
Arctic surface layer, 186–187
Arctic surface water, 186
Atlantic layer, 187–188
Atlantic water, 186
Canada Basin deep water, 188
deep waters, 188
Eurasian Basin deep water, 188
Greenland Sea deep water, 188
lower Arctic intermediate water, 188
Norwegian Sea deep water, 188
polar intermediate water, 188
polar water, 186
upper Arctic intermediate water, 188
Arctic region
AIDJEX, 155
deep-water formation, 207
floe motion, SAR data, 161
ice pack, SAR data, 161
MIZEX, 157
open water during winter, 66
satellite passive-microwave data on, 153
stratification, one-dimensional predictions, 376
Arctic shelf/estuary systems, 198–201
Arctic shelf waters
distribution, 188–190
T–S scheme, 190
Atmosphere, large-scale modeling, 33
Automatic weather stations project, 19–20
Average received power, for radar, 133
Averaging correlations, effect on drag coefficients, 35
AVHRR, *see* Advanced Very High Resolution Radiometer (NOAA 9/10)

Backscatter cross sections, 133
first-year ice, 138–139
contrast reversals, 144
seasonal variations, 144
frequency and incidence angle effects on ice type and water signatures, 139–141
ice roughness effects, 139
in situ observations, 161
instrumentations, ground-based and helicopter-mounted, 161
Kirchoff approximations for rough-surface scattering, 148–149
modeling, 147–151
multiyear ice, 138–139
contrast reversals, 144
seasonal variations, 144
surface scattering, 148
volume scattering, 148
Barents Sea
ice margin simulation, 364
sea ice
extent of, 75, 77
rafted pancake, 59
salinity/thickness relationship, 93
Baroclinic behavior, eddies and fronts, 226
Baroclinic instability, 226
Baroclinicity, effect on drag coefficients, 35
Barotropic behavior, eddies and fronts, 226
Barotropic instability, 226
Bathymetry
Arctic Ocean, 173
Southern Ocean, 173
Beaufort Sea
AIDJEX, 17–19

Beaufort Sea Gyre, 61–62
frontal systems, 238
sea ice
c-axis orientation, 97
ice pack, SAR data, 161
salinity/thickness relationship, 93
shorefast ice, 85
temperature vs salinity and buoyancy frequency vs salinity, 204
Beaufort Sea Gyre
circulation pattern, 61–62, 181–182
simulated drift pattern, 339
Bering Sea
coastal polynyas in, 275–276
frontal systems, 238–241
ice edge
simulations, 373–375
upwelling, 273
ice edge front, 240–242
heat fluxes, 241, 271
seasonal variation, 240–242
ice extent, interannual variability, 4
MIZEX, 20
pigment distribution, 152
polynyas, 66
structural front in, 230, 239
Biological activity
spaceborne sensors for, table, 128
visible and infrared sensors for, 129
Blue ice, 52
Bottom features, mesoscale activity and, 228
Bottom waters, *see also* Deep waters
production, 205–209
in the Greenland Sea, 207
modeling, 361
near-boundary and open-ocean convection, 205–207
Northern hemisphere, 207
simulation, Greenland Sea, 368, 370
Southern hemisphere, 208–209
in Weddell Sea, 208–209
Southern Ocean, T–S schemes
Antarctic, 192
Ross Sea, 193
Weddell Sea, 192–193
Boundary layers
planetary
Arctic Ice Dynamics Joint Experiment, 17–19
atmospheric, linked atmospheric–oceanic Ekman spiral velocities, 6–8
Ekman layer, 6–12
MIZEX, 20–23
modeling, 23–24
geostrophic drag coefficient, 25
numerical, 28–30
similarity, 25–28
oceanic
bottomed by a pycnocline, 8
linked atmospheric–oceanic Ekman spiral velocities, 6–8
parameters and definitions, table, 11
turbulence in, 10
velocity profile in, 6–8
winds in, 6–7
under-ice rotational
advective term, 291–293
measurements from, 310–314
Reynolds stress, 292–293, 317–318
surface layer profile measurements, 316–317
total transport in, 318
turbulent processes, 296–298
heuristic model for, 302–309
scales governing, 298–302
Bowen ratio, 39
Bransfield Strait, open-ocean convection, 206
Brewster angle effects, 137
Brightness temperature
sea ice, 145–147
seasonal variations, 146–147
Brine
effects on electromagnetic wave penetration, 135
in sea ice, 81, 87–88
explusion, 90
flushing, 90–91
gravity drainage, 90
mass salt initially trapped as, 88
pockets, migration, 90
removal mechanisms, 89–90
seasonal variation, 88
volume, calculation, 88
Bulk parametrizations
ice–ocean models with, 376–378
for mixing processes, 373
Buoyancy
effect on length scale of turbulence in the RBL, 299–300

flux
expression for, 300
at ice-ocean interface, 324-327
sources of, in ice-covered RBL, 300

Cabbeling instability, in Southern Ocean, 361
Canadian Archipelago
ice extent, 75
ice thickness, 72
polynyas, 276-277
North Water, 276-277
Penny Strait, 278
Terra Nova, 277
shear zones, 77
shorefast ice, 77
Centripetal acceleration, 293-294
Chimneys
bottom-water formation and, 368
as mesoscale phenomena, 272
modeling, 375
Weddell Gyre
heat loss from deep water in, 209
vertical distribution of temperature, 268, 272
Chlorophyll *a*, remote sensing, 151
Chukchi Sea
coastal current, 239-240
frontal systems, 238-243
ice edge front, 242-243
heat fluxes, 271
sea ice, *c*-axis orientation, 97
shorefast ice, 85
Circulation
large-scale
Arctic Ocean current systems
Beaufort Gyre, 181-182
Bering Strait exchange, 180
East Greenland Current, 179-180
Fram Strait exchange, 178-180
surface currents, 180-182
Transpolar Drift, 180-181
undercurrents, 182-183
West Spitsbergen Current, 178-179
Southern Ocean current systems
Antarctic Circumpolar Current, 183-184
Antarctic Coastal Current, 184-185
Weddell Gyre, 185
Weddell-Scotia Confluence, 185
ocean, models for
large-scale, 358-360
process studies, 360-362
sea ice
Antarctic, 63-65
Arctic, 61-62
Beaufort Sea Gyre, 61-62
Transpolar Drift Stream, 61-62
thermohaline
Arctic shelf/estuary systems, 198-201
deep- and bottom-water production, 205-209
halocline ventilation, 202-205
Closure problem, of turbulence, 298
Clouds, effect on radiative processes, 41
Coastal Zone Color Scanner (Nimbus-7), 151-152
Color algorithms, 152
Color sensors, 151-152
Congelation growth, sea ice
Arctic region, 79-81, 83
columnar, 79-81, 83
Weddell Sea, 115
Conservation equations, 291-292
Constitutional supercooling, sea ice, 81
Constitutive law, for sea ice, 338-342
Continental margins, mesoscale activity and, 228
Continuity equations
ice motion, 337-338
oceanic flow, 291
Contrast reversals, between first-year and multiyear ice, 144, 154
Convection
Arctic Ocean, 207
deep
modeling, 370, 375-376
Weddell Sea polynyas, 375-376
Greenland Sea, 207
ingredients, 205
near-boundary and open-ocean, 205-207
Southern Ocean, 208-209
Weddell Gyre, 208-209
Weddell Sea polynyas, modeling, 375-376
Coriolis acceleration, 293-294
Coriolis force, effect on planetary boundary layer dynamics, 35
Crystalline structure, sea ice, 97
Antarctic, 107-115
Arctic, 100-107
c-axis orientation, 97-100

Current systems
  Arctic Ocean
    Beaufort Gyre, 181–182
    Bering Strait exchange, 180
    East Greenland Current, 179–180
    Fram Strait exchange, 178–180
    surface currents, 180–182
    Transpolar Drift, 180–181
    undercurrents, 182–183
    West Spitsbergen Current, 178–179
  barotropic, 226
  frontal systems associated with, 228
  mesoscale, long-period fluctuations, 226
  Southern Ocean
    Antarctic Circumpolar Current, 183–184
    Antarctic Coastal Current, 184–185
    Weddell Gyre, 185
    Weddell–Scotia Confluence, 185

Deep convection
  modeling, 370, 375–376
  in Weddell Sea polynyas, 375–376
Deep waters, *see also* Bottom waters
  Arctic Ocean, T–S schemes
    Canada Basin, 188
    Eurasian Basin, 188
    Greenland Sea, 188
    Norwegian Sea, 188
  North Atlantic, 191–192
  production, 205–209
    Greenland Sea, 207
    near-boundary and open-ocean convection, 205–207
    Northern hemisphere, 207
    Southern hemisphere, 208–209
  Southern Ocean, T–S schemes
    circumpolar, 191
    Weddell Sea, 192
Deformation, sea ice, 66–71
Density, calculation, 295
Density fields, frontal systems, 229
Desalination, sea ice
  effects on structural properties, 82
  temperature effects, 88
Dissipation method, for surface stress measurement, 16
Drag coefficients, 33–37
  buoyancy flux at ice–ocean interface, 324–327
  conversion to roughness length, 321–322
  dimensional analysis-derived, 14
  effects of
    averaging, 35
    baroclinicity, 35
    inversions, 35
    latitude, 35
    local nonequilibrium, 35
    roughness, 34–35
    stratification, 34
    surface temperature magnitude and humidity, 35
    wind magnitude, 35
  heat flux coefficients and, 39
  ice–ocean stress measurements
    combination methods, 318
    direct Reynolds stress, 317–318
    force balance method, 318–320
    log profile method, 316–317
    momentum integral methods, 318
  interfacial stress components, 316
  internal wave drag, 327–330
  momentum flux from internal waves, 316, 327–330
  skin friction, 316
  under-ice roughness effects, 314–322
Drainage, brine from sea ice, 90
Drake Passage–Scotia Sea
  eddy systems, 265–267
  frontal system, 244–246
Drift rates
  Antarctic sea ice, 63, 65
  Arctic sea ice, 61–63
Dynamic instabilities, 226
Dynamic models, sea ice, 337–342
Dynamic–thermodynamic models, sea ice, 351–357

East Greenland Current, 178–180
  branches of, 179
  dynamical forcing, 179–180
  large-scale fully coupled ice–ocean models, 363–364
  pack ice advected with, 235–236
  transport estimates, 179, 231–233
East Greenland Polar Front, 230
  advection of eddies into, 256
  currents, 233
  dynamic instability, 254
  eddy fields, 252, 254

mesoscale heat transfer across, 269
subsurface temperature structures, 233–235
temperature and salinity
vertical distributions, 232
vertical profiles, 235
time scale, 225
East Wind Drift, 63
Eddies
analytical models, 251
Antarctic, 264–269
Arctic
eastern, 252–261
western, 261–264
baroclinic behavior, 226
barotropic behavior, 226
detection, 251
distribution, 250–251
Drake Passage–Scotia Sea, 265–267
Fram Strait, 252–256
generation, 263–264
generation mechanisms, 228, 251, 259–261
Greenland Sea, 251
heat flux coefficients, 14
horizontal scale, 224
Labrador Sea, 261
large-eddy-simulation model, 298
lateral fluxes, 269–272
marginal ice zone, 261
mesoscale, 250–269
Molley Deep-associated, 257–260
numerical modeling, 251, 256
remote sensing, 251
seaward of shelf break in Arctic Ocean, 262
shelf regions, 261–262
spaceborne sensors for, table, 128
submesoscale coherent vortices, 263–264
theoretical model for, 264
time scale, 225
vertical fluxes, 272–273
viscosity, 10
Weddell Sea, 267–269
Eddy correlation formula
computation of lateral heat flux via, 269
cross-frontal heat for Bering Sea ice edge front, 271
for surface stress, 15
Eddy diffusivity, expression for, 297–298
Ekman layer, atmospheric, 6–12
classical solution, 10–12
similarity modeling, 25–28
Electrically Scanning Microwave Radiometer (Nimbus-5), ice distribution in Arctic and Antarctic regions, 153
Electromagnetic waves, penetration depth, 135, 137, 144–145
Emissivity
Brewster angle effects, 137
calculation, 133–135
first-year ice, 137, 139
multiyear ice, 137, 139, 151
sea ice, modeling, 149, 151
Energy balance, at ice–water interface, 49, 53
Equatorward boundaries, mesoscale activity near, 228–229
ESMR, *see* Electrically Scanning Microwave Radiometer (Nimbus-5)
Estuarine circulation, Arctic Ocean, 198–201
Expansion coefficients, salinity and temperature, 295–296
Expulsion, brine from sea ice, 90

Fast ice, *see* Shorefast ice
First-year ice
active microwave backscatter, 138–139
backscatter cross sections
contrast reversals, 144
seasonal variations, 144
cross-sectional view, 142
definition, 48
geometry, for theoretical penetration models, 137–138
internal scatterers, 137
microwave emissivity, 137, 139
microwave signature, 135
passive microwave return, modeling, 149
penetration depth of electromagnetic waves, 137
Flow fluctuations, *see* Fluctuations, flow
Fluctuations, flow
long-period, of mesoscale currents, 226
mechanisms of, 226–227
Flushing, brine from sea ice, 90
Force balance, on sea ice, 59–64
Force balance method, for ice–ocean stress determination, 318–320
Form drag, 316

Fram Strait
AVHRR data, 157
East Greenland Current, 179–180
exchange of water in, 178–180
mesoscale eddies, 252–256
ice distribution along summer ice zone, 253
instability mechanisms, 254–255
origins, 254–255
MIZEX data, 252
ocean circulation and frontal structure, 231
oceanic heat flux, 53
recirculation of Atlantic waters, 178–179
sea ice
brightness temperature, 145–147
crystalline structure, 100–107
drift pattern, 234
exiting via, structure, 85
floes, 63
pancake ice, 80
salinity profiles of first-year and multiyear ice cores, 94
salinity/thickness relationship, 93
snow pack, 144–145
snow thicknesses on floes in, 55
West Spitsbergen Current, 178–179
Frazil, 83–84
Antarctic region, 59, 84–85
Arctic region, 84–85
episodic formation, 107
floes in Fram Strait, 104
formation, 79, 111–112
Weddell Sea ice, 107
Free drift, 338
Freezing point
seawater, 78–79
UNESCO formula for saline water, 296
Freshwater inputs, *see also* River inflow
to world ocean, 175
Friction velocity scale, 298–299
Frontal systems
Antarctic, 243–247
Antarctic Polar Frontal zone, 245
Drake Passage–Scotia Sea, 244–246
Scotia front, 244
Weddell front, 244, 246–247
Weddell–Scotia Confluence, 244, 246–247
Arctic
eastern, 230–238
East Greenland Current-associated, 231–233
East Greenland Polar Front, 225, 230, 233–235
Labrador Sea, 237–238
West Spitsbergen Current-associated, 236
western, 238–243
Bering Sea winter ice edge, 240–242
marginal ice zone-associated, 240
northward flow-associated, 239
seaward of summer baroclinic coastal currents, 239–240
structural, 238–239
types in, 238–239
baroclinic behavior, 226
barotropic behavior, 226
central Polar basin, 247–250
horizontal scales for, 248
northeast-oriented density front, 247–248
Ross Sea-associated, 248
Weddell Sea-associated, 248, 250
currents associated with, 228
density fields, 229
ice edge, 229–230
marginal ice zone-associated, 228
occurrence, 230
permanent oceanic, 228
salinity, lateral and vertical gradients, 229
spaceborne sensors for, table, 128
structural, 230
temperature, lateral and vertical gradients, 229
time scales, 225
along water masses, 230

GCMs, *see* General circulation models
General circulation models
air–ice–sea interaction, 33
for large-scale modeling of polar-region atmosphere, 33
sea ice conditions and, 33
Geosat ice index, 155
Geostrophic current, equation for, 294
Geostrophic drag coefficient model, for surface stress, 25
Geostrophic wind
pack ice velocity and, 25

prediction of sea ice drift with, 61
Gravity drainage, brine from sea ice, 90
Grease ice, 79
Greenland
ice thickness north of, 72
latent-heat polynya off northeastern coast, 275–276
polynyas, 66
Greenland Sea
active lidar system, 152
bottom-water formation, simulation, 368, 370
deep-water formation, 207
mesoscale eddies, 251
MIZEX, 20, 252
Odden area, satellite passive-microwave data, 154
open-ocean convection, 205
sea ice
concentration, SMMR data, 153
extent of
interannual variability, 4
seasonal variation, 75
ice edge upwelling, 273
ice margin, simulation, 364
salinity/thickness relationship, 93
shorefast ice along fiords, 77

Halocline
formation, 201–202
maintenance by shelf/estuarine processes, 203–205
structure, mechanisms for, 203
ventilation, 199, 202–205
Heat conduction, *see also* Heat fluxes
sea ice
away from bottom toward surface, 49, 53
at upper surface, 49, 52
Heat flux coefficients, 37–40
Bowen ratio, 39
drag coefficients and, 39
seasonal variation, 38
sensible, 37
stratification effects, 39
wind speed effects, 39
Heat fluxes, *see also* Heat conduction
at ice–ocean interface, 322–327
sea ice
conducted at upper surface, 49, 52
conducted away from bottom to surface, 49, 53
latent, 49, 51–52
oceanic
Antarctic, 57–58
Arctic, 53
effect on equilibrium thickness, 53–54
sensible, 49, 51–52
turbulent, 51–52, 57
in thermodynamic ice models, 343–351
Heat loss, from sea ice, melting- or sublimation-related, 49, 52
Heat transfer, mesoscale, 269–272
across East Greenland Polar Front, 269
computation via the eddy correlation formula, 269
in marginal ice zone eddies, 269–270
marginal ice zone frontal systems
Bering Sea, 271
Chukchi Sea, 271
Drake Passage, 271–272
Labrador Sea, 269–270
Humidity, effect on drag coefficients, 35
Hydrology
Arctic Ocean, 175–176
Southern Ocean, 176

Ice edge
fronts, 229–230
Bering Sea, 240–242
Chukchi Sea, 242–243
Labrador Sea, 270–271
Weddell Sea, 248, 250
marginal ice zone, *see* Marginal ice zone
simulations, Bering Sea, 373–375
upwelling
modeling, 367–368
upward transport and, 272–273
Ice index, 155
Ice–ocean interface, heat and mass flux at, 322–327
Ice–ocean models, 362–363, 375–379
large-scale fully coupled, 363–365
mesoscale, 365–375
Ice–ocean stress
determination
combination methods, 318
direct Reynolds stress, 317–318

force balance method, 318–320
log profile method, 316–317
momentum integral methods, 318
form drag, 316
momentum flux from internal waves, 316, 327–330
roughness lengths, 321–322
skin friction, 316
Ice sheets
deformation, 67–68
entrainment of sediment in, 87
evolution during summer
first-year ice cross-section, 142
multiyear ice cross-section, 143
formation, 79
structure, 81, 83
Infrared remote sensors, 124–125, 151–152, 163
Instability theory, 226–227
Instantaneous field of view, 129
Integral radar equation for distributed targets, 133
Intermediate waters, T–S schemes
lower Arctic, 188
polar, 188
upper Arctic, 188
Internal waves
drag from, 327–330
spaceborne sensors for, table, 128
Inversions, temperature, effect on drag coefficients, 35

Kara Sea, sea ice, *c*-axis orientation, 97, 99
Katabatic winds, in air–sea–ice interactions, 19
Keel, of deforming ice, 67–68
Kinematic stress, scale for, 299
Kirchoff approximations, for rough-surface scattering, 148–149
Kotzebue Sound, sea ice, *c*-axis orientation, 98–99

Labrador Sea
frontal systems, 237–238, 270–271
ice edge fronts, heat fluxes, 270–271
ice extent, 76–77
marginal ice zone eddies, 261
meanders, evolution with time, 237
open-ocean convection, 205
Langmuir circulations, 6
Large-eddy-simulation model, 298
Large-scale circulation
Arctic Ocean current systems
Beaufort Gyre, 181–182
Bering Strait exchange, 180
East Greenland Current, 179–180
Fram Strait exchange, 178–180
surface currents, 180–182
Transpolar Drift, 180–181
undercurrents, 182–183
West Spitsbergen Current, 178–179
Southern Ocean current systems
Antarctic Circumpolar Current, 183–184
Antarctic Coastal Current, 184–185
Weddell Gyre, 185
Weddell–Scotia Confluence, 185
thermohaline
Arctic shelf/estuary systems, 198–201
deep- and bottom-water production, 205–209
Northern hemisphere, 207
Southern hemisphere, 208–209
halocline ventilation, 202–205
Large-scale interactions
GCMs, 33
ice edge record and, 32
surface pressure maps and, 25, 32
Large-scale modeling
fully coupled ice–ocean interaction, 363–365
GCMs, 33
ice edge record and, 32
ocean circulation, 358–360
surface pressure maps and, 32
Laser profiles, sea ice surface topography, 68
Latent heat flux, 49, 51–52
Latent-heat polynyas, 274–277
Lateral fluxes, frontal and eddy-associated, 269–272
Latitude, effect on planetary boundary layer dynamics, 35
Law of the wall, 299
Leads
in sea ice, 65–66
spaceborne sensors for, table, 127
Length scale, for vertical exchange, 299–300

Local nonequilibrium, effect on drag coefficients, 35
Log profile method, for ice–ocean stress determination, 316–317
Lomonosov Ridge Experiment (LOREX), 247
Longwave radiation
  emitted by ice surface, 49–51
  incoming, 49–51

Marginal ice zone, 4–5
  Arctic Cyclone Experiment, 20
  drag coefficients, 20, 34–35
  dynamic processes, SAR data, 157–159
  Fram Strait, summer ice distribution along, 253
  frontal activity, 228, 240
  heat fluxes over, 39–40, 269–270
    in the Bering Sea, 271
    in the Chukchi Sea, 271
    in the Labrador Sea, 269–270
  mesoscale eddies
    eastern Arctic, 252, 261
    Labrador Sea, 261
  modeling, 349–351, 365–373
  surface waves, 160–161
Marginal Ice Zone Experiments (MIZEX), 20–23, 156
  AVHRR data, 157
  heat and mass balance studies, 327
  mesoscale processes in Greenland Sea, 252
  salinity profiles of first-year and multiyear ice, 93–94
Mass fluxes, at ice–ocean interface, 322–327
McMurdo Sound
  sea ice
    platelet ice, 115
    salinity, 96
  shorefast ice, 77
Meanders
  evolution with time, Labrador Sea, 237
  horizontal scales, 224–225
  ice edge, 160
  modeling, 368
Melting, sea ice, 49, 52
  Antarctic, 58
  Arctic, 56–57
Melt ponds, 56–57
Melt pools, 139
Mesoscale processes
  Arctic Ocean eastern basin, 229
  baroclinic behavior, 226
  baroclinic instability, 226
  barotropic behavior, 226
  barotropic instability, 226
  bottom topographic features and, 228
  continental margins and, 228
  distribution, large-scale, 227–229
  dynamic instabilities, 226–227
  eddies, *see* Eddies
  fluctuations, long-period, 226
  fronts, *see* Frontal systems
  horizontal scales, 224–225
  ice–ocean models, 365–375
  minimum length scale, 225
  near equatorward boundaries, 228
  in permanently ice-covered regions, 229
  radius of deformation
    definition, 225
    external, 225–226
    internal, 226
  time scales, 225
Microwave imaging
  algorithms using active- and passive-microwave data, 154–155
  average received power, 133
  backscatter cross sections
    first-year and multiyear ice, 138–139
    frequency and incidence angle effects on ice type and water signatures, 139–141
    ice roughness effects, 139
  Brewster angle effects, 137
  dielectric constant, 135
  electromagnetic spectrum, 125
  emissivity
    calculation, 133–135
    first-year ice, 137, 139
    multiyear ice, 137, 139
  integral radar equation for distributed targets, 133
  Microwave Scanning Radiometer
    parameters measured, table, 131
    swath, resolution, and revisit time/day, table, 131
  planetary boundary layer parameters, 30–31
  radar altimeters
    parameters measured, table, 130

swath, resolution, and revisit time/day, table, 130
radar scattering coefficient, 133
radiometers, 133–135
satellite sea data sources, table, 130–131
signatures of first-year and multiyear ice, 135, 137, 144
Special Scanning Microwave Imager
parameters measured, table, 130
swath, resolution, and revisit time/day, table, 130
synthetic-aperture radar
parameters measured, table, 131
swath, resolution, and revisit time/day, table, 131
Microwave Scanning Radiometer (MOS-1)
parameters measured, table, 131
swath, resolution, and revisit time/day, table, 131
Microwave signatures
first-year ice, 135
modeling of passive microwave return, 149
multiyear ice, 135, 137
during summer
first-year ice, 144
multiyear ice, 144
Mid Ocean Dynamics Experiments (MODE, POLYMODE), 250
Mixing-length hypothesis, 297–298
length scale for vertical exchange and, 299–301
Mixing processes
bulk parametrization for, 373
effect on vertical fluxes, 272–273
mesoscale, vertical, 272–273
second-moment turbulence closure model, 373
MIZEX experiments, *see* Marginal Ice Zone experiments
Models and modeling
coastal polynyas, wind-driven, 274
coupled ice–ocean, 362–363
large-scale, 363–365
mesoscale, 365–375
eddy formation
near Molley Deep, 260
offshore in Arctic Ocean, 264
general circulation, 33
geostrophic drag coefficient, 25
large-eddy-simulation, 298
large-scale
fully coupled ice–ocean interaction, 363–365
GCMs, 33
ice edge record and, 32
ocean circulation, 358–360
surface pressure maps and, 32
mesoscale eddies, 251, 256
methods, 23–30
numerical modeling, 28–30
ocean, 357–358
large-scale circulation, 358–360
process studies, 360–362
planetary boundary layer, 23–24
geostrophic drag coefficient method, 25
numerical method, 28–30
similarity method, 25–28
radar backscatter from sea ice, 147–151
river inflow effects on water column structure, 200–201
sea ice, 335–337
coupled ice–ocean, 375–379
dynamic, 337–342
dynamic–thermodynamic, 351–357
ridge distribution, 71
thermodynamic, 342–351
similarity modeling, 25–28
turbulent flux in the RBL, 302–309
upwelling, 273
Molley Deep eddy, 257–260
detection, 257–258
generation, 259–261
horizontal dimensions, 258–259
Momentum balance, sea ice, 59–64
Momentum equations
for ice motion, 337–338
for oceanic flow, 292
Momentum flux, from internal waves, 316, 327–330
Momentum integral methods
ice–ocean stress determination, 318
for surface stress measurement, 16–17
Monin–Obukhov length, 15
Morphology, sea-ice, large-scale, 65–71
Multispectral Electronic Self-Scanning Radiometer (MOS-1), 131
Multispectral Scanner (Landsat), 130
Multispectral Scanner (Spot), 130
Multiyear ice
active microwave backscatter, 138–139

air bubbles in, 137
backscatter cross sections
contrast reversals, 144
seasonal variations, 144
cross-sectional view, 143
definition, 48
emissivity, 137, 139
modeling, 151
geometry, for theoretical penetration models, 137–138
microwave signature, 135
seasonal variations in, 137
during summer, 144
passive microwave return, modeling, 149
penetration depth of electromagnetic waves, 137

Net radiation
incoming and outgoing longwave, 50–51
solar, 50
total, 50–51
North Atlantic deep water, 191–192
North Atlantic ice concentration, SMMR data, 153
North Pole, ice thickness, 72
North Water polynya, 276–277
Norwegian Sea, sea ice extent, 77
Numerical modeling, planetary boundary layer, 28–30

Obukhov length, 300–301
Ocean color, 151–152
Ocean height, radar altimetry, 155
Oceanic heat flux
Antarctic, 57–58
Arctic, 53
effect on sea ice equilibrium thickness, 53–54
Ocean models
coupled ice–ocean, 362–363, 375–379
large-scale circulation, 358–360
large-scale fully-coupled ice–ocean, 363–365
mesoscale ice–ocean, 365–375
process studies, 360–362
Optical Line Scanner (DMSP), 130
Optical properties, polar atmospheres and surfaces, 41
Optical sensors
information provided by, 163
resolution, 129
Oxygen concentrations, water masses in Arctic Mediterranean and Southern Ocean, 197, 199

Pack ice, 3–4
advected with East Greenland Current, 235–236
Beaufort Sea, SAR data, 161
motion
Ekman's solution, 6
satellite data, 31
velocity, geostrophic wind and, 25
Pancake ice
formation, 79
rafted, 58–59
Penetration depth
electromagnetic waves, 135, 137
snow effects, 145
Penny Strait polynya, 278
Planetary boundary layer
AIDJEX, 17–19
Ekman layer, 6–12
linked atmospheric–oceanic Ekman spiral velocities, 6–8
MIZEX, 20–23
modeling, 23–24
geostrophic drag coefficient, 25
numerical, 28–30
similarity, 25–28
oceanic
bottomed by a pycnocline, 8
linked atmospheric–oceanic Ekman spiral velocities, 6–8
parameters and definitions, table, 11
turbulence in, 10
velocity profile in, 6–8
winds in, 6–7
Polar basin, frontal structures in, 247–250
Polarization ratio, for sea ice concentration, 153–154
Polynyas
characterization, 273–274
formation, 274
latent-heat, 274–277
morphology, 65–66
sensible-heat, 277–279

Weddell
deep-water renewal in, 209
formation, 66
Porosity parameter, for sea ice, 88
Probability density function, sea ice, 72–73
Profile method, for surface stress measurement, 13, 16–17
Prudhoe Bay, sea ice salinity, 96

Quasi-geostrophic eddies, *see* Eddies, mesoscale

Radar
average received power, 133
integral equation for distributed targets, 133
scattering coefficient, 133
Radar Altimeter (ESA ERS-1), 131
Radar Altimeter (GEOSAT), 131
Radar altimeters, 163
ice index, 155
ocean height measurements, 155
parameters measured, table, 130
shape of return pulse, 155
swath, resolution, and revisit time/day, table, 130
Radiation
exchanges, parametrization, 40–42
longwave
emitted by ice surface, 49–51
incoming, 49–51
net
incoming and outgoing longwave, 50–51
solar, 50
total, 50–51
shortwave
Antarctic, 57
Arctic, 53, 57
flux passing through to ice interior, 49, 52, 57
incoming, 49–50
Radiative fluxes, 49–51
parametrization, 40–42
in thermodynamic ice models, 343–351
Radiometers, emissivity calculation, 133–135
Radius of deformation
definition, 225
external, 225–226
internal, 226
Rafted pancakes, 58–59
RBL, *see* Rotational boundary layer
Real-aperture radar, 124
resolution, 125, 129
Regional variations, sea ice morphology, 68
Remote sensing
algorithms
for sea ice type and concentration, 157
using active- and passive-microwave data, 154–155
backscatter information, 161
forces affecting ice floe drift, 160
ice concentration
in situ observations vs airborne data, 154
satellite passive-microwave data, 153–155
ice distribution
satellite passive-microwave data, 153–154
seasonal variations, 154
ice drift kinematic data, 160–161
ice index, 155–156
in situ observations and, 161
meandering ice edges, 160
mesoscale eddies, 251
MIZEX program, 157
ocean height, 155
planetary boundary layer parameters, 30–31
sled-based scatterometers and, 161
surface waves, 160–161
synthetic-aperture radar images, 157–159
Remote sensors
active, 124
high resolution vs swath width coverage, 163, 166
infrared, 124–125, 151–152, 163
microwave, *see* Microwave imaging
optimum instrumentation for polar oceanography, 129
passive, 124, 151–152, 163
planned missions for polar information, table, 164–165
real-aperture radars, 124–125, 129
resolution, 125, 129
satellite sea ice data sources, table, 130–131

spaceborne, available for observations, table, 126–128
synthetic-aperture radar, *see* Synthetic-aperture radar
visible, 124–125, 151–152, 163
wavelengths for, 124–125
Residence times
ice floes in Arctic basin, 63
sea ice in Weddell Sea, 63, 65
water masses in Arctic Mediterranean and Southern Ocean, 197, 201
Resolution
instantaneous field of view, 129
optical sensors, 129
real-aperture radar, 125, 129
remote sensors, 125, 129
synthetic-aperture radar, 129
Return Atlantic Current, 231
Reynolds stress, 292–293
direct measurement, 317–318
Richardson number, 14
Ridges, sea ice, 67–68
Antarctic, 68, 71
Arctic, 68
distribution, statistical models, 71
Ross Sea, 71
River inflow, *see also* Freshwater inputs
effect on
ice cover, modeling, 365
water column structure, 200–201
over Arctic shelves, 198–201
Rossby radius of deformation, *see* Radius of deformation
Ross Ice Shelf, sea ice accretion, 77–78
Ross Sea
automatic weather stations project, 19–20
bottom water, T–S scheme, 193
frontal structures, 248
ice circulation in, 63
near-boundary convection, 205
ridging in, 71
salinity gradients, modeling, 362
Rotational boundary layer
advective term, 291
Reynolds stress, 292–293
turbulent processes
heuristic model for, 302–309
under-ice, 296–302
Roughness
Kirchoff approximations for rough-surface scattering, 148–149
sea ice surface
effect on
backscatter signature, 139
drag coefficients, 34–35
morphology, 66–71
under-ice
buoyancy flux at ice–ocean interface, 324–327
drag coefficients and, 314–322
ice–ocean stress measurements
combination methods, 318
direct Reynolds stress, 317–318
force balance method, 318–320
log-profile method, 316–317
momentum integral methods, 318
morphology, 67–68
Roughness lengths
conversion of drag coefficients to, 321–322
undersurface, 321–322
Rubble fields, of sea ice, 67–68

Sail, of deforming ice, 67–68
Salinity
East Greenland Polar Front
vertical distributions, 232
vertical profiles, 235
expansion coefficient, 295–296
frontal systems, lateral and vertical gradients, 229
Molley Deep eddy, vertical distribution, 259
sea ice, 88–91
bulk, 79, 88
effects on thermal conductivity, 52–53
thickness/salinity relationship, 92–93
Southern Ocean mixed-layer, simulation, 377–378
Weddell Sea
surface distribution from Scotia Sea to, 246
vertical distribution along summer ice edge, 249
Salinity–temperature classifications, *see* Temperature–salinity classifications
Salt
balances at ice–ocean interface, 323–324
conservation equation, 292
content of sea ice, 87–88
distribution coefficient

for amount rejected into oceanic mixed layer, 91
for amount retained during freezing of sea ice, 91
initially trapped as brine, 88
SAR, *see* Synthetic-aperture radar
Satellites
planned missions for polar information, table, 164–165
remote sensors available for observing sea ice and ice-free ocean parameters, table, 126–128
sea ice data sources, table, 130–131
Satellite sensing, *see* Remote sensing
Scanning Multichannel Microwave Radiometer (Nimbus-7)
ice concentration
in Greenland Sea and North Atlantic, 153
in Weddell Sea, 154
ice distribution data, 154
sea ice brightness temperature measurements, 145–147
Scatterometers
measurement of planetary boundary layer parameters with, 30–31
sled-based, 161
Scotia front, 244
Scotia Sea, temperature, vertical distribution, 246
Sea ice
aging
changes during, 88–89
effect on electromagnetic wave penetraton, 135
albedo, 49
Antarctic, 58
Arctic, 51
algae in, 87–88
Arctic region
floe motion, SAR data, 161
ice pack, SAR data, 161
backscatter cross sections, modeling, 147–151
blue ice, 52
brightness temperature, 145–147
brine
distribution, 82
explusion mechanism, 90
flushing, 90–91
gravity drainage, 90
pockets, migration, 90
removal mechanisms, 89–90
sensitivity to temperature changes, 82
trapped, 81
c-axis orientation, 81, 83, 97–100, 105–106
circulation
Antarctic, 63–65
Arctic, 61–62
classification of, 48
columnar congelation growth, 79–81, 83
concentration
algorithm for calculation of, 153–155
calculation, 155
in constitutive laws, 341
dynamic–thermodynamic models, 351–357
in situ observations and airborne sensor data, 154
polarization ratio, 153–154
SAR data, 157
satellite passive-microwave data, 153
spaceborne sensors for, table, 126
conditions, GCMs and, 33
constitutional supercooling, 81
constitutive law, 338–342
cover
Arctic Ocean, 176–177
dynamic–thermodynamic models, 353–355
simulation
long-term, 355–357
seasonal variations, 348–349
Southern Ocean, 177
crystalline structure, 97–100
Antarctic, 107–115
Arctic, 100–107
platelike crystals, 114–115
retextured ice crystals, 104
decay
Antarctic, 57–59
Arctic, 49–57
large-scale, 49–59
thermodynamic models, 342–351
deformation, 67
depth, Southern Ocean, simulation, 377–378
desalination effects on structural properties, 82
distribution
satellite passive-microwave data, 153

seasonal variations, passive microwave sensing, 154
simulation, 365–366
distribution coefficients for salt, 91
drift, simulations, 338–342
emissivity, modeling, 149, 151
energy balance at ice–water interface, 49, 53
extent of, 75–78
Antarctic, 58, 76
Arctic, 75–76
Arctic Ocean, 76, 176–177
satellite passive-microwave data, 154
seasonal sea ice zone, 76–77
Southern Ocean, 177
spaceborne sensors for, table, 126
first-year
active microwave backscatter, 138–139
backscatter cross sections
contrast reversals, 144
seasonal variations, 144
cross-sectional view, 142
definition, 48
differentiation, 82–83
geometry, for theoretical penetration models, 137–138
internal scatterers, 137
microwave signature, 135
passive microwave return, modeling, 149
penetration depth of electromagnetic waves, 137, 144–145
floe size distributions, spaceborne sensors for, table, 127
force balance, 59–61
formation, initial, 79
frazil, 79, 83–84
Antarctic, 59
Arctic, 84
formation mechanisms, 111–112
granular vs columnar ice, 85
grease ice, 79
growth
Antarctic, 57–59
Arctic, 49–57
large-scale, 49–59
simulation, 365–366
small-scale, 78–88
thermodynamic models, 342–351
heat conduction
away from bottom toward surface, 49, 53
at upper surface, 49, 52
heat fluxes
conducted at upper surface, 49, 52
conducted away from bottom to surface, 49, 53
latent, 49, 51–52
oceanic
Antarctic, 57–58
Arctic, 53
effect on equilibrium thickness, 53–54
sensible, 49, 51–52
turbulent, 51–52, 57
heat loss from melting or sublimation, 49, 52
ice sheets
formation, 79
structure, 81, 83
inclusions, 87–88
keel, 67–68
kinematics, spaceborne sensors for, table, 127
laser profiles (airborne), 68
leads, 65–66
spaceborne sensors for, table, 127
longwave radiation
emitted by ice surface, 49–51
incoming, 49–51
melting, 49, 52
Antarctic, 58
Arctic, 56–57
melt pools, 139
mixed-layer depth, temperature, and salinity, simulation, 377–378
models, 335–337
coupled ice–ocean, 362–363, 375–379
large-scale, 363–365
mesoscale, 365–375
dynamic, 337–342
dynamic–thermodynamic, 351–357
thermodynamic, 342–351
momentum balance, 59–64
morphology, large-scale, 65–71
motion, momentum and continuity equations for, 337–338
multiyear
active microwave backscatter, 138–139
air bubbles in, 137
backscatter cross sections
contrast reversals, 144
seasonal variations, 144
cross-sectional view, 142
definition, 48

differentiation, 82–83
emissivity modeling, 151
geometry, for theoretical penetration models, 137–138
microwave signature, 135
passive microwave return, modeling, 149
penetration depth of electromagnetic waves, 137, 144–145
net radiation
incoming and outgoing longwave, 50–51
solar, 50
total, 50–51
pancake ice
formation, 79
rafted, Antarctic, 58–59
in Weddell Sea, 107
polynyas, 65–66
probability density function, 72–73
radiative fluxes, 49–51
remote sensing, *see* Remote sensing
residence times
floes in Arctic basin, 63
Weddell Sea, 63, 65
ridges, 67–68
roughness, 66–71
effect on backscatter cross sections, 139
rubble fields, 67–68
sail, 67–68
salinity, 88–91
Antarctic, 95–96
Arctic, 92–85, 92–95
bulk, 79
Southern Ocean, simulation, 377–378
satellite data sources, table, 130–131
sediment in, 87
shear zones, 77
shorefast ice, 77–78
shortwave (solar) radiation
Antarctic, 57
Arctic, 53, 57
flux passing through to ice interior, 49, 52, 57
incoming, 49–50
snow cover
Antarctic, 58
Arctic, 53–56
effects on remote sensing, 144–145
snow ice, 83–85
snowpack effects on backscatter signature, 139, 144
snow thicknesses, 55
sonar profiles, 68
structure
small-scale, 78–88
temperature effects, 82
sublimation, 52
surface temperature, modeling, 348–349
temperature profiles, 49–50
thermal conductivity, 52–53
thickness
Antarctic, 58–59
Arctic, 53–56
dynamic–thermodynamic models, 351–357
effect of oceanic heat fluxes, 53–54
modeling, 348, 350
salinity/thickness relationship, 92–93
simulation, Southern Ocean, 377–378
spaceborne sensors for, table, 126
thickness distribution, 71–75
spaceborne sensors for, table, 126
type
algorithm for calculation of, 153–155
effect on backscatter cross sections, 139
SAR data, 157
spaceborne sensors for, table, 126
spectral gradient ratio, 153
zonation
Antarctic, 76–78
Arctic, 75–78
Sea of Okhotsk
ice extent, 76–77
polynya in, 278–279
Seasonal sea ice zone, 76–77
Seasonal variations
circulation in an Arctic shelf estuary, 199, 202
heat fluxes, 38
sea ice
backscatter cross sections, first-year and multiyear ice, 144
Bering Sea ice edge, 240–242
brightness temperature, 146–147
distribution, passive microwave sensing, 154
drift, dynamic–thermodynamic models, 351–357
extent, 75–78
Antarctic, 58, 76
Arctic, 75–76
microwave signatures of multiyear ice, 137

morphology, 68
penetration depth of electromagnetic waves, 144–145
ridging in Ross Sea, 71
simulations, 348–349
SMMR data, 154
solar radiation, 50–51
Seawater
freezing point, 78–79
UNESCO formula for freezing point, 296
SeaWIFS, 151
Second-moment turbulence closure model, 373
Sensible heat flux, 49, 51–52
Sensible heat polynyas, 277–279
Shear zones, between fast and moving ice, 77
Shelf/estuary systems
Arctic, 198–201
halocline maintenance by, 203–205
Shelf regions, western Arctic, mesoscale eddies, 264
Shelf waters
Antarctic
deep ice shelf water, 195
distribution in Weddell Sea, 208
high-salinity, 194
ice shelf water, 195
low-salinity, 194
modification by melting of ice shelves, 208
T–S scheme, 193–195
warm core, 195
Arctic
distribution, 188–190
T–S scheme, 190
Shorefast ice, 77–78
Shortwave (solar) radiation
Antarctic, 57
Arctic, 53, 57
flux passing through to ice interior, 49, 52, 57
incoming, 49–50
Silicate content, water masses in Arctic Mediterranean and Southern Ocean, 197, 200
Similarity model, for the planetary boundary layer, 25–28
Skin friction, 316
SMMR, *see* Scanning Multichannel Microwave Radiometer (Nimbus-7)
Snow cover
Antarctic, 58
Arctic, 53–56
effects on remote sensing, 144–145
surface temperature, modeling, 348–349
Snow depth, effect on sea ice equilibrium thickness, 54–56
Snow ice, 83–85
Snowpack
effects on backscatter signature, 139, 144
evolution during summer
first-year ice cross-section, 142
multiyear ice cross-section, 143
Snow thickness, 55
Sonar profiles, sea ice, 68, 72
Southern Ocean
Antarctic Circumpolar Current, 63
bathymetry, 173
bottom-water formation, 208–209
cabbeling instability, 361
congelation growth in, 59
convection in, 208–209
current systems
Antarctic Circumpolar Current, 183–184
Antarctic Coastal Current, 184–185
Weddell Gyre, 185
Weddell–Scotia Confluence, 185
East Wind Drift, 63
geographic nomenclature for, 174
hydrology, 176
mesoscale features, 227–229
open-ocean convection in, 208–209
sea ice
circulation, 63
cover, 177
depth, simulation, 377–378
growth and decay, 57–59
seasonal equilibrium response, various parameters, simulation, 377–378
volumetric comparison with Arctic Mediterranean, 195–198
water masses, T–S scheme, 190–195
Antarctic bottom water, 192–193
Antarctic shelf waters, 193–195
Antarctic surface layer, 191
Antarctic surface water, 191
circumpolar deep water, 191
high-salinity shelf water, 194–195
ice shelf water, 195

low-salinity shelf water, 194–195
North Atlantic deep water, 191–192
Ross Sea bottom water, 193
transitional layers, 191
warm core shelf water, 195
Weddell deep water, 192
Weddell Sea bottom water, 192–193
winter water, 191
Special Scanning Microwave Imager
parameters measured, table, 130
swath, resolution, and revisit time/day, table, 130
Special Scanning Microwave Imager (DMSP), characterization and parameters measured by, 130
Spectral gradient ratio, for sea ice type, 153
SSM/I, *see* Special Scanning Microwave Imager
Statistical models, of sea ice ridge distribution, 71
Stratification, Arctic region, one-dimensional predictions, 376
Stratification effects
on drag coefficients, 34
on heat flux coefficients, 39
Stratification parameters, for ocean applications, 4–15
Stress
kinematic, scale for, 299
laws for ice, 338–342
surface, *see* Surface stress
Structural frontal systems, 230
in the western Arctic, 238–239
Submesoscale coherent vortices, 263–264
Surface Currents, in Arctic Ocean, 180–182
Surface layer, atmospheric, 12–15
flux coefficients, 13–15
Surface pressure maps, large-scale interactions and, 25, 32
Surface roughness, effect on drag coefficients, 34–35
Surface stress
measurement methods
AIDJEX, 16
aircraft observations, 16
dissipation method, 16
eddy correlation method, 15
momentum integral techniques, 16–17
from near-surface observations, 15–16
profile method, 13, 16–17
modeling methods, 23–24
geostrophic drag coefficient, 25
numerical, 28–30
similarity, 25–28
Surface temperature, magnitude, effect on drag coefficients, 35
Surface waters
Arctic Ocean, T–S schemes
Arctic surface layer, 186–187
Arctic surface water, 186
Atlantic water, 186
polar water, 186
Southern Ocean
Antarctic surface water, T–S scheme, 191
transitional layers, 191
winter water, T–S scheme, 191
Surface waves, effect on MIZ ice structure, 160
Synoptic eddies, *see* Eddies, mesoscale
Synthetic-aperture radar
algorithms, ice type and concentration, 157
data from, 157
dynamic processes in marginal ice zone, 157–159
parameters measured, table, 131
planned missions, 163
potential of, 163
resolution, 129
swath, resolution, and revisit time/day, table, 131
wave penetration into ice, 161

Temperature
air–surface difference, 15
conservation equation, 292
East Greenland Polar Front
vertical distributions, 232
vertical profiles, 235
effects on sea ice
brine pocket formation, 90
structure, 82
thermal conductivity, 52–53
expansion coefficient, 295–296
frontal systems, lateral and vertical gradients, 229
inversions, effect on drag coefficients, 35
Molley Deep-associated eddy, vertical distribution, 259

from Scotia Sea to Weddell Sea, vertical distribution, 246
sea ice, 49–50
sea surface, spaceborne sensors for, table, 127
at snow and ice surfaces, modeling, 348–349
surface magnitude, effect on drag coefficients, 35
Weddell Gyre
heat loss from deep water in, 209
vertical distribution associated with convective eddy, 268, 272
Weddell Sea, vertical distributions along summer ice edge in, 249
Temperature–salinity classifications
Arctic Ocean water masses, 185–190
Arctic shelf waters, 188–189
Arctic surface layer, 186–187
Arctic surface water, 186
Atlantic layer, 187–188
Atlantic water, 186
Canada Basin deep water, 188
classes of, 195–196
deep waters, 188
Eurasian Basin deep water, 188
Greenland Sea deep water, 188
lower Arctic intermediate water, 188
Norwegian Sea deep water, 188
oxygen concentrations, 197, 199
polar intermediate water, 188
polar water, 186
renewal times, 197, 201
silicate content, 197, 200
volumetric comparison with Southern Ocean, 195–198
Southern Ocean water masses, 190–195
Antarctic bottom water, 192–193
Antarctic shelf waters, 193–195
Antarctic surface layer, 191
Antarctic surface water, 191
circumpolar deep water, 191
classes of, 197
high-salinity shelf water, 194–195
ice shelf water, 195
low-salinity shelf water, 194–195
North Atlantic deep water, 191–192
oxygen concentrations, 197, 199
renewal times, 197, 201
Ross Sea bottom water, 193
silicate content, 197, 200
transitional layers, 191
volumetric comparison with Arctic Mediterranean, 195–198
warm core shelf water, 195
Weddell deep water, 192
Weddell Sea bottom water, 192–193
winter water, 191
Terra Nova polynya, 277
Thermal sensors, 163
Thermodynamic models, sea ice, 342–351
Thermodynamics, sea ice growth and decay, 49–59
albedo, 49
Antarctic, 58
Arctic, 51
Antarctic, 57–59
Arctic, 49–57
blue ice, 52
energy balance at ice–water interface, 49, 53
frazil
Antarctic, 59
Arctic, 84–85
heat conduction
away from bottom toward surface, 49, 53
at upper surface, 49, 52
heat fluxes
conducted at upper surface, 49, 52
conducted away from bottom to surface, 49, 53
latent, 49, 51–52
oceanic
Antarctic, 57–58
Arctic, 53
effect on equilibrium thickness, 53–54
sensible, 49, 51–52
turbulent, 51–52, 57
heat loss from melting or sublimation, 49, 52
longwave radiation
emitted by ice surface, 49–51
incoming, 49–51
melting, 49, 52
Antarctic, 58
Arctic, 56–57
net radiation
incoming and outgoing longwave, 50–51
solar, 50
total, 50–51

radiative fluxes, 49–51
rafted pancakes, Antarctic, 58–59
shortwave (solar) radiation
Antarctic, 57
Arctic, 53, 57
flux passing through to ice interior, 49, 52, 57
incoming, 49–50
snow cover
Antarctic, 58
Arctic, 53–56
snow thicknesses, 55
sublimation, 52
temperature profiles, 49–50
thermal conductivity, 52–53
thickness
Antarctic, 58–59
Arctic, 53–56
effect of oceanic heat fluxes, 53–54
Thickness, sea ice
Antarctic, 56, 73–75
Arctic, 56, 72–73
distribution, 71–75, 126
equilibrium
Antarctic, 58–59
Arctic, 53–56
effect of oceanic heat fluxes, 53–54
salinity/thickness relationship, 92–93
spaceborne sensors for, table, 126
Transpolar Drift
circulation pattern, 61–62, 180–181
simulation, 338–339
T–S schemes, *see* Temperature–salinity classification
Turbulence
in planetary boundary layer, 10
in under-ice RBL, 296–298
characteristics, 297
closure problem, 298
eddy diffusivity, 297–298
friction velocity scale, 298–299
heuristic model for, 302–309
length scale, factors affecting, 299–301
mixing-length hypothesis, 297–298
scales governing, 298–302
vertical flux, 297
Turbulence closure model, second-moment, 373
application to upper ocean, 378–379
Turbulent heat flux, 51–52, 57
in thermodynamic ice models, 343–351

Undercurrents, in Arctic Ocean, 182–183
Upwelling
ice edge
modeling, 367–368
upward transport and, 272–273
numerical models, 273

Ventilation
direct, of abyssal Arctic Ocean, 207
halocline, 202–205
Vertical fluxes
expression for, 297
frontal and eddy-associated, 272–273
length scale for exchange, 299
Visible and Thermal Infrared Radiometer (MOS-1), 131
Visible remote sensors, 124–125, 151–152, 163
Volumetric analyses, Arctic Mediterranean and Southern Ocean, 195–198

Water masses
Arctic Ocean
deep- and bottom-water production, 205–207
oxygen concentrations, 197, 199
residence times, 197, 201
silicate content, 197, 200
T–S scheme, 185–186
Arctic surface layer, 186–187
Atlantic layer, 187–188
deep waters, 188
shelf waters, 188–190
volumetric comparison with Southern Ocean, 195–198
water classes in, 195–196
Southern Ocean
deep- and bottom-water production, 205–209
oxygen concentration, 197, 199
residence times, 197–201
silicate content, 197, 200
T–S scheme, 190–195
Antarctic bottom water, 192–193
Antarctic shelf waters, 193–195
Antarctic surface layer, 191
circumpolar deep water, 191–192
volumetric comparison with Arctic Mediterranean, 195–198
water classes in, 197

Wavelengths, for remote sensors, 124–125
Waves
  internal
    drag from, 327–330
    spaceborne sensors for, table, 128
  sea and swell gravity, spaceborne sensors for, table, 128
Weddell Gyre, 185
  convection within, 208–209
  heat loss from deep water via chimney mechanism, 209
  open-ocean convection, 205, 208
  temperature, vertical distribution associated with convective eddy, 268, 272
Weddell Polynya
  deep-water renewal in, 209
  development, simulation, 355
  formation, 66
  heat transport by vertical mixing, 279
Weddell–Scotia Confluence, 185, 244, 246–247
Weddell Sea
  automatic weather stations project, 19–20
  bottom water
    formation, 208
    T–S scheme, 192–193
  eddies, 267–269
  frontal structures, 248, 250
  ice shelf water, distribution, 208
  near-boundary convection, 205, 208
  polynyas, 66, 209, 279
    deep convection in, modeling, 375–376
  salinity
    gradients, modeling, 362
    vertical distribution along summer ice edge, 249
  sea ice
    concentration
      satellite passive-microwave data, 154
      SMMR data, 154
    congelation ice, 115
    crystalline structure, 107–115
    extent of, 76
    frazil, 84, 107
    growth and decay in, 57–59
    ice pack, simulation, 355
    pancake ice, 107
    residence times, 63, 65
    salinity, 95–96
    thickness, 73–75
  temperature, vertical distribution
    along late summer ice edge, 249
    from Scotia Sea to, 246
West Spitsbergen Current, 178–179
  frontal systems, 236
  temporal variability, 178
  transport estimates, 178
  Whaler's Bay polynya, 278
Wilkes Land, near-boundary convection, 205
Wind magnitude, effect on drag coefficients, 35
Winds
  atmospheric Ekman layer, 6–12
  in atmospheric PBL, 6–7
  atmospheric surface layer, 12–15
Wind speed, effect on heat flux coefficients, 39
Wind stress, 5–6
World Meteorological Organization, taxonomy for sea ice classification, 48

Zonation, sea ice
  Antarctic, 76–78
  Arctic, 75–78